UC San Diego

UC San Diego Electronic Theses and Dissertations

Title

Secular and recent trends in the geochemistry of the Réunion hotspot and other global hotspots

Permalink

https://escholarship.org/uc/item/8294s7rf

Author

Peters, Bradley

Publication Date

2016

Supplemental Material

https://escholarship.org/uc/item/8294s7rf#supplemental

Peer reviewed|Thesis/dissertation

eScholarship.org Powered by the California Digital Library
University of California

UNIVERSITY OF CALIFORNIA, SAN DIEGO

Secular and recent trends in the geochemistry of the Réunion hotspot and other global hotspots

A dissertation submitted in partial satisfaction of the requires for the degree of Doctor of Philosophy

in

Earth Sciences

by

Bradley James Peters

Committee in charge:

Professor James M.D. Day, Chair
Professor Paterno Castillo
Professor David Hilton
Provessor David Stegman
Professor Mark Thiemens

2016

Copyright

Bradley James Peters, 2016

All rights reserved

The dissertation of Bradley James Peters is approved and is acceptable in quality and form for publication on microfilm and electronically.

_____

_____

_____

_____

_____

Chair

University of California, San Diego

2016

EPIGRAPH

No one can love the country as much as I do. For surely woods, trees, and rocks produce the echo which man desires to hear.

Ludwig van Beethoven

TABLE OF CONTENTS

LIST OF SUPPLEMENTAL FILES

Table A3.5 is submitted as an electronic attachment to this dissertation.

LIST OF FIGURES

LIST OF TABLES

ACKNOWLEDGEMENTS

If you've had to put up with me anytime in the last five years, chances are you deserve to occupy this space. James, my advisor, knows this every time I appear in his office doorway at an inconvenient time or whenever I send him an email just to say I've used up something in the lab and could he please order more. Trying to see eye-to-eye with one of geochemistry's most respected researchers is a tall task, and I and all those around me know how much I've benefited from the challenge. James has given me the opportunity to see rocks on the other side of the world (twice), to meet some of the most important people in our field and to work in a state-of-the-art lab without ever having to worry about funding. For this, I owe him a great debt of gratitude…until I retire. And maybe a little after.

Further, I couldn't have asked for a more responsive and supportive committee. Pat, whose insight was invaluable while I developed the Sr-Nd chemistry method, always helps me think about the bigger picture (particularly with regard to TITAN). Dave Hilton, who supported my interest in noble gas geochemistry by generously offering the use of his lab and lab technician, has been an unyielding source of good conversation, both scientific and non-scientific. Dave Stegman, who is never unwilling to challenge a geochemical idea with a geophysical constraint, has given me the perspective to always try to ground my hypotheses in a qualitatively physical reality. And, finally, Mark, who is always enthusiastic about everything scientific and makes me feel like I'm doing a good job, no matter what. Thank you, guys, thank you, thank you.

Outside of these faculty members, who are at least temporarily contractually obligated to be interested in my future, there are others to which I am grateful. I profusely thank Peter Lonsdale, who provided me with the shipboard experience I so badly wanted when I came to SIO. I'm grateful also to Larry Taylor, who helped me think critically about how I use petrology to make geochemical arguments and who is just a darn good host. And to my co-authors, and my erstwhile co-authors: Phil Janney, Claude Herzberg, Chris Vidito, Richard Greenwood and Jenny Gibson…I've learned a lot from each of you. A particular thanks to my undergraduate thesis advisor, Brent Owens, who I think somewhat unknowingly cultivated my passion for petrology and geochemistry, but who was in reality the start of it all.

Thanks are due to my SIO cohort, which miraculously did not disperse despite our research interests becoming more entrenched. In particular thanks are due my officemate, Jasmeet, who has been a punchingbag for my stress as I equally have for her. I'm also grateful to my labmates – Kim, Diana, Chris, Caitlin, Jorge and Demian – even when there wasn't a lab for us. You have all helped me keep perspective on my life as a Ph.D. student, as a scientist and as a human. Many thanks are due to all of the GRD and SIO office staff, including Gilbert, Adam, Maureen (her holiness), Maureen, Denise, Monica, Megan, Laura, Tina, Azzure and Anne. You're all so *good*, and for that reason it's been so easy for me to focus on my job.

OK, now, my friends and family. Those who have seen my stress at its maximum and its minimum. My parents, Jim and Josephine, who wish I called more but understand that often my hands are on a pipet. My grandmother, Didi, who also wishes I called more but, because she has her Ph.D., too, she "gets it." My brother, AJ, who through his unbelievable ability to converse intelligently about everything has actually served as a valuable think-tank for my geological ideas. Also Fleabag, who doesn't care but sometimes wishes he did. Thanks to my best friend Erin, as well, who has always known I'm still there even though I'm in this black hole. Much gratitude to Corinne, who was dependable through it all and taught me how to just relax and do a headstand. And unsurpassed thanks to my partner, Justin, who has perfected the smile-and-knod approach to our conversations and tries to be awake when I leave work everyday. To everyone else: I'm still only beginning to know the impact of your support.

Chapter 2, in full, is a reformatted version of the material as it appeared in *Geochemistry Geophysics Geosystems* 2012, as Peters, B.J. and J.M.D. Day (2014) Assessment of relative Ti, Ta and Nb (TITAN) enrichments in ocean island basalts: Geochemistry, Geophysics, Geosystems, 15(11), 4424-4444. The dissertation author was the primary investigator and first author of this paper and completed all of the analysis presented therein.

Chapter 3, in full, is a reformatted version of the material as it appeared in Earth and Planetary Science Letters 2016, as Peters, B.J., J.M.D. Day and L.A. Taylor (2016)

Early mantle heterogeneities in the Réunion hotspot source inferred from highly siderophile elements in cumulate xenoliths: *Earth and Planetary Science Letters*, 448, 150-160. The dissertation author was the primary investigator and first author of this paper and conducted all of the analyses presented therein.

Chapter 4, in full, is a reformatting of material in preparation for submission to Earth and Planetary Science Letters 2016, as Peters, B.J., J.M.D. Day, R.C. Greenwood, D.R. Hilton and J. Gibson (2016) Helium-oxygen-osmium isotopic and elemental constraints on the mantle sources of the Deccan Traps. The dissertation author was the primary investigator and first author of this paper.

Chapter 5, in full, is a reformatting of material in preparation for submission to Nature 2016, as Peters, B.J. and J.M.D Day (2016) A definitive link between plume head and plume tail volcanism. The dissertation author was the primary investigator and first author of this paper and conducted all of the analyses presented therein.

VITA

2007-2011	B.S. with Honors, Geology; Monroe Scholar - The College of William and Mary in Virginia
2011	Intern – Naval Research Enterprise Internship Program
2011-2012	Regents Fellow – Scripps Institution of Oceanography, University of California, San Diego
2012-2014	Teaching Assistant – Scripps Institution of Oceanography, University of California, San Diego
2013-2014	Research Assistant – Scripps Institution of Oceanography, University of California, San Diego
2013	M.S., Earth Science – Scripps Institution of Oceanography, University of California, San Diego
2015-2016	Devendra & Aruna Lal Fellow – Scripps Institution of Oceanography, University of California, San Diego
2016	Ph.D., Earth Sciences – Scripps Institution of Oceanography, University of California, San Diego

PUBLICATIONS

Peters, B.J. (2011) Mineralogical and geochemical constraints on the origin of ferruginous quartzites in the Chopawamsic Terrane, Piedmont Province, Virginia: B.S. honors thesis, College of William and Mary, VA, 98 pp.

Day, J.M.D., B.J. Peters and P.E. Janney (2014) Oxygen isotope systematics of South African olivine melilitites and implications for HIMU mantle reservoirs: Lithos, 202, 76-84.

Peters, B.J. and J.M.D. Day (2014) Assessment of relative Ti, Ta and Nb (TITAN) enrichments in ocean island basalts: Geochemistry, Geophysics, Geosystems, 15(11), 4424-4444.

Peters, B.J., J.M.D. Day and L.A. Taylor (2016) Early mantle heterogeneities in the Réunion hotspot source inferred from highly siderophile elements in cumulate xenoliths: Earth and Planetary Science Letters, 448, 150-160.

ABSTRACT OF THE DISSERTATION

Secular and recent trends in the geochemistry of the Réunion hotspot and other global hotspots

by

Bradley James Peters

Doctor of Philosophy in Earth Sciences

University of California, San Diego, 2016

Professor James M.D. Day, Chair

The origins of volcanic activity at intraplate “hotspot” localities cannot be easily explained by fundamental principles of plate tectonics. Decades of geochemical and geophysical research have produced controversial hypotheses that attempt to explain the physical mechanism of magma generation and the origin of the magmas in the deep Earth. The mantle plume hypothesis conjectures that hotspot volcanism results from upwelling of buoyant mantle material from the deep Earth, which may carry recycled crust and lithosphere that resided on Earth’s surface billions of years ago. One requirement of the

plume hypothesis is that initial, intense stages of hotspot volcanism, which exist only in the geologic record, are genetically linked to later, waning stages of volcanism observed on Earth today. Physiographic evidence exists in several global localities, including the Réunion hotspot, that appears to link large igneous province volcanism to oceanic volcanism, however geochemical evidence linking the two is tenuous. Here, I demonstrate that certain trace element signatures of global hotspots are unlikely to reflect their mantle source in the same way as isotope systems. Next, I show that igneous rocks on Réunion possess a unique geochemical and isotopic signature that make them distinct from igneous rocks from other global hotspots. Finally, I interrogate the composition of the Deccan Traps mantle source in two ways. First, I use early-formed mineral phases to evaluate the presence of recycled material in the Deccan Traps mantle source. Second, I use lava compositions to re-construct a lithospheric and crustal assimilation history for Deccan Traps parental magmas and attempt to relate the composition of this parental magma to that of Réunion. Considering all chapters together, I show that these two volcanic provinces likely share a mantle source with a common composition, and that this source contains a small amount of recycled material. In addition, I provide new evidence that the Réunion mantle source was formed early in Earth's history and remained isolated from other mantle domains for long periods of geologic time.

Chapter 1:

Introduction

Although plate tectonics provides a satisfactory explanation for the majority of Earth's volcanism, the origin of magmatism that occurs far from tectonic plates remains controversial. Intraplate "hotspots" are areas of active volcanism that are distinct from volcanoes occurring within island arcs or oceanic and continental spreading centers, though some share a geographic position with these features. Hotspots typically host effusive but frequent eruptions of geochemically distinct basaltic lavas. In many locations, these eruptions form an age progressive sequence that appears to move thousands of kilometers over millions of years. A foundational theory regarding the origins of hotspot volcanism holds that hotspots are formed by active upwelling of mantle material that impinges on the base of the lithosphere and causes volcanic eruptions at the surface [e.g., Morgan, 1971]. Such upwelling may initially carry an immense amount of material that generates a large volume of magma. The ascent of this magma may be sufficient to cause continents to break up [e.g., Devey & Stephens, 1991] and may erupt with such intensity that it causes global

climate change [e.g., Self et al., 2008]. Additionally, hotspots have the capability of exhuming material residing deep in the Earth that may have remained intact for billions of years [e.g., Cabral et al., 2013]. Notwithstanding these tantalizing characteristics of hotspots, many questions remain regarding the cause of mantle upwelling and the origins of the material that is upwelled.

Relatively low-volume, long-lived volcanism characterizes many of the hotspots known today, including Hawaii, Iceland and the Galapagos. These islands typically erupt a geochemically distinct lava type known as ocean island basalt (OIB). Many researchers attempt to understand the structure and evolution of the mantle using OIB. An abundance of geochemical and geophysical studies of OIB demonstrate that Earth's mantle contains many physically and chemically distinct domains [e.g., Gast, 1968; Hofmann, 1988; van der Hilst et al., 1997] that may mix or interact at many length and time scales. OIB from a single hotspot define geochemical signatures that may reflect interaction between these domains [Zindler & Hart, 1986; Hofmann, 1997; Stracke, 2012] and OIB from different hotspot localities may represent mantle domains that are not present in the source of other hotspots. However, these signatures are frequently masked by processes that act to change the composition of OIB during their transit to the surface [e.g., O'Hara, 1996; Class & Goldstein, 1997; Millet et al., 2008]. One primary job of geochemists is to separate the chemical signals that derive from these secondary processes from those that reflect the deeper origins of lavas.

In the geologic past, some hotspots are thought to have experienced a time of rapid, high-volume volcanism. The evidence of these episodes is preserved in large igneous provinces (LIP), many of which represent an original lava volume of more than one million cubic kilometers [e.g., Schoene et al., 2015]. The environmental consequences of these events were likely disastrous, and their close temporal association with mass extinctions [e.g., Chung et al., 1998; Kamo et al., 2003; Schoene et al., 2010] strongly implies that their impacts were global. LIP are commonly located on continental margins, possibly because the vigor of their eruptions is sufficient to change the speed and direction of tectonic plates [e.g., Cande & Stegman, 2011]. Much like hotspot islands, LIP are often comprised of a distinct lava type known as a continental flood basalt (CFB). CFB are geochemically distinct from OIB in many ways, but CFB and OIB from the same hotspot are often though to share a common origin in the deep Earth, despite a notable absence of geochemical and geophysical data supporting this hypothesis. For example, the physiographic link between the modern Tristan da Cunha-Gough hotspot and the Etendeka-Paraná flood basalt province is appealing evidence that the two are related, but it is difficult to reconcile geochemical differences between the two areas [e.g., Thompson et al., 2001]. One major factor that contributes to this difficulty is that continental crust, through which CFB commonly erupt, frequently leaves a chemical fingerprint on an ascending CFB magma such that the original composition of the magma is masked [e.g., Day, 2016]. In this way, the relationship between OIB and CFB may be obscured.

The islands of Réunion, Mauritius and Rodrigues (together, the Mascarene Islands) are OIB edifices related to recent volcanism on the Réunion hotspot. Réunion hotspot activity began around 65 million years ago with the eruption of the Deccan Traps, a LIP, on the Indian continent [e.g., Wellman & McElhinny, 1970; Kaneoka & Haramura, 1973; Widdowson et al., 2000]. As India moved northwest, the hotspot erupted the Laccadive Islands and the Chagos-Laccadive Ridge in a roughly southeasterly line. Later, the Central Indian Ridge (CIR) passed over the hotspot at about 34 million years ago [Duncan et al., 1990]. West of the CIR, the hotspot formed the submarine Mascarene Ridge and the islands of Mauritius (10 million years – 40 thousand years ago) [e.g., McDougall & Chamalaun, 1969; Moore et al., 2011] and Réunion (2.1 million years ago – present) [e.g., Gillot et al., 1994] in a roughly linear chain. Rodrigues Island, which lies east of the hotspot track, hosts rocks of ages between 1.3 and 1.6 million years old [McDougall et al., 1965] (no historical eruptions are known), and is connected to the Mascarene Ridge by the Rodrigues Ridge, which erupted 8 – 10 million years ago [Duncan et al., 1990]. On the other side of the island, it is connected to the CIR by a series of en-echelon submarine volcanic ridges known as the Three Magi and Gasitao Ridges. Rodrigues is geochemically distinct from Mauritius and Réunion in that is has a helium isotopic signature similar to lavas seafloor spreading centers ($^3He/^4He = 8\pm1\ R_A$) [Graham, 2002; Füri et al., 2011]. In addition, the chemical composition of CIR lavas acquires a distinct hotspot "flavor" at latitudes approaching the latitude of Rodrigues [Murton et al., 2005; Nauret et al., 2006; Füri et al., 2011]. This supports conclusion that there is active geochemical interaction between the Réunion hotspot and the CIR near Rodrigues occurring in the shallow mantle.

The oldest rocks erupted by the Réunion hotspot are those comprising the Deccan Traps volcanic province of India, which were erupted between 67 and 64 million years ago [e.g., Courtillot et al., 1986; Duncan & Pyle, 1988; Widdowson et al., 2000]. Although many Deccan rocks share some of the geochemical characteristics of Mascarene lavas, such as distinct helium isotopic signature [Basu et al., 1993], there are many geochemical trends represented by various formations of the Deccan. For example, there is evidence of variable assimilation of continental crust and/or lithosphere into hotspot magmas [e.g., Cox & Hawkesworth, 1985; Mahoney et al., 1992; Peng et al., 1994, 1998; Melluso et al., 1995, 2006]. However, the composition of lavas from volcanic provinces in the northwest Deccan Traps may be distinct from those of other Deccan lavas flows [Melluso et al., 1995, 2006; Peng & Mahoney, 1995], which may reflect unique conditions of magma ascent in this region. The composition of Deccan Traps lavas that are thought to be least affected by crustal assimilation and other processes acting during the transit of magmas lie between the compositions of Réunion OIB and seafloor spreading center lavas [Mahoney, 1988; Lightfoot et al., 1990]. Thus, although the Deccan lava pile appears stratigraphically homogenous, we find a rich array of geochemical signatures present even in neighboring lava flows.

In order to evaluate the origin of lavas collected as geological samples at the surface, it is important to consider the processes that acted on those lavas before they reached the surface. The compositions of lavas are changed during transit as they begin to cool, because the composition of the first solids formed in a magma are distinct from the composition of the magmas that formed them. In addition, magmas may partially melt the

wall rocks of magma chambers and thus partially aquire the geochemical signature of these wall rocks. Magma chambers may periodically receive deliveries of new magma batches with a distinct geochemistry, which would modify their composition further still. It is critical to resolve the effects of these processes independently so that the composition of an original, parental magma can be known.

Arguably, one of the most important tools in a geochemist's toolbox are isotope systems. Isotopes are atoms of a single element that have a variable number of neutrons, such that the mass of the atom changes without changing the identity of an element. For example, oxygen is an element that most commonly has ten neutrons, but approximately 0.04% of natural oxygen atoms have eleven neutrons and approximately 0.2% of natural oxygen atoms have twelve neutrons. These three types of atoms represent the three primary isotopes of oxygen: oxygen-16 (with a mass of 16 atomic mass units), oxygen-17 and oxygen-18, respectively. The vast majority of atoms were formed by interstellar processes at the beginning of the Solar System's history and some are continually produced in the sun. Other, heavier atoms cannot be formed in the sun and must have formed during supernovae before the birth of our solar system. An even smaller group of atoms are produced naturally by radioactive decay of other atoms. Atoms that decay are known as parents and the atoms they become are known as daughters, and this decay occurs at a measurable and constant rate. However, the rate of radioactive decay depends on the number of radioactive parents present in a system, such that the fastest rate of decay occurs when there are many radioactive parents and this rate slows as parent isotopes are lost to the decay process. This process can be arithmetically represented by a decay constant, λ,

which is treated as an unchangeable property of a radioactive isotope. Using an isotope's half life, which is arithmetically related to its decay constant, geochemists can calculate the amount of radioactive decay that has occurred over long periods of geologic time.

Evaluating the mantle sources to hotspot volcanism heavily relies on these facts. If one knows the composition of the mantle with respect to a particular radioactive parent-daughter pair at the beginning of Earth's history, one can calculate the same composition that exists in the mantle today if the mantle remained undisturbed through geologic time. Arranged in a useful way, geochemists most typically use one form of the radioactive decay equation to accomplish this:

$$C = C_0 + P * (e^{\lambda t} - 1)$$

In this equation, C is the amount of daughter isotope present today, C_0 is the amount of daughter isotope present at the beginning of radioactive decay, P is the amount of parent isotope present today and t is the amount of time elapsed since the beginning of radioactive decay. Geochemists can replace terms like C and P with isotope ratios, which can then be measured by mass spectrometry. In this dissertation, this is accomplished for the parent-daughter isotope systems ^{87}Rb-^{87}Sr, ^{147}Sm-^{143}Nd and ^{187}Re-^{187}Os. From this basis, geochemists can predict the isotopic compositions of various Earth materials that might contribute to hotspot volcanoes based on the age, composition and history of those materials. For example, it is thought that hotspots may tap into a reservoir of ancient oceanic crust that was subducted in early Earth history [e.g., Hofmann & White, 1982]. Using the isotopic composition of modem oceanic crust, which can be measured in the laboratory, one can predict the isotopic composition of that crust after it has transited

through Earth's mantle and thus know the geochemical signature of one possible contributor to a hotspot volcano. Of course, many assumptions are used in creating this scenario, and it is the geochemist's job to create a sophisticated numerical model that reflects natural systems as accurately as possible without exceeding the computational capacity of their equipment.

Isotopes occupy a preferred role in geochemistry because many magmatic processes, such as partial melting and fractional crystallization, do not change the isotopic composition of a magma. In addition, in most cases a crystal that solidifies out of a magma can be expected to acquire an isotopic signature identical to that of a magma. The same is not always true for trace elements because each mineral phase has a unique relative preference for each element. For example, the mineral phase olivine has a high preference for the element chromium [e.g., Adam & Green, 2006]; therefore, a solidifying olivine will take on a higher concentration of chromium that what is present in the magma from which it forms. This preference is termed "compatibility" or "incompatibility" depending on the specific preference of a mineral for any given element. Compatibility behavior poses a significant problem for geochemists evaluating the origins of trace element signatures that is not encountered when evaluating the origins of isotopic signatures. Numerical models predicting the behavior of trace elements in magmatic systems must be particularly careful to account for all possible processes affecting each element.

Chapter 2 of this dissertation tackles this problem as it relates to global OIB. Enrichments in Ti, Ta and Nb ("TITAN" elements) relative to elements of similar

incompatibility have been recognized in several global hotspots, and may be correlated with He and Os isotopic signatures [e.g., Jackson et al., 2008]. Statistically persistent trace element patterns in magmatic systems have been interpreted as direct representations of the composition of the magma source [e.g., Arevalo & McDonough, 2010]. I show that, absent fractional crystallization and mid-ocean ridge basalt (MORB) contamination of OIB source magmas, TITAN anomalies bear no significant correlation to $^{3}He/^{4}He$ ratios and occur in hotspots thought to tap distinct mantle reservoirs. Further, I show that partial melting of primitive mantle [McDonough & Sun, 1995] can generate positive Ta and Nb anomalies, and Ti is strongly enriched during fractional crystallization. These results strongly support particular caution when analyzing trace element data, as they can be altered by secondary differentiation processes in the lithosphere and crust, which most likely operate in all magmatic settings.

Chapter 3 examines the highly siderophile element (HSE) and Os isotope characteristics of cumulate xenoliths and lavas from Réunion Island. It reinforces the relatively invariant Os isotopic signature of Réunion and argues that the parental magma to Réunion volcanism possesses a highly fractionated HSE signature that is not generated by shallow differentiation processes such as partial melting and fractional crystallization. The origin of this fractionated HSE pattern may be related to Réunion possessing a deep mantle source that has remained intact through long periods of geologic time. In one scenario, the fractionated signature may be acquired from meteorites that impacted Earth early in its history. The existence of these meteorites is evidenced by lunar impact breccias, but this unusual composition has not been found in the present-day inventory of meteorites.

In a second scenario, the fractionated signature may be acquired in a distinct deep-mantle domain as Earth's core formed that then remained relatively protected from meteoritic contributions early Earth history. Regardless of whether either of these scenarios is true, the survival of these fractionated signatures strongly supports the notion that the Réunion mantle source has remained isolated for long geologic periods of time because interaction with most known Earth reservoirs would conspire to obliterate this unique signature.

Chapter 4 interrogates the composition of the mantle source to the Deccan Traps using the helium, oxygen and osmium isotopic composition of mineral phases, as well as the major and minor element composition of olivine. While the compositions of most Deccan Traps lavas are strongly affected by assimilation of crustal and lithospheric material, early-formed mineral phases such as olivine may preserve a signature similar to the mantle source of the Deccan. Study of olivine with later formed phases presents a progressive picture of crustal assimilation that is acquired during magma ascent. Isotopic and elemental data support a limited role for recycled material in the Deccan source, representing approximately 20-25% of the Deccan primary magma. However, the correlation between isotopic and elemental data is indistinct and may reflect a divergence of behavior between each elemental and isotopic system. The method is able to successfully distinguish between the contributions of continental crust and recycled material to the compositions of olivine.

Chapter 5 discusses the Sr, Nd and Os isotopic and HSE compositions of a wide range of Deccan lavas. Using the unique sensitivity of Os isotopes to crustal contamination,

it identifies various magmatic assimilants, including continental lithospheric mantle, lower and upper crust, that contribute to the isotopic compositions of Deccan lavas. Then, using a calculated Sr, Nd and Os isotopic composition of Réunion lavas, it attempts to geochemically link the two ends of the Réunion hotspot. Isotopic data show a strong affinity for a calculated Réunion endmember, which strongly implies that the Réunion hotspot source has remained invariant through long periods of geologic time. To conclude, this chapter discusses the implications of such a link for the mantle plume theory of hotspot volcanism.

Chapter 6 summarizes the main conclusions of each study and indicates areas of further research in the study of hotspots using geochemistry.

References

Arevalo, R. Jr. and W.F. McDonough (2010) Chemical variations and regional diversity observed in MORB: Chemical Geology, 271, 70-85.

Adam, J. and T. Green (2006), Trace element partitioning between mica- and amphibole-bearing garnet lherzolite and hydrous basanitic melt: 1. Experimental results and the investigation of controls on partitioning behavior: Contributions to Mineralogy and Petrology, 152, 1-17, doi:10.1007/s00410-006-0085-4.

Basu, A.R., P.R. Renne, D.K. DasGupta, F. Teichmann and R.J. Poreda (1993) Early and late alkali igneous pulses and a high-^{3}He plume origin for Deccan flood basalts: Science, 261, 902-906.

Cabral, R.A., M.G. Jackson, E.F. Rose-Koga, K.T. Koga, M.J. Whitehouse, M.A. Antonelli, J. Farquhar, J.M.D. Day and E.H. Hauri (2013) Anomalous Sulphur isotopes in plume lavas reveal deep mantle storage of Archaean crust: Nature, 496, 490-493.

Cande, S.C. and D.R. Stegman (2011) Indian and African plate motions driven by the push force of the Réunion plume head: Nature, 475, 47-52.

Chung, S.-L., B.-M. Jahn, W. Ganyao, C.-H. Lo and C Bollin (1998) The Emeishan flood basalt in SW China: A mantle plume initiation model and its connection with continental breakup and mass extinction at the Permian-Triassic boundary, *in* Flower, M.F.J., S.-L. Chung, C.-H. Lo and T.-Y. Lee (*eds.*) Mantle Dynamics and Plate Interactions in East Asia: American Geophysical Union, Washington, DC, 47-58.

Class, C. and S.L. Goldstein, (1997) Plume-lithosphere interactions in the ocean basins: constraints from the source mineralogy: Earth and Planetary Science Letters, 150, 245-260.

Courtillot, V., J. Besse ,D. Vandamme, R. Motigny, J.-J. Jaeger and H. Cappetta (1986) Deccan flood basalts at the Cretaceous/Tertiary boundary?: Earth and Planetary Science Letters, 80, 361-374.

Cox, K.G. and C.J. Hawkesworth (1985) Geochemical stratigraphy of the Deccan Traps at Mahabaleshwar, Western Ghats, India, with implication for open system magmatic processes: Journal of Petrology, 26(2), 355-377.

Devey, C.W. and W.E. Stephens (1991) Tholeiitic dykes in the Seychelles and the original spatial extent o the Deccan: Journal of the Geological Society, 148, 979-983.

Duncan, R.A. & D.G. Pyle (1988) Rapid eruption of the Deccan flood basalts at the Cretaceous/Tertiary boundary: Nature, 333, 841-843.

Duncan, R.A., J. Backman and L.C. Peterson (1990) The volcanic record of the Réunion hot spot: Proceedings of the Ocean Drilling Program, Scientific Results, 115, 3-10.

Füri, E., D.R. Hilton, B.J. Murton, C. Hémond, J. Dyment and J.M.D. Day (201) Helium isotope vriations between Réunion Island and the Central Indian Ridge (17°-21°S): New evidence for ridge-hot spot interaction: Journal of Geophysical Research, 116, B02207.

Gast, P.W. (1968) Trace element fractionation and the origin of tholeiitic and alkaline magma types: Geochimica et Cosmochimica Acta, 32, 1057-1086.

Gillot, P.-Y., J.-C. Lefevre and P.-E. Nativel (1994) Model for the structural evolution of the volcanoes of Réunion Island: Earth and Planetary Science Letters, 122, 291-302.

Graham, D.W. (2002) Noble gases in MORB and OIB: observational constraints for the characterization of mantle source reservoirs: Reviews in Mineralogy and Geochemistry, 46, 247-318.

van der Hilst, R.D., S. Widiyantoro and E.R. Engdahl (1997) Evidence for deep mantle circulation from global tomography: Nature, 386, 578-584.

Hofmann, A.W. (1988) Chemical differentiation of the Earth: the relationship between mantle, continental crust, and oceanic crust: Earth and Planetary Science Letters, 90, 297-314.

Hofmann, A.W. (1997) Mantle geochemistry: the message from oceanic volcanism: Nature, 385, 219-229.

Hofmann, A.W. and W.M. White (1982), Mantle plumes from ancient oceanic crust: Earth and Planetary Science Letters, 57, 421-436, doi:10.1016/0012-821X(82)90161-3.

Jackson, M.G., S.R. Hart, A.E. Sal, N. Shimizu, M.D. Kurz, J.S. Blusztajn and A.C. Skovgaard (2008) Globally elevated titanium, tantalum and niobium (TITAN) in ocean island basalts with high 3He/4He: Geochemistry, Geophysics, Geosystems, 9(4), 21 pp.

Kamo, S., G.K. Czamanske, Y. Amelin, V.A. Fedorenko, D.W. Davis and V.R. Trofimov (2003) Rapid eruption of Siberian flood-volcanic rocks and evidence for coincidence with the Permian-Triassic boundary and mass extinction at 251 Ma: Earth and Planetary Science Letters, 214, 75-91.

Kaneoka, I. and H. Haramura (1973) K/Ar ages of successive lava flows from the Deccan Traps, India: Earth and Planetary Science Lettres, 18, 229-236.

Lightfoot, P.C., C.J. Hawkesworth, C.W. Devey, N.W. Rogers and P.W.C. Van Calsteren (1990) Source and differentiation of Deccan Trap lavas: Implications of geochemical and mineral chemical variations: Journal of Petrology, 31(5), 1165-1200.

Mahoney, J.J. (1988) Deccan Traps, *in* J.D. Macdougall (ed.) Continental flood basalts, Kluwer Academic Publishers, Dordrecht, 151-194.

Mahoney, J.J., A.P. Le Roex, Z.X. Peng, R.L. Fisher and J.H. Natland (1992) Southwestern limits of Indian Ocean ridge mantle and the origin of low-$^{206}Pb/^{204}Pb$ mid-ocean ridge basalt: isotope systematics of the central Southwest Indiann Ridge (17°-50°E): Journal of Geophysical Research, 97, 19771-19790.

McDonough, W.F. and S.-s. Sun (1995) The composition of the Earth: Chemical Geology, 120, 223-253.

McDougall, I. and F.H. Chamalaun (1969) Isotopic dating and geomagnetic polarity studies on volcanic rocks from Mauritius, Indian Ocean: Geological Society of America Bulletin, 80, 1419-1442.

McDougall, I., B.G.J. Upton and W.J. Wadsworth (1965) A geological reconnaissance of Rodriguez Island, Indian Ocean: Nature, 206, 26-27.

Melluso, J., L. Beccaluva, P. Brotzu, A. Gregnanin, A.K. Gupta, L. Morbidelli and G. Traversa (1995) Constraints on the mantle sources of the Deccan Traps from the petrology and geochemistry of basalts of Gujarat State (Western India): Journal of Perology, 36(5), 1393-1432.

Melluso, L., J.J. Mahoney and L. Dallai (2006) Mantle sources and crustal input as recorded in high-Mg Deccan Traps basalts of Gujarat (India): Lithos, 89, 259-274.

Millet, M.-A., R. Douelance, P. Schiano, K. David and C. Bosq (2008) Mantle plume heterogeneity versus shallow-level interactions: A case study, the São Nicolau Island, Cape Verde archipelago: Journal of Volcanology and Geothermal Research, 176, 265-276.

Moore, J., W.M. White, D. Paul, R.A. Duncan, W. Abouchami and S.J.G. Galer (2011) Evolution of shiled-building and rejuvenescent volcanism of Mauritius: Journal of Volcanology and Geothermal Research, 207, 47-66.

Morgan, W.J. (1971) Convection plumes in the lower mantle: Nature, 230, 42-43.Murton, B.J., A.G. Tindle, J.A. Milton and D. Sauter (2005) Heterogeneity in southern

Central Indian Ridge MORB: Implications for ridge-hot spot interaction: Geochemistry, Geophysics, Geosystems, 6(3), 24 pp.

Nauret, F., W. Abouchami, S.J.G. Galer, A.W. Hofmann, C. Hémond, C. Chauvel and J. Dyment (2006) Correlated trace element-Pb isotope enrichments in Indian MORB along 18-20°S, Central Indian Ridge: Earth and Planetary Science Letters, 245, 137-152.

O'Hara, M.J. (1996) Volcanic plumbing and the space problem-thermal and geochemical consequences of large-scale assimilation in ocean island development: Journal of Petrology, 39, 1077-1089.

Peng, Z.X. and J.J. Mahoney (1995) Drillhole lavas from the northwestern Deccan Traps, and the evolution of the Réunion hotspot mantle: Earth and Planetary Science Letters, 134, 169-185.

Peng, Z.X., J. Mahoney, P. Hooper, C. Harris and J. Beane (1994) A role for lower continental crust in flood basalt genesis? Isotopic and incompatible element study of the lower six formation of the western Deccan Traps: Geochimica et Cosmochimica Acta, 58, 267-288.

Peng, Z.X., J.J. Mahoney, P.R. Hooper, J.D. Macdougall and P. Krishnamurthy (1998) Basalts of the northeastern Deccan Traps, India: Isotopic and elemental geochemistry and relation to the southwestern Deccan stratigraphy: Journal of Geophysical Research, 103, 29843-29865.

Schoene, B., J. Guex, A. Bartolini, U. Schaltegger and T.J. Blackburn (2010) Correlating the end-Triassic mass extinction and flood basalt volcanism at the 100 ka level: Geology, 38(5), 387-390.

Schoene, B., K.M. Samperton, M.P. Eddy, G. Keller, T. Adatte, S.A. Bowring, S.F.R. Khadri and B. Gertsch (2015) U-Pb geochronology of the Deccan Traps and relation to the end-Cretaceous mass extinction: Geology, 347, 182-185.

Self, S., S. Blake, K. Sharma, M. Widdowson and S. Sephton (2008) Sulfur and chlorine in late Cretaceous Deccan magmas and eruptive gas release: Science, 319, 1654-1657.

Stracke, A. (2012) Earth's heterogeneous mantle: A product of convection-driven interaction between crust and mantle: Chemical Geology, 330-331, 274-299.

Thompson, R.N., S.A. Gibson, A.P. Dickin and P.M. Smith (2001) Early Cretaceous basalt and picrate dykes of the southern Etendeka region, NW Namibia: Windows into the role of the Tristan mantle plume in Paraná-Etendeka magmatism: Journal of Petrology, 42(11), 2049-2081.

Wellman, P. and M.W. McElhinny (1970) K-Ar age of the Deccan Traps, India: Nature, 227, 595-596.

Widdowson, M., M.S. Pringle and O.A. Fernandez (2000) A post K-T boundary (early Palaeocene) age for Deccan-type feeder dykes, Goa, India: Journal of Petrology, 41(7), 1177-1194.

Zindler, A. and S. Hart (1986) Chemical geodynamics: Annual Review of Earth and Planetary Science, 14, 493-571.

Chapter 2:

Assessment of relative Ti, Ta and Nb (TITAN) enrichments in ocean island basalts

Abstract

The sensitivity of trace element concentrations to processes governing solid-melt interactions has made them valuable tools for tracing the effects of partial melting, fractional crystallization, metasomatism and similar processes on the composition of a parental melt. Recent studies of ocean island basalts (OIB) have sought to correlate Ti, Ta and Nb (TITAN) anomalies to isotopic tracers, such as $^{3}He/^{4}He$ and $^{187}Os/^{188}Os$ ratios, which may trace primordial deep mantle sources.

A new compilation of global OIB trace element abundance data indicates that positive TITAN anomalies, though statistically pervasive features of OIB, may not be compositional features of their mantle sources. OIB show a range of Ti ($Ti/Ti^{*}=0.28-2.35$), Ta ($Ta/Ta^{*}=0.11-93.4$) and Nb ($Nb/Nb^{*}=0.13-17.8$) anomalies that show negligible correlations with $^{3}He/^{4}He$ ratios, indicating that TITAN anomalies are not derived from the

less-degassed mantle source traced by high-$^{3}He/^{4}He$. Positive TITAN anomalies can be modelled using variable degrees (0.1-10%) of non-modal batch partial melting of garnet-spinel lherzolite at temperatures and pressures considered typical for OIB petrogenesis, and subjecting this partial melt to fractional crystallization and assimilation of mid-ocean ridge basalt-like crust (AFC). Correlations of TITAN anomalies with modal abundances of olivine and clinopyroxene in porphyritic Canary Islands lavas provide empirical support for this process and indicate that high abundances of these phases in OIB may create misleading trace element anomalies on primitive mantle-normalized spider diagrams. Because partial melting and AFC are common to all mantle-derived magmas, caution should be used when attributing TITAN anomalies to direct sampling of recycled or deep mantle sources by hotspots.

2.1 Introduction

Ocean island basalts (OIB) sample geochemical heterogeneities in the convecting mantle that preserve an enriched trace element signature relative to mid-ocean ridge basalts (MORB) [e.g., Sun, 1980; Schilling, 1985; Hofmann, 2003; White, 2010; Stracke, 2012]. However, interpretations of melt provenance in general are complicated by partial melting and differentiation processes [e.g., DePaolo, 1981; Klein & Langmuir, 1987], which can yield lavas with distinct trace element signatures at a single hotspot [e.g., Macdonald & Katsura, 1964; Gast, 1968; Schilling & Winchester, 1969; Moore et al., 1982]. Assuming that geographically or temporally persistent trace element signatures imply a constant source requires that partial melting and differentiation have a commanding influence on

the overall measured trace element composition of OIB. However, continued refinement of experimentally and empirically determined partition coefficients [e.g., Hart & Dunn, 1993; Adam & Green, 2006; Heber et al., 2007] has improved assessment of the impact of partial melting and fractional crystallization on trace element concentrations to obtain information on OIB parental magma composition.

In contrast to absolute abundances of trace elements, certain trace element ratios (e.g., Ti/Eu and Y/Ho) have been shown to be relatively constant under MORB-like melting conditions and may therefore be characteristic of magma source regions [e.g., Arevalo & McDonough, 2010; Jenner & O'Neill, 2012]. There have been numerous attempts to determine which trace element ratios are most statistically consistent in OIB and MORB, and thus most likely impervious to modification after partial melting of their mantle source [Hofmann et al., 1986; Halliday et al., 1995; Arevalo & McDonough, 2010; Jenner & O'Neill, 2012]. Recently, many of these "canonical" trace element ratios were shown to be sufficiently variable on a global scale that they are unlikely to directly reflect the inter-element composition of their mantle source [Arevalo & McDonough, 2010]. Further, well-understood geologic processes clearly contribute to certain trace element ratios, such as La/Yb (garnet residual to melting) [Clague & Frey, 1982] and Eu/Eu* (oxidation state) [Drake, 1975], suggesting that the relationship between measured and source trace element ratios should be closely examined.

In classic theory, the isotopic compositions of melts are impervious to partial melting and fractional crystallization and are therefore direct impressions of mantle sources

and later contaminants. OIB show isotopic enrichments that trend toward end-member compositions, such as HIMU (high-μ; high $^{238}U/^{204}Pb$), enriched mantle components (EM-1 and EM-2) and Focus Zone (FOZO) [e.g., Gast et al., 1964; Zindler & Hart, 1986; Hart et al., 1992; Jackson et al., 2007; Day et al., 2009; White, 2010; Stracke, 2012]. The origins of many of these reservoirs are considered to reflect geological processes such as subduction of high-U/Pb oceanic crust (HIMU) [Hofmann & White, 1982], or pelagic (EM1) [e.g. Blichert-Toft et al., 1999; Eisele et al., 2002] or terrigenous sediments (EM2) [e.g., Jackson et al., 2007], allowing models to be developed for their respective trace element compositions [e.g., Chauvel et al., 1992]. However, the trace element signatures of these reservoirs are not empirically well-known, and studies relating measured trace element and isotopic compositions of these reservoirs are in their infancy [e.g., Hart et al., 1997; Willbold & Stracke, 2006; Hart & Jackson, 2014].

Relative enrichments of Ti, Ta and Nb ("TITAN") have been noted in some intraplate magmas (**Figure 2.1**) [e.g., Fitton et al., 1997; Dixon et al., 2002; Saal et al., 2007]. The enrichments are statistically anomalous to concentrations expected from relative compatibility alone (**Figure 2.2**) and thus they have garnered interest as a unique feature of OIB. Apparent global correlations of these enrichments with $^{3}He/^{4}He$, a proxy for deep mantle contributions to OIB, were noted and explained by Jackson et al. [2008] as representing coupled contributions from low-$^{3}He/^{4}He$, high TITAN recycled oceanic crust and high-$^{3}He/^{4}He$, low TITAN recycled oceanic lithosphere. If the correlation between $^{3}He/^{4}He$ and relative TITAN enrichments is robust, it may indicate that the deep, primitive mantle has preferentially retained Ti, Ta and Nb on long geologic timescales

($>10^9$ yr). Possible reasons for this include preferential Ti retention [e.g., Jackson et al., 2008], or large ion lithophile element (LILE) mobility in down-going slabs [e.g. Zack & John, 2007] replenishing the depleted upper mantle, however neither of these processes are presently supported by direct, empirical observations.

Mantle source reservoirs to OIB have distinct relative enrichments or depletions in TITAN elements based on previous work. For example, HIMU-type OIB may have flat-to-negative Ti anomalies [McDonough, 1991; Hart & Gaetani, 2006; Jackson et al., 2008] and positive Nb and Ta anomalies [Weaver, 1990; Chauvel et al., 1992]. EM1-type OIB hosts relatively flat Ti and flat-to-positive Ta and Nb anomalies [Honda & Woodhead, 2005; Jackson et al., 2008]. EM2 contains negative Ti, Ta and Nb anomalies [Farley et al., 1992; Workman et al., 2004; Jackson et al., 2007]. MORB and depleted MORB mantle (DMM)-type basalts have variable, but typically flat Ti and positive Ta and Nb anomalies [Workman & Hart, 2005; Hart & Gaetani, 2006; Arevalo & McDonough, 2010]. In addition, parental melt compositions of MORB are thought to have similar, flat Ti and positive Ta and Nb anomalies [Jenner & O'Neill, 2012]. No empirically known mantle reservoir has uniformly positive Ti, Ta and Nb anomalies. In this contribution, we revisit the significance of TITAN anomalies and evaluate whether the deep, primitive mantle is a plausible reservoir of relative TITAN enrichments, or whether TITAN anomalies reflect petrogenetic processes.

2 Methods

2.2.1 Definition of terms

We define Ti, Ta and Nb (TITAN) anomalies as:

$$\mathrm{Ti/Ti^*} = Ti_N/\sqrt{(Sm_N \times Tb_N)} \qquad \text{(Equation 1)}$$

$$\mathrm{Ta/Ta^*} = Ta_N/\sqrt{(Th_N \times La_N)} \qquad \text{(Equation 2)}$$

$$\mathrm{Nb/Nb^*} = Nb_N/\sqrt{(Th_N \times La_N)} \qquad \text{(Equation 3)}$$

In all cases, *N* indicates normalization to the primitive mantle compositions of McDonough [2000] (in ppm, Ti = 1200, Ta = 0.037, Nb = 0.66, Sm = 0.41, Tb = 0.1, Th = 0.08, La = 0.65), which are based on the values of McDonough & Sun [1995]. We choose primitive mantle for normalization to enable comparison with other studies of mantle geochemistry; normalizing to bulk Earth or chondritic values do not substantially change the numerical values of TITAN anomalies (see *Supplementary Information*). Positive anomalies are represented by values greater than one, negative anomalies by values less than one and perfectly "flat" anomalies by a value of exactly one. We compare these trace element anomalies to $^3He/^4He$ ratios, reported relative to the atmospheric $^3He/^4He$ ratio (R_A) of 1.38×10^{-6}. Helium isotopes are a proven tool for constraining mantle heterogeneity, with present-day mantle degassing of ^3He representing one of the most fundamental observations of terrestrial evolution [e.g., Clarke et al., 1969; Lupton & Craig, 1975]. This is because, unlike ^4He, which is predominantly a byproduct of radioactive decay of U and Th, ^3He is mainly primordial in origin and was trapped during the earliest stages of planetary accretion. Consequently, He isotopes provide direct evidence for the preservation of relatively undegassed, primordial reservoirs in the present-day mantle.

Reference MgO refers to the calculated MgO composition of a theoretical OIB parental magma. It is used to calculate all other trace element abundances of the same parental magma using methods described below; these abundances and resulting ratios are referred to as “parental”. “Measured” abundances and ratios refer to those determined directly from sampled rocks by geochemical analyses. “TITAN-involved” elements are Ti, Ta, Nb and their normalizing elements La, Sm, Tb and Th. Parental melts are those delivered to the base of the lithosphere and are assumed to be in chemical equilibrium with their mantle source; these are altered by shallow-level differentiation processes during migration to the surface.

2.2.2 Data assembly and filtering

Geochemical and isotopic data for OIB were assembled using the GEOROC online database as a bibliographic tool; data were compiled directly from published literature tables in order to compare analytical techniques. For a complete list of data sources that are not cited in this article, please refer to *Supplementary Information*.

All assembled geochemical data were filtered according to a number of tests designed to exclude samples compromised by extensive post- or syn-crystallization processes that may affect their compositions or by low-quality analytical methods, and samples from settings that may be geochemically unrelated to hotspot volcanism (e.g., proximate seafloor ridges). Data acquired by standard and carefully reported acquisition methods (X-ray fluorescence, XRF; instrumental neutron activation analysis, INAA; inductively coupled plasma mass spectrometry, ICP-MS; high precision liquid

chromatography, HPLC; etc.) were used without prejudice. All He abundance and isotopic data from olivine and clinopyroxene acquired by melting or by crushing in vacuo were accepted, however He analyses on glass were only accepted if He gas concentrations were equal to, or greater than, 20 ncc STP·g^{-1}. In total, data from approximately 3,100 samples from a variety of global hotspots were included in the study; approximately 500 possible data points were excluded for reasons mentioned above. Of the included data, approximately 2,100 samples from the hotspots of the Canary Islands, Cape Verde, the Comoros, the Galapagos, Hawaii, Iceland, Kerguelen, Reunion and Samoa were used for parental melt calculations and numerical modeling because these hotspots have a greater volume of available geochemical data and thus are capable of producing the most statistically robust data correlations.

2.2.3 Calculation of reference MgO and parental TITAN anomalies

TITAN compositions of OIB parental melts were determined using reference MgO compositions, which were calculated in two independent ways (both are explained in more detail in *Supplementary Information*). First, hotspot MgO arrays were used to determine the influence of olivine accumulation on plots of Al_2O_3 versus MgO [e.g., Klein & Langmuir, 1987]. Inflection points on these arrays were interpreted to correspond to MgO compositions uninfluenced by olivine accumulation or extraction, analogous to parental magmas that have not experienced fractional crystallization. In the second method, reference MgO was determined using theoretical forsterite-whole rock equilibria. Whole rock Mg# (Mg#=Mg/[Mg + Fe]) were regressed against forsterite contents of olivine for lavas from each hotspot and a reference Mg# was calculated using the average forsterite

content of each hotspot. Reference MgO was regressed from hotspot arrays of whole rock Mg# versus MgO. Quantitative comparison with experimental olivine Mg/Fe equilibria [Roeder & Emslie, 1970] was also undertaken; however, only some measured olivine compositions from individual hotspots fit with their experimental data. Those that do not may represent accumulative olivine, consistent with the preferential sampling of ankaramites, picrites and olivine-phyric basalts in many OIB studies. Consequently, the visual method of determining reference MgO was used, although the two methods result in similar calculated parental TITAN anomalies (*Supplementary Information*).

Parental TITAN anomalies were determined using two methods. In the first, data arrays for each relevant element or oxide (TiO_2, Nb, Ta and the normalizing elements Sm, Tb, La and Th) were regressed against measured MgO contents and the reference MgO value was used to determine a parental concentration for each element in each hotspot. Parental TITAN anomalies were then recalculated using the equations above. In the second method, data arrays for measured TITAN anomalies (Ti/Ti*, Ta/Ta* and Nb/Nb*) were regressed against MgO and parental TITAN anomalies were determined using reference MgO values. Parental TITAN anomalies calculated from the two methods are similar, but results from the first method were preferred because the second excludes samples for which TITAN anomalies cannot be calculated because only some of the necessary TITAN and normalizing elements are analyzed or reported (for example, a sample analyzed for Th but not Ta would be included in the first method, but not the second, because measured Ta/Ta* cannot be calculated for this sample). In both methods, the calculated parental concentrations or anomalies are relatively insensitive to the exact value for reference MgO

because the data arrays generally have shallow slopes versus MgO. Error introduced from the subjective nature of reference MgO determination is accordingly minimized; for full details on the calculation of errors on parental TITAN anomalies, please see *Supplementary Information.*

2.2.4 Model setup and parameters

Numerical models are presented predicting distributions of TITAN elements versus $^{3}He/^{4}He$ and $^{187}Os/^{188}Os$ ratios after ubiquitous partial melting and AFC processes. We choose to model non-modal, batch partial melting [Shaw, 1970] because it is likely that the rate of chemical reactions between residual, solid mantle and partial melt are fast relative to the rate of magma transport in the mantle [e.g., Hirose & Kushiro, 1993]. We use primitive mantle composition [McDonough, 2000] as an initial mantle composition because it is likely that hotspots, regardless of their mantle source reservoir(s), are partially generated from, or assimilate, some amount of ambient, primitive mantle during ascent [e.g., Hauri, 1996; Sobolev et al., 2005, 2007; Gurenko et al., 2009; Day et al., 2009, 2010]. For all hotspots, we model partial melting that begins in the garnet stability field but has a variable contribution from melting in the spinel stability field and a variable total degree of partial melting, with values for both of these parameters selected based on the lithospheric thickness underlying a given hotspot. We primarily use mineral partition coefficients from the high temperature and pressure experiments of Adam & Green [2006] because they consider a relatively complete array of trace elements and mineral phases in a single experiment, which permits a consistent view of partitioning between trace elements. However, we also use partition coefficients from other experiments and studies

[Hart & Brooks, 1974; Okamoto, 1979; Villemant et al., 1981; Lemarchand et al., 1987; McKenzie & Onions, 1991; Ewart & Griffin, 1992; Nielsen, 1992; Sobolev et al., 1996; Nash & Crecraft, 1985; Nikogosian & Sobolev, 1997; Heber et al., 2007; Day, 2013] that consider trace elements and mineral phases not included in Adam & Green [2006] (for a complete listing, please see **Table 2.4**). For REE not given in Adam & Green [2006], partition coefficients are interpolated based on available REE partition coefficients to ensure continuity in the partial melt model (**Figure 2.3**).

Results from a set degree of partial melting are used as initial conditions for modelling AFC processes in the presence of MORB-like oceanic crust [Workman & Hart, 2005]. We use the equations of Nishimura [2012], which are derived from the foundational modeling of DePaolo [1981] and Powell [1984], to calculate instantaneous and integrated compositions of phenocrysts during magma chamber cooling. Crystal accumulation is simulated by assuming that partial settling of suspended phenocrysts in a cooling magma chamber results in differing abundances of phenocrysts in erupted lavas and thus differing bulk rock chemistry; calculated residual magma and phenocryst compositions are accordingly re-convolved across an appropriate range of volumetric phenocryst abundances (maxima of 50-60 mass percent). However, as $^{3}He/^{4}He$ ratios are measured on phenocryst phases, calculated He isotopic compositions are not re-convolved with the residual magma.

For a complete model explanation, including model parameters, equations and results please refer to *Supplementary Information*.

2.3 Results

2.3.1 TITAN compositions of hotspots and their parental melts

Our compilation of global OIB geochemistry shows negligible correlations between measured TITAN anomalies and $^{3}He/^{4}He$ ratios (**Figure 2.4**). Many samples with elevated $^{3}He/^{4}He$ ratios (greater than the MORB value of 8 ± 1 R_A; e.g., Graham, 2002] have negative TITAN anomalies, and others with low-$^{3}He/^{4}He$ have positive TITAN anomalies. For example, the Canary Islands host low-$^{3}He/^{4}He$, high-TITAN ankaramites (**Figure 2.1**) and Cape Verde lavas with $^{3}He/^{4}He > 10$ frequently have flat-to-negative TITAN anomalies. There are apparent positive correlations between TITAN anomalies and $^{3}He/^{4}He$ within individual hotspots (e.g., Galapagos, Samoa), however the statistical significance of these correlations is variable (e.g., **Figure 2.4D-2.4F**).

Reference MgO compositions used to calculate the TITAN composition of OIB parental magmas range from 5.9-13.0 wt.%, and are reported with calculated parental TITAN anomalies in **Table 2.1**. Hotspots thought to contain a deep mantle component, such as Samoa, generally have higher reference MgO than other hotspots; however, they do not uniformly possess higher parental TITAN anomalies (**Figure 2.5**). Calculated parental Ti/Ti* (0.89-1.18), Ta/Ta* (0.88-2.35) and Nb/Nb* (0.97-1.91) vary widely between hotspots, and all parental Ti anomalies are indistinguishable from Ti/Ti*=1 (i.e., no anomaly) within the calculated uncertainties (**Figure 2.5A**; **Table 2.1**). Parental TITAN anomalies show weak to moderate correlations to $^{3}He/^{4}He$, with Ti/Ti* displaying the statistically weakest correlation ($R^2 = 0.13$) and Ta/Ta* displaying the strongest correlation

(R^2 = 0.55), versus $^3He/^4He$ (**Figure 2.5A-C**). Parental Ti anomalies show weak correlations to parental Ta and Nb anomalies, however there is a moderately robust correlation between parental Ta and Nb anomalies (**Figure 5D-F**).

Comparisons of TITAN anomalies to "scorecard" metrics for mantle plumes (*Supplementary Information*) [Courtillot et al., 2003; Anderson, 2005] yield poor correlations. Hotspot "scores" aim to qualitatively judge the probability that hotspot volcanism is fueled by mantle plumes, which may derive from the deep mantle, with higher scores representing a higher probability of a plume component. Many components of the scores condense quantitative measurements, such as geoid swell and heat flow, into qualitative bins.

2.3.2 Model Results

Numerical modeling reveals that small to moderate degrees of partial melt of primitive mantle (0.001-10%) [McDonough, 2000], thought to be a contributor to OIB parental melts in many settings [e.g., McKenzie & Bickle, 1988; McKenzie & O'Nions, 1991; Watson & McKenzie, 1991], yield positive Ta and Nb anomalies (**Figure 2.6**), particularly when a greater proportion of melting occurs in the spinel stability field (**Figure 2.7A-B**); blends of high and low degree partial melts coming from different depths may create a magma with variable TITAN anomalies. Increasing degrees of partial melting (up to 1%) are predicted to generate complex distributions of Ta/Ta* relative to La/Yb ratios (**Figure 2.7**). The origin of these distributions is rooted in increasingly efficient dilution of Ta with increasing melting in the garnet stability field, as Ta is relatively compatible in

garnet compared to Nb. Titanium anomalies, on the other hand, are more typically modestly positive or negative (**Figure 2.6**), with melting in the spinel stability field generating more negative Ti/Ti* (**Figure 2.7**). Fractional crystallization of olivine and clinopyroxene, two of the most abundant phenocryst phases in OIB, produces a solid phase in a theoretical magma chamber with large, positive Ti, Ta and Nb anomalies (**Figure 2.6**). However, since many trace elements are relatively incompatible in these phases, absolute abundances of trace elements are 10-to-1000 times lower than in the crystallizing magma. Residual liquids to this fractional crystallization maintain TITAN anomalies that are essentially flat, though arithmetically positive (**Figure 2.6**). Reconvolving calculated liquid and solid compositions to create a theoretical porphyritic rock results in generation of significant positive Ti anomalies and modestly positive Ta and Nb anomalies.

Distributions of TITAN anomalies after partial melting of DMM [Workman & Hart, 2005] show similar patterns to distributions after partial melting of primitive mantle. However, as DMM probably hosts positive Ta and Nb anomalies, the distribution fields of these anomalies are higher than for primitive mantle. For Ta/Ta*, melting of DMM produces more exaggerated dilution peaks than for melting of primitive mantle, and these peaks persist through the highest degree of partial melting in the spinel field (**Figure 2.7**). The melting of DMM may be of particular importance when considering measured geochemistry of basalts originating from hotspots erupting through oceanic crust. We give each hotspot individual consideration in generating final models, though we present only results for Iceland in the main text. For a more comprehensive discussion of the model, please refer to *Supplementary Information*.

2.3.3 Empirical relationship between mineral accumulation and TITAN anomalies

Although classic petrological studies of OIB have presented information on mineral phase abundance, few studies offer this information combined with detailed geochemistry. Day et al. [2010] reported modal abundances for lava and xenolith samples from the Canary Islands with accompanying whole rock geochemical analyses. Regression analysis of TITAN anomalies versus the sum of olivine and clinopyroxene modal abundances (**Figure 2.8**) yields a moderately robust correlation with Ti/Ti* ($r^2 = 0.56$) while regressions against Ta/Ta* and Nb/Nb* yield weak correlations ($r^2<0.01$ and $r^2 = 0.03$, respectively). Correlations of TITAN anomalies to bulk rock MgO contents in this dataset (**Figure 2.8**) are better for Ta/Ta* ($r^2 = 0.05$) and Nb/Nb* ($r^2 = 0.14$), though slightly worse than with modal proportions of olivine and clinopyroxene for Ti/Ti* ($r^2 = 0.40$).

2.4 Discussion

The use of trace element ratios as direct reflections of mantle source composition presumes that the partitioning behavior of each trace element is predictable throughout the generation and differentiation of the source magma, and that assimilation and homogenization of melt extracts, both during magma ascent and during AFC processes, are readily detectible [e.g., Stracke & Bourdon, 2009]. However, knowledge of partitioning is largely limited to experimental data, which are, in turn, constrained by the researchers' choice of experimental conditions, and to numerical modeling [e.g., Arevalo & McDonough, 2010]. For these reasons, the use of trace element ratios as diagnostic tracers of mantle source regions should be carefully assessed. We consider the origin of TITAN

anomalies from several perspectives, including new consideration of the impact of partial melting and AFC processes on the TITAN compositions of OIB parental melts.

2.4.1 Geographic scale of TITAN anomalies

Trace element abundances and ratios can be altered by a variety of geologic processes. By contrast, while isotopic ratios of OIB may be susceptible to crustal assimilation after volatile outgassing (e.g., He isotopes; Condomines et al., 1983) or fractional crystallization of compatible elements (e.g., Os isotopes; Reisberg et al., 1993), they are generally considered more robust tracers of OIB mantle sources. This is one explanation as to why generally accepted tracers of deep, primitive mantle components to OIB sources, such as $^{3}He/^{4}He$ ratios, bear no significant correlation to measured Ti, Ta and Nb anomalies in a global survey of OIB (**Figure 2.4A-2.4C**). However, correlations between TITAN anomalies and $^{3}He/^{4}He$ appear to be moderately robust within single hotspots (e.g., **Figure 2.4D-2.4F**), indicating that there may be a source control on TITAN anomalies that is regional rather than global. The idea that measured TITAN anomalies are appropriate tracers of an OIB source reservoir at the single-hotspot scale is unlikely for three reasons: first, many hotspots are thought to have multiple small-scale source compositional trends, yet they display relatively coherent distributions of TITAN anomalies across these trends (e.g., **Figure 2.4E**); second, with the exception of Ti/Ti* and the two cases presented in **Figures 2.4E** and **2.4F**, many hotspot arrays of TITAN versus $^{3}He/^{4}He$ are flat or have no obvious correlation, implying that Ta and Nb anomalies are decoupled from helium isotopes and the mantle reservoir(s) that they trace; and third, combining relatively robust correlations of TITAN anomalies versus radiogenic isotopes

across multiple hotspots with similar geochemical properties diminishes the correlation, suggesting that it is generally inappropriate to extrapolate geochemical trends of single hotspots to gain information about recognized mantle reservoirs to many hotspots.

Identification of trace element ratios in MORB that are faithful recorders of DMM composition has also been attempted on a global scale [e.g., Arevalo & McDonough, 2010]. When considering a global dataset, it becomes clear that trends in trace element ratios that are observable from smaller or geographically limited datasets [e.g., Jochum et al., 1983] may be misleading in terms of identifying a common composition for DMM. In view of this, conceptual and numerical models offering explanations for the origin of positive TITAN anomalies ought to be global in scale. Jackson et al. [2008] argue that generation models should apply only to the highest-$^{3}He/^{4}He$ samples, but provide no reason to divorce these samples from other samples from the same hotspot that lack this geochemical trait. Application of their model to other samples from hotspots with high-$^{3}He/^{4}He$, and not just the highest-$^{3}He/^{4}He$ samples, requires OIB parental reservoirs to assimilate recycled oceanic materials of many distinct ages, and for lava suites to represent mixtures of very old (up to 3 Ga) and very young (> 1 Ga) oceanic lithosphere [Jackson et al., 2008, their Figure 2]. In addition, their model requires addition of recycled oceanic crust much younger than 1 Ga when considering only $^{3}He/^{4}He$ ratios, but exclusively crust >1 Ga when considering $^{3}He/^{4}He$ and $^{187}Os/^{188}Os$ ratios of OIB. Both of these physical predictions may be unlikely in hotspot sources, and their existence would further obscure a single mantle source for positive TITAN anomalies. Instead, we offer an approach to

determining the origin of TITAN anomalies that can explain a common origin across single and multiple hotspots.

2.4.2 General trends in parental TITAN anomalies

Global parental TITAN anomalies vary widely between hotspots (**Table 2.1**). Hotspots with an overall more primitive geochemistry (reference MgO >10 wt.%) may have positive or negative parental TITAN anomalies, and those with a more evolved geochemistry have flat or positive parental TITAN anomalies. The Comoros is the only hotspot with relatively flat to negative parental Ti, Ta and Nb anomalies, which are consistent with it lying within the EM source spectrum and possibly having a continental crustal component [Class et al., 2009]. However, the EM1 'flavor' of the Comoros is inconsistent with the presence of significantly negative parental Ta/Ta*, which should be the inverse in recycled pelagic materials, and may indicate that its uniformly negative parental TITAN anomalies are the result of partial melting or differentiation (see below). Iceland has a relatively strong positive parental Ta anomaly and a relatively flat parental Ti anomaly, which may reflect a long-term history of interaction with DMM [e.g., Doucet et al., 2002, 2005; Peate et al., 2009; Koornneef et al., 2012]; relatively flat parental Ti anomalies are shared by a number of hotspots located near mid-ocean ridges (e.g., Cape Verde). Parental Nb/Nb* is the most difficult attribute to explain by OIB mantle sources alone; for example, the distinctly-EM2 hotspot Samoa has a positive parental Nb/Nb*, while the EM2 mantle reservoir is thought to host negative Nb anomalies [Farley et al., 1992; Workman et al., 2004; Jackson et al., 2007].

Calculated parental magma compositions bear moderate to poor correlations to $^{3}He/^{4}He$ ratios (**Figure 2.5**). Hotspots with average $^{3}He/^{4}He$ ratios lower than MORB (8 R_A) have both positive and negative calculated parental anomalies; for example, the Canaries has higher calculated parental Ta/Ta* and Nb/Nb* than several high-$^{3}He/^{4}He$ hotspots (**Figure 2.5**). In addition, several high-$^{3}He/^{4}He$ hotspots (e.g., Reunion, Samoa) have calculated parental Ta/Ta* and Nb/Nb* that are lower than those for hotspots with MORB-like $^{3}He/^{4}He$. According to these calculations, there is no apparent correlation between the TITAN and $^{3}He/^{4}He$ compositions of OIB source magmas.

Comparison of trace element abundances, which are measured on bulk rock powders, to $^{3}He/^{4}He$, which are measured on phenocrysts, or glass, is procedurally problematic. If fractional crystallization is responsible for the production of positive TITAN anomalies, then the analysis of a fresh, porphyritic OIB, like a picrite (olivine ± cr-spinel) or an ankaramite (clinopyroxene + olivine ± spinel) is likely to yield excesses of both $^{3}He/^{4}He$ and TITAN. This is one explanation why correlations are observed in the TITAN versus $^{3}He/^{4}He$ arrays (**Figure 2.4**), which must use porphyritic rocks in many OIB settings, is absent in the arrays of calculated parental TITAN versus average hotspot $^{3}He/^{4}He$ arrays (**Figure 2.5**), which may include both aphanitic and porphyritic rocks. This is particularly true for Ti/Ti*, which also shows the strongest empirical correlation to olivine and clinopyroxene accumulation amongst Canary Island OIB (**Figure 2.8**), and is compatible in oxide minerals [e.g., Okamoto, 1979]. The result of combined partial melting-AFC models can simulate typical distributions of Ti/Ti* against $^{3}He/^{4}He$ and $^{187}Os/^{188}Os$ ratios in OIB (**Figure 2.9**), providing theoretical support for this process.

Whatever the origin of these characteristics, their occurrence warrants consideration of magma differentiation processes as the origin of TITAN anomalies.

Although parental Ti/Ti* is not correlated to parental Ta/Ta* or parental Nb/Nb*, parental Ta/Ta* shows a moderately robust correlation to parental Nb/Nb* (**Figure 2.5F**). Although this implies that there is a common origin to these anomalies, it does not require that they are source features; instead, it is equally possible from the correlation that the relationship is source- or process-based. It is also noteworthy that Hawaii does not lie on this trend, indicating that if Ta and Nb anomalies have a common origin, it cannot be global in nature and either anomaly may be affected by melt sources or processes that do not affect the other.

2.4.3 The origin of Ti anomalies

Titanium is unique amongst the TITAN-involved elements for several reasons. First, its bulk distribution coefficient at high temperatures and pressures is not the product of anomalous incompatibility in a single phase, rather, it is roughly equally incompatible in all common igneous silicate mineral phases; second, it has a relatively high compatibility in oxides; and third, it is the only anomaly for which analysis by multiple methods is particularly common (as TiO_2 is commonly measured by XRF while Sm and Tb cannot be measured by XRF) – all other TITAN-involved elements, including occasionally TiO_2, may be analyzed using a single instrument, such as an ICP-MS. The third problem is of particular concern because of uncertainties introduced in comparing abundance data obtained from two different methods. However, we generally find that XRF and ICP-MS

analyses for minor elements agree within sample sets, so we find no reason to summarily disregard Ti anomalies calculated from the results of multiple methods of analysis.

Titanium's relatively low incompatibility in mantle mineral phases means that partial melting is not the origin of positive Ti anomalies in OIB (**Figure 2.7A** & **2.7C**). Rather, preferential retention of Ti in pyroxene and garnet generates negative anomalies in partial melts that diminish with increasing degrees of partial melting. This result agrees with those of Prytulak & Elliott [2007], who show that the TiO_2 contents of OIB cannot be explained by partial melting alone. One notable exception is Iceland, which is thought to represent one of the highest degrees of partial melting amongst OIB because it traverses the Central Atlantic Ridge: Iceland has a slightly positive average measured Ti anomaly (Ti/Ti^*_{avg} = 0.72-1.49, preferred value 1.02) and TiO_2 contents that can be explained by partial melting [Prytulak & Elliott, 2007]. According to our model, positive Ti/Ti* may also be observed in OIB originating from a parental magma derived from ≥ ca. 5% partial melting of primitive mantle without invoking an unusually enriched or recycled source.

Positive Ti anomalies can be generated through AFC processes in magma chambers hosted by MORB-like oceanic crust. At low temperatures and pressures, Ti is highly compatible in magnetite and other oxide phases, which are frequently included in olivine crystals (e.g., in accumulative picrites and ankaramites). This generates positive Ti anomalies even at low degrees of AFC and phenocryst accumulation, even when the phenocrysts contain a low proportion of oxide (≤ 5 mass %; e.g., **Figure 2.8**). Many hotspots are thought to result from low degrees of mantle partial melting [e.g., McKenzie

& Bickle, 1988; McKenzie & O'Nions, 1991; Watson & McKenzie, 1991], and thus positive Ti anomalies cannot be theoretically generated without invoking AFCunless the source has a substantially positive Ti/Ti* (e.g., **Figure 2.7**).

This notion is generally supported by empirical data. In a survey of Canary Island basalts, Day et al. [2010] found that Ti/Ti* increases with increasing modal abundance of olivine and clinopyroxene, two common phenocryst phases in OIB. However, the Canary Island hotspot has relatively low-$^{3}He/^{4}He$ (typically $\leq 8R_A$) [Day & Hilton, 2011], requiring input from only the oceanic crustal source envisioned by Jackson et al. [2008] without contribution from their oceanic lithospheric source, a situation with an unclear physical likelihood, and which is inconsistent with the isotopic and geochemical compositions of Canary Island lavas [Day et al., 2010; Day & Hilton, 2011].

2.4.4 The origin of Ta and Nb anomalies

Because Ta and Nb are members of the same chemical period, it is expected that they should exhibit similar physical properties in natural environments. However, Ta analyses are often unreliable because normal laboratory procedures, especially the use of tungsten carbide (W-C) crushing and grinding preparation devices, may cause Ta contamination. In addition, precise analysis of Ta by ICP-MS is difficult due to its low abundance, possible instability in solution [e.g., Jenner et al., 1990], and its nearly mono-isotopic occurrence as ^{181}Ta. The fact that Ta/Ta* is often arithmetically greater than Ti/Ti* or Nb/Nb* in a given sample, and that some samples (e.g., from the Galapagos) have measured Ta/Ta* that well exceed any known mantle OIB source, may indicate that these

concerns are producing anomalies of a magnitude that are physically unlikely. Nonetheless, as mentioned previously, parental Ta/Ta* shows a moderately robust correlation to parental Nb/Nb*, suggesting that analytical artifacts confuse, rather than completely compromise the available OIB Ta dataset (**Figure 2.5F**). Thus, although the origins of Ta and Nb anomalies are best considered in unison, special care should be taken when ascribing meaning to Ta anomalies as they may be affected by analytical artifacts.

Tantalum and Nb are anomalously incompatible at high temperatures and pressures when compared to their normalizing elements La and Th [Adam & Green, 2006], which generates positive Ta and Nb anomalies at low degrees of partial melting (<10%) of either primitive mantle or DMM (**Figure 2.7**). However, because Ta is less incompatible in garnet than La and Th by a factor of ~2 [Adam & Green, 2006], negative Ta anomalies are generated at extremely low degrees of partial melting (<1%) in the garnet stability field. Over normal intervals of partial melting, however, positive Ta and Nb anomalies can be generated in melts from source materials with positive or negative Ta and Nb anomalies, effectively masking the original mantle source signature. Thus, even if the ultimate origin of OIB in the deep mantle possesses TITAN anomalies, it is unlikely that geochemical measurements of hotspot lavas accurately represent them.

Crustal AFC processes in the presence of MORB-like crust may further alter the TITAN composition of parental hotspot materials. At low temperatures and pressures, the compatibility relationship between Ta, Nb, La and Th reverses: Ta and Nb have anomalously low incompatibility in common phenocryst phases (by a factor of 10-100, see

Supplementary Information for partition coefficient sources) compared to neighboring elements on trace element spidergrams. This would result in accumulation of crystals in crustal magma chambers with large positive Ta and Nb anomalies, though lower absolute concentrations of all incompatible elements with low degrees of AFC (**Figure 2.6**). In addition, MORB is hosts positive Ta and Nb anomalies [Arevalo & McDonough, 2010], which counteract Ta and Nb extraction by crystallizing phenocrysts. The result is flat to modestly positive Ta and Nb anomalies in the residual magma and large positive Ta and Nb anomalies in phenocrysts (**Figure 2.6**). Since the phenocryst phases have lower absolute abundances of TITAN-involved elements, convolving the calculated phenocryst composition with the composition of the residual liquid results in a dilution of Ta and Nb anomalies in the liquid-phenocryst composite. Our model predicts this would create modestly positive Ta and Nb anomalies in a resulting porphyritic rock, however these results generally underestimate the measured distribution of Ta and Nb anomalies amongst global OIB (**Figure 2.9**). Thus, although the magnitude of measured Ta and Nb anomalies in OIB can be explained by partial melting, it cannot be explained by normative crustal AFC processes.

One possible origin of the underestimate of Ta and Nb anomalies is enrichment of TITAN-involved elements through lithospheric metasomatism, which is not considered in our model. Understanding of the distribution of high field strength elements (HFSE, including Ti, Ta and Nb) in the upper mantle has been challenging [McDonough et al., 1992; Bodinier et al., 1993; Eggins et al., 1998], mainly due to the extreme incompatibility of these elements in common upper mantle mineral phases [Adam & Green, 1994, 2006].

The problem of Ti is partially solved by the extreme affinity of oxides and Ca-perovskite for Ti [e.g., Nielsen, 1992; Kato et al., 1988], however discovering the identity of the mineral hosts for the much more scarce elements Ta and Nb has proven to be more difficult. Bodinier et al. [1996] report high concentrations of Nb, Ta and other elements in metasomatic phlogopite rims coating spinel crystals in peridotites and mantle xenoliths. In spite of the small volume of the rims, they argue that they may comprise up to 90% of the budget of HFSE in mantle xenoliths. The importance of amphibole, another trace mineral phase in the upper mantle [Oxburgh, 1964], to the Nb contents of mantle xenoliths has also been explored [Eggins et al., 1998]. Spinel and phlogopite are unstable in the lower mantle [e.g., Akimoto & Syono, 1967; Sudo & Tatsumi, 1990] and would decompose on a subducting slab, losing their trace elements either to fluid flow or to other mineral phases in which the trace elements are more incompatible. Trace element signatures of residual spinel or phlogopite would therefore not be expected in melting products of recycled subducted crust. In contrast, spinel rim metasomatism is thought to occur in the shallow, sub-oceanic and sub-continental lithosphere [Bodinier et al., 1996], thus a deep mantle origin for TITAN anomalies generated by this process is unlikely.

2.4.5 The role of a recycled oceanic crust and lithosphere source to OIB in TITAN anomalies

Jackson et al. [2008] argue that the origin of TITAN anomalies in OIB lies in an ideal mixture of high-TITAN, low-$^{3}He/^{4}He$ recycled oceanic crust and low-TITAN, high-$^{3}He/^{4}He$ recycled oceanic lithosphere. Though recycled oceanic crust and lithosphere are commonly recognized components to OIB parental materials, it may be unlikely that they

retain these expected compositions on billion-year timescales, and are known to have a $^{3}He/^{4}He$ ratio that is less than DMM [e.g., Moreira & Kurz, 2001]. However, we argue they are unlikely sources of positive TITAN anomalies in OIB, even if their expected TITAN signatures can be retained through partial melting and magma differentiation and the $^{3}He/^{4}He$ ratio of recycled ancient lithosphere were higher.

2.4.5.1 Effects of fluid mobility during subduction

Changes in the trace element geochemistry of oceanic crust can occur during subduction due to dewatering [e.g., Pearce, 1983], increasing pressure [e.g., Tatsumi, 1989] or partial melting of the slab [e.g., Defant & Drummond, 1990; Defant, et al., 1992; Yogodzinski & Keleman, 1998; Castillo, 2012], which could impact the composition of OIB parental materials derived from recycled oceanic crust. The former two processes are not suspected to affect changes in the TITAN composition of a downgoing slab because they preferentially affect large ion lithophile elements, which do not include the TITAN-involved elements. Some researchers suggest there is modest mobility of Sm in slab-derived fluids [Pearce, 1983; Pearce et al., 1995; Barry et al., 2006], but this effect may be isolated to the unique conditions of subduction in the Sandwich Islands and is thus unlikely to significantly affect global distributions of TITAN anomalies. Normal fluid movement during subduction is not known to significantly mobilize TITAN-involved elements.

2.4.5.2 Effects of partial melting during subduction

Partial melting and dehydration of down-going slabs may also affect the geochemistry of the resulting recycled sources to OIB. In addition to arc volcanics, these

processes result in the production of a unique brand of rocks known as adakites [Defant & Drummand, 1990], which may contain varying contributions from slab melts. If a slab contains a relatively high proportion of rutile, it may become enriched in Ti, Ta and Nb during subduction [e.g., Rudnick et al., 2000; Jackson et al., 2008], presuming that rutile remains a refractory phase. This notion is generally supported by commonly negative Ti anomalies in adakites [e.g., Drummond et al., 1992; Yogodzinski et al., 1995] and arc volcanics [e.g., Perfit et al., 1980], which would serve as a complement to positive Ti anomalies in the down-going slab, and by xenolithic eclogites, which host enrichments in Ta and Nb relative to La [Rudnick et al., 2000]. However, the scale and ubiquity of slab melting is disputed [see, e.g., Castillo, 2012], which would diminish TITAN enrichment, and commonly held geochemical models for HIMU-type lavas, which are thought to derive from recycled oceanic crust and lithosphere [e.g., Chauvel et al., 1992; Moreira & Kurz, 2001], have flat-to-negative Ti anomalies [McDonough, 1991; Woodhead, 1996; Hauri & Hart, 1997; Hart & Gaetani, 2006]. Further, the Réunion hotspot, which is thought to be comparatively isolated from recycling processes [Schiano et al., 2012], has consistently positive TITAN anomalies and positive calculated parental anomalies (**Figure 2.5**). Finally, even if eclogites preserve positive TITAN anomalies, rutile must be consumed during partial melting of deeply subducted slabs. Experiments conducted by Gaetani et al. [2008] indicate rutile is consumed between 4-22% partial melt, but there are no empirical constraints on the degree of melting of this refractory reservoir, and this range is well in excess of the commonly held OIB partial melt interval of <10% [e.g., Klein & Langmuir, 1987; McKenzie & Bickle, 1988]. These high degrees of partial melting also contraindicate selective melting of high-TITAN, low-$^{3}He/^{4}He$ oceanic crust over low-TITAN, high-

$^{3}He/^{4}He$ oceanic lithosphere to fuel hotspots such as the Canary Islands. If refractory rutile does generate positive TITAN anomalies in OIB parental melts, our knowledge of the composition of recycled oceanic crust vis-à-vis measured OIB does not support the survival of these anomalies through partial melting and magma differentiation during and after subduction.

2.4.5.3 Origins of OIB parental magmas

OIB sources cannot be limited to recycled oceanic crust and lithosphere [Niu & O'Hara, 2003], but are frequently envisioned as mixtures of recycled crust and/or lithosphere and ambient mantle [e.g., Hauri, 1996; Sobolev et al., 2005, 2007; Gurenko et al., 2009; Day et al., 2009, 2010]. Estimates of possible OIB mantle source components have distinct trace element compositions [e.g., McDonough, 1991; Weaver, 1990; Chauvel et al., 1992; Farley et al., 1992; Workman et al., 2004; Honda & Woodhead, 2005; Workman & Hart, 2005; Hart & Gaetani, 2006; Jackson et al., 2007] that may contribute in varying amounts to an OIB parental magma. Homogenization of these mantle sources with ambient, primitive mantle, which we show forms melts with positive Ta and Nb anomalies, and subjugation to AFC, may result in an OIB parental melt with positive TITAN anomalies regardless of the composition of the mantle source. Thus, ascribing TITAN anomalies to any one hypothesized mantle source to OIB is not warranted by the common conceptual understanding of mantle geochemistry.

2.4.6 Reconsideration of relative incompatibility in OIB

Since the importance of partial melting and differentiation cannot be overlooked when considering incompatible trace elements in all geologic systems, it is important to hold a critical view of relative incompatibility during all stages of magma production. Traditional spider diagram plots hold that Nb and Ta are less incompatible than Th, but more incompatible than La. In contrast, a compilation of experimental and calculated partition coefficients indicates that this may not be true for rocks with olivine, clinopyroxene and oxides as major solidus or phenocryst phases (**Figure 2.3**). In fact, this particular combination of phenocryst phases, which are not typically shared by non-hotspot rocks, shows a pattern of K_D values that is similar to the pattern of trace elements noted in porphyritic OIB (e.g., **Figure 2.1**). Taken together, these observations indicate that care should be taken when identifying geochemical anomalies on trace element plots that summarily assign relative properties to elements across a wide variety of geologic settings. A new consideration of the ordering of elements on trace-element spidergrams may be needed to address this issue (see *Supplementary Information*).

2.5 Conclusions

Common enrichments in Ti, Ta and Nb relative to elements of similar incompatibility in OIB do not appear to represent characteristics of recycled crust and lithosphere from the deep mantle. We show that:

(1) A global compilation of OIB geochemistry shows no relationship between Ti, Ta and Nb (TITAN) anomalies and measured $^{3}He/^{4}He$ ratios; calculated parental TITAN anomalies also show little relationship to $^{3}He/^{4}He$ ratios, buoyancy flux, and plume "scores."

(2) Measured Ta anomalies exceed those of any known OIB source reservoir, which may partly reflect contamination occurring during sample preparation and/or from analytical error;

(3) Positive TITAN anomalies occur in low-$^{3}He/^{4}He$ samples from the Canary Islands and the Comoros and, inversely, negative TITAN anomalies occur in elevated $^{3}He/^{4}He$ samples from Cape Verde and Samoa, which would indicate long-term decoupling of the two parameters;

(4) Positive TITAN anomalies are measured in OIB lavas from and calculated to be present in the parental magma for the Reunion hotspot, which is generally considered to be isolated from the recycling process thought to be the source of TITAN enrichments;

(5) HIMU, which is thought to represent the melt product of recycled oceanic crust, has, flat-to-negative Ti anomalies, which contradicts the notion that positive Ti anomalies would be generated by Ti retention in rutile during subduction;

(6) TITAN anomalies can arise from lithospheric metasomatism that enriches HFSE in phlogopite rims on rutile, diminishing the need to invoke melting of rutile-bearing subducted oceanic crust an lithosphere in the source of all hotspots with positive TITAN anomalies;

(7) Numerical models of partial melting and AFC processes simulate distributions of Ti anomalies, $^{187}Os/^{188}Os$ and $^{3}He/^{4}He$ for many hotspots that resemble measured data. Further, modal abundance data for Canary Islands OIB show moderately robust positive correlations between clinopyroxene and olivine abundance and Ti anomalies, demonstrating a clear AFC control on positive Ti anomalies. These

models also show that significant positive Ta and Nb anomalies can be generated by partially melting primitive mantle under typical hotspot melting conditions. This means that even if Ti, Ta and/or Nb enrichments are systematically present in high-$^{3}He/^{4}He$ OIB source materials, it is unlikely that they remain unaltered from their mantle sources to be sampled at hotspot volcanoes.

Taken together, these arguments indicate that TITAN enrichments amongst OIB may not be representative of OIB source compositions, but are rather attributable primarily to the effects of melt homogenization and AFC processes on parental magma compositions. It further implies that late-stage differentiation processes are capable of generating globally pervasive geochemical signatures observed in a variety of geological settings. For OIB magmas, which form in unique pressure-temperature conditions in which olivine and clinopyroxene are on the solidus, this means that traditional conceptions of relative element incompatibility may be inadequate to identify meaningfully anomalous trace element compositions. Careful consideration of modal abundance of phenocryst phases in future studies may reveal that fractional crystallization processes operating on OIB magmas demand rethinking of the ordering of trace elements on spidergrams, which are presently used for a wide variety of rocks with distinct petrogeneses (see *Supplementary Information*).

Acknowledgements

The authors thank associate editor C.-T. Lee, reviewer S. Hart and an anonymous reviewer for their comments, which substantially improved this paper. This work was made possible through support from the National Science Foundation (EAR-1116089).

Chapter 2, in full, is a reformatted version of the material as it appears in Earth and Planetary Science Letters: Peters, B.J. and J.M.D. Day (2014) Assessment of relative Ti, Ta, and Nb (TITAN) enrichments in ocean island basalts: Geochemistry, Geophysics, Geosystems, 15, 4424-4444. I was the primary investigator and author of this paper and of this chapter.

Table and Figures

Table 2.1: Reference MgO compositions used in the calculation of parental TITAN anomalies and calculated average TITAN anomalies for nine primary global hotspots. Ranges of MgO correspond to possible locations of inflection points on hotspot arrays of Al_2O_3 versus MgO arrays. Ranges in parental anomalies correspond to anomaly minima and maxima based on propagation of standard or reported error for geochemical analyses (see text).

Hotspot	Reference MgO (wt. %)	Reference MgO Range (wt. %)	Parental Ti/Ti*	Parental Ti/Ti* Range	Parental Ta/Ta*	Parental Ta/Ta* Range	Parental Nb/Nb*	Parental Nb/Nb* Range
Reunion	13.0	11.5 - 15.5	1.07	0.75 - 1.59	1.27	0.74 - 2.09	1.15	0.71 - 1.83
Hawaii	12.6	11.6 - 14.1	0.89	0.66 - 1.22	1.74	1.51 - 1.99	1.90	1.62 - 2.27
Samoa	12.0	10.8 - 13.4	1.12	0.85 - 1.43	1.51	1.18 - 1.62	1.21	1.06 - 1.42
Comoros	11.0	10.0 - 11.5	0.89	0.73 - 1.07	0.88	0.72 - 1.04	0.97	0.80 - 1.18
Canaries	10.0	8.75 - 11.5	1.02	0.88 - 1.23	1.52	1.15 - 1.79	1.43	1.08 - 1.84
Iceland	9.7	8.9 - 10.8	1.02	0.72 - 1.49	2.12	1.56 - 3.03	1.51	1.04 - 2.22
Cape Verde	8.3	7.6 - 9.1	1.00	0.84 - 1.20	1.74	1.43 - 2.11	1.51	1.23 - 1.84
Galapagos	7.0	6.3 - 7.7	1.19	0.90 - 1.57	2.33	1.86 - 3.04	1.69	1.27 - 2.27
Kerguelen	5.9	4.9 - 6.7	1.11	0.85 - 1.45	1.27	1.00 - 1.60	1.12	0.86 - 1.44

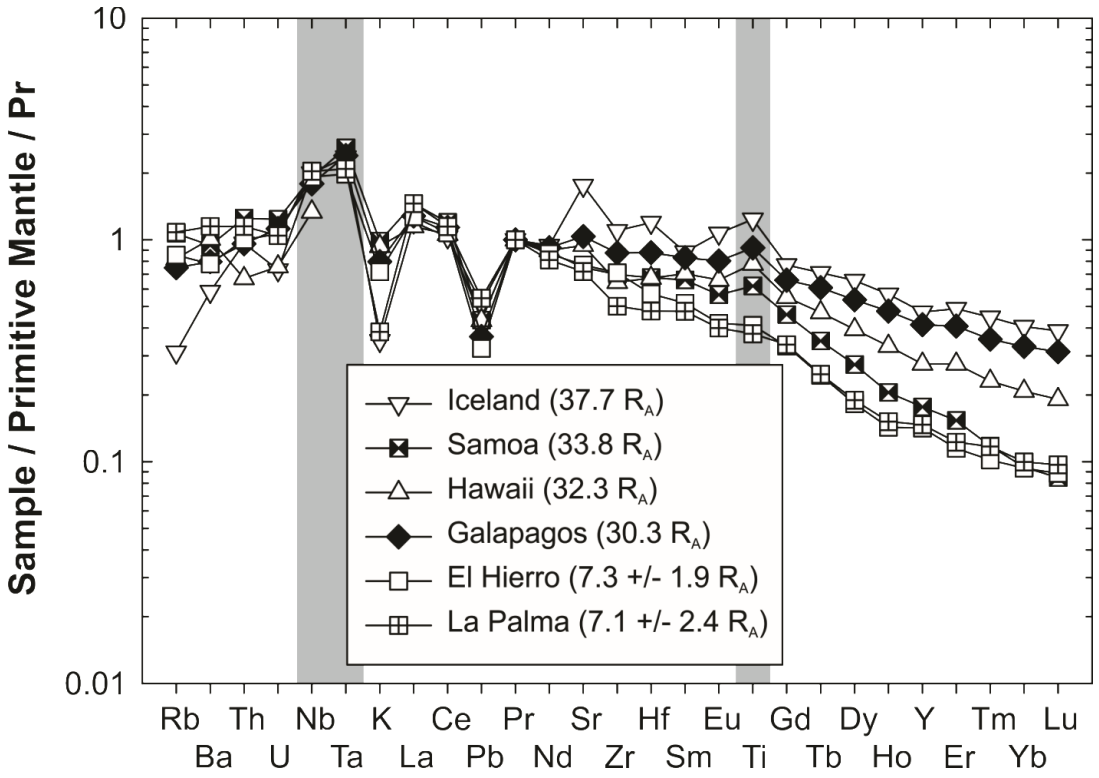

Figure 2.1: Examples of titanium, tantalum and niobium (TITAN) enrichments in ocean island basalts double normalized to primitive mantle [McDonough & Sun, 1995] and Pr. Shown are four samples with high-^{3}He/^{4}He presented in Jackson et al. [2008] along with two samples from El Hierro and La Palma (Canary Islands) with lower ^{3}He/^{4}He [Day et al., 2010; Day & Hilton, 2011]. Note the elevated Ti relative to Sm and Tb and the elevated Ta and Nb relative to La and Th (shaded areas).

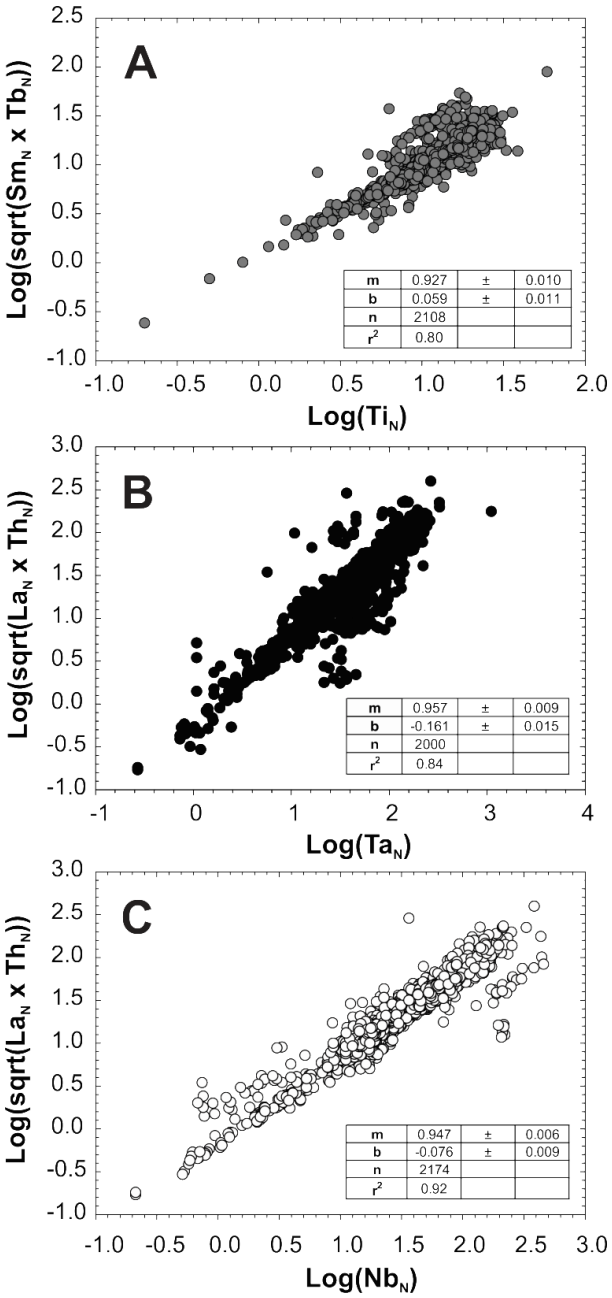

Figure 2.2: Log-log co-variation plots for Ti (A), Ta (B) and Nb (C; together, TITAN) and their normalizing elements in ocean island basalts (OIB). Values of slopes (m) are given with 95% confidence limits for a bivariate least-squares regression. Deviations from a unitary slope (m = 1) indicate a deviation in TITAN values from that expected from relative element compatibility (according to the order of elements on the plot) alone. In all three plots, slopes are distinguishable from unity, indicating that TITAN anomalies are a statistically pervasive feature of OIB. Data sources are listed in *Supplementary Information*, number of points for each plot varies according to availability and data filtering.

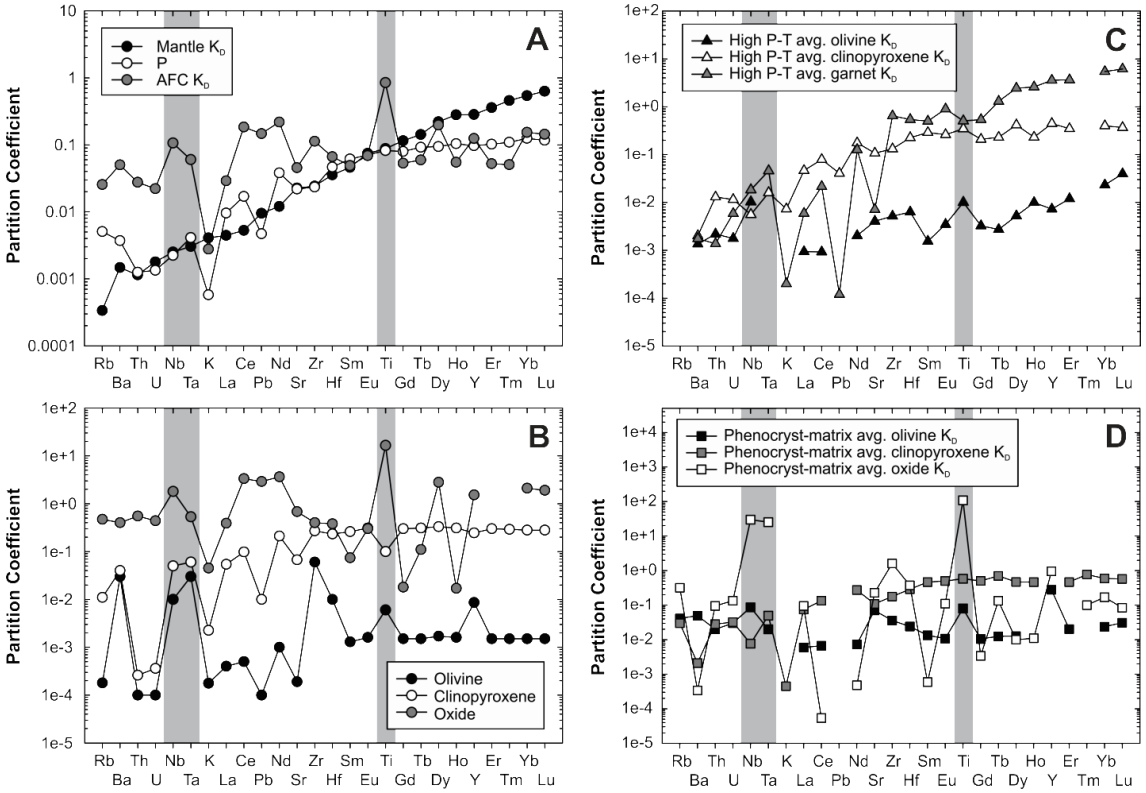

Figure 2.3. Summary of partition coefficients used in partial melting (A) and AFC (A and B) models. Average high pressure-temperature (C) and matrix-phenocryst (D) partition coefficients from literature data (excluding those used in the models) surveying lithologies included in typical OIB suites are presented for comparison. In panel A, P is the bulk distribution coefficient of minerals that comprise the melt phase. Oxide phase partition coefficients are a composite of spinel, ilmenite and rutile K_D. Partition coefficients for AFC show strong affinities for TITAN in the solid phase, providing one explanation as to the origin of the anomalies. Data sources for panels A and Bare listed in *Supplementary Information*. Data sources for panels C and D: Beattie [1994]; Ewart & Griffin [1994]; Fujimaki et al. [1984]; Green et al. [2000]; Hart & Dunn [1993]; Hauri et al. [1994]; Higuchi & Nagasawa [1969];Jenner et al. [1994]; Johnson [1994]; Kennedy et al. [1993]; Lemarchand et al. [1987; excluding those used in the models]; Matsui et al. [1977]; Nielsen et al. [1992]; Schnetzler & Philpotts [1970]; Skulski et al. [1994]; Stimac & Hickmott [1994]; Tuff & Gibson [2007]; Zack & Brumm [1988].

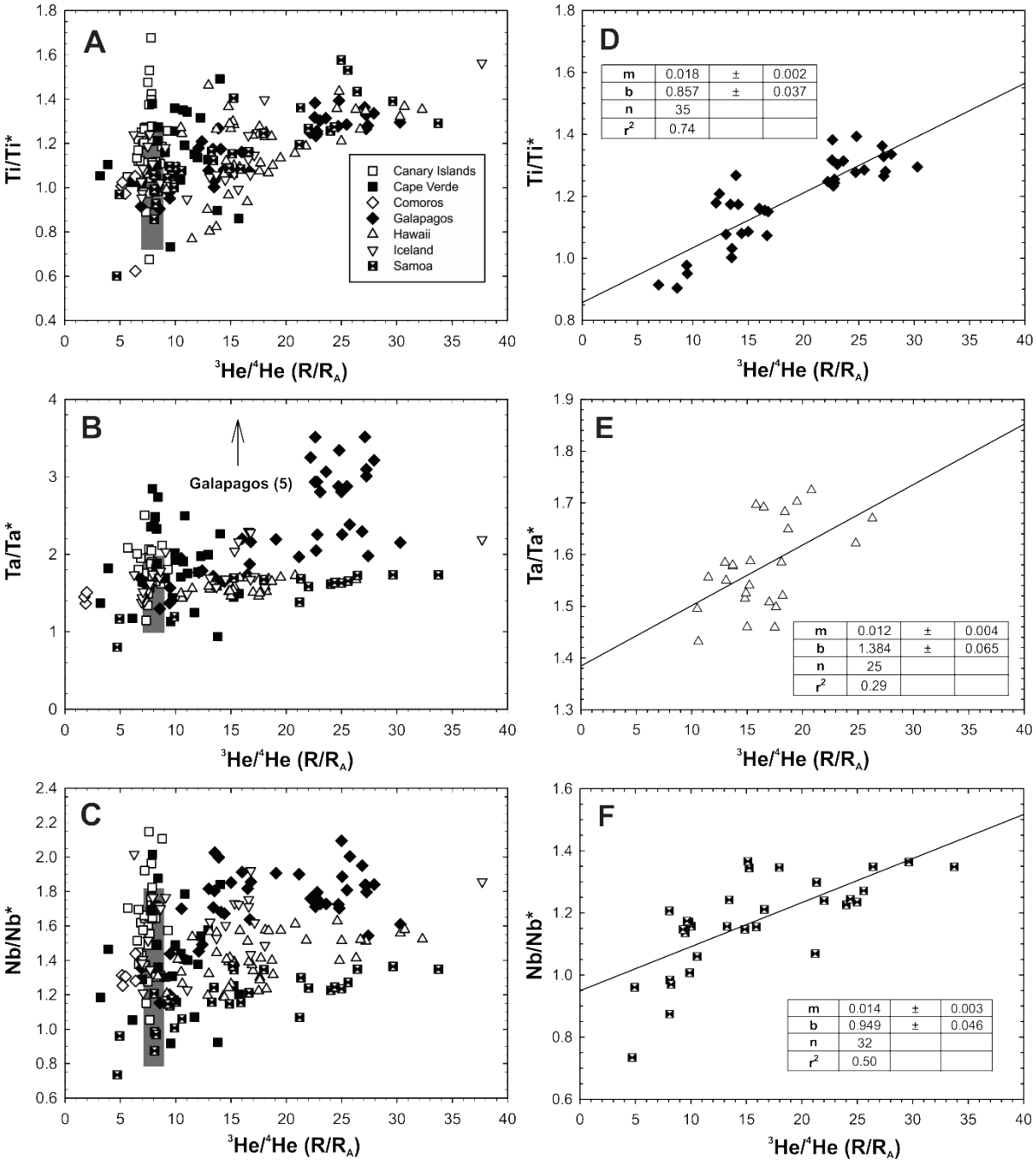

Figure 2.4: Compilations of $^{3}He/^{4}He$ versus (A) Ti/Ti*, (B) Ta/Ta* and (C) Nb/Nb* for a global dataset of OIB and examples of positive trends amongst arrays of single hotspots from (D) Galapagos, (E) Hawaii and (F) Samoa with bivariate least-squares regressions and statistics. MORB values are represented as a gray region in A-C and is taken as $^{3}He/^{4}He = 8 \pm 1R_A$ [Graham, 2002]; MORB trace element analyses are from Arevalo & McDonough [2010] and region represents 2σ deviation from average. Data sources are noted in *Supplementary Information*. Anomalous Ta/Ta* data from the Galapagos are reported in Naumann, et al. [2002] and Geist, et al. [2006].

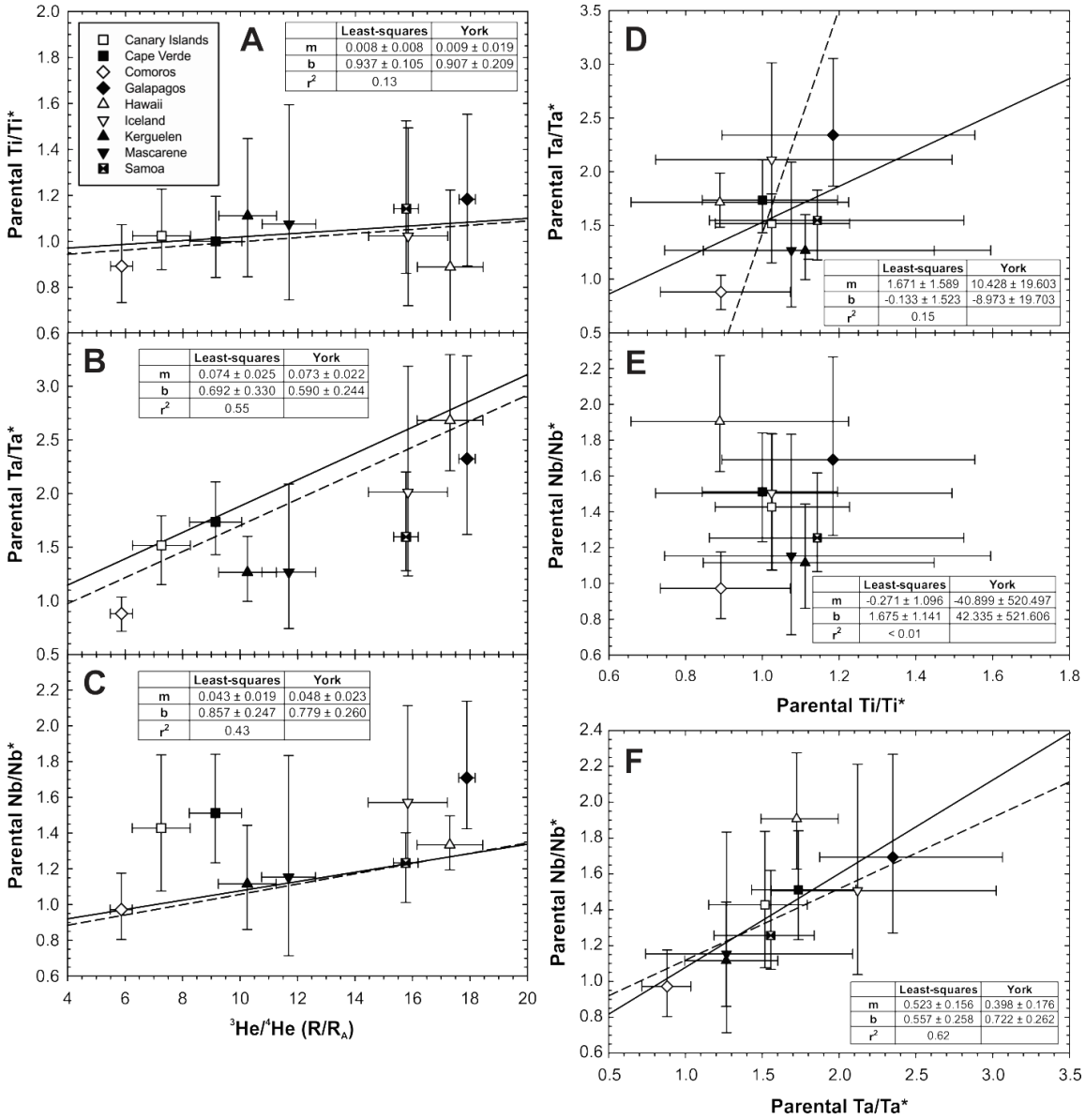

Figure 2.5: Calculated parental TITAN anomalies versus $^{3}He/^{4}He$ within individual OIB locations and correlations between parental TITAN anomalies. Calculated parental TITAN anomalies and error bars are determined by methods described in the text; $^{3}He/^{4}He$ values are averages and average 2σ deviations of compiled data. The most robust correlations are observed between $^{3}He/^{4}He$ and Ta anomalies. None of the correlations are sufficiently robust to link positive TITAN anomalies to a primitive component traced by He isotopes. York-type regressions (dashed) are calculated using the average of the asymmetric TITAN error bars; least-squares regressions (solid) are presented for comparison; regression lines are not show in panel E due to the low r^2 value

Figure 2.6: Model steps simulating stages of OIB volcanism and their effect on trace element geochemistry of idealized primitive mantle (PM) [McDonough & Sun, 1995]. Normalized to itself, PM initially appears as a flat line (A), and is then is subjected to 2% partial melting in the garnet stability field, resulting in the PM-normalized liquid composition in B. As the melt body ascends into the spinel stability field, spinel-residual melts homogenize with the original melt resulting in an overall composition as in C (3% cumulative partial melt; 20% in spinel stability field). This parental mantle magma ascends into a crustal magma chamber and is subjected to AFC processes with final liquid and crystal compostions shown in D after removal of 20 mass percent liquid. Theoretical composite rocks are then formed from mixtures of the residual, aphyric liquid and the precipitated minerals, generating a clinopyroxene- and olivine-phyric rock of varying phenocryst proportion shown in E. In the upper curve of E, representing 10 volume percent phenocrystic rock, Ti anomalies remain negative, and modest positive Ta and Nb anomalies are displayed. In the lower curve, representing a 50 volume percent phenocrystic rock, the Ti anomaly has increased dramatically, and Ta and Nb anomalies are within the ranges of many measured OIB. Model details are found in the text and further explanation, including calculation procedures and a list of model parameters, are found in *the Supplementary Information*.

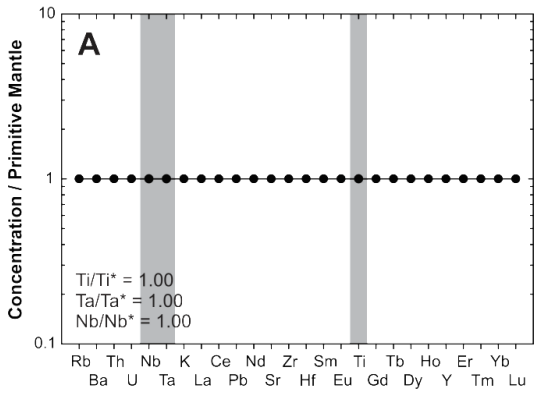
A
Concentration / Primitive Mantle
10
1
0.1
Ti/Ti* = 1.00
Ta/Ta* = 1.00
Nb/Nb* = 1.00
Rb Th Nb K Ce Nd Zr Sm Ti Tb Ho Er Yb
Ba U Ta La Pb Sr Hf Eu Gd Dy Y Tm Lu

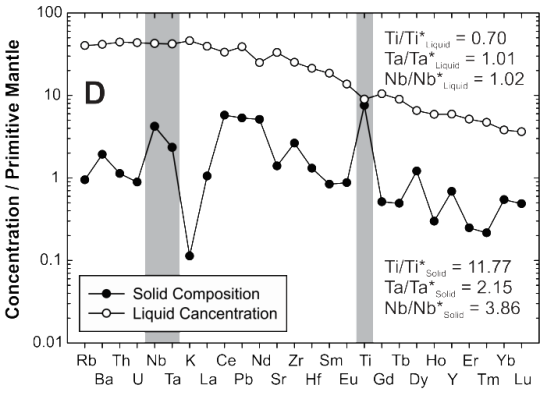
D
Concentration / Primitive Mantle
100
10
1
0.1
0.01
Ti/Ti*Liquid = 0.70
Ta/Ta*Liquid = 1.01
Nb/Nb*Liquid = 1.02
Ti/Ti*Solid = 11.77
Ta/Ta*Solid = 2.15
Nb/Nb*Solid = 3.86
Solid Composition
Liquid Cancentration
Rb Th Nb K Ce Nd Zr Sm Ti Tb Ho Er Yb
Ba U Ta La Pb Sr Hf Eu Gd Dy Y Tm Lu

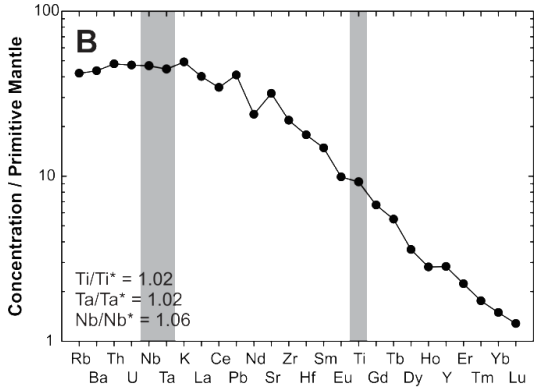
B
Concentration / Primitive Mantle
100
10
1
Ti/Ti* = 1.02
Ta/Ta* = 1.02
Nb/Nb* = 1.06
Rb Th Nb K Ce Nd Zr Sm Ti Tb Ho Er Yb
Ba U Ta La Pb Sr Hf Eu Gd Dy Y Tm Lu

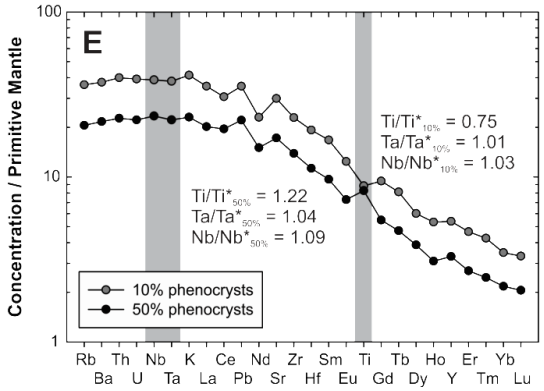
E
Concentration / Primitive Mantle
100
10
1
Ti/Ti*10% = 0.75
Ta/Ta*10% = 1.01
Nb/Nb*10% = 1.03
Ti/Ti*50% = 1.22
Ta/Ta*50% = 1.04
Nb/Nb*50% = 1.09
10% phenocrysts
50% phenocrysts
Rb Th Nb K Ce Nd Zr Sm Ti Tb Ho Er Yb
Ba U Ta La Pb Sr Hf Eu Gd Dy Y Tm Lu

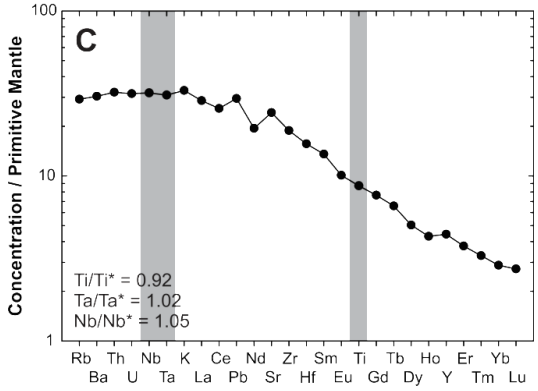
C
Concentration / Primitive Mantle
100
10
1
Ti/Ti* = 0.92
Ta/Ta* = 1.02
Nb/Nb* = 1.05
Rb Th Nb K Ce Nd Zr Sm Ti Tb Ho Er Yb
Ba U Ta La Pb Sr Hf Eu Gd Dy Y Tm Lu

Figure 2.7: Theoretical distributions of TITAN anomalies versus La/Yb, a common index of partial melting, according to numerical models of partial melting described in the text and in *Supplementary Information* and illustrated in **Figure 2.6**. Melting of primitive mantle (PM) and depleted MORB mantle (DMM) is simulated. Boxed decimals represent the fraction of melting in the garnet stability field along the solid lines they overlap and printed percentages represent the degree of partial melting along the dotted lines they abut. Panel (A) shows distributions of both Ti/Ti* (black lines) and Nb/Nb* (gray lines) as well as measured distributions in Icelandic lavas (black region – Ti/Ti*; gray region – Nb/Nb*, both within 2σ of hotspot average TITAN anomaly). Similar distributions are shown for Ta/Ta* (B) and for all TITAN anomalies after melting of DMM (C-E). Distributions of Icelandic lavas are similarly shown in shaded gray regions, however they are not shown in panel (E) because they span nearly the entire range of the plot. These measured ranges are due only in part to partial melting, so their correspondence to model bounds should not be narrowly interpreted. Tantalum anomalies uniquely show large changes in slope across a typical interval of OIB partial melting (0 – 10%) because Ta is significantly less incompatible in clinopyroxene at high pressures than either La or Th, generating initially lower Ta anomalies before continued partial melting dilutes this signature.

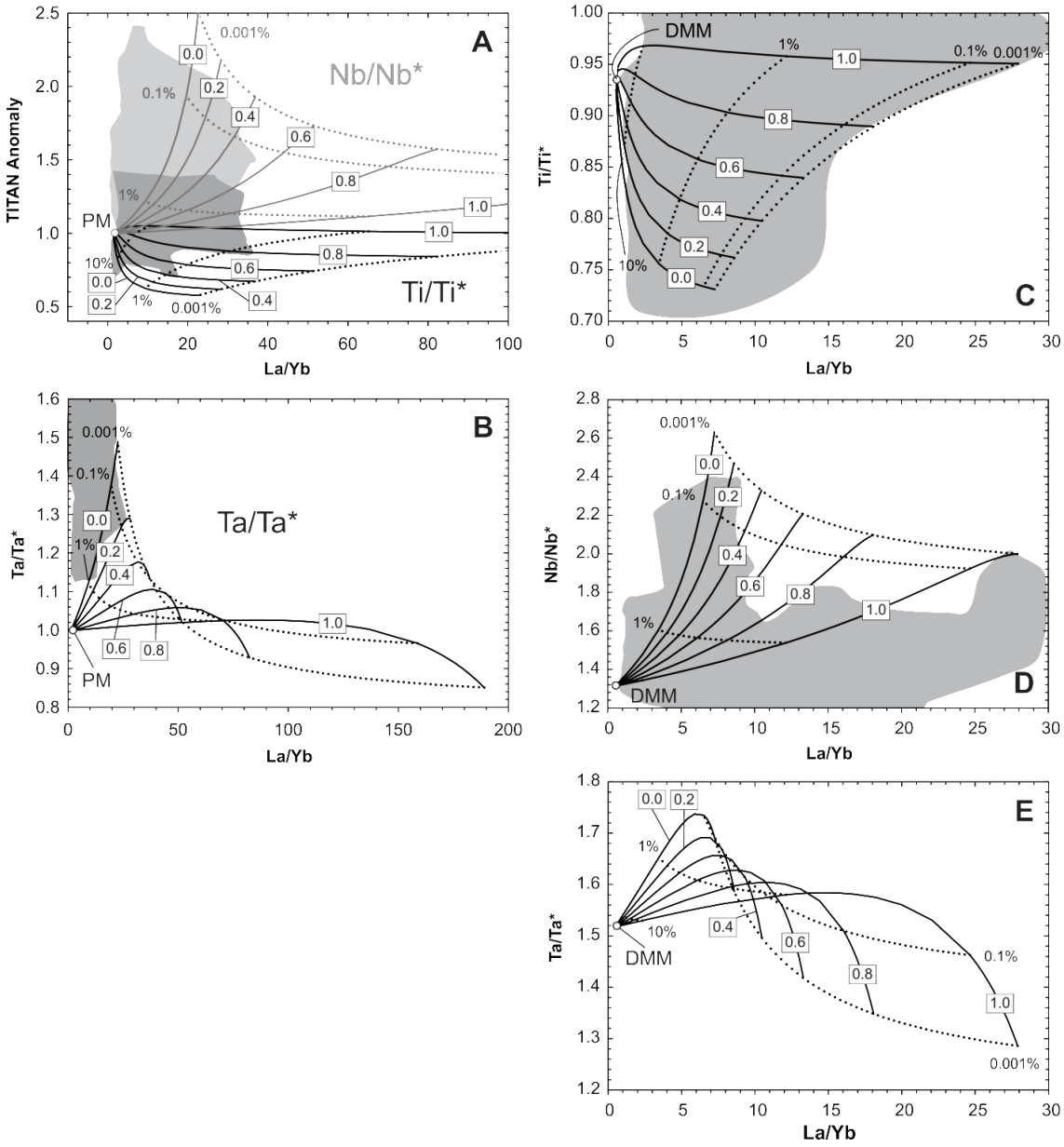
A
Nb/Nb*
Ti/Ti*
TITAN Anomaly
La/Yb
PM
0.001%
0.1%
1%
10%
0.0
0.2
0.4
0.6
0.8
1.0
B
Ta/Ta*
C
Ti/Ti*
DMM
D
Nb/Nb*
E

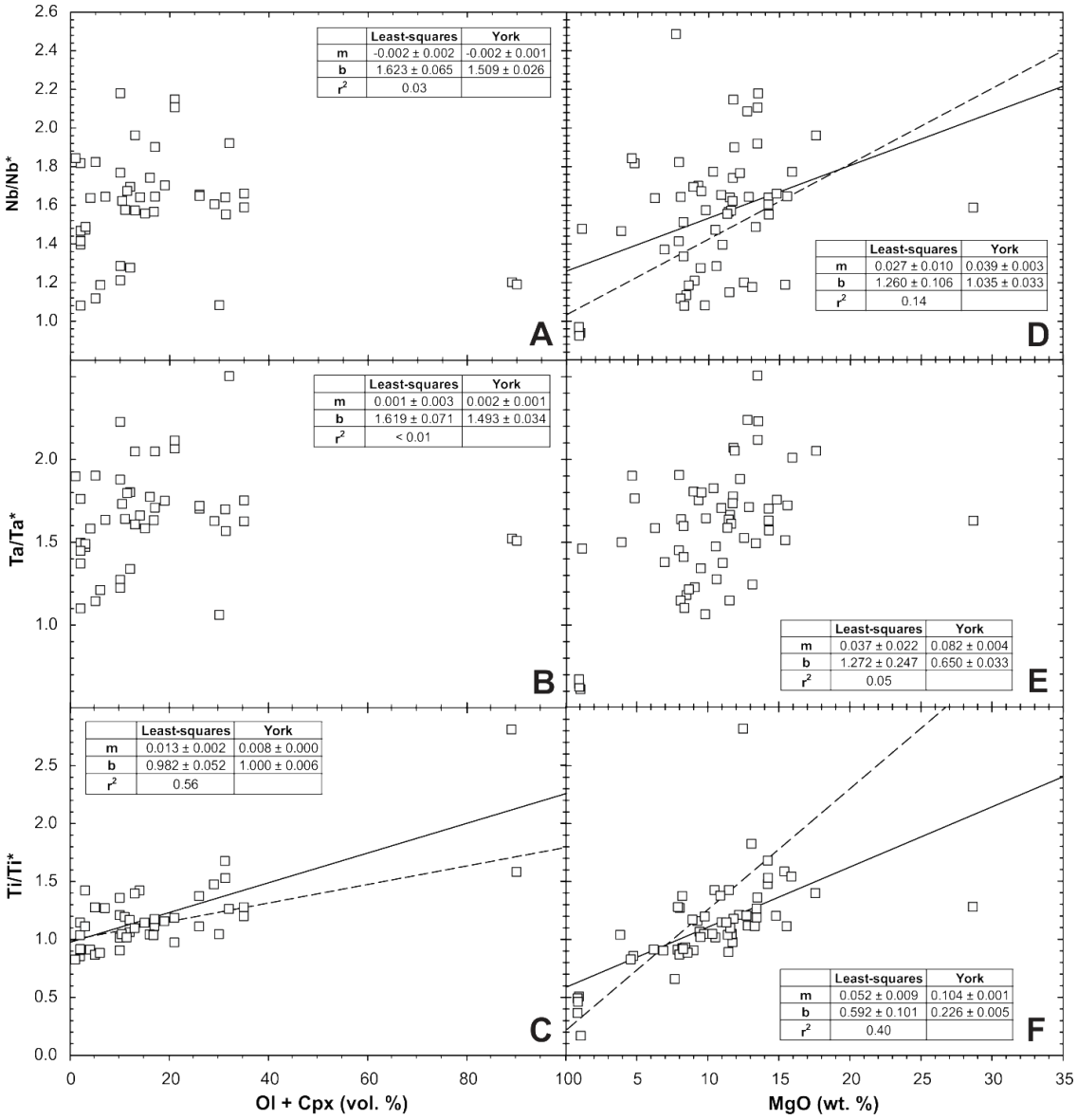

Figure 2.8: TITAN anomalies versus modal olivine and clinopyroxene and bulk rock MgO contents for OIB from the Canary Islands, a relatively low-$^{3}He/^{4}He$ hotspot [Day et al., 2010]. Titanium anomalies are the best correlated with modal mineralogy and MgO contents while Ta anomalies are least correlated with these parameters. The two points with the highest modal olivine and clinopyroxene in A-C and the corresponding points in D-F are olivine-clinopyroxene cumulate xenoliths. Many of the plotted samples contain oxide phases (spinel, chromite) as accessory mineral phases. Evolved samples lacking olivine and clinopyroxene are excluded from panels A-C. Tabulated statistics are shown for York-type (dashed) and least-squares (solid) regressions, but the regressions are only plotted if $r^2 > 0.10$.

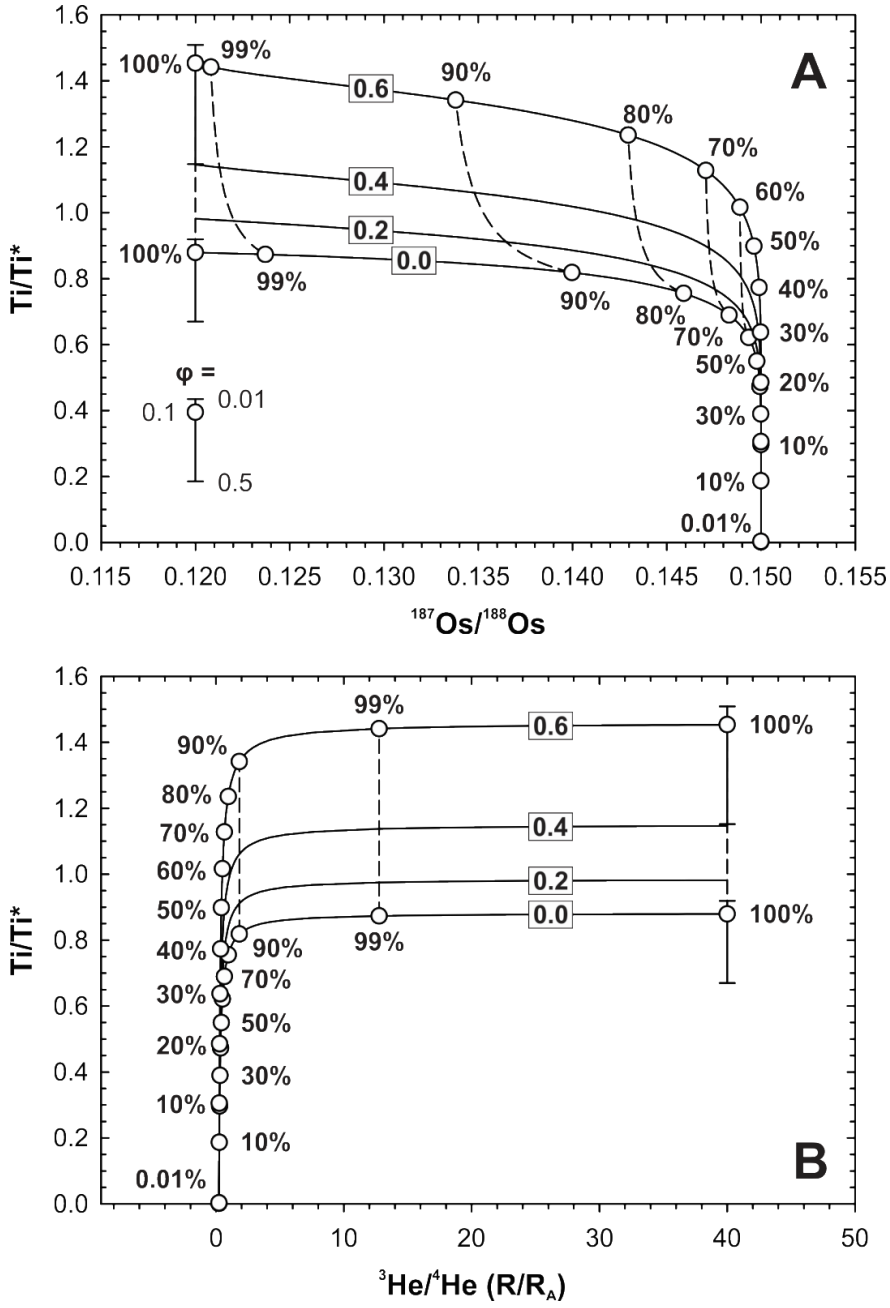

Figure 2.9: Model results for distributions of Ti anomalies versus $^{187}Os/^{188}Os$ and $^{3}He/^{4}He$. Boxed percentages refer to phenocryst accumulation (mass fraction) and unboxed percentages refer to the mass proportion of remaining magma after AFC. Total crystal accumulation in the magma chamber (φ) is fixed at 10 mass percent, "error bars" surrounding undifferentiated (100%) points depict the effect of changes in this parameter, as illustrated in panel A. For other model parameters, see *Supplementary Information***.** The model is meant to present a possible explanation for the coupling of particular ranges of Ti anomalies and $^{3}He/^{4}He$ or $^{187}Os/^{188}Os$ ratios; it is not intended to re-interpret literature data to represent ubiquitous crustal contamination.

References

Adam, J. and T. H. Green (1994), The effects of pressure and temperature on the partitioning of Ti, Sr and REE between amphibole, clinopyroxene and basanitic melts: Chemical Geology, 117, 219-233, doi:10.1016/0009-2541(94)90129-5.

Adam, J. and T. Green (2006), Trace element partitioning between mica- and amphibole-bearing garnet lherzolite and hydrous basanitic melt: 1. Experimental results and the investigation of controls on partitioning behavior: Contributions to Mineralogy and Petrology, 152, 1-17, doi:10.1007/s00410-006-0085-4.

Akimoto, S. and Y. Syono (1967), High pressure decomposition of some titanate spinels: Journal of Chemical Physics, 47, 1813-1817.

Anderson, D.L. (2005), Scoring hotspots: The plume and plate paradigms: Geological Society of America Special Paper 388, 31-54, doi:10.1130/2005.2388(04).

Arevalo, R. Jr. and W. F. McDonough (2010), Chemical variations and regional diversity observed in MORB: Chemical Geology, 271, 2010, 70-85, doi:10.1016/j.chemgeo.2009.12.013.

Barry, T. L., J. A. Pearce, P. T. Leat, I. L. Millar and A. P. le Roex (2006) Hf isotope evidence for selective mobility of high-field-strength elements in a subduction setting: South Sandwich Islands: Earth and Planetary Science Letters, 252, 223-244, doi:10.1016/j.epsl.2006.09.034.

Beattie, P. (1994), Systematics and energetics of trace-element partitioning between olivine and silicate melts: Implications for the nature of mineral/melt partitioning: Chemical Geology, 117, 57-71, doi:10.1016/0009-2541(94)90121-X.

Blichert-Toft, J., F. A. Frey and F. Albarède (1999), Hf isotope evidence for pelagic sediments in the source of Hawaiian basalts: Science, 285, 879-882, doi:10.1126/science.285.5429.879.

Bodinier, J.-L., C. Merlet, R. M. Bendini, F. Simien, M. Remaidi and C. J. Garrido (1996), Distribution of niobium, tanatulum, and other highly incompatible trace elements in the lithospheric mantle: The spinel paradox: Geochimica et Cosmochimica Acta, 60(3), 54/5-550, doi:10.1016/0016-7037(95)00431-9.

Castillo, P. R. (2012), Adakite petrogenesis: Lithos, 134-135, 304-316, doi:10.1016/j.lithos.2011.09.013.

Chauvel, C., A. W. Hofmann and P. Vidal (1992), HIMU-EM: The French Polynesian connection: Earth and Planetary Science Letters, 110, 99-119, doi:10.1016/0012-821X(92)90042-T.

Clague, D.A. and F.A. Frey (1982), Petrology and trace element geochemistry of the Honolulu Volcanics, Oahu: Implications for the oceanic mantle below Hawaii: Petrology, 23(3), 447-504, doi:10.1093/petrology/23.3.447.

Clarke, W. B., M. A. Beg and H. Craig (1969), Excess ^{3}He in the sea: Evidence for terrestrial primordial helium: Earth and Planetary Science Letters, 6, 213-220, doi:10.1016/0012-821X(69)90093-4.

Class, C., S.L. Goldstein and S.B. Shirey (2009), Osmium isotopes in Grande Comore lavas: a new extreme among EM-type mantle end members: Earth and Planetary Science Letters, 284, 219-227.

Condomines, M., Gronvold, K., Hooker, P.J., Muehlenbachs, K., O'Nions, R.K., Oskarsson, N., Oxburgh, E.R. (1983) Helium, oxygen, strontium and neodymium isotope relationships in Icelandic volcanoes, Earth and Planetary Science Letters, 66, 125-136.

Courtillot, V., A. Davaille, J. Besse and J. Stock (2003), Three distinct types of hotspots in the Earth's mantle: Earth and Planetary Science Letters, 205, 295-308, doi:10.1016/S0012-821X(02)01048-8.

Day, J. M. D., D. G. Pearson, C. G. Macpherson, D. Lowry and J.-C. Carracedo (2009), Pyroxenite-rich mantle formed by recycled oceanic lithosphere: Oxygen-osmium isotope evidence from Canary Island lavas: Geology, 37, 555-558, doi:10.1130/G25613A.1.

Day, J. M. D., D. G. Pearson, C. G. Macpherson, D. Lowry and J.-C. Carracedo (2010), Evidence for distinct proportions of subducted oceanic crust and lithosphere in HIMU-type mantle beneath El Hierro and La Palma, Canary Islands: Geochimica et Cosmochimica Acta, 74(22), 6565-6589, doi:10.1016/j.gca.2010.08.021.

Day, J. M. D. and D. R. Hilton (2011), Origin of ^{3}He/^{4}He ratios in HIMU-type basalts constrained from Canary Island lavas: Earth and Planetary Science Letters, 305, 226-234, doi:10.1016/j.epsl.2011.03.006.

Day, J. M. D. (2013), Hotspot volcanism and highly siderophile elements: Chemical Geology, 341, 50-74, doi:10.1016/j.chemgeo.2012.12.010.

Defant, M. J. and M. S. Drummond (1990), Derivation of some modern arc magmas by melting of young subducted lithosphere: Nature, 347, 662-665, doi:10.1038/347662a0.

Defant, M. J., T. E. Jackson, M. S. Drummond, J. Z. De Boer, H. Bellon, M. D. Feigenson, R. C. Maury and R. H. Stewart (1992), The geochemistry of young volcanism throughout western Panama and southeastern Costa Rica: an overview: Journal of the Geological Society of London, 149, 569-579, doi:10.1144/gsjs.149.4.05.69.

DePaolo, D. J. (1981), Trace element and isotopic effects of combined wall rock assimilation and fractional crystallization: Earth and Planetary Science Letters, 53, 189-202, doi:10.1016/0012-821X(81)90153-9.

Dixon, J.E., L. Leist, C. Langmuir and J.-G. Schilling (2002) Recycled dehydrated lithosphere observed in plume-influenced mid-ocean-ridge basalt: Nature, 420, 385-389, doi:10.1038/nature01215.

Doucet, S., D. Weis, J. S. Scoates, K. Nicolaysen, F. A. Frey and A. Giret (2002), The depleted mantle component in Kerguelen archipelago basalts: Petrogenesis of tholeiitic-transitional basalts from the Loranchet Peninsula: Journal of Petrology, 43(7), 1341-1366, doi:10.1093/petrology/43.7.1341.

Doucet, S., J.S. Scoates, D. Weis and A. Giret (2005) Constraining the components of the Kerguelen mantle plume: A Hf-Pb-Sr-Nd isotopic study of picrites and high-MgO basalts from the Kerguelen Archipelago: Geochemistry Geophysics Geosystems, 6(4), doi:10.1029/2004GC000806.

Drake, M. J. (1975), The oxidation state of europium as an indicator of oxygen fugacity: Geochimica et Cosmochimica Acta, 39, 55-64, doi:10.1016/0016-7037(75)90184-2.

Eggins, S. M., R. L. Rudnick and W. F. McDonough (1998), The composition of peridotites and their minerals: a laser-ablation ICP-MS study: Earth and Planetary Science Letters, 154, 53-71, doi:10.1016/S0012-821X(97)00195-7.

Eisele, J., M. Sharma, S. J. G. Galer, J. Blichert-Toft, C. W. Devey and A. W. Hofmann (2002), The role of sediment recycling in EM-1 inferred from Os, Pb, Hf, Nd, Sr isotope and trace element systematics of the Pitcairn hotspot: Earth and Planetary Science Letters, 196, 197-212, doi:10.1016/S0012-821X(01)00601-X.

Ewart, A. and W. L. Griffin (1994), Application of proton-microprobe data to trace-element partitioning in volcanic rocks: Chemical Geology, 117, 251-284, doi:10.1016/0009-2541(94)90131-7.

Farley, K. A., J. H. Natland and H. Craig (1992), Binary mixing of enriched and undegassed (primitive?) mantle components (He, Sr, Nd, Pb) in Samoan lavas: Earth and Planetary Science Letters, 111, 183-199, doi:10.1016/0012-821X(92)90178-X.

Fitton, J.G., A.D. Saunders, M.J. Norry, B.S. Hardarson and R.N. Taylor (1997), Thermal and chemical structure of the Iceland plume: Earth and Planetary Science Letters, 153, 197-208, doi:10.1016/S0012-821X(97)00170-2.

Fujimaki, H., M. Tatsumoto and K.-I. Aoki (1984), Partition coefficients of Hf, Zr, and REE between phenocrysts and groundmasses: Journal of Geophysical Research, 89, B662-B672, doi:10.1029/JB089iS02p0B662.

Gaetani, G.A., P.D. Asimow and E.M. Stolper (2008) A model for rutile saturation in silicate melts with applications to eclogite partial melting in subduction zones and mantle plumes: Earth and Planetary Science Letters, 272, 720-279, doi:10.1016/j.epsl.2008.06.002.

Gast, P. W., G. R. Tilton and C. Hedge (1964), Isotopic composition of lead and strontium from Ascension and Gough Islands: Science, 145, 1181-1185, doi:10.1126/science.145.3637.1181.

Gast, P. W. (1968), Trace element fractionation and the origin of tholeiitic and alkaline magma types: Geochimica et Cosmochimica Acta, 32, 1057-1086,doi:10.1016/0016-7037(68)90108-7.

Geist, D.J., D.J. Fornari, M.D. Kurz, K.S. Harpp, S.A. Soule, M.R. Perfit and A.M. Koleszar (2006), Submarine Fernandina: Magmatism at the leading edge of the Galápagos hot spot: Geochemistry, Geophysics, Geosystems, 7(12), 27 pp, doi:10.1029/2006GC001290.

Graham, D. W. (2002), Noble gas isotope geochemistry of mid-ocean ridge and ocean island basalts: characterization of mantle source reservoirs. *In:* Porcelli, D., C. J. Ballentine and R. Wieler (eds.), Noble gases in geochemistry and cosmochemistry: Reviews in Mineralogy and Geochemistry, 47, 247-319, doi:10.2138/rmg.2002.47.8.

Green, T.H., J.D. Blundy, J. Adam and G.M. Yaxley (2000), SIMS determination of trace element partition coefficients between garnet, clinopyroxene and hydrous basaltic liquids at 2-7.5 GPa and 1080-1200°C: Lithos, 53, 165-187, doi:10.1016/S0024-4937(00)00023-2.

Gurenko, A. A., T. H. Hansteen and H.-U. Schmincke (1996), Evolution of parental magmas of Miocene shield basalts of Gran Canaria (Canary Islands): constraints from crystal, melt and fluid inclusions in minerals: Contributions to Mineralogy and Petrology, 124, 422-435, doi:10.1007/s004100050201.

Halliday, A. N., D.-C. Lee, S. Tommasini, G. R. Davies, C. R. Paslick, J. G. Fitton and D. E. James (1995), Incompatible trace elements in OIB and MORB and source

enrichment in the sub-oceanic mantle: Earth and Planetary Science Letters, 133, 379-395, doi:10.1016/0012-821X(95)00097-V.

Hart, S. R. and C. Brooks (1974), Clinopyroxene-matrix partitioning of K, Rb, Cs, Sr and Ba: Geochimica et Cosmochimica Acta, 38, 1799-1806, doi:10.1016/0016-7037(74)90163-X.

Hart, S.R., E.H. Hauri, L.A. Oschmann and J.A. Whitehead (1992), Mantle plumes and entrainment: Isotopic evidence: Science, 256, 517-520, doi:10.1126/science.256.5056.517.

Hart, S.R. and T. Dunn (1993), Experimental Cpx/melt partitioning of 24 trace elements: Contributions to Mineralogy and Petrology, 113, 1-8, doi:10.1007/BF00320827.Hart, S.R., J. Bluszajn, W.E. LeMasurier and D.C. Rex (1997) Hobbs Coast Cenozoic volcanism: Implications for the West Antarctic rift system: Chemical Geology, 139, 223-248, doi:10.1016/S0009-2541(97)00037-5.

Hart, S. R. and G. A. Gaetani (2006), Mantle Pb paradoxes: the sulfide solution: Contributions to Mineralogy and Petrology, 152, 295-308, doi:10.1007/s00410-006-0108-1.

Hart, S.R. and M.G. Jackson (2014), Ta'u and Ofu/Olosega volcanoes: The "twin sisters" of Samoa, their P, T, X melting regime, and global implications: Geochemistry, Geophysics, Geosystems, 15, doi:10.1002/2013GC006221.

Hauri, E. H. (1996), Major-element variability in the Hawaiian mantle plume: Nature, 382, 415-419, doi:10.1038/382415a0.

Hauri, E.H., T.P. Wagner and T.L. Grove (1994), Experimental and natural partitioning of Th, U, Pb and other trace elements between garnet, clinopyroxene and basaltic melts: Chemical Geology, 117, 149-166, doi:10.1016/0009-2541(94)90126-0.

Hauri, E. H. and S. R. Hart (1997), Rhenium abundances and systematics in oceanic basalts: Chemical Geology, 139, 185-205, doi:10.1016/S0009-2541(97)00035-1.

Heber, V. S., R. A. Brooker, S. P. Kelley and B. J. Wood (2007), Crystal-melt partitioning of noble gases (helium, neon, argon, krypton, and xenon) for olivine and clinopyroxene: Geochimica et Cosmochimica Acta, 71, 1041-1061, doi: 10.1016/j.gca.2006.11.010.

Higuchi, H. and H. Nagasawa (1969) Partition of trace elements between rock-forming minerals and the host volcanic rocks: Earth and Planetary Science Letters, 7(3), 281-287, doi:10.1016/0012-821X(69)90066-1.

Hirose, K. and I. Kushiro (1993), Partial melting of dry peridotites at high pressures: determination of compositions of melts segregated from peridotite using aggregates of diamonds: Earth and Planetary Science Letters, 114: 477-489, doi:10.1016/0012-821X(93)90077-M.

Hofmann, A.W. and W.M. White (1982), Mantle plumes from ancient oceanic crust: Earth and Planetary Science Letters, 57, 421-436, doi:10.1016/0012-821X(82)90161-3.

Hofmann, A. W., K. P. Jochum, M. Seufert and W. M. White (1986), Nb and Pb in oceanic basalts: new constraints on mantle evolution: Earth and Planetary Science Letters, 79, 33-45, doi:10.1016/0012-821X(86)90038-5.

Hofmann, A. W. (2003), Sampling mantle heterogeneity through oceanic basalts: isotopes and trace elements. *In:* Carlson, R.W., Holland, H.D. and Turekian, K.K. (eds.) Treatise on Geochemistry: The mantle and core, 66-101, Elsevier, New York., doi:10.1016/B0-08-043751-6/02123-X.

Honda, M. and J. D. Woodhead (2005), A primordial solar-neon enriched component in the source of EM-I-type ocean island basalts from the Pitcairn seamounts, Polynesia: Earth and Planetary Science Letters, 236, 597-612, doi: 10.1016/j.epsl.05.038.

Jackson, M. G., S. R. Hart, A. A. P. Koppers, H. Staudigel, J. Konter, J. Blusztajn, M. Kurz and J. A. Russell (2007), The return of subducted continental crust in Samoan lavas: Nature, 448, 684-687, doi:10.1038/nature06048.

Jackson, M. G., S. R. Hart, A. E. Saal, N. Shimizu, M. D. Kurz, J. S. Blusztajn, A. C. Skovgaard (2008), Globally elevated titanium, tantalum, and niobium (TITAN) in ocean island basalts with high $^{3}He/^{4}He$: Geochemistry, Geophysics, Geosystems, 9, Q04027, doi:10.1029/2007GC001876.

Jochum, K. P, A. W. Hofmann, E. Ito, H. M. Seufert and W. M. White (1983), K, U and Th in mid-ocean ridge basalt glasses and heat production, K/U and K/Rb in the mantle: Nature, 306, 431-436, doi:10.1038/306431a0.

Johnson, K.T.M. (1994), Experimental cpx/ and garnet/melt partitioning of REE and other trace elements at high pressures: petrogenetic implications: Mineralogical Magazine, 58, 454-455.

Jenner, G. A., H. P. Longerich, S. E. Jackson and B. J. Fryer (1990), ICP-MS – A powerful tool for high-precision trace-element analysis in Earth sciences: Evidence from analysis of selected U.S.G.S. reference samples: Chemical Geology, 83, 133-148, doi:10.1016/0009-2541(90)90145-W.

Jenner, G.A., S.F. Foley, S.E. Jackson, T.H. Green, B.J. Fryer and H.P. Longerich (1994) Determination of partition coefficients for trace elements in high pressure-temperature experimental run products by laser ablation microprobe-inductively coupled plasma-mass spectrometry (LAM-ICP-MS): Geochimica et Cosmochimica Acta, 58, 5099-5103, doi:10.1016/0016-7037(93)90611-Y.

Jenner, F. E. and H. St.C. O'Neill (2012), Analysis of 60 elements in 616 ocean floor basaltic glasses: Geochemistry Geophysics Geosystems, 13(1), 11 pp, doi:10.1029/2012GC004088.

Kato, T., A. E. Ringwood and T. Irifune (1988), Experimental determination of element partitioning between silicate perovskites, garnets and liquids: constraints on early differentiation of the mantle: Earth and Planetary Science Letters, 89, 123-145, doi:10.1016/0012-821X(88)90038-6.

Johnson, K.T.M. (1994), Experimental cpx/ and garnet/melt partitioning of REE and other trace elements at high pressures: petrogenetic implications: Mineralogical Magazine, 58, 454-455.

Klein, E. M. and C. H. Langmuir (1987), Global correlations of ocean ridge basalt chemistry with axial depth and crustal thickness: Journal of Geophysical Research, 92(B8), 8089-8115, doi:10.1029/JB092iB08p08089.

Koornneef, J. M., A. Stracke, B. Bourdon, M. A. Meier, K. P. Jochum, B. Stoll and K. Grönvold (2012), Melting of a two-component source beneath Iceland: Journal of Petrology, 53(1), 127-157, doi:10.1093/petrology.egr059.

Lemarchand, F., B. Villemant and G. Calais (1987), Trace element distribution coefficients in alkaline series: Geochimica et Cosmochimica Acta, 51, 1071-1081, doi:10.1016/0016-7037(87)90201-8.

Lupton, J. E. and H. Craig (1975), Excess ^{3}He in oceanic basalts: evidence for terrestrial primordial helium: Earth and Planetary Science Letters, 26, 133-139, doi:10.1016/0012-821X(75)90080-1.

Macdonald, G. A. and T. Katsura (1964), Chemical composition of Hawaiian lavas: Journal of Petrology, 5(1), 82-133, doi:10.1093/petrology/5.1.82.

Matsui, Y., N. Onuma, H. Nagasawa, H. Higuchi and S. Banno (1977), Crystal structure control in trace element partition between crystal and magma: Tectonics, 100, 315-324.

McDonough, W. F. (1991), Partial melting of subducted oceanic crust and isolation of its residual eclogitic lithology: Philosophical Transactions of the Royal Society of London, 335, 181-192, doi:10.1098/rsta.1991.0055.

McDonough, W.F. (2000), The composition of the Earth, *in*: Teisseyre, R. and E. Majewski (eds.), Earthquake thermodynamics and phase transformations in the Earth's interior: International Geophysics Series, 76, 3-23.

McDonough, W. F., H.-G. Stosch and N. G. Ware (1992), Distribution of titanium and the rare earth elements between peridotitic minerals: Contributions to Mineralogy and Petrology, 110, 321-328, doi:10.1007/BF00310747.

McDonough, W. F. and S.-S. Sun (1995), The composition of the Earth: Chemical Geology, 120, 223-253, doi:10.1016/0009-2541(94)00140-4.

McKenzie, D. and M. J. Bickle (1988), The volume and composition of melt generated by extension of the lithosphere: Journal of Petrology, 29(3), 625-679, doi:10.1093/petrology/29.3.625.

McKenzie, D. and R. K. O'Nions (1991), Partial melt distributions from inversion of rare earth element concentrations: Journal of Petrology, 32(5), 1021-1091, doi:10.1093/petrology/32.5.1021.

Moore, J. G., A. Clague and W. R. Normark (1982), Diverse basalt types from Loihi seamount, Hawaii: Geology, 10, 88-92, doi:10.1130/0091-7613(1982)10<88:DBTFLS.2.0.CO;2.

Moreira, M. and M. D. Kurz (2001), Subducted oceanic lithosphere and the origin of the 'high μ' basalt helium isotopic signature: Earth and Planetary Science Letters, 189, 49-57, doi:10.1016/S0012-821X(01)00341-5.

Nash, W. P and H. R. Crecraft (1985), Partition Coefficients for trace elements in silicic magmas: Geochimica et Cosmochimica Acta, 49, 2309-2322, doi:10.1016/0016-7037(85)90231-5.

Naumann, T., D. Geist and M. Kurz (2002), Petrology and Geochemistry of Volcán Cerro Azul: Petrologic diversity among the Western Galápagos volcanoes: Journal of Petrology, 32(5), 859-883, doi:10.1093/petrology/43.5.859.

Nielsen, R. L. (1992), BIGD.FOR: A FORTRAN program to calculate trace-element partition coefficients for natural mafic and intermediate composition magmas: Computers & Geosciences, 18(7), 773-788, doi:10.1016/..98-3004(92)90024-L.

Nielsen, R.L., W.E. Gallahan and F. Newberger (1992), Experimentally determined mineral-melt partition coefficients for Sc, Y and REE for olivine, orthopyroxene, pigeonite, magnetite and ilmenite: Contributions to Mineralogy and Petrology, 110, 488-499, doi:10.1007/BF00344083.

Nikogosian, I. K. and Sobolev, A. V. (1997), Ion-microprobe analysis of melt Inclusions in olivine: experience in estimating the olivine-melt partition coefficients of trace elements: Geochemistry International 35: 119-126.

Nishimura, K. (2012), A mathematical model of trace element and isotopic behavior during simultaneous assimilation and imperfect fractional crystallization: Contributions to Mineralogy and Petrology, 164, 427-440, doi:10.1007/s00410-012-0745.

Niu, Y. and M. J. O'Hara (2008), Global correlations of ocean ridge basalt chemistry with axial depth: a new perspective: Journal of Petrology, 49(4), 633-664, doi:10.1093/petrology.egm051.

Okamoto, K. (1979), Geochemical study on magmatic differentiation of Asama Volcano, central Japan. Journal of the Geological Society of Japan 85(8): 525-535.

Oxburgh, E. R. (1964), Petrological evidence for the presence of amphibole in the upper mantle and its petrogenetic and geophysical implications: Geological Magazine, 101(1), 19 pp, doi:10.1017/S001675680004841X.

Pearce, J. A. (1983), Role of sub-continental lithosphere in magma genesis at active continental margins: in Hawkesworth, C.J. and M.J. Norry (eds.), Continental basalts and mantle xenoliths: Shiva, Nantwich, 230-249.

Pearce, J. A., P. E. Baker, P. K. Harvey and I. W. Luff (1995), Geochemical evidence for subduction fluxes, mantle melting and fractional crystallization beneath the South Sandwich island arc: Journal of Petrology, 36(4), 1073-1109, doi:10.1093/petrology/36.4.1073.

Peate, D.W., J.A. Baker, S.P. Jakobsson, T.E. Waight, A.J.R. Kent, N.V. Grassineau and A.C. Skovgaard (2009) Historic magmatism on the Reykjanes Peninsula, Iceland: a snap-shot of melt generation at a ridge segment: Contributions to Mineralogy and Petrology, 157, 359-382, doi:10.1007/s00410-008-0339-4.Perfit, M. R., D. A. Gust, A. E. Bence, R. J. Arculus and S. R. Taylor (1980), Chemical characteristics of island-arc basalts: implications for mantle sources: Chemical Geology, 30: 227-256, doi:10.1016/0009-2541(80)90107-2.

Powell, R. (1984), Inversion of the assimilation and fractional crystallization (AFC) equations; characterization of contaminants from isotope and trace element relationships in volcanic suites: Journal of the Geological Society, 141, 447-452, doi:10.1144/gsjgs.141.3.0447.

Prytulak, J. and T. Elliott (2007), TiO_2 enrichment in ocean island basalts: Earth and Planetary Science Letters, 263, 388-403, doi:10.1016/k.epsl.2007.09.015.

Reisberg, L., Zindler, A., Marcantonio, F., White, W., Wyman, D., Weaver, B., 1993. Os isotope systematics in ocean island basalts. Earth and Planetary Science Letters, 120, 149-167.

Roeder, P. L. and R. F. Emslie (1970), Olivine-liquid equilibrium: Contributions to Mineralogy and Petrology, 29, 275-289, doi:10.1007/BF00371276.

Rudnick, R.L., M. Barth, I. Horn and W.F. McDonough (2000) Rutile-bearing refractory eclogites: Missing link between continents and depleted mantle: Science, 287, 278-281, doi:10.112/science.287.5451.278.

Saal, A.E., M.D. Kurz, S.R. Hart, J.S. Blusztajn, J. Blichert-Toft, Y. Liang and D.J. Geist (2007), The role of lithospheric gabbros on the composition of Galapagos lavas: Earth and Planetary Science Letters, 257, 391-406, doi:10.1016/j.epsl.2007.02.040.

Schilling, J.-G. and J. W. Winchester (1969), Rare earth contribution to the origin of Hawaiian lavas: Contributions to Mineralogy and Petrology, 23, 27-37, doi:10.1007/BF00371330.

Schilling, J.-G. (1985), Upper mantle heterogeneities and dynamics: Nature, 314, 62-67, doi:10.1038/314062a0.

Schnetzler, C.C. and J.A. Philpotts (1970) Partition coefficients of rare-earth elements between igneous matrix material and rock-forming mineral phenocrysts—II: Geochimica et Cosmochimica Acta, 34(3), 331-340, doi:10.1016/0016-7037(70)90110-9.

Shaw, D.M. (1970), Trace element fractionation during anatexis: Geochimica et Cosmochimica Acta, 34, 237-243, doi:10.1016/0016-7037(0)90009-8.

Skulski, T., W. Minarik and E.B. Watson (1994), High-pressure experimental trace-element partitioning between clinopyroxene and basaltic melts: Chemical Geology, 117, 127-147.

Sobolev, A. V., A. A. Migdisov and M. V. Portnyagin (1996), Incompatible element partitioning between clinopyroxene and basalt liquid revealed by the study of melt inclusions in minerals from Troodos Lavas, Cyprus: Petrology, 4(3), 307-317.

Sobolev, A. V., A. W. Hofmann, S. V. Sobolev and I. K. Nikogosian (2005), An olivine-free mantle source of Hawaiian shield basalts: Nature, 434, 590-597, doi:10.1038/nature03411.

Sobolev, A. V., A. W. Hofmann, D. V. Kuzmin, G. M. Yaxley, N. T. Arndt, S.-L. Chung, L. V. Danyushevsky, T. Elliott, F. A. Frey, M. O. Garcia, A. A. Gurenko, V. S. Kamenetsky, A .C. Kerr, N. A. Krivolutskaya, V. V Matvienkov, I. K. Nikogosian, A. Rocholl, I. A. Sigurdsson, N. M. Sushchevskaya and M. Teklay (2007), The

amount of recycled crust in sources of mantle-derived melts: Science, 316, 412-418, doi: 10.1126/science.1138113.

Stracke, A. and B. Bourdon (2009), The importance of melt extraction for tracing mantle heterogeneity: Geochimica et Cosmochimica Acta, 73, 218-238, doi:10.1016/j.gca.2008.10.015.

Stracke, A. (2012), Earth's heterogeneous mantle: A product of convection-driven interaction between crust and mantle: Chemical Geology, 330-331: 274-299, doi:10.1016/j.chemgeo.2012.08.007.

Stimac, J. and D. Hickmott (1994), Trace-element partition coefficients for ilmenite, orthopyroxene and pyrrhotite in rhyolite determined by micro-PIXE analysis: Chemical Geology, 117, 313-330, doi:10.1016/0009-2541(94)90134-1.

Sudo, A. and Y. Tatsumi (1990), Phlogopite and K-amphibole in the upper mantle: implication for magma genesis in subduction zones: Geophysical Research Letters, 17(1), 29-32, doi:10.1029/GL017i001p00029.

Sun, S.-S. (1980), Lead isotopic study of young volcanic rocks from mid-ocean ridges, ocean islands and island arcs: Philosophical Transactions of the Royal Society of London, 297, 409-445, doi:10.1098/rsta.1080.0224.

Tatsumi, Y. (1989), Migration of fluid phases and genesis of basalt magmas in subduction zones: Journal of Geophysical Research, 94(B4), 4697-4707, doi:10.1029/JB094iB04p04697.

Tuff, J. and S.A. Gibson (2007), Trace-element partitioning between garnet, clinopyroxene and Fe-rich picritic melts at 3 to 7 GPa: Contributions to Mineralogy and Petrology, 153(4), 369-387, doi:10.1007/s00410-006-0152-x.

Villemant, B., H. Jaffrezic, J.-L. Joron and M. Treuil (1981), Distribution coefficients of major and trace element; fractional crystallization in the alkali basalt series of Chaine des Puys (Massif Central, France): Geochimica et Cosmochimica Acta, 45, 1997-2016, doi:10.1016/0016-7037(81)90055-7.

Watson, S. and D. McKenzie (1991), Melt generation by plumes: A study of Hawaiian volcanism: Journal of Petrology, 32(3), 501-537, doi:10.1093/petrology/32.3.501.

Weaver, B. L. (1990), Geochemistry of highly-undersaturated ocean island basalt suites from the South Atlantic Ocean: Fernando de Noronha and Trinidade islands: Contributions to Mineralogy and Petrology, 105, 502-515, doi:10.1007/BF00302491.

Workman, R. K., S. R. Hart, M. Jackson, M. Regelous, K. A. Farley, J. Blusztajn, M. Kurz and H. Staudigel (2004), Recycled metasomatized lithosphere as the origin of the enriched mantle II (EM2) end-member: Evidence from the Samoan volcanic chain: Geochemistry Geophysics Geosystems, 5(4), 44 pp, doi:10.1029/2003GC000623.

Workman, R. K. and S. R. Hart (2005), Major and trace element composition of the depleted MORB mantle (DMM): Earth and Planetary Science Letters, 231, 53-72, doi:10.1016/j.epsl.2004.12.005.

White, W. M. (2010), Ocean island basalts and mantle plumes: The geochemical perspective: Annual Review of Earth and Planetary Sciences, 38, 113-160, doi:10.1146/annurev-earth-040809-152450.

Willbold, M. and A. Stracke (2006), Trace element composition of mantle end-members: Implications for recycling of oceanic and upper and lower continental crust: Geochemistry Geophysics Geosystems, 7(4), 30 pp, doi:10.1029/2005GC001005.

Woodhead, J. D. (1996), Extreme HIMU in an oceanic setting: the geochemistry of Mangaia Island (Polynesia), and temporal evolution of the Cook-Austral hotspot: Journal of Volcanology and Geothermal Research, 72, 1-19, doi:10.1016/0377-0273(96)0002-9.

Yogodzinski, G. M., R. W. Kay, O. N. Volynets, A. V. Koloskov and S.M. Kay (1995), Magnesian andesite in the western Aleutian Komandorsky region: Implications for slab melting and processes in the mantle wedge: Geological Society of America Bulletin, 107(5), 505-519, doi:10.1130/0016-7606(1995)107,0505:MAITWA.2.3.CO;2.

Yogodzinski, G. M. and P.B. Kelemen (1998), Slab melting in the Aleutians: implications of an ion probe study of clinopyroxene in primitive adakite and basalt: Earth and Planetary Science Letters, 158, 53-65, doi:10.1016/S0012-821X(98)00041-7.

Zack, T. and R. Brumm (1998), Ilmenite/liquid partition coefficients of 26 trace elements determined through ilmenite/clinopyroxene partitioning in garnet pyroxenite, *in:* Gurney, J.J., J.L. Gurney, M.D. Pascoe and S.H. Richardson (eds.) 7th International Kimberlite Conference, Red Roof Design, Cape Town, 986-988.

Zack, T. and T. John (2007), An evaluation of reactive fluid flow and trace element mobility in subducting slabs: Chemical Geology, 239, 199-216, doi:10.1016/j.chemgeo.2006.10.020.

Zindler, A. and S. Hart (1986), Chemical geodynamics: Annual Review of Earth and Planetary Sciences, 14, 493-571.

Supplementary Information

2.6 Data sources for OIB compilation.

References are indexed to hotspot localities in **Table 2.2**.

[1] Gurenko, A. A., K. A. Hoernle, F. Hauff, H.-U. Schmincke, D. Han, Y.N. Miura and I. Kaneoka (2006), Major, trace element and Nd-Sr-Pb-O-He-Ar isotope signatures of shield stage lavas from the central and western Canary Islands: Insights into mantle and crustal processes: Chemical Geology, 233, 75-112, doi:10.1016/j.chemgeo.2006.02.016.

[2] Hoernle, K. J. and G. R. Tilton (1991), Sr-Nd-Pb isotope data for Fuerteventura (Canary Islands) basal complex and subaerial volcanics: applications to magma genesis and evolution: Schweizerische mineralogiache und petrographische Mittellungen, 71, 3-18, doi:10.5169/seals-54342.

[3] Neumann, E.-R., E. Wulff-Pedersen, S. L. Simonsen, N. J. Pearson, J. Marti and J. Mitjavila (1999), Evidence for fractional crystallization of periodically refilled magma chambers in Tenerife, Canary Islands: Journal of Petrology, 40(7), 1089-1123, doi:10.1093/petroj/40.7.1089.

[4] Day, J. M. D., D. G. Pearson, C. G. Macpherson, D. Lowry and J. C. Carracedo (2010), Evidence for distinct proportions of subducted oceanic crust and lithosphere in HIMU-type mantle beneath El Hierro and La Palma, Canary Islands: Geochimca et Cosmochimica Acta, 74(22), 6565-6589, doi:10.1016/j.gca.2010.08.021.

[5] Day, J. M. D. and D. R. Hilton (2011), Origin of $^{3}He/^{4}He$ ratios in HIMU-type basalts constrained from Canary Island lavas: Earth and Planetary Science Letters, 305: 226-234, doi:10.1016/j.epsl.2011.03.006.

[6] Vance, D., J. O. H. Stone and R. K. O'Nions (1989), He, Sr and Nd isotopes in xenoliths from Hawaii and other oceanic islands: Earth and Planetary Science Letters, 96, 147-160, dor:10.1016/0012-821X(89)90129-5.

[7] Hilton, D. R., C. G. Macpherson and T. R. Elliott (2000), Helium isotope ratios in mafic phenocrysts and geothermal fluids from La Palma, the Canary Islands (Spain): Implications for HIMU mantle sources: Geochimica et Cosmochimica Acta, 64(12), 2119-2132, doi:10.1016/S0016-7037(00)00358-6.

[8] Schmincke, H.-U. and B. Segschneider (1998), 12. Shallow submarine to emergent basaltic shield volcanism of Gran Canaria: Evidence from drilling into the volcanic apron, *In*: Weaver, P.P.E., H.-U. Schmincke, J.V. Firth and W. Duffield (Eds.),

Proceedings of the Ocean Drilling Program, Scientific Results, 157, 141-181, doi:10.2973/odp.proc.sr.157.110.1998.

[9] Cousens, B. L., F. J. Spera and G. R. Tilton (1990), Isotopic patterns in silicic ignimbrites and lava flows of the Mogan and lower Fataga Formations, Gran Canaria, Canary Islands: temporal changes in mantle source composition: Earth and Planetary Science Letters, 96, 319-335, doi:10.1016/0012-821X(90)90010-U.

[10] Schmincke, H.-U., A. Klügel, T. Hansteen, K. Hoernle and P. van den Bogaard (1998), Samples from the Jurassic ocean crust beneath Gran Canaria, La Palma and Lanzarote: Earth and Planetary Science Letters, 163, 343-360, doi:10.1016/S0012-821X(98)00168-X.

[11] Thomas, L .E., C. J. Hawkesworth, P. Van Calsteren, S. P. Turner and N. W. Rogers (1999), Melt generation beneath ocean islands: A U-Th-Ra isotope study from Lanzarote in the Canary Islands: Geochimica et Cosmochimica Acta, 63(23-24), 4081-4099, doi:10.1016/S0016-7037(99)00310-5.

[12] Bryan, S. E., J. Martí and M. Leosson (2002), Petrology and geochemistry of the Bandas del Sur Formation, Las Cañadas edifice, Tenerife (Canary Islands): Journal of Petrology, 43(10), 1815-1856, doi:10.1093/petrology/43.10/1815.

[13] Ahijado, A., R. Casillas and A. Hernández-Pacheco (2001), The dyke swarms of Amanay Massif, Fuerteventura, Canary Islands (Spain): Journal of Asian Earth Sciences, 19: 333-345, doi:10.1016/S1367-9120(99)0066-8.

[14] Lundstrom, C. C., K. Hoernle and J. Gill (2003), U-series disequilibria in volcanic rocks from the Canary Islands: Plume versus lithospheric melting: Geochimica et Cosmochimica Acta, 67(21), 4153-4177, doi:10.1016/S0016-7037(03)00308-9.

[15] Aulinas, M., D. Gimeno, J. L. Fernandez-Turiel, L. Font, F. J. Perez-Torrado, A. Rodriguez-Gonzalez and G. M. Nowell (2010), Small-scale mantle heterogeneity on the source of the Gran Canaria (Canary Islands) Pliocene-Quaternary magmas: Lithos, 119, 377-392, doi:10.1016/j.lithos/2010.07.016.

[16] Wiesmaier, S., F. M. Deegan, V. R. Troll, J. C. Carracedo, J. P. Chadwick and D. M. Chew (2011), magma mixing in the 1100 AD Montaña Reventada composite lava flow, Tenerife, Canary Islands: interaction between rift zone and central volcano plumbing systems: Contributions to Mineralogy and Petrology, 162, 651-669, doi:10.1007/s00410-010-0596-x.

[17] Doucelance, R., S. Escrig, M. Moreira, C. Gariépy and M.D. Kurz (2003), Pb-Sr-He isotope and trace element geochemistry of the Cape Verde Archipelago: Geochimica et Cosmochimica Acta, 67(19), 3717-3733, doi:10.1016/S0016-7037(03)00161-3.

[18] Gerlach, D. C., R. A. Cliff, G. R. Davies, M. Norry and N. Hodgson (1988), Magma sources of the Cape Verdes Archipelago: Isotopic and trace element constraints: Geochimica et Cosmochimica Acta, 52, 2979-2992, doi:10.1016/0016-7037(88)90162-7.

[19] Jørgensen, J. Ø. and P. M. Holm (2002), Temporal variation and carbonatite contamination in primitive ocean island volcanics from São Vicente, Cape Verde Islands: Chemical Geology, 192, 249-267, doi:10.1016/S0009-2541(02)00198-5.

[20] Escrig, S., R. Doucelance, M. Moreira and C. J. Allègre (2005), Os isotope systematics in Fogo Island: Evidence for lower continental crust fragments under the Cape Verde southern islands: Chemical Geology, 219, 93-113, doi:10.1016/j.chemgeo.2005.02.011.

[21] Holm, P. M., J. R. Wilson, B. P. Christensen, L. Hansen, S. L. Hansen, M. Hein, A. K. Mortensen, R. Pedersen, S. Plesner and M.K. Runge (2006), Sampling the Cape Verde mantle plume: Evolution of melt compositions on Santo Antão, Cape Verde Islands: Journal of Petrology, 47(1), 145-189, doi:10.1093/petrology/egi071.

[22] Christensen, B. P., P. M. Holm, A. Jambon and J. R. Wilson (2001), Helium, argon and lead isotopic composition of volcanics from Santo Antão and Fogo, Cape Verde Islands: Chemical Geology, 178, 127-142, doi:10.1016/S0009-2541(01)00261-3.

[23] Madeira, J., J. Mata, C. Mourão, A. B. da Silveira, S. Martins, R. Ramalho and D. L. Hoffmann (2010), Volcano-stratigraphic and structural evolution of Brava Island (Cape Verde) based on $^{40}Ar/^{39}Ar$, U-Th and field constraints: Journal of Volcanology and Geothermal Research, 196, 219-235, doi:10.1016/j.jvolgeores.2010.07.010.

[24] Hildner, E., A. Klügel and T. H. Hansteen (2012), Barometry of lavas from the 1951 eruption of Fogo, Cape Verde islands: Implication for historic and prehistoric magma plumbing systems: Journal of Volcanology and Geothermal Research, 217-218, 73-90, doi:10.1016/j.jvolgeores.2011.12.014.

[25] Mourão, C., M. Moreira, J. Mata, A. Raquin and J. Madeira (2012), Primary and secondary processes constraining the noble gas signatures of carbonatites and silicate rocks from Brava Island: evidence for a lower mantle origin of the Cape Verde plume: Contributions to Mineralogy and Petrology, 163, 995-1009, doi:10.1007/s00410-011-0711-7.

[26] Ryabchikov, I. D., T. Ntaflos, G. Kurat and L. N. Kogarko (1995), Glass-bearing xenoliths from Cape Verde: evidence for a hot rising mantle jet: Mineralogy and Petrology, 55, 217-237, doi:10.1007/BF01165119.

[27] Class, C. and S. L. Goldstein (1997), Plume-lithosphere interactions in the ocean basins: constraints from the source mineralogy: Earth and Planetary Science Letters, 150, 245-260, doi:10.1016/S0012-821X(97)0089-7.

[28] Class, C., S. L. Goldstein, R. Altherr and P. Bachèlery (1998), The process of plume-lithosphere interactions in the ocean basins-the case of Grand Comore: Journal of Petrology, 39(5), 881-903, doi:10.1093/petroj/39.5.881.

[29] Class, C, S. L. Goldstein, M. Stute, M. D. Kurz and P. Schlosser (2005), Grand Comore Island: A well-constrained "low $^{3}He/^{4}He$" mantle plume: Earth and Planetary Science Letters, 233, 391-409, doi:10.1016/j.epsl/2005.02.029.

[30] Class, C., S. L. Goldstein and S. B. Shirey (2009), Osmium isotopes in Grande Comore lavas: A new extreme among a spectrum of EM-type mantle endmembers: Earth and Planetary Science Letters, 284, 219-227, doi:10.1016/j.epsl.2009.04.031.

[31] Kaneoka, I., N. Takaoka and B. G. J. Upton (1986), Noble gas systematics in basalts and a dunite nodule from Réunion and Grand Comore islands, Indian Ocean: Chemical Geology, 59, 35-42, doi:10.1016/0168-9622(86)90055-2.

[32] Flower, M. F. J. (1971), Rare earth element distribution in lavas and ultramafic xenoliths from the Comores archipelago, western Indian Ocean: Contributions to Mineralogy and Petrology, 31, 335-346, doi:10.1007/BF00371153.

[33] Späth, A., A. P. le Roex and R. A. Duncan (1996), The geochemistry of lavas from the Comores Archipelago, western Indian Ocean: Petrogenesis and mantle source region characteristics: Journal of Petrology, 37(4), 961-991, doi:10.1093/petrology/37.4.961.

[34] Reynolds, R. W. and D. J. Geist (1995), Petrology of lavas from Sierra Negra volcano, Isabela Island, Galápagos archipelago: Journal of Geophysical Research, 100(B12), 24537-24553, doi:10.1029/95JB02809.

[35] Handley, H. K., S. Turner, K. Berlo, C. Beier and A. E. Saal (2011), Insights into the Galápagos plume from uranium-series isotopes of recently erupted basalts: Geochemistry Geophysics Geosystems, 12, 16 pp, doi:10.1029/2011GC003676.

[36] Naumann, T., D. Geist and M. Kurz (2002), Petrology and geochemistry of Volcán Cerro Azul: Petrologic diversity among the western Galápagos volcanoes: Journal of Petrology, 43(5), 859-883, doi:10.1093/petrology/43.5.859.

[37] Harpp, K. S., D. J. Fornari, D. J. Geist and M. D. Kurz (2003), Genovesa submarine ridge: A manifestation of plume-ridge interaction in the northern Galápagos Islands: Geochemistry Geophysics Geosystems, 4(9), 27 pp, doi:10.1029/2003GC000531.

[38] Geist, D. J., D. J. Fornari, M. D. Kurz, K. S. Harpp, S. A. Soule, M. R. Perfit and A. M. Koleszar (2006), Submarine Fernandina: Magmatism at the leading edge of the Galápagos hot spot: Geochemistry Geophysics Geosystems, 7(12), 27 pp, doi:10.1029/2006GC001290.

[39] Kurz, M. D. and D. Geist (1999), Dynamics of the Galapagos hotspot from helium isotope geochemistry: Geochimica et Cosmochimica Acta, 63(23-24), 4139-4156, doi:10.1016/S0016-7037(99)00314-2.

[40] Kurz, M. D., J. Curtice, D. Fornari, D. Geist and M. Moreira (2009), Primitive neon from the center of the Galápagos hotspot: Earth and Planetary Science Letters, 286, 23-34, doi:10.1016/j.epsl.2009.06.008.

[41] Saal, A. E., M. D. Kurz, S. R. Hart, J. S. Blusztajn, J. Blichert-Toft, Y. Liang and D. J. Geist (2007), The role of lithospheric gabbros on the composition of Galapagos lavas: Earth and Planetary Science Letters, 257, 391-406, doi:10.1016/j.epsl.2007.02.040.

[42] Gibson, S. A. and D. Geist (2010), Geochemical and geophysical estimates of lithospheric thickness variation beneath Galápagos: Earth and Planetary Science Letters, 300, 275-386, doi:10.1016/j.epsl/2010.10.002.

[43] Nusbaum, R. L., M. W. Colgan, D. E. Lawton and M. D. Glascock (1991), Mineralogic constraints on the magmatic history of Volcán Darwin flank lava at Urvina Bay, Islá Isabela, Galápagos Islands: Journal of Volcanology and Geothermal Research, 47, 359-366, doi:10.1016/0377-0273(91)90011-N.

[44] Cullen, A., E. Vicenzi and A. R. McBirney (1989), Plagioclase-ultraphyric basalts of the Galapagos Archipelago: Journal of Volcanology and Geothermal Research, 37, 325-337, doi:10.1016/0377-0273(89)90087-5.

[45] Batis, H. W. and M. M. Lindstrom (1980), Geology, petrography, and petrology of Pinzon Island, Galapagos Archipelago: Contributions to Mineralogy and Petrology, 72, 367-386, doi:10.1007/BF00371345.

[46] Allan, J. F. and T. Simkin (2000), Fernandina Volcano's evolved, well-mixed basalts: Mineralogical and petrological constraints on the nature of the Galapagos plume: Journal of Geophysical Research, 105(B3), 6017-6041, doi:10.1029/1999JB900417.

[47] Graham, D. W., D. M. Christie, K. S. Harpp and J. E. Lupton (1993), Mantle plume helium in submarine basalts from the Galápagos platform: Science, 262, 2023-2026, doi:10.1126/science.262.5142.2023.

[48] Raquin, A. and M. Moreira (2009), Atmospheric $^{38}Ar/^{36}Ar$ in the mantle: Implications for the nature of the terrestrial parent bodies: Earth and Planetary Science Letters, 2009, 551-558, doi:10.1016/j.epsl.2009.003.

[49] Garcia, M. O., D. Hanano, A. Flinders, D. Weis, G. Ito and M. D. Kurz (2012), Age, geology, and geochemistry of Mahukona volcano, Hawai'i: Bulletin of Volcanology, 74, 1445-1463, doi:10.1007/s00445-012-0602-4.

[50] Hanyu, T., J.-I. Kimura, M. Katakuse, A. T. Calvert, T. W. Sisson and S. Nakai (2010), Source materials for inception stage Hawaiian magmas: Pb-He isotope variations for early Kilauea: Geochemistry Geophysics Geosystems, 11, 25 pp, doi:10.1029/2009GC002760.

[51] Kimura, J.-I., T. W. Sisson, N. Nakano, M. L. Coombs and P. W. Lipman (2006), Isotope geochemistry of early Kilauea magmas from the submarine Hilina bench: The nature of the Hilina mantle component: Journal of Volcanology and Geothermal Research, 151, 51-72, doi:10.1016/j.jvolgeores.2005.07.024.

[52] Wanless, V. D., M. O. Garcia, F. A. Trusdell, J. M. Rhodes, M. D. Norman, D. Weis, D. J. Fornari, M. D. Kurz and H. Guillou (2006), Submarine radial vents on Mauna Loa volcano, Hawai'i: Geochemistry Geophysics Geosystems, 7(5), 28 pp, doi:10.1029/2005GC001086.

[53] Ren, Z.-Y., T. Hanyu, T. Miyazaki, Q. Chang, H. Kawabata, T. Takahashi, Y. Hirahara, A.R.L. Nichols and Y. Tatsumi (2009), Geochemical differences of the Hawaiian shield lavas: Implications for melting process in the heterogeneous Hawaiian mantle plume: Journal of Petrology, 50(8), 1553-1573, doi:10.1093/petrology/egh076.

[54] Kaneoka, I., T. Hanyu, J. Yamamoto and Y. N. Miura (2002), Noble gas systematics of the Hawaiian volcanoes based on the analysis of Loihi, Kilauea and Koolau submarine rocks. *In:* Takahashi, E., P. W. Lipman, M. O. Garcia, J. Naka and S. Aramaki (eds.), Hawaiian volcanoes: Deep underwater perspectives: Geophysical Monograph, American Geophysical Union, 128, 373-389, doi:10.1029/GM128p0373.

[55] Lipman, P. W., J. M. Rhodes and G. B. Dalrymple (1990), The Ninole basalt – Implications for the structural evolution of Mauna Loa volcano, Hawaii: Bulletin of Volcanology, 53, 1-19, doi:10.1007/BF00680316.

[56] Frey, F. A., W. S. Wise, M. O. Garcia, H. West, S.-T. Kwon and A. Kennedy (1990), Evolution of Mauna Kea volcano, Hawaii: Petrologic and geochemical constraints on postshield volcanism: Journal of Geophysical Research, 95(B2), 1271-1300, doi:10.1029/JB095iB02p01271.

[57] Frey, F. A., M. O. Garcia, W. S. Wise, A. Kennedy, P. Gurriet and F. Albarede (1991), The evolution of Mauna Kea volcano, Hawaii: Petrogenesis of tholeiitic and alkalic basalts: Journal of Geophysical Research, 96(B9), 14347-14375, doi:10.1029/91JB00940.

[58] Spengler, S. R. and M. O. Garcia (1988), Geochemistry of the Hawi lavas, Kohala volcano, Hawaii: Contributions to Mineralogy and Petrology, 99, 90-104, doi:10.1007/BF00399369.

[59] Yang, H.-J., F. A. Frey, M. O. Garcia and D. A. Clague (1994), Submarine lavas from Mauna Kea volcano, Hawaii: Implications for Hawaiian shield stage processes: Journal of Geophysical Research, 99(B8), 15577-15594, doi:10.1029/94JB00895.

[60] Leeman, W. P., D. C. Gerlach, M. O. Garcia and H. B. West (1994), Geochemical variations in lavas from Kahoolawe volcano, Hawaii: Evidence for open system evolution of plume-derived magmas: Contributions to Mineralogy and Petrology, 116: 62-77, doi:10.1007/BF00310690.

[61] Rhodes, J. M., S. Huang, F. A. Frey, M. Pringle ad G. Xu (2012), Compositional diversity of Mauna Kea shield lavas recovered by the Hawaii Scientific Drilling Project: Inferences on source lithology, magma supply, and the role of multiple volcanoes: Geochemistry Geophysics Geosystems, 13(3), 28 pp, doi:10.1029/2011GC003812.

[62] Garcia, M. O., L. Swinnard, D. Weis, A. R. Greene, T. Tagami, H. Sano and C. E. Gandy (2010), Petrology, geochemistry and geochronology of Kaua'i lavas over 4.5 Myr: Implications for the origin of rejuvenated volcanism and the evolution of the Hawaiian plume: Journal of Petrology, 51(7), 1507-1540, doi:10.1093/petrology/egq027.

[63] Van der Zander, I., J. M. Sinton and J. J. Mahoney (2010), Late shield-stage silicic magmatism at Wai'anae volcano: Evidence for hydrous crustal melting in Hawaiian volcanoes: Journal of Petrology, 51(3), 671-701, doi:10.1093/petrology/egp094.

[64] Hanano, D., D. Weis, J. S. Scotes, S. Aciego and D. J. DePaolo (2010), Horizontal and vertical zoning of heterogeneities in the Hawaiian mantle plume from the geochemistry of consecutive postshield volcano pairs: Kohala-Mahukona and Mauna Kea-Hualalai: Geochemistry Geophysics Geosystems, 11(1), 22 pp, doi:10.1029/2009GC002782.

[65] Dixon, J., D. A. Clague, B. Cousens, M. L. Monsalve and J. Uhl (2008), Carbonatite and silicate melt metasomatism of the mantle surrounding the Hawaiian plume: Evidence from volatiles, trace elements, and radiogenic isotopes in rejuvenated-stage lavas from Niihau, Hawaii: Geochemistry Geophysics Geosystems, 9(9), 34 pp, doi:10.1029/2008GC002076.

[66] Xu, G., F. A. Frey, D. A. Clague, W. Abouchami, J. Blichert-Toft, B. Cousens and M. Weisler (2007), Geochemical characteristics of west Molokai shield- and postshield-stage lavas: Constraints on Hawaiian plume models: Geochemistry Geophysics Geosystems, 8(8), 40 pp, doi:10.1029/207GC001608.

[67] Clague, D. A., J. B. Paduan, W. C. McIntosh, B. L. Cousens, A. S. Davis and J. R. Reynolds (2006), A submarine perspective of the Honolulu volcanics, Oahu: Journal of Volcanology and Geothermal Research, 151, 279-307, doi:10.1016/j.jvolgeores.2005.07.036.

[68] Lipman, P. W., T. W. Sisson, M. L. Coombs, A. Calvert and J.-I. Kimura (2006), Piggyback tectonics: Long-term growth of Kilauea on the south flank of Mauna Loa: Journal of Volcanology and Geothermal Research, 151, 73-108, doi:10.1016/j.jvolgeores.205.07.032.

[69] Huang, S., F. A. Frey, J. Blichert-Toft, R. V. Fodor, G. R. Bauer and G. Xu (2005), Enriched components in the Hawaiian plume: Evidence from Kahoolawe volcano, Hawaii Geochemistry Geophysics Geosystems, 6(11), 21 pp, doi:10.1029/2005GC001012.

[70] Gaffney, A. M., B. K. Nelson and J. Blichert-Toft (2005), Melting the Hawaiian plume at 1-2 Ma as recorded at Maui Nui: The role of eclogite, peridotite, and source mixing: Geochemistry Geophysics Geosystems, 6(10), 30 pp, doi:10.1029/2005GC000927.

[71] Sims, K. W. W., D. J. DePaolo, M. T. Murrell, W. S. Baldridge, S. Goldstein, D. Clague and M. Jull (1999), Porosity of the melting zone and variations in the solid mantle upwelling rate beneath Hawaii: Inferences from ^{238}U-^{230}Th-^{226}Ra and ^{235}U-^{231}Pa disequilibria: Geochemica et Cosmochimica Acta, 63(23-24), 4119-4138.

[72] Jackson, M. C., F. A. Frey, M. O. Garcia and R. A. Wilmoth (1999), Geology and geochemistry of basaltic lava flows and dikes from the Trans-Koolau tunnel, Oahu, Hawaii: Bulletin of Volcanology, 60, 381-401, doi:10.1007/s004450050239.

[73] Chen, C.-Y., F.A. Frey and M. O. Garcia (1990), Evolution of alkalic lavas at Haleakala volcano, east Maui, Hawaii: Contributions to Mineralogy and Petrology, 105, 197-218, doi:10.1007/BF00678986.

[74] Roden, M. F., F. A. Frey and D. A. Clague (1984), Geochemistry of tholeiitic and alkalic lavas from the Koolau range, Oahu, Hawaii: implications for Hawaiian volcanism: Earth and Planetary Science Letters, 69, 141-158, doi:10.1016/0012-821X(84)90079-7.

[75] Clague, D. A. and G. B. Dalrymple (1988), Age and petrology of alkalic postshield and rejuvenated-stage lava from Kauai, Hawaii: Contributions to Mineralogy and Petrology, 99, 202-218, doi:10.1007/BF00371461.

[76] Frey, F. A., M. O. Garcia and M. F. Roden (1994), Geochemical characteristics of Koolau volcano: Implications of intershield geochemical differences among Hawaiian volcanoes: Geochemica et Cosmochimica Acta, 58(5), 1441-1462, doi:10.1016/0016-7037(94)90548-7.

[77] Chen, C.-Y. and F. A. Frey (1983), Origin of Hawaiian tholeiite and alkalic basalt: Nature, 302, 785-789, doi:10.1038/302785a0.

[78] West, H. B. and W. P. Leeman (1994), The open-system geochemical evolution of alkalic cap lavas from Haleakala crater, Hawaii, USA: Geochimica et Cosmochimica Acta, 58(3), 773-796, doi:10.1016/0016-7037(94)90505-3.

[79] Chen, C.-Y., F. A. Frey, M. O. Garcia, G. B. Dalrymple and S. R. Hart (1991), The tholeiite to alkalic basalt transition at Haleakala volcano, Maui, Hawaii: Contributions to Mineralogy and Petrology, 106, 183-200, doi:10.1007/BF00306433.

[80] Tanaka, R. and E. Nakamura (2005), Boron isotopic constraints on the source of Hawaiian shield lavas: Geochemica et Cosmochimica Acta, 69(13), 3385-3399, doi:10.1016/j.gca.2005.03.009.

[81] Clague, D. A. and J. G. Moore (2002), The proximal part of the giant submarine Wailau landslide, Molokai, Hawaii: Journal of Volcanology and Geothermal Research, 113, 259-287, doi:10.1016/S0377-0273(01)00261-X.

[82] Xu, G., F. A. Frey, D. A. Clague, D. Weis and M. H. Beeson (2005), East Molokai and other Kea-trend volcanoes: Magmatic processes and sources as they migrate away from the Hawaiian hot spot: Geochemistry Geophysics Geosystems, 6(5), 28 pp, doi:10.1029/2004GC000830.

[83] Ren, Z.-Y., E. Takahashi, Y. Orihashi and K. T. M. Johnson (2004), Petrogenesis of tholeiitic lavas from the submarine Hana ridge, Haleakala volcano, Hawaii: Journal of Petrology, 45(10), 2067-2099, doi:10.1093/petrology.egh076.

[84] Gaffney, A. M., B. K. Nelson and J. Blichert-Toft (2004), Geochemical constraints on the role of oceanic lithosphere in intra-volcano heterogeneity and West Maui, Hawaii: Journal of Petrology, 45(8), 1663-1687, doi:10.1093/petrology.egh029.

[85] Breddam, K. (2002), Kistufell: Primitive melt from the Iceland mantle plume: Journal of Petrology, 43(2), 345-373, doi:10.1093/petrology/43.2.345.

[86] Macpherson, C. G., D. R. Hilton, J. M. D. Day, D. Lowry and K. Grönvold (2005), High-$^{3}He/^{4}He$, depleted mantle and low-$\delta^{18}O$ recycled oceanic lithosphere in the source of central Iceland magmatism: Earth and Planetary Science Letters, 233(3-4), 411-427, doi:10.1016/j.epsl.2005.02.037.

[87] Hilton, D. R., K. Grönvold, C. G. Macpherson and P. R. Castillo (1999), Extreme $^{3}He/^{4}He$ ratios in northwest Iceland: constraining the common component in mantle plumes: Earth and Planetary Science Letters, 173, 53-60, doi:10.1016/S0012-821X(99)00215-0.

[88] Condomines, M., K. Grönveld, P. J. Hooker, K. Muehlenbachs, R. K. O'NIons, N. Óskarsson and E. R. Oxburgh (1983), Helium, oxygen, strontium and neodymium isotopic relationships in Icelandic volcanics: Earth and Planetary Science Letters, 66, 125-136, doi:10.1016/0012-821X(83)90131-0.

[89] Breddam, K., M. D. Kurz and M. Storey (2000), Mapping out the conduit of the Iceland mantle plume with helium isotopes: Earth and Planetary Science Letters, 176, 45-55., doi:10.1016/S0012-821X(99)00313-1.

[90] Dixon, E. T. (2003), Interpretation of helium and neon isotopic heterogeneity in Icelandic basalts: Earth and Planetary Science Letters, 206, 83-99, doi:10.1016/S0012-821X(02)01071-3.

[91] Peate, D. W., K. Breddam, J. A. Baker, M. D. Kurz, A. K. Barker, T. Prestvik, N. Grassineau and A. C. Skovgaard (2010), Compositional characteristics and spatial distribution of enriched Icelandic mantle components: Journal of Petrology, 51(7), 1447-1475, doi:10.1093/petrology/egq025.

[92] Debaille, V., R. G. Trønnes, A. D. Brandon, T. E. Waight, D. W. Graham, C.-T. A. Lee (2009), Primitive off-rift basalts from Iceland and Jan Mayen: Os-isotopic evidence for a mantle source containing enriched subcontinental lithosphere: Geochimica et Cosmochimica Acta, 73, 3423-3449, doi:10.1016/j.gca.2009.03.002.

[93] Macdonald, R., D. W. McGarvie, H. Pinkerton, R. L. Smith and Z. A. Palacz (1990), Petrogenetic evolution of the Torfajökull volcanic complex, Iceland I. Relationship between the magma types: Journal of Petrology, 31(2), 429-459, doi:10.1093/petrology/31.2.429.

[94] McGarvie, D. W., R. Macdonald, H. Pinkerton and R. L. Smith (1990), Petrogenetic evolution of the Torfajökull volcanic complex, Iceland II. The role of magma mixing: Journal of Petrology, 31(2), 461-481, doi:10.1093/petrology/31.2.461.

[95] Révillon, S., N. T. Arndt, E. Hallot, A. C. Kerr and J. Tarney (1999), Petrogenesis of picrites from the Caribbean Plateau and the North Atlantic magmatic province: Lithos, 49, 1-21, doi:10.1016/S0024-4937(99)00038-9.

[96] Kempton, P. D., J. G. Fitton, A. D. Saunders, G. M. Nowell, R. N. Taylor, B. S. Hardarson and G. Pearson (2000), The Iceland plume in space and time: a Sr-Nd-Pb-Hf study of the North Atlantic rifted margin: Earth and Planetary Science Letters, 177, 255-271, doi:10.1016/S0012-821X(00)00047-9.

[97] Slater, L., D. McKenzie, K. Grönvold and N. Shimizu (2001), Melt generation and movement beneath Theistareykir, NE Iceland: Journal of Petrology, 42(2), 321-354, doi:10.1093/petrology/42.2.321.

[98] Prestvik, T., S. Goldberg, H. Karlsson and K. Grönvold (2001), Anomalous strontium and lead isotope signatures in the off-rift Öræfajökull central volcano in south-east Iceland: Evidence for enriched endmembers(s) of the Iceland mantle plume?: Earth and Planetary Science Letters, 190, 211-220, doi:10.1016/S0012-821X(01)00390-9.

[99] Skovgaard, A. C., M. Storey, J. Baker, J. Blusztajn and S. R. Hart (2001), Osmium-oxygen isotopic evidence for a recycled and strongly depleted component in the Iceland mantle plume: Earth and Planetary Science Letters, 194, 259-275, doi:10.1016/S0012-821X(01)00549-0.

[100] Stracke, A., A. Zindler, V. J. M. Salters, D. McKenzie, J. Blichert-Toft, F. Albarède and K. Grönvold (2003), Theistareykir revisited: Geochemistry Geophysics Geosystems, 4(2), 49 pp, doi:10.1029/2001GC000201.

[101] Jónasson, K. (2005), Magmatic evolution of the Heiðarsporður ridge, NE-Iceland: Journal of Volcanology and Geothermal Research, 147, 109-124, doi:10.1016/j.jvolgeores.2005.03.009.

[102] Mattsson, H. B. and N. Oskarsson (2005), Petrogenesis of alkaline basalts at the tip of a propagating rift: Evidence from the Heimaey volcanic centre, south Iceland: Journal of Volcanology and Geothermal Research, 147, 245-267, doi:10.1016/j.jvolgeores.2005.04.004.

[103] Kokfelt, T. F., K. Hoernle, F. Hauff, J. Fiebig, R. Werner and D. Garbe-Schönberg (2006), Combined trace element and Pb-Nd-Sr-O isotope evidence for recycled oceanic crust (upper and lower) in the Iceland mantle plume: Journal of Petrology, 47(9), 1705-1749, doi: 10.1093/petrology/egl025.

[104] Zellmer, G. F., K. H. Rubin, K. Grönvold and Z. Jurado-Chichay (2008), On the recent bimodal magmatic processes and their rates in the Torfajökull-Veidivötn

area, Iceland: Earth and Planetary Science Letters, 269, 388-398, doi:10.1016/j.epsl.2008.02.026.

[105] Kitagawa, H., K. Kobayashi, A. Makishima and E. Nakamura (2008), Multiple pulses of the mantle plume: Evidence from Tertiary Icelandic lavas: Journal of Petrology, 49(7), 1365-1396, doi:10.1093/petrology/egn029.

[106] Maclennan, J. (2008), Concurrent mixing and cooling of melts under Iceland: Journal of Petrology, 49(11), 1931-1953, doi:10.1093/petrology/egn052.

[107] Kuritani, T., T. Yokoama, H. Kitagawa, K. Kobayashi and E. Nakamura (2011), Geochemical evolution of historical lavas from Askja volcano, Iceland: Implications for mechanisms and timescales of magmatic differentiation: Geochimica et Cosmochimica Acta, 75, 570-587, doi:10.1016/j.gca.2010.10.009.

[108] Koornneef, J. M., A. Stracke, B. Bourdon, M. A. Meier, K. P. Jochum, B. Stoll and K. Grönvold (2012), Melting of a two-component source beneath Iceland: Journal of Petrology, 53(1), 127-157, doi:10.1093/petrology.egr059.

[109] Bosshard, S. A., H. B. Mattsson and G. Hetényi (2012), Origin of internal flow structures in columnar-jointed basalt from Hrepphólar, Iceland: I. Textural and geochemical characterization: Bulletin of Volcanology, 74, 1645-1666, doi:10.1007/s00445-012-0623-z.

[110] Kurz, M. D., P. S. Meyer and H. Sigurdsson (1985), Helium isotopic systematics within the neovolcanic zones of Iceland: Earth and Planetary Science Letters, 74, 291-305, doi:10.1016/S0012-821X(85)80001-7.

[111] Moreira, M., K. Breddam, J. Curtice and M. D. Kurz (2001), Solar neon in the Icelandic mantle: new evidence for an undegassed lower mantle: Earth and Planetary Science Letters, 185, 15-23, doi:10.1016/S0012-821X(00)00351-4.

[112] Dixon, E. T., M. Honda, I. McDougal, I. H. Campbell and I. Sigurdsson (2000), Preservation of near-solar neon isotopic ratios in Icelandic basalts: Earth and Planetary Science Letters, 180, 309-324, doi:10.1016/S0012-821X(00)00164-3.

[113] Brandon, A. D., D. W. Graham, T. Waight and B. Gautason (2007), ^{186}Os and ^{187}Os enrichments and high-$^{3}He/^{4}He$ sources in the Earth's mantle: Evidence from Icelandic picrites: Geochimica et Cosmochimica Acta, 71, 4570-4591, doi:10.1016/j.gca.2007.07.015.

[114] Füri, E., D. R. Hilton, S. A. Haldórsson, P. H. Barry, D. Hahm, T.P. Fischer and K. Grönvold (2010), Apparent decoupling of the He and Ne isotope systematics of the Icelandic mantle: The role of He depletion, melt mixing, degassing fractionation

and air interaction: Geochimica et Cosmochimica Acta, 74, 3307-3332, doi:10.1016/j.gca.2010.03.023.

[115] Trønnes, R. G. (1990), Basaltic melt evolution of the Hengill volcanic system, SW Iceland, and evidence for clinopyroxene assimilation in primitive tholeiitic magmas: Journal of Geophysical Research, 95(B10), 15893-15910, doi:10.1029/JB095iB10p15893.

[116] Maclennan, J., D. McKenzie, K. Gronvöld, L. Slater (2001), Crustal accretion under northern Iceland: Earth and Planetary Letters, 191, 295-310, doi:10.1016/S0012-821X(01)00420-4.

[117] Valbracht, P. J., M. Honda, T. Matsumoto, N. Mattielli, I. McDougall, R. Ragettli and D. Weis (1996), Helium, neon and argon isotope systematics in Kerguelen ultramafic xenoliths: implications for mantle source signatures: Earth and Planetary Science Letters, 138, 29-38, doi:10.1016/0012-821X(95)00226-3.

[118] Trull, T., S. Nadeau, F. Pineau, M. Polvé and M. Javoy (1993), C-He systematics in hotspot xenoliths: Implications for mantle carbon contents and carbon recycling: Earth and Planetary Science Letters, 118, 43-64, doi:10.1016/0012-821X(93)90158-6.

[119] Weis, D., F. A. Frey, A. Giret and J.-M. Cantagrel (1998), Geochemical characteristics of the youngest volcano (Mount Ross) in the Kerguelen archipelago: Inferences for magma flux, lithosphere assimilation and composition of the Kerguelen plume: Journal of Petrology, 39(5), 973-994, doi:10.1093/petroj/39.5.973.

[120] Yang, H.-J., F. A. Frey, D. Weis, A. Giret, D. Pyle and G. Michon (1998), Petrogenesis of the flood basalts forming the northern Kerguelen archipelago: Implications for the Kerguelen plume: Journal of Petrology, 39(4), 711-748, doi:10.1093/petroj/39.4.711.

[121] Gautier, I., D. Weis, J.-P. Mennessier, P. Vidal, A. Giret and M. Loubet (1990), Petrology and geochemistry of the Kerguelen archipelago basalts (southern Indian Ocean): Evolution of the mantle sources from ridge to intraplate position: Earth and Planetary Science Letters, 100, 59-76, doi:10.1016/0012-821X(90)90176-X.

[122] Storey, M., A. D. Saunders, J. Tarney, P. Leat, M. F. Thirlwall, R.N. Thompson, M. A. Menzies and G. F. Marriner (1988), Geochemical evidence for plume-mantle interactions beneath Kerguelen and Heard islands, Indian Ocean: Nature, 336, 371-374, doi:10.1038/336371a0.

[123] Weis, D., F. A. Frey, H. Leyrit and I. Gautier (1993), Kerguelen archipelago revisited: geochemical and isotopic study of the Southeast Province lavas: Earth and Planetary Science Letters, 118, 101-119, doi:10.1016/0012-821X(93)90162-3.

[124] Frey, F. A., D. Weis, H.-J. Yang, K. Nicolaysen, H. Leyrit and A. Giret (2000), Temporal geochemical trends in Kerguelen Archipelago basalts: evidence for decreasing magma supply from the Kerguelen plume: Chemical Geology, 164, 61-80, doi:10.1016/S0009-2541(99)00144-8.

[125] Doucet, S., D. Weis, J. S. Scoates, K. Nicolaysen, F. A. Frey and A. Giret (2002), The depleted mantle component in Kerguelen archipelago basalts: Petrogenesis of tholeiitic-transitional basalts from the Loranchet Peninsula: Journal of Petrology, 43(7), 1341-1366, doi:10.1093/petrology/43.7.1341.

[126] Doucet, S., M. Moreira, D. Weis, J. S. Scoates, A. Giret and C. Allègre (2006), Primitive neon and helium isotopic compositions of high-MgO basalts from the Kerguelen archipelago, Indian Ocean: Earth and Planetary Science Letters, 241, 65-79, doi:10.1016/j.epsl.2005.10.025.

[127] Fretzdorff, S. and K. M. Haase (2002), Geochemistry and petrology of lavas from the submarine flanks of Réunion Island (western Indian Ocean): Implications for magma genesis and the mantle source: Mineralogy and Petrology, 75, 153-184, doi:10.1007/s007100200022.

[128] Vlastélic, I., T. Staudacher and M. Semet (2005), Rapid change of lava composition from 1998 to 2002 and Piton de la Fournaise (Réunion) inferred from Pb isotopes and trace elements: Evidence for variable crustal contamination: Journal of Petrology, 46(1), 79-107, doi:10.1093/petrology/egh062.

[129] Nohda, S., I. Kaneoka, T. Hanyu, S. Xu and K. Uto (2005), Systematic variation of Sr-, Nd- and Pb-isotopes with time in lavas of Mauritius, Réunion hotspot: Journal of Petrology, 46(3), 505-522, doi:10.1093/petrology/egh085.

[130] Paul, D., W. M. White and J. Blichert-Toft (2005), Geochemistry of Mauritius and the origin of rejuvenescent volcanism on ocean island volcanoes: Geochemistry Geophysics Geosystems, 6(6), 22 pp, doi:10.1029/2004GC000883.

[131] Sheth, H. C., J. J. Mahoney and A. N. Baxter (2003), Geochemistry of lavas from Mauritius, Indian Ocean: Mantle sources and petrogenesis: International Geology Review, 45(9), 780-797, doi:10.2747/0020-6814.45.9.780.

[132] Paul, D., V. S. Kamenetsky, A. W. Hofmann and A. Stracke (2007), Compositional diversity among primitive lavas of Mauritius, Indian Ocean: Implications for mantle sources: Journal of Volcanology and Geothermal Research, 164, 76-94, doi:10.1016/j.jvolgeores.2007.04.004.

[133] Vlastélic, I., A. Peltier and T. Staudacher (2007), Short-term (1998-2006) fluctuations of Pb isotopes at Piton de la Fournaise volcano (Reunion Island): Origins and constraints on the size and shape of the magma reservoir: Chemical Geology, 244, 202-220, doi:10.1016/j.chemgeo.2007.06.015.

[134] Moore, J., W. M. White, D. Paul, R. A. Duncan, W. Abouchami and S. J. G. Galer (2011), Evolution of shield-building and rejuvenescent volcanism of Mauritius: Journal of Volcanology and Geothermal Research, 207, 47-66, doi: 10.1016/j.jvolgeores.2011.07.005.

[135] Graham, D., J. Lupton, F. Albarède and M. Condomines (1990), Extreme temporal homogeneity of helium isotopes at Piton de la Fournaise, Réunion Island: Nature, 347, 545-548, doi:10.1038/347545a0.

[136] Staudacher, T., P. Sarda and C. J. Allègre (1990), Noble gas systematics of Réunion Island, Indian Ocean: Chemical Geology, 89, 1-17, doi:10.1016/0009-2541(90)90057-E.

[137] Fisk, M. R., B. G. J. Murton, C. E. Ford and W. M. White (1988), Geochemical and experimental study of the genesis of magmas of Reunion Island, Indian Ocean: Journal of Geophysical Research, 93(B5), 4933-4950, doi:10.1029/JB093iB05p04933.

[138] Baxter, A. N., B. G. J. Upton and W. M. White (1985), Petrology and geochemistry of Rodrigues Island, Indian Ocean: Contributions to Mineralogy and Petrology, 89, 90-101, doi:10.1007/BF01177594.

[139] Füri, E., D. R. Hilton, B. J. Murton, C. Hémond, J. Dyment and J. M. D. Day (2011), Helium isotope variations between Réunion Island and the Central Indian Ridge (17°-21°S): New evidence for ridge-hot spot interaction: Journal of Geophysical Research, 116, B02207, doi:10.1029/2010JB007609.

[140] Sobolev, A. V. and I. K. Nikogosian (1994), Petrology of long-lived mantle plume magmatism: Hawaii, Pacific, and Reunion Island, Indian Ocean: Petrology, 2, 111-144.

[141] Schiano, P., K. David, L. Vlastelic, A. Gannoun, M. Klein, F. Nauret and P. Bonnand (2012), Osmium isotope systematics of historical lavas from Piton de la Fournaise (Réunion Island, Indian Ocean): Contributions to Mineralogy and Petrology, 164(5), 16 pp, doi:10.1007/s00410-012-0774-0.

[142] Bovin, P. and P. Bachèlery (2009), Petrology of 1977 to 1998 eruptions of Piton de la Fournaise, La Réunion Island: Journal of Volcanology and Geothermal Research, 184, 109-125, doi:10.1016/j.jvolgeores.2009.01.012.

[143] Workman, R. K., S. R. Hart, M. Jackson, M. Regelous, K. Farley, J. Blusztajn, M. Kurz and H. Staudigel (2004), Recycled metasomatized lithosphere as the origin of the Enriched Mantle II (EM2) end-member: Evidence from the Samoan volcanic chain: Geochemistry Geophysics Geosystems, 5(4), 44 pp, doi:10.1029/2003GC000623.

[144] Farley, K. A., J. H. Natland and H. Craig (1992), Binary mixing of enriched and undegassed (primitive?) mantle components (He, Sr, Nd, Pb) in Samoan lavas: Earth and Planetary Science Letters, 111, 183-199, doi:10.1016/0012-821X(92)90178-X.

[145] Palacz, Z. A. and A. D. Saunders (1986), Coupled trace element and isotope enrichment in the Cook-Austral-Samoa islands, southwest Pacific: Earth and Planetary Science Letters, 79, 270-280, doi:10.1016/0012-821X(86)90185-8.

[146] Jackson, M. G., S. R. Hart, A. A. P. Koppers, H. Staudigel, J. Konter, J. Blusztajn, M. Kurz and J. A. Russell (2007), Evidence for the return of subducted continental crust in Samoan lavas: Nature, 448, 684-687, doi:10.1038/nature06048.

[147] Jackson, M. G., M. D. Kurz and S. R. Hart (2009), Helium and neon isotopes in phenocrysts from Samoan lavas: Evidence for heterogeneity in the terrestrial high-$^{3}He/^{4}He$ mantle: Earth and Planetary Science Letters, 287, 519-528, doi:10.1029/2008GC002324.

[148] Jackson, M. G., S. R. Hart, J. G. Konter, A. A. P. Koppers, H. Staudigel, M. D. Kurz, J. Blusztajn and J. M. Sinton (2010), Samoan hot spot track on a "hot spot highway": Implications for mantle plumes and a deep Samoan mantle source: Geochemistry Geophysics Geosystems, 11(12), 24 pp, doi:10.1029/2010GC003232.

[149] Pearce, J. A., P. D. Kempton and J. B. Gill (2007), Hf-Nd evidence for the origin and distribution of mantle domains in the SW Pacific: Earth and Planetary Science Letters, 260, 98-114, doi:10.1016/j.epsl.2007.05.023.

[150] Poreda, R. J. and K. A. Farley (1992), Rare gases in Samoan xenoliths: Earth and Planetary Science Letters, 113, 129-144, doi:10.1016/0012-821X(92)90215-H.

[151] Hahm, D., D. R. Hilton, P. R. Castillo, J. W. Hawkins, B. B. Hanan and E. H. Hauri (2012), An overview of the volatile systematics of the Lau Basin – Resolving the effects of source variation, magmatic degassing and crustal contamination: Geochemica et Cosmochimica Acta, 85, 88-113, doi:10.1016/j.gca.2012.02.007.

[152] Hauri, E. H. and S. R. Hart (1997), Rhenium abundances and systematics in oceanic basalts: Chemical Geology, 139, 185-205, doi:10.1016/S0009-2541(97)00035-1.

[153] Jackson, M. G. and S. B. Shirey (2011), Re-Os isotope systematics in Samoan shield lavas and the use of Os-isotopes in olivine phenocrysts to determine primary magmatic compositions: Earth and Planetary Science Letters, 312, 91-101, doi:10.1016/j.epsl.2011.09.046.

[154] Gaffney, A. M., B. K. Nelson, L. Reisberg and J. Eiler (2005), Oxygen-osmium isotope systematics of West Maui lavas: A record of shallow-level magmatic processes: Earth and Planetary Science Letters, 239, 122-139, doi:10.1029/2005GC000927.

[155] Sen, I. S., M. Bizimis, G. Sen and S. Huang (2011), A radiogenic Os component in the oceanic lithosphere? Constraints from Hawaiian pyroxenite xenoliths: Geochimica et Cosmochimica Acta, 75, 4899-4916, doi:10.1016/j.gca.2011.06.068.

[156] Jackson, M. G., S. R. Hart, A. E. Saal, N. Shimizu, M. D. Kurz, J. S. Blusztajn, A. C. Skovgaard (2008), Globally elevated titanium, tantalum, and niobium (TITAN) in ocean island basalts with high $^{3}He/^{4}He$: Geochemistry, Geophysics, Geosystems, 9, Q04027, doi:10.1029/2007GC001876.

[157] Hart, S.R. and M.G. Jackson (2014), Ta'u and Ofu/Olosega volcanoes: The "twin sisters" of Samoa, their P, T, X melting regime, and global implications: Geochemistry, Geophysics, Geosystems, 15, doi:10.1002/2013GC006221.

2.7 Supplementary discussion of data collection and quantitative methods for determining compositions of parental magmas

Because we employ a number of methods to determine the composition of hotspot parental magmas, and the results depend on what data are included, we compare the relative strengths and weaknesses of our data collection and quantitative methods here. We apply several geochemical filters to exclude misleading data or data from highly altered samples. Two methods were used to determine reference MgO, which represents the MgO contents of the parental magma, and two methods were employed to use reference MgO to determine the TITAN contents of parental magmas.

2.7.1 Data Collection and Filtering

Data was gathered from a variety of studies on OIB and related rocks. In order to maximize data inclusion, cross-referencing of samples for which geochemical data is included in multiple publications was attempted. However, where sample data were not explicitly cross-referenced in article text or tables, samples were cross-referenced by identifying common c-authors and sample names. Similarly, parent rocks to mineral separate were identified by common root sample names.

Several data filters were employed to ensure inclusion of only the highest quality data in calculations of parental TITAN anomalies. Samples not meeting the following criteria were excluded from these calculations:

- Whole-rock MgO contents of at least 5.3 wt. % (a discrimination also used by Jackson et al., 2008)
- Samples suggested in article texts to be substantially altered by crustal contamination or assimilation
- Data published in 1980 or later
- Major elements plus loss on ignition totaling less than 97.5 wt.% (for XRF data)
- Loss on ignition greater than 5 wt.%

Samples that do not meet the first two criteria but do meet the last three were included in determinations of hotspot reference MgO; samples that do not meet any one of the last three criteria were excluded from all consideration. For an example of the effect of these filters on major hotspots, please see **Table 2.3**.

2.7.2 Use of primitive mantle as normalizing values for calculating TITAN anomalies

The primitive mantle composition of McDonough [2000] is used to normalize trace element measurements for TITAN element calculations and other applications. This normalization scheme is chosen primarily for its ubiquity; however other researchers prefer to normalize trace-element data to other reservoirs, such as chondrite or bulk Earth. However, normalizing the data shown in this paper using these reservoirs does not substantially change the numerical value of TITAN anomalies (see **Table 2.4**).

2.7.3 Reference MgO method 1: Visual determination of MgO

In mafic lavas, MgO is typically used as an index of differentiation. Mg# may also be used, but its calculation when the redox state of Fe is not analyzed is not straightforward (see Section 2.8). In plots of Al_2O_3 versus MgO, an inflection point typically appears in OIB data arrays. This inflection point represents the transition between olivine and clinopyroxene accumulation (MgO greater than inflection point value) and olivine and clinopyroxene removal (MgO less than inflection point value) [e.g. Day et al., 2010]. In large datasets, this inflection point may be obscured, however plots of $\log(Al_2O_3)$ versus log(MgO) may be used to help determine the inflection point. We determine a range for each hotspot inside which the inflection point exists, and then choose a preferred value inside this range (e.g., **Figure 2.10**). Many hotspots have reference MgO greater than 10 wt. %, which is expected for mafic lavas.

Choosing inflection points on large arrays is subjective and complicated by inclusion of rocks with distinct differentiation histories or distinct provenance, which may obscure a single identifiable reference MgO. Nevertheless, many hotspot data arrays have identifiable inflection points in Al_2O_3 versus MgO plots. In cases where they do not, the inflection points become clearer on plots of $\log(Al_2O_3)$ versus log(MgO) [e.g., Norman & Garcia,1999]. For verification in hotspots with large data arrays, data were split into sub-groups based on geographical location, and inflection points from these sub-arrays were identified and compared in order to corroborate the selected reference MgO values for the entire hotspot.

2.7.4 Reference MgO method 2: Average forsterite contents in equilibrium with whole rocks

Roeder and Emslie [1970] provide experimental constraints on the chemical conditions of equilibrium olivine crystallization. Hotspot data arrays mirror the shape of these equilibrium constraints, although, as expected, a number of data points lie outside this ideal equilibrium (**Figure 2.11**; for a more detailed discussion of Mg# calculations, please see Section 2.8). The origin of this misfit may reflect highly variable degrees of magma differentiation in the history of each hotspot, pressure-temperature conditions of magma ascent that do not match those of Roeder & Emslie [1970], or accumulation of xenocrystic olivine.

We determine the average forsterite contents for each hotspot and use this to determine a corresponding reference Mg# that is both within the dataset and in chemical equilibrium with melt. We then regress Mg# against whole rock MgO within each hotspot to determine a corresponding MgO value for the reference Mg#, which is then used as the hotspot reference MgO. Although this method has an experimental constraint that the first method lacks, we prefer the first method because each olivine dataset will likely contain xenocrystic olivine that we cannot identify by their chemical attributes alone, and which would skew the reference MgO determination. However, results from the two methods agree well (**Figure 2.12**).

2.7.5 Parental TITAN anomaly calculation method 1: Component calculation

Within each hotspot, reference MgO was regressed against each TITAN-involved element to obtain the contents of each of these elements in theoretical parental magmas. Minimum and maximum reference MgO were similarly regressed to propagate the error of each reference MgO determination. TITAN anomalies were then re-calculated using the equations presented in the text.

2.7.6 Parental TITAN anomaly calculation method 2: Direct calculation

In the second method, reference MgO was regressed against TITAN anomalies calculated from measured data for each hotspot to determine parental TITAN anomalies. Similarly, reference MgO minima and maxima were propagated to determine error ranges on each parental TITAN anomaly. We prefer the first method because the second excludes samples for which one or more components of an anomaly calculation are not reported in data sources. For example, a sample with only XRF analysis might have reported TiO_2, Nb, La and Th contents that could be used in method 1 but would be excluded from method 2 because no TITAN anomaly can be calculated from these data. There is agreement between the two methods, however parental TITAN anomalies determined by direct calculation are systematically greater than those determined by component calculation (**Figure S4**), which could be a result of data exclusion from the latter method. Whatever the origin of the deviation, we use the first method for calculating parental TITAN anomalies for our results.

2.7.7 Calculation of error on parental TITAN anomalies

Errors on calculated parental TITAN compositions were determined by propagation of reported data precision through the preferred methods detailed above. Where precisions were unreported, standard precision of ±8% for XRF, ±5% for INAA and HPLC and ±2% for ICP-MS were assumed. Concentrations of TITAN-involved elements and MgO were then re-calculated using reported values plus or minus reported or standard precision. A range of possible parental TITAN anomalies were calculated from these parameters, and ranges were typically within ±30%, with maxima typically showing greater deviation from preferred values than minima (**Table 2.1**). In nearly all cases, reported precision was better than these standard values for their respective methods and we therefore find no reason to summarily exclude any data collected by any standard method of acquisition. Indeed, because different analytical methods have different relative strengths for the study of a given element, errors on calculated parental TITAN anomalies are often minimized when data is derived from more than one acquisition method. Nonetheless, where data acquired by more than one method were available for a single element in a single sample, ICP-MS was preferred over INAA, which in turn was preferred over XRF. This generally avoids situations where multiple analytical methods are used to determine concentrations of elements used in a single TITAN anomaly calculation. It is only possible to determine Nb/Nb* from XRF data alone because the XRF method is not routinely used to measure Sm, Tb or Ta, which are required elements in Ti/Ti* and Ta/Ta* calculations.

2.7.8 Comparison of parental magma compositions to hotspot scorecards.

The parental magma compositions calculated using these methods bear little relationship to "scorecard" metrics [Courtillot et al., 2003; Anderson, 2005] (**Figure 2.14**).

References

Anderson, D.L. (2005), Scoring hotspots: The plume and plate paradigms: Geological Society of America Special Paper 388, 31-54, doi:10.1130/2005.2388(04).

Courtillot, V., A. Davaille, J. Besse and J. Stock (2003), Three distinct types of hotspots in the Earth's mantle: Earth and Planetary Science Letters, 205, 295-308, doi:10.1016/S0012-821X(02)01048-8.

Day, J. M. D., D. G. Pearson, C. G. Macpherson, D. Lowry and J.-C. Carracedo (2010), Evidence for distinct proportions of subducted oceanic crust and lithosphere in HIMU-type mantle beneath El Hierro and La Palma, Canary Islands: Geochimica et Cosmochimica Acta, 74(22), 6565-6589, doi:10.1016/j.gca.2010.08.021.

Jackson, M. G., S. R. Hart, A. E. Saal, N. Shimizu, M. D. Kurz, J. S. Blusztajn, A. C. Skovgaard (2008), Globally elevated titanium, tantalum, and niobium (TITAN) in ocean island basalts with high $^{3}He/^{4}He$: Geochemistry, Geophysics, Geosystems, 9, Q04027, doi:10.1029/2007GC001876.

McDonough, W.F. (2000), The composition of the Earth, *in*: Teisseyre, R. and E. Majewski (eds.), Earthquake thermodynamics and phase transformations in the Earth's interior: International Geophysics Series, 76, 3-23.

Norman, M.D. and M.O. Garcia (1999), Primitive magmas and source characteristics of the Hawaiian plume: petrology and geochemistry of shield picrites: Earth and Planetary Science Letters, 168, 27-44, doi:10.1016/S0012-821X(99)0043-6.

Roeder, P. L. and R. F. Emslie (1970), Olivine-liquid equilibrium: Contributions to Mineralogy and Petrology, 29, 275-289, doi:10.1007/BF00371276.

Wasson, J.T. and G.W. Kallemeyn (1988), Compositions of chondrites: Philosophical Transactions of the Royal Society, London, 325, 146-154, doi:10.1098/rsta.1988.0066.

2.8 Iron oxidation state recalculation method from analytically determined total iron

Many commonly used instrumental methods for determining the abundance of elements in geological materials are unable to differentiate between the oxidation states of a given element, usually due to the minute differences in their atomic weight. The oxidation state of Fe can have an important bearing on arguments regarding the origins of melts, particularly when there is a desire to compare the chemistry of olivine, which incorporates only ferrous iron and excludes ferric iron, to the chemistry of the bulk host rock. The oxidation state of Fe can be determined by titration, but this is not frequently undertaken due to the time and cost involved. In our calculation of parental MgO contents based on olivine compositions, it is necessary to know the redox state of Fe to calculate Mg#. In instances where published literature does not include data regarding the oxidation state of iron, or where analysis is not considered necessary, it is therefore necessary to attempt a calculated prediction of the redox state of Fe based on chemical principles.

In the case that the redox state of Fe is not analytically determined, OIB geochemists will frequently use a constant ratio of 0.9 for the proportion of FeO relative to total Fe oxide. For primitive basalts, analytical data of FeO and Fe_2O_3 frequently conform to this ratio, however the compilation of global OIB presented here, which includes both primitive and more evolved OIB, shows a much broader range of $FeO/(FeO + Fe_2O_3)$ (**Figure 2.15**). It is therefore clear that a more rigorous, data-focused approach to calculating FeO is necessary in order to accurately know whole-rock Mg# and determine

whether olivines are in chemical equilibrium with their host rocks. Here, we outline such a calculation following the method of Robin-Popieul et al. [2012], which was developed for studying the oxidation state of Fe in komatiites.

The presence of ferrous iron (Fe^{2+}) is predominantly controlled by the presence or absence of olivine in rocks, thus felsic rocks, which do not typically contain olivine, retain high proportions of ferric iron (Fe^{3+}) relative to mafic rocks, which can contain olivine. Ferric iron, on the other hand, is typically incorporated into the structures of felsic minerals such as feldspars. Given a large body of Fe redox state analyses on both felsic and mafic rocks, it is possible to approximate the value of $Fe_2O_3/(FeO+Fe_2O_3)$ in general categories of rocks: felsic, mafic, and ultramafic. In addition, a value of typical MgO contents can be assigned, which provides a sensitive measure of the differentiation process causing evolution of rocks from ultramafic to mafic to felsic, to these categories of rocks. The result is a kinked line (**Figure 2.16A**).

The use of a kinked line rather than a curve is supported by the unique phase equilibria governing the genesis of felsic versus mafic rocks. However, we consider also the case where the proportion of ferric to ferrous iron is governed by a curve using the same three tie points as in **Figure 2.16A**, and the difference between these two approaches (**Figure 2.16B**). The propagated deviation in whole-rock Mg# between these two approaches remains below 1% over typical values of Fe and Mg in OIB, though it increases slightly with increasing Fe contents (**Figure 2.17**).

The comparison of these calculations to measured olivine chemistry is not circular because: (1) the assignment of redox states occurs independently of the modal abundance of olivine in the sample on which the calculations are done and (2) whole rock MgO contents are controlled by mineral processes including, *but not limited to*, olivine accumulation. The following equations must be applied to all samples in order to conserve the redox potential of a given magma:

$$For\ 25 < wt.\%\ MgO < 50, \frac{Fe_2O_3}{(FeO+Fe_2O_3)} = \frac{0.1}{(25-50)} * MgO + 25 * \frac{0.1}{(50-25)} + 0.1 \quad \text{(S1)}$$

$$For\ wt.\%\ MgO < 25, \frac{Fe_2O_3}{(FeO+Fe_2O_3)} = \frac{0.2}{(0-25)} * MgO + 25 * \frac{0.1}{(25-0)} + 0.2 \quad \text{(S2)}$$

Because analytical abundance determinations typically rely on counts representing relative concentrations of atoms, it is necessary to also conserve the number of atoms present in the system. This is accomplished by a third equation:

$$Fe_2O_{3\ total} = Fe_2O_3 + FeO * \frac{m_{Fe}+\frac{3}{2}*m_O}{m_{FeO}} \quad \text{(S3)}$$

If we solve the system of equations A1 and A3, we can provide a predictive calculation of FeO and Fe_2O_3 for each sample in the range 25 < MgO < 50 wt. %:

$$Fe_2O_3 = Fe_2O_{3\ total} - 1.11 * \frac{Fe_2O_{3\ total}*(0.8+0.004*MgO)}{(-0.004*MgO+0.2)*(-0.11)+1.11} \quad \text{(S4)}$$

$$FeO = Fe_2O_{3\ total} * \frac{(0.8+0.004*MgO)}{(-0.004*MgO+0.2)*(-0.11)+1.11} \quad \text{(S5)}$$

Similarly, for samples containing up to 25 wt. % MgO, we solve the system of A2 and A3 to yield:

$$Fe_2O_3 = Fe_2O_{3\ total} - 1.11 * \frac{Fe_2O_{3\ total}*(0.7+0.008*MgO)}{(-0.008*MgO+0.3)*(-0.11)+1.11} \quad \text{(S6)}$$

$$FeO = Fe_2O_{3\ total} * \frac{(0.7+0.008*MgO)}{(-0.008*MgO+0.3)*(-0.11)+1.11} \quad \text{(S7)}$$

When used in calculations of Mg#, the results of this method differ up to >20% compared to the use of a constant ratio of $FeO/(FeO + Fe_2O_3) = 0.9$ (**Figure 2.18**), and therefore define unique data arrays relative to the experimental olivine equilibrium constraints of Roeder & Emslie (1970) (**Figure 2.19**). To test the relative accuracy of the two methods of determining Mg#, we use a dataset of OIB for which FeO and/or Fe_2O_3 are analytically determined. For these data, values for FeO and Fe_2O_3 are summed and treated as total Fe, and then FeO is recalculated using a flat ratio and using the method described above. The results are used to calculate Mg#, and these values are compared to values of Mg# calculated directly from the analyzed data. The results, shown in **Figure 2.20**, show that Mg# calculated from the method described here more closely match Mg# determined from explicit analysis of FeO than Mg# calculated using a constant ratio of $FeO/(FeO + Fe_2O_3) = 0.9$. We therefore prefer this method over using a constant ratio of FeO relative to total Fe.

References

Robin-Popieul, C.C.M., N.T. Arndt, C. Chauvel, G.R. Byerly, A.V. Sobolev and A. Wilson (2012), A new model for Barberton komatiites: deep critical melting with high melt retention: Journal of Petrology, 53(11), 2191-2229, doi:10.1093/petrology/egs042.

Roeder, P. L. and R. F. Emslie (1970), Olivine-liquid equilibrium: Contributions to Mineralogy and Petrology, 29, 275-289, doi:10.1007/BF00371276.

2.9 Discussion of partial melting-AFC model of trace element and radiogenic isotope compositions of OIB

In the article text, a two-stage numerical model is presented to show the effect of partial melting and assimilation-fractional crystallization on the composition of the primitive mantle (**Figure 2.6**). The model begins with performance of calculations to determine the effect of low degree (0.001-10%), non-modal batch partial melting of the mantle on the primitive mantle composition of McDonough & Sun [1995] and the DMM composition of Workman & Hart [2005] according to the equation of Shaw [1970]:

$$\frac{C_L}{C_0} = \frac{1}{D_0 + F(1-P)} \qquad \text{(S8)}$$

In this equation, C_L is the element concentration in the melt, C_0 is the initial element concentration in the mantle, D_0 is the bulk distribution coefficient of the element at the onset of melting, and P is the bulk distribution coefficient of the minerals that comprise the melt. For exploration of the impact of partial melting on mantle composition (**Figure 2.7**), a primitive mantle mineralogy with proportions of 0.4/0.4/0.1/0.1 (olivine / orthopyroxene / clinopyroxene / garnet or spinel) as the primitive OIB source is thought to be a mixture between pyroxenite and peridotite mantle [e.g., Sobolev et al., 2007; Vidito et al., 2013]. When modeling partial melting of DMM, proportions of 0.55/0.25/0.15/0.05 are used, as it is likely that the upper mantle has become relatively depleted in orthopyroxene after melting events. Partition coefficients are primarily derived from reported high temperature and pressure experimental data, and are reported with their sources in **Table 2.5**. The selection of primitive mantle composition for the model starting point was based on

frequency of citation, however it is noted that alternative calculations of primitive mantle do not have substantially different TITAN compositions (**Table 2.6**).

The ascent of mantle partial melts is likely a punctuated process that includes ponding of magmas in lithospheric or crustal magma chambers, which can have a measurable impact on the trace element compositions of erupted magmas [Bowen, 1928]. Thus, we use the results of the primitive mantle partial melt models (as it is likely that hotspot parental materials derive from a source approaching a primitive mantle composition) over typical partial melting intervals of hotspots (ca. 0.1-10%) as initial conditions for further models simulating the effects of assimilation and fractional crystallization (AFC) on residual magma and phenocryst phases in a magma chamber. Exact choice of degree of partial melting has little numerical impact on the final model as the shape of the model bounds is primarily determined by differences in source and assimilant concentrations of Os and He. Instantaneous and average trace element and isotopic compositions of a magma chamber solid, liquid and magma (liquid plus solid) were calculated using the equations of Nishimura [2012], which are derived from those of DePaolo [1981] and Powell [1984]. We assume instantaneous chemical equilibrium exists between the magma chamber liquid and the surface of phenocrysts. Growing crystals hence become ‘zoned’ with respect to their trace element and isotopic compositions, and the average phenocryst composition is calculated by integrating over the AFC history of the magma chamber.

Suspended crystals in a magma chamber are likely to at least partially settle, creating regions of varying phenocryst accumulation in a magma chamber. These variably phenocryst-rich regions of the magma chamber are taken to be responsible for varying abundances of phenocrysts in OIB. The trace element and isotopic compositions of porphyritic OIB is simulated by taking a weighted average of the magma chamber liquid and the average composition of phenocrysts based on a range of typical volumetric phenocryst accumulation observed in OIB (0-60 mass percent). This final step is particularly important to garner a theoretical understanding of TITAN compositions in OIB relative to He isotopic compositions because He isotope analysis requires the use of a porphyritic sample. Thus, any sample measure for He isotopes is necessarily going to have a bulk geochemistry, including TITAN elements, that is biased towards the composition of the phenocrysts. If the typical OIB phenocrysts assemblage preserves trace element signatures with elevated TITAN, it becomes more likely that porphyritic OIB will host positive TITAN anomalies.

Although numerical modeling of He isotopes is not typically undertaken, we take a conservative approach to modeling He isotopic compositions. We use partition coefficients for He from Heber et al. [2007], which were determined using methods that avoid the problems complicating previous determinations of noble gas partition coefficients [e.g., Ozima & Podosek, 2002]. One major problem with use of these partition coefficients is that they do not account for gases trapped in mineral fluid inclusions, which are precipitated from magma chamber liquids. Although our modeling of structural He cannot account for He trapped in mineral inclusions, we argue that because fluid inclusions precipitate from a

crystallizing magma in a manner similar to phenocrysts, our model of the average He isotopic composition of phenocrysts closely approximates the He isotopic composition of fluid inclusions. In addition, the difference between calculated isotopic compositions of solid and liquid phases in the magma is small, meaning that error introduced by underestimating the relative mass of precipitate phases (phenocryst and fluid inclusions) is also relatively small. Further, because modeled compositions of Ti/Ti* converge over large ranges of modeled $^{3}He/^{4}He$, error in the He isotopic model is not likely to change the ability of the model to fit measured data.

The resulting model generally fits distributions of measured Ti/Ti* versus $^{3}He/^{4}He$ and $^{187}Os/^{188}Os$ for a variety of hotspots, however we plot them without measured data as we do not believe that the model demands re-interpretation of all OIB samples to reflect only two set source and assimilant end members. Rather, it is more likely that trace element and, in particular, isotopic compositions reflect a degree of source heterogeneity and inputs from sources not considered by the model. We thus present the model as a possible explanation for the co-variance of Ti anomalies with $^{3}He/^{4}He$ and $^{187}Os/^{188}Os$, but not as a necessary explanation for the co-variances.

The model generally under-predicts magnitudes of Ta/Ta* and Nb/Nb* across a realistic range of model parameters because whereas magnitudes of Ti/Ti* respond strongly to modal abundance of metal oxides, Ta and Nb are not as compatible in oxide structures. Thus, the model fails to explain all but the lowest magnitudes of Ta/Ta* and

Nb/Nb*. However, the model can generate sufficiently positive Ta and Nb anomalies through partial melting alone (**Figure 2.7**).

Our model simulates magma compositions using a variety of parameters. Variable model parameters include the proportion of partial melting in garnet versus spinel stability fields (G) and the cumulative percent of mantle melting, which are both varied based on crustal thickness around each hotspot. The ratio of assimilation to fractional crystallization (r_{AFC}) is unconstrained by empirical data and is thus used to maximize model fit, but is generally left invariant at $r_{AFC} = 0.3$. The total proportion of solid phases in the theoretical magma chamber, which is a required constant in the derivations of Nishimura [2012], is taken as 0.1. The phenocryst assemblage of the theoretical OIB is 78/17/5 (olivine/clinopyroxene/oxide) and is based on typical modal abundances amongst phenocryst-rich OIB. The composition of the magma chamber wall rock, which contaminates the crystallizing magma, is taken as DMM composition [Workman & Hart, 2005; Arevalo & McDonough, 2010], with idealized $^{3}He/^{4}He$ and $^{187}Os/^{188}Os$ endmembers based on general distributions of OIB data and oceanic crust. A summary of model parameters is given in **Table 2.7**, and our selected partition coefficients and their respective sources are given in **Table 2.6** and **Table 2.8**.

The results of the models show that elemental incompatibility during partial melting and AFC processes may be responsible for TITAN anomalies. If this is true, given that trace-element spidergrams are intended to order elements in terms of their relative incompatibility, the particular combination of OIB solidus mineral phases may demand

that the order of incompatible elements be changed in such a plot. An appropriate re-ordering is difficult to determine as OIB have vastly different proportions of olivine, clinopyroxene and oxide phases. However, using binned modal abundance and geochemical data from Day et al. (2010), four potential re-orderings are proposed (**Figure 2.21**). These are not meant to be applied to any OIB, but rather as a guideline to show how modal abundance can affect overall incompatibilities of trace elements.

References

Adam, J. and T. Green (2006), Trace element partitioning between mica- and amphibole-bearing garnet lherzolite and hydrous basanitic melt: 1. Experimental results and the investigation of controls on partitioning behaviour: Contributions to Mineralogy and Petrology (152), 1-17, doi:10.1007/s00410-006-0085-4.

Arevalo, R. Jr. and W. F. McDonough (2010), Chemical variations and regional diversity observed in MORB: Chemical Geology, 271, 2010, 70-85, doi:10.1016/j.chemgeo.2009.12.013.

Bowen, N.L. (1928), The evolution of the igneous rocks: Princeton University Press, Princeton, NJ.

Day, J.M.D. (2013), Hotspot volcanism and highly siderophile elements: Chemical Geology, 341, 50-74, doi:10.1016/j.chemgeo.2012.12.010.

DePaolo, D.J. (1981), Trace element and isotopic effects of combined wallrock assimilation and fractional crystallization: Earth and Planetary Science Letters, 53, 189-202, doi: 10.1016/0012-821X(81)90153-9.

Elkins, L.K., G.A. Gaetani, K.W.W. Sims (2008), Partitioning of U and Th during garnet pyroxenite partial melting: Constraints on the source of alkaline ocean island basalts, doi:10.1016/j.epsl.2007.10.034.

Ewart, A. and W.L. Griffin (1994), Application of proton-microprobe data to trace-element partitioning in volcanic rocks: Chemical Geology, 117, 251-284, doi:10.1016/0009-2541(94)90131-7.

Hart, S.R. and C. Brooks (1974), Clinopyroxene-matrix partitioning of K, Rb, Cs, Sr and Ba: Geochimica et Cosmochimica Acta, 38, 1799-1806, doi:10.1016/0016-7037(74)90163-X.

Heber, V.S., R.A. Brooker, S.P. Kelley, B.J. Wood (2007), Crystal-melt partitioning of noble gases (helium, neon, argon, krypton, and xenon) for olivine and clinopyroxene: Geochimica et Cosmochimica Acta, 71, 1041-1061, doi:10.1016/j.gca.2006.11.010.

Jagoutz, E., H. Palme, H. Baddenhausen, K. Blum, M. Cendales, G. Dreibus, B. Spettel, V. Lorenz and H. Wänke (1979) The abundances of major, minor and trace elements in the earth's mantle as derived from primitive ultramafic nodules: Proceedings of the Lunar and Planetary Science Conference, 10, 2031-2050.

Kelemen, P.B., N. Shimizu, T. Dunn (1993), Relative depletion of niobium in some arc magmas and the continental crust: partitioning of K, Nb, La and Ce during melt/rock reaction in the upper mantle: Earth and Planetary Science Letters, 120, 111-134, doi:10.1016/0012-821X(93)90234-Z.

Lemarchand, F., B. Villemant and G. Calais (1987), Trace element distribution coefficients in alkaline series: Geochimica et Cosmochimica Acta, 51, 1071-1081, doi:10.1016/0016-7037(87)90201-8.

Lyubetskaya, T. and J. Korenaga (2007) Chemical composition of Earth's primitive mantle and its variance: 1. Method and results: Journal of Geophysical Research, 112, B03211, doi:10.1029/2005JB004233.

McDonough, W.F. (2000), The composition of the Earth, *in*: Teisseyre, R. and E. Majewski (eds.), Earthquake thermodynamics and phase transformations in the Earth's interior: International Geophysics Series, 76, 3-23.

McDonough, W. F. and S.-S. Sun (1995), The composition of the Earth: Chemical Geology, 120, 223-253, doi:10.1016/0009-2541(94)00140-4.

McKenzie, D. and R.K. O'Nions (1991), Partial melt distributions from inversion of rare earth element concentrations: Journal of Petrology, 32(5), 1021-1091, doi:10.1093/petrology/32.5.1021.

Nash, W.P and H.R. Crecraft (1985), Partition Coefficients for trace elements in silicic magmas: Geochimica et Cosmochimica Acta, 49, 2309-2322, doi:10.1016/0016-7037(85)90231-5.

Nielsen, R.L. (1992), BIGD.FOR: A Fortran program to calculate trace-element partition coefficients for natural mafic and intermediate composition magmas: Computers & Geosciences, 18(7), 773-788, doi:10.1016/0098-3004(92)90024-L.

Nikogosian, I.K. and Sobolev, A.V. (1997), Ion-microprobe analysis of melt Inclusions in olivine: experience in estimating the olivine-melt partition coefficients of trace elements: Geochemistry International 35: 119-126.

Nishimura, K. (2012), A mathematical model of trace element and isotopic behavior during simultaneous assimilation and imperfect fractional crystallization: Contributions to Mineralogy and Petrology, 164, 427-440, doi:10.1007/s00410-012-0745.

Okamoto, K. (1979), Geochemical study on magmatic differentiation of Asama Volcano, central Japan. Journal of the Geological Society of Japan 85(8): 525-535.

Ozima, M. and F. A. Podosek (2002), Noble gas geochemistry: Cambridge University Press, Cambridge, United Kingdom.

Palme, H. and H. St. C. O'Neill (2003) Cosmochemical estimates of mantle composition, *in*: Holland, H.D. and K.K. Turekian (eds.), Treatise on Geochemistry, Volume 2, The Mantle and Core, 1-38, Elsevier, New York, doi:10.1016/B0-08-043751-6/02177-0.

Powell, R. (1984), Inversion of the assimilation and fractional crystallization (AFC) equations; characterization of contaminants from isotope and trace element relationships in volcanic suites: Journal of the Geological Society of London, 141, 447-452, doi:10.1144/gsjgs.141.3.0447.

Shaw, D.M. (1970) Trace element fractionation during anatexis: Geochimica et Cosmochimica Acta, 34, 237-243, doi:10.1016/0016-7037(70)90009-8.

Sobolev, A.V., A.A. Migdisov and M.V. Portnyagin (1996), Incompatible element partitioning between clinopyroxene and basalt liquid revealed by the study of melt inclusions in minerals from Troodos Lavas, Cyprus: Petrology, 4(3), 307-317.

Sobolev, A. V., A. W. Hofmann, D. V. Kuzmin, G. M. Yaxley, N. T. Arndt, S.-L. Chung, L. V. Danyushevsky, T. Elliott, F. A. Frey, M. O. Garcia, A. A. Gurenko, V. S. Kamentsky, A.C. Kerr, N.A. Krivolutskaya, V. V. Matvienkov, I. K. Nikogosian, A. Rocholl, I. A. Sigurdsson, N. M. Sushchevskaya and M. Teklay (2007), The amount of recycled crust in sources of mantle-derived melts: Science, 316, 412-417, doi:10.1126/science.1138113.

Workman, R.K. and S.R. Hart (2005), Major and trace element composition of the depleted MORB mantle: Earth and Planetary Science Letters, 231, 53-72, doi:10.1016/j.epsl.2004.12.005.

Vidito, C., C. Herzberg, E. Gazel, D. Geist and K. Harpp (2013), Lithological structure of the Galápagos Plume: Geochemistry, Geophysics, Geosystems, 14(10), 4214-4240, doi:10.1002/ggge.20270.

Villemant, B., H. Jaffrezic, J.-L. Joron and M. Treuil (1981), Distribution coefficients of major and trace element; fractional crystallization in the alkali basalt series of Chaine des Puys (Massif Central, France): Geochimica et Cosmochimica Acta, 45, 1997-2016, doi:10.1016/0016-7037(81)90055-7.

Supplementary Tables and Figures

Table 2.2: Table of the nine hotspots primarily studied and corresponding indexed references. References are listed in *Supplementary Information* text.

Hotspot	Reference range
Canary Islands	1 - 16
Cape Verde	17 - 26
Comoros	27 - 33
Galapagos	34 - 48, 156
Hawaii	49 – 84, 154 – 156
Iceland	85 – 116, 156
Kerguelen	6, 117 - 126
Reunion	31, 127 - 142
Samoa	143 – 153, 156-157

Table 2.3: Example of the number of samples filtered using criteria mentioned in *Supplementary Information*. Some samples are excluded by multiple factors.

	Hawaii	**Iceland**	**Galapagos**	**Samoa**
Total samples	796	542	186	173
Total filtered samples	103	89	34	38
Samples filtered by low MgO contents	94	86	30	30
Samples filtered by high LOI	2	0	0	0
Samples filtered by low major element + LOI total	8	5	4	11

Table 2.4: Example of TITAN calculations using various normalization schemes. PM: primitive mantle (McDonough, 2000), CI: chondrite Ivuna (Wasson & Kallemeyn, 1988); BE: bulk Earth (McDonough, 2000). The largest difference between PM-normalized TITAN values (preferred) and another normalization reservoir are for CI-normalized Ta and Nb anomalies, which arise due to the low Sm and Tb contents of CI relative to PM. Maximum variation is less than 20%.

	SEL 97	**OFU-04-06**	**KK 18-8**	**NSK 97-214**
Ti/Ti*$_{PM}$	1.14	0.45	0.88	0.82
Ti/Ti*$_{CI}$	1.19	0.47	0.92	0.86
Ti/Ti*$_{BE}$	1.16	0.46	0.90	0.84
Ta/Ta*$_{PM}$	2.95	5.35		3.33
Ta/Ta*$_{CI}$	2.48	4.49		2.80
Ta/Ta*$_{BE}$	2.93	5.31		3.31
Nb/Nb*$_{PM}$	2.51	3.96	2.31	2.50
Nb/Nb*$_{CI}$	2.22	3.51	2.04	2.21
Nb/Nb*$_{BE}$	2.52	3.98	2.31	2.51

Table 2.5: Partition coefficients for numerical modeling of partial melting and references (bracketed). References: [1] Adam & Green (2006); [2] McKenzie & O'Nions (1991); [3] Elkins, et al. (1991); [4] Hart & Brooks (1974); [5] Kelemen, et al. (1993); [6] Day (2013).

	Ol		Opx		Cpx		Gar		Sp	
Rb	0.0004	[1]	0.0038	[1]	0.020313	[1]	0.002	[1]	0.029	[3]
Ba	0.0001	[1]	0.0036	[1]	0.014664	[1]	0.0011	[1]	0.0006	[3]
Th	0.00017	[1]	0.0005	[1]	0.00525	[1]	0.0011	[1]	0.013	[3]
U	0.00026	[1]	0.0007	[1]	0.0052	[1]	0.00355	[1]	0.03	[3]
Nb	0.00007	[1]	0.0007	[1]	0.0103	[1]	0.0015	[1]	0.0006	[3]
Ta	0.0004	[1]	0.0008	[1]	0.018525	[1]	0.00195	[1]	0.0004	[2]
K	0.000177	[4]	0.0001	[5]	0.00225	[4]	0.00001	[1]		
La	0.0001	[1]	0.0006	[1]	0.046875	[1]	0.00125	[1]	0.01	[2]
Ce	0.001	[1]	0.0017	[1]	0.08	[1]	0.00285	[1]	0.01	[2]
Pb	0.001	[1]	0.0001	[1]	0.020371	[1]	0.02	[1]	0.0005	[3]
Nd	0.003	[1]	0.004	[1]	0.1775	[1]	0.024	[1]	0.01	[2]
Sr	0.001	[1]	0.0021	[1]	0.10425	[1]	0.003	[1]	0.0047	[3]
Zr	0.0015	[1]	0.0099	[1]	0.102625	[1]	0.115	[1]	0.0081	[3]
Hf	0.0024	[1]	0.017	[1]	0.20875	[1]	0.085	[1]	0.003	[3]
Sm	0.002	[1]	0.011	[1]	0.29	[1]	0.145	[1]	0.01	[2]
Eu	0.00298	Interp.	0.0195	Interp.	0.324	Interp.	0.412	Interp.	0.01	[2]
Ti	0.013	[1]	0.1	[1]	0.2725	[1]	0.175	[1]	0.048	[2]
Gd	0.00413	Interp.	0.0262	Interp.	0.359	Interp.	0.832	Interp.	0.01	[2]
Tb	0.0025	[1]	0.03	[1]	0.4225	[1]	1.09	[1]	0.01	[2]
Dy	0.00797	Interp.	0.0426	Interp.	0.404	Interp.	2.00	Interp.	0.01	[2]
Ho	0.00605	[1]	0.048	[1]	0.45375	[1]	2.705	[1]	0.01	[2]
Y	0.0055	[1]	0.046	[1]	0.4225	[1]	2.72	[1]	0.002	[3]
Er	0.0136	Interp.	0.063	Interp.	0.4017	Interp.	3.59	Interp.	0.01	[2]
Tm	0.01355	[1]	0.071	[1]	0.43375	[1]	4.75	[1]	0.01	[2]

Table 2.5 Partition coefficients for numerical modeling of partial melting and references (continued)

Yb	0.05	[1]	0.077	[1]	0.3975	[1]	5.625	[1]	0.01	[2]
Lu	0.0325	[1]	0.09	[1]	0.3975	[1]	6.765	[1]	0.01	[2]
Os	2.066667	[6]	0.3	[6]	0.3	[6]				

Table 2.6: Literature compositions of primitive mantle as comparisons to the starting point selected for the models [McDonough, 2000]. None of the calculations results in a TITAN anomaly that is substantially different from 1.00; in the case of Nb/Nb*, partial melt models show that the increase in Nb/Nb* well exceeds the difference from 1.00 shown here (**Figure 2.7**).

	McDonough (2000)	**Jagoutz et al. (1979)**	**Palme & O'Neill (2003)**	**Lyubetskaya & Korenaga (2007)**
Ti	1200	1300	1280	0.95
Nb	0.66	0.9	0.588	0.46
La	0.65	0.63	0.686	0.508
Sm	0.41	0.38	0.431	0.324
Tb	0.1		0.105	0.08
Ta	0.037	0.04	0.04	0.0302
Th	0.08	0.094	0.0834	0.0626
Ti/Ti*	1.00	1.02	1.02	1.01
Ta/Ta*	1.00		1.03	1.03
Nb/Nb*	1.00		0.85	0.88

Table 2.7: Model parameters for OIB hotspot localities. For an explanation of variables, please see the text of *Supplementary Information*.

G	0.9
Cumulative melting	5%
$\mathbf{r_{AFC}}$	0.3
AFC $\boldsymbol{\theta_{ol}}$	78
AFC $\boldsymbol{\theta_{opx}}$	0
AFC $\boldsymbol{\theta_{cpx}}$	17
AFC $\boldsymbol{\theta_{ox}}$	5
$\boldsymbol{\varphi}$	0.1
V	0 - 0.6
$\mathbf{(^3He/^4He)_{Assimilant}\ (R/R_A)}$	0.05
$\mathbf{(^{187}Os/^{188}Os)_{Assimilant}}$	0.15

Table 2.8: Partition coefficients for numerical modeling of AFC processes and references (bracketed). References: [1] McKenzie & O'Nions (1991); [2] Villemant, et al. (1981); [3] Hart & Brooks (1974); [4] Nikogosian & Sobolev (1997); [5] Adam & Green (2006); [6] Sobolev, et al. (1996); [7] Heber, et al. (2007); [8] Day (2013); [9] Nielsen (1992); [10] Ewart & Griffin (1992); [11] Nash & Crecraft (1985); [12] Okamoto (1979); [13] Lemarchand, et al. (1987).

	Ol		Opx		Cpx		Ox	
Rb	0.00018	[1]	0.0006	[1]	0.011	[1]	0.47	[2]
Ba	0.03	[2]	0.0036	[5]	0.04	[2]	0.4	[2]
Th	0.0001	[1]	0.0001	[1]	0.00026	[1]	0.55	[2]
U	0.0001	[1]	0.0001	[1]	0.00036	[1]	0.44	[2]
Nb	0.01	[1]	0.0007	[5]	0.05	[1]	1.8	[9]
Ta	0.03	[2]	0.0008	[5]	0.06	[2]	0.53	[2]
K	0.000177	[3]	0.045		0.00225	[3]	0.045	[12]
La	0.0004	[1]	0.002	[1]	0.054	[1]	0.39	[2]
Ce	0.0005	[1]	0.003	[1]	0.098	[1]	3.34	[11]
Pb	0.0001	[1]	0.0013	[1]	0.01	[1]	2.9	[10]
Nd	0.001	[1]	0.0068	[1]	0.21	[1]	3.633333	[11]
Sr	0.00019	[1]	0.007	[1]	0.067	[1]	0.68	[2]
Zr	0.06	[2]	0.0099	[5]	0.27	[2]	0.4	[2]
Hf	0.01	[1]	0.01	[1]	0.233	[1]	0.38	[2]
Sm	0.0013	[1]	0.01	[1]	0.26	[1]	0.074	[12]
Eu	0.0016	[1]	0.013	[1]	0.31	[1]	0.3	[2]
Ti	0.006	[1]	0.024	[1]	0.1	[1]	16.5	[12]
Gd	0.0015	[1]	0.016	[1]	0.3	[1]	0.018	[13]
Tb	0.0015	[1]	0.019	[1]	0.31	[1]	0.11	[12]
Dy	0.0017	[1]	0.022	[1]	0.33	[1]	2.8	[11]
Ho	0.0016	[1]	0.026	[1]	0.31	[1]	0.017	[13]
Y	0.008625	[4]	0.046	[5]	0.245	[6]	1.523333	[10]
Er	0.0015	[1]	0.03	[1]	0.3	[1]		
Tm	0.0015	[1]	0.04	[1]	0.29	[1]		
Yb	0.0015	[1]	0.049	[1]	0.28	[1]	2.1	[11]
Lu	0.0015	[1]	0.06	[1]	0.28	[1]	1.903333	[11]
He	0.00017	[7]			0.0002	[7]		
Os	2.066667	[8]	0.3	[8]	0.3	[8]	100	[8]

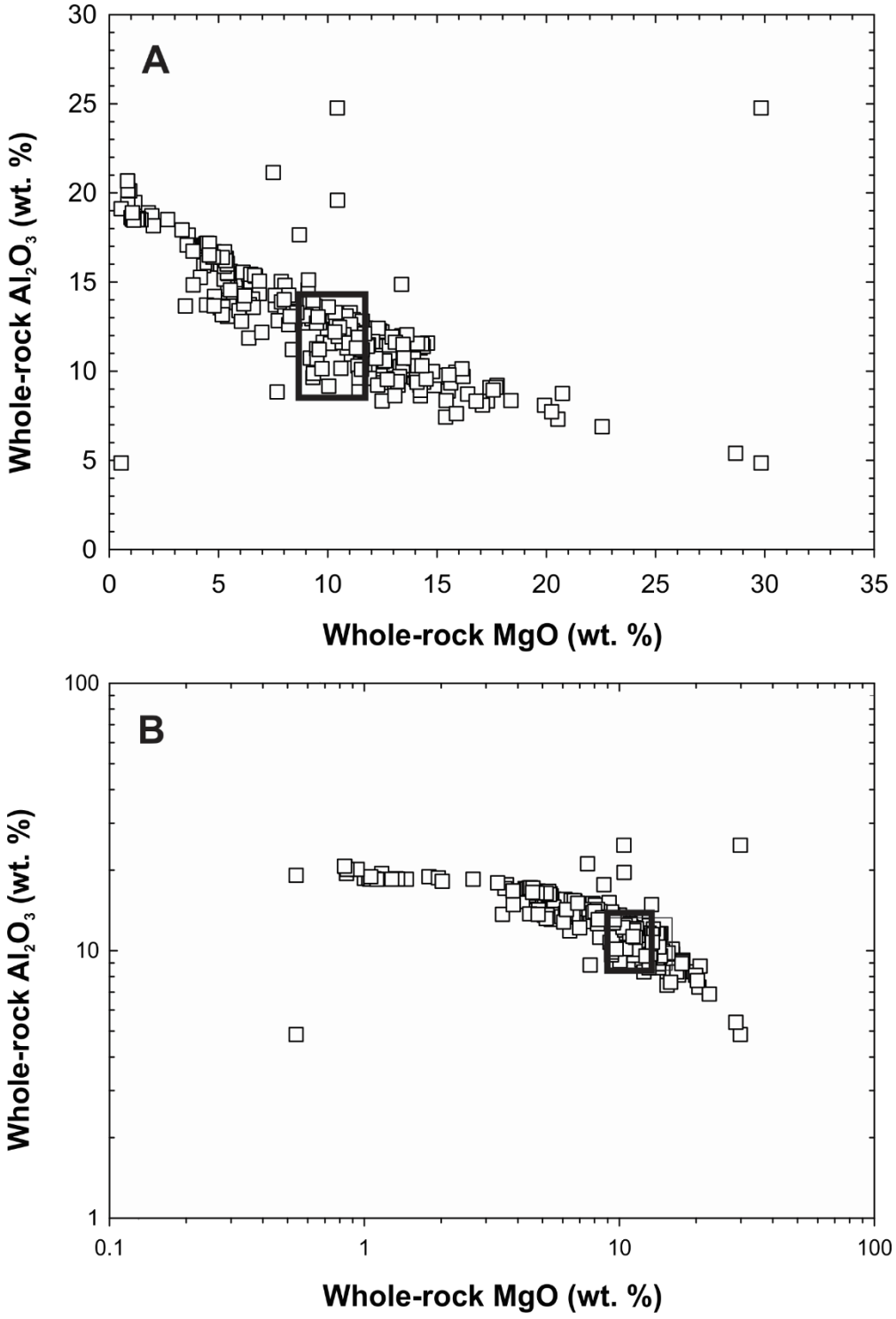

Figure 2.10: Example of visual determination of reference MgO using Canary Island OIB. Black boxes represent areas in which the inflection point is expected to occur. Preferred reference MgO for this hotspot is 10 wt. %.

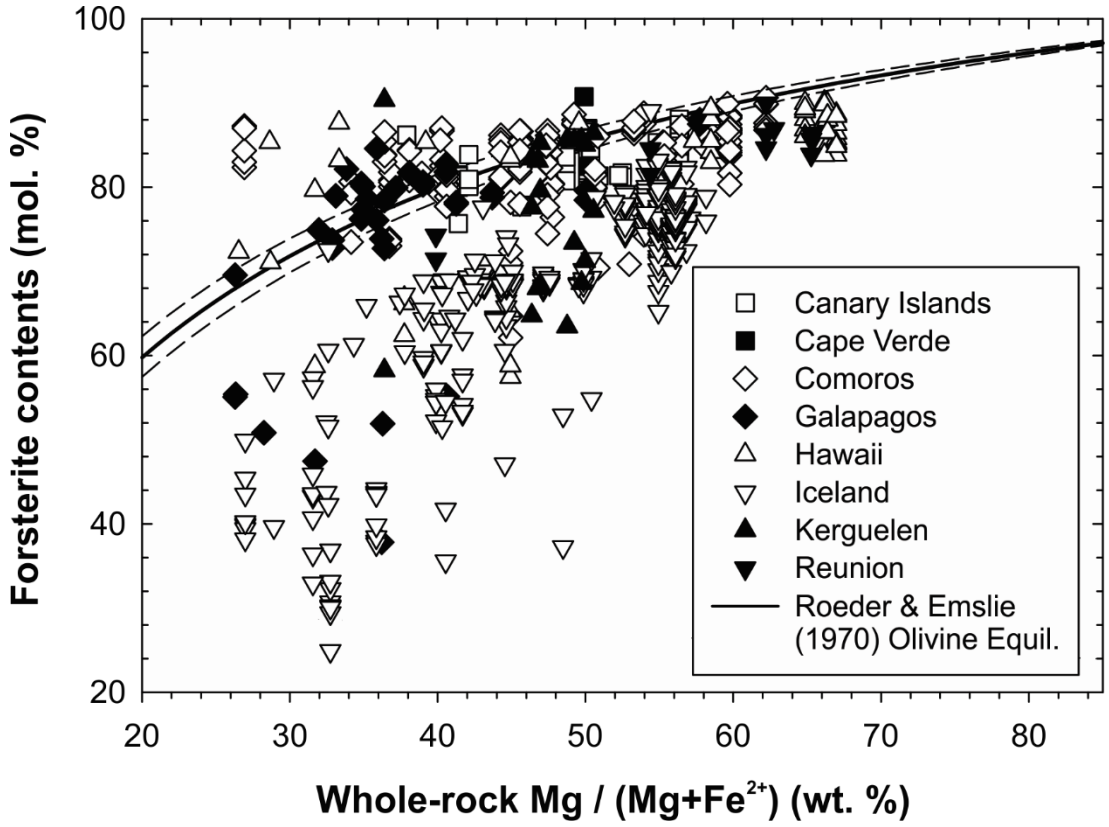

Figure 2.11: Olivine compositions and corresponding whole-rock Mg# from hotspots. A number of olivines lie outside the narrow range of experimental equilibrium determined by Roeder & Emslie [1970]. For a more detailed explanation of the calculation of FeO from measured total Fe, please see *Supplemental Information* text.

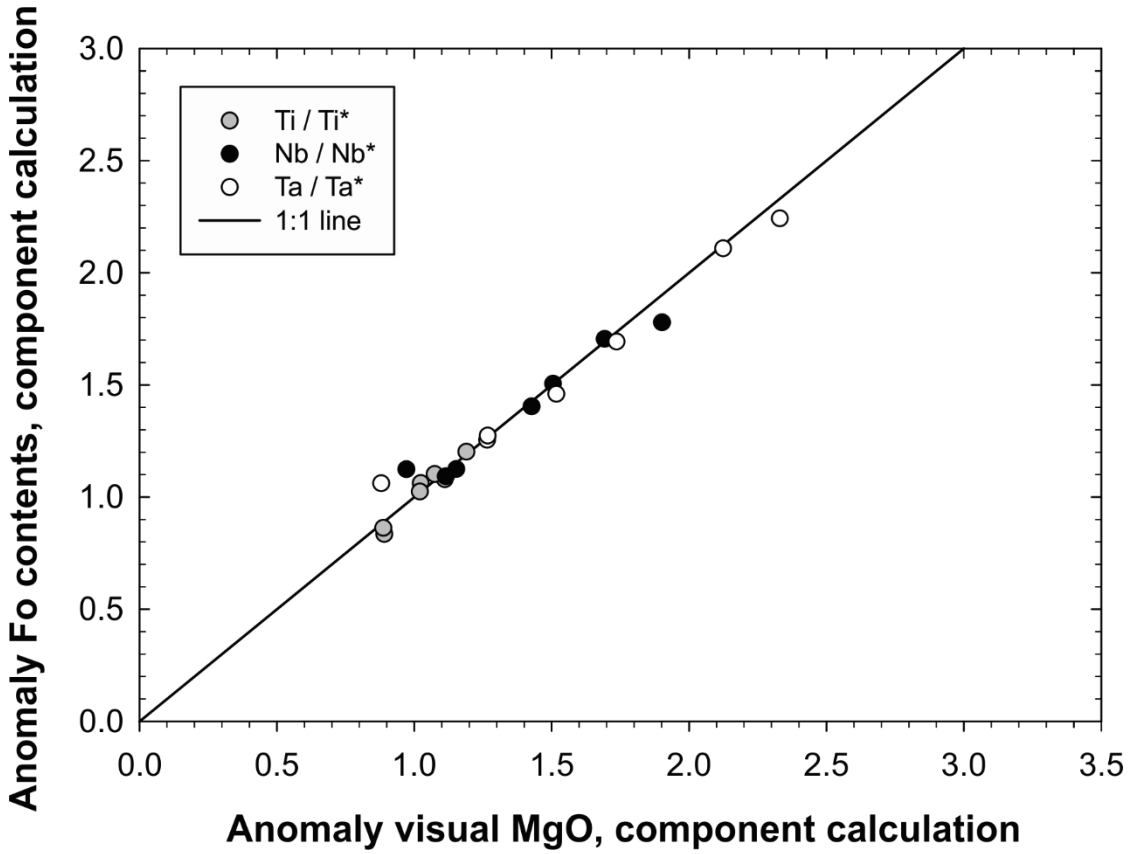

Figure 2.12: Comparison of parental TITAN anomalies determined from reference MgO determined by two methods: a visual estimate of reference MgO and olivine equilibria (see text for explanation of each method). Both methods result in similar calculated parental TITAN anomalies.

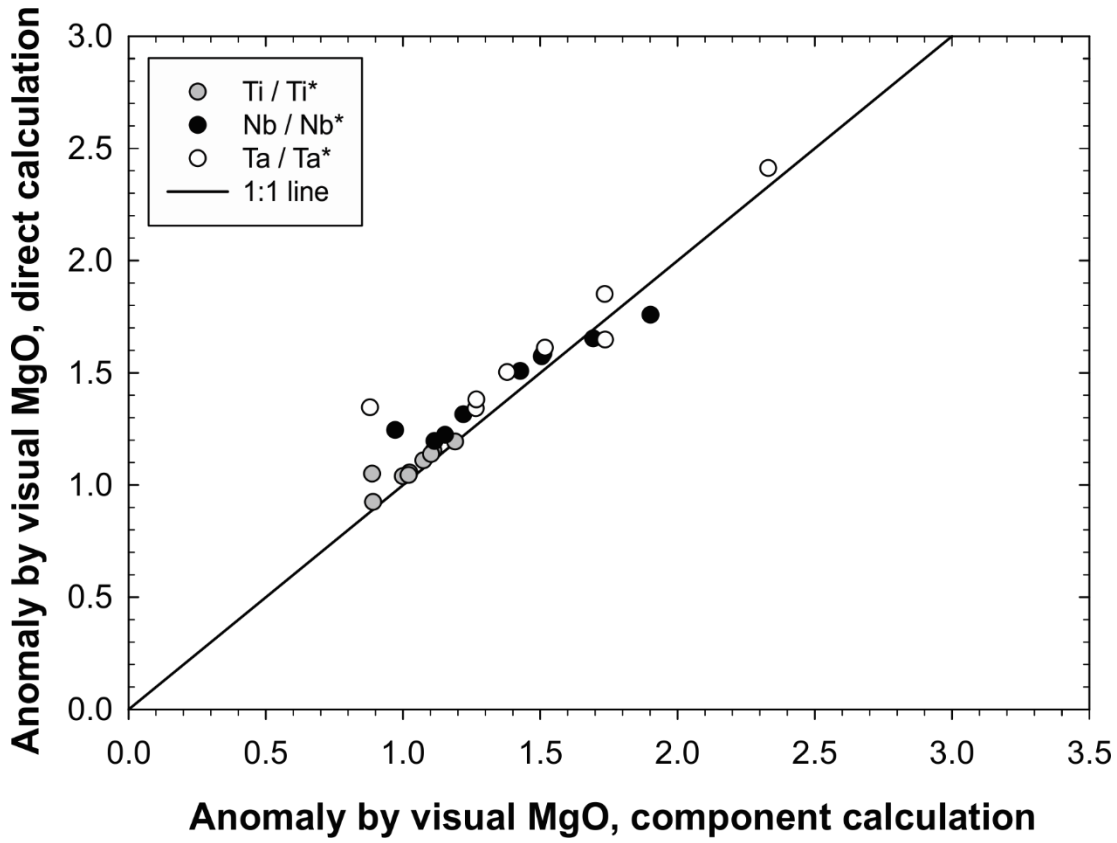

Figure 2.13: Comparison of parental TITAN anomalies determined from visually-determined reference MgO contents and either direct or component calculation, as described in the text. Anomalies directly regressed against reference MgO values are systematically higher than those determined by regression of reference MgO against TITAN-involved elements and recalculation of parental TITAN anomalies (or the inverse of this).

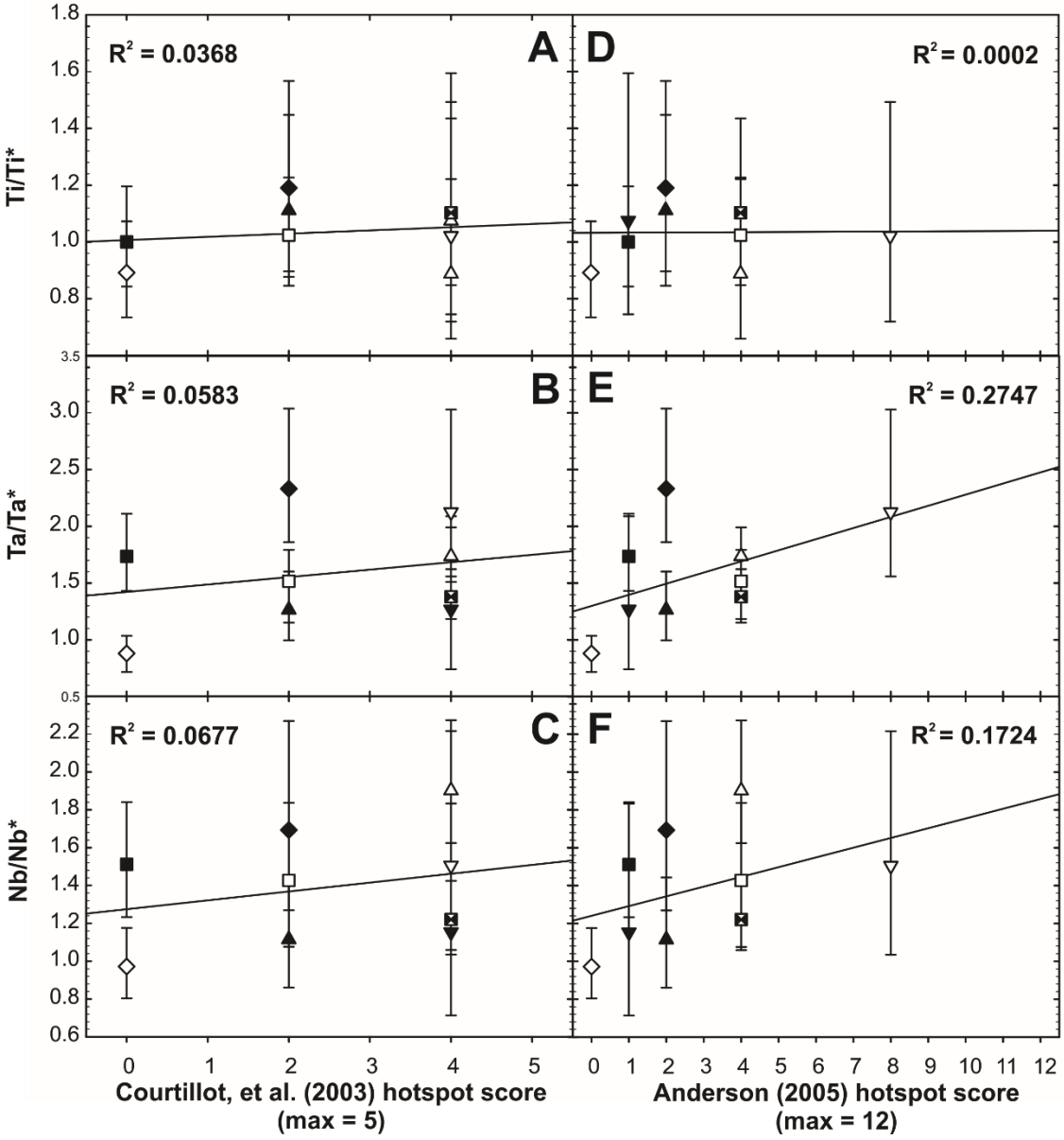

Figure 2.14: Parental TITAN anomalies (as in **Figure 2.5**) versus hotspot "scorecards" [Courtillot et al., 2003; Anderson, 2005] for a plume origin to OIB volcanism. All parental anomalies show poor to very poor correlations, indicating that the primitive component possibly proxied by a higher score is not present in the source of the positive TITAN anomalies. Symbols as in **Figure 2.5**.

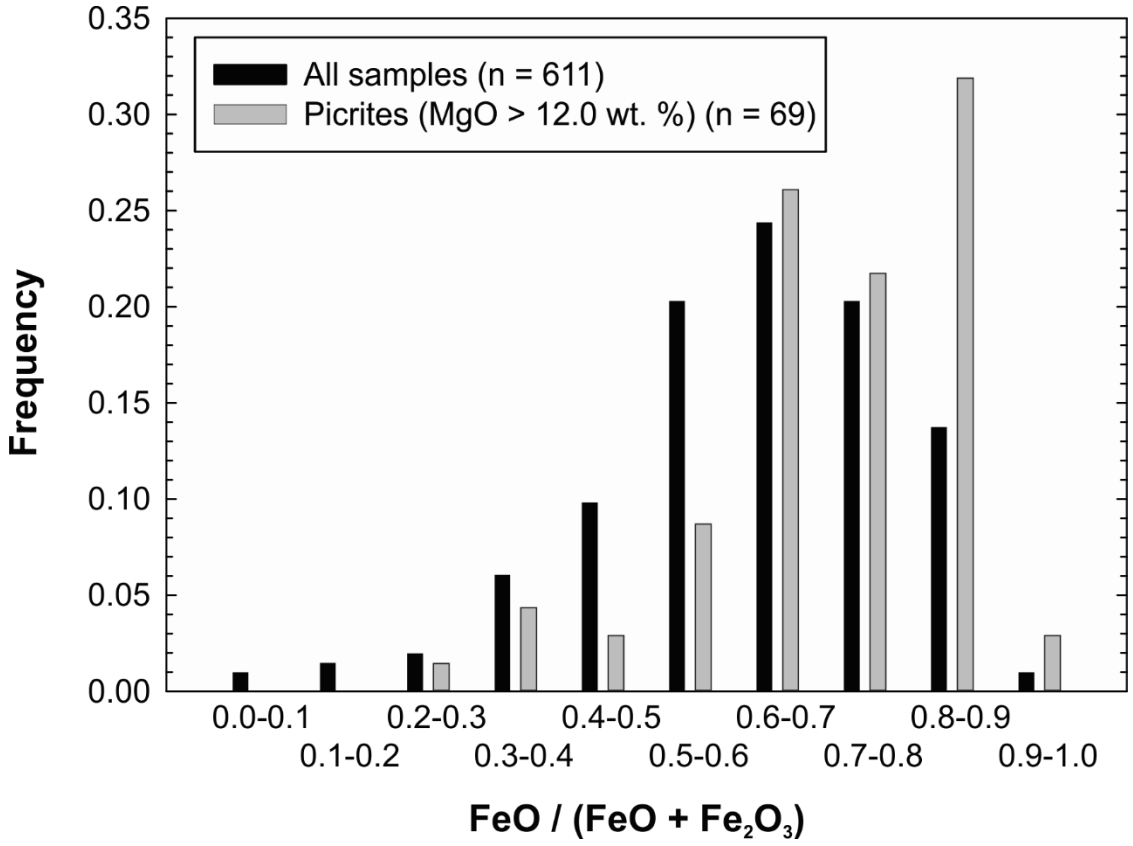

Figure 2.15: Relative abundances of FeO relative to total Fe in OIB and a subset of picritic (primitive) OIB.

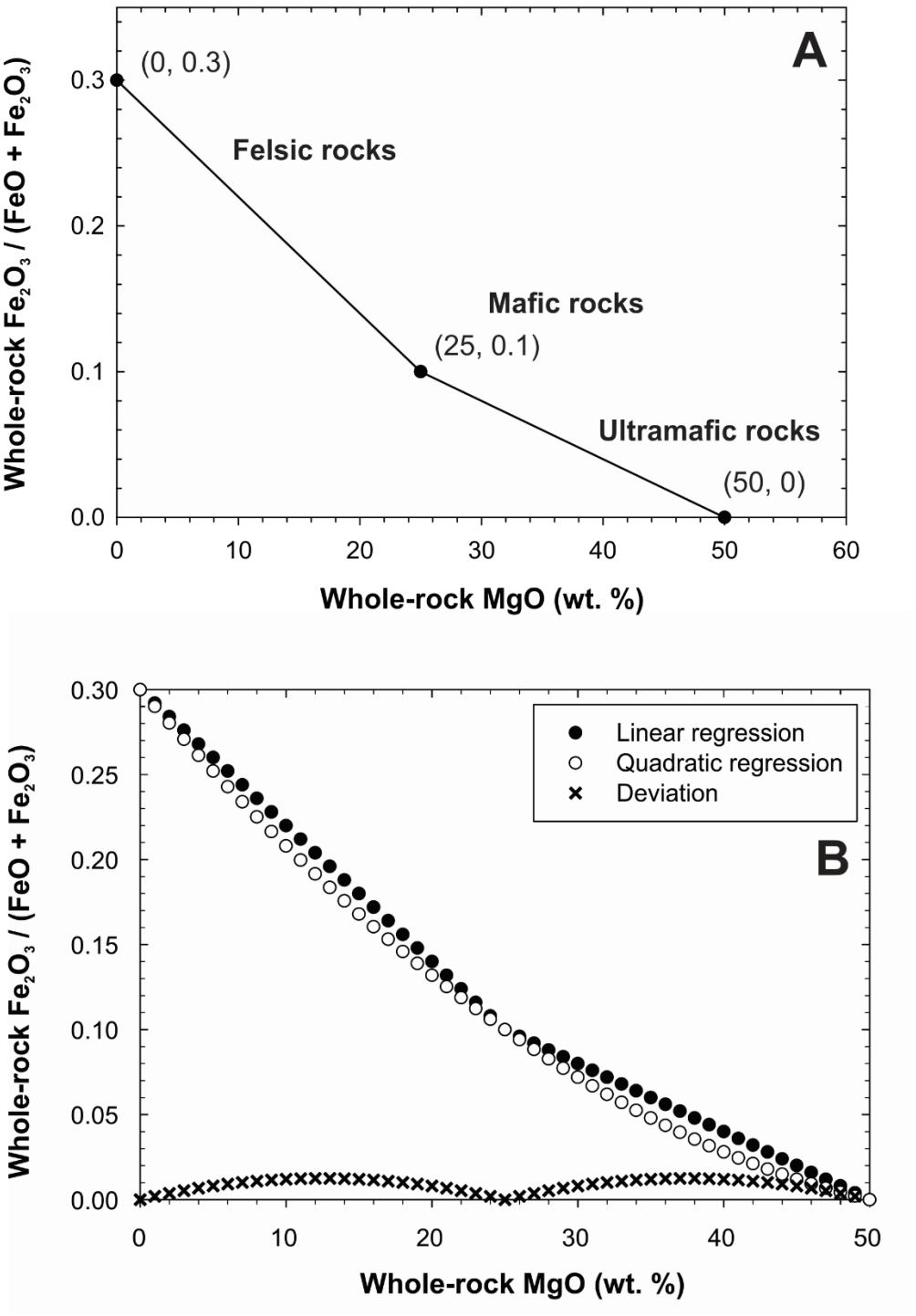

Figure 2.16: (A) Theoretical Fe redox state based on olivine accumulation in typical categories of geological materials. (B) Linear and quadratic approaches to recalculating Fe oxidation state and absolute deviation between the two methods.

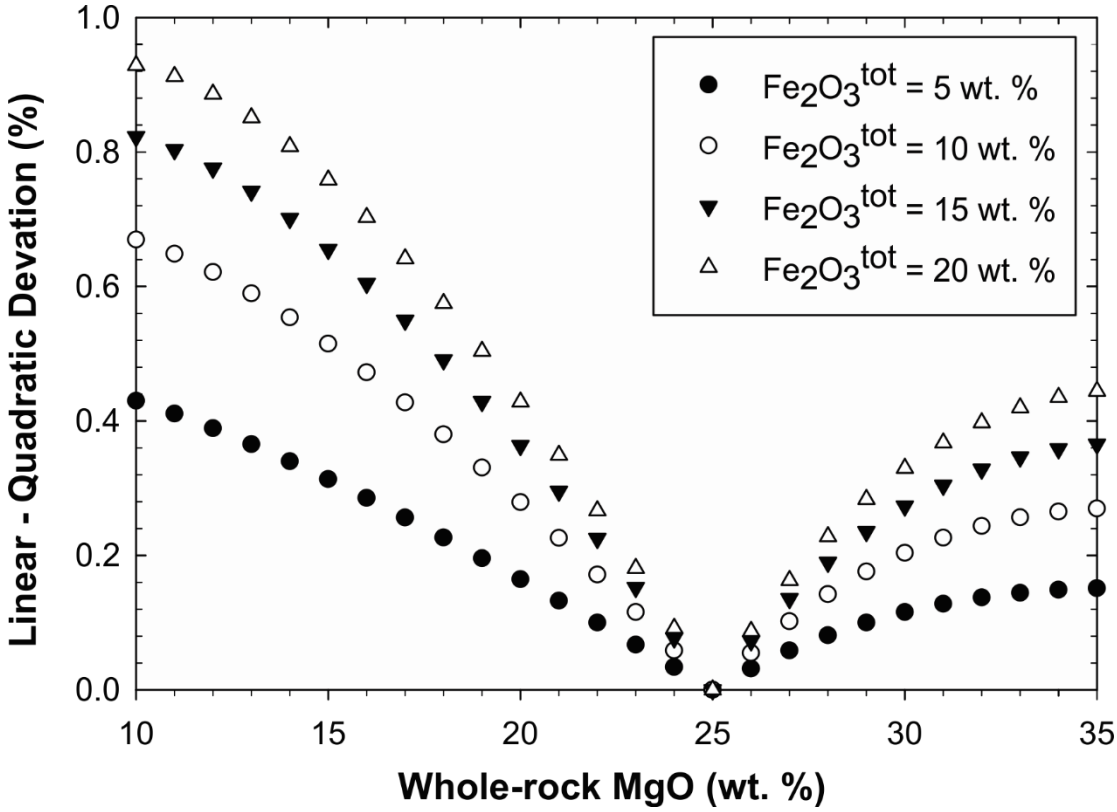

Figure 2.17: Propagated deviation on whole-rock Mg# for various values of total Fe content over a range of typical MgO contents for OIB using the two methods described in *Supplementary Information* text Percent deviation remains below 1% even for very high Fe contents.

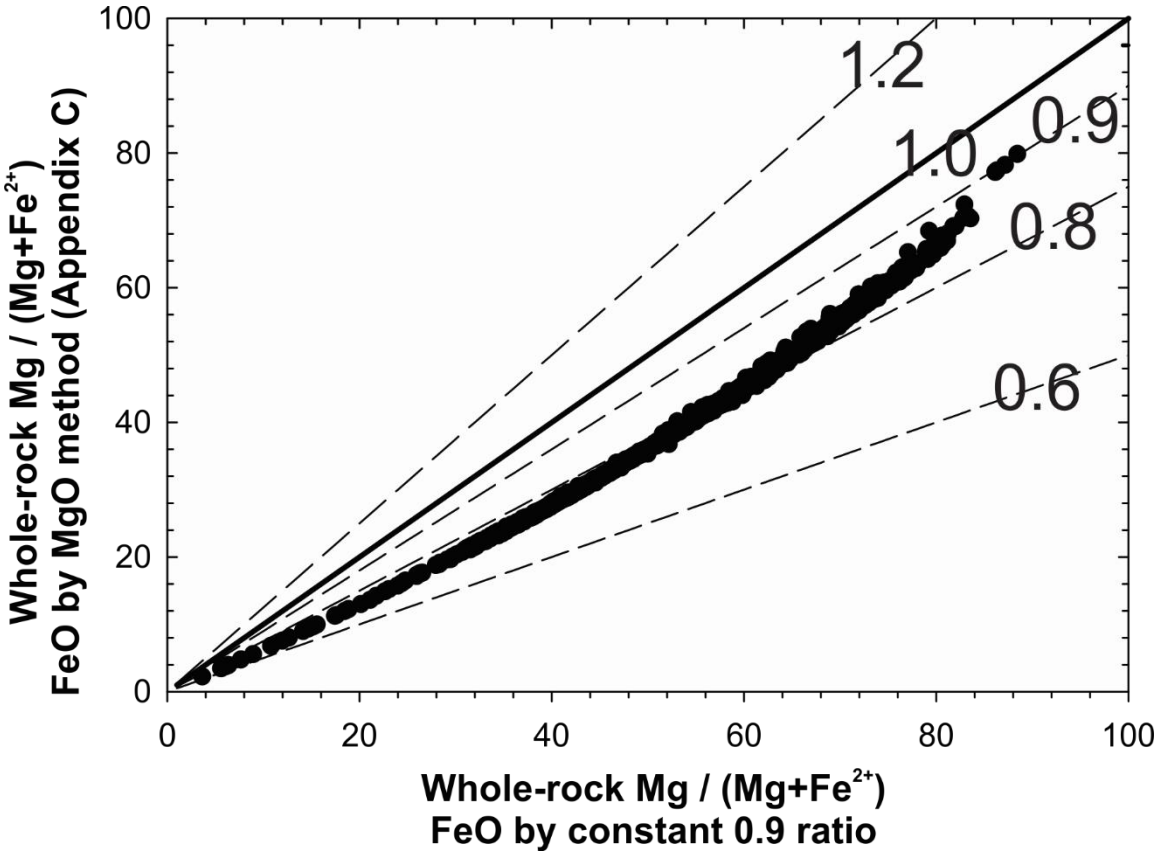

Figure 2.18: Comparison of methods of determining FeO (and, by this, Fe^{2+}) from total Fe data when propagated to calculations of Mg# (Mg# = Mg / (Mg+Fe^{2+})). A 1:1 line (solid, bold) and other lines of constant ratio (dashed) are given with their respective slopes.

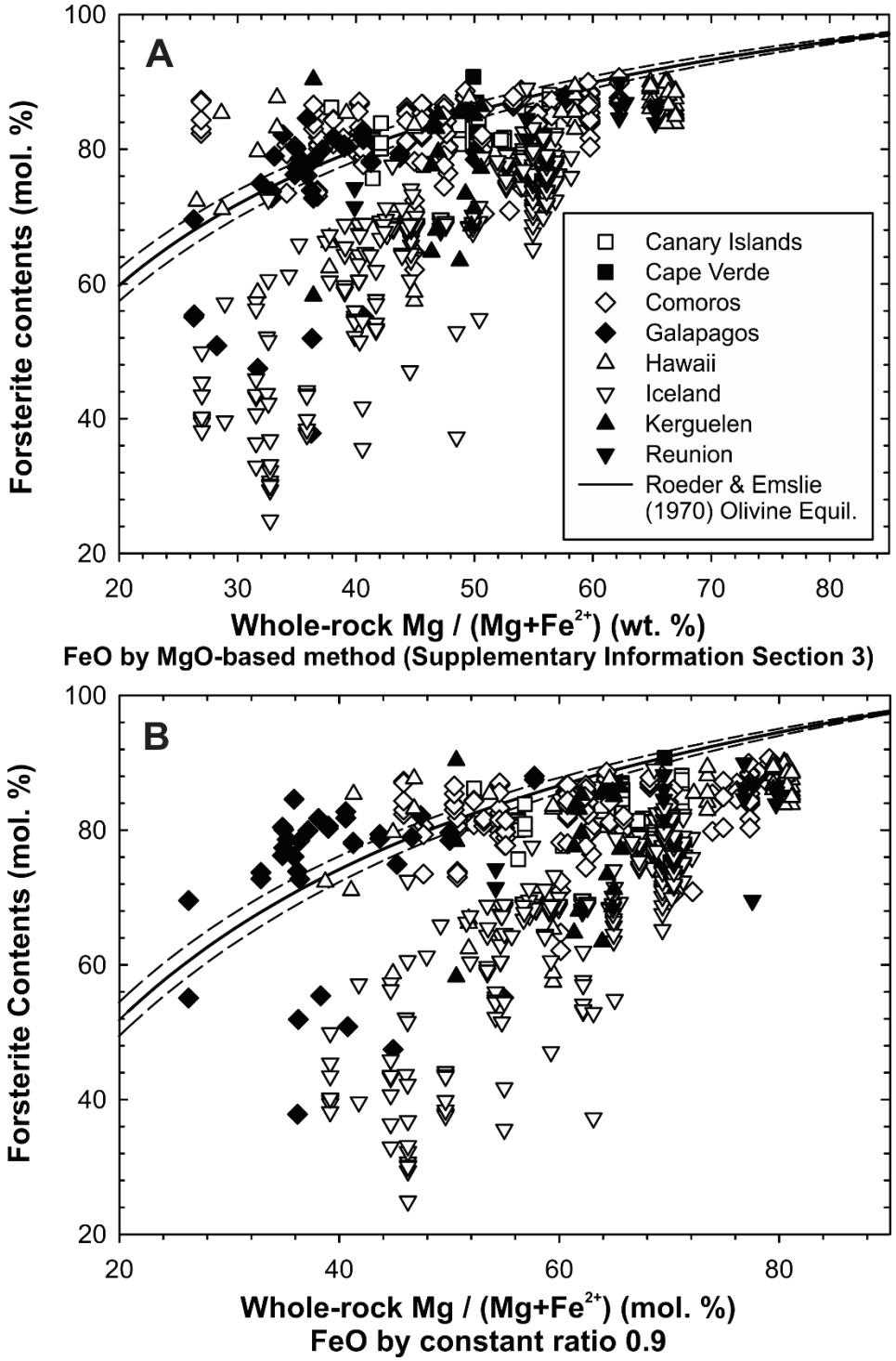

Figure 2.19: Olivine and whole-rock data for global OIB plotted with experimental equilibrium bounds of Roeder & Emslie [1970]. (A) shows Mg# calculated using FeO determined by the method described in Section 3 of the Supplementary Information; (B) shows Mg# using a constant ratio of $FeO/(FeO + Fe_2O_3) = 0.9$.

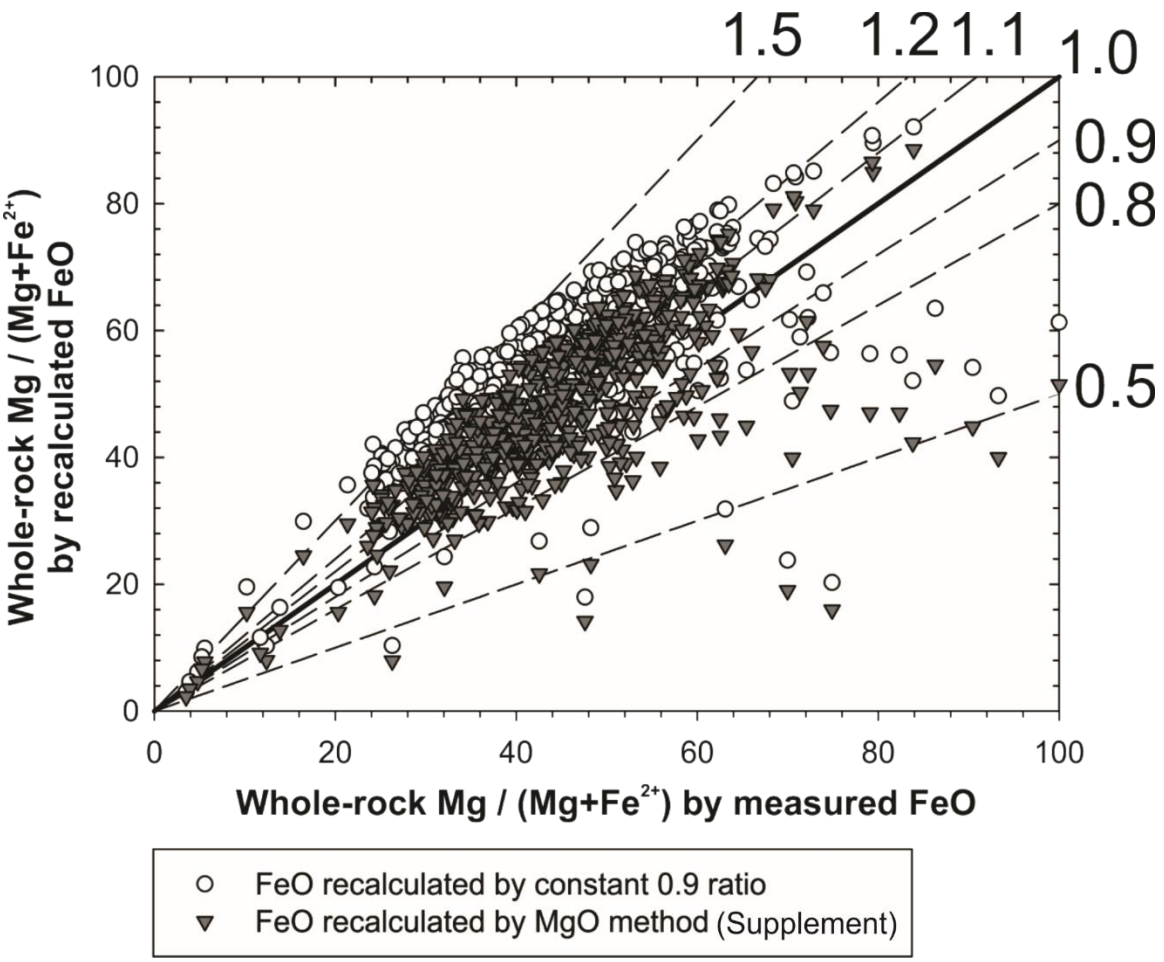

Figure 2.20: Comparison of Mg# calculated from measured redox states of Fe and re-calculations of redox state using the method described in Section 3 of the Supplementary Information and a constant ratio of $FeO/(FeO + Fe_2O_3) = 0.9$. A 1:1 line (solid, bold) and other lines of constant ratio (dashed) are given with their respective slopes. Mg# calculated using the method described in Section 3 of the Supplementary Information are a closer statistical fit with measured data than are Mg# calculated using a constant ratio of FeO to total Fe.

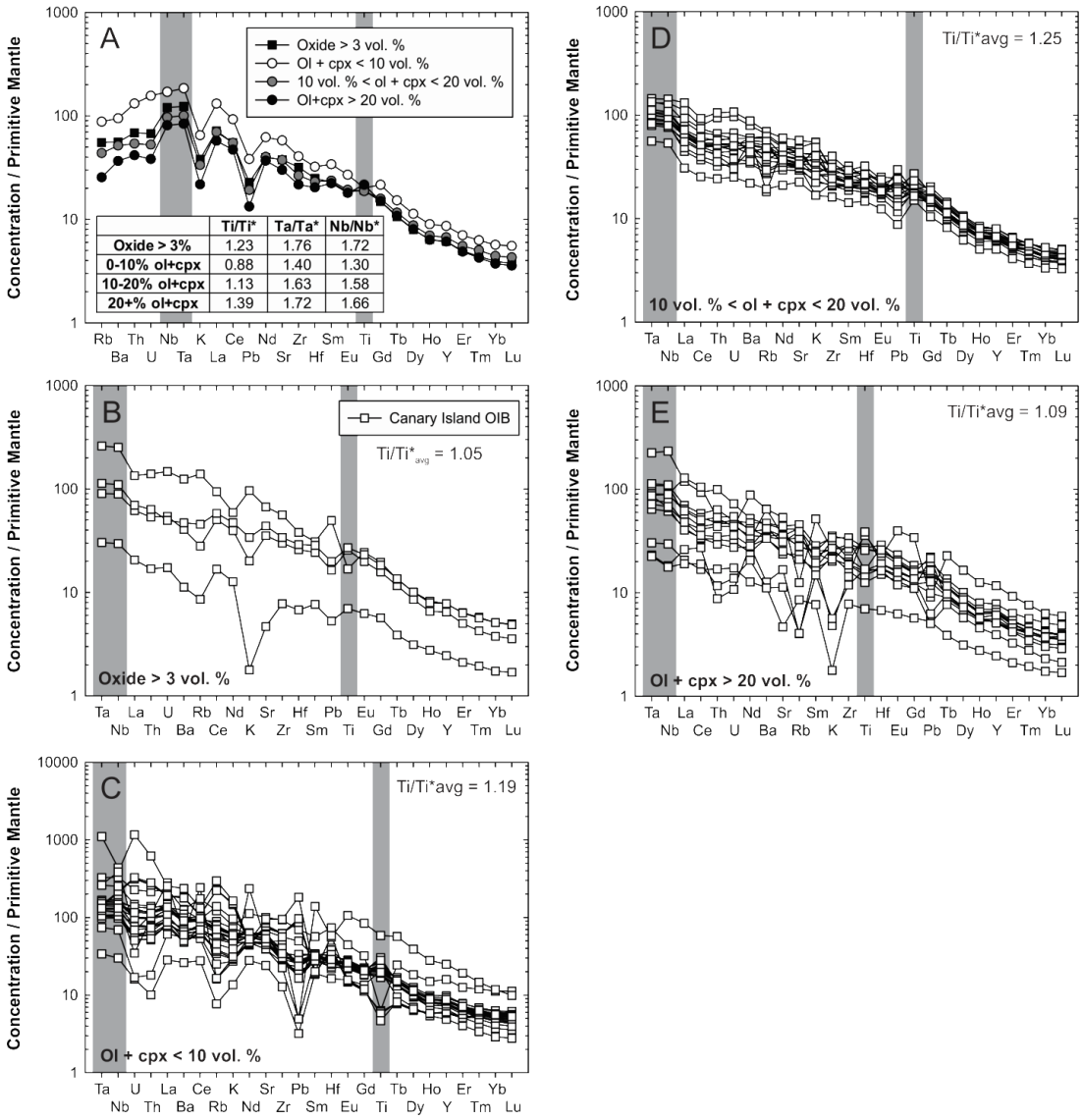

Figure 2.21: Re-ordering of trace element spider diagrams based on relative incompatibilities of elements in OIB with various accumulations of olivine, clinopyroxene and oxide phenocryst phases for (A) typical ordering, (B) oxide accumulation >3 vol. %; (C) <10 vol.%; (D) between >3 vol. % and (E) >20 vol. % olivine and clinopyroxene. Accumulation of oxides, which strongly prefer HFSE (**Table 2.14**, **2.16**), generally cause TITAN anomalies of the highest magnitude. In all cases, re-ordering the elements based on overall compatibility results in Ta and Nb being shifted to the far left, indicating that they are the most incompatible elements in these systems; this new position means that Ta and Nb anomalies can no longer be calculated. Titanium shifts variably, and in all cases Ti/Ti* becomes closer to 1. These re-ordering options are not meant to suggest re-use, but show how modal abundance of mineral phases in OIB may cause relative elemental incompatibilities that differ from those presented in a traditional spidergram; the most appropriate ordering of incompatible trace elements may be closely linked to modal mineral abundances.

Chapter 3:

Early mantle heterogeneities in the Réunion hotspot source inferred from highly siderophile elements in cumulate xenoliths

Abstract

Ultramafic cumulate rocks form during intrusive crystallization of high-MgO magmas, incorporating relatively high abundances of compatible elements, including Cr and Ni, and high abundances of the highly siderophile elements (HSE: Os, Ir, Ru, Pt, Pd, Re). Here, we utilize a suite of cumulate xenoliths from Piton de la Fournaise, La Réunion (Indian Ocean), to examine the mantle source composition of the Réunion hotspot using HSE abundances and Os isotopes. Dunite and wherlite xenoliths and associated lavas from the Piton de la Fournaise volcanic complex span a range of MgO contents (46 to 7 wt.%), yet exhibit remarkably homogeneous $^{187}Os/^{188}Os$ (0.1324 ± 0.0014, 2σ), representing the Os-isotopic composition of Réunion hotspot primary melts. A significant fraction of the xenoliths also have primitive upper-mantle (PUM) normalized HSE patterns with elevated

Ru and Pd (PUM-normalized Ru/Ir and Pd/Ir of 0.8–6.3 and 0.2–7.2, respectively). These patterns are not artifacts of alteration, fractional crystallization, or partial melting processes, but rather require a primary magma with similar relative enrichments. Some highly olivine-phyric (>40 modal percent olivine) Piton de la Fournaise lavas also preserve these relative Ru and Pd enrichments, while others preserve a pattern that is likely related to sulfur saturation in evolved melts.

The estimate of HSE abundances in PUM indicates high Ru/Ir and Pd/Pt values relative to carbonaceous, ordinary and enstatite chondrite meteorite groups. Thus, the existence of cumulate rocks with even more fractionated HSE patterns relative to PUM suggests that the Réunion hotspot samples a yet unrecognized mantle source. The origin of fractionated HSE patterns in Réunion melts may arise from sampling of a mantle source that experienced limited late accretion (<0.2% by mass) compared with PUM (0.5–0.8%), possibly involving impactors that were distinct from present-day chondrites, or limited core–mantle interactions. Given the remarkably homogeneous Os, Pb, and noble-gas isotopic signatures of Réunion, which plot near the convergence point of isotopic data for many hotspots, such a conclusion provides evidence for an early differentiated and subsequently isolated mantle domain that may be partially sampled by some ocean island basalts.

3.1 Introduction

Geochemical studies of lavas from hotspot volcanoes have yielded information that is foundational to knowledge about Earth's deep mantle. In particular, high-$^{3}He/^{4}He$ [e.g.,

Kurz et al., 1982; Hilton et al., 1999; Stuart et al., 2003], solar-like $^{20}Ne/^{22}Ne$ [Moreira & Kurz, 2001] (**Figure 3.1**), or coupled ^{186}Os-^{187}Os enrichments in some ocean-island basalt (OIB) lavas [e.g., Walker et al., 1995; Brandon et al., 1998; 1999; Ireland et al., 2011] have been interpreted as potential indicators of deep-mantle source signatures [e.g., Craig & Lupton, 1976; Kurz et al., 1982; Humayun, 2011]. However, these signatures have not been clearly linked to early-formed, relatively primitive or minimally depleted reservoirs that are distinct from the upper, depleted MORB mantle (DMM). Positive identification of deep- or primitive-mantle sources to volcanism has proven difficult because, apart from noble gases, the majority of isotope systems measured routinely in OIB (e.g., Sr-Nd-Hf-Pb) are broadly lithophile in character. As a result, they tend to be enriched in crustal or sedimentary rocks ($>>\mu g\ g^{-1}$) which, when they are assimilated into magmas, can overwhelm isotopic or elemental signatures imparted from 'peridotitic' mantle sources ($<\mu g\ g^{-1}$). One way to circumvent this problem is to measure highly siderophile elements (HSE: Os, Ir, Ru, Pt, Pd, Re), many of which exhibit compatible behavior, in OIB. The HSE represent a suite of geochemically similar, highly to moderately compatible elements, which can be dominated by mantle (peridotite/pyroxenite) components in OIB, due to the corresponding low concentrations of these elements in crustal rocks [Day, 2013]. The potential for using the HSE and the radiogenic ^{187}Re-^{187}Os and ^{190}Pt-^{186}Os systems that are embedded within them to examine deep-mantle contributions to hotspot volcanic rocks has been previously recognized [Walker et al., 1994, 1995; Brandon et al., 1998; 1999; Ireland et al., 2011, Humayun, 2011]. However, a significant impediment has been that relatively low concentrations of these elements are preserved in many OIB lavas, since the HSE are efficiently removed during fractional crystallization. This leads to compatible HSE (Os, Ir,

Ru) concentrations about an order of magnitude less in OIB lavas than in their mantle sources and complicates interpretations of HSE signatures [Day, 2013].

A novel means with which to elucidate the composition of hotspot mantle sources is to use cumulate rocks that can be found as xenoliths within OIB lavas. Cumulate xenoliths are formed by fractional crystallization of early-crystallizing mineral phases such as spinel, olivine, and pyroxene during the ascent of mantle-derived melts to the surface, and may additionally host HSE-bearing sulfides. For this reason, cumulate rocks tend to be relatively enriched in compatible elements and leave a magma residuum that possesses a significantly different composition than before fractional crystallization, becoming progressively depleted in compatible major-, minor-, and trace-elements as crystallization progresses [e.g., Wager et al., 1960; Jackson & Wright, 1970]. Additionally, because cumulate phases are fractionated early in magma ascent, they are less susceptible to crustal contamination than extrusive lavas. The abundance of cumulate rocks at many hotspots, including Hawaii [e.g., Clague, 1988], the Canary Islands [e.g., Widom et al., 1999; Day et al., 2010], the Azores [Mattiolli et al., 1997], and Réunion [e.g., Babkine et al., 1966; Upton & Wadsworth, 1972] provides a means to quantitatively evaluate the composition of hotspot parental magmas.

In this contribution, we appraise aspects of the composition of the Réunion primary magma through combined analysis of cumulate xenoliths and associated lavas. Compared with other ocean-island locations, the Réunion hotspot has been noted for its remarkable isotopic homogeneity in terms of He [e.g., Graham et al., 1990; Füri et al., 2011], Sr [e.g.,

McDougall & Compston, 1965; Albarède & Tamagnan, 1988; Fisk et al., 1988; Albarède et al., 1997], Nd [e.g., Fisk et al., 1988; Albarède et al., 1997; Luais, 2004; Bosch et al., 2008], Pb [e.g., Vlastélic et al., 2005, 2007, 2009], and Os isotopes [Roy-Barman & Allègre, 1995; Schiano et al., 2012; Gannoun et al., 2015], signatures that persist even in submarine strata [Fretzdorff & Haase, 2002]. Additionally, Réunion plots near the center of the Sr-Nd-Pb isotopic arrays of hotspots [Bosch et al., 2008], rather than displaying a pronounced affinity for one or more of the recognized mantle end-members (**Figure 3.1**). Geochemical evidence, including limited $^{187}Os/^{188}Os$ variations that are marginally more radiogenic than modern-day chondrites [Roy-Barman & Allègre, 1995, Schiano et al., 2012; Gannoun et al., 2015], and a broadly chondritic Th/U signature [Vlastélic et al., 2006] supports a negligible role for recycled materials in the Réunion mantle source. Rather than channeling a mixed signal from multiple mantle-source domains, as inferred for many other OIB, it is possible that Réunion magmas are derivates of a mantle source that has been effectively isolated from recycling processes through much of Earth history. Consistent with this hypothesis, Réunion magmatic products lie on a ~4.4 Ga geochron in Pb isotope space (**Figure 3.1C;** *Supplementary Information*). We show that this ancient source also preserves early mantle HSE heterogeneities and Re/Os that make it distinct from the bulk silicate Earth estimate derived from mantle peridotites [Becker et al., 2006].

3.2 Samples and Methods

A total of 29 cumulate and 13 associated basaltic lava samples from Piton de la Fournaise were selected for study. Petrography and modal analysis were performed at the *Scripps Isotope Geochemistry Laboratory (SIGL),* Scripps Institution of Oceanography,

using identical protocols to those described in Day et al. [2014]. Major- and minor-element mineral compositions were obtained primarily from polished mounts containing olivine, clinopyroxene, and spinel, and as polished-thick sections, at the University of Tennessee using a Cameca SX 100 electron microprobe analyzer. A total of 430 olivine, 294 clinopyroxene, and 246 spinel grains were analyzed in cumulate xenolith samples. Bulk-rock major- and select trace-element abundance analyses were performed by X-ray fluorescence (XRF) at Franklin & Marshall University using a PW 2404 PANalytical XRF vacuum spectrometer, following the procedures outlined in Boyd and Mertzman [1987]. Silicate, oxide, and sulfide phases were measured for the HSE, Cu and W by laser ablation inductively coupled plasma mass spectrometry (LA-ICP-MS) in samples CH0701 Dunite and CH0706B. Bulk-rock trace-element abundances were determined on 100 mg of homogenized powder, using analytical procedures similar to those described in Day et al. [2014], and utilizing a *ThermoScientific* iCAPq-c quadrupole inductively coupled plasma mass spectrometer (ICP-MS) in standard mode. Bulk-rock osmium isotope and HSE abundance analyses were performed at the on ~1 g of homogenized powder according to methods described in Day et al. [2016] and were appropriately oxide and blank corrected. Precision for $^{187}Os/^{188}Os$, determined by repeated measurement of a 35 pg UMCP Johnson-Matthey standard was better than ± 0.3 % for cumulate runs (2 σ; 0.11381 ± 0.00032; n = 12). Repeated measurement of this standard during analyses of RU07 and RU15 samples, which took place several months after analyses of CH07 samples, averaged $^{187}Os/^{188}Os$ = 0.11408 ± 0.00017 (n = 5) and samples measured at this time were normalized to a standard measurement of 0.11381 to enable comparisons between these data. Run statistics for HSE generally indicate <5 % relative standard deviation. Average HSE blanks for cumulate

analyses were (in pg): 14.5 ± 14 [Os], 74.8 ± 86 [Ir], 109 ± 34 [Ru], 50.5 ± 18.7 [Pt], 37.3 ± 57.4 [Pd], and 8.9 ± 4.6 [Re] Full methods information along with tabulated run statistics can be found in the *Appendix*.

3.3 Results

Tabulated whole-rock and mineral geochemical and isotopic data and associated figures are provided in the *Appendix*. Most of the studied Piton Chisny cumulate xenoliths are equigranular dunites with low clinopyroxene contents (0.6-3.1 modal %). Two samples, CH0701Dunite and CH0703Dunite, have relatively high abundances of clinopyroxene (~2-3 modal %). Sample CH0703B is the sole wherlite of the suite, and it possesses distinct mineral chemistry. Approximately one-third of the dunites have a yellow-green color, and the remaining samples are weakly to strongly discolored with a reddish-purple hue. There are, however, no clear distinctions between the bulk chemistry of any of the dunite samples (*Supplementary Information*). Roughly one-third of the cumulate xenoliths contain trace sulfide that is observable in thin section. Sulfide grains occur primarily as silicate-hosted grains (generally <10 μm diameter) with rare, larger interstitial sulfide (up to 50 μm diameter). The large sulfides typically display subequal proportions of pentlandite and pyrrhotite, with rare chalcopyrite occurring exclusively in olivine-hosted grains. Forsterite contents of the cumulate xenoliths span a restricted range from Fo_{80} to Fo_{89} and are generally more Mg-rich than those of Piton de la Fournaise lavas ($Fo_{84.0\ \pm 0.9}$) [Füri et al., 2011]; wherlite sample CH0703B has the lowest forsterite contents ($Fo_{82.0\ \pm 0.9}$), while discolored dunite sample CH0706A has the highest forsterite contents ($Fo_{88.1\ \pm 0.3}$). Olivine formula units of Ca average 0.03 and are consistent across samples. Ranges for pyroxene

compositions are $En_{44-51}Wo_{39-49}Fs_{5-11}$, with no distinguishable differences between rock type or coloration. Spinels are highly chromian, with an average Cr# of 57 ± 5 (1σ).

Piton Chisny xenoliths have high bulk-rock MgO contents (33.1 to 46.4 wt. %, **Figure 3.2**) and low SiO_2 contents (37.5 to 41.1 wt. %), with a range of Mg-numbers (82.7 to 91.0). Most samples have low CaO contents (0.26 to 1.08 wt. %), except those with significant clinopyroxene accumulation (e.g., CH0701Dunite, CH0703B and CH0703Dunite; 1.81 to 7.74 wt. %). Wherlite sample CH0703B has lower proportions of Fe_2O_3(T) and MgO compared with the other Piton Chisny xenoliths, reflecting greater accumulation of pyroxene and/or amphibole relative to olivine. Correlations between MgO and Fe_2O_3 (T), along with elevated concentrations of Ni and Cr, reflect the importance of olivine accumulation over the accumulation of other mineral phases. Relatively high levels of moderately incompatible elements (e.g., Sc, V, Zn) may reflect additional influence from Cr-spinel and clinopyroxene fractionation. For many major- and trace-element systems, the xenolith and lava samples share a common differentiation trend (e.g., **Figure 3.2**). A brief discussion of the major-element characteristics of Piton de la Fournaise lavas is provided in the *Supplementary Information*.

Concentrations of the rare earth elements (REE) in the cumulate xenoliths are depleted relative to Réunion lavas and to primitive mantle (**Figure 3.3**). The xenoliths display a dominant trough-like pattern, reflecting REE compatibility in olivine and a subordinate, concave-down pattern, reflecting REE compatibility in clinopyroxene. Lava samples display a range in absolute REE concentrations, but highly consistent relative

abundances of the REE with primitive mantle-normalized La/Yb varying from 5.0 to 6.9. Concentrations of elements enriched in crustal materials, such as W (1-50 ng g^{-1}) are low in the cumulate xenoliths. The xenoliths have positive Ta anomalies ($Ta/Ta^* = [Ta/(Th \times La)]_{PM}^{0.5}$ = 0.91-2.92; PM indicates normalization to primitive mantle for the respective elements) [McDonough & Sun, 1995], variable Pb anomalies ($Pb/Pb^* = [Pb/(La \times Nd)]_{PM}^{0.5}$ = 0.06-28.9) and negative Sr anomalies ($Sr/Sr^* = [Sr/(Pr \times Hf)]_{PM}^{0.5}$ = 0.13-1.01). Lavas preserve positive Ta anomalies (Ta/Ta^* = 1.67-1.86) and flat-to-negative Sr anomalies (Sr/Sr^* = 0.84-0.95), but possess strongly negative Pb anomalies (Pb/Pb^* = 0.26-0.45) that do not correlate with chalcophile-element abundances (*Supplementary Information*). Differences between "canonical" trace-element ratios in Réunion OIB compared to other OIB indicate that mineral fractionation processes have a dominant effect on incompatible-element compositions; for example, Nb/U values (37.0-42.5) are relatively low with respect to typical OIB (Nb/U = 52 ± 11) [Hofmann, 2007]. Correlations between Cu and ratios of chalcophile elements indicate that sulfide phases exert control over the abundances of certain trace elements in all samples (**Figure 3.4**, *Supplementary Information*), despite a lack of observed sulfide in some polished thin sections. *In situ* measurements of oxides by LA-ICP-MS indicate that these phases contain appreciable Cu and may be partially responsible for Cu abundances in the cumulate xenoliths (*Supplementary Information*).

Piton Chisny cumulate xenoliths contain between 0.27 and 3.9 ng g^{-1} ($[Os/Ir]_{PUM}$ = 2.7 ± 1.5, 1σ) and generally elevated abundances of Ru (0.9 to 5.93 ng g^{-1}, $[Ru/Ir]_{PUM}$ = 2.6 ± 1.4) and Pd (0.21 to 21.3 ng g^{-1}, $[Pd/Ir]_{PUM}$ = 2.1 ± 1.9, 2σ). Iridium abundances range

from 0.14 to 3.1 ng g^{-1}, and Re abundances are generally low, ranging from 0.001 to 0.266 ng g^{-1}. Abundances of Pt in xenoliths vary widely from 0.08 to 13.3, with $[Pt/Ir]_{PUM} = 1.0 \pm 1.0$. Host lavas show a similar relative range of HSE abundances, but have generally lower absolute abundances (Ru = 0.156 to 1.42 ng g^{-1}; Pd = 0.65 to 10 ng g^{-1}). Concentrations of Re in the lavas are generally higher (0.045 to 2.48 ng g^{-1}) than in the cumulate xenoliths. Primitive upper-mantle-normalized HSE patterns for the majority of cumulate xenoliths exhibit a dominant "sawtooth" pattern with relative enrichments in Ru and Pd, and subordinate patterns lacking relative Pd enrichments or containing relative Re enrichments (**Figure 3.5**). Parameterizations of these patterns show no relationship to each other, or to tracers of lithophile and chalcophile differentiation processes, or long-term Re/Os fractionation (*Supplementary Information*). The PUM-normalized HSE patterns of lavas show that some samples have similar sawtooth patterns to the cumulate xenoliths; others have hyperbolic distributions of the HSE, with high relative enrichments in Re, and some are a hybrid of these two patterns (**Figure 3.5**).

Cumulate xenoliths and lavas have a narrow range of $^{187}Os/^{188}Os$ values that are indistinguishable from one another (0.1324 ± 0.0014, $n = 33$, and 0.1325 ± 0.0015, $n = 11$, respectively; standard deviations are 2σ). These values are consistent with published Os-isotopic data for Réunion lavas (0.1325 ± 0.0029, $n = 57$) [Schiano et al., 2012; Gannoun et al., 2015], indicating that magmatic fractionation is unlikely to affect the Os-isotopic compositions of Piton de la Fournaise lavas [e.g., Gannoun et al., 2015]. Measured $^{187}Os/^{188}Os$ values are greater than both the estimate of the primitive upper mantle [$^{187}Os/^{188}Os = 0.1296 \pm 0.0008$; e.g., Meisel et al., 2001] and chondrites [e.g., Horan et al.,

2003], with average cumulate and lava γOs[1] values of 3.8 ± 1.1 and 3.9 ± 1.2, respectively, relative to chondrite ($^{187}Os/^{188}Os$ = 0.12757). Nonetheless, the Réunion hotspot source is less radiogenic than $^{187}Os/^{188}Os$ measured at many other hotspot localities, in particular HIMU-type OIB [e.g., Hauri & Kurz, 1997; Mukhopadhyay et al., 2003; Lassiter et al., 2003; Gaffney et al., 2005; Day et al., 2009; 2010; Ireland et al., 2009, 2011; Day, 2013], but are more radiogenic than classic EM2-type OIB lavas from Samoa [e.g., Jackson & Shirey, 2011].

3.4 Discussion

The petrological and geochemical characteristics of the ultramafic xenoliths found at Piton Chisny are consistent with an accumulative origin. They exhibit petrological characteristics of cumulate rocks including association of olivine and clinopyroxene and lack of orthopyroxene, which is more common in upper mantle rocks. Olivine in equilibrium with depleted upper mantle are expected to have ~$Fo_{89.5}$ [Workman & Hart, 2005] or greater, while the average of Piton Chisny xenoliths is less than Fo_{85}. This average is indistinguishable from cumulates extracted in the Grand Brûlé drill core, which records a continuous sequence of basalt-gabbro-dunite/wherlite under the Piton de la Fournaise terrain [Augé et al., 1989; Rançon et al., 1989]. Most importantly, the xenoliths and lavas share common differentiation trajectories (**Figure 3.2,** *Supplementary Information*), implying that they share a mutual primary-magma composition. The conclusion that the

[1] $\gamma Os = \left[\frac{(\frac{^{187}Os}{^{188}Os})_{Sample}(T)}{(\frac{^{187}Os}{^{188}Os})_{Mantle}(T)} - 1\right] * 100$, T indicates isotopic compositions at time, T.

xenoliths are cumulate rocks is consistent with assumptions of noble-gas studies that have employed Piton Chisny xenoliths to study Réunion mantle sources, showing high-$^{3}He/^{4}He$ and near-Solar $^{20}Ne/^{22}Ne$ [Trieloff et al., 2002; Buikin et al., 2005; Füri et al., 2011]. In the following discussion, post-magmatic alteration effects and cumulate petrogenetic processes are considered, followed by an assessment of the possible causes for relative Ru, Pd and Re enrichments measured in Piton Chisny cumulate xenoliths.

3.4.1 Post-magmatic alteration and petrogenetic controls on cumulate xenoliths and lavas

In Piton Chisny cumulate xenoliths, the most obvious effect of alteration is the strong red to purple discoloration present in some xenoliths. Although the discoloration is not clearly correlated with changes in modal mineralogy, it is most commonly found in intergranular spaces, implying it resulted from fluid-mediated alteration processes. The similarity in the bulk geochemistry of fresh and discolored cumulate xenoliths demonstrates that this modification was largely isochemical, but that it caused local oxidation to some cumulate xenoliths. For example, average Fe^{2+}/Fe^{*} (molar proportion of ferrous to total Fe) is essentially indistinguishable between discolored and fresh samples (0.92 ± 0.03 versus 0.88 ± 0.05), and both types of xenolith exhibit relatively low levels of oxidation compared to lavas (0.1 to 0.97). Bulk-rock abundances of transition metals and spinel Fe^{3+} contents are also similar between the fresh and discolored groups. However, intergrowth patterns occur on silicate-spinel boundaries, which may arise from replacement of ferrous Fe near the edges of olivine grains (*Supplementary Information*). Small quantities of these oxidized minerals, therefore, appear capable of producing the

large color difference observed in the cumulate xenoliths, without significantly affecting their bulk chemistry. Critically, $^{187}Os/^{188}Os$ values and the HSE-pattern sub-groups do not vary systemically between the fresh and the discolored xenoliths, suggesting that late-stage alteration to some cumulate xenoliths did not strongly affect HSE compositions.

Post-emplacement infiltration of basaltic melt can also affect the bulk geochemistry of cumulate rocks before they have fully compacted [e.g., Mathez, 1995; Holness et al., 2007], and may equally disturb the geochemistry of an entire sample suite. Mineralogical evidence for this process, such as the presence of plagioclase or other fine-grained material, is absent in Piton Chisny cumulate xenoliths. Piton Chisny cumulate xenoliths have low Al_2O_3 (<1 wt. %, except wherlite sample CH0703B, which has 1.72 wt. %), and this element is uncorrelated to HSE abundances or Ru/Ir, Pd/Pt and Re/Pd. This excludes the possibility that the HSE patterns are affected by basaltic-melt infiltration processes. Additionally, concentrations of all HSE are uncorrelated to $^{187}Os/^{188}Os$, diminishing the possibility that Os isotopes were perturbed by melt infiltration. For the lavas, it is likely that some Re loss has occurred through degassing under high fO_2 conditions [e.g., Bennett et al., 2000; Lassiter et al., 2003; Norman et al., 2004; Day et al., 2010; Gannoun et al., 2015], but this is probably not a concern for the deeply crystallized cumulates (*Supplementary Information*).

Rare earth element patterns show clear mineralogical control and many of the features of major- and trace-element concentrations in the cumulate xenoliths can be attributed to element compatibility in olivine (*Supplementary Information*). Those dunites

that contain little clinopyroxene have concave-up patterns, whereas the three samples with significant clinopyroxene have concave-down patterns. This latter pattern is consistent with element compatibility in clinopyroxene, which is known to have a preference for the middle REE relative to the light and heavy REE [e.g., Fujimaki et al., 1984] compared to olivine. The REE are also generally more incompatible in olivine than in clinopyroxene, meaning that even a small modal volume of clinopyroxene can control the REE composition of a dunite. Concentrations of the lightest and heaviest REE are broadly similar between the two groups, demonstrating that mineral fractionation alone is insufficient to overcome pervasive negatively sloped REE patterns likely present in the OIB parental magma. Indeed, normalized REE abundances in Piton de la Fournaise lavas are remarkably smooth with limited variation in absolute abundances (La_N/Yb_N = 5.0-6.9; **Figure 3.3**), highlighting the remarkable homogeneity of Réunion partial melts. Ubiquitous positive Ti anomalies in cumulate xenoliths (Ti/Ti* = 1.01-6.89), which are mediated by olivine and spinel accumulation, reflect the regularity of mineral fractionation in these rocks. Sulfides also clearly affect xenolith compositions (**Figure 3.4**, *Supplementary Information*). Thus, many trace-element variations observed in the Piton Chisny xenoliths can be reasonably explained by fractional crystallization and/or partial-melting processes occurring during Réunion magmatism.

3.4.2 HSE in Réunion lavas and cumulate xenoliths

Most Piton Chisny cumulate xenoliths display saw-toothed HSE patterns with relative depletions in Ir, Pt, and Re (high Ru/Ir and Pd/Pt), when normalized to either CI chondrite [Horan et al., 2003], or the estimate for the primitive upper mantle (PUM)

[Becker et al., 2006]. These patterns are not analytical artifacts. We used identical methods to those employed by Day et al. [2016], who have shown that identical results are obtained using conventional digestion or HF-desilicification methods in volcanic rocks spanning a range of compositions. Further, standard peridotite and lava reference materials analyzed using these methods do not exhibit the characteristic patterns observed in the Chisny cumulate xenoliths. Here, we conceptually equate PUM to the bulk silicate earth (BSE), since the terrestrial crust hosts a minor fraction of the total HSE (<< 1 %). Consequently, relative fractionation of the HSE in the cumulate xenoliths is greater than that in the PUM, or the BSE. Either a hitherto-unrecognized petrogenetic process causes significant HSE inter-element fractionation, or the cumulate xenoliths inherited this signature from their mantle source. There are also cumulate xenoliths with relative enrichments in Re and/or Pt relative to Pd (**Figure 3.5**), and we first focus on explaining the causes of the HSE patterns from these xenoliths.

Most OIB lavas are known to have highly variable inter-element fractionations of the HSE, but generally have PUM-normalized Ru/Ir and Pd/Pt values < 1, and have high Re/Os [e.g., Ireland et al., 2009; Day et al., 2010], which contrasts strongly with the patterns measured for the majority of Piton Chisny xenoliths. In basaltic magmas, HSE are highly compatible (Os, Ir, Ru) to compatible (Pt, Pd), or moderately incompatible (Re). These typically exhibit parallel liquid lines of descent, controlled by olivine and spinel fractionation [Crocket, 2000; Puchtel & Humayun, 2001; Puchtel et al., 2004; Jamais et al., 2008; Ireland et al., 2009; Day, 2013]. The HSE also have strong but variable affinities for sulfide [Barnes et al., 1985; Hart & Ravizza, 1996; Burton et al., 1999; Ballhaus et al.,

2006; Gannoun et al., 2007], leading to relatively high Re/Os value in sulfide-residual melts [Roy-Barman et al., 1998; Alard et al., 2000; Gannoun et al., 2004; Day, 2013]. Thus, cumulate xenoliths with Re enrichments (**Figure 3.5B**) may represent relatively late-stage differentiates in the subsurface cumulate pile. *In situ* analysis of Re in the cumulate xenoliths shows relative enrichment of Re in oxide phases that may explain the relative enrichments in Re observed for some samples (*Supplementary Information*).

Relative enrichments in Pt, or the absence of strong depletions in Pt, are more difficult to explain by such a mechanism. Cumulate xenoliths from Piton Chisny that have the greatest enrichments in Pt are also generally the most HSE-enriched (**Figure 3.5**). In addition, all clinopyroxene-bearing dunites have flat-to positive trends across Pt. The same trend, however, is also observed in samples without appreciable clinopyroxene. Current knowledge of Pt partitioning underscores the relatively low incompatibility of Pt in tholeiitic melts [Jamais et al., 2008; Pitcher et al., 2009; Ireland et al., 2009] relative to alkali basalts [Day, 2013], particularly in relatively evolved melts [Jamais et al., 2008]. However, while evolved melts occur on Réunion (*Supplementary Information*), they are not well-represented in the suite of lavas that we measured. Furthermore, the relatively high HSE abundances in some of the Pt-enriched xenoliths, and their similar forsterite contents to the other measured cumulate xenoliths, indicate that singular fractionation processes involving either silicate phases, such as clinopyroxene, or Pt-based alloys may be responsible for these variations. Alard et al. [2000] noted that interstitial sulfides host strong relative enrichments in Pd that may influence bulk-rock Pd/Pt in the opposite direction to that seen in the Chisny cumulate xenoliths. Indeed, the majority of sulfides

observed in Chisny xenoliths are olivine-hosted rather than interstitial, and the magnitude of relative Pd enrichments noted for this type of sulfide are significantly less than for interstitial sulfides. *In situ* analysis of oxides, sulfides, and silicates in samples CH0701 Dunite and CH0706B reveal PUM-normalized Pd/Pt values >1 in all cumulate mineral phases; this strongly argues for a similar relative enrichment in the Réunion parental magma (*Supplementary Information*).

Given that cumulate xenoliths with relative Re and Pt enrichments can be explained by petrogenetic processes, we investigate the possibility that the general saw-toothed shape of PUM-normalized patterns of some Piton Chisny xenoliths reflects similar processes. We present a null-hypothesis fractional-crystallization model utilizing empirically determined partition coefficients and assuming a parental melt that is relatively unfractionated, with respect to the HSE (**Figure 3.6A**). The results permit the generation of a cumulate from a parental melt with relative enrichments in Ru and Pd; however, the model also predicts significant depletion in the incompatible HSE (e.g., Pt, Pd, Re), relative to the compatible HSE (Os, Ir, Ru), which is not observed in the Piton Chisny xenoliths. Correspondingly, these calculations also mean that partial melting is not likely to be responsible for the HSE fractionations, as a reversely fractionated signature would be implied under the conditions of partial melting assumed for Réunion when using the same partition coefficients [e.g., Rehkämper et al., 1999; Day, 2013]. Fractional crystallization or partial melting models, therefore, fail to explain the characteristic sawtooth patterns of many of the Piton Chisny xenoliths. Instead, the HSE signatures must be imparted from the Réunion mantle source.

Petrological modeling utilizing the same partition coefficients demonstrates that a source with pre-existing relative enrichments in Ru, Pd, and Re can produce a cumulate and residual magma with compositions that closely match those observed in the Re-enriched cumulate xenoliths and lavas with hyperbolic HSE patterns, respectively (**Figure 3.6B**). This result provides compelling evidence that Piton de la Fournaise lavas preserve HSE fractionations from a parental magma that inherited Ru/Ir and Pd/Pt fractionations from their mantle source. The presence of similar sawtooth HSE patterns in lavas with high modal proportions of olivine also implies that this signature was acquired within accumulative olivine. For example, a simple arithmetic model indicates 10-60% accumulation of olivine, which is comparable to the modal abundance of olivine in the appropriate samples, can account for the sawtooth patterns present in lavas (*Supplementary Information*). Samples with intermediate abundances of modal olivine may preserve features of the sawtooth fractionated pattern or the hyperbolic pattern; this is dependent on the proportion of accumulated to late-crystallizing olivine. These results strongly support the mode-of-origin for the fractionated HSE patterns preserved in the majority of Piton Chisny xenoliths as being inherited directly from their parental magma.

3.4.3 A non-chondritic source for Réunion

The possibility that the Réunion mantle source was segregated early in Earth's history and remained relatively unaffected by recycling processes has been suggested previously. In particular, relatively low time-integrated Th/U [Vlastélic et al., 2006], $^{3}He/^{4}He$ [e.g., Trieloff et al., 2002; Füri et al., 2011], $^{187}Os/^{188}Os$ [e.g., Schiano et al., 2011; Gannoun et al., 2015], Ne [e.g., Trieloff et al., 2002], and Sr-Nd-Pb isotopic compositions

[Bosch et al., 2008] might indicate that the Réunion mantle source derives from a relatively undifferentiated reservoir. Using the MgO and Ir composition of Piton de la Fournaise lavas that have not experienced S saturation, we calculate the Ir composition of the Réunion parental magma to be 0.41 ng g^{-1} (0.29-0.54 ng g^{-1}, 1σ propagated error) at 35 wt. % MgO, and lower than for other hotspots (e.g., **Figure 3.7**). Using the HSE/Ir values of the same samples, we calculate the concentrations of Os, Ru, Pt, Pd and Re to be 1.01 (0.36-2.0), 0.42 (0.29-0.54), 1.09 (0.49-1.9), 4.18 (0-11), 11 (0-36) and 0.64 (0-2.0) ng g^{-1}, respectively (1σ propagated error). These estimated concentrations are consistent with fractionated Ru/Ir, Pd/Pt, and Re/Pd relative to PUM observed in the cumulates, but are generally lower in abundance compared to PUM and similarly calculated parental compositions of other OIB. If this signature represents the composition of the Réunion mantle source, its composition is certainly non-chondritic.

The relatively unradiogenic $^{187}Os/^{188}Os$ signature of Réunion (0.1324 ± 0.0014) compared to other OIB also supports the idea that its mantle source is non-chondritic. If a Réunion mantle source, represented by CI chondrites [Horan et al., 2003], were isolated at 4.4 Ga [Vlastélic et al., 2006], its present-day Os-isotopic signature requires a $^{187}Re/^{188}Os$ value that is approximately 22 percent higher than that measured for Chondrite Ivuna in order to evolve to its current $^{187}Os/^{188}Os$ value. If this mantle source subsequently interacted with depleted mantle domains [e.g., Gannoun et al., 2015], then we overestimate the HSE concentrations of the source and underestimate the age at which it was isolated from the rest of the mantle. Thus, the Réunion mantle source would be even more geochemically unique than we suggest here. The unique, highly fractionated HSE pattern

observed in Piton de la Fournaise xenoliths are dissimilar to patterns measured in oceanic crust and lithosphere [e.g. Rehkämper et al. 1999; Luguet et al., 2003] or continental crust and lithosphere [e.g., Peucker-Ehrenbrink & Jahn, 2001; Ackerman et al., 2009], which may be present in the sources of other hotspots. Indeed, the unique geochemistry of the Réunion source material may also indicate it melts deeper in the mantle than other hotspot sources (*Supplementary Information*). Given these conditions, we explore the possible origins of an early-formed, non-chondritic Réunion mantle source and the implications for the existence of such a source.

We propose two possibilities to explain the highly fractionated HSE patterns of the Réunion source. First, if the source of the Réunion primary magma is ultimately in the deepest mantle, chemical contributions from Earth's core could impart a strongly fractionated HSE pattern on a source-domain later insulated from the geochemical effects of chondritic late accretion. Results of high-pressure experiments indicate that liquid silicate-metal partitioning is not equivalent for all of the HSE, and core formation may have left a mantle residuum with elevated Ru/Ir and Pd/Pt values, but extremely low absolute HSE abundances [e.g., Mann et al., 2012]. If a small amount of liquid metal from the core were re-entrained into a deep-mantle domain and then cooled [e.g., Humayun, 2011], this could partially replenish HSE abundances and still maintain elevated Pd/Pt and Re/Pd values. Mixing between a solid metal formed by this process and the mantle residuum left over after core formation could produce a domain that has similar HSE fractionations to measured Piton Chisny cumulate xenoliths (**Figure 3.8A-B**). However, extremely high calculated metal/silicate partition coefficients for the most compatible HSE (Os, Ir, Ru,

e.g., D_{Os} = 8064) mean that these elements are entirely stripped from Earth's mantle during core differentiation, thus preserving the original chondritic relative proportions in the core. Mixing between the residual mantle and metallic core material, therefore, causes the mantle to immediately re-acquire the chondritic Ru/Ir signature of the metal, even at vanishingly small added masses. This problem may be avoided by incorporating quantitative constraints on HSE fractionation by sulfide liquid at high temperatures and pressures, which may also cause Ru/Ir fractionation [e.g., Laurenz et al., 2015]. For the less-compatible and incompatible HSE (Pt, Pd and Re), the model predicts retention of a fractionated signature with elevated Pd/Pt and Re/Pd in the mantle, after a limited degree of remixing between the mantle and solid metal from the core. If this mantle domain were subjected to a low degree (<0.2 % by mass) of chondritic late accretion, its composition would closely match Ir, Ru, and Pt abundances calculated for the Réunion source (**Figure 3.8C**).

Second, the source could represent a mantle domain that was differentiated during or after late accretion by non-chondritic or heterogeneous materials in an open silicate system. Previous workers have suggested that late-accretion materials may not be well-represented by measured chondrites, but rather reflect a population of impactors that are no longer preserved in the meteorite collection [e.g., Pattou et al., 1996; Becker et al., 2006; Puchtel et al., 2008]. For example, similar HSE patterns to the PUM, with elevated Ru/Ir and Pd/Pt values have been observed in lunar breccias [e.g., Puchtel et al., 2008; Sharp et al., 2014]. Alternatively, recent constraints provided by refined geochemical modeling [e.g., Rubie et al., 2011] and geochemical data [Walker et al., 2015], indicate that the Earth

may have resided in a chemically heterogeneous proto-planetary disk. Accretion of asteroidal material possessing variable chemistry may produce anomalously fractionated HSE patterns, relative to fractionations observed in a single meteorite family. Additionally, mixing of highly fractionated or heterogeneous-accreted material with primitive Earth material hosting little or no HSE fractionation relative to chondrites, could produce domains of variable HSE fractionation, effectively erasing a homogeneous chondritic or non-chondritic signature existing before late accretion.

Importantly, the two proposed models of lower mantle processes and non-chondritic late accretion are not mutually exclusive. For example, a deep-mantle domain that inherited a fractionated HSE signature from core-mantle interaction may also have experienced variable contributions from non-chondritic late impactors; however, the degree of this accretion would be unknown without constraints on the HSE compositions of the impactors themselves. The unique contributions of the two alternatives are that the first does not require that late accretion was non-chondritic, whereas the second does not require that the Réunion source experienced core contributions. However, both explanations can account for the unusually low calculated HSE abundances in the Réunion source, which cannot otherwise easily be explained by conventional late-accretion models. Evidence from the HSE, therefore, strongly supports the notion that the Réunion source represents an early differentiated mantle domain that became chemically isolated from the bulk silicate Earth before the termination of late accretion. Future high-pressure and temperature metal-silicate and sulfide-partitioning data may be able to fully account for the magnitude of calculated HSE abundances in the lower mantle during core formation. If this

were the case, it could mean that the Réunion mantle source was isolated even earlier, before the onset of late accretion.

Heterogeneous distribution of the daughter isotopes to short-lived radiogenic isotope systems (e.g., ^{146}Sm-^{142}Nd and ^{182}Hf-^{182}W) have provided complementary evidence for the existence of persistent, distinct mantle domains that formed early in Earth's history [e.g., Caro et al., 2003, 2006; Boyet & Carlson, 2005; Bennett et al., 2007; Caro & Bourdon, 2010; Willbold et al., 2011; Touboul et al., 2012, 2014; Debaille et al., 2013; Rizo et al., 2013]. If the Réunion mantle source experienced minimal contributions from late accretion, Réunion igneous rocks may also possess modestly positive ε^{142}Nd, but either positive or negative μ^{182}W, depending on the relative contribution of core material to the extant Hf-W system. However, the lack of correlation between Ru/Ir, Pd/Pt and Re/Pd values (*Supplementary Information*) implies that there were multiple processes involved in the formation of the Réunion source-domain. If this were the case, it may provide a mechanism by which the source could simultaneously contain elevated Ru/Ir, Pd/Pt, and Re/Pd values, but also lack positive ε^{142}Nd and μ^{182}W.

3.5 Conclusions

Piton Chisny cumulate xenoliths preserve evidence for non-chondritic HSE inter-element fractionations in the Réunion mantle source. Combined with the unique features of Réunion's radiogenic isotopic signature, this evidence may be a repercussion of a strong influence from a deep, primitive source that is less refractory than either ambient upper mantle or other mantle sources to hotspot magmas. The origin of this fractionated pattern

requires further investigation from studies of extinct radionuclides and nucleosynthetic effects, but may be due to either: (1) addition of a non-chondritic exogenous component during late accretion, or (2) limited contribution from core material after Earth differentiation that was insulated from the geochemical consequences of late accretion. In either case, it demonstrates that the Réunion hotspot has the greatest potential of all OIB studied to date for sampling a mantle domain that has been effectively isolated from the convecting upper mantle through much of Earth's history.

Acknowledgements

The authors thank Richard Walker for discussions and Allan Patchen for technical assistance with EMP analyses. We are grateful to two anonymous reviewers and EPSL editor Dr. Bernard Marty for their thoughtful comments, which substantially improved the quality of this work. Field work was supported by the National Geographic Society (NGS 8330-07), the Geological Society of America (GSA 10539-14) and by a generous donation from Dr. Robert Rex. General support was provided from NSF EAR grants 1116089 and 1447130 to JMDD and the Devendra and Aruna Lal Fellowship to BJP. These sources of funding are gratefully acknowledged. The authors declare no conflicts of interest.

Chapter 3, in full, is a reformatted version of the material as it appears in Earth and Planetary Science Letters: Peters, B.J., J.M.D. Day and L.A. Taylor (2016) Early mantle heterogeneities in the Réunion hotspot source inferred from highly siderophile elements in cumulate xenoliths: Earth and Planetary Science Letters, 448, 150-160. I was the primary investigator and author of this paper and of this chapter.

Figures

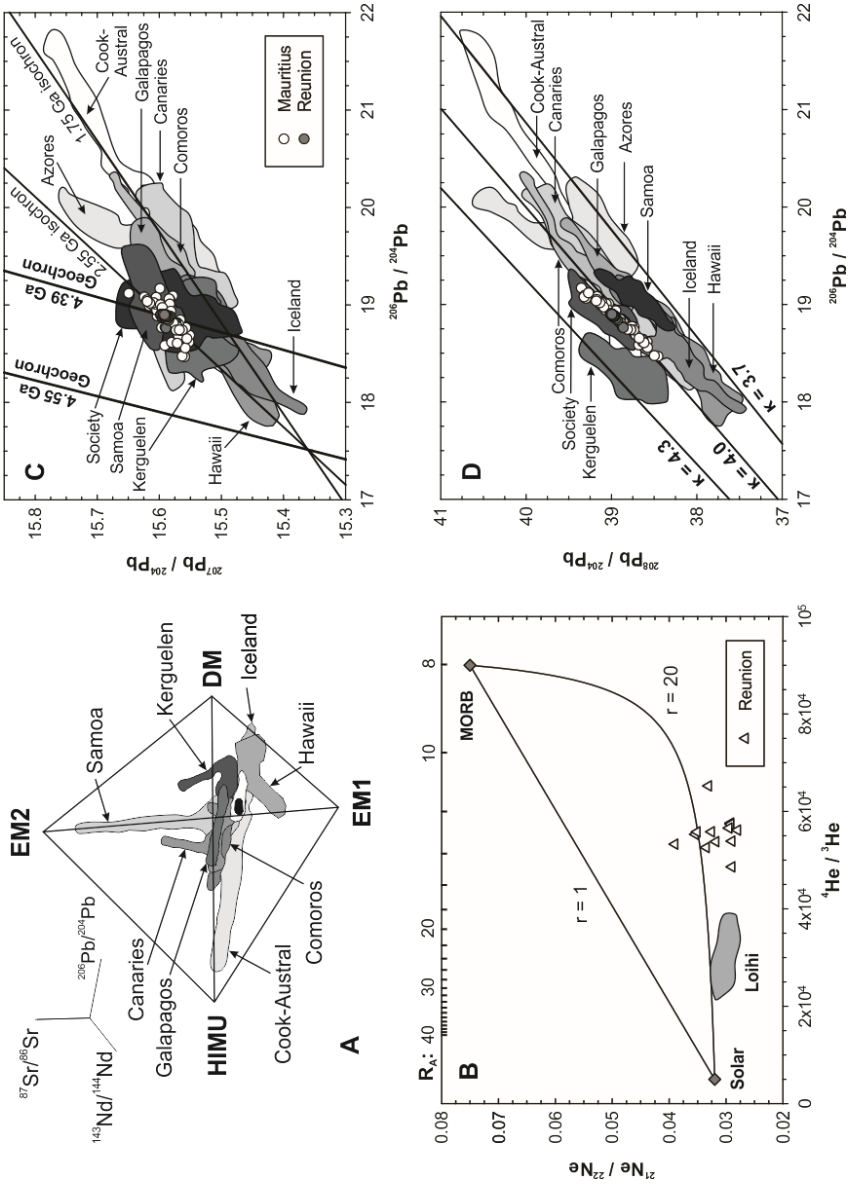

Figure 3.1: (A) The Sr-Nd-Pb isotope mantle tetrahedron, showing the location of Mauritius (white field) and Réunion (Piton de la Fournaise – black field superimposed on the Mauritius field) relative to other selected OIB locations; (B) noble-gas characteristics of Réunion basalts [Kaneoka et al., 1986; Staudacher et al., 1990] compared with Loihi basalts [Honda et al., 1993] and the solar noble gas signature [Moreira & Kurz 2001]; (C) $^{206}Pb/^{204}Pb$-$^{207}Pb/^{204}Pb$ characteristics of Réunion and Mauritius basalts compared to those of other hotspots, isochrons calculated using $\mu = 8.0$; (D) $^{206}Pb/^{204}Pb$-$^{208}Pb/^{204}Pb$ characteristics of Réunion and Mauritius basalts compared to those of other OIB ($\kappa = {}^{232}Th/^{238}Pb = 4.0$).

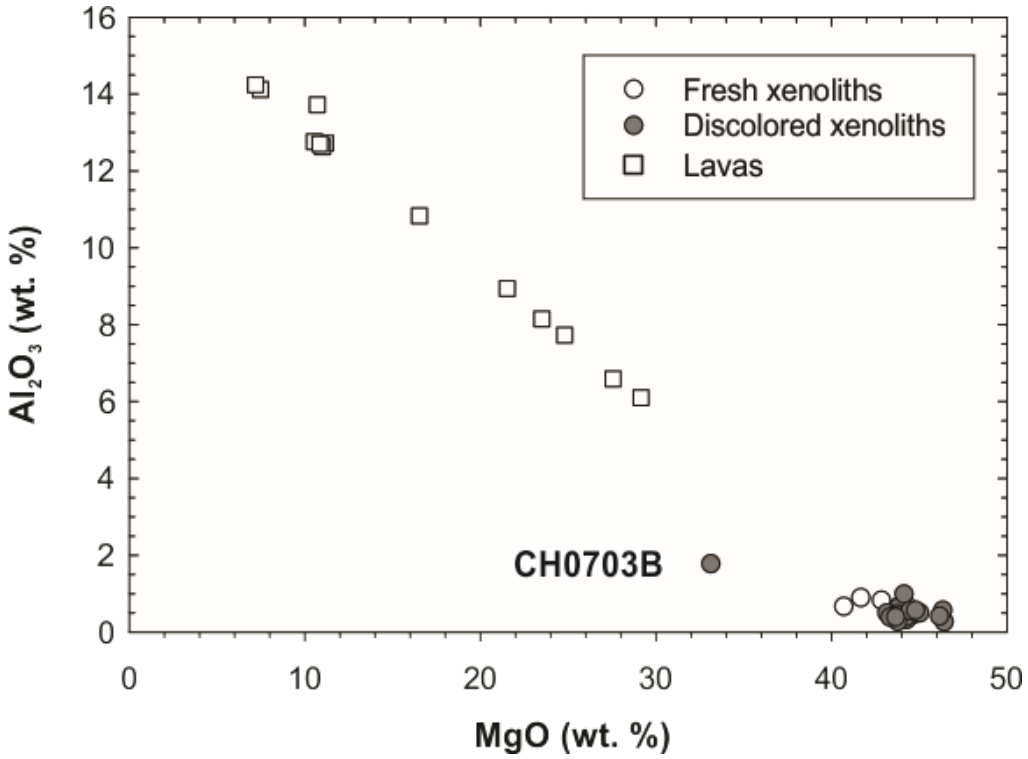

Figure 3.2: Example of major-element variations for Piton Chisny cumulate xenoliths (circles) and Piton de la Fournaise lavas (squares).

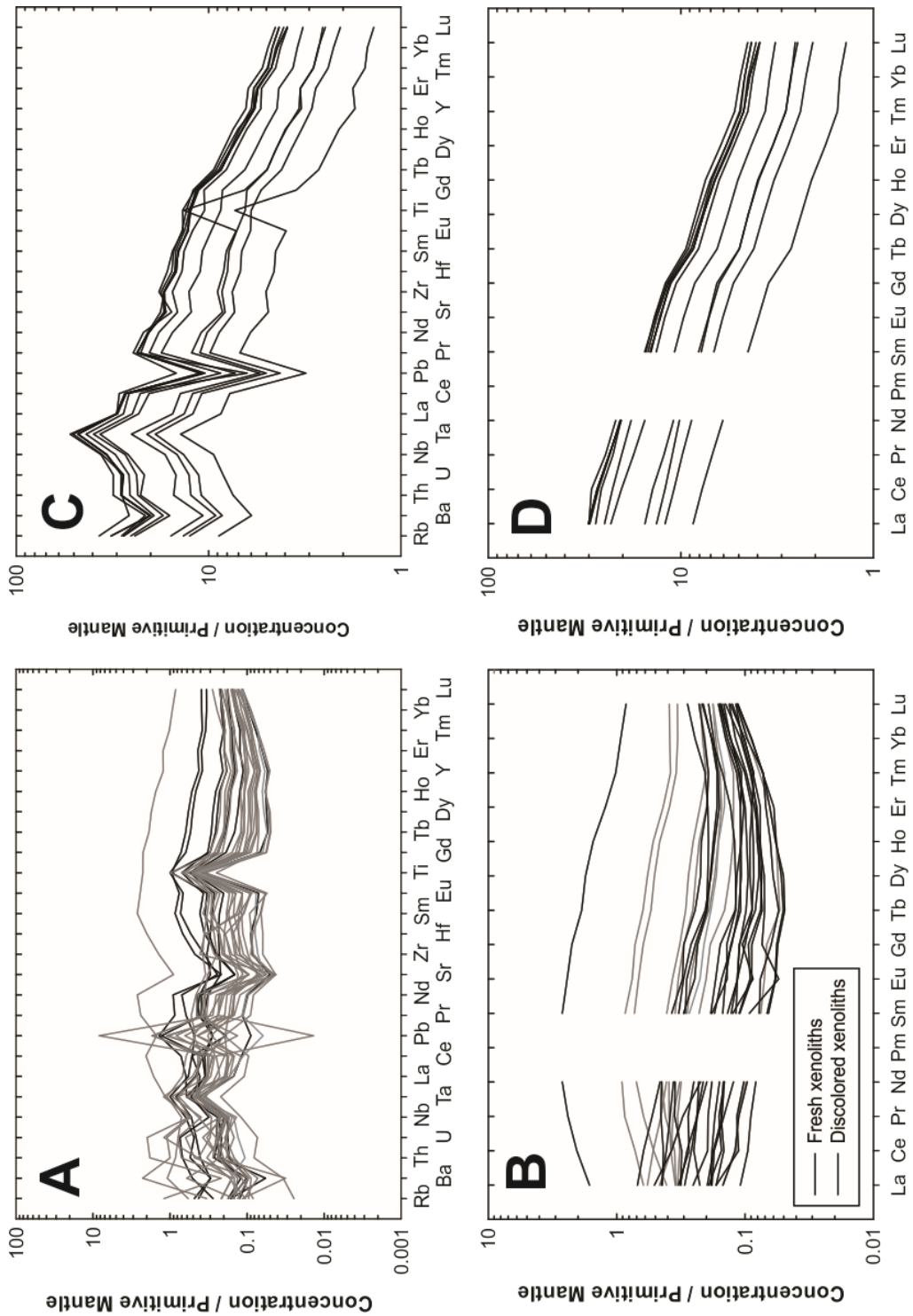

Figure 3.3: Primitive mantle-normalized trace element variation and rare earth element diagrams for Piton Chisny cumulate xenoliths (A, B) and Piton de la Fournaise lavas (C, D). Primitive-mantle normalization from McDonough & Sun [1995].

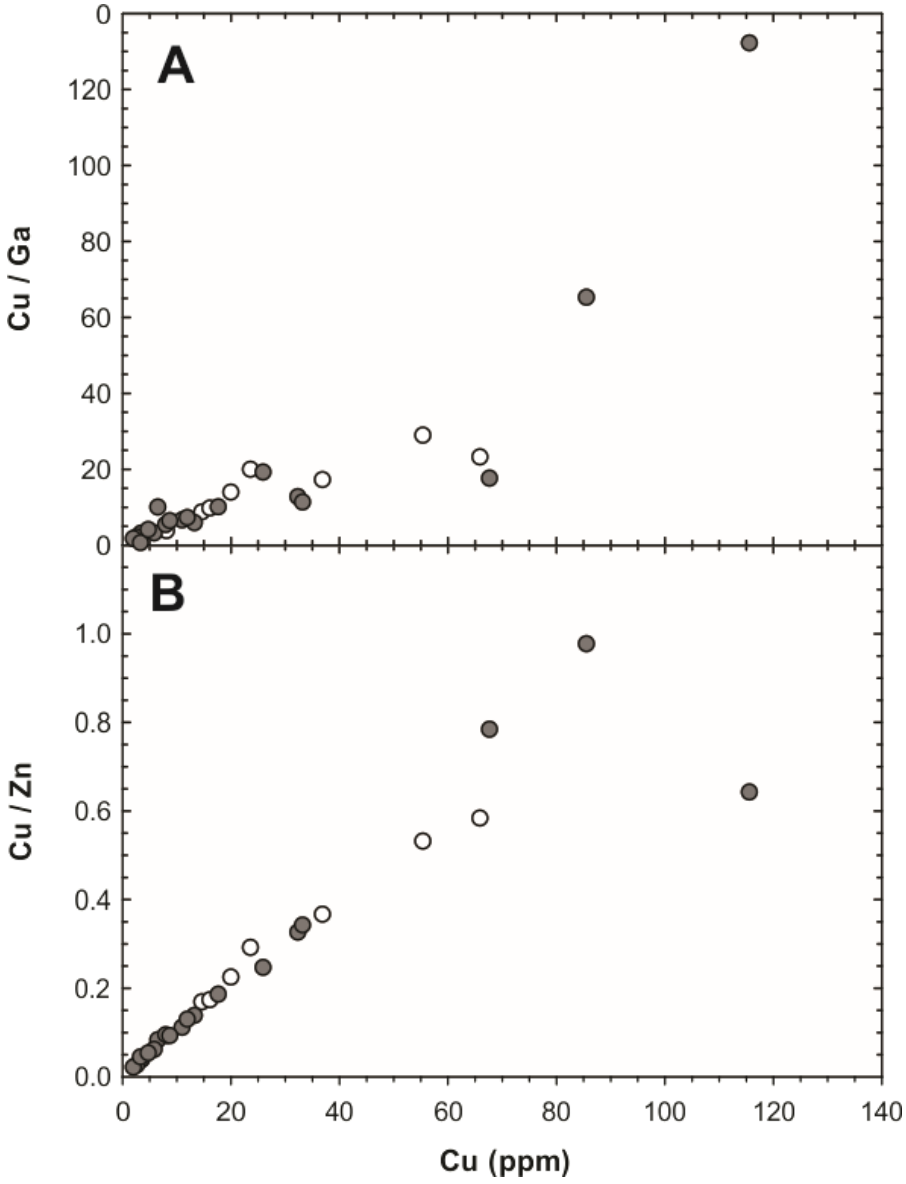

Figure 3.4: Co-variations of Cu and chalcophile element ratios in Piton Chisny cumulate xenoliths. Symbols as in **Figure 3.2**. Correlation coefficients are (A) $r^2 = 0.77$ and (B) $r^2 = 0.86$.

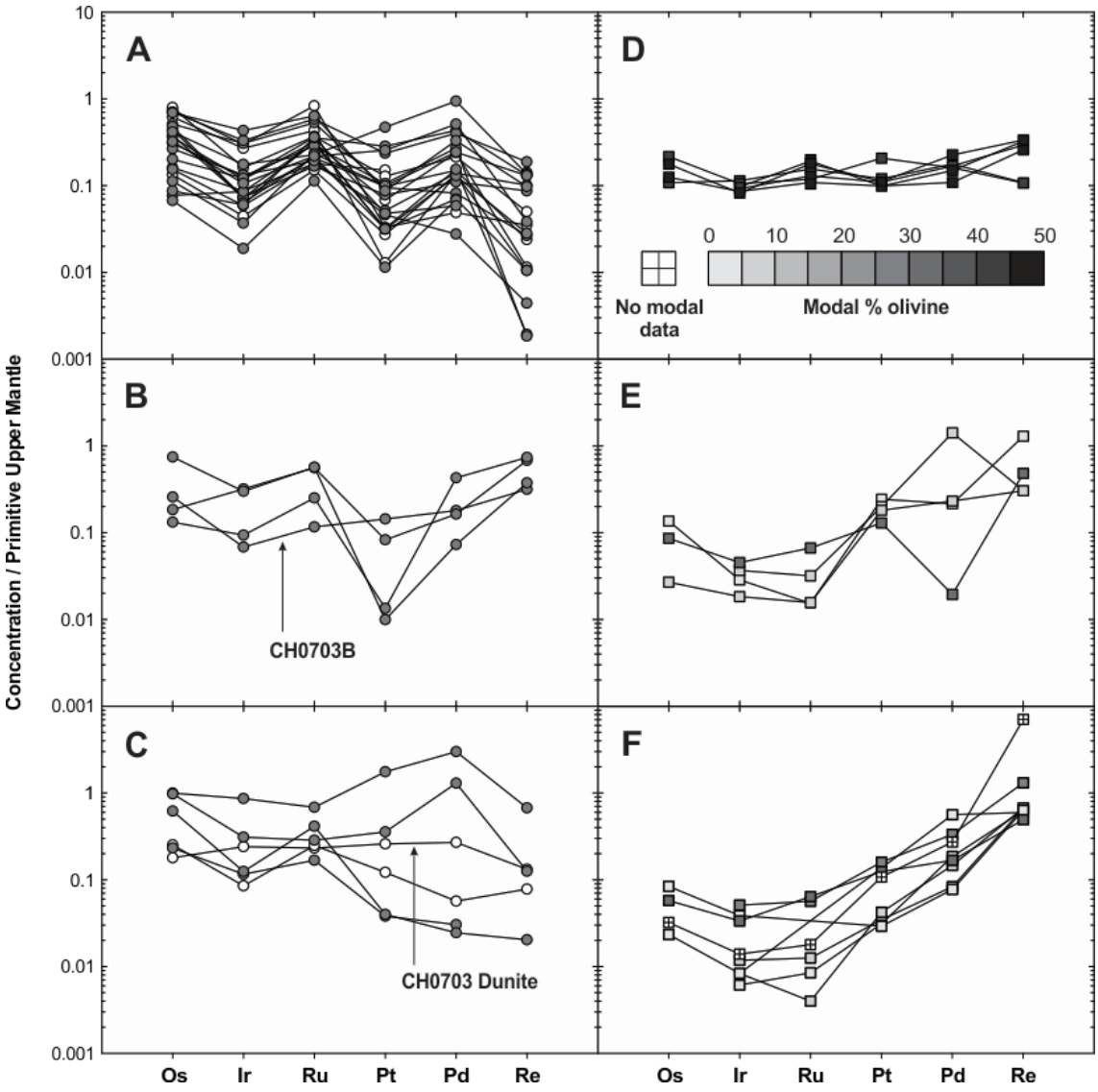

Figure 3.5: Primitive upper-mantle normalized highly siderophile element patterns for Piton Chisny cumulate xenoliths (A-C, symbol colors as in **Figure 3.2**) and Piton de la Fournaise lavas (D-F, symbols color coded according to modal proportion of olivine using the scale in panel D). Primitive mantle normalization from Becker et al. [2006].

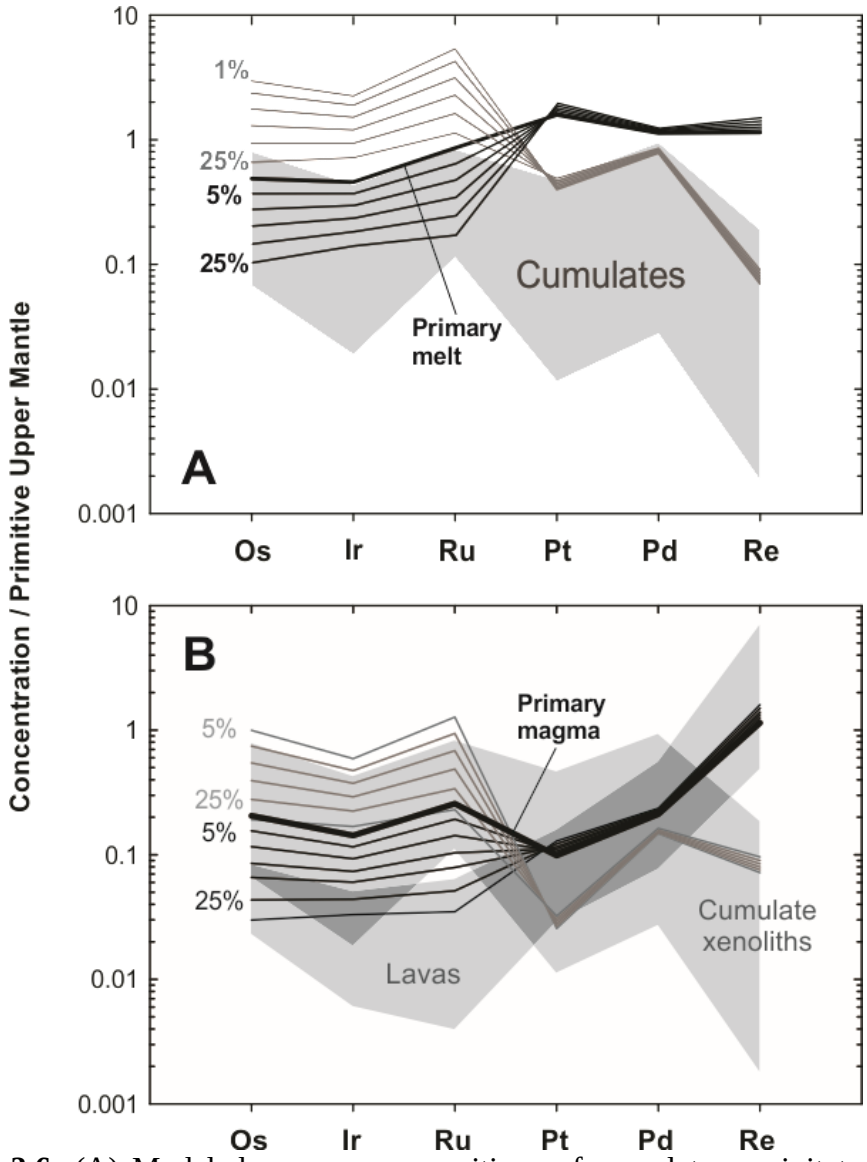

Figure 3.6: (A) Modeled average compositions of cumulate precipitated by fractional crystallization (gray lines) from a primary magma (heavy black line) that lacks Ru/Ir, Pd/Pt and Re/Pd enrichments (composition from Day, 2013) and the composition of a corresponding residual melt after fractional crystallization (black lines). Gray region: range of Piton Chisny cumulate compositions; percentages: mass proportion of primary magma lost to fractional crystallization. Partition coefficients are those for 12 wt.% MgO parental melt to alkali basalt as reported in Day [2013]. Primitive mantle normalization from Becker et al. (2006). (B) Fractional crystallization model for a theoretical Réunion primary magma (heavy black line) possessing elevated Ru/Ir, Pd/Pt and Re/Pd. Compositions of the residual melt and the average composition of the cumulate xenoliths are shown by the black and gray lines, respectively; measured HSE compositions for cumulate xenoliths and lavas are shown in the dark and light gray shaded regions, respectively. Percentages refer to mass loss from primary magma. The effect of these models on lava HSE compositions are discussed in the *Supplementary Information*.

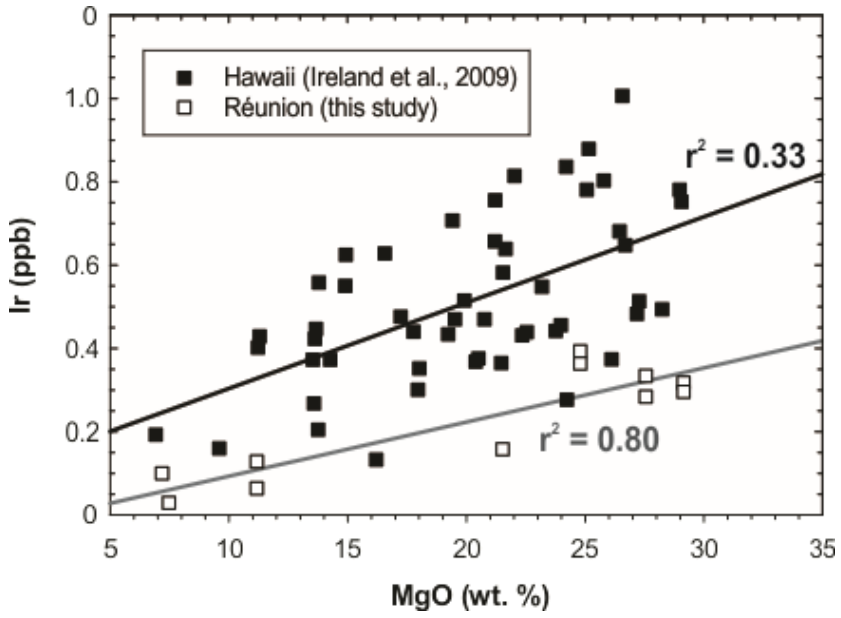

Figure 3.7: Correlation of MgO to Ir for Hawaiian lavas [Ireland et al., 2009] and Piton de la Fournaise lavas that do not display the hyperbolic HSE patterns noted in the text. Least-squares regression lines and fit statistics for the two sample suites (Hawaii, black; Réunion, gray) are provided for reference.

Figure 3.8: (A) Modeled HSE composition of core after 25% extraction of Earth's mass into the core (solid gray line) from an initially chondritic body (solid black line) [Horan et al., 2003] based on silicate-metal partitioning experiments of Mann et al. [2012], P of 60 GPa and T of 4250 K. Dashed gray lines are compositions of solid metal precipitated from small amounts of liquid metal entrained from the core into the residual mantle [e.g., Humayun, 2011] based on liquid metal-solid metal partitioning experiments of Chabot & Jones [2003]; percentages represent degree of solidification. (B) Curves for mixing between solid metal precipitated as 1% by mass of liquid metal (as in panel a) and a calculated residual silicate mantle left behind after core formation. Percentages refer to proportion solid metal involved in the metal-silicate mixing. (C) Mixing between 99.99% residual silicate mantle and 0.01% solid metal (as in panel B) and chondrite [Horan et al., 2003], simulating late accretion. Calculated composition of primary Réunion magma shown for reference (see text for details). Symbols as in **Figure 3.2**.

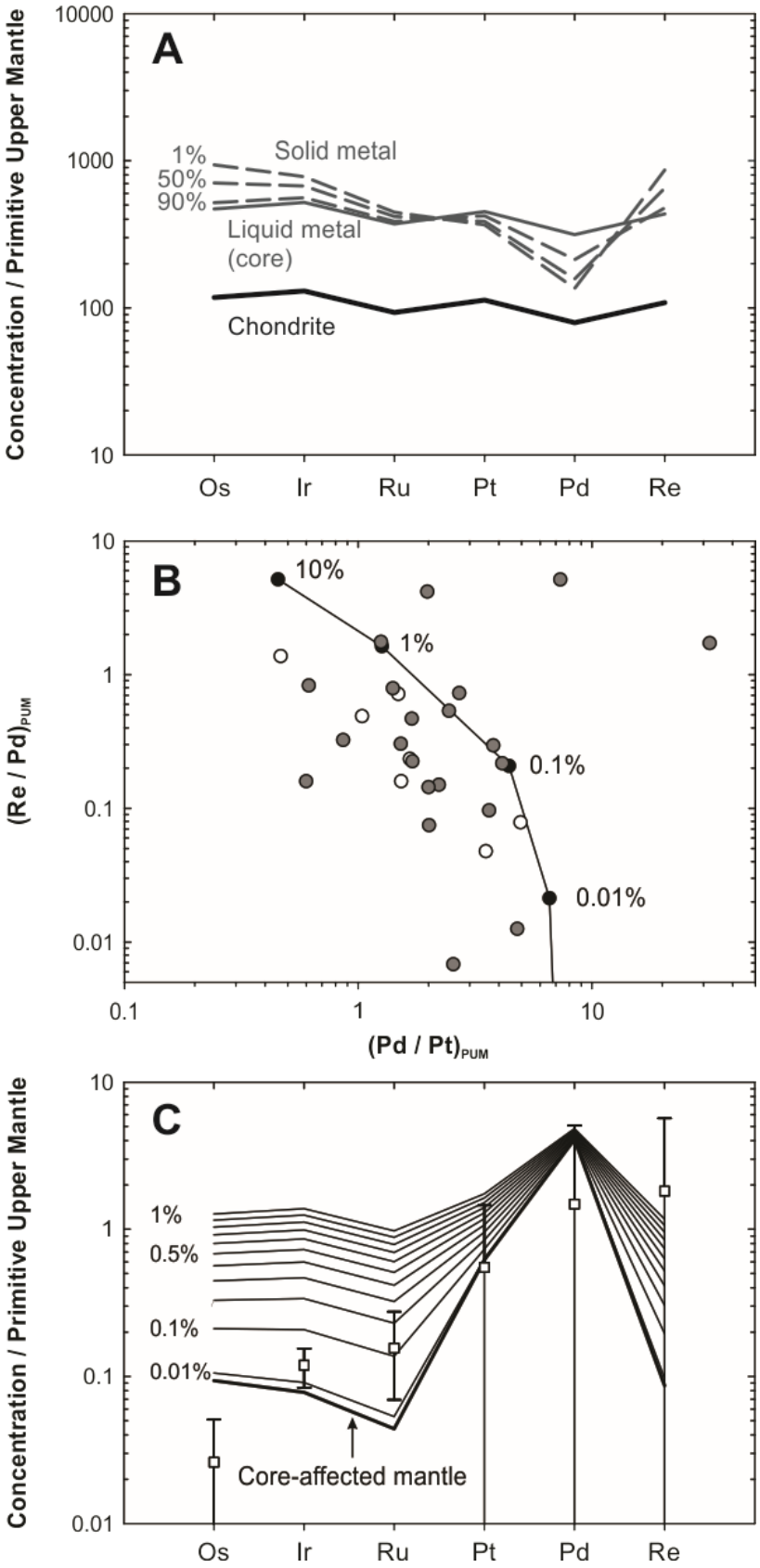
A
Concentration / Primitive Upper Mantle
10000
1000
100
10
1%
50%
90%
Solid metal
Liquid metal
(core)
Chondrite
Os
Ir
Ru
Pt
Pd
Re
B
(Re / Pd)PUM
(Pd / Pt)PUM
10%
1%
0.1%
0.01%
0.1
1
10
0.01
C
Concentration / Primitive Upper Mantle
1%
0.5%
0.1%
0.01%
Core-affected mantle

References

Ackerman, L., R.J. Walker, I.S. Puchtel, L. Pitcher, E. Jelínek and L. Strnad (2009) Effects of melt percolation on highly siderophile elements and Os isotopes in subcontinental lithospheric mantle: a study of the upper mantle profile beneath Central Europe: Geochimica et Cosmochimica Acta, 73, 2400-2414.

Alard, O., W.L. Griffin, J.P. Lorand, S.E. Jackson and S.Y. O'Reilly (2000) Non-chondritic distribution of the highly siderophile elements in mantle sulphides: Nature, 407, 891-894.

Albarède, F. and V. Tamagnan (1988) Modelling the recent geochemical evolution of the Piton de la Fournaise Volcano, Réunion Island, 1931-1986: Journal of Petrology, 29(5), 997-1030.

Albarède, F., B. Luais, G. Fitton, M. Semet, E. Kaminski, B.G.J. Upton, P. Bachélery an J.-L. Cheminée (1997) The geochemical regimes of Piton de la Fournaise Volcano (Réunion) during the last 530,000 years: Journal of Petrology, 38(2), 171-201.

Augé, T., P. Lerebour and J.-P. Rançon (1989) The Grand Brûlé exploration drilling: New data on the deep framework of the Piton de la Fournaise volcano. Part 3: Mineral chemistry of the cumulate rocks: Journal of Volcanology and Geothermal Research, 36, 139-151.

Babkine, J., F. Conquéré and J.-C. Vilminot (1966) Nodules de peridotite et cumulats d'olivine: Bulletin de la Société Française de Mineralogie et Cristallographie, 89, 262-268.

Ballhaus, C., C. Bockrath, C. Wohlgemuth-Ueberwasser, V. Laurenz and J. Berndt (2006) Fractionation of the noble metals by physical processes: Contributions to Mineralogy and Petrology, 152, 667-684.

Barnes, S.J., A.J. Naldrett and M.P. Gorton (1985) The origin of the fractionation of platinum-group elements in terrestrial magmas: Chemical Geology, 53, 303-323.

Becker, H., M.F. Horan, R.J. Walker, S. Gao, J.-P. Lorand and R.L. Rudnick (2006) Highly siderophile element composition of the Earth's primitive upper mantle: constraints from new data on peridotite massifs and xenoliths: Geochimica et Cosmochimica Acta, 70, 4528-4550.

Bennett, V.C., M.D. Norman and M.O. Garcia (2000) Rhenium and platinum element group element abundances correlated with mantle source components in Hawaiian picrites: sulphides in the plume: Earth and Planetary Science Letters, 183, 513-526.

Bennett, V.C., A.D. Brandon and A.P. Nutman (2007) Coupled ^{142}Nd-^{143}Nd isotopic evidence for Hadean mantle dynamics: Science, 318, 1907-1910.

Bosch, D., J. Blichert-Toft, F. Moynier, B.K. Nelson, P. Telouk, P.-Y. Gillot and F. Albarede (2008) Pb, Hf and Nd isotope compositions of the two Réunion volcanoes (Indian Ocean): A tale of two small-scale mantle "blobs"?: Earth and Planetary Science Letters, 265, 748-765.

Boyd, F.R. and S.A. Mertzman (1987) Composition and structure of the Kaapvaal lithosphere, southern Africa, *in* Mysen, B.O., *ed.*, Magmatic processes – physiochemical principles: Geochemical Society Special Publications, 1, 13-24.

Boyet, M. and R.W. Carlson (2005) ^{142}Nd evidence for early (>4.53 global differentiation of silicate earth: Science, 309, 576-581.

Brandon, A.D., R.J. Walker, J.W. Morgan, M.D. Norman and H.M. Prichard (1998) Coupled ^{186}Os and ^{187}Os evidence for core-mantle interaction: Science, 280, 1570-1574.

Brandon, A.D., M.D. Norman, R.J. Walker and J.W. Morgan (1999) ^{186}Os-^{187}Os systematics of Hawaiian picrites: Earth and Planetary Science Letters, 174, 25-42.

Buikin, A., M. Trieloff, J. Hopp, T. Althaus, E. Korochantseva, W.H. Schwarz and R. Altherr (2005) Noble gas isotopes suggest deep mantle plume source of late Cenozoic mafic alkaline volcanism in Europe: Earth and Planetary Science Letters, 230, 143-162.

Burton, K.W., P. Schiano, J.-L. Birck and C.J. Allègre (1999) Osmium isotope disequilibrium between mantle minerals in a spinel-lherzolite: Earth and Planetary Science Letters, 172, 311-322.

Caro, G., B. Bourdon, J.-L. Birck and S. Moorbath (2003) ^{146}Sm-^{142}Nd evidence from Isua metamorphosed sediments for early differentiation of Earth's mantle: Nature, 423, 428-432.

Caro, G., B. Bourdon, J.-L. Birck and S. Moorbath (2006) High-precision ^{142}Nd/^{144}Nd measurements in terrestrial rocks: constraints on the early differentiation of Earth's mantle: Geochimica et Cosmochimica Acta, 70, 164-191.

Caro, G. and B. Bourdon (2010) Non-chondritic Sm/Nd ratio in the terrestrial planets: consequences for the geochemical evolution of the mantle-crust system: Geochimica et Cosmochimica Acta, 74, 3333-3349.

Clague, D.A. (1988) Petrology of ultramafic xenoliths from Loihi Seamount, Hawaii: Journal of Petrology, 29(6), 1161-1186.

Craig, H. and J.E. Lupton (1976) Primordial neon, helium, and hydrogen in oceanic basalts: Earth and Planetary Science Letters, 31, 369-385.

Crocket, J.H. (2000) PGE in fresh basalt, hydrothermal alteration products, and volcanic incrustations of Kilauea volcano, Hawaii: Geochimica et Cosmochimica Acta, 64(10), 1791-1807.

Day, J.M.D. (2013) Hotspot volcanism and highly siderophile elements: Chemical Geology, 341, 60-74.

Day, J.M.D., D.G. Pearson, C.G. Macpherson, D. Lowry and J.-C. Carracedo (2009) Pyroxenite-rich mantle formed by recycled oceanic lithosphere: Oxygen-osmium isotope evidence from Canary Island lavas: Geology, 37, 555-558.

Day, J.M.D., D.G. Pearson, C.G. Macpherson, D. Lowry and J.-C. Carracedo (2010) Evidence for distinct proportions of subducted oceanic crust and lithosphere in HIMU-type mantle beneath El Hierro and La Palma, Canary Islands: Geochimica et Cosmochimica Acta, 74, 6565-6589.

Day, J.M.D., B.J. Peters and P.E. Janney (2014) Oxygen isotope systematics of South African olivine melilitites and implications for HIMU mantle reservoirs: Lithos, 202-203, 76-84.

Day J.M.D., Waters C. L., Schaefer B. F., Walker R. J., & Turner, S. (2016). Use of Hydrofluoric Acid Desilicification in the Determination of Highly Siderophile Element Abundances and Re-Pt-Os Isotope Systematics in Mafic-Ultramafic Rocks. Geostandards and Geoanalytical Research, 40, 49-65.

Debaille, V., C. O'Neill, A.D. Brandon, P. Haenecour, Q.-Z. Yin, N. Mattielli and A.H. Treiman (2013) Stagnant-lid tectonics in early Earth revealed by ^{142}Nd variations in late Archean rocks: Earth and Planetary Science Letters, 373, 83-92.

Fisk, M.R., B.G.J. Upton and C.E. Ford (1988) Geochemical and experimental study of the genesis of magmas of Reunion Island, Indian Ocean: Journal of Geophysical Research, 93(B5), 4933-4950.

Fretzdorff, S. and K.M. Haase (2002) Geochemistry and petrology of lavas from the submarine flanks of Réunion Island (western Indian Ocean): implications for magma genesis and the mantle source: Mineralogy and Petrology, 75, 153-184.

Fujimaki, H., M. Tatsumoto and K.-I. Aoki (1984) Partition coefficients of Hf, Zr, and REE between phenocrysts and groundmass: Journal of Geophysical Research, 89, B662-B672.

Füri, E., D.R. Hilton, B.J. Murton, C. Hémond, J. Dyment and J.M.D. Day (2011) Helium isotope variations between Réunion Island and the Central Indian Ridge (17°-21°S): new evidence for ridge-hot spot interaction: Journal of Geophysical Research, 116, B02207.

Gaffney, A.M., B.K. Nelson, L. Reisberg and J. Eiler (2005) Oxygen-osmium isotope systematics of West Maui lavas: A record of shallow-level magmatic processes: Earth and Planetary Science Letters, 239, 122-139.

Gannoun, K.W. Burton, L.H. Thomas, I.J. Parkinson, P.V. Calsteren and P. Schiano (2004) Osmium isotope heterogeneity in the constituent phases of mid-ocean ridge basalts: Science, 303, 70-72.

Gannoun, A., K.W. Burton, I.J. Parkinson, O. Alard, P. Schiano and L.E. Thomas (2007) The scale and origin of the osmium isotope variations in mid-ocean ridge basalts: Earth and Planetary Science Letters, 259, 541-556.

Gannoun, A., I. Vlastélic and P. Schiano (2015) Escape of unradiogenic osmium during sub-aerial lava degassing: Evidence from fumarolic deposits, Piton de la Fournaise, Réunion Island: Geochimica et Cosmochimica Acta, 166, 312-326.

Graham, D., J. Lupton, F. Albarede and M. Condomines (1990) Extreme temporal homogeneity of helium isotopes at Piton de la Fournaise, Réunion Island: Nature, 347, 545-548.

Hart, S.R. and G.E. Ravizza (1996) Os partitioning between phases in lherzolite and basalt: American Geophysical Union Monograph, 95, 123-144.

Hauri, E.H. and M.D. Kurz (1997) Melt migration and mantle chromatography, 2: a time-series Os isotope study of Mauna Loa volcano, Hawaii: Earth and Planetary Science Letters, 153, 21-36.

Hilton, D.R., K. Grönvold, C.G. Macpherson and P.R. Castillo (1999) Extreme $^{3}He/^{4}He$ ratios in northwest Iceland: constraining the common component in mantle plumes: Earth and Planetary Science Letters, 173, 53-60.

Hofmann, A.W. (2007) Sampling mantle heterogeneity through oceanic basalts: isotopes and trace elements, *in:* Holland, H.D. and T.K. Turekian, Treatise on Geochemistry, 2, 1-44.

Holness, M.B., M.A. Hallworth, A. Woods and R.E. Sides (2007) Infiltration metasomatism of cumulates by intrusive magma replenishment: the wavy horizon, Isle of Rum, Scotland: Journal of Petrology, 48(3) 563-587.

Honda, M., I. McDougall, D.B. Patterson, A. Doulgeris and D.A. Clague (1993) Noble gases in submarine pillow basalt glasses from Loihi and Kilauea, Hawaii: A solar component in the Earth: Geochimica et Cosmochimica Acta, 57, 859-874.

Horan, M.F., R.J. Walker, J.W. Morgan, J.N. Grossman and A.E. Rubin (2003) Highly siderophile elements in chondrites: Chemical Geology, 196, 5-20.

Humayun, M. (2011) A model for osmium isotopic evolution of metallic solids at the core-mantle boundary: Geochemistry Geophysics Geosystems, 12(3), 23 pp.

Ireland, T.J., R.J. Walker and M.O. Garcia (2009) Highly siderophile element and ^{187}Os isotope systematics of Hawaiian picrites: implications for parental melt composition and source heterogeneity: Chemical Geology, 260, 112-128.

Ireland, T.J., R.J. Walker and A.D. Brandon (2011) ^{187}Os-^{187}Os systematics of Hawaiian picrites revisited: new insights into Os isotopic variations in ocean island basalts: Geochimica et Cosmochimica Acta, 75, 4456-4475.

Jackson, E.D. and T.L. Wright (1970) Xenoliths in the Honolulu Volcanic Series, Hawaii: Journal of Petrology, 11(2), 405-430.

Jackson, M.G. and S.B. Shirey (2011) Re-Os systematics in Samoan shield lavas and the use of Os-isotopes in olivine phenocrysts to determine primary magmatic compositions: Earth and Planetary Science Letters, 312, 91-101.

Jamais, M. J.C. Lassiter and G. Brügmann (2008) PGE and Os-isotopic variations in lavas from Kohala Volcano, Hawaii: constraints on PGE behavior and melt/crust interaction: Chemical Geology, 250, 16-28.

Kaneoka, I., N. Takaoka and B.G.J. Upton (1986) Noble gas systematics in basalts and a dunite nodule from Réunion and Grand Comore Islands, Indian Ocean: Chemical Geology, 59, 35-42.

Kurz, M.D., W.J. Jenkins and S.R. Hart (1982) Helium isotopic systematics of oceanic islands and mantle heterogeneity: Nature, 297, 43-47.

Lassiter, J.C., J. Blichert-Toft, E.H. Hauri and H.G. Barsczus (2003) Isotope and trace element variations in lavas from Raivavae and Rapa, Cook-Austral Islands: constraints on the nature of HIMU- and EM-mantle and the origin of mid-plate volcanism in French Polynesia: Chemical Geology, 202, 115-138.

Laurenz, V., D.C. Rubie, D.J. Frost and A.K. Vogel (2015) Sulfide-silicate partitioning of the HSEs and S-solubility in peridotite melt at high P and T: Goldschmidt Abstracts, 2015, 1786.

Luais, B. (2004) Temporal changes in Nd isotopic composition of Piton de la Fournaise magmatism (Réunion Island, Indian Ocean): Geochemistry, Geophysics, Geosystems, 5(1), 17 pp.

Luguet, A., J.-P. Lorand and M. Seyler (2003) Sulfide petrology and highly siderophile element geochemistry of abyssal peridotites: a coupled study of samples from the Kane Fracture Zone (45°W 23°20N, MARK area, Atlantic Ocean): Geochimica et Cosmochimica Acta, 67(8) 1553-1570.

Mann, U., D.J. Frost, D.C. Rubie, H. Becker and A. Audétat (2012) Partitioning of Ru, Rh, Pd, Re, Ir and Pt between liquid metal and silicate at high pressures and high temperatures – implications for the origin of highly siderophile element concentrations in Earth's mantle: Geochimica et Cosmochimica Acta, 84, 593-613.

Mathez, E.A., Magmatic metasomatism and formation of the Merensky reef, Bushveld Complex: Contributions to Mineralogy and Petrology, 119, 277-286.

Mattioli, M. B.G.J. Upton and A. Renzulli (1997) Sub-volcanic crystallization at Sete Cidades volcano, São Miguel, Azores, inferred from mafic and ultramafic nodules: Mineralogy and Petrology, 60, 1-26.

McDonough, W.F. and S.-s. Sun (1995) The composition of the Earth: Chemical Geology, 120, 223-253.

McDougall, I. and W. Compston (1965) Strontium isotopic composition and potassium-rubidium ratios in some rocks from Réunion and Rodriguez, Indian Ocean: Nature, 207, 252-253.

Meisel, T., R.J. Walker, A.J. Irving and J.-P. Lorand (2001) Osmium isotopic compositions of mantle xenoliths: a global perspective: Geochimica et Cosmochimica Acta, 65(8), 1311-1323.

Moreira, M. and M.D. Kurz (2001) Subuducted oceanic lithosphere and the origin of the 'high μ' basalt helium isotopic signature: Earth and Planetary Science Letters, 189, 49-57.

Mukhopadhyay, S., J.C. Lassiter, K.A. Farley and S.W. Bogue (2003) Geochemistry of Kauai shield-stage lavas: Implications for the chemical evolution of the Hawaiian plume: Geochemistry, Geophysics, Geosystems, 4(1), 32 pp.

Norman, M.D., M.O. Garcia and V.C. Bennett (2004) Rhenium and chalcophile elements in basaltic glasses from Ko'olau and Moloka'i volcanoes: magmatic outgassing and composition of the Hawaiian plume: Geochimica et Cosmochimica Acta, 68(18), 3761-3777.

Pattou, L., J.P. Lorand and M. Gros (1996) Non-chondritic platinum-group element ratios in the Earth's mantle: Nature, 379, 712-715.

Peucker-Ehrenbrink, B. and B.-M. Jahn (2001) Rhenium-osmium isotope systematics and platinum group element concentrations: loess and the upper continental crust: Geochemistry Geophysics Geosystems, 2, 22 pp.

Pitcher, L., R.T. Helz, R.J. Walker and P. Piccoli (2009) Fractionation of the platinum-group elements and Re during crystallization of basalt in Kilauea Iki Lava Lake, Hawaii: Chemical Gelology, 260, 196-210.

Puchtel, I.S. and M. Humayun (2001) Platinum group element fractionation in a komatiitic basalt lava lake: Geochimica et Cosmochimica Acta, 65, 2979-2993.

Puchtel, I.S. A.D Brandon and M. Humayun (2004) Precise Pt-Re-Os isotope systematics of the mantle from 2.7-Ga komatiites: Earth and Planetary Science letters, 224, 157-174.

Puchtel, I.S., R.J. Walker, O.B. James and D.A. Kring (2008) Osmium isotope and highly siderophile element systematics of lunar impact melt breccias: implications for the late accretion history of the Moon and Earth: Geochimica et Cosmochimica Acta, 72, 3022-3042.

Rançon, J.-P., P. Lerebour and T. Augé (1989) The Grand Brûlé exploration drilling: New data on the deep framework of the Piton de la Fournaise volcano. Part 1: Lithostratigraphic units and volcanostructural implications: Journal of Volcanology and Geothermal Research, 36, 139-151.

Rehkämper, M., A.N. Halliday, J.G. Fitton, D.-C. Lee, M. Weineke and N.T. Arndt (1999) Ir, Ru, Pt, and Pd in basalts and komatiites: new constraints for the geochemical behavior of the platinum-group elements in the mantle: Geochimica et Cosmochimica Acta, 63(22), 3915-3934.

Rizo, H., M. Boyet, J. Blichert-Toft, J. O'Neil, M.T. Rosing and J.-L. Paquette (2013) The elusive Hadean enriched reservoir revealed by ^{142}Nd deficits in Isua Archaean rocks: Nature, 491, 96-100.

Roy-Barman, M. and C.J. Allègre (1995) ^{187}Os/^{186}Os in oceanic island basalts: tracing oceanic crust recycling in the mantle: Earth and Planetary Science Letters, 129, 145-161.

Roy-Barman, M., G.J. Wasserburg, D.A. Papanastassiou and M. Chaussidon (1998) Osmium isotopic compositions and Re-Os concentrations in sulfide globules from basaltic glasses: Earth and Planetary Science Letters, 154, 331-347.

Rubie, D.C., D.J. Frost, U. Mann, Y. Asahara, F. Nimmo, K. Tsuno, P. Kegler, A. Holzheid and H. Palme (2011) Heterogeneous accretion, composition and core-mantle differentiation of the Earth: Earth and Planetary Science Letters, 301, 31-42.

Schiano, P., K. David, I. Vlastélic, A. Gannoun, M. Klein, F. Nauret and P. Bonnand (2012) Osmium isotope systematics of historical lavas from Piton de la Fournaise (Réunion Island, Indian Ocean): Contributions to Mineralogy and Petrology, 164(5), 805-820.

Sharp, M., I. Gerasimenko, L.C. Loudin, J. Liu, O.B. James, I.S. Puchtel and R.J. Walker (2014) Characterization of dominant impactor signature for Apollo 17 impact melt rocks: Geochimica et Cosmochimica Acta, 131, 62-80.

Staudacher, T., P. Sarda and C.J. Allègre (1990) Noble gas systematics of Réunion Island, Indian Ocean: Chemical Geology, 89, 1-17.

Stuart, F.M., S. Lass-Evans, J.G. Fitton and R.M. Ellam (2003) High $^{3}He/^{4}He$ ratios in picritic basalts from Baffin Island and the role of a mixed reservoir in mantle plumes: Nature, 2003, 57-59.

Touboul, M., I.S. Puchtel and R.J. Walker (2012) ^{182}W evidence for long-term preservation of early mantle differentiation products: Science, 355, 1065-1070.

Touboul, M., J. Liu, J. O'Neil, I.S. Puchtel and R.J. Walker (2014) New insights into the Hadean mantle revealed by ^{182}W and highly siderophile element abundances of supracrustal rocks from the Nuvvuagittuq greenstone belt, Quebec, Canada: Chemical Geology, 383, 63-75.

Trieloff, M., J. Kunz and C.J. Allègre (2002) Noble gas systematics of the Réunion mantle plume source and the origin of primordial gases in Earth's mantle: Earth and Planetary Science Letters, 200, 297-313.

Upton, B.G.J. and W.J. Wadsworth (1972) Aspects of magmatic evolution on Reunion Island: Philosophical Transactions of the Royal Society, 271, 105-130.

Vlastélic, I., T. Staudacher and M. Semet (2005) Rapid change of lava composition from 1998 to 2002 at Piton de la Fournaise (Réunion) inferred from Pb isotopes and trace elements: Evidence for variable crustal contamination: Journal of Petrology, 46(1), 79-107.

Vlastélic, I., E. Lewin and T. Staudacher (2006) Th/U and other geochemical evidence for the Réunion plume sampling a less differentiated mantle domain: Earth and Planetary Science Letters, 248, 379-393.

Vlastélic, I., A. Peltier and T. Staudacher (2007) Short-term (1998-2006) fluctuations of Pb isotopes at Piton de la Fournaise volcano (Reunion Island): Origins and constraints on the size and shape of the magma reservoir: Chemical Geology, 244, 202-220.

Vlastélic, I., C. Deniel, C. Bosq, P. Télou, P. Boivin, P. Bachelery, V. Famin and T. Staudacher (2009) Pb isotope geochemistry of Piton de la Fournaise historical lavas: Journal of Volcanology and Geothermal Research, 184, 63-78.

Wager, L.R., G.M. Brown and W.J. Wadsworth (1960) Types of igneous cumulates: Journal of Petrology, 1(1), 73-85.

Walker, R.J., J.W. Morgan, M.F. Horan, C.K. Czamanske, E.J. Krogstad, V.A., Fedorenko and V.E. Kunilov (1994) Re-Os isotopic evidence for an enriched-mantle source for the Noril'sk-type, ore-bearing intrusions, Siberia: Geochimica et Cosmochimica Acta, 4179-4197.

Walker, R.J., J.W. Morgan and M.F. Horan (1995) Osmium-187 enrichment in some plumes: evidence for core-mantle interaction? Science, 11, 819-822.

Walker, R.J., K. Bermingham, J. Liu, I.S. Puchtel, M. Touboul and E.A. Worsham (2015) In search of late-stage planetary building blocks: Chemical Geology, 311, 125-142.

Widom, E., K.A. Hoernle, S.B. Shirey and H.-U. Schmincke (1999) Os isotope systematics in the Canary Islands and Madeira: lithospheric contamination and mantle plume signatures: Journal of Petorlogy, 40(2), 279-296.

Willbold, M., T. Elliott and S. Moorbath (2011) The tungsten isotopic composition of the Earth's mantle before the terminal bombardment: Nature, 477, 195-199.

Workman, R.K. and S.R. Hart (2005) Major and trace element composition of the depleted MORB mantle (DMM): Earth and Planetary Science Letters, 231, 53-72.

Supplementary Information

3.6 Supplementary introduction to the Réunion hotspot

Numerous mantle source end-members have been identified in ocean island basalts (OIB), including HIMU ($\mu = {}^{238}U/{}^{204}Pb$) [e.g., Hofmann & White, 1982; Hanyu et al., 2011], enriched mantle (EM1 and EM2 end-members, or a continuous spectrum) [e.g., Zindler & Hart, 1986; Class & Goldstein, 1997; Class et al., 2009], depleted mantle (DMM) [e.g., Workman & Hart, 2005] and a source at the intersection of these compositional arrays, often termed as the focus zone, or 'FOZO' [e.g. Hart et al., 1992; Hanan & Graham, 1996; Day et al., 2010; Stracke, 2012]. These end-members have distinct isotopic signatures that have been proposed to result from authigenic mantle differentiation [e.g., Ballentine et al., 1997], subducted oceanic crust and lithosphere [e.g., Hawkesworth et al., 1979; Hofmann & White, 1982; White & Hofmann, 1982; Day et al., 2009, 2010], recycled pelagic clay [e.g., Weaver et al., 1986; le Roex et al, 1990; Cousens et al., 1994; Blichert-Toft et al, 1999], continental crust and lithosphere [e.g., Mahoney et al., 1989, 1996; Hanan et al., 2004; Willbold & Stracke, 2006, 2010], or sediments of various origin [e.g., White & Dupre, 1986; Plank & Langmuir, 1998; Plank, 2005; Elliott et al., 2007]. Studies of these OIB lavas indicate that many hotspots span a range of Sr-Nd-Pb isotopic ratios consistent with sources that combine multiple end-members [c.f., Stracke, 2012]. Rather than displaying a pronounced affinity for one or more of the recognized mantle endmembers, Réunion plots near the center of the Sr-Nd-Pb isotopic arrays of hotspots [Bosch et al., 2008] (**Figure 3.1**).

Piton Chisny is located on the western flank of the Piton de la Fournaise volcanic complex of Réunion Island, Indian Ocean. Carbon-14 dating of charcoal from the Piton Chisny edifice indicates that it last erupted between 1200 and 1060 years ago [Albarède et al., 1997; Sigmarsson et al., 2005]. Volcanism has recently occurred in the *enclos* of Piton de la Fournaise with three eruptions occurring in 2015. Prior to this, geologically recent volcanism occurred around the older Piton des Neiges volcanic complex, which comprises the remainder of Réunion Island, and before this on the neighboring islands of Mauritius and Rodrigues (together referred to as the Mascarene Islands, **Figure 3.9**). Northwest of the Mascarene Islands, age-progressive volcanism trending through the Chagos-Laccadive Ridge links Réunion to late-Cretaceous and early-Paleocene volcanism of the Deccan Traps, a large igneous province on the Indian subcontinent [e.g., Wellman & McElhinny, 1970; Kaneoka & Haramura, 1973; Duncan et al., 1990; Widdowson et al., 2000; Moore et al., 2011]. As a result, Réunion is considered the active terminus of intraplate "hotspot"-type volcanism, and has been postulated to reflect the impingement of a buoyant mantle plume on the base of the African Plate [e.g., Courtillot et al., 2003].

Early geological surveys of Réunion noted the presence of wherlite and dunite xenoliths at Piton Chisny [Babkine et al., 1966; Upton & Wadsworth, 1972]. To date, work has been done on Chisny xenoliths for noble gases, with the cumulate xenoliths having the highest $^{3}He/^{4}He$ of measured Réunion samples at ~14 R_a (where $R_a = {}^{3}He/^{4}He_{sample}/{}^{3}He/^{4}He_{air}$, where $^{3}He/^{4}He_{air} = 1.38 \times 10^{6}$) and relatively high gas contents, allowing the measurement of Ne, Ar, Xe isotope systematics [Trieloff et al., 2002; Buikin

et al., 2005; Füri et al., 2011]. As well as finding that Réunion has lower $^{3}He/^{4}He$ values than Icelandic or Hawaiian mantle sources (up to 50 R_a) [Stuart et al., 2003], previous studies have shown that the Réunion mantle source has $^{40}Ar/^{36}Ar$ (11,000 ±200) intermediate between mid-ocean ridge basalts (MORB = 32,000 ± 4000) and Loihi seamount (8000 ± 1000) or Iceland OIB (6500 ± 150), as well as excess nucleogenic ^{21}Ne [Trieloff et al., 2002; Buikin et al., 2005]. A petrological study of wherlite and gabbro xenoliths from the Bellcombe ash member of the Piton de la Fournaise complex was conducted by Upton et al. [2000]. Olivine from these xenoliths is ferroan (up to Fo_{69}), with Mg- and Ca-rich clinopyroxene and variable modal abundances of plagioclase and oxide minerals. Petrological modelling in their study supported clinopyroxene fractionation before plagioclase, indicating a deep origin for these cumulate xenoliths. Lithostratigraphic analysis of the Grand Brûlé drill core, taken from the eastern flank of Piton de la Fournaise, generally supports this model, with the highest modal clinopyroxene occurring in deep cumulate units (2.5-3.0 km) [Rançon et al., 1989]. Geophysical studies have also identified large bodies with seismic velocities consistent with cumulate material underling much of Réunion [Gallart et al., 1999]. Taken together, this evidence demonstrates that fractional crystallization, cumulate formation and associated differentiation processes play a major role in the composition of erupted lavas on Réunion.

3.7 Supplementary methods information

A total of 29 cumulate and 13 associated basaltic lava samples from Piton de la Fournaise were selected for study. Petrography and modal analysis were performed at the *Scripps Isotope Geochemistry Laboratory (SIGL),* Scripps Institution of Oceanography,

using identical protocols to those described in Day et al. [2014]. Major- and minor-element mineral compositions were obtained primarily from polished mounts containing olivine, clinopyroxene and spinel, and as polished thick sections, at the University of Tennessee, using a Cameca SX-100 electron probe micro analyzer (EMP). All analyses were made with an accelerating potential of 15 keV and a beam size of 1 μm. Beam currents were 30 nA for olivine and pyroxene and 20 nA for spinel. Both natural and synthetic standards were used to calibrate the EMP and were measured throughout analytical sessions to ensure data quality. Background and peak counting times used were 20-30 s and standard PAP correction procedures were used. Detection limits were ≤0.02 wt. % for Si, Al, Mg, Ca, Na, K and P and <0.04 wt. % for Fe, Ti, Mn, V, Ni and Cr. Detailed, tabulated precision and detection limit data are available as part of the *Supplementary Information*.

Laser ablation ICP-MS analyses of phases in CH0701 and CH0706B were performed using a *New Wave Research* UP213 (213 nm) laser-ablation system coupled to a *ThermoScientific* iCAPq C ICP-MS. Analyses were done using pits with a 100 μm-diameter, a laser repetition rate of 5 Hz, and a photon fluence of 3.5 J/cm^2. Oxide production (UO/U and Th/O) was 0.03% for the analytical session. Ablation analysis took place in a 3 cm^3 ablation cell. The cell was flushed with a He-gas flow of ~0.7 L/min to enhance production and transport of fine aerosols, and was mixed with an Ar carrier-gas flow of ~1 L/min before reaching the torch. Each analysis consisted of ~60 s data collection. Backgrounds on the sample gas were collected for ~20 s followed by ~40 s of laser ablation. Washout time between spots was >120 s. Data were collected in time-resolved mode so effects of inclusions, mineral zoning, and possible penetration of the laser

beam to underlying phases could be evaluated. Plots of counts per second versus time were examined for each analysis, and integration intervals for the gas background and the sample analysis were selected. Standardization was performed using the Coahuila and Hoba iron meteorites, the compositions of which are known very well for LA-ICP-MS HSE abundance measurements [e.g., Walker et al., 2008].

Major and select trace element abundance analyses were performed by X-ray fluorescence (XRF) at Franklin & Marshall University using a PW 2404 PANalytical XRF vacuum spectrometer following the procedures outlined in Boyd and Mertzman [1987]. Precision and accuracy are estimated using repeat analyses of preparations of USGS standard BHVO-2 giving long-term reproducibility (2σ absolute standard deviation, n = 13) at ± 0.13 for SiO_2, ± 0.01 for TiO_2, ± 0.09 for Al_2O_3, ± 0.63 for FeO, ± 0.47 for Fe_2O_3, ± 0.10 for $Fe_2O_3^T$, ± 0.01 for MnO, ± 0.04 for MgO, ± 0.07 for CaO, ± 0.03 for Na_2O, ± 0.01 for K_2O, and ± <0.01 for P_2O_5. Accuracy for the average of 13 runs of BHVO-2 relative to USGS accepted values is estimated at <0.2 % for SiO_2 and TiO_2, <1 % for Al_2O_3, MgO, Fe_2O_3(T), CaO, Na_2O, P_2O_5, and <3 % for K_2O.

Trace-element abundances were determined using 100 mg of homogenized rock powder at the *SIGL*, using analytical procedures similar to those described in Day et al. (2014). Powder was precisely weighed and digested in a 1:4 mixture of concentrated Optima-grade HNO_3:HF for >72 Hrs at 150 ˚C on a hotplate. Samples were prepared with rock standards (BHVO-2, BIR-1, and BCR-2) and total procedural blanks. After drying down and sequential HNO_3 digestion steps to break-down fluorides, clear sample solutions

were diluted by a factor of 5000 in 2 % HNO_3 and doped with a 1 ppb In solution to monitor instrumental drift. Solutions were measured using a *ThermoScientific* iCAPq-c quadrupole inductively coupled plasma-mass spectrometer (ICP-MS) in standard mode. Reproducibility of the reference materials was generally better than 3 % (RSD) for standards, and element abundances were generally within error (1σ standard deviation) of the recommended values, with trace element concentrations determined by ICP-MS generally agreeing with those determined by XRF.

Osmium isotope and HSE abundance analyses were performed at the *SIGL* using methods described in Day et al. [2016]. The use of HF-desilicificiation in mafic-ultramafic rocks is discussed in that paper, and comparative standard reference material data are also presented, illustrating the robustness of the method. Precisely weighed homogenized powders were digested in sealed borosilicate Carius tubes, with isotopically enriched multi-element spikes (^{99}Ru, ^{106}Pd, ^{185}Re, ^{190}Os, ^{191}Ir, ^{194}Pt), and 10 mL of a 2:3 mixture of multiply Teflon distilled HCl, and Teflon distilled HNO_3 that had been expunged of Os. Samples were digested to a maximum temperature of 270 ˚C in an oven for 72 hours. Osmium was triply extracted from the acid using CCl_4 and then back-extracted into HBr [Cohen & Waters, 1996], prior to purification by micro-distillation [Birck et al., 1997]. Rhenium and the other HSE were recovered and purified from the residual solutions using standard anion exchange separation techniques [Day et al., 2016]. Isotopic compositions of Os were measured in negative-ion mode on a *ThermoScientific* Triton thermal ionization mass spectrometer at the *SIGL*. Rhenium, Pd, Pt, Ru and Ir were measured using a *Cetac* Aridus II desolvating nebuliser coupled to a *ThermoScientific* iCAPq-c ICP-MS in standard

mode. Offline corrections for Os involved an oxide correction, an iterative fractionation correction using $^{192}Os/^{188}Os = 3.08271$, a ^{190}Os spike subtraction, and finally, an Os blank subtraction. Precision for $^{187}Os/^{188}Os$, determined by repeated measurement of a 35 pg UMCP Johnson-Matthey standard was better than ± 0.3 % for cumulate runs (2 St. Dev.; 0.11381 ± 0.00032; n = 12). Repeated measurement of this standard during analyses of RU07 and RU15 samples, which took place several months after analyses of CH07 samples, averaged $^{187}Os/^{188}Os = 0.11408 \pm 0.00017$ (n = 5) and a correction to the samples measured at that time was applied to equate the average standard analyses. Measured Re, Ir, Pt, Pd and Ru isotopic ratios for sample solutions were corrected for mass fractionation using the deviation of the standard average run on the day over the natural ratio for the element, and all reported values are blank corrected. Total procedural blanks (n = 6) run with CH07 samples had a median corrected value of $^{187}Os/^{188}Os = 0.1370$, with a median [Os] of 9.2 pg. Average HSE abundances of these blanks were (in picograms) 74.8 ± 86 [Ir], 109 ± 34 [Ru], 50.5 ± 18.7 [Pt], 37.3 ± 57.4 [Pd], and 8.9 ± 4.6 [Re]. One blank run for Os and two for other HSE were run with the RU07 and RU15 samples. The Os yielded a $^{187}Os/^{188}Os$ ratio of 0.1932 ± 0.0054 and [Os] of 1.2 pg, and the HSE blanks averaged 80 pg Ir, 140 pg Ru, 23 pg Pt, 42 pg Pd and 11 pg Re. Full tabulated blank percentages are available in the *Appendix*.

3.8 Petrography of Piton Chisny cumulate xenoliths and major element chemistry of xenoliths and lavas

Most of the studied Piton Chisny cumulate xenoliths are equigranular dunites with limited clinopyroxene contents (typically 0.6-3.1 modal %). Approximately one-third of these samples have a yellow-green color, and have well-developed intergranular textures, with grain sizes typically less than 5 mm. Hereafter, these samples are referred to as 'fresh' cumulate xenoliths. The remaining samples are weakly to strongly discolored with a reddish-purple hue (**Figure 3.10**). In the less-strongly discolored samples, the discoloration propagates through intergranular spaces, while in more strongly discolored samples, grain cores are also typically discolored. Discolored samples contain higher proportions of accessory minerals including clinopyroxene and, more rarely, amphibole. Clinopyroxene occasionally occurs in distinct zones, but more commonly forms thin mantles around oxide grains, or is dispersed throughout a sample (**Figure 3.11**). However, twinning and exsolution of clinopyroxene is uncommon, making positive identification challenging in plane- or cross-polarized light. Where present, undulose extinction and deformation lamellae of accessory clinopyroxene is more common in strongly discolored samples and, in these samples, olivine generally shows more blighted textures such as embayments and exsolution to oxide phases. In areas of polished thick sections where this is common, olivine frequently shows symplectic texture, indicating that discoloration may be mediated by high-temperature fluids or chemical compaction events.

Three samples, CH0701Dunite, CH0703B and CH0703Dunite, have notable abundances of clinopyroxene. In CH0701Dunite and CH0703Dunite, clinopyroxene occurs predominantly in small, fine-grained veins (3 mm width, 5-50 μm grain diameter) that host only trace amounts of olivine. The veins have sharp contacts with surrounding

host rock and display no visible alteration or remineralization of surrounding material. In some circumstances, trace interstitial calcite in the veins is found in the host less than 1 cm from the vein boundary. Sample CH0703B is the sole wherlite of the cumulate suite, and has higher proportions of accessory amphibole, though this phase composes less than 1 % of its modal volume.

The only ubiquitous accessory mineral phase is spinel, which occurs both in intergranular spaces and as inclusions in olivine and makes up between 0.5 and 4.6 modal % of samples. In fresh samples, spinel grains are typically smaller and more diffuse, have sharp contacts with surrounding phases and occur in intergranular spaces, implying that they accumulated in equilibrium with proximate phases. In contrast, strongly discolored samples commonly have larger and more widespread spinel grains that are surrounded by zones of strong olivine exsolution, or are mantled by micron-sized grains of clinopyroxene (**Figure 3.11**). Rims of spinel grains and surrounding grains commonly show cubic intergrowth microtextures in reflected light (**Figure 3.11**) and surrounding grains are sometimes embayed to accommodate spinel growth. While Cr-spinel is the dominant opaque phase, magnetite intergrowths are not uncommon, especially in discolored cumulate xenoliths.

Approximately one-third of the cumulate xenoliths contain trace amounts of sulfide phases. Sulfide grains occur primarily as tiny, olivine-hosted grains (generally <10 μm diameter) with subordinate, larger interstitial sulfide (up to 50 μm diameter). The large sulfides typically display subequal proportions of pentlandite and pyrrhotite (**Figure 3.11**)

with rare chalcopyrite occurring exclusively in olivine-hosted grains. Poor response to polishing combined with their small grain sizes meant that limited quantitative mineral chemical data were obtained for the sulfides. An overview of mineral chemistry is given in **Figure 3.12** and discussed in the main text.

Both fresh and discolored cumulate xenoliths display similar major element characteristics, including similar concentrations of Fe, which have been shown to produce red colors in precipitates of oxidized fluids [e.g., Walker, 1986]. Average TiO_2, Al_2O_3 and CaO contents, which have the greatest proportional differences between the fresh and discolored groups, are elevated in the fresh group relative to the discolored group by 0.03 wt. %, 0.12 wt. % and 0.19 wt. %, respectively (**Figure 3.13**). These small differences indicate that differences in accumulation of major element oxides from exogenous sources is probably not responsible for the color distinction between fresh and discolored cumulate xenoliths. Furthermore, neither group shows relatively elevated Fe^{2+}/Fe^* or loss on ignition (LOI) relative to the other, implying that if an oxidized mineral phase is involved in the color change, very low abundances of that phase are required to produce the observed colors (**Figure 3.14**). Trace element characteristics are indistinguishable between the two groups (**Figure 3.13**) and cumulate xenoliths show evidence for sulfide control of chalcophile elements, including Cu, Zn and Ga (**Figure 3.15**).

Piton de la Fournaise lavas are compositionally basaltic and basanitic, with generally low concentrations of alkali metals (**Figure 3.16**). The MgO contents are variable (7.2 to 29.2 wt. %) and correlate strongly with the modal abundance of olivine (3-46 percent, r^2 =

0.98; *Appendix*). Abundances of Al_2O_3 and CaO are generally high (6.1 to 14.2 wt. % and 4.9 to 11.2 wt. %, respectively), especially in lavas collected on or near Piton Chisny, which have the least olivine and therefore the greatest ratios of plagioclase to olivine. Major element patterns also show significant influence from clinopyroxene and olivine fractionation, consistent with studies of other Réunion OIB [e.g., Albarède & Tamagnan, 1988; Albarède, et al., 1997; Fretzdorff & Haase, 2002; Vlastélic, et al., 2005]. On plots of major elements versus MgO contents, clear differentiation trends are present that intersect the region of relatively invariant cumulate compositions (**Figure 3.14**).

3.9 Supplementary discussion of petrological controls on cumulate xenolith and lava geochemistry

A number of differentiation processes can alter the composition of igneous rocks. For example, hydrothermal alteration is common in volcanic complexes and can modify the mineralogy and bulk chemistry of rocks [e.g., Schiffman & Staudigel, 1994; Crocket, 2000; Marks et al., 2010]. Lavas examined in this study are not visibly altered. Nonetheless, previous studies of OIB lavas have recognized that Re concentrations are typically much lower than MORB, with a number of studies attributing this feature to magmatic degassing of Re [Bennett et al., 2000; Lassiter et al., 2003; Norman et al., 2004; Day et al., 2010]. An increase in fO_2 promotes the loss of Re [Borisov & Jones, 1999], suggesting that at the oxidation state relevant to OIB petrogenesis (FMQ), the rate of Re loss from a magma will increase by an order of magnitude per increasing log unit of fO_2. Sub-aerial eruptions from Réunion preserve evidence for an increase in fO_2 during magmatic emplacement, from

FMQ -1.8 up to FMQ +3 [Boivin and Bachélery, 2009]. High temperature (>350 °C) gas condensate deposits at Piton de la Fournaise have been shown to be enriched in Re (24 to 79 ng g^{-1}) by almost two orders of magnitude with respect to corresponding lavas (0.130 to 0.137 ng g^{-1}), while the Os abundances of the condensates are similar to those of the lavas (14 to 132 pg g^{-1}) [Gannoun et al., 2015]. These observations provide a clear role for the outgassing and loss of some HSE, especially Re, from the lavas. However, because at least some Réunion cumulates form at depths >2.5 km [Rançon et al., 1989], degassing would have to begin relatively deeply if it were to affect the Re concentrations of the cumulate xenoliths. It has also been argued that Os isotope systematics can also be affected by degassing processes. High-temperature gas condensates (Na–K sulfates; 384 to 400 °C) from Piton de la Fournaise yielded $^{187}Os/^{188}Os$ values that were lower (0.124–0.129) than nearby lavas and may be attributable to preferential mobilization of mantle sulfides carried by magmas [Gannoun et al., 2015]. The extreme consistency of measured $^{187}Os/^{188}Os$ in Réunion magmatic rocks from across the Piton de la Fournaise complex diminishes the possibility that this process operates on a large scale. Nonetheless, these results imply that the Réunion mantle source may be more radiogenic with respect to Os than previously known, and that this source has been subsequently diluted by interaction with a DMM-like component with low $^{187}Os/^{188}Os$. Care must be exercised to identify isotopic fractionation or mixing patterns amongst samples associated with active degassing sites.

Relative enrichments in Pt are more difficult to explain through magmatic processes. Relative enrichments in Pt have been noted in some ophiolite orthopyroxenites [O'Driscoll et al., 2015], but orthopyroxene is absent in the Piton Chisny cumulate

xenoliths and rare in Piton de la Fournaise lavas. Cumulate xenoliths from Piton Chisny that have the greatest enrichments in Pt are also generally the most HSE-enriched. In addition, all clinopyroxene-bearing dunites have flat-to positive trends across Pt. Current knowledge of Pt partitioning underscores the relatively low incompatibility of Pt in tholeiitic melts [Jamais et al., 2008; Pitcher et al., 2009; Ireland et al., 2009] relative to alkali basalts [Day, 2013], particularly in relatively evolved melts [Jamais et al., 2008]. Evolved lavas are known in the Piton de la Fournaise complex [e.g., Nativel et al., 1979; Albarède & Tamagnan, 1988; Albarède et al., 1997; Upton et al., 2000; Fretzdorff & Haase, 2002; Boivin & Bachèlery, 2009], but are more abundant in the post-shield phase Piton de Neiges [Upton & Wadsworth, 1972; Nativel, 1976; Gillot & Nativel, 1982; Fisk et al., 1988; Fretzdorff & Haase, 2002] and are not represented in the suite of lavas that we measured. It is possible that relatively Pt-enriched xenoliths may represent a distinct spatial generation of cumulate formation that derives from low-MgO magmas either in shallow depths of the Piton de la Fournaise complex or deeper levels of post-shield tholeiitic magmatism in the Piton de Neiges complex, which likely underlies the western edge of Piton de la Fournaise. Differences in the composition of a magma is known to affect bulk partitioning of HSE [Day, 2013], and this may additionally explain generally higher abundances of the HSE in cumulate xenoliths that also have relative enrichments in Pt.

To investigate the possible effects of fractional crystallization on the HSE compositions of the cumulate xenoliths, we performed laser ablation (LA) ICP-MS analyses on sulfide, oxide and silicate phases of sample CH0701Dunite, a fresh, clinopyroxene-bearing dunite, and sample CH0706B, a sulfide-bearing discolored dunite

(**Figure 3.17**). In sulfide phases pentlandite and chalcopyrite, these data reveal subequal PUM-normalized Ru and Ir and PUM-normalized Re/Pd <1. Iron oxides contain appreciable Cu (1-177 ppm) and high PUM-normalized Re/Pd and Ru/Ir, but variable HSE concentrations. These ratios are highly variable in clinopyroxene, with PUM-normalized Re/Pd both less than and greater than 1 and flat-to-negative Ru anomalies. However, all measured phases have high PUM-normalized Pd/Pt (2-46), strongly implying that relative enrichments in Pd are not petrologically controlled, but rather imparted from the Réunion parental magma.

In order to investigate the implications of these results for the cumulate xenoliths, we employ three tests for petrological controls on relative HSE enrichments. First, we calculate a HSE mass balance for samples with modal mineralogy information and compare this information with measured HSE patterns (**Figure 3.17**). We find that fractionation of Ru from Ir observed in the LA-ICP-MS data greatly under-predicts measured bulk rock Ru/Ir. Given that Ir is below the LA-ICP-MS detection limit in olivine from both samples, it seems most likely that oxides, despite their omnipresence in the cumulate xenoliths, do not mask the Ru/Ir composition of the Réunion parental magma. If they did, we would expect the mass balance calculation to fully account for the measured PUM-normalized Ru/Ir ratios of the cumulate xenoliths. In the case of PUM-normalized Pd/Pt and Re/Pd ratios, the mass balance calculation greatly over-predicts the ratios of the cumulate xenoliths, which again strongly supports the notion that the Réunion parental melt possesses relative excesses of Pd.

Second, we plot measured HSE fractionations versus modal mineralogy data (**Figure 3.18**). We find no strong relationship between modal clinopyroxene and PUM-normalized Ru/Ir and Pd/Pt ratios, but we do see a positive relationship between modal clinopyroxene and PUM-normalized Re/Pd ratios. We acknowledge that this could potentially represent a petrological control on relative Re excesses, but tend to discount this possibility for three reasons. First, the correlation is supported by only four samples containing clinopyroxene, including the one wherlite sample in which the mineral phase control on relative HSE concentrations is presumably different from the dunites. Second, the LA-ICP-MS data indicate distinct fractionation of Re from Pd in our two selected samples, with clinopyroxene possessing a PUM-normalized Re/Pd ratio >1 in sample CH0701 Dunite and <1 in sample CH0706B. Third, few cumulate xenoliths contain appreciable modal clinopyroxene, and among these samples there are both relative Re enrichments and relative Re depletions. Relative HSE enrichments also show no particular relationship to opaque phases. Although these phases comprise both oxides and sulfides, our LA-ICP-MS data indicate that both phases possess PUM-normalized Re/Pd >1. Further, sulfides contain PUM-normalized Ru/Ir ≈1, implying that the presence of sulfide alone would not dramatically change the PUM-normalized Ru/Ir ratios of all opaque phases, particularly given the abundance of oxides relative to sulfides.

Finally, we plot elemental tracers of clinopyroxene, oxide and sulfide accumulation versus relative HSE enrichments (**Figure 3.19**). Clinopyroxene is most effectively traced by CaO in dunites, since Ca is highly incompatible in olivine. Oxides are traced by W because the LA-ICP-MS data indicate appreciable amounts of this element in oxides

relative to other analyzed phases, and because W is highly incompatible in silicates. The relative contributions of sulfide phases are traced with Ni/Cu ratios, as our LA-ICP-MS data indicate appreciable differences in the PUM-normalized Pd/Pt and Re/Pd ratios of pentlandite and chalcopyrite. Both sulfide phases show near-flat Ru anomalies, so this ratio should not trace the relative contributions of these phases to the bulk-rock Ru/Ir budget, however, given the flat patters about Ru, sulfides should not strongly affect bulk rock Ru anomalies in either direction. We find no clear relationship between these elemental tracers and PUM-normalized Ru/Ir, Pd/Pt and Re/Pd ratios.

While it is clear from the LA-ICP-MS data that certain phases in the cumulate xenoliths do fractionate HSE, it is unlikely that sulfide accumulation strongly affects bulk-rock PUM-normalized Ru/Ir ratios, or that any of the observed fractionations can unequivocally explain the pervasive relative enrichments in Ru and Pd observed in the cumulate xenoliths. Our data may indicate that relative Re enrichments may not reflect the HSE composition of the Réunion primary melt. Additional study of Re fractionation in cumulates may reveal more specific information about the impact of silicate, sulfate and oxide fractionation on the relative concentrations of this element.

Several features of major and trace element concentrations in the cumulate xenoliths can be attributed to element compatibility in olivine. For example, Pb is the only chalcophile element on typical trace element diagrams (e.g., **Figure 3.3**), and its abundance is likely controlled by accumulation or removal of sulfides from cumulate sources, which is consistent with negative Pb anomalies in Piton de la Fournaise lavas (Pb/Pb* = 0.26-

0.45), since they are generally free of significant modal sulfide. However, correlations of Pb/Pb* to chalcophile elements and inter-chalcophile element correlations are poor (**Figure 3.4**), indicating that the low abundances of Pb either makes them poor candidates for mineral fractionation proxies, or that sulfide exerts little control on bulk rock Pb compositions. By contrast, Sr is compatible in plagioclase [e.g., Villemant et al., 1981], and since the cumulate xenoliths are devoid of plagioclase they also lack positive Sr anomalies (Sr/Sr* = 0.84-0.95). Common Ti enrichments in cumulate xenoliths (Ti/Ti* = 1.01-6.89) and most lavas (Ti/Ti* = 0.98-2.12) likely reflect relatively high compatibility of Ti in olivine relative to the REE [e.g., Adam & Green, 2006], but also significant accumulation of Ti-bearing spinel.

Compared to Ti, Sr and Pb anomalies, Ta anomalies are more difficult to explain by fractional crystallization [Jackson et al., 2008; Peters & Day, 2014], partially because the extremely low abundances of Ta in OIB makes their compatibility behavior difficult to experimentally constrain. However, the nearly ubiquitous presence of positive Ta anomalies in both the cumulate xenoliths (Ta/Ta* = 0.77-3.20) and lavas (Ta/Ta* = 1.67-1.86) and strong correlations between Ti and Ta anomalies implies that there is a petrological control to these features that is most likely mediated by a mineral phase that is common to both the cumulate xenoliths and lavas. One possibility is that these anomalies are generated by partial melting [e.g., Peters & Day, 2014], since both Ta and Nb (average Nb/Nb* = 0.42-2.01 for cumulate xenoliths, 1.10-1.23 for lavas) are anomalously incompatible [Adam & Green, 2006], and this would explain positive Ta anomalies in both

the cumulate xenoliths and the lavas. However, the consistent relative Ta enrichments may mean that this is a source signal that is decoupled from Nb.

It is impossible to account for fractionation that may be introduced by unique sulfide or metal phases that do not appear in available thin sections (e.g., alloy phases). Nevertheless, these phases can dominate the HSE profiles of rocks in which they are present, and may introduce significant nuggeting effects. Replicate analyses of our samples sometimes yield different HSE patterns (c.f., samples CH0704 and CH0705Y), which probably reflects heterogeneous distribution of HSE in bulk powders. It is unlikely that partitioning between hypothetical and unidentified phases have any strong influence on HSE fractionations because correlations of Ru/Ir, Pd/Pt and Re/Pd are poor despite well-resolved behavior of many chalcophile elements in the cumulate xenoliths.

3.10 Temperature-depth constraints on partial melting and cumulate formation

Using the parameterized model of Lee et al. [2009] it is possible to estimate the pressure and temperature conditions under which lavas from Piton de la Fournaise are in equilibrium with ultramafic material of varying composition (**Figure 3.20**). This model and other thermobarometric models have been used to determine the pressure-temperature (P-T) conditions of mantle melting based on calculated primary magma compositions [Dasgupta et al., 2010; Hart & Jackson, 2014]. Here, the parameterization is extended to determine the P-T conditions under which parental magmas to measured lavas are in

equilibrium with a variety of olivine forsterite compositions ("target" forsterite). This allows assessment of both the P-T conditions under which the primary magmas were in equilibrium with the ambient upper mantle ($Fo_{89.5}$) [Workman & Hart, 2005], but also equilibrium conditions for more primitive mantle with higher forsterite contents [e.g., Thompson & Gibson, 2000]. The model cannot account for unique geological processes that may strongly affect parental magma compositions, such as fluid fluxes and slab melting, but it is considered to be well-calibrated to various tectonic environments [Lee et al., 2009].

In order to determine magma compositions that are in equilibrium with various forsterite contents, olivine was quantitatively added or subtracted from measured bulk compositions of Piton de la Fournaise lavas. The method of accomplishing this is similar to that described by Lee et al. [2009] but also uses our measured iron oxidation state data, varying the increment at which olivine is added with the degree of disequilibrium with target olivine compositions. Some ascending magmas will experience net accumulation rather than net loss of olivine and will eventually erupt as picrites, oceanites, or other olivine-phyric lavas. Because the dataset presented here is limited to bulk-rock powders, some of which contain large proportions of accumulated olivine, some of these lavas will appear to be in equilibrium with olivine of erroneously high Fo content. This cautionary possibility may be countered by quantitatively subtracting olivine from olivine-accumulative lavas such that the calculated magma compositions can intersect the actual composition of the parental melt. We include both olivine-rich and olivine-poor Réunion lava samples in the model to illustrate any impact of olivine accumulation.

Thermobarometric model estimates indicate that Piton de la Fournaise melts were last in equilibrium with $Fo_{89.5}$ olivine between 1.40 (52 km) and 5.50 GPa (204 km) and between 1270 and 1660°C (**Figure 3.20**). The lowest model pressures and temperatures are from lavas collected at the locality of the Piton Chisny cumulate xenoliths, and are likely different compared with other Piton de la Fournaise lavas for two reasons. First, they have relatively high loss on ignition (LOI), which were used to represent H_2O contents, and this lowers calculated pressures and temperatures in the Lee et al. [2009] model. Clearly, LOI and H_2O contents are not identical measures, but this is commonly how the model is applied, enabling comparison of published datasets. Second, as these lavas have close spatial association with the Piton Chisny cumulate xenoliths, these are the most likely to be substantially affected by accumulative olivine from distinct magma batches, which may affect final calculated P-T.

To compare the thermobarometric results to calculated P-T conditions of lavas from other hotspots, similar datasets were carefully selected to plot alongside Réunion lavas at a target of $Fo_{89.5}$ (**Figure 3.20**). These published data have similar analytes, including LOI and iron oxidation state, and are treated identically to the Réunion data in terms of the primary magma composition calculation. Lavas from the selected datasets return substantially lower P-T conditions of their primary magmas than those of Piton de la Fournaise lavas. It is unlikely that these inferred conditions are strongly affected by olivine accumulation, as both the Réunion and comparative lavas have widely varying modal olivine.

Calculated thermobarometric conditions for primary magmas in equilibrium with a more ferroan olivine composition similar to those measured in Piton Chisny xenoliths (Fo_{85}; 0.89-2.30 GPa or 33 to 85 km; 1170-1410°C, **Figure 3.20**) are lower than those for higher target forsterite values ($Fo_{89.5}$). However, the predicted P-T conditions still exceed those expected for a crustal origin for the cumulate xenoliths if the oceanic crust beneath Réunion is only 9-15 km thick [Gallart et al., 1999; Torsvik et al., 2013], or possibly thicker due to underplating beneath Réunion Island itself [Gallart et al., 1999; Gupta et al. 2010]. Only consideration of the group of lowest forsterite contents among the cumulate xenoliths (ca. Fo_{82}) brings the cumulate xenoliths closer to crustal pressures and temperatures, as does consideration of alternative geothermometers [e.g., Putirka, 2005]. These results emphasize that the returned P-T estimates are highly model-dependent, but all models suggest that the cumulate xenoliths formed at the base of the crust at the crust-mantle transition, as has been hypothesized for xenoliths at other hotspots [e.g., Sen, 1988; Sen & Jones, 1990]. The model results provide further support for a shallow, accumulative rather than mantle origin for the ultramafic xenoliths. Further, if the calculated P-T conditions of Réunion parental magma genesis are accurate relative to other hotspots, the model is consistent with anomalously deep mantle melting beneath Réunion Island.

3.11 Supplementary discussion of petrological modeling

The main text presents a null hypothesis model showing that, given current knowledge of HSE partitioning in basaltic systems, a parental magma lacking relative Ru and Pd enrichments cannot precipitate a cumulate with enrichments similar to Piton Chisny

cumulate xenoliths (**Figure 3.6A**). However, a parental magma with these enrichments can produce a primitive upper mantle-normalized HSE pattern that is very similar to the range of compositions of cumulate xenoliths possessing the 'sawtooth' pattern (**Figure 3.6B**). Certain lavas also show a more muted sawtoothed distribution of HSE (**Figure 3.5**), and these tend to be the most olivine-phyric of the sample set. Modeled mixing between the modeled residual magma composition and calculated corresponding cumulate material from **Figure 3.6B** produces similar patterns to these olivine-phyric samples (**Figure 3.21**). If the majority of olivine grains in these rocks are inherited from cumulate sources, it may explain why these samples display a sawtooth pattern rather than the common hyperbolic pattern found in other cumulate xenoliths.

The main text also discusses consideration of the HSE contents of Réunion lavas relative to those of other hotspot lavas. We find that, compared to the well-characterized sample set of Ireland et al [2009], Réunion lavas are systematically depleted in the HSE (**Figure 3.22**) and thus correspond to an OIB parental magma that is unusually deficient in these elements. The text then explores the possibility that, if Réunion is derived from an early-sequestered mantle domain [e.g., Vlastélic et al., 2009], it may have been partially or wholly exempt from acquisition of HSE during late accretion. However, the lack of correlation between the various relative HSE enrichments (**Figure 3.23**) demonstrates that they do not likely share a common process origin. However, separation and degassing of Re from ascending magmas by volcanic gasses [e.g., Gannoun et al., 2015] may preclude correlations of this relative enrichment. Further, a lack of correlation between the relative

enrichments and primitive mantle-normalized La/Yb values and Pb/Pb* strongly implies they are not related to partial melting or differentiation of sulfides (**Figure 3.23**).

Supplementary Figures

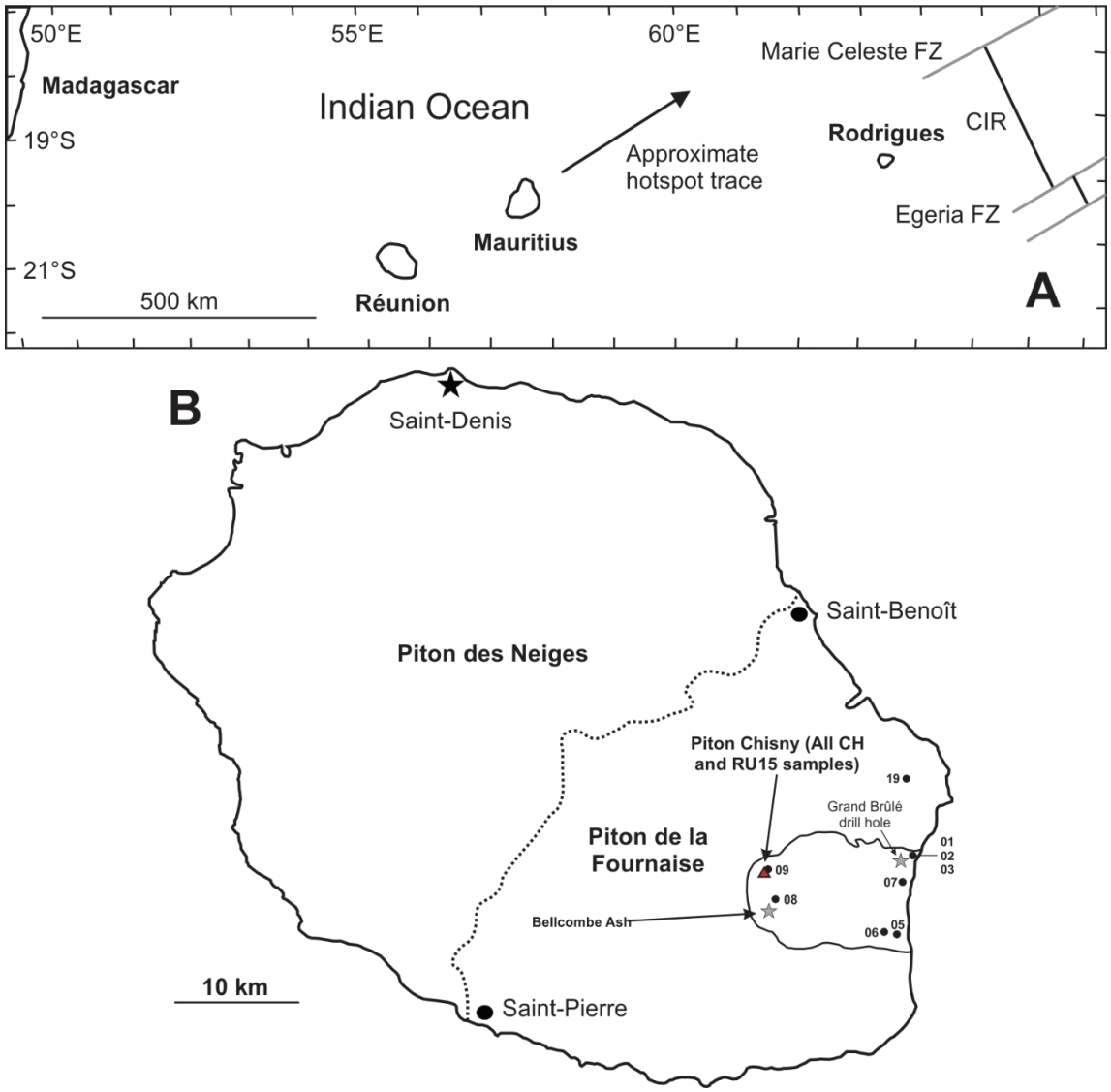

Figure 3.9: (A) Outline map of southwest Indian Ocean showing the location of Réunion, Mauritius and Rodrigues (the Mascarene Islands) relative to Madagascar and the Central Indian Ridge (CIR, FZ: fracture zone). The Réunion hotspot trace extends northeast from Réunion Island towards India and the Cretaceous-age Deccan Traps. (B) Outline map of Réunion Island noting the location Piton Chisny (red triangle) and of lavas examined in this study (black dots with numbers), with locations referred to in the text, including the Bellcombe Ash. Dotted line denotes approximate boundary between Piton des Neiges and Piton de la Fournaise lava flows according to Vlastélic et al. [2005], and the ovular shape set into the Piton de la Fournaise region denotes the approximate boundaries of the Piton de la Fournaise *enclos*.

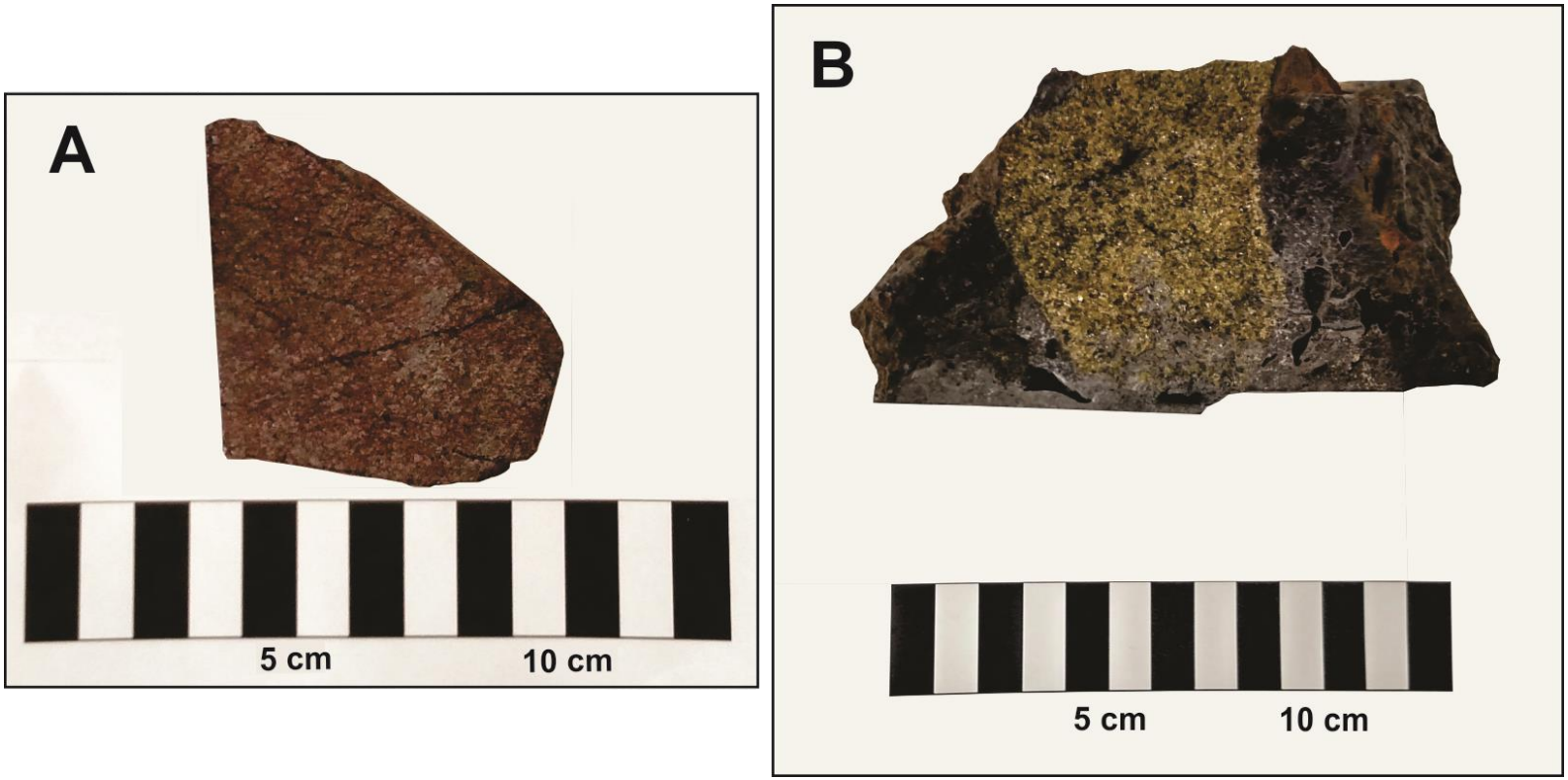

Figure 3.10: Photographs of representative Chisny dunite xenoliths, showing discolored sample CH0705C (excised from host lava, A) and fresh Piton Chisny xenolith sample CH1515 (B) that is still embedded in the host-lava.

Figure 3.11: Photomicrographs of features of Piton Chisny cumulate xenoliths. Some cumulate xenoliths show minor discoloration that propagates through intergranular spaces (S), while some other xenoliths show extensive discoloration (B). In discolored samples, complex intergrowth textures and exsolution of Cr-spinel can occur (C). Clinopyroxene occurs as a minor (<10 modal %) phase in some dunites and is usually present as small veins (D), or as clusters (E). Spinels are ubiquitous and occasionally display cubic intergrowth structures along boundaries with silicates (F). Small sulfide grains are found in approximately one-third of the cumulate rocks and are typically pyrrhotite and pentlandite (G), or are too small to positively identify (H). Other accessory minerals that are occasionally found in discolored samples include amphibole (J). ol: olivine; cpx: clinopyroxene; chr: chromite; po: pyrrhotite; pn: pentlandite; sulf: sulfide (undifferentiated); amph: amphibole.

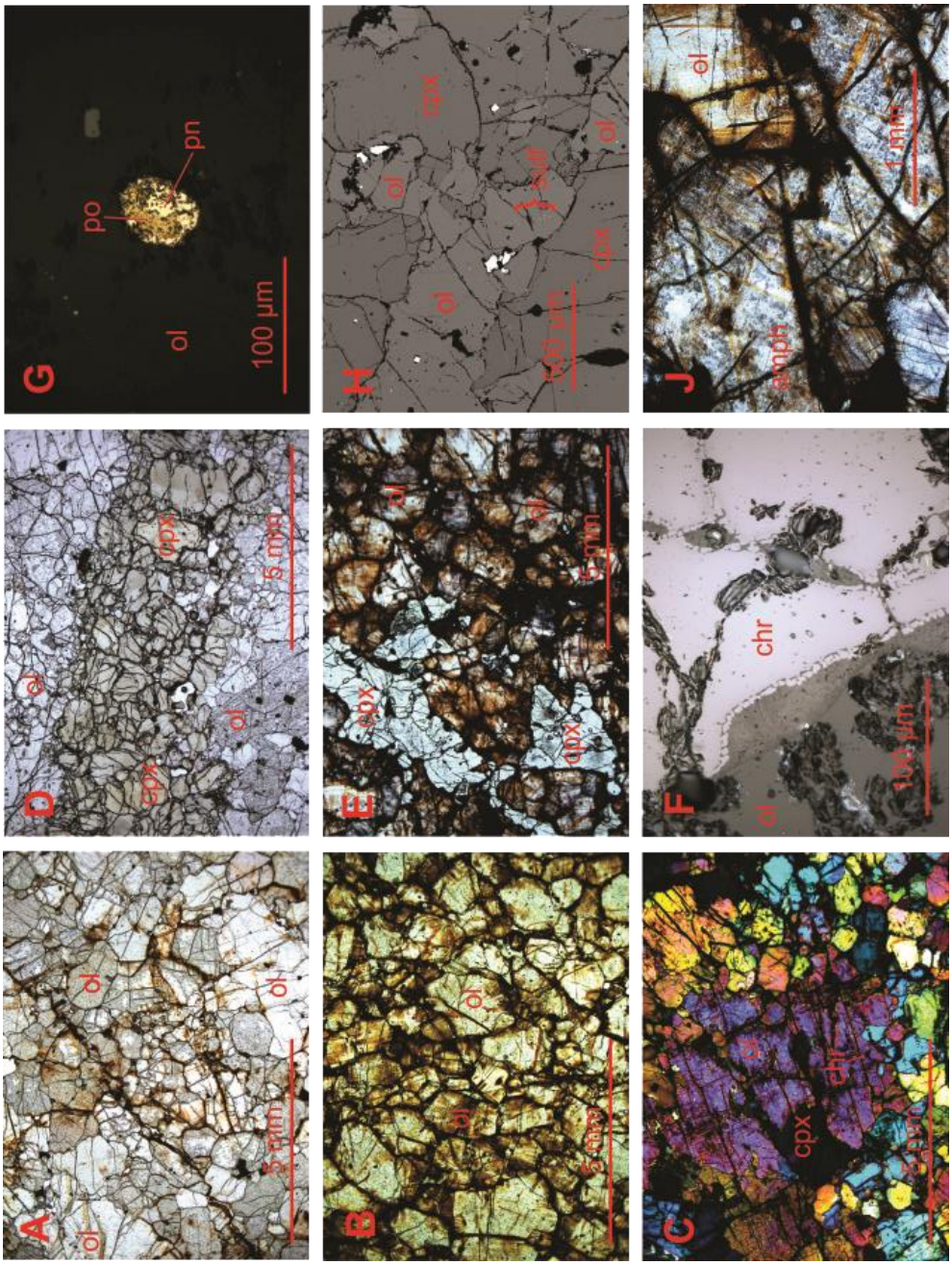
A
ol
ol
ol
5 mm
B
ol
ol
ol
5 mm
C
ol
cpx
chr
cpx
5 mm
D
ol
cpx
ol
cpx
5 mm
E
ol
ol
cpx
cpx
5 mm
F
chr
ol
100 µm
G
pn
po
ol
100 µm
H
cpx
ol
ol
cpx
cpx
ol
100 µm
J
ol
amph
1 mm

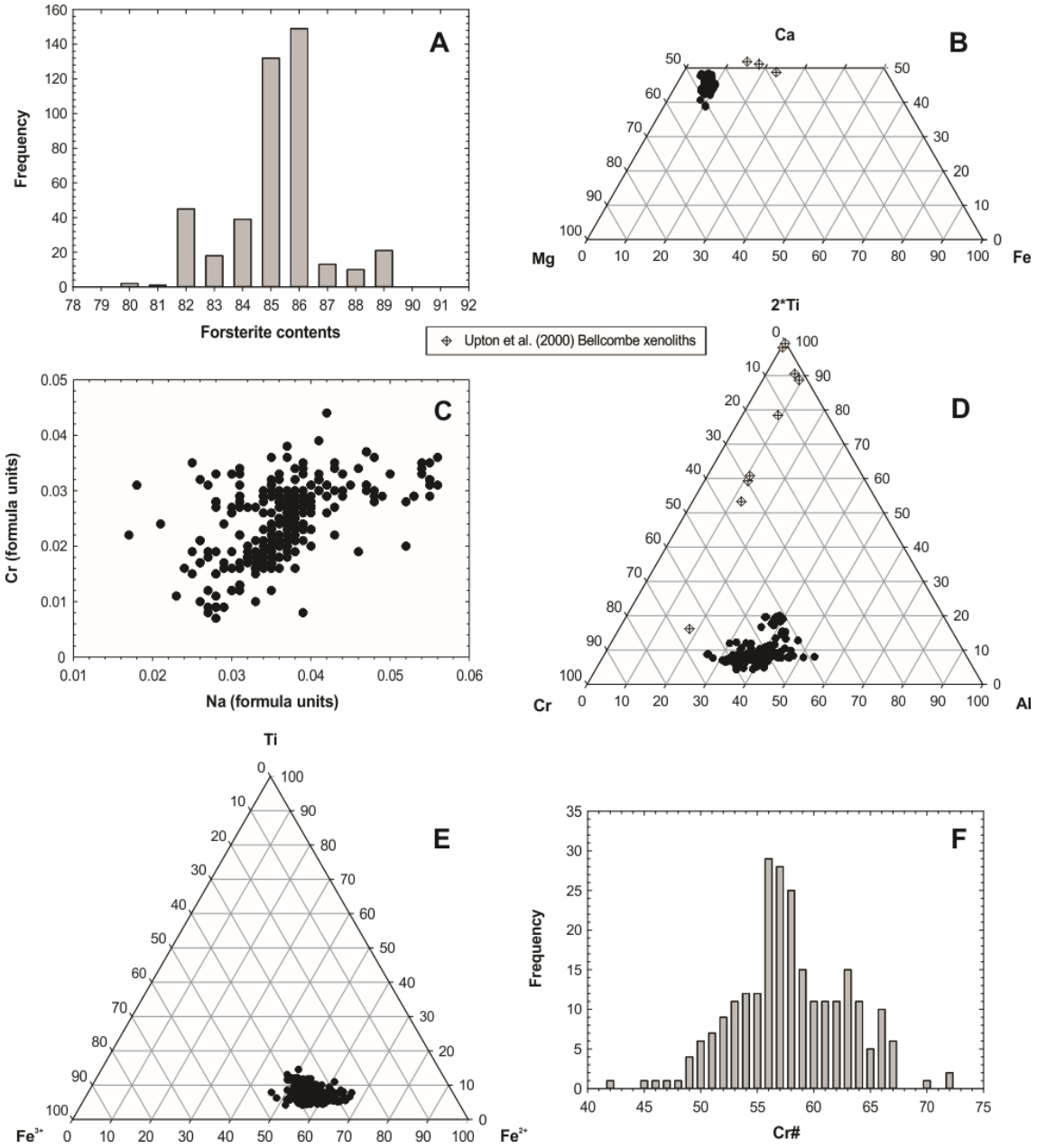

Figure 3.12: Mineral compositions of Piton Chisny cumulate xenoliths and Bellcombe Ash xenoliths [Upton et al., 2000] showing: (A) distribution of olivine forsterite contents; (B) a pyroxene quadrilateral for dunite and wherlite xenoliths; (V) Cr-Na co-variation for clinopyroxene; (D-E) composition and Fe oxidation state of spinel; and (F) distribution of Cr# for spinel.

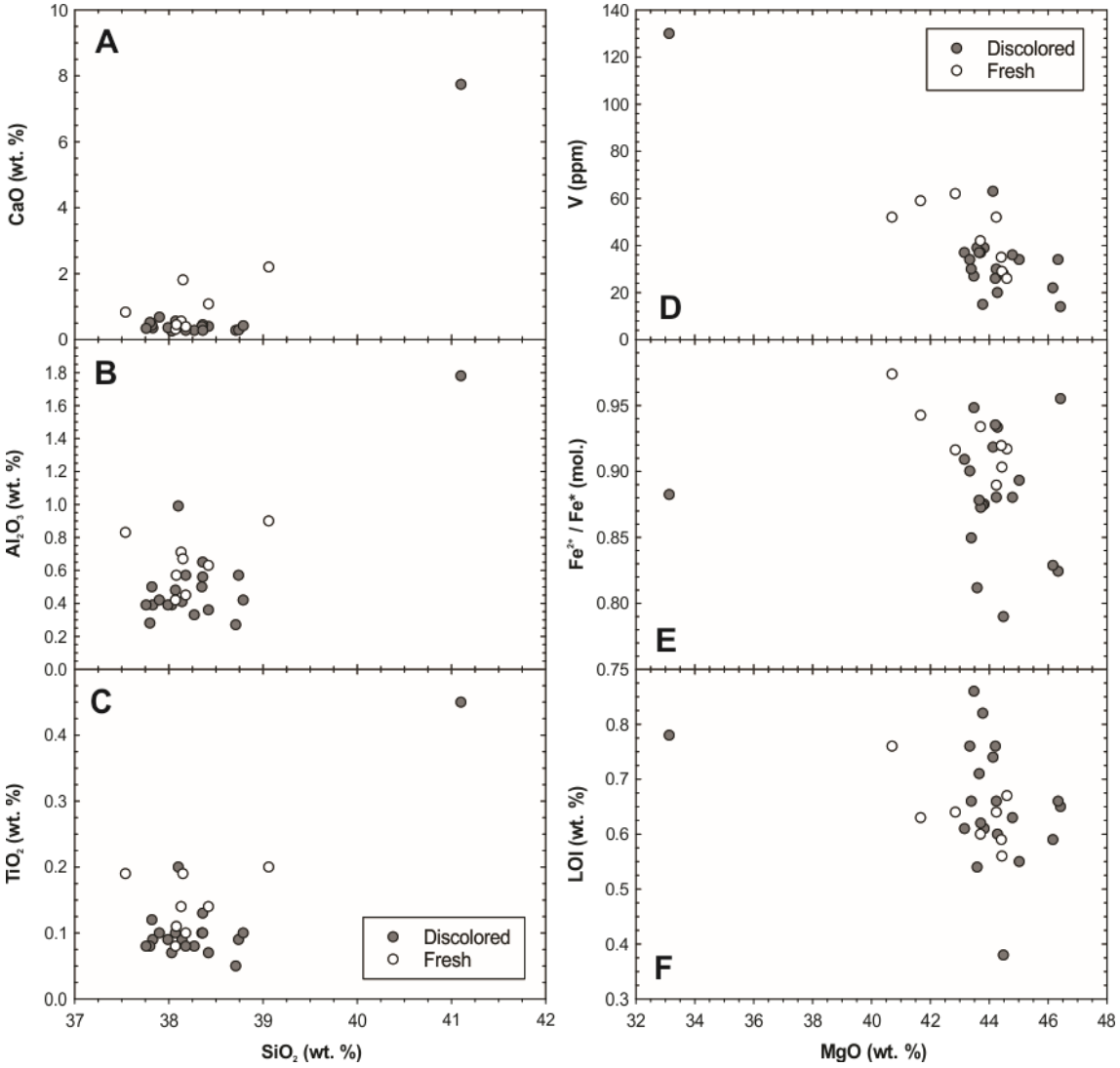

Figure 3.13: Major element and major-trace element variation diagrams showing variations within the discolored and fresh subsets of Piton Chisny cumulate xenoliths.

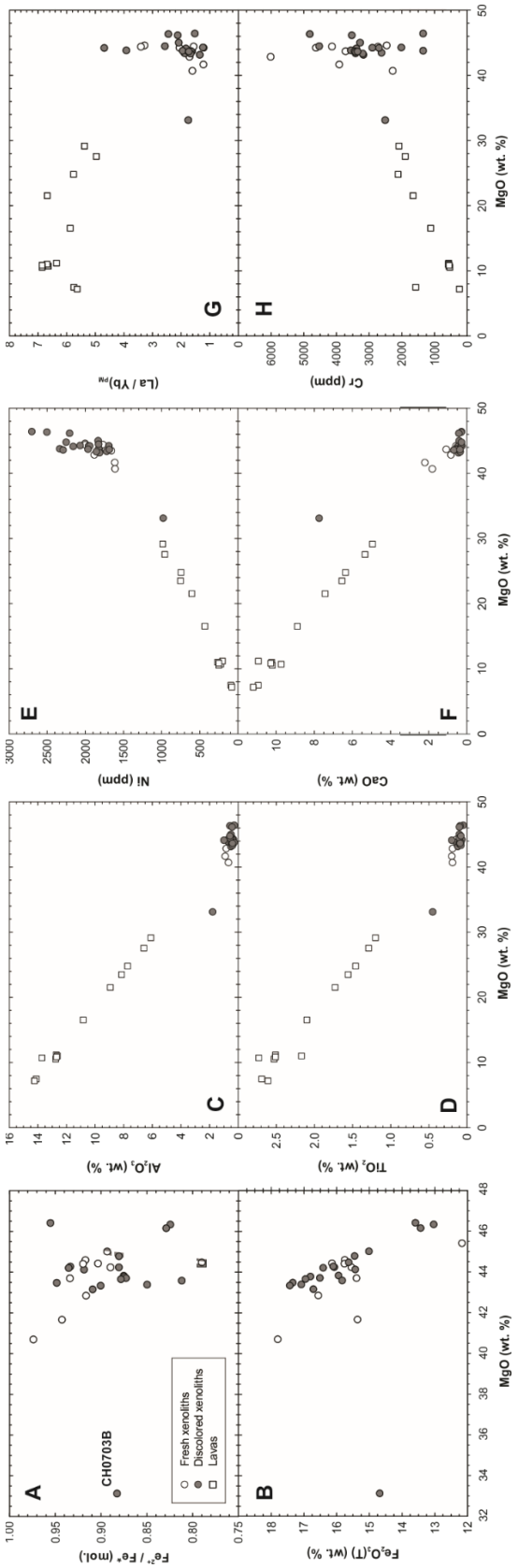

Figure 3.14: Major and trace element variations for Piton Chisny cumulate xenoliths (circles) and Piton de la Fournaise lavas (squares).

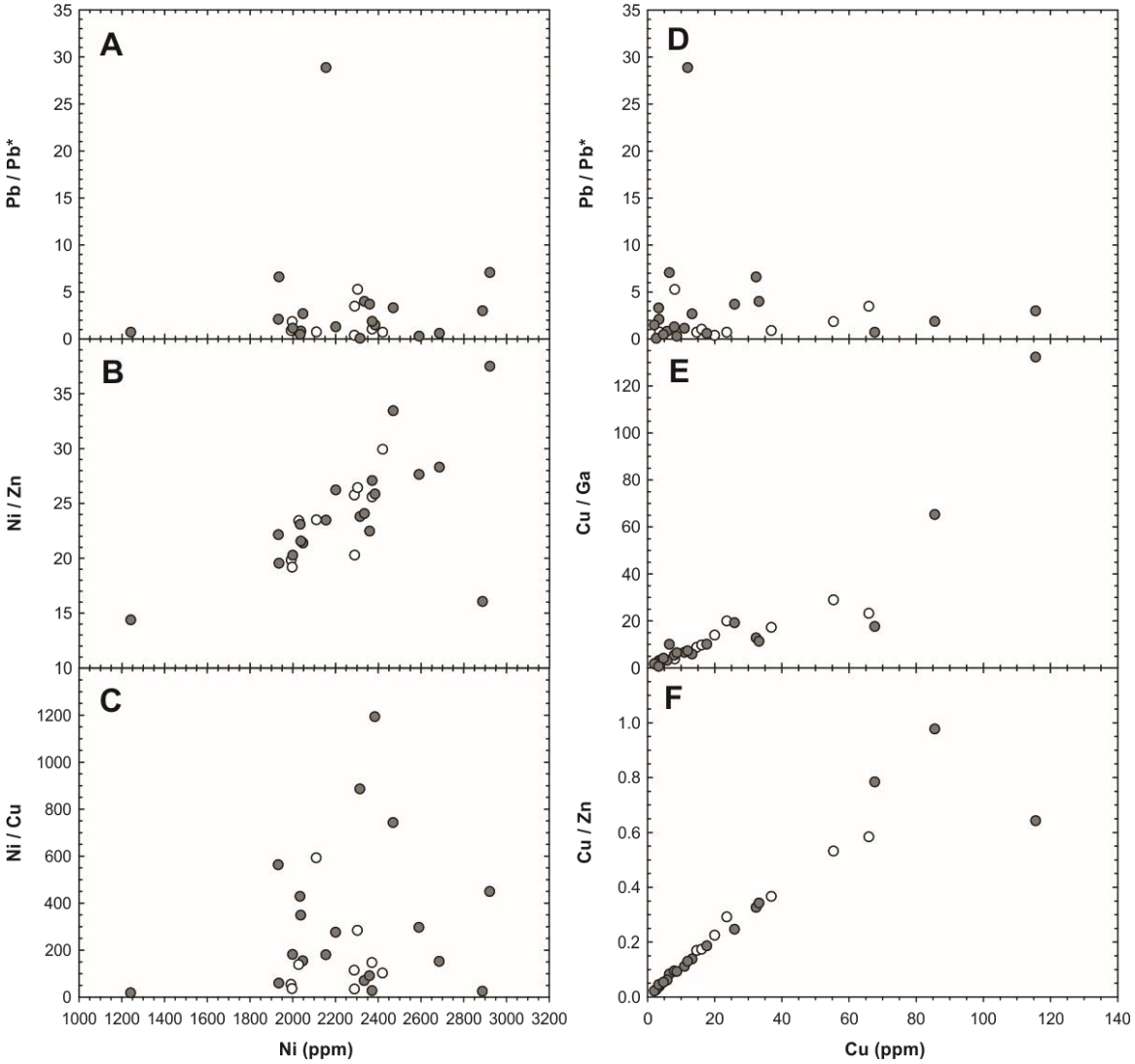

Figure 3.15: Co-variations of chalcophile elements and Pb anomalies in Piton Chisny cumulate xenoliths. $Pb/Pb^* = Pb_n / (La_n \times Nd_n)^{0.5}$, where N means normalized to primitive mantle [McDonough & Sun, 1995]. Symbols as in **Figure 3.2**, main text. Maximum correlation coefficients are (E) $r^2 = 0.77$ and (F) $r^2 = 0.86$.

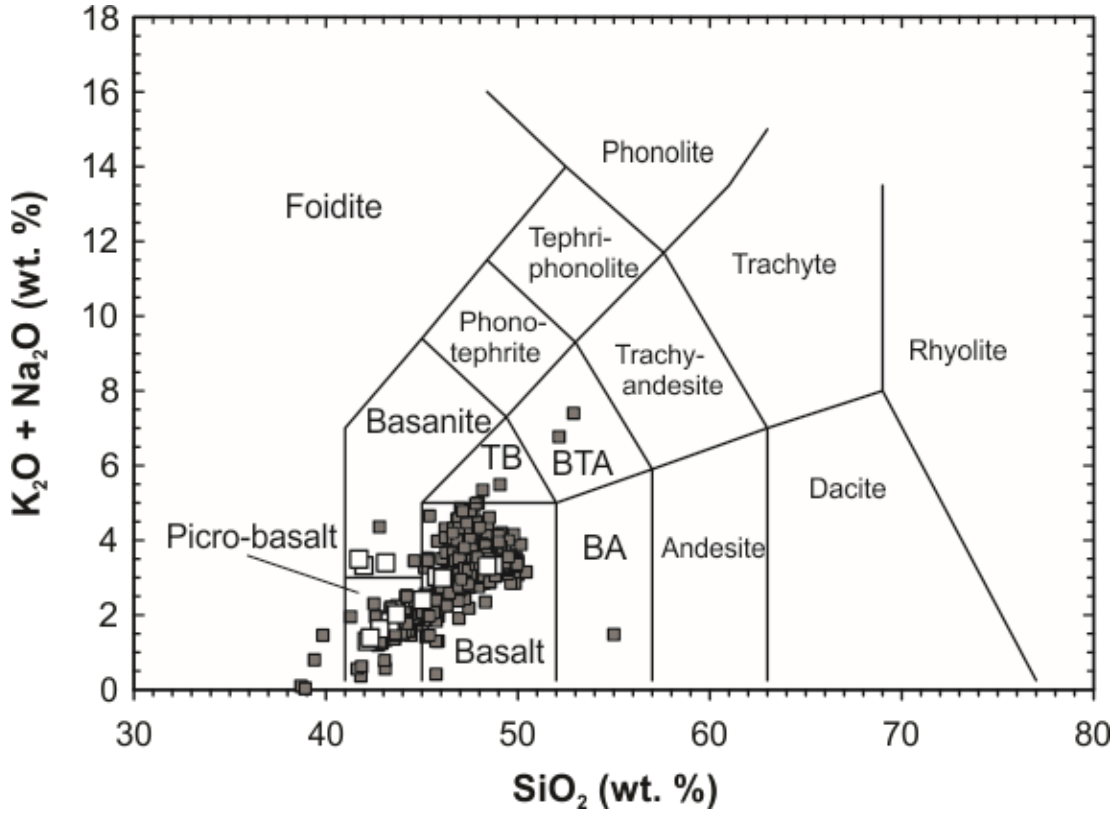

Figure 3.16: Total alkali versus silica diagram for Réunion lavas from the literature (dark gray squares) and this study (larger white squares). TB: trachy-basalt; TBA: basaltic trachyandesite; BA: basaltic andesite.

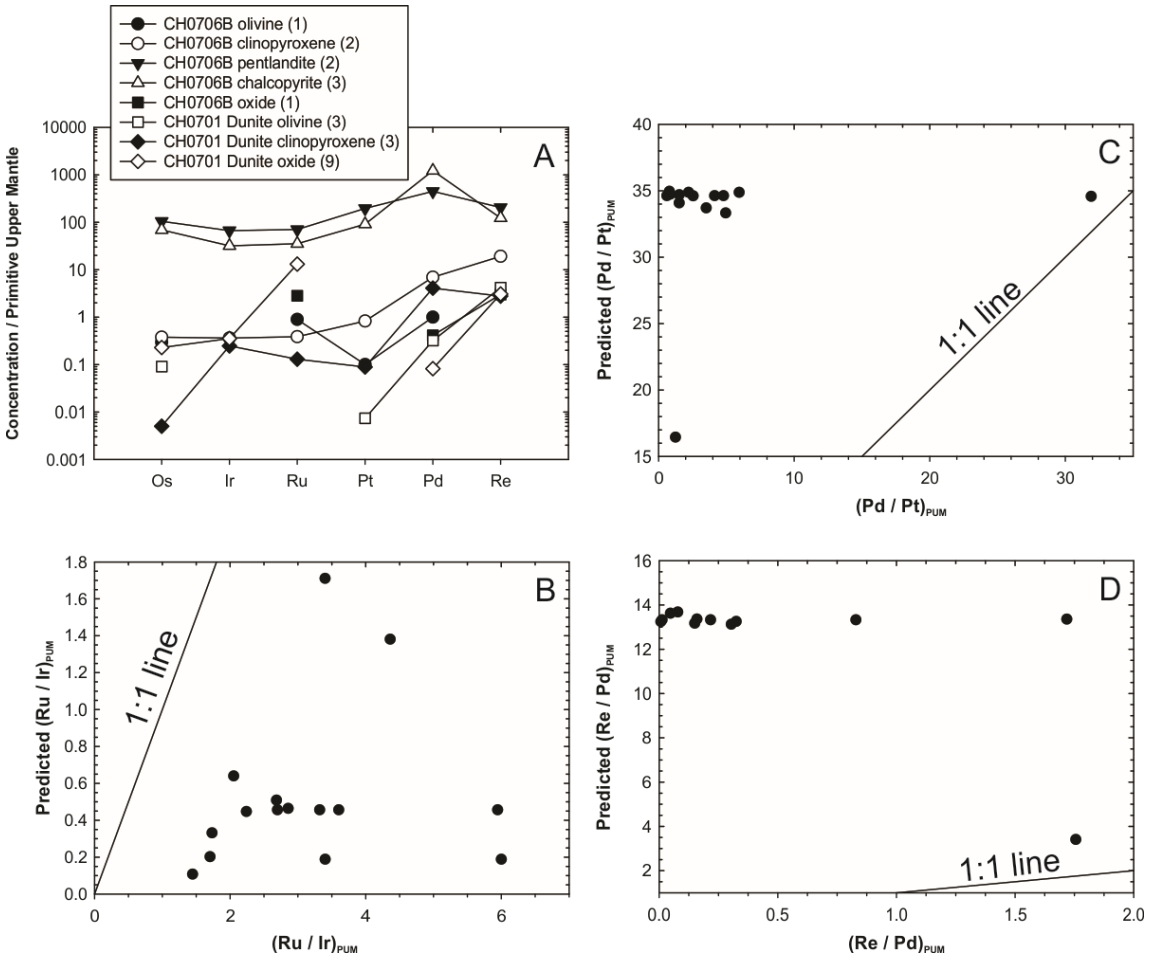

Figure 3.17: (a) PUM-normalized HSE concentrations of silicate, sulfide and oxide minerals measured by LA-ICP-MS. (b-d) Measured relative HSE enrichments versus 'predicted' relative HSE enrichments calculated from mass balance constraints and HSE concentrations in minerals shown in (a). PUM normalization values from Becker et al. (2006).

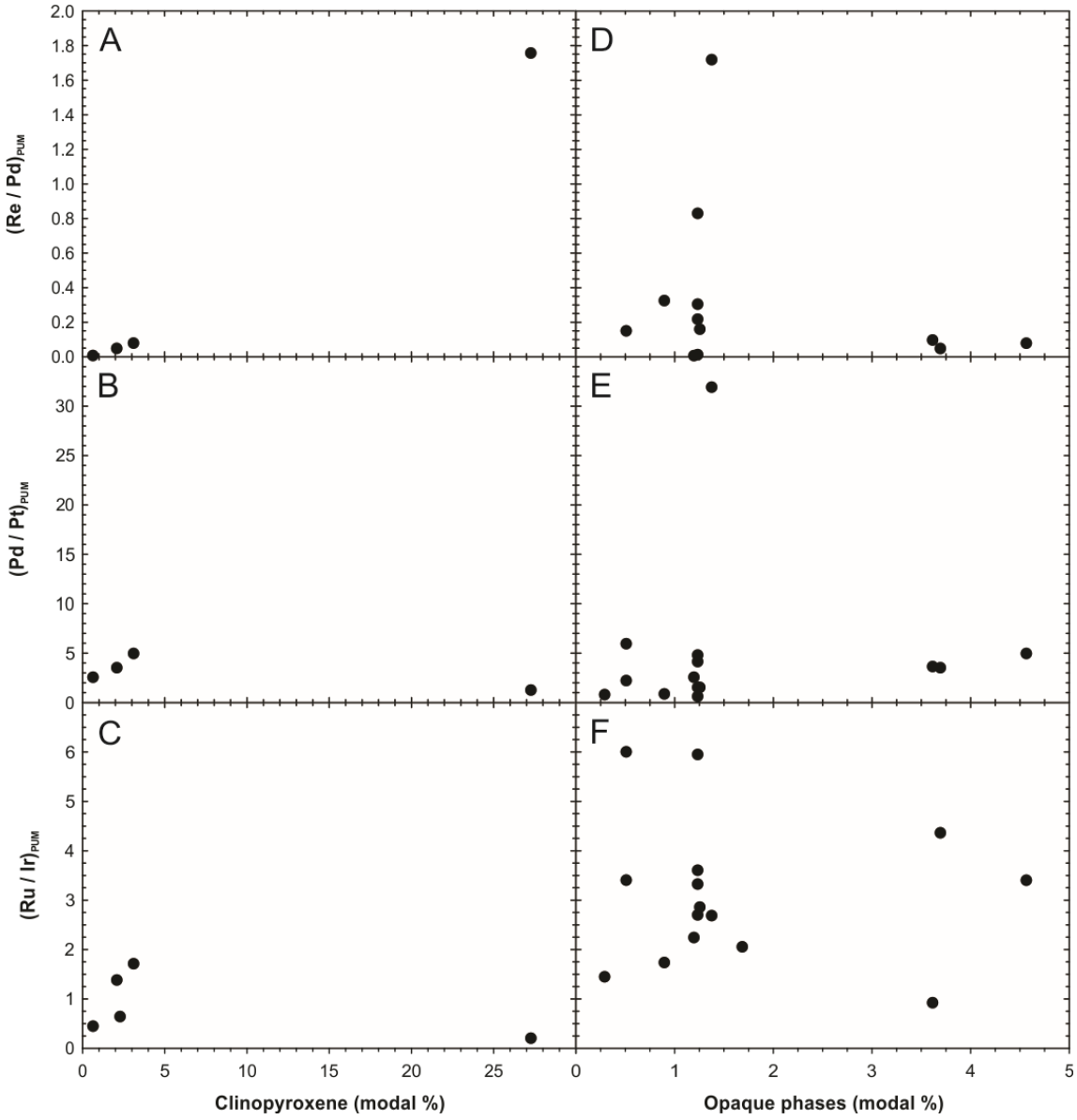

Figure 3.18: Modal abundances of clinopyroxene and opaque phases determined by *ImageJ* versus measured relative HSE enrichments.

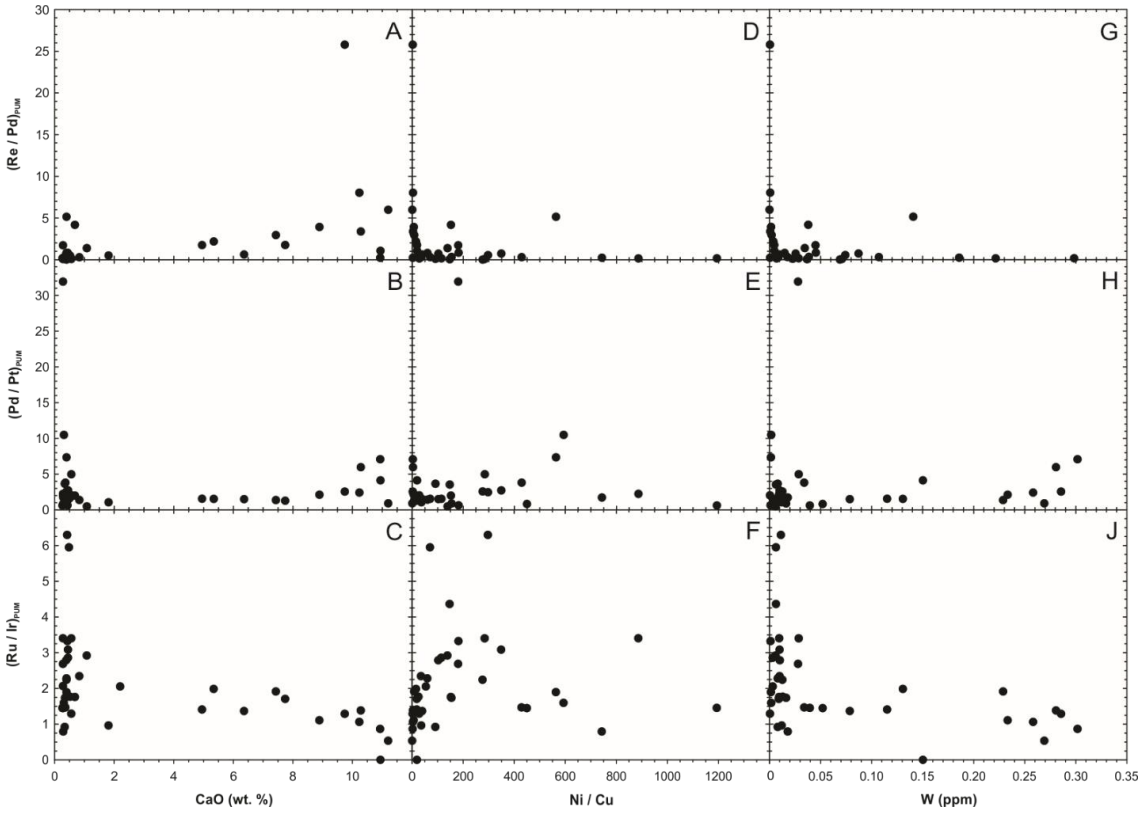

Figure 3.19: (A-C) CaO concentrations of bulk cumulate xenoliths, tracing clinopyroxene contents, (D-F) Ni/Cu ratios, tracing relative pentlandite and chalcopyrite contents and (G-J) W concentrations, tracing oxide contents, versus measured relative HSE enrichments.

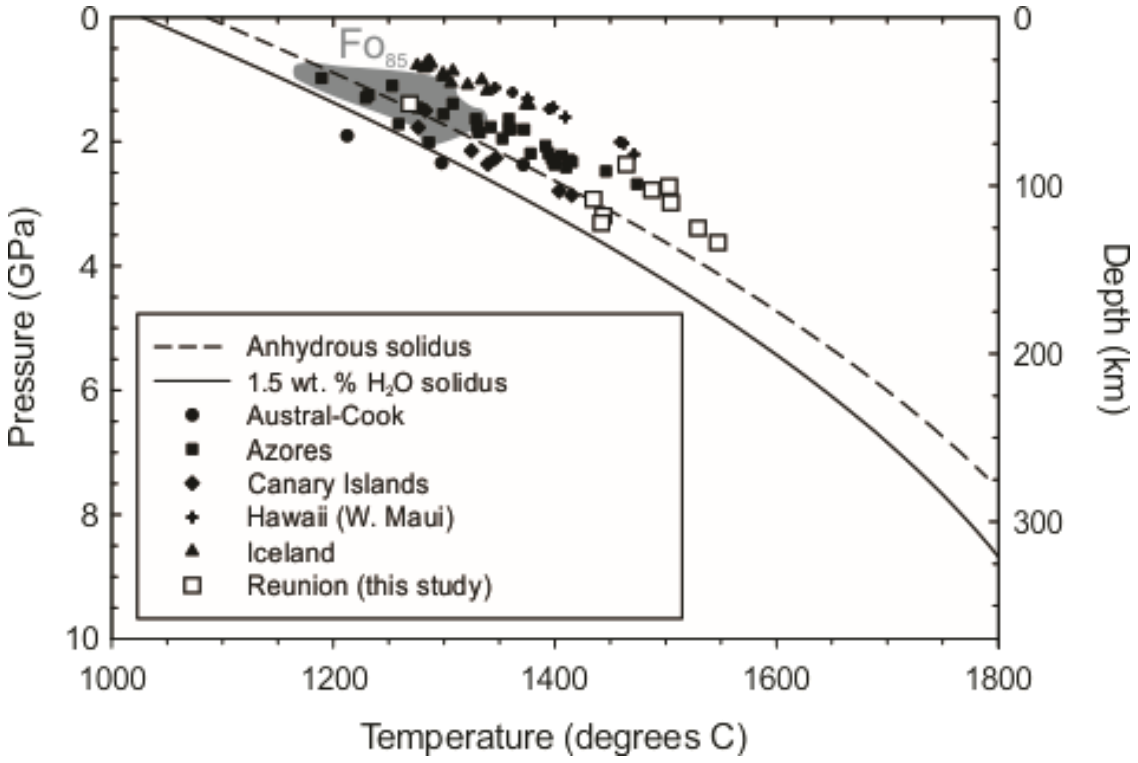

Figure 3.20: Model pressure-temperature conditions (after Lee et al., 2009) for calculated primary magmas in equilibrium with $Fo_{89.5}$ (squares, Réunion and other symbols) from measured compositions of Piton de la Fournaise lavas. Gray shaded region shows range of pressure-temperature conditions for primary magmas in equilibrium with Fo_{85} (e.g., average cumulate forsterite contents). Solidi calculated from empirical model of Katz et al. [2003]. Geochemical data sources: Herzberg et al. [2014]; Praegel & Holm [2006]; Skovgaard et al. [2008].

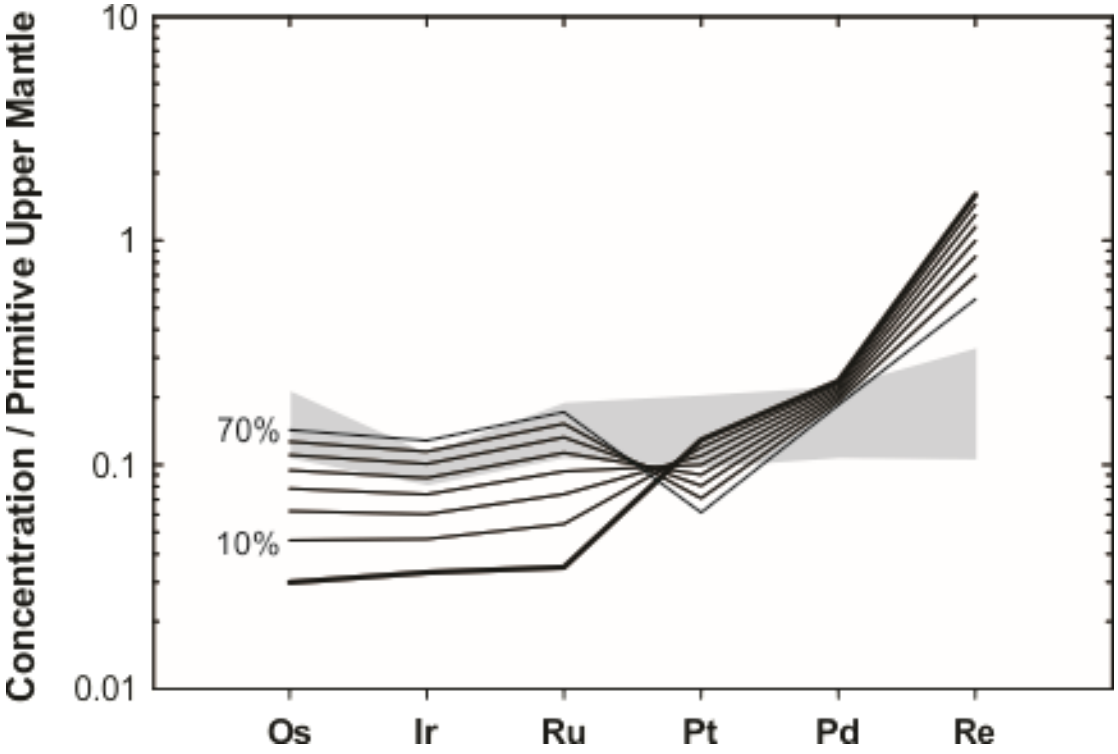

Figure 3.21: Mixing between a calculated cumulate (as hypothetical xenocrysts) and its residual magma after 30% solidification (as in **Figure 3.6**, main text); percentages note proportion of added cumulate. Gray region is measured values of Piton de la Fournaise lavas preserving the sawtooth pattern.

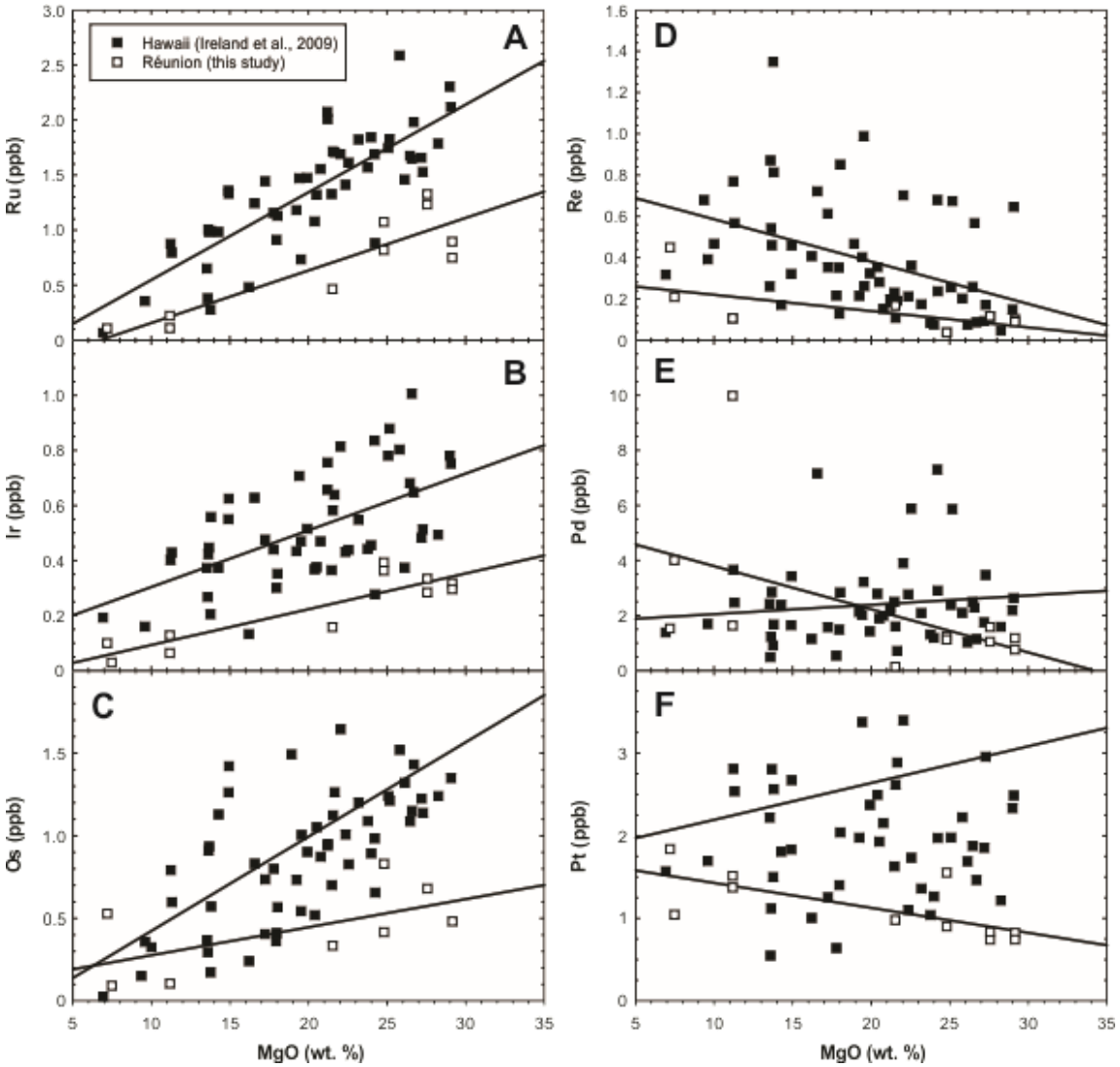

Figure 3.22: Correlations of MgO to HSE for Hawaiian lavas [Ireland et al., 2009] and Piton de la Fournaise lavas that do not display the hyperbolic trend noted in the text. Trend lines for the two sample suits are provided for reference.

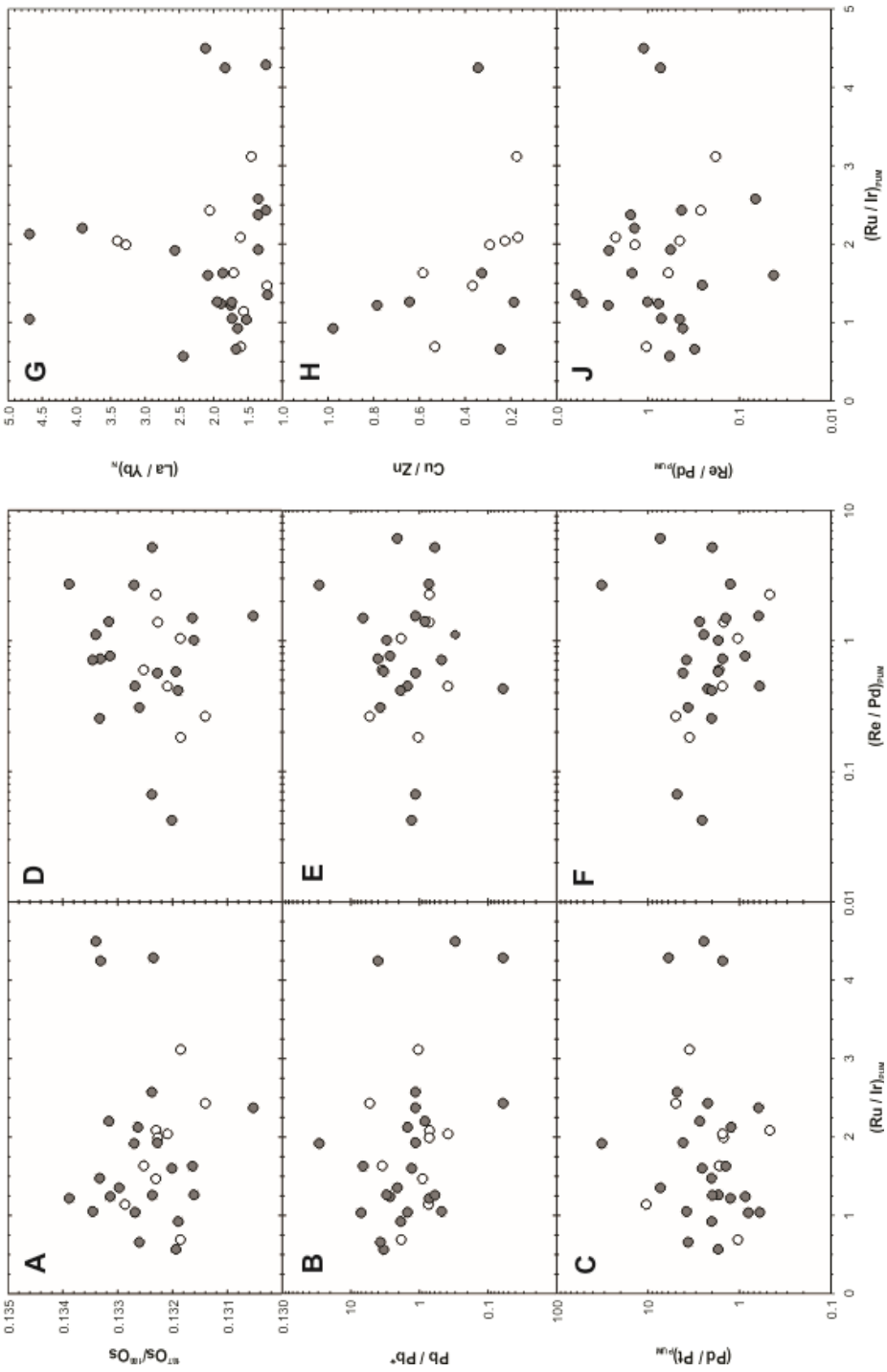

Figure 3.23: Correlations of relative Ru and Re enrichments to Os isotopes (A and D, respectively), Pb anomalies (B and E, respectively) and relative Pd enrichments (C and F, respectively). Correlation of relative Ru enrichments to primitive mantle-normalized La/Yb values (G), Cu/Zn values H) and relative Re enrichments (J). Pb/Pb* and Cu/Zn serve as indices of chalcophile differentiation processes (c.f., **Figure 3.4**) and La/Yb values as an index of partial melting.

Chapter 4:

Helium-oxygen-osmium isotopic and elemental constraints on the mantle sources of the Deccan Traps

Abstract

The Deccan Traps, a 65 Ma continental flood basalt province located in western India, is one of the largest short-lived magmatic events to have occurred on Earth. The nature and composition of its mantle source(s), however, have been difficult to resolve due to extensive assimilation of continental crust. To circumvent this issue we have analyzed early-formed olivine grains from MgO-rich (up to 15.7 wt.%) lavas that likely formed before substantial crustal assimilation occurred. We compare mineral chemistry and He-O-Os isotope compositions with bulk rock major- and trace-element abundances and $^{187}Os/^{188}Os$. Helium isotope compositions for the olivine grains generally show strong influence from crustal assimilation (<3 R_A), but one ankaramite sample from the Pavagadh volcanic complex has a $^{3}He/^{4}He$ ratio of 10.7 R_A, which is slightly lower than the range of

$^{3}He/^{4}He$ measured for present-day Réunion volcanism (~12-14 R_A). Olivine separates span a more restricted range in $^{187}Os/^{188}Os$ (0.1267 to 0.1443) compared with their host lavas (0.1186 to 0.5010), with the separates reflecting a parental magma composition less affected by lithospheric or crustal interaction than for the bulk-rocks.

High-precision analyses of olivine compositions indicate the presence of a signature similar to pyroxenite in Deccan mantle sources, with up to 25% of the parental magma representing this source. However, pyroxenite signatures are remarkably similar to those expected to arise as a result of assimilation of continental crust. Weak correlations exist between X_{px} (range: 0.2-0.7) and $^{3}He/^{4}He$, $\delta^{18}O$ and $^{187}Os/^{188}Os$. Robust relationships between these parameters may be precluded due to a lack of simple two reservoir source mixing, requiring multiple mantle domains with distinct compositions, or because X_{px} may partially reflect assimilation of continental crust. Geochemical similarities exist between Deccan Traps olivines ($^{3}He/^{4}He$ = >10 R_A; $^{187}Os/^{188}Os_i$ = 0.1311 ±24) and Réunion cumulate rocks ($^{3}He/^{4}He$ = 12 to 14 R_A; $^{187}Os/^{188}Os_i$ = 0.1324 ±14). These relationships imply that a characteristic geochemical 'fingerprint' may have persisted in the mantle plume that fed the Deccan Traps, since its inception at 65 Ma, to ongoing eruptions occurring on Réunion up to the present-day.

4.1 Introduction

The elemental and isotopic compositions of basaltic lavas can reveal the nature of their mantle sources, including the identity of mantle lithologies involved in partial melting [e.g., Yaxley & Green, 1998], or evidence for the return of ancient subducted materials to

Earth's surface [Morgan, 1971; Hofmann & White, 1982; White & Hofmann, 1982]. It has been shown that modification and metasomatism of peridotite mantle by subducted oceanic lithosphere may significantly alter the bulk composition of hotspot melts [Yaxley & Green, 1998], possibly resulting in the formation of mixed peridotite-pyroxenite/eclogite lithologies [Hirschmann & Stolper, 1996; Sobolev et al., 2005, 2007; Day et al., 2009] with different bulk compositions than ambient peridotite mantle [e.g., Herzberg & O'Hara, 2002; Herzberg, 2011]. Melting in the presence of these distinct lithologies is thought to produce olivine with distinct major and minor element compositions [Herzberg, 2011; Vidito et al., 2013; Herzberg et al., 2013, 2014]. The degree with which these signatures correlate with olivine and bulk rock isotopic tracers, however, is poorly constrained. One study of Icelandic lavas has offered evidence for positive correlations between pyroxenite and peridotite end-members and Os isotopes [Sobolev et al., 2008], but understanding of the cause of these variations remains limited.

A potential method for better understanding the origins of hotspot magmas is to combine multiple radiogenic and stable isotope systems (e.g., He-O-Os) with high-precision geochemistry for individual mineral phases, such as olivine. For example, noble gases provide evidence that primordial gas signatures exist in the mantle [e.g., Clarke et al., 1969; Lupton & Craig, 1975; Stuart et al., 2003] that have maintained high-$^{3}He/^{4}He$ (greater than the depleted upper mantle value of 8 ±1 R_A; R_A is the $^{3}He/^{4}He$ ratio of air, 1.38×10^{-6}; Graham, 2002) due to their high time-integrated $^{3}He/(U+Th)$ [e.g., Kurz et al., 1982; Allègre et al., 1983; Kaneoka, 1983; O'Nions & Oxburgh, 1983]. Contrastingly, the radiogenic ^{187}Re-^{187}Os system can provide time-integrated information on the sources of

melts, as Os is highly compatible, being in low quantities in crustal materials compared to melt-extracted domains, and is incorporated into early crystallizing mineral phases [e.g., Day, 2013; Gannoun et al., 2015]. Oxygen is the primary constituent of silicate and oxide minerals, and is a major element in the mantle, crust and surface reservoirs. Oxygen isotopes (^{16}O, ^{17}O and ^{18}O) show mass dependent fractionated by kinetic and equilibrium effects, with decreasing fractionation with increasing temperature [e.g., Bigeleisen and Mayer, 1947]. For this reason, $^{18}O/^{16}O$ provides a sensitive record of relatively low temperature (<500˚C) hydrological and hydrothermal processes occurring in the crust and lithosphere [Gregory & Taylor, 1981; Staudigel et al., 1995]. Materials containing a recording of these processes can be effectively recycled and returned at hotspot volcanoes while retaining their oxygen isotope signatures [e.g., Eiler, 2001; Day et al., 2009]. Combining study of these isotopes and major-element mineral chemistry, all of which can be effectively measured in olivine grains, has the potential to elucidate the relationship between mantle petrology and the isotopic composition of mantle sources and their derivative magmas.

Here, we use this approach to investigate one of the largest short-lived magmatic events in Earth history, the eruption of the Deccan Traps of western India. Deccan Traps lavas are well-characterized in terms of their major and trace element abundances and Sr-Nd-Pb isotope systematics, and reveal both crust- and MORB-like influences [Allègre et al., 1982; Mahoney et al., 1982; Melluso et al., 1995, 2006; Peng & Mahoney, 1995], as well as strong fractional crystallization and differentiation trends [e.g., Krishnamurthy, 1971]. However, concomitant assimilation and fractional crystallization (AFC) processes

have effectively served to obscure contributions from mantle sources. To ameliorate these issues, we searched for olivine with relatively high forsterite contents (>80) from olivine-phyric Deccan lavas. In other magmatic systems, such high-Fo olivines are thought to crystallize relatively early, and prior to other crystallizing phases (e.g., clinopyroxene, plagioclase, oxides). A limited number of basalts and picrites that display this primitive character have been previously identified in the Deccan Traps [Krishnamurthy & Cox, 1977; Krishnamurthy et al., 2000]. However olivine in basalts erupted through thick crust and lithosphere may have experienced modification that can limit positive identification of their mantle source(s) [Sobolev et al., 2007], even when they have high forsterite contents. Petrological and isotopic analyses are therefore likely to be mutually complementary in the study of mantle sources to hotspot volcanism. This contribution provides the first combined He-O-Os isotope and high-precision olivine elemental composition study of any continental flood basalt (CFB), to explore the identity of Deccan Traps parental magmas.

4.2 Samples and Methods

Samples were collected from Gujarat and Maharashtra States in January 2014, and are from areas with lava flows and dikes associated with Deccan Traps magmatism. The samples used in this study represent some of the most olivine-phyric basalts of a much larger suite of basaltic rocks from the Deccan Traps collected during a 2014 field campaign (>200 samples). In hand sample, most specimens contain a combined 5 to 15 volume percent olivine and clinopyroxene phenocrysts, and many of the samples also contain plagioclase phenocrysts. Sample 47B is the sole ankaramite of the suite, and contains ~50% olivine and clinopyroxene phenocrysts.

Bulk-rock major- and select trace-element abundance analyses were performed by X-ray fluorescence (XRF) at Franklin & Marshall University using a *PW 2404 PANalytical* XRF vacuum spectrometer following the procedures outlined in Boyd and Mertzman [1987]. Trace-element abundances were determined on 100 mg of homogenized bulk-rock and 5 to 100 mg of homogenized mineral separate powder at the *SIGL*, using a *ThermoScientific* iCAPq-c quadrupole inductively coupled plasma mass spectrometer (ICPMS) following analytical procedures similar to those described in Day et al. [2014]. Major element data for mineral separates were determined using a dilute solution of their respective trace-element solutions. Bulk-rock $^{187}Os/^{188}Os$ and Re and Os abundance analyses were performed at the *SIGL* using 1 g of homogenized powder according to methods described in Day et al. [2016] and were appropriately oxide, blank, and standard corrected. Rhenium, Ir, Ru, Pt and Pd abundances were determined by isotope-dilution using the iCAPq-c ICPMS, and Os abundance and $^{187}Os/^{188}Os$ were determined by isotope-dilution using a *ThermoScientific* Triton thermal ionization mass spectrometer in negative ion mode. Olivine trace-element, HSE abundances and Os isotopes were determined using identical methods, using between 0.1 and 0.4 g of powder, depending on the availability of clean mineral separates from each sample.

Helium isotope analyses were performed in the Fluid and Volatiles Laboratory at Scripps Institution of Oceanography. Melt and/or fluid inclusions containing He were released by crushing under vacuum for 150 seconds, which avoids release of structural He from the crystal lattice [Hilton et al., 1993; Graham et al., 1998; Scarsi, 2000]. Procedural

blanks were obtained by running the crusher without sample for the same period of time. The average blank was 8.2×10^{-11} cm^3 ^4He (STP), representing an average of 2.7% ^4He released from samples. Helium released by crushing was expanded into a stainless steel gas preparation line and purified of Ne after being sequentially exposed to a Ti getter at 750˚C (30 min), which is then cooled to 400˚C, a liquid N-cooled charcoal trap after cooling to 400˚C, a SAES© Zr-Al getter at room temperature and a He-cooled charcoal trap. Following purification, He was allowed into a dual collector noble gas mass spectrometer (*MAP 215E*) for static $^3He/^4He$ analysis by peak jumping [Shaw et al., 2006]. Neon concentrations were monitored to correct for contamination effects arising from imperfect instrument vacuum and/or the presence of air in the mineral lattice [Hilton et al., 1992]. Raw sample ratios were normalized to SIO Pier air (1 R_A). Olivine powders collected from the on-line crushers MAP after He analysis were used for replicate trace element and Os-isotopic analyses in a manner similar to that described previously [Day et al., 2015].

Olivine major and trace element data were obtained on the *Jeol JXA-8200* Electron Microprobe analyzer at Rutgers University according to the method of Sobolev et al. [2007] and with a current of 300 nA and an accelerating voltage of 20 kV. Count times were 50 s for Si, 80 s for Mg, 100 s for Fe and 150 s for Mn, Ni and Ca. Calibration analyses were performed on synthetic fayalite, tephroite and Ni_2SiO_2 as well as Kakanui Augite (USNM 122142), and drift correction was accomplished by repeated analyses of the San Carlos olivine standard. Average detection limits were 45 ppm for Si, 50 ppm for Mg, 28 ppm for Fe, 20 ppm for Ca, 23 ppm for Mn and 20 ppm for Ni; average errors were 0.06%

for Si, 0.07% for Mg, 0.08% for Fe, 0.65% for Ca, 0.86% for Mn and 0.88% for Ni. Analyses with deviations from 100% of ±2% for oxide proportions and ±1% for stoichiometry were excluded. A total of 325 high-precision analyses on seven Deccan lavas were obtained after reconnaissance EMP and backscatter imaging intended to identify homogenous and high-Fo olivine phenocrysts. Samples with relatively high modal olivine were analyzed *in situ* using 30 µm thin sections, while samples with low modal olivine were analyzed using grain mounts.

Oxygen isotope analyses were performed at the Open University, UK, using an infrared laser-assisted fluorination system according to methods described in Miller et al. [1999]. Recent analytical precision of this system, based on replicate analyses of an internal obsidian standard, is ±0.017‰ (2σ) for $\delta^{18}O$ [Greenwood et al., 2015]. All analyses are reported in delta notation as

$$\delta^{18}O = \left(\frac{{}^{18}O/{}_{16}O\ sample}{{}^{18}O/{}_{16}O\ VSMOW} - 1\right) * 1000$$

where VSMOW refers to the Vienna Standard Mean Ocean Water reference material. Full tabulated geochemical data are available in the *Appendix*, and more detailed methods information is available in the *Supplementary Information*.

4.3 Olivine compositions

Major and minor element compositions of olivine from the Deccan rocks vary widely, with average forsterite content of 81 ±9 (2σ), Ni and Ca contents of 485-3099 and

190-5784 ppm, respectively, and Fe/Mn of 50-85. We use these high-precision data to infer the lithology of the mantle sources to Deccan Traps volcanism. Previous petrological modeling efforts [e.g., Herzberg et al., 2013, 2014; Vidito et al., 2013] preferred to focus on olivine with >Fo_{90} because highly magnesian olivines are more likely to derive from sources that fractionated only olivine. Unfortunately, such compositions are rare amongst surveyed Deccan olivine grains and so we focus the petrological modeling effort on the highest-forsterite olivine available.

Large (>0.5 g) mass mineral separates from DC14-05, DC14-10B, DC14-47B, DC14-68, DC14-111 and MMF7 were measured for major and trace elements and Os isotopes. While olivine is used for all high-precision *in situ* analyses and O isotopic measurements, some of these samples did not contain sufficient olivine to separate for chemical digestion. We compare the compositions of plagioclase separates from DC14-68 and DC14-111 and clinopyroxene separates from DC14-10B and MMF7 to the compositions of olivine separates in DC14-05 and DC14-47B. The presence of plagioclase and clinopyroxene is particularly evident in the high Al_2O_3 contents of some of the mineral separates (4.4 to 30 wt.%) and the presence of plagioclase is evident from the relative enrichments in Eu and Sr in DC14-68 and DC14-111. Clinopyroxene separates from samples DC14-10B and MMF7 are strongly enriched in Cr (>2000 ppm). In all cases, when parental melt compositions are calculated for the mineral separates, using the partition coefficients of Fujimaki et al. [1984] and McKenzie & O'Nions [1991], they yield melts that would broadly be in equilibrium with their host rock (*Supplementary Information*), implying that the separates and bulk rocks represent a single magmatic system.

Olivine separates have the least radiogenic $^{187}Os/^{188}Os$ (0.1267-0.1308) compared to clinopyroxene (0.139-0.163) and plagioclase (0.144-0.146) separates. On average, mineral separates have a smaller range of measured $^{187}Os/^{188}Os$ (0.1267 to 0.1461) than their respective bulk rocks (0.1186 to 0.5010), but broadly similar Os contents (average of 0.31±0.28 and 0.32 ±0.58 ppb, respectively, **Figure 4.1**). These values overlap and extend $^{187}Os/^{188}Os$ measured previously by Allègre et al. [1999]. However, the $^{187}Re/^{187}Os$ composition of the lavas in this study are generally much lower than those measured by Allègre et al. [1999], consistent with a higher initial $^{187}Os/^{188}Os$ that is equal to the composition of the Réunion parental magma [Peters et al., 2016], with no significant difference between bulk rocks and mineral separates.

Most Deccan Traps mineral separates have low $^{3}He/^{4}He$ (0.6-4.2 R_A, 2σ), however, olivine separate DC14-47B has a ratio of 10.7 ±0.2 R_A. These results are similar to the measurements reported previously for associated Deccan ultramafic rocks, carbonatites and nephelinites (up to 14 R_A [Basu et al., 1993]). Olivine separates have $\delta^{18}O$ of 4.9-7.4‰, which is similar to or higher than the mantle range [Mattey et al., 1994] and are highly variable (average 5.9 ±1.3‰). The variability in these results may be influenced by inclusions present in the olivine. For example, ilmenite, a common olivine inclusion, is known to fractionate oxygen isotopes up to +1.2‰ [e.g., Bindeman, 2008], and may partially explain the higher values in our dataset. Such values may therefore be regarded as maxima, but do not change our overall interpretations of the data. One sample, DC14-53, has a $\delta^{18}O$ value of 12.8‰, which is doubtlessly reflecting the composition of

inclusions or other non-olivine material, and we exclude it from further consideration. Besides this sample, $\delta^{18}O$ values are similar to published $\delta^{18}O$ for Deccan Traps lavas (6.4 to 7.4‰ for plagioclase, 5.4 to 7.1‰ for pyroxene, 5.9-6.7‰ for olivine) [Peng et al., 1994; Melluso et al., 2006] and range to higher values than the two published Réunion samples (4.72‰ for olivine) [Boivin & Bachèlery, 2009].

4.4 Discussion

4.4.1 Crustal assimilation

Parental magmas to Deccan Traps volcanism likely reflect geochemical signatures from their mantle sources, as well as from materials through which they ascended, such as lithosphere and crust. These materials could potentially include upper mantle domains, including depleted MORB mantle and continental lithosphere, as well as lower and upper continental crust. Here, we make the simple assumption that early-formed mineral phases are most likely to be precluded from substantial crustal assimilation. The combined analysis of olivine, an early-formed phase, and likely later formed phases such as clinopyroxene and plagioclase, reveals progressive assimilation of crustal materials through the ascent of Deccan Traps parental magmas (**Figure 4.2**). Lower continental crust possesses moderate $\delta^{18}O$ [Kempton & Harmon, 1992] and $^{187}Os/^{188}Os$ [Asmerom & Walker, 1998], whereas upper continental crust contains high $\delta^{18}O$ [Hart et al., 1999] and $^{187}Os/^{188}Os$ [Esser & Turekian, 1993]. Olivine separates plot close to a Réunion-like source ($\delta^{18}O$ = 4.72‰, $^{187}Os/^{188}Os$ = 0.1324 ±0.0014) [Boivin & Bachèlery, 2009; Peters et al., 2016]: however, an alternative interpretation would imply incorporation of up to ~20% DMM-like material or ~10% lower crustal material. Given the range of published $\delta^{18}O$

measured for Réunion lavas [e.g., Boivin & Bachèlery, 2009], which is similar to those measured in the most olivine-phyric samples, we interpret that olivine compositions represent a more pure Réunion-like endmember with relatively little crustal or lithospheric contamination. On the other hand, the compositions of clinopyroxene and plagioclase separates imply assimilation of 20-40% lower crustal materials with possible subsequent assimilation of <10% upper crustal materials. These characteristics are reflected in the trace element compositions of the rocks that host these separates, with highly olivine-phyric samples plotting near a Réunion-like composition and clinopyroxene- and plagioclase-phyric samples possessing a signature that may arise from assimilation of <50% lower continental crust and later assimilation of <30% upper continental crust. Olivine separates and analyses from their host rocks are therefore the most likely to provide the most faithful record of parental magma compositions.

Crustal assimilation may also affect measured $^{3}He/^{4}He$. Assimilation of crustal material containing high $(U+Th)/^{3}He$ and low $^{3}He/^{4}He$ into degassed melts can impart radiogenic $^{3}He/^{4}He$ signatures into ascending magmas, or can increase the rate of ^{4}He production in erupted lavas. Calculated ^{4}He production rates given bulk rock and mineral separate compositions [c.f., Day et al., 2015] in this study yield production totals that are greater than measured ^{4}He, implying that decay of U and Th strongly impacted $^{3}He/^{4}He$ signatures. These effects may be exacerbated by He loss during magmatism such that measured $^{3}He/^{4}He$ is much lower than the $^{3}He/^{4}He$ of the Deccan parental magmas (*Supplementary Information*). In young rocks, the relationship between [He] and $^{3}He/^{4}He$ can reveal information about the effect of degassing on $^{3}He/^{4}He$ signatures. However, due

to their age, Deccan lavas are universally degassed but possess both high- and low-$^{3}He/^{4}He$, making the impact of ^{4}He production difficult to directly trace. Although cosmogenic production of ^{3}He can also change measured $^{3}He/^{4}He$, it is unlikely that this affected any of our samples because high erosion rates in the Deccan [e.g., Dessert et al., 2000] mean that the residence time of flows at the surface is relatively short. It is therefore our inference that our maximum measured $^{3}He/^{4}He$ value of 10.7 R_A represents a minimum for the Deccan Traps source.

4.4.2 Petrological modeling

The goal of our petrological modeling is to understand the relative contributions of pyroxenite, generated from reaction with recycled crust, and ambient mantle peridotite,that contributed to the source of the Deccan Traps. We selected glass 30.12, which was produced in an experiment on fertile peridotite KR-4003 [Walter, 1998], as our assumed peridotite-source parental composition because it is experimentally well-characterized and has served as the basis for similar petrological modeling on other hotspot materials [e.g., Herzberg et al., 2014]. The assumptions and drawbacks of selecting such an idealized peridotite source material are discussed in detail in Herzberg et al. [2014], and we similarly use a Ni content of 521 ppm for calculations involving this glass. Attempts to invert measured lava compositions to determine a primary magma composition are made difficult because of extensive clinopyroxene and plagioclase accumulation, however sample DC14-47B returns a valid primary magma composition from MELTS3 despite some clinopyroxene accumulation [Herzberg & Asimow, 2015]. Calculated liquid lines of descent calculated for KR-4003 and DC14-47B using PETROLOG software

[Danyushevsky & Plechov, 2011] show that our samples lie within likely compositional ranges for lavas derived from magma chambers with similar starting compositions (**Figure 4.3**). In addition, these liquid lines of descent predict fractionation of olivine before later-formed plagioclase and clinopyroxene. Given the strong overlap in valid compositions between KR-4003 and DC14-47B, the likelihood that clinopyroxene has affected the calculation of a primary melt to DC14-47B, and the common use of KR-4003 as an assumed peridotite source in similar petrological modeling, we prefer the use of KR-4003 as a representative of the peridotite fraction of the Deccan mantle source.

Olivine compositions in equilibrium with KR-4003 and its partial melts are shown in **Figure 4.4**, assuming olivine as the sole residual phase. The model is computed using methods similar to those described in Herzberg & O'Hara [2002] and Herzberg [2011], which thoroughly document the model assumptions and limitations. Our model does not compute the effects of orthopyroxene residuum in the mantle source, and this has a small but notable impact on the model results [e.g., Herzberg et al., 2014]. Calculated parental magmas span a range of compositions but are closely associated with MORB olivine, which have a peridotite source [Sobolev et al., 2007; Herzberg, 2011]. Derivative magmas extracted from the parental magma when it contains approximately 18 or 12 wt.% MgO overlap the Ni compositions of high-forsterite olivine from highly olivine-phyric Deccan Traps samples, which are most likely to faithfully reflect the Deccan mantle source. However, the Ca and Fe/Mn composition of sample DC14-05 in particular cannot be explained by derivation from a solely peridotite source. There is a close relationship between MORB olivine, which likely reflects a dominantly peridotite source, and

calculated parental magmas to KR-4003. We prefer a parental magma with 12 wt.% MgO based on differentiation studies of studied lavas (*Supplementary Information*) and a fixed $D_{NiO}(cpx)/D_{NiO}(ol)$ of 0.175 [e.g., Herzberg et al., 2013].

Because hotspot lavas are thought to derive from sources derived from interaction of peridotite and pyroxenite [e.g., Sobolev et al., 2005; 2007], we additionally consider the effect of mixing between fertile mantle melts and dacitic melts on olivine compositions in equilibrium with these primary magmas (**Figure 4.4**). Dacite is recognized as a likely melt product of recycled oceanic crust, which may react with ambient mantle peridotite to form pyroxenite, or a pyroxene and garnet-rich secondary peridotite [Yaxley & Green, 1998]. In some mantle xenoliths, textural evidence supports the formation of orthopyroxene at the expense of olivine in melt-infiltrated lherzolites, with geochemical constraints requiring the infiltrating melt to possess an evolved composition [e.g., Liu et al., 2005]. Petrological experiments have also documented the formation of pyroxenite resulting from the interaction of lherzolite and silicic or evolved magmas [Wang et al., 2013] and the formation of dacitic liquids from pyroxenite [Zhang et al., 2012], or directly from eclogite [Pertermann & Hirschmann, 2003; Spandler et al., 2008]. However, interaction of a fertile mantle melt with evolved, silicic materials would also be expected during the ascent of a magma through thick continental crust. Mixing between fertile mantle melts and charnokite melts [Litvinovsky et al., 2000], representing lower Indian crust, or rhyolite melts [Ratajeski et al., 2005], representing upper crust, may affect the compositions of olivine in equilibrium with primary magmas in ways similar to dacite (**Figure 4.4**). Only Fe/Mn,

which is relatively high in dacite melts compared to charnokite and rhyolite melts, would behave substantially differently during this process.

Our model seeks to capture the effects of mixing between a recycled component to hotspot volcanism, represented by dacite A200K [Pertermann & Hirschmann, 2003], with assumed NiO contents of 0.36 wt.% [Herzberg et al., 2014] or a crustal component represented by rhyolite run 1624 of Rajateski et al. [2005] and ambient mantle peridotite. Although modeling of crustal assimilation (**Figure 4.2**) implies a dominant role for lower crust, which may contain material similar to charnokite, in late-formed mineral phases, for the parameters of our modeling rhyolite represents a similar, but more extreme compositional endmember that would therefore constrain the minimum expected contribution from crustal sources. As the proportion of dacite melt is increased, olivine in equilibrium with the calculated parental magma and its derivatives are relatively enriched in Ni and Fe/Mn, and relatively depleted in Ca (**Figure 4.5A-C**). Assimilation of rhyolitic materials produces indistinguishable derivative magmas in terms of their Ni and Ca compositions (**Figure 4.5D-F**). Derivative melts of peridotite-dacite and peridotite-rhyolite interaction can explain the distribution of all Deccan olivine compositions from all samples. For Fe/Mn, high proportions of dacite melts are needed to account for the highest measured olivine Fe/Mn in Deccan lavas, and increasing proportions of rhyolite melt cannot easily explain the compositions of crustally contaminated or relatively uncontaminated samples. The model implies that limited recycled material (<25%) is needed to explain the Ni, Ca and Fe/Mn compositions of the least crustally contaminated samples. However, inclusion of certain other mineral phases, including clinopyroxene and

garnet in the parental magma computations could alter these liquid lines of descent [Herzberg et al., 2013]. In particular, for phases that are unique to dacite, charnokite or rhyolite, inclusion of these phases in petrological modeling may help better explain the relative contributions of pyroxenite and crustal reservoirs in both crustally contaminated and uncontaminated samples.

To complement these petrological models, we further calculate empirical X_{px}, or pyroxenite contents, for our measured olivine and for a compilation of literature data. The X_{px} parameter has appeared in various forms [Sobolev et al., 2008; Gurenko et al., 2009, 2011], and we select the definition of Gurenko et al. [2011] for this study because it requires the fewest analytes and thus broadens the inclusion of literature data, and further produces more tightly constrained results than parameterizations that involve Mn. The equation used is:

$$X_{px} = 1.341 * 10^{-3} \times \left[Ni \times \frac{FeO}{MgO}\right] - 0.437$$

where X_{px} refers to the weight fraction of pyroxenite-derived melt in the olivine parental magma, Ni is in ppm and FeO and MgO are in wt.%. Low values of X_{px} infer limited contributions from pyroxenite-type sources, whereas high values imply a strong pyroxenite contribution. Importantly, X_{px} cannot differentiate between crustal assimilation and pyroxenite in the same way as the detailed models. We find that many OIB localities have well-defined X_{px} frequency peaks, whereas CFB tend to have broader distributions of X_{px} (**Figure 4.6**) that may be explained by variable influence of crustal materials on the X_{px} parameter, thus dampening the signal from recycled materials. In addition, we find that the

distribution of X_{px} is statistically indistinguishable between CFB and OIB localities when considered across many studies, and in particular the average X_{px} of Deccan CFB (0.38 ±0.20) and Réunion OIB (0.41 ±0.23) are indistinguishable and generally have a lower calculated X_{px} component than most OIB or CFB (**Figure 4.6**).

4.4.3 Mantle sources to Deccan volcanism inferred from He-O-Os isotopes

Helium, oxygen and osmium isotopes have proven to be invaluable tracers of mantle sources to hotspot volcanism [e.g., Basu et al., 1993; Gurenko et al., 2009, 2011; Day et al., 2010, Day & Hilton, 2011; Füri et al., 2011]. Despite the proven ability to accurately measure all of these isotope systems in olivine separates, they have rarely been considered in unison. Many of the samples considered here come from areas of the Deccan recognized as possessing the most primitive geochemical signatures [e.g., Melluso et al., 2006], and they are therefore ideally suited for placing constraints on the provenance of Deccan parental magmas. Our samples and previously measured Deccan rocks [Basu et al., 1993] reveal $^{3}He/^{4}He$ above the mid-ocean ridge basalt average (MORB; 8 ±1 R_A) [Graham, 2002] and OIB that show affinity for depleted MORB mantle [Day & Hilton, 2011] and are within the range of other primitive CFB provinces thought to derive from deep mantle sources [Marty et al., 1996; Scarsi & Craig, 1996; Dodson et al., 1997; Stuart et al., 2000, 2003; Hilton et al., 2011; Halldórsson et al., 2014]. Additionally, these results are similar to He-isotopic measurements on olivine from Réunion OIB [Kaneoka et al., 1986; Graham et al., 1990; Staudacher, et al, 1990; Füri et al., 2011], which lie within a remarkably confined range (11.1 to 14.9 R_A) compared to other OIB. Although our sample 47B lies below this range, it represents a minimum $^{3}He/^{4}He$ signature for parental magmas

to our suite because all Deccan lavas were likely subjected to a greater degree of crustal assimilation, and are older, than Réunion lavas (*Supplementary Information*). Mineral separates also demonstrate that the Deccan mantle source has a relatively unradiogenic $^{187}Os/^{188}Os$ signature.

Previous models of Deccan sources have typically focused on crustal and lithospheric contaminants to a primitive Réunion-like source, without being able to independently examine the processes responsible for the formation of that mantle source. Coupled variations in He-O-Os isotopes have been used to discriminate between relative contributions of recycled oceanic crust and lithosphere in the source of OIB [e.g., Day et al., 2009; 2010; Day & Hilton, 2011]. We consider the provenance of the Deccan parental magma in terms of three mantle sources (**Figure 4.7**): (1) recycled oceanic crust that has been efficiently degassed, resulting in low $^{3}He/^{4}He$ (~1 R_A), variable $\delta^{18}O$ (5-8‰) and $^{187}Os/^{188}Os$ of 0.96 (representing oceanic crust with $^{187}Os/^{188}Os$ = 0.15, recycled over 1 Ga); (2) recycled oceanic lithosphere that has maintained $^{3}He/^{4}He$ of 6 R_A because it was protected from extensive degassing, $\delta^{18}O$ of 4 [e.g., Moreira & Kurz, 2001; Day et al., 2009, 2010] and $^{187}Os/^{188}Os$ of 0.120 [e.g., Standish et al., 2002]; (3) a Réunion-like high-$^{3}He/^{4}He$ (15 R_A) component with $\delta^{18}O$ of 4.72, which represents the sole oxygen isotope measurement on olivine for Réunion [Boivin & Bachèlery, 2009], but with a Réunion-like $^{187}Os/^{188}Os$ of 0.1324 ±0.0014 [Peters et al., 2016].

In a plot of $^{3}He/^{4}He$ versus $\delta^{18}O$, olivine and plagioclase separates define a pseudo-mixing line between a Réunion-like source and recycled oceanic crust. However, these

compositions are most likely due to post-eruptive degassing rather than a true representation of recycled materials, however one plagioclase separate possesses a higher $\delta^{18}O$ that may represent either crustal assimilation (**Figure 4.2**) or a degassed sample derived from a parental magma that incorporated recycled materials. In $^{3}He/^{4}He$ versus $^{187}Os/^{188}Os$ space, similar degassing trends are visible, but may also represent degassing of a parental magma that incorporated limited (<10%) recycled crustal material. In $^{187}Os/^{188}Os$ versus $\delta^{18}O$ space, where degassing does not pose the same issues, the crustal contamination trend of **Figure 4.2** is also evident. If this trend is not due to crustal contamination, several plagioclase and clinopyroxene samples closely parallel a mixing line between a Réunion-like source and recycled oceanic crust (<30%), or may represent mixtures of both recycled oceanic lithosphere and crust. Similarly to the petrological models, evidence for recycled sources to the Deccan Traps parental magma may be difficult to distinguish from the effects of crustal assimilation. Olivine separate continue to plot near the Réunion-like source, implying that they reflect a source that contains little recycled material. Since these separates are the least likely to preserve a record of crustal contamination, we interpret a maximum recycled component of up to 20% recycled oceanic crust, a result similar to those of the petrological models.

4.4.4 The relationship between petrological models and isotopic evidence

Given the similar quantitative estimates for recycled material given by the petrological and isotopic data, we compare these data with the intention of determining whether these combined geochemical systematics are capable of tracing the same processes occurring within the Earth. We observe weak, positive correlations between X_{px} and

$^{3}He/^{4}He$, $\delta^{18}O$ and $^{187}Os/^{188}Os$ for both our new data on Deccan materials and a compilation of literature data from studies of OIB and CFB (**Figure 4.8**). A positive correlation between X_{px} and $^{187}Os/^{188}Os$ is logical because recycled crustal materials, which are thought to form pyroxenite reservoirs, and their MORB progenitors, are expected to have relatively radiogenic Os isotope signatures [e.g., Roy-Barman & Allègre, 1995; Schiano et al., 1997; Day et al., 2009], whereas the primitive mantle is estimated to have $^{187}Os/^{188}Os$ of 0.1296 ±0.0008 [Meisel et al., 2001]. This relationship is also unsurprising as the parameter was originally conceived with respect to the Os isotope systematics of recycled materials [Sobolev et al., 2008]. Similarly, recycled oceanic crust may have $\delta^{18}O$ as high as 15‰ [e.g., Day et al., 2009] whereas ambient mantle has lower $\delta^{18}O$ (5.2 ±0.3‰) [Eiler, 2001], and hydrothermally altered, recycled lithosphere may have $\delta^{18}O$ that is lower still (to 0‰) [Eiler, 2001; Day et al., 2009]. However, layer-3 crustal gabbros are also known to have low $\delta^{18}O$ (to 1‰), and their participation in the pyroxenite generation process would change the nature of this mixing relationship.

The meaning of a positive relationship between X_{px} and $^{3}He/^{4}He$ is more difficult to explain, since recycled domains would be highly degassed and possess low-$^{3}He/^{4}He$ [c.f., Hahm et al., 2009]. A meaningful correlation of $^{3}He/^{4}He$ and X_{px} may be precluded by overprinting of He isotopic signatures during magma ascent. For example, if subduction and mantle processing of recycled crust eliminates virtually all He, the X_{px}-$^{3}He/^{4}He$ relationship would be obliterated because the He signature of pyroxenite would be easily overwritten by mantle material containing higher [He]. This result may be improved if examined using young geological materials that may not have experienced substantial

degassing (e.g., intrusive rocks). Similarly, in systems that lack evidence for substantial crustal assimilation, a quantitatively satisfying relationship between X_{px} and $^{187}Os/^{188}Os$ or $\delta^{18}O$ may be easier to derive. The existence of qualitatively similar estimates for recycled materials in the source of a highly degassed and crustally contaminated province such as the Deccan is highly promising for such work.

4.4.5 A petrological and geochemical link between Deccan and Réunion volcanism

The Deccan Traps and Réunion Island, respectively, are considered to represent the 'head' and 'tail' components of a canonical mantle plume [e.g., Richards et al., 1989]. Such a relationship would suggest that their mantle sources share a similar composition and provenance that persisted in Earth's mantle for 65 Ma. Olivine separates, which formed before the Deccan Traps parental magma assimilated a substantial amount of crustal material, possess isotopic compositions that are broadly similar to geologically recent Réunion lavas and cumulates [e.g., Schiano et al., 2012; Peters et al., 2016]. For example, they have mantle-like $\delta^{18}O$ and relatively unradiogenic $^{187}Os/^{188}Os$ compared to most global hotspots. In addition, one olivine separate possesses elevated $^{3}He/^{4}He$ (10.7 R_A), which represents a minimum value for the Deccan Traps parental magma because all Deccan lavas are highly degassed. This value approaches those known for Réunion lavas [e.g., Füri et al., 2011], which are distinctive and more restricted in range compared to other global hotspots. These characteristics together have led some to propose that Réunion parental magmas may be minimally influenced by recycled materials [e.g., Vlastélic et al., 2006; Peters et al., 2016]. Similarly, little to no recycled input is required to explain the Ni contents of high-forsterite olivine from the most primitive Deccan lavas, and a maximum

of ~25% is needed to explain the Ca and Fe/Mn characteristics of olivine from the same rocks. This implies that the link between Deccan and Réunion volcanism is not just geochemical and physiographic, but also petrological.

4.5 Concluding Remarks

Petrological modeling provides strong evidence that primary magmas to the Deccan Traps contained a significant proportion (up to 25%) of pyroxenite that may have derived from recycled crustal materials. However, assimilation of continental crust compounds direct assessment of the influence of a mafic mantle component, as it is difficult to differentiate the effect of pyroxenite from crustal lithologies. Although petrological and geochemical indicators of mantle sources may be intimately related, they may be decoupled because differentiation has affected each in a different manner. However, measurements of He, O and Os isotopes in mineral separates support a limited role for recycled materials in the Deccan Traps mantle source. Further, they strongly suggest that the Deccan mantle source possesses elevated, but not extreme $^{3}He/^{4}He$ and relatively unradiogenic $^{187}Os/^{188}Os$, which are also unique features of Réunion lavas. This similarity is particularly striking given the volcanic trace connecting the Deccan and Réunion volcanic provinces.

Acknowledgements

We are grateful to Hetu Sheth for provision of the MMF7 sample. Field work was supported by the National Geographic Society grants (NGS 8330-07 and GEFNE28-11), and general support was provided from NSF EAR grants 1116089 and 1447130 to JMDD,

1019489 to DRH, and the Devendra and Aruna Lal Fellowship to BJP. These sources of funding are gratefully acknowledged. The authors declare no conflicts of interest.

Chapter 4, in full, is a reformatted version of material in preparation for submission to Earth and Planetary Science Letters as Peters, B.J., J.M.D. Day, R.C. Greenwood, D.R. Hilton and J. Gibson (2016) Helium-oxygen-osmium isotopic and elemental constraints on the mantle sources of the Deccan Traps: *in preparation*. I was the principal investigator and author of this paper and of this chapter.

Figures

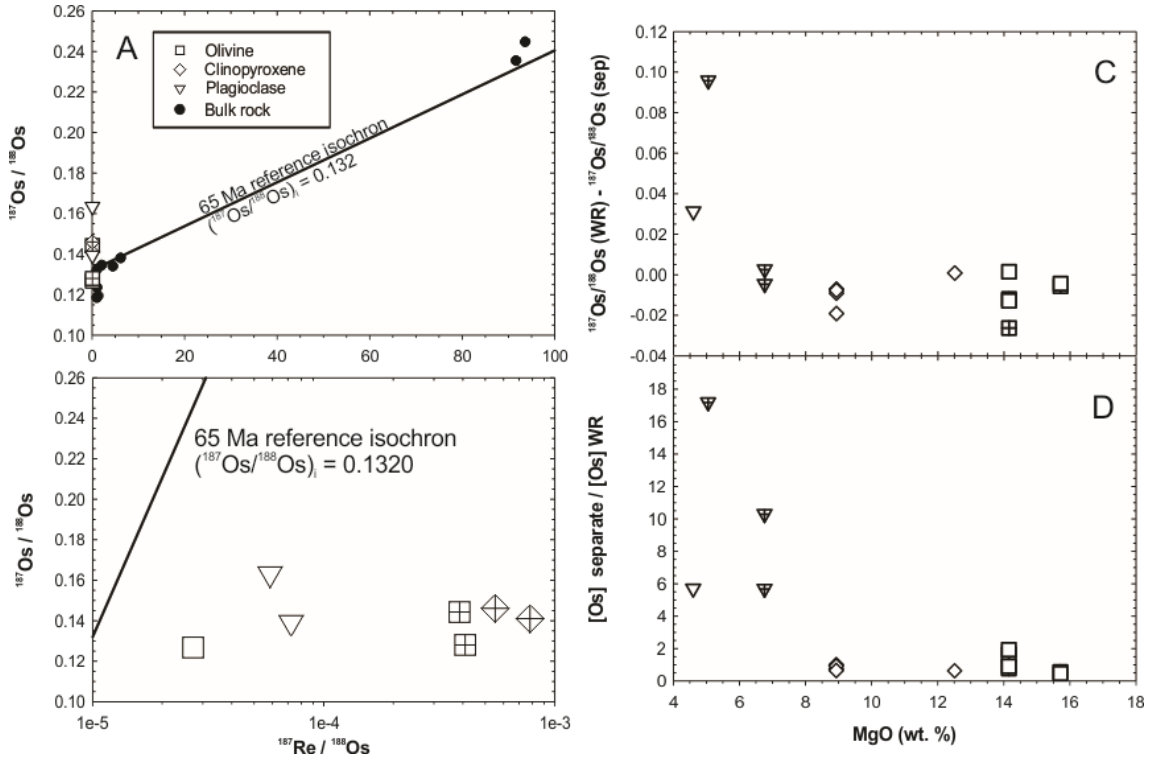

Figure 4.1: (A) Re-Os composition of Deccan lavas and mineral separates included in this study. Near-isochronous behavior results in an initial $^{187}Os/^{188}Os$ of 0.1311 ±0.0024 and an age of 68 ±16 Ma. Shown is a reference isochron representing 65 Ma, the commonly-accepted age of the Deccan Traps, anchored to a Reunion $^{187}Os/^{188}Os$ ratio of 0.132. This ratio is distinct from the near-chondritic initial for the Deccan Traps estimated by Allegre et al. (1999). An expanded view of (A) is provided in panel (B). Comparison of (C) $^{187}Os/^{188}Os$ and (D) Os concentrations between mineral separate and bulk rock analyses shown against bulk rock MgO. The greatest magnitude of difference for [Os] and $^{187}Os/^{188}Os$ is observed in the most evolved (low MgO) samples. Symbols with crosses represent Os isotope analyses completed on recycled MAP powders.

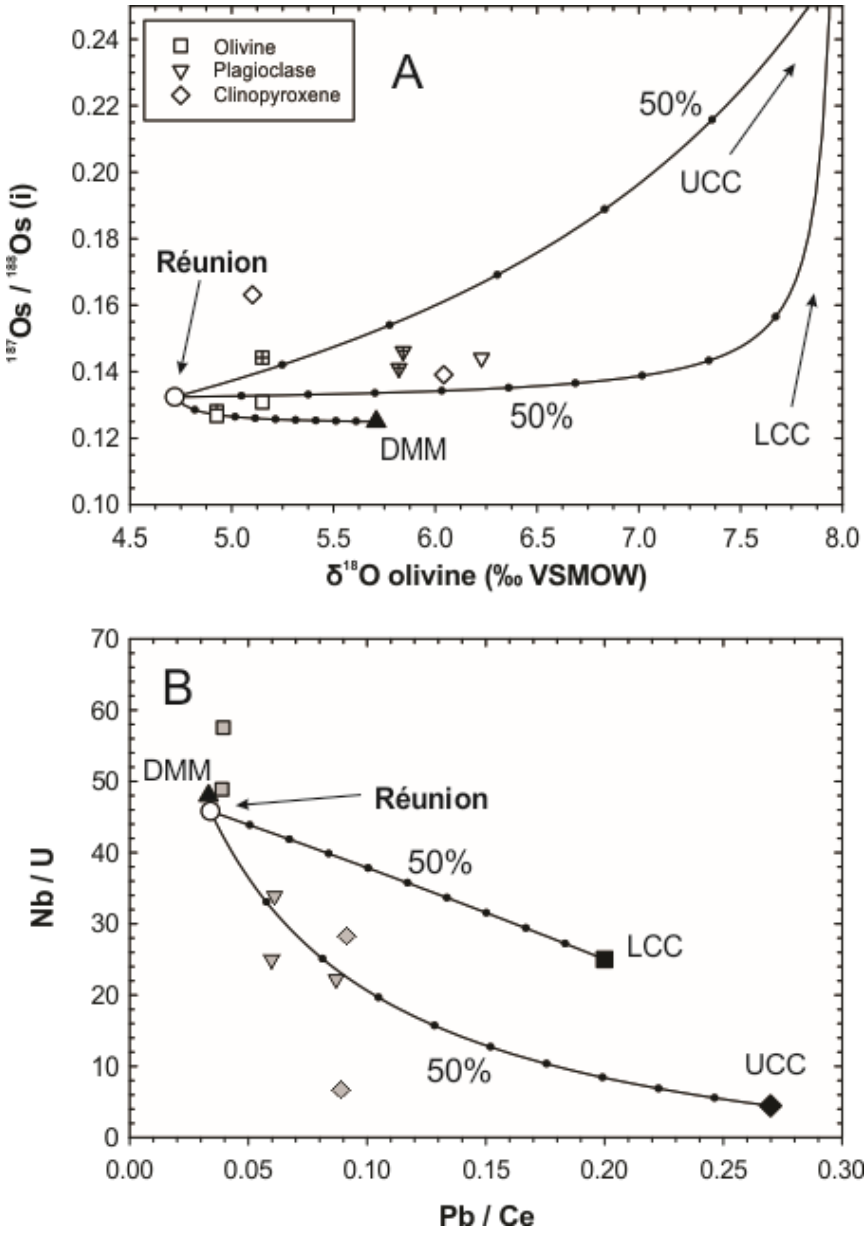

Figure 4.2: Assimilation models for a Réunion-like source [Peters et al., 2016; Boivin & Bachèlery, 2009; unpublished data] with upper continental crust (UCC), lower continental crust (LCC) and depleted MORB mantle (DMM), with 10% intervals noted by dots. Symbols as in **Figure 4.1**.

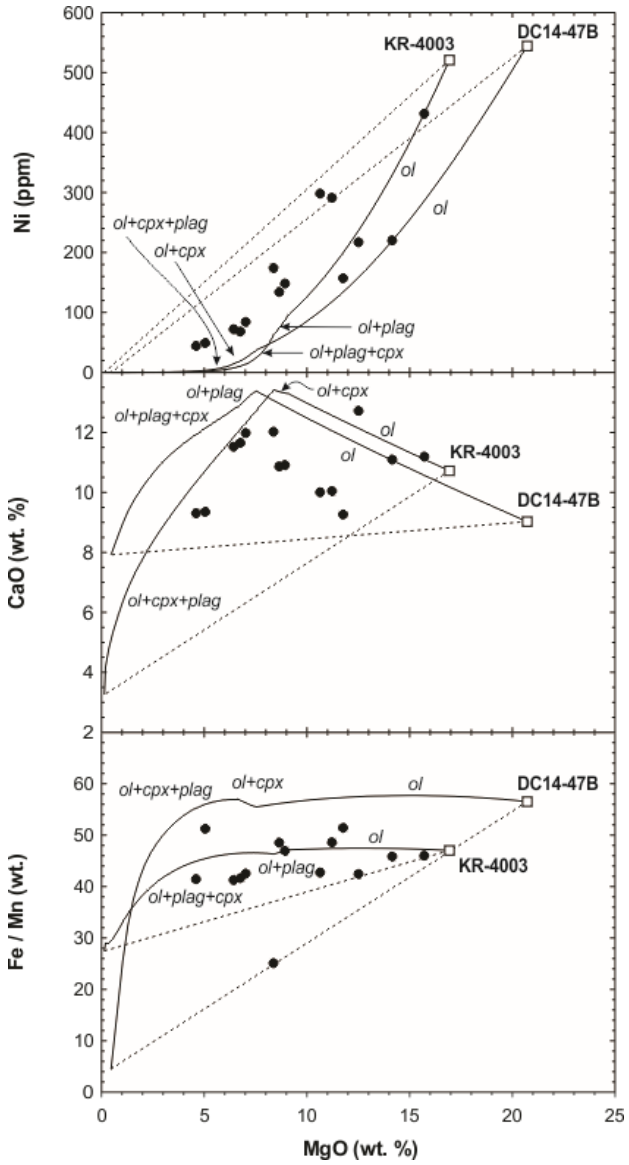

Figure 4.3: Liquid lines of descent (LLD) for experiment 30.12 on peridotite KR-4003 [Walter, 1998] and an inverted composition for DC14-47B, each of which may represent a derivate of the Deccan parental magma, calculated using PETROLOG software [Danyushevsky & Plechov, 2011]. Dashed lines represent the bounds of all possible mixing lines between magmas fractionated to varying extents along the LLD. Solid circles are bulk rock compositions of studied host lavas to mineral separates. In both cases, olivine is expected to be the first fractionating phase, followed by plagioclase and clinopyroxene in short succession.

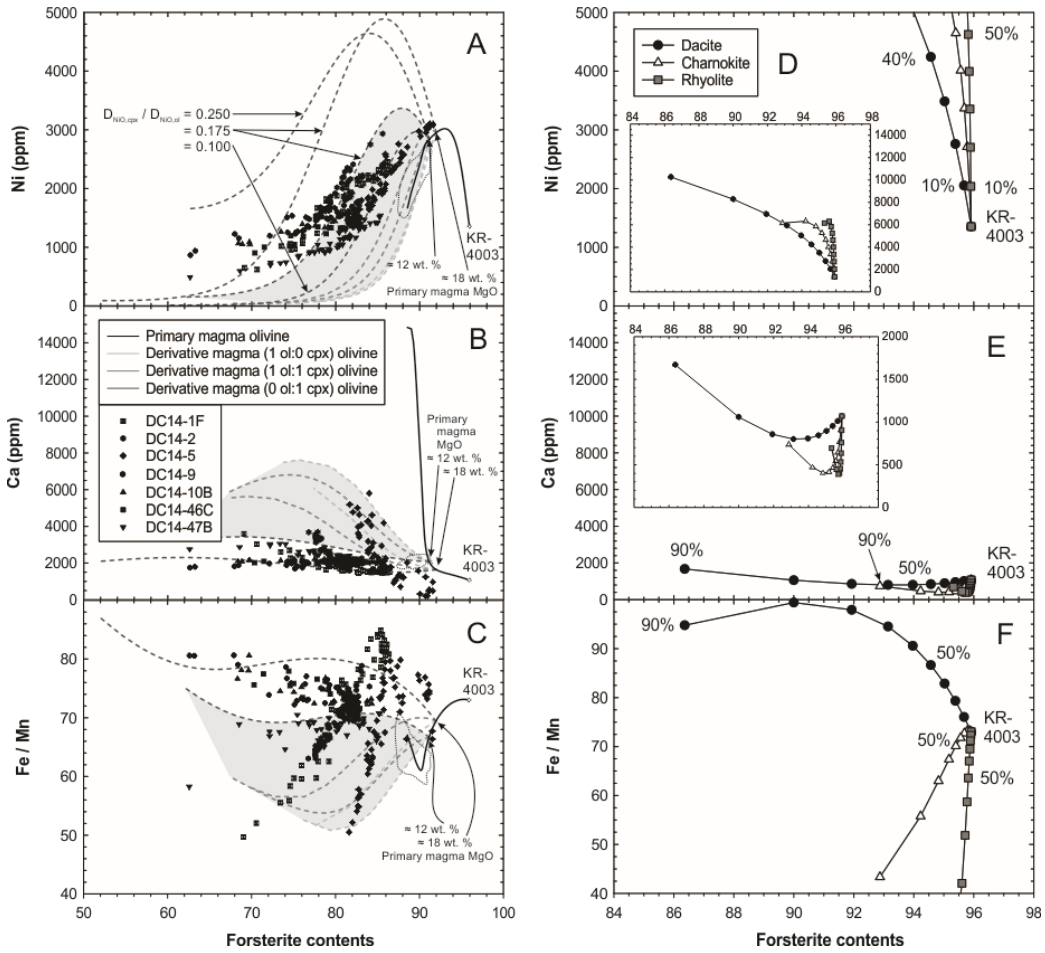

Figure 4.4: Nickel (A), Ca (B) and Fe/Mn (C) versus forsterite contents for measured olivine compositions and model curves. Black curves represent olivine in equilibrium with parental magmas derived directly from peridotite and gray curves represent compositions of olivine in equilibrium with derivative magmas as olivine and clinopyroxene are extracted. Shown for illustration are derivative magmas separating from the parental magma when the latter contains 18 to 12 wt.% MgO. Curves representing the compositions of derivative magmas appear darker with increasing modal clinopyroxene (0-100%). For Ni, the partition coefficient for Ni in clinopyroxene is fixed proportionally to the partition coefficient of Ni in olivine; the constant of proportionality is varied for illustration where the ratio of olivine to clinopyroxene is 0:1, as shown in panel (A). For all other calculations of Ni in clinopyroxene, $D_{Ni}(cpx)/D_{Ni}(ol)$ is fixed to 0.175 as a preferred value. Preferred model olivine compositions are shown in the gray fields, and represent 12 wt.% MgO in the parental magma with 0-100% olivine fractionation in the derivative magma. Fields of MORB olivine [Sobolev et al., 2007] are shown for reference in the stippled fields. (D-F) Compositions of olivine in equilibrium with primary magmas representing mixtures between fertile peridotite (KR-4003) and dacite, charnokite or rhyolite. Mixing intervals are represented by symbols placed in 10% intervals. Main panels preserve y-axis scaling of (A-C), insets have distinct scales to view extent of mixing.

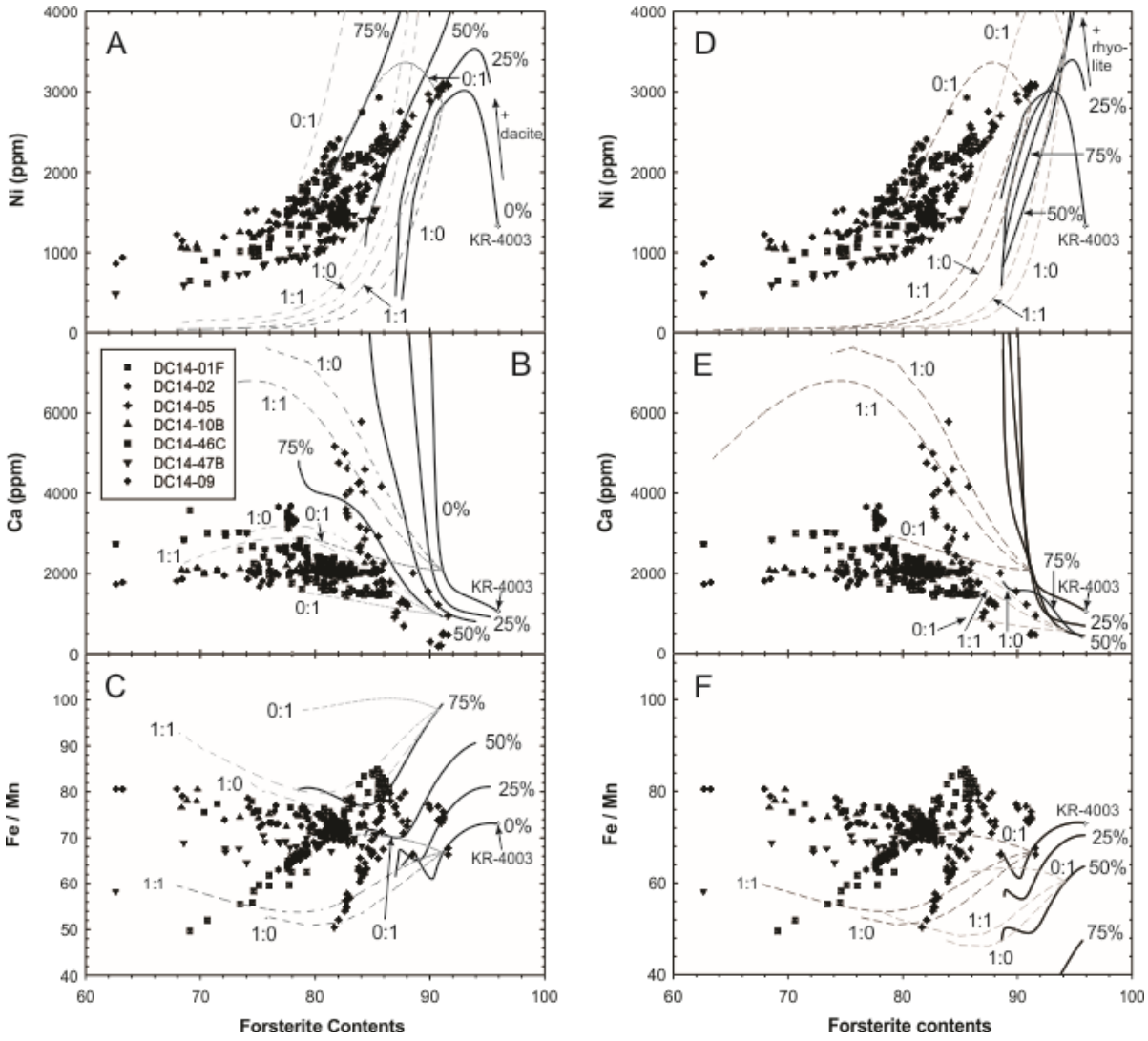

Figure 4.5: Nickel (A, D), Ca (B, E) and Fe/Mn (C, F) versus forsterite contents for measured olivine compositions (symbols) versus model compositions (curves). Black curves represent olivine in equilibrium with parental magmas derived directly from mixtures between peridotite and dacite A200K [Pertermann & Hirschmann, 2003] (A-C) or rhyolite run 1624 [Ratajeski et al., 2005] (D-F), indicated by percentages. Olivine in equilibrium with derivative magmas extracted from a parental magma containing 12 wt.% MgO are represented by the gray curves. Ratios along these curves represent the proportion of olivine to clinopyroxene extracted from the derivative magmas.

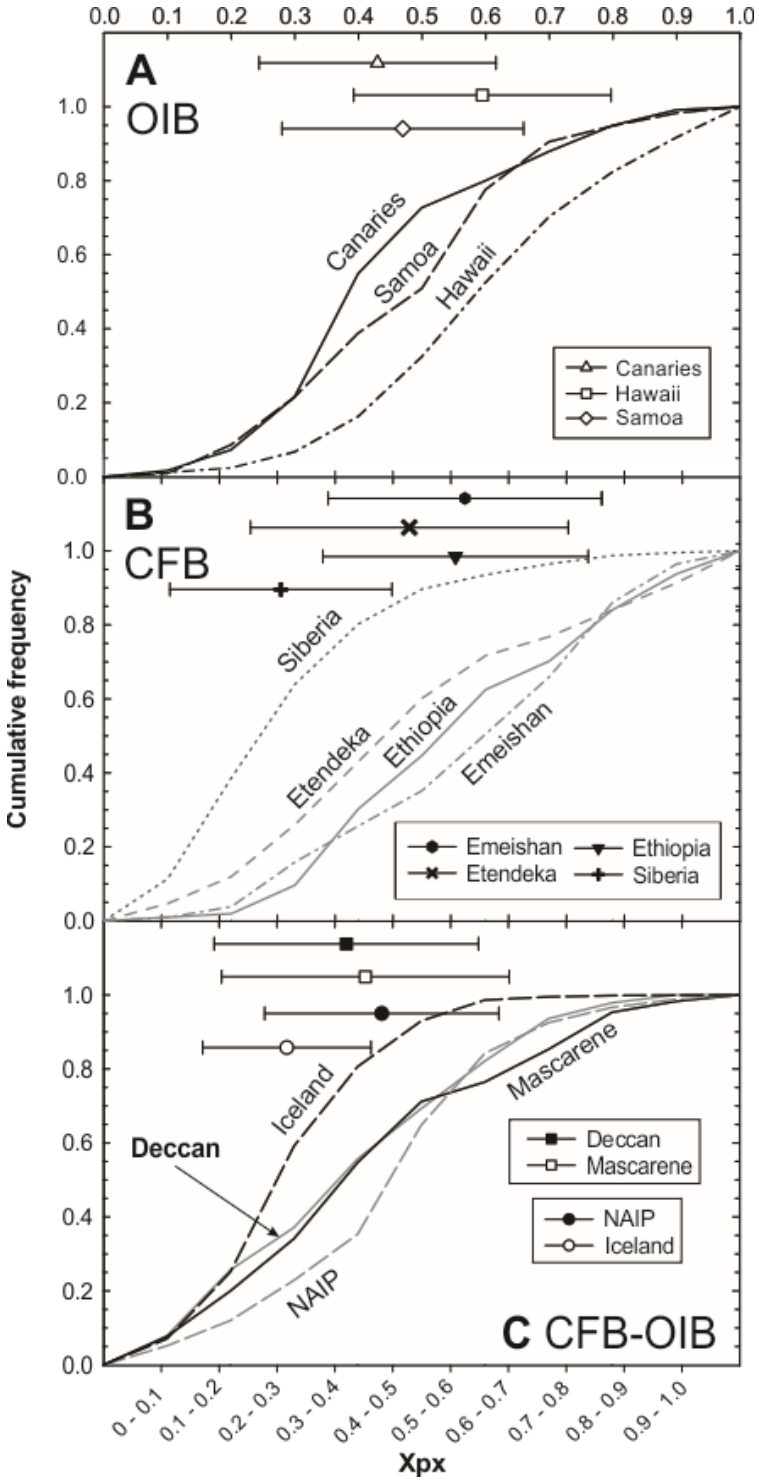

Figure 4.6: Cumulative frequency distributions of X_{px} in OIB (A), CFB (B) and paired CFB-OIB (C) with averages and one standard deviation shown as bars above the curves according to the upper y-axis. X_{px} is calculated according to the equation in the text, and values less than 0 or greater than 1 are excluded (*Supplementary Information*). Symbols and brackets represent averages and 2σ deviation for each locality.

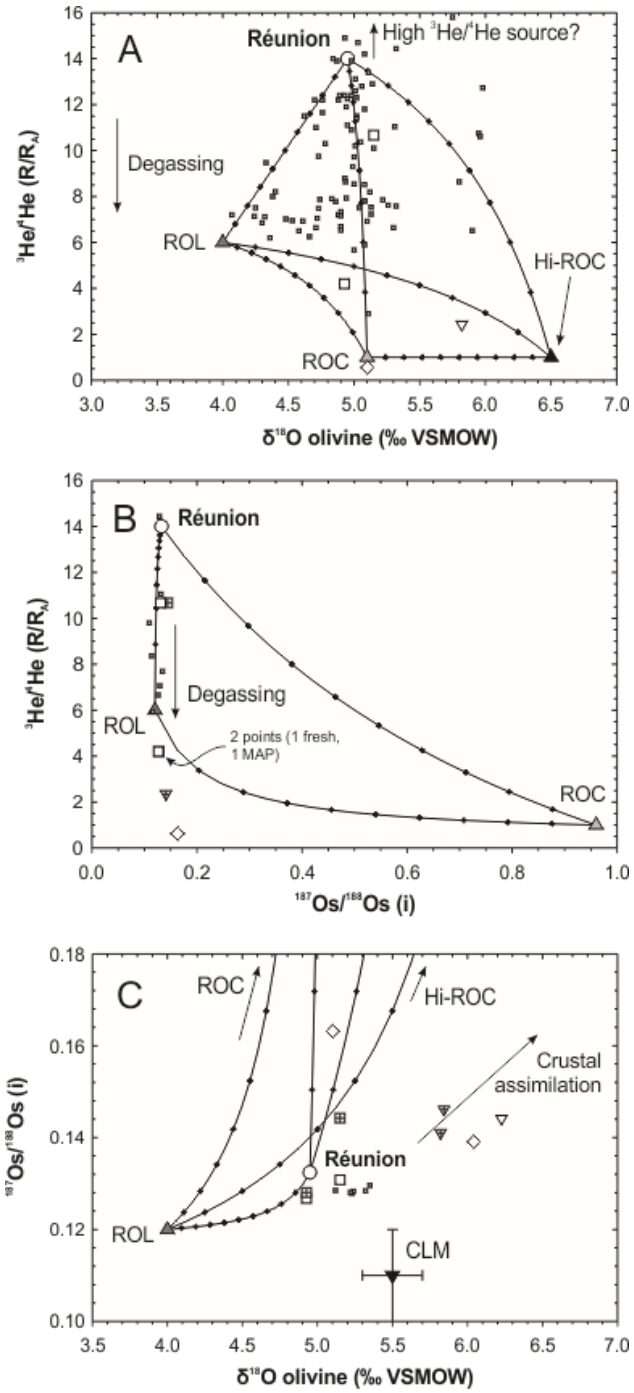

Figure 4.7: Olivine He-O-Os isotopic systematics and models representing mixtures between mantle domains that may serve as the source to Deccan Traps (open symbols as in **Figure 4.1**) and other CFB (small black squares) and OIB (small gray squares) volcanism. Dots denote 10% intervals of mixing; ROC and ROL are recycled oceanic crust and lithosphere, respectively. Full model parameters are tabulated in the *Appendix*. Data sources: Barry et al. [2015]; Day et al. [2010, 2015]; Eiler et al. [1996, 1997]; Gurenko et al. [2006]; Jackson et al. [2011]; Kurz et al. [1987]; Macpherson et al. [2005]; Peate et al. [2010]; Skovgaard et al. [2001]; Wang et al. [2003]; Workman et al. [2008].

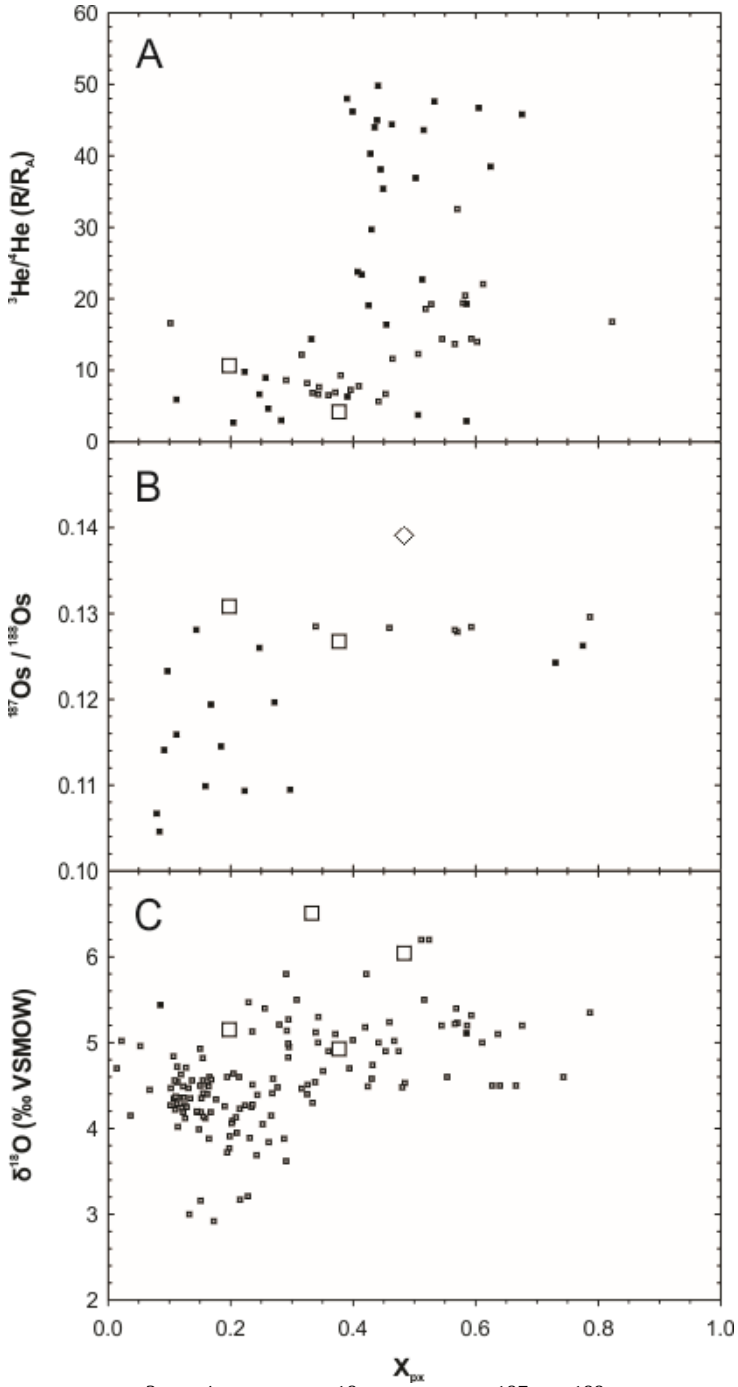

Figure 4.8: X_{px} versus $^3He/^4He$ (A), $\delta^{18}O$ (B) and $^{187}Os/^{188}Os$ (C) for Deccan olivine and literature compilation of CFB and OIB olivine analyses. Symbols as in **Figure 4.1** and **Figure 4.7**. Data sources: Barry et al. [2015]; Bernstein et al. [1998, 2006]; Bindeman et al. [2008]; Day et al. [2015]; Eiler et al [2000]; Francis [1985]; Garcia et al. [1998, 2008]; Gurenko et al. [2006]; Hanyu et al. [2007]; Hauri & Hart [1994]; Jackson & Shirey [2011]; Jackson et al. [2014]; Jeffcoate et al. [2007]; Kaneoka et al. [2002]; Kurz et al. [1987]; Kyser et al. [1981, 1982]; Macpherson et al. [2005]; Pernet-Fisher et al. [2015]; Starkey et al. [2009]; Thompson et al. [2007]; Wang et al. [2011]; Workman et al. [2008].

References

Allègre, C.J., B. Dupre, P. Richard, D. Rousseau and C. Brooks (1982) Subcontinental versus suboceanic mantle, II. Nd-Sr-Pb isotopic comparison of continental tholeiites with mid-ocean ridge tholeiites, and the structure of the continental lithosphere: Earth and Planetary Science Letters, 57, 25-34, doi:10.1016/0012-821X(82)90170-4.

Allègre, C.J., T. Staudacher, P. Sarda and M. Kurz (1983) Constraints on the evolution of Earth's mantle from rare gas systematics: Nature, 303, 762-766, doi:10.1038/303762a0.

Allègre, C.J., J.L. Birck, F. Campas and V. Courtillot (1999) Age of the Deccan traps using ^{187}Re-^{187}OS systematics: Earth and Planetary Science Letters, 170, 197-204.

Asmerom, Y. and R.J. Walker (1998) Pb and Os isotopic constraints on the composition and rheology of the lower crust: Geology, 26(4), 359-362.

Barry, P.H., D.R. Hilton, J.M.D. Day, J.F. Pernet-Fisher, G.H. Howarth, T. Magna, A.M. Agashev, N.P. Pokhilenko, L.N. Pokhilenko and L.A. Taylor (2015) Helium isotopic evidence for modificiation of the cratonic lithosphere during the Permo-Triassic Siberian flood basalt event: Lithos, 216-217, 73-80.

Basu, A.R., P.R. Renne, D.K. DasGupta, F. Teichmann and R.J. Poreda (1993) Early and late alkali igneous pulses and a high-^{3}He plume origin for Deccan flood basalts: Science, 261, 902-906.

Bernstein, S., P.B. Kelemen and C.K. Brooks (1998) Depleted spinel harzburgite xenoliths in Tertiary dykes from east Greenland: Restites from high degree melting: Earth and Planetary Science Letters, 154, 221-235.

Bernstein, S., K. Hanghøj, P.B. Kelemen and C.K. Brooks (2006) Ultra-depleted, shallow cratonic mantle beneath West Greenland: Dunitic xenoliths from Ubekendt Ejland: Contributions to Mineralogy and Petrology, 152, 335-347.

Bigeleisen, J. and M.G. Mayer (1947) Calculation of equilibrium constants for isotopic exchange reactions: Journal of Chemical Physics, 15, 261–267.

Bindeman, I. (2008) Oxygen isotopes in mantle and crustal magmas as revealed by single crystal analysis: Reviews in Mineralogy and Geochemistry, 69, 445-478.

Bindeman, I.N., A.A. Gurenko, O. Sigmarsson and M. Chaussidon (2008) Oxygen isotope heterogeneity and disequilibria of olivine crystals in large volume Holocene basalts from Iceland: Evidence for magmatic digestion and erosion of Pleistocene hyaloclastites: Geochimica et Cosmochimica Acta, 72, 4397-4420.

Boivin, P. and P. Bachèlery (2009) Petrology of 1977 to 1998 eruptions of Piton de la Fournaise, La Réunion Island: Journal of Volcanology and Geothermal Research: 184, 109-125.

Boyd, F.R. and S.A. Mertzman (1987) Composition and structure of the Kaapvaal lithosphere, southern Africa, *in:* Mysen, B.O. (ed.) Magmatic Processes: Physicochemical Principles: Geochemical Society Special Publications, 1, 13-24.

Clarke, W.B., M.A. Beg and H. Craig (1969) Excess ^{3}He in the sea: evidence for terrestrial primordial helium: Earth and Planetary Science Letters, 6, 213-220, doi:10.1016/0012-821X(69)90093-4.

Danyushesky, L.V. and P. Plechov (2011) Petrolog3: integrated software for modeling crystallization processes: Geochemistry Geophysics Geosystems, 12, Q07021, doi:10.1029/2011GC003516.

Day, J.M.D. (2013) Hotspot volcanism and highly siderophile elements: Chemical Geology, 341, 60-74.

Day, J. M. D. and D. R. Hilton (2011), Origin of ^{3}He/^{4}He ratios in HIMU-type basalts constrained from Canary Island lavas: Earth and Planetary Science Letters, 305, 226-234, doi:10.1016/j.epsl.2011.03.006.

Day, J.M.D., D.G. Pearson, C.G. Macpherson, D. Lowry and J.-C. Carracedo (2009) Pyroxenite-rich mantle formed by recycled oceanic lithosphere: Oxygen-osmium isotope evidence from Canary Island lavas: Geology, 37, 555-558.

Day, J. M. D., D. G. Pearson, C. G. Macpherson, D. Lowry and J.-C. Carracedo (2010), Evidence for distinct proportions of subducted oceanic crust and lithosphere in HIMU-type mantle beneath El Hierro and La Palma, Canary Islands: Geochimica et Cosmochimica Acta, 74(22), 6565-6589, doi:10.1016/j.gca.2010.08.021.

Day, J.M.D., B.J. Peters and P.E. Janney (2014) Oxygen isotope systematics of South African olivine melilitites and implications for HIMU mantle reservoirs: Lithos, 202-203, 76-84.

Day, J.M.D., P.H. Barry, D.R. Hilton, R. Burgess, D.G. Pearson and L.A. Taylor (2015) The helium flux from the continents and ubiquity of low-^{3}He/^{4}He recycled crust and lithosphere: Geochimica et Cosmochimica Acta, 153, 116-133.

Day, J.M.D., C.L. Waters, B.F. Schaefer, R.J. Walker and S. Turner (2016) Use of hydrofluoric acid desilicification in the determination of highly siderophile element abundances and Re-Pt-Os isotope systematics in mafic-ultramafic rocks: Geostandards and Geoanalytical Research, 40, 49-65.

Dessert, C., B. Dupré, L.M. François, J. Schott, J. Gaillardet, G. Chakrapani and S. Bajpai (2000) Erosion of Deccan Traps determined by river geochemistry: impact on the global climate and the $^{87}Sr/^{86}Sr$ of seawater: Earth and Planetary Science Letters, 188, 459-474.

Dodson, A., B.M. Kennedy and D.J. DePaolo (1997) Helium and neon isotopes in the Imnaha Basalt, Columbia River Basalt Group: Evidence for a Yellowstone plume source: Earth and Planetary Science Letters, 150, 443-451.

Eiler, J.M. (2001) Oxygen isotope variations of basaltic lavas and upper mantle rocks: Reviews in Mineralogy and Geochemistry, 43, 319-364, doi:10.2138/gsrmg.43.1.319.

Eiler, J.M., K.A. Farley, J.W. Valley, A.W. Hofmann and E.M. Stolper (1996) Oxygen isotope constraints on the sources of Hawaiian volcanism: Earth and Planetary Science Letters, 144, 453-468.

Eiler, J.M., K.A. Farley, J.W. Valley, E.H. Hauri, H. Craig, S.R. Hart and E.M. Stolper (1997) Oxygen isotope variations in ocean island basalt phenocrysts: Geochimica et Cosmochimica Acta, 61, 2281-2293.

Eiler, J.M., K. Grönvold and N.E. Kitchen (2000): Oxygen isotope evidence for the origin of chemical variations in lavas from the Theistareykir volcano in Iceland's northern volcanic zone: Earth and Planetary Science Letters, 184, 269-286.

Esser, B.K. and K.K. Turekian (1993) The osmium isotopic composition of the continental crust: Geochimica et Cosmochimica Acta, 57, 3093-3104.

Francis, D.M. (1985) The Baffin Bay lavas and the value of picrites as analogues of primary magmas: Contributions to Mineralogy and Petrology, 89, 144-154.

Fujimaki, H., M. Tatsumoto and K.-I. Aoki (1984) Partition coefficients of Hf, Zr and REE between phenocrysts and groundmass: Journal of Geophysical Research, 89, B662-B672.

Füri, E., D.R. Hilton, B.J. Murton, C. Hémond, J. Dyment and J.M.D. Day (201) Helium isotope vriations between Réunion Island and the Central Indian Ridge (17°-21°S): New evidence for ridge-hot spot interaction: Journal of Geophysical Research, 116, B02207.

Gannoun, A., I. Vlastélic and P. Schiano (2015) Escape of unradiogenic osmium during sub-aerial lava degassing: Evidence from fumarolic deposits, Piton de la Fournaise, Réunion Island: Geochimica et Cosmochimica Acta, 166, 312-326.

Garcia, M.O. E. Ito, J.M. Eiler and A.J. Pietruszka (1998) Crustal contamination of Kilauea volcano magma revealed by oxygen isotope analyses of glass and olivine from Pu'u O'o eruption lavas: Journal of Petrology, 39, 803-817.

Garcia, M.O, E. Ito and J.M. Eiler (2008) Oxygen isotope evidence for chemical interaction of Kilauea historical magmas with basement rocks: Journal of Petrology, 49, 757-769.

Graham, D. W. (2002), Noble gas isotope geochemistry of mid-ocean ridge and ocean island basalts: characterization of mantle source reservoirs. *In:* Porcelli, D., C. J. Ballentine and R. Wieler (eds.), Noble gases in geochemistry and cosmochemistry: Reviews in Mineralogy and Geochemistry, 47, 247-319, doi:10.2138/rmg.2002.47.8.

Graham, D., J. Lupton, F. Albaréde and M. Condomines (1990) Extreme temporal homogeneity of helium isotopes at Piton de la Fournaise, Réunion Island: Nature, 347, 545-549.

Graham, D.W., L.M. Larsen, B.B. Hanan, M. Storey, A.K. Pedersen and J.E. Lupton (1998) Helium isotope composition of the early Iceland mantle plume inferred from the Tertiary picrites of West Greenland: Earth and Planetary Science Letters, 160, 241-255.

Greenwood, R.C., J.-A. Barrat, E.R.D. Scott, H. Haack, P.C. Buchanan, I.A. Franchi, A. Yamaguchi, D. Johnson, A.W.R. Bevan and T.H. Burbine (2015) Geochemistry and oxygen isotope composition of main-group pallasites and olivine-rich clasts in mesosiderites: Implications for the "Great Dunite Shortage" and HED-mesosiderite connection: Geochimica et Cosmochimica Acta, 169, 115-136.

Gregory, R.T. and H.P. Taylor (1981) An oxygen isotope profile in a section of Cretaceous oceanic crust, Samail ophiolite, Oman: evidence for $\delta^{18}O$ buffering of the ocean by deep (>5 km) seawater-hydrothermal circulation at mid-ocean ridges: Journal of Geophysical Research, 86, 2737-2755, doi:10.1029/JB086iB04p02737.

Gurenko, A.A., K.A. Hoernle, F. Hauff, H.-U. Schmincke, D. Han, Y.N. Miura and I. Kaneoka (2006) Major, trace element and Nd-Sr-Pb-O-He-Ar isotope signatures of shield stage lavas from the central and western Canary Islands: Insights into mantle and crustal processes: Chemical Geology, 233, 75-112.

Gurenko, A., A.V. Sobolev, K.A. Hoernle, F. Hauff and H.-U. Schmincke (2009) Enriched, HIMU-type peridotite and depleted recycled pyroxenite in the Canary plume: a mixed-up mantle: Earth and Planetary Science Letters, 277, 514-524, doi:10.1016/j.epsl.2008.11.013.

Gurenko, A.A., I.N. Bindeman and M. Chaussidon (2011) Oxygen isotope heterogeneity of the mantle beneath the Canary Islands: insights from olivine phenocrysts: Contributions from Mineralogy and Petrology, 162, 349-363.

Hahm, D., P.R. Castillo, and D.R Hilton (2009) A deep mantle source of high $^{3}He/^{4}He$ ocean island basalts (OIB) inferred from Pacific near-ridge seamounts. Geophys. Res. Lett. 36, L20316, doi:10.1029/2009GL040560 (5 pages).

Halldórsson, S.A., D.R. Hilton, P. Scarsi, T. Abebe and J. Hopp (2014) A common mantle plume source beneath the entire Earth African Rift System revealed by coupled helium-neon systematics: Geophysical Research Letters, 41, 2304-2311.

Hanyu, T., K.T.M. Johnson, N. Hirano and Z.-Y. Ren (2007) Noble gas geochronology study of the Hana Ridge, Haleakala volcano, Hawaii; implications to the temporal change of magma source and the structural evolution of the submarine ridge: Chemical Geology, 238, 1-18.

Hart, S.R., J. Blusztajn, H.J.B. Dick, P.S. Meyer and K. Muehlenbachs (1999) The fingerprint of seawater circulation in a 500-meter section of ocean crust gabbros: Geochimica et Cosmochimica Acta, 63, 4059-4080.

Hauri, E.H. and S.R. Hart (1993) Re-Os isotope systematics of HIMU and EMII oceanic island basalts from the South Pacific Ocean: Earth and Planetary Science Letters, 114, 353-371, doi:10.1016/0012-821X(93)90036-9.

Herzberg, C. (2011) Identification of source lithology in the Hawaiian and Canary Islands: Implications for origins: Journal of Petrology, 52, 113-146, doi:10.1093/petrology/egq075.

Herzberg, C. and M.J. O'Hara (2002) Plume-associated ultramafic magmas of Phanerozoic age: Journal of Petrology, 43, 1857-1883, doi:10.1093/petrology/43.10.1857.

Herzberg, C. and P. Asimow (2015) PRIMELTS3 MEGA.XLSM software for primary magma calculation: Peridotite primary magma MgO contents from the liquidus to the solidus: Geochemistry, Geophysics, Geosystems, 16, 563-578.

Herzberg, C., P. Asimow, D. Ionov, C. Vidito, M.G. Jackson and D. Geist (2013) Nickel and helium evidence for melt above the core-mantle boundary: Nature, 493, 393-397.

Herzberg, C., R.A. Cabral, M.G. Jackson, C. Vidito, J.M.D. Day and E.H. Hauri (2014) Phantom Archean crust in Mangaia hotspot lavas and the meaning of heterogeneous mantle: Earth and Planetary Science Letters, 396, 97-106, doi:10.1016/j.epsl.2014.03.065.

Hilton, D.R., J.A. Hoogewerff, M.J. Van Bergen, and K. Hammerschmidt (1992) Mapping magma sources in the east Sunda-Banda arcs, Indonesia: constraints from helium isotopes: Geochimica et Cosmochimica Acta, 56, 851-859.

Hilton, D.R. K. Hammerschmidt, S. Teufel and H. Freidrichsen (1993) Helium isotope characteristics of Andean geothermal fluids and lavas: Earth and Planetary Science Letters, 120, 265-282, doi:10.1016/0012-821X(93)90244-4.

Hilton, D.R., S.A. Halldorsson, P.H. Barry, T.P. Fische , J.M. de Moor, F. Mangasini, C.J. Ramirez and P. Scarsi (2011) Helium isotopes at Rungwe volcanic province, Tanzania and the origin of East African plateau: Geophysical Research Letters, 38, L21304.

Hofmann, A.W. and W.M. White (1982), Mantle plumes from ancient oceanic crust: Earth and Planetary Science Letters, 57, 421-436, doi:10.1016/0012-821X(82)90161-3.

Jackson, M.G. and S.B. Shirey (2011) Re-Os isotope systematics in Samoan shield lavas and the use of Os-isotopes in olivine phenocrysts to determine primary magmatic compositions: Earth and Planetary Science Letters, 312, 91-101.

Jackson, M.G., S.R. Hart, J.G. Konter, M.D. Kurz, J. Blustajn and K.A. Farley (2014) Helium and lead isotopes reveal the geochemical geometry of the Samoan plume: Nature, 514, 355-358.

Jeffcoate, A.B., T.R. Elliott, S. Kasemann, D.A. Ionov, K.M. Cooper and R.A. Brooker (2007) Li isotope fractionation in peridotites and mafic melts: Geochimica et Cosmochimica Acta, 71, 202-218.

Kaneoka, I. (1983) Noble gas constraints on the layered structure of the mantle: Nature, 302, 698-700.

Kaneoka, I., N. Takaoka and B.G.J. Upton (1986) Noble gas systematics in basalts and a dunite nodule from Réunion and Grand Comore Islands, Indian Ocean: Chemical Geology, 59, 35-42.

Kaneoka, I., H. Takeshi, J. Yamamoto and Y.N. Miura (2002) Noble gas systematics of the Hawaiian volcanoes based on the analysis of Loihi, Kilauea and Ko'olau submarine rocks, *in* E. Takahashi, P.W. Lipman, M.O. Garcia, J. Naka and S. Aramaki (eds.) Hawaiian volcanoes: Deep underwater perspectives: American Geophysical Union, Washington, DC, 373-389.

Kempton, P.D. and R.S Harmon (1992) Oxygen isotope evidence for large-scale hybridization of the lower crust during magmatic underplating: Geochimica et Cosmochimica Acta, 56, 971-986.

Krishnamurthy, P. (1971) Petrology of the dyke rocks of the western portions of Rajpipla hills, Broach district, Gujarat, India: Bulletin Volcanologique, 35(4), 930-946.

Krishnamurthy, P. and K.G. Cox (1977) Picrite basalts and related lavas from the Deccan Traps of western India: Contributions to Mineralogy and Petrology, 62, 53-75, doi:10.1007/BF00371027.

Krishnamurthy, P., K. Gopalan and J.D. Macdougall (2000) Olivine compositions in picrite basalts and the Deccan volcanic cycle: Journal of Petrology, 41(7), 1057-1069.

Kurz, M.D., W.J. Jenkins and S.R. Hart (1982) Helium isotopic systematics of oceanic islands and mantle heterogeneity: Nature, 297, 43-47, doi:10.1038/297043a0.

Kurz, M.D., M.O. Garcia, F.A. Frey and P.A. O'Brien (1987) Temporal helium isotope variations within Hawaiian volcanoes: Basalts from Mauna Loa and Haleakala: Geochimica et Cosmochimica Acta, 51, 2905-2914.

Kyser, T.K., J.R. O'Neil and I.S.E. Carmichael (1981) Oxygen isotope thermometry of basic lavas and mantle nodules: Contributions to Mineralogy and Petrology, 77, 11-23.

Kyser, T.K., J.R. O'Neil and I.S.E. Carmichael (1982) Genetic relations among basic lavas and ultramafic nodules: Evidence from oxygen isotope compositions: Contributions to Mineralogy and Petrology, 81, 88-102.

Litvinovsky, B.A., I.M. Steele and S.M. Wickham (2000) Silicic magma formation in overthickened crust: melting of charnokite and leucogranite at 15, 20 and 25 kbar: Journal of Petrology, 41(5), 717-737.

Liu, Y., S. Gao, C.-T.A. Lee, S. Hu, X. Liu and H. Yuan (2005) Melt-peridotite interactions: links between garnet pyroxenite and high-Mg# signature of continental crust: Earth and Planetary Science Letters, 234, 39-57.

Lupton, J.E. and H. Craig (1975) Excess ^{3}He in oceanic basalts: Evidence for terrestrial primordial helium: Earth and Planetary Science Letters, 26, 133-139.

Macpherson, C.G., D.R. Hilton, J.M.D. Day, D. Lowry and K. Grönvold (2005) High-$^{3}He/^{4}He$ depleted mantle and low-$\delta 18O$, recycled oceanic lithosphere in the source of central Iceland magmatism: Earth and Planetary Science Letters, 233, 411-427.

Mahoney, J., J.D. Macduogall, G.W. Lugmair, A.V. Murali, M. Sankar Das and K. Gopalan (1982) Origin of the Deccan Trap flows at Mahabaleshwar inferred from Nd and Sr isotopic and chemical evidence: Earth and Planetary Science Letters, 60, 47-60, doi:10.1016/0012-821X(82)90019-X.

Marty, B., R. Pik and Y. Gezahegn (1996) Helium isotopic variations in Ethiopian plume lavas: nature of magmatic sources and limit on lower mantle contribution: Earth and Planetary Science Letters, 144, 223-237.

Mattey, D., D. Lowry, C. Macpherson (1994) Oxygen isotopes composition of mantle peridotite: Earth and Planetary Science Letters, 128, 231-241.

McKenzie, D. and R.K. O'Nions (1991) Partial melt distributions from inversion of rare earth element concentrations: Journal of Petrology, 32(5), 1021-1091.

Meisel, T., R.J. Walker, A.J. Irving and J.-P. Lorand (2001) Osmium isotopic compositions of mantle xenoliths: a global perspective: Geochimica et Cosmochimica Acta, 65(8), 1311-1323.

Melluso, J., L. Beccaluva, P. Brotzu, A. Gregnanin, A.K. Gupta, L. Morbidelli and G. Traversa (1995) Constraints on the mantle sources of the Deccan Traps from the petrology and geochemistry of basalts of Gujarat State (Western India): Journal of Petrology, 36(5), 1393-1432, doi:10.1093/petrology/36.5.1393.

Melluso, L., J.J. Mahoney and L. Dallai (2006) Mantle sources and crustal input as recorded in high-Mg Deccan Traps basalts of Gujarat (India): Lithos, 89, 259-274, doi:10.1016/j.lithos.2005.12.007.

Miller, M.F., I.F. Franchi, A.S. Sexton and C.T. Pillinger (1999) High precision $\delta^{17}O$ isotope measurements of oxygen from silicates and other oxides: methods and applications: Rapid Communications in Mass Spectrometry, 13, 1211-1217.

Morgan, W.J. (1971) Convection plumes in the lower mantle: Nature, 230, 42-43, doi:10.1038/230042a0.

Moreira, M. and M.D. Kurz (2001) Subducted oceanic lithosphere and the origin of the 'high μ' basalt helium isotopic signature: Earth and Planetary Science Letters, 189, 49-57.

O'Nions, R.K. and E.R. Oxburgh (1983) Heat and helium in the Earth: Nature, 306, 429-431, doi:10.1038/306429a0.

Peate, D.W., K. Breddam, J.A. Baker, M.D. Kurz, A.K. Barker, T. Prestvik, N. Grassineau and A.C. Skovgaard (2010) Compositional characteristics and spatial distribution of enriched Icelandic mantle components: Journal of Petrology, 51, 1447-1475.

Peng, Z.X. and J.J. Mahoney (1995) Drillhole lavas from the northwestern Deccan Traps, and the evolution of the Réunion hotspot mantle: Earth and Planetary Science Letters, 134, 169-185, doi:10.1016/0012-821X(95)00110-X.

Peng, Z.X., J. Mahoney, P. Hooper, C. Harris and J. Beane (1994) A role for lower continental crust in flood basalt genesis? Isotopic and incompatible trace element study of the lower six formations of the western Deccan Traps: Geochimica et Cosmochimica Acta, 58, 267-288.

Pernet-Fisher, J.F., G.H. Howarth, D.G. Pearson, S. Woodland, P.H. Barry, N.P. Pokhilenko, L.N. Pokhilenko, A.M. Agashev and L.A. Taylor (2015) Plume impingement on the Siberian SCLM: Evidence from Re-Os isotope systematics: Lithos, 218-219, 141-154.

Pertermann, M. and M.M. Hirschmann (2003) Anhydrous partial melting experiments on MORB-like eclogite: phase relations, phase compositions and mineral-melt partitioning of major elements at 2-3 GPa: Journal of Petrology, 44(12), 2173-2201.

Peters, B.J., J.M.D. Day and L.A. Taylor (2016) Early mantle heterogeneities in the Réunion hotspot source inferred from highly siderophile elements in cumulate xenoliths: Earth and Planetary Science Letters, 448, 150-160.

Ratajeski, K., T.W. Sisson, A.F. Glazner (2005) Experimental and geochemical evidence for derivation of the El Capitan Granite, California, by partial melting of hydrous gabbroic lower crust: Contributions to Mineralogy and Petrology, 149, 713-734.

Rocha-Junior, E.R.V., I.S. Puchtel, L.S. Marques, R.J. Walker, F.B. Machado, A.J.R. Nardy, M. Babinski and A.M.G. Figueiredo (2012) Re-Os isotope and highly siderophile element systematics of the Paraná continental flood basalt system: Earth and Planetary Science Letters, 337-338, 164-173.

Roy-Barman, M. and C.J. Allègre (1995) $^{187}Os/^{186}Os$ in oceanic island basalts: tracing oceanic crust recycling in the mantle: Earth and Planetary Science Letters, 129, 145-161.

Scarsi, P. (2000) Fractional extraction of helium by crushing of olivine and clinopyroxene phenocrysts: effects on the $^{3}He/^{4}He$ measured ratio: Geochmica et Cosmochimica Acta, 64, 3751-3762, doi:10.1016/S0016-7037(00)00419-1.

Scarsi, P. and H. Craig (1996) Helium isotope ratios in Ethiopian Rift basalts: Earth and Planetary Science Letters, 144, 505-516.

Schiano, P., J.-L. Birck and C.J. Allègre (1997) Osmium-strontium-neodymium-lead isotopic covariations in mid-ocean ridge basalt glasses and the heterogeneity of the upper mantle: Earth and Planetary Science Letters, 150, 363-379.

Schiano, P., K. David, L. Vlastelic, A. Gannoun, M. Klein, F. Nauret and P. Bonnand (2012), Osmium isotope systematics of historical lavas from Piton de la Fournaise

(Réunion Island, Indian Ocean): Contributions to Mineralogy and Petrology, 164(5), 16 pp, doi:10.1007/s00410-012-0774-0.

Shaw, A.M., D.R. Hilton, T.P. Fischer, J.A. Walker and G.A. De Leeuw (2006) Helium isotope variations in mineral separates from Costa Rica and Nicaragua: assessing crustal contributions, timescale variations and diffusion related mechanisms: Chemical Geology, 230, 124-139, doi:10.1016/j.chemgeo.2005.12.003.

Skovgaard, A.C., M. Storey, J.A. Baker and J. Blusztajn (2001) Osmium-oxygen isotopic evidence for a recycled and strongly depleted component in the Iceland mantle plume: Earth and Planetary Science Letters, 194, 259-275.

Sobolev, A. V., A. W. Hofmann, S. V. Sobolev and I. K. Nikogosian (2005), An olivine-free mantle source of Hawaiian shield basalts: Nature, 434, 590-597, doi:10.1038/nature03411.

Sobolev, A. V., A. W. Hofmann, D. V. Kuzmin, G. M. Yaxley, N. T. Arndt, S.-L. Chung, L. V. Danyushevsky, T. Elliott, F. A. Frey, M. O. Garcia, A. A. Gurenko, V. S. Kamenetsky, A .C. Kerr, N. A. Krivolutskaya, V. V Matvienkov, I. K. Nikogosian, A. Rocholl, I. A. Sigurdsson, N. M. Sushchevskaya and M. Teklay (2007), The amount of recycled crust in sources of mantle-derived melts: Science, 316, 412-418, doi: 10.1126/science.1138113.

Sobolev, A.V., A.W. Hofmann, G. Brügmann, V.G. Batanova and D.V. Kuzmin (2008) A quantitative link between recycling and Osmium isotopes: Science, 321, 536.

Spandler, C., G. Yaxley, D.H. Green and A. Rosenthal (2008) Phase relation and melting of anhydrous K-bearing eclogite from 1200 to 1600°C and 3 to 5 GPa: Journal of Petrology, 49(4), 771-795.

Standish, J.J, S.R. Hart, J. Blustajn, H.J.B. Dick and K.L. Lee (2002) Abyssal peridotite osmium isotopic compositions from Cr-spinel: Geochemistry Geophysics Geosystems, 3(1), 24 pp.

Starkey, N.A., F.M. Stuart, R.M. Ellam, J.G. Fitton, S. Basu and L.M. Larsen: Helium isotopes in early Iceland plume picrites: Constraints on the composition of the high 3He/4He mantle (2009): Earth and Planetary Science Letters, 277, 91-100.

Staudacher, T., P. Sarda and C.J. Allegre (1990) Noble gas systematics of Réunion Island, Indian Ocean: Chemical Geology, 89, 1-17.

Staudigel, H., G.R. Davies, S.R. Hart, K.M. Marchand and B.M. Smith (1995) Large-scale isotopic Sr, Nd and O isotopic anatomy of altered oceanic crust-DSDP/ODP sites 417/418: Earth and Planetary Science Letters, 130, 169-185.

Stuart, F.M., R.M. Ellam, P.J. Harrop, J.G. Fitton and B.R. Bell (2000) Constraints on mantle plumes from the helium isotopic composition of basalts from the British Tertiary Igneous Province: Earth and Planetary Science Letters, 177, 273-285.

Stuart, F.M., S. Lass-Evans, J.G. Fitton and R.M. Ellam (2003) High $^{3}He/^{4}He$ ratios in picritic basalts from Baffin Island and the role of a mixed reservoir in mantle plumes: Nature, 424, 57-59, doi:10.1038/nature01711.

Thompson, R.N., A.J.V. Richer, P.M. Antoshechkina, D.G. Pearson, G.M. Nowell, C.J. Ottley, A.P. Dickin, V.L. Hards, A.-K. Nguno and V. Niku-Paavola (2007) The origin of CFB magmatism: Multi-tiered intracrustal picrate-rhyolite magmatic plumbing at Spitzkoppe, western Namibia, during early Cretaceous Etendeka magmatism: Journal of Petrology, 48, 1119-1154.

Vidito, C., C. Herzberg, E. Gazel, D. Geist and K. Harpp (2013), Lithological structure of the Galápagos Plume: Geochemistry, Geophysics, Geosystems, 14(10), 4214-4240, doi:10.1002/ggge.20270.

Vlastélic, I., E. Lewin and T. Staudacher (2006) Th/U and other geochemical evidence for the Réunion plume sampling a less differentiated mantle domain: Earth and Planetary Science Letters, 248, 379-393, doi:10.1016/j.epsl.2006.06.003.

Walter, M.J. (1998) Melting of garnet peridotite and the origin of komatiite and depleted lithosphere: Journal of Petrology, 39, 29-60, doi:10.1093/petroj/39.1.29.

Wang, C., Y. Liang, W. Xu and N. Dygert (2013) Effect of melt composition on basalt and peridotite interaction: laboratory dissolution experiments with applications to mineral compositional variations in mantle xenoliths from the North China Craton: Contributions to Mineralogy and Petrology, 166, 1469-1488.

Wang, Z., N.E. Kitchen and J.M. Eiler (2003) Oxygen isotope geochemistry of the second HSDP core: Geochemistry Geophysics Geosystems, 4, 29 pp.

Wang, Z. C. Bucholz, B. Skinner, N. Shimizu and J. Eiler (2011) Isotope constraints on the origin of high-Cr garnets from kimberlites: Earth and Planetary Science Letters, 312, 337-347.

White, W.M. and A.W. Hofmann (1982) Sr and Nd isotope geochemistry of oceanic basalts and mantle evolution: Nature, 296, 821-825, doi:10.1038/296821a0.

Workman, R.K., J.M. Eiler, S.R. Hart and M.G. Jackson (2008) Oxygen isotopes in Samoan lavas: Confirmation of continent recycling: Geology, 36, 551-554.

Yaxley, G.M. and D.H. Green (1998) Reactions between eclogite and peridotite: Mantle refertilisation by subduction of oceanic crust: Swiss Journal of Geosciences, 78(2), 243-255.

Zhang, J., C. Wang and Y. Wang (2012) Experimental constraints on the destruction mechanism of the North China Craton: Lithos, 149, 91-99.

Supplementary Information

4.6 Supplementary discussion regarding the use of residual powders from helium isotope analysis

Major, trace and highly siderophile element (HSE) abundances and $^{187}Os/^{188}Os$ were determined by ICPMS and N-TIMS on powders produced during He isotope analyses using the MAP solenoid crushers. The intention was to provide replicate HSE and Os-isotope analyses for olivine separates, which are limited in mass, and to determine U and Th abundances on the same powders on which $^{3}He/^{4}He$ analyses were accomplished. Analytical methods were otherwise identical to those described. As expected, we observe strong enrichment in W imparted from the WC crushers in the MAP powders, and additionally note large systematic excesses in Cu (up to 231 ppm over the fresh aliquots) and Mo (up to 1.2 ppm over fresh aliquots). The smallest differences were observed for Li and the REE. Differences in HSE concentrations varied independently of W contributions, but with large excesses in HSE/Ir ratios for the DC14-05 MAP powder over the fresh powder, but generally smaller positive and negative differences between the DC14-47B MAP and fresh powders. Variations in $^{187}Os/^{188}Os$ were less than 4% between the MAP and fresh powders; less than natural variability between bulk powder aliquots of the same sample. Because of these uncertainties, we do not use the HSE concentrations of the MAP powders for modeling or calculations.

4.7 Supplementary discussion of bulk rock and mineral separate geochemistry

Deccan traps lavas from which mineral separates were extracted range from relatively primitive to evolved (Mg# = 21 to 77) and have generally elevated Al_2O_3 (7.9 to 14.2 wt.%) and CaO (9.3 to 12.7 wt.%). The three lavas collected in the Kutch region are basanites, while all others are basalts (**Figure 4.9**). All lavas have steeply dipping incompatible element trends (e.g., La/Yb = 2.5 to 27.6). In contrast, mineral separates define more shallowly dipping rare earth element (REE) slopes (La/Yb = 1.4 to 24.1, **Figure 4.10**). Samples from the northwestern Deccan generally exhibit greater incompatible trace element enrichment than those found elsewhere in the Deccan, in good agreement with previous findings [e.g., Mahoney et al., 1985; Melluso et al., 2002, 2006].

The intention of this study is to analyze mantle source contributions to Deccan volcanism using early-formed mineral phases. However, most Deccan basalts are not olivine-phyric and therefore only two mineral separates (corresponding to samples DC14-05 and 47B) are pure olivine. Separate MMF7 likely represents mostly olivine with a small contribution from plagioclase. Two of the mineral separates (corresponding to samples DC14-10B, 68 and 111) have strong contributions from plagioclase, which is reflected in their high Al_2O_3 (26-30 wt.%) and positive Eu anomalies (**Figure 4.10**). Separate DC14-10B likely also contains significant clinopyroxene, as evidenced by its high Cr contents (>2000 ppm). Every effort was made to separate these phases for individual analysis, however this was not always possible due to similarities in body color between olivine,

clinopyroxene (where present) and plagioclase. Analysis of a variety of positively identified mineral phases permits analysis of the characteristics of both the early-stage (using olivine) and late-stage (using plagioclase) parental magmas.

The role of accumulative phases in Deccan igneous rocks has been previously discussed [e.g., Chatterjee & Sheth, 2015]. Accumulative olivine complicates interpretation of rocks compositions if the accumulating phases are non-cognate. For our samples, olivine phenocrysts are likely to be in equilibrium with their respective host rocks, based on Mg/(Mg+Fe) ratios in equilibrium with the host-rock, and complementary REE patterns (**Figure 4.10**).

Subaerial weathering can alter the composition of volcanic rocks. Bulk samples have a range of LOI (1.8 to 3.7 wt.%) that are negatively correlated to Al_2O_3 and Fe^{2+}/Fe^* ($Fe^{2+}/(Fe^{2+} + Fe^{3+})$ by mole; r^2 of 0.42 and 0.43, respectively). Additionally, there are weak positive correlations between bulk-rock LOI contents and Cs and Ba contents in corresponding mineral separates (both with r^2 of 0.30), raising the possibility that fluid-mediated weathering controls some facets of lava compositions. However, we deliberately avoided analysis of elements that appeared to be affected by weathering using these simple filters. To avoid alteration effects to O and He, we used fresh mineral grains and, for helium isotopic analyses, short crushing times, to avoid release of structurally-hosted He [e.g., Graham et al., 1998; Hilton et al., 1993; Scarsi, 2000].

Figures

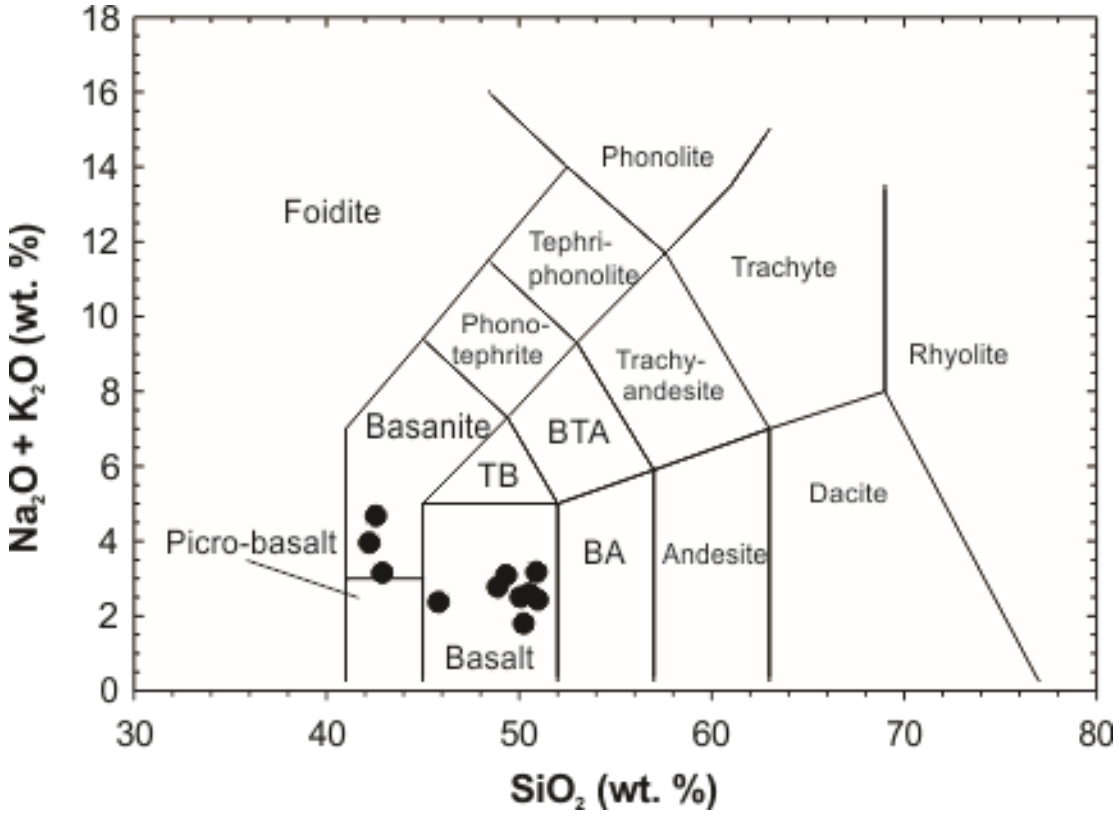

Figure 4.9: Total alkalis versus silica plot for Deccan Traps lavas examined in this study.

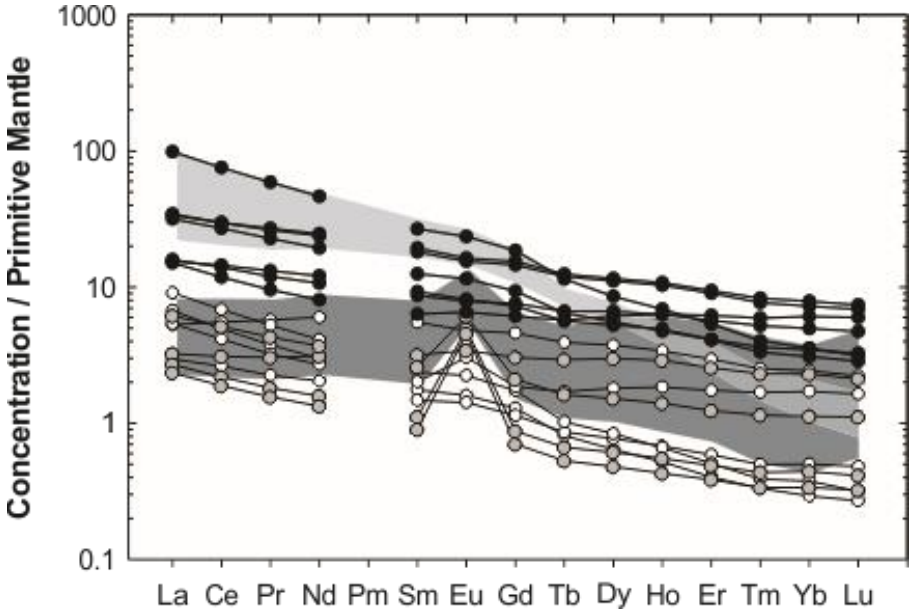

Figure 4.10: Primitive mantle normalized rare earth element (REE) compositions of olivine separates (open circles), plagioclase and clinopyroxene separates (gray circles) and bulk rocks (black circles). Dark gray region represents range of compositions expected for bulk rocks based on REE partitioning into plagioclase; light gray region represents the same for olivine, and middle gray represents the overlap between these two regions. Plagioclase fractionation generally predicts lower bulk rock contents due to higher REE partition coefficients of this phase and also predicts larger positive Eu anomalies. Fractional crystallization model utilizes coefficients of Fujimaki et al. [1984]. Primitive mantle normalization from McDonough & Sun [1995].

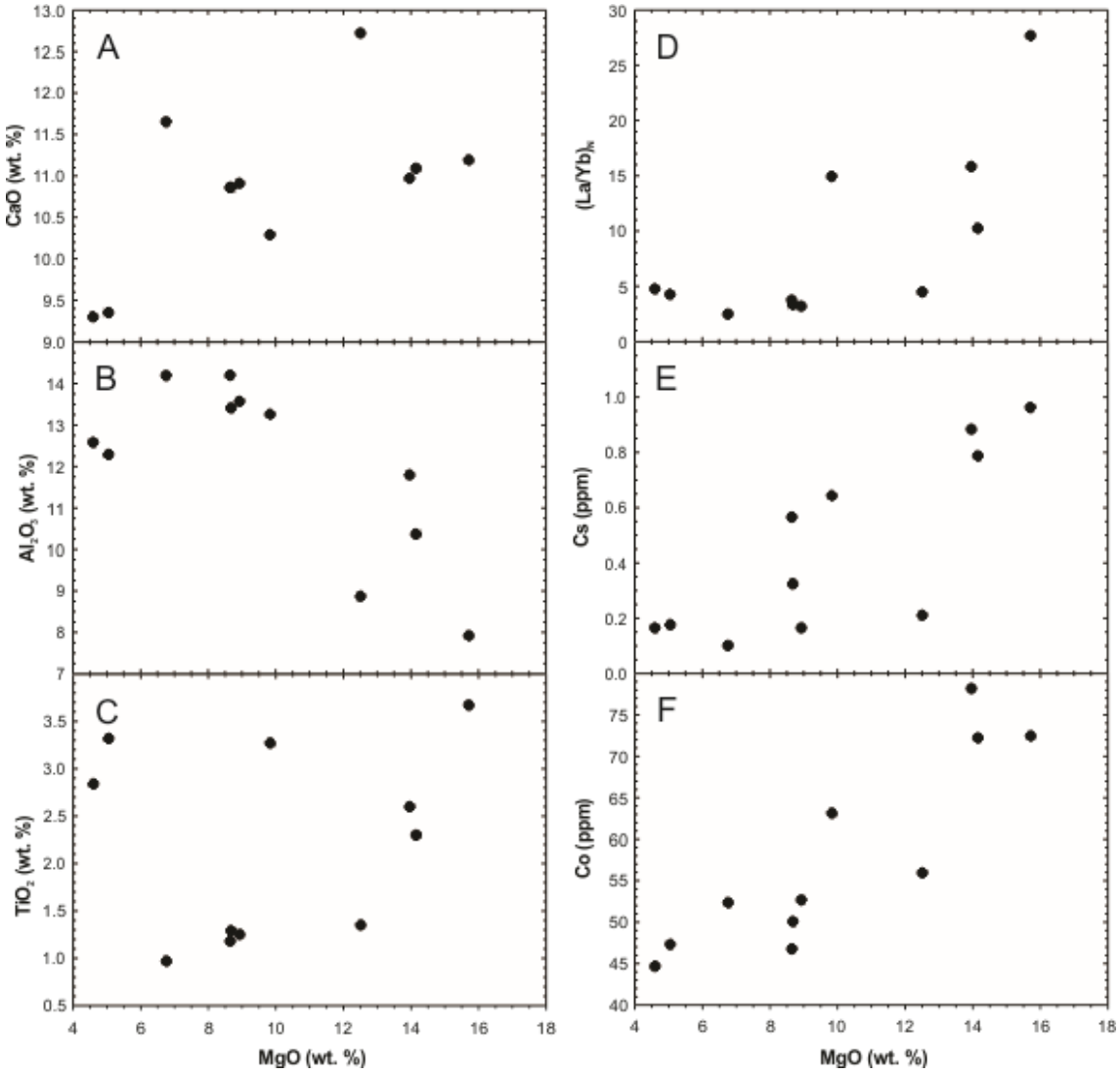

Figure 4.11: Whole-rock MgO versus (A) CaO, (B) Al_2O_3, (C) TiO_2, (D) primitive-mantle normalized La/Yb [McDonough & Sun, 1995], (E) Cs, (F) Co for samples corresponding to separates referenced in the study.

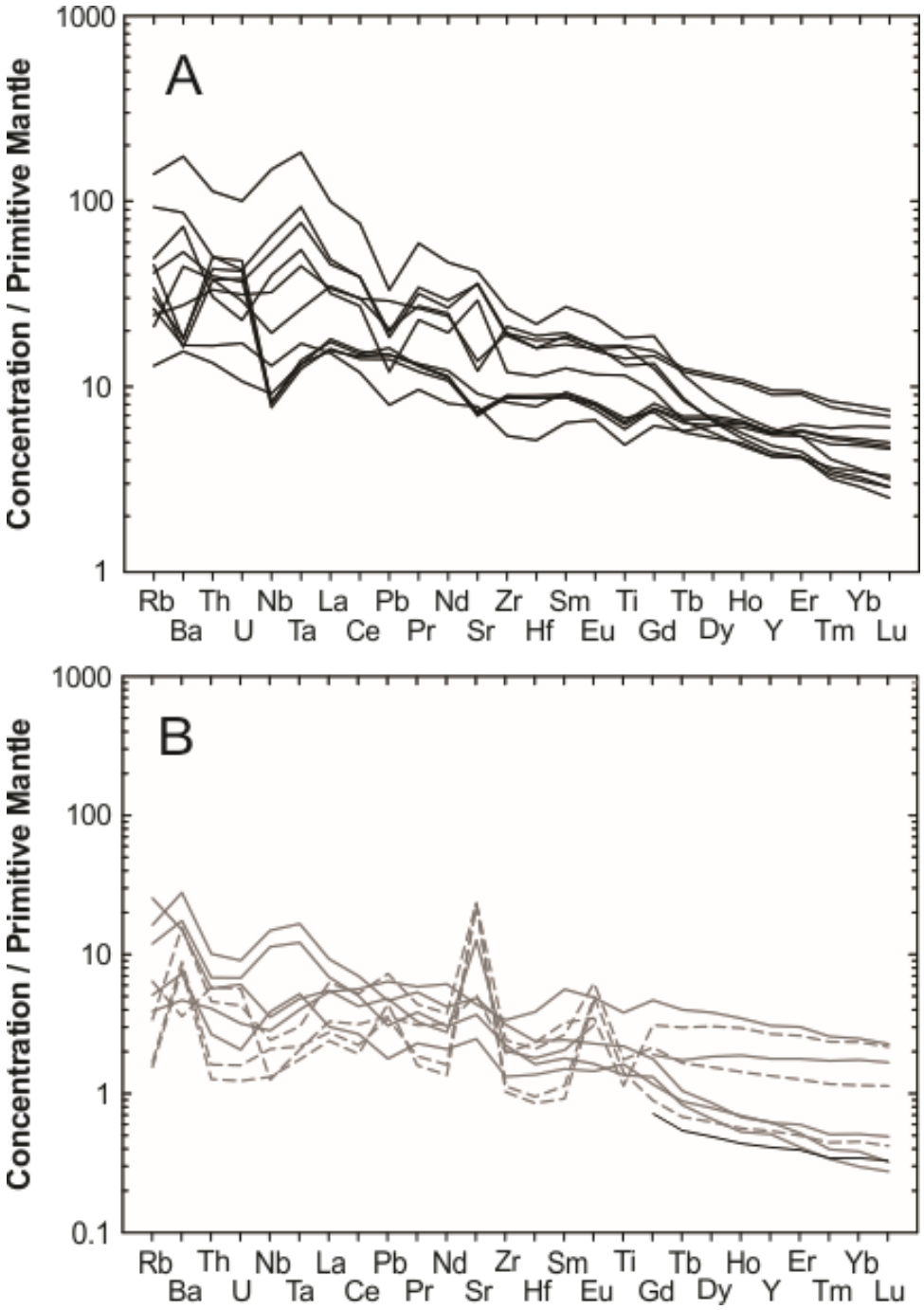

Figure 4.12: Primitive mantle-normalized trace element variation diagram for Deccan Traps (A) basalts hosting separates involved in this study and (B) olivine and clinopyroxene (solid lines) and plagioclase (dashed lines) separates. Primitive mantle normalization from McDonough & Sun [1995].

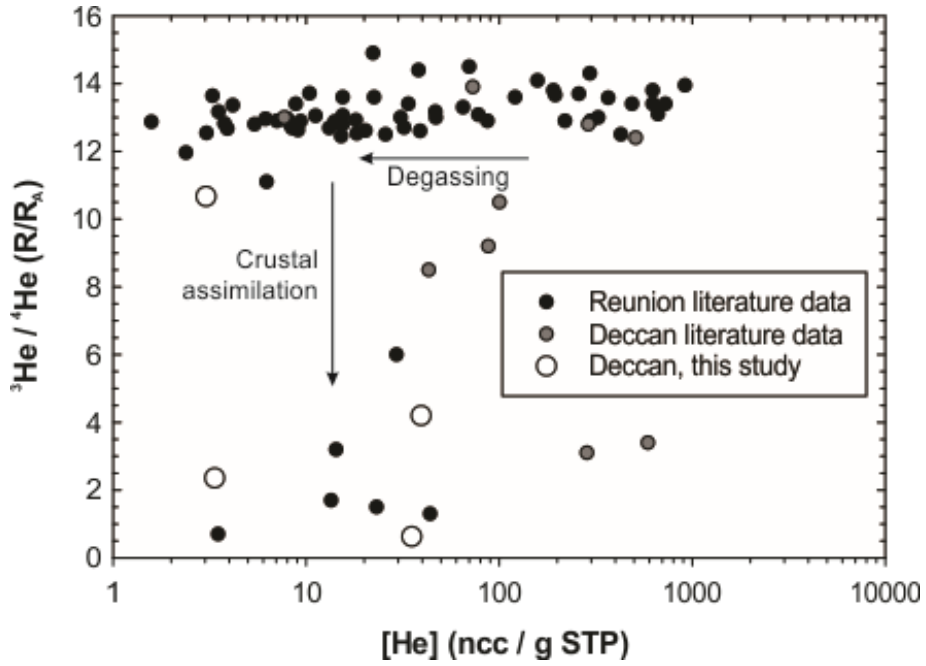

Figure 4.13: Helium isotopic composition versus helium concentrations for published Réunion [Kaneoka et al., 1986; Graham et al., 1990; Staudacher et al., 1990; Füri et al., 2000] and Deccan [Basu et al., 1993], and data from this study. Degassing and concomitant addition of crustal He will lower ^{3}He/^{4}He ratios trapped within olivine.

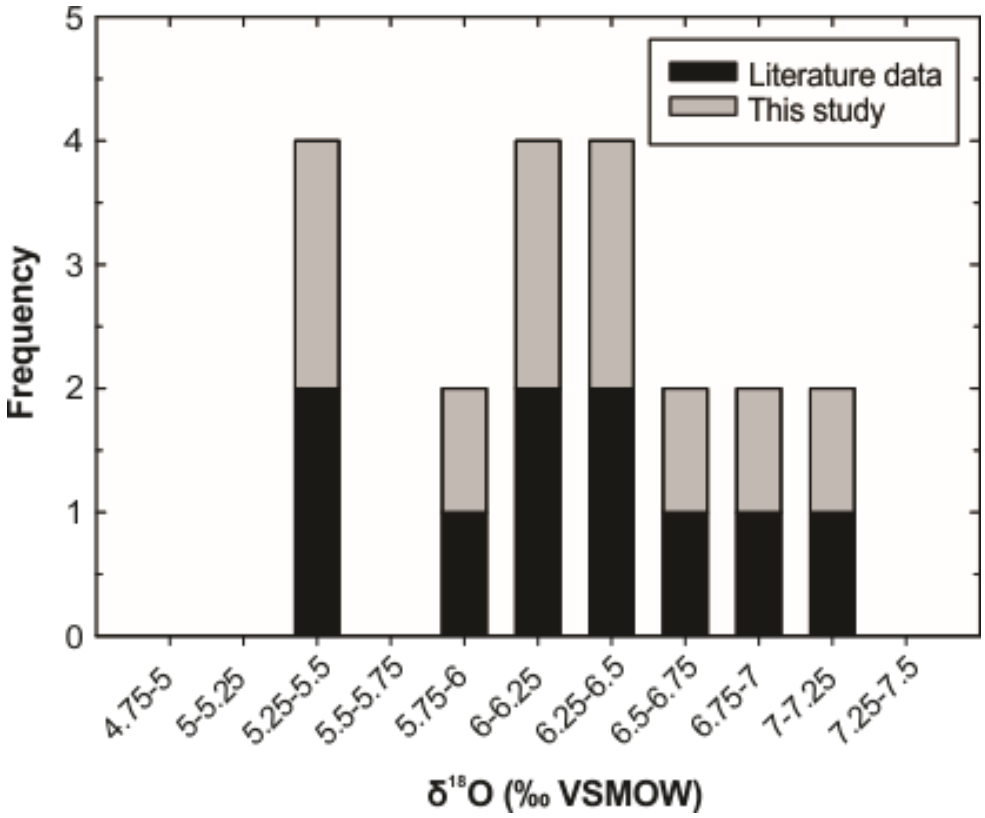

Figure 4.14: Histogram of oxygen isotope data for Deccan Traps olivine from this study and literature olivine and clinopyroxene. Literature data from Peng et al. [2004] and Melluso et al. [2006].

References

Basu, A.R., P.R. Renne, D.K. DasGupta, F. Teichmann and R.J. Poreda (1993) Early and late alkali igneous pulses and a high-^{3}He plume origin for Deccan flood basalts: Science, 261, 902-906.

Chatterjee, N. and H. Sheth (2015) Origin of the Powai ankaramite, and the composition, P-T conditions of equilibration and evolution of the primary magmas of the Deccan tholeiites: Contributions of Mineralogy and Petrology, 169, 24 pp.

Fujimaki, H., M. Tatsumoto and K.-I. Aoki (1984) Partition coefficients of Hf, Zr and REE between phenocrysts and groundmass: Journal of Geophysical Research, 89, B662-B672.

Füri, E., D.R. Hilton, B.J. Murton, C. Hémond, J. Dyment and J.M.D. Day (201) Helium isotope vriations between Réunion Island and the Central Indian Ridge (17°-21°S): New evidence for ridge-hot spot interaction: Journal of Geophysical Research, 116, B02207.

Graham, D., J. Lupton, F. Albaréde and M. Condomines (1990) Extreme temporal homogeneity of helium isotopes at Piton de la Fournaise, Réunion Island: Nature, 347, 545-549.

Graham, D.W., L.M. Larsen, B.B. Hanan, M. Storey, A.K. Pedersen and J.E. Lupton (1998) Helium isotope composition of the early Iceland mantle plume inferred from the Tertiary picrites of West Greenland: Earth and Planetary Science Letters, 160, 241-255.

Hilton, D.R. K. Hammerschmidt, S. Teufel and H. Freidrichsen (1993) Helium isotope characteristics of Andean geothermal fluids and lavas: Earth and Planetary Science Letters, 120, 265-282, doi:10.1016/0012-821X(93)90244-4.

Kaneoka, I., N. Takaoka and B.G.J. Upton (1986) Noble gas systematics in basalts and a dunite nodule from Réunion and Grand Comore Islands, Indian Ocean: Chemical Geology, 59, 35-42.

Mahoney, J.J., J.D. Macdougall, G.W. Lugmair, K. Gopalan and P. Krishnamurthy (1985) Origin of contemporaneous tholeiitic and K-rich alkalic lavas: a case study from the northern Deccan Plateau, India: Earth and Planetary Science Letters, 72, 39-53.

McDonough, W.F. and S.-s. Sun (1995) The composition of the Earth: Chemical Geology, 120, 223-253.

Melluso, J., L. Beccaluva, P. Brotzu, A. Gregnanin, A.K. Gupta, L. Morbidelli and G. Traversa (1995) Constraints on the mantle sources of the Deccan Traps from the petrology and geochemistry of basalts of Gujarat State (Western India): Journal of Petrology, 36(5), 1393-1432, doi:10.1093/petrology/36.5.1393.

Melluso, L., J.J. Mahoney and L. Dallai (2006) Mantle sources and crustal input as recorded in high-Mg Deccan Traps basalts of Gujarat (India): Lithos, 89, 259-274, doi:10.1016/j.lithos.2005.12.007.

Peng, Z.X., J. Mahoney, P. Hooper, C. Harris and J. Beane (1994) A role for lower continental crust in flood basalt genesis? Isotopic and incompatible trace element study of the lower six formations of the western Deccan Traps: Geochimica et Cosmochimica Acta, 58, 267-288.

Peters, B.J., J.M.D. Day and L.A. Taylor (2016) Early mantle heterogeneities in the Réunion hotspot source inferred from highly siderophile elements in cumulate xenoliths: Earth and Planetary Science Letters, 448, 150-160.

Scarsi, P. and H. Craig (1996) Helium isotope ratios in Ethiopian Rift basalts: Earth and Planetary Science Letters, 144, 505-516.

Staudacher, T., P. Sarda and C.J. Allègre (1990) Noble gas systematics of Réunion Island, Indian Ocean: Chemical Geology, 89, 1-17.

Chapter 5:

A definitive link between plume head and plume tail volcanism

Abstract

Mantle plumes are long-lived, thermo-chemically anomalous upwellings that cause voluminous intraplate magmatism, and are thought to have occurred throughout the geological record [Wilson, 1963; Morgan, 1971]. Models of plumes typically invoke initial plume 'heads' that impinge upon the lithosphere causing large-scale volcanism, followed by plume 'tails' that represent long-lived, lower volume and persistent magmatism [Richards et al., 1989]. The Réunion hotspot preserves clear physiographic links between a 'plume head' in the Cretaceous-Paleogene aged Deccan Traps of India and present-day active intraplate volcanism on Réunion Island. Efforts to geochemically link Deccan and Réunion volcanic rocks, however, have been impeded by assimilation of lithospheric material within Deccan magmas [Mahoney et al., 1982; Peng et al., 1995]. Here, we present new Os isotope and highly siderophile element (HSE: Os, Ir, Ru, Pt, Pd, Re) abundance data for Deccan volcanic rocks that

demonstrate for the first time a clear geochemical link between plume head and tail volcanism. Use of compatible elements like the HSE can circumvent the complexities introduced by lithospheric assimilation because these elements are relatively scarce in the crust and are concentrated in primary mantle melts [Day, 2013]. We define initial $^{3}He/^{4}He$ ($>13R_A$), $^{87}Sr/^{86}Sr_T$ (0.70419 ±0.00006), εNd_T (5.1 ±0.2), and $^{187}Os/^{188}Os_T$ (0.1324 ±0.0014) compositions for Deccan lavas that are identical to those of Reunion Island [e.g., Peters et al., 2016] Our results provide firm geochemical evidence for a compositionally distinct mantle plume that has generated magmatism for about 65 Ma, and are inconsistent with models that explain magmatism by continuous melting of shallow mantle reservoirs.

5.1 Main Text

The origin of intraplate, "hotspot" volcanism remains a controversial issue in the Earth Sciences, though two theories have gained most traction. One model conjectures that thermo-chemically buoyant mantle plumes upwell from the deep mantle and initiate volcanism, including short-lived high-volume magmatism that may be associated with major tectonic [Cande & Stegman, 2011] and environmental [e.g., Self et al., 2008] events. The other suggests that intraplate magmatism is caused by shallow-melting in response to tectonic processes, producing short-lived and low-volume events [Koppers et al., 2003].

A key argument in support of a mantle plume origin for intraplate volcanoes is the association between CFB erupted at the edge of cratons during continental break-up, and oceanic island basalts (OIB) [e.g., Richards et al., 1989]. In addition to the Réunion hotspot

(**Figure 5.1**), this has been observed for the Parana-Etendeka CFB and Tristan-Gough OIB and the North Atlantic Igneous Province (NAIP) and present-day Icelandic volcanism. However, in these cases, the physiographic evidence for a mantle plume origin is not as strongly matched by the geochemistry. For example, Tristan possesses low-$^{3}He/^{4}He$ [Graham, 2002] and the search for a common geochemical source to NAIP-Iceland is complicated by hotspot-ridge interaction [Schilling, 1973] and crustal contamination [Day, 2016]. Therefore, the hypothesis that modern OIB are supported by plumes transporting deep mantle material is not strongly supported by the crucial observation of a geochemical connection between OIB and CFB volcanism.

Here we report new $^{87}Sr/^{86}Sr$, $^{143}Nd/^{144}Nd$ and $^{187}Os/^{188}Os$ isotope data, along with major-, trace- and HSE abundance data for greater than 60 samples spanning a broad geographic range of the Deccan Traps CFB province of India (*Appendix*, *Supplementary Information*). The Deccan Traps are thought to represent the initial phase of the Réunion hotspot at the Cretaceous-Paleogene boundary [Wellman & McElhinny, 1970] and likely produced in $>10^{6}$ km^{3} of lava [Jay & Widdowson, 2008] in <1 Ma [Schoene et al., 2015]. The Deccan province is physiographically linked to modern volcanism on Réunion Island by a chain of extinct volcanic features comprising the Chagos-Laccadive Ridge and the Mascarene Plateau. Geophysical evidence indicates that active volcanism on Réunion is sustained by a columnar low-velocity mantle anomaly that appears to transport material from the D" layer [Montelli et al., 2004]. Fractionated HSE patterns with high Pd/Pt and Ru/Ir, a remarkably consistent Os-isotopic signature (0.1324 ±0.0014) and elevated,

consistent $^{3}He/^{4}He$ [Füri et al., 2011] in Réunion igneous rocks also argue for contributions from a distinct, deep mantle source [Peters et al., 2016].

In contrast, an extensive differentiation history has necessitated focus on the relative contributions of crust and lithosphere to Deccan lava geochemistry, rather than on the compositions of its mantle sources [Peng et al., 1994; Bhattacharya et al., 2013]. The Deccan Traps are predominantly underlain by 40-50 km of continental crust and ~150 km of SCLM [Gupta et al., 2003] with areas overlying rift zones having considerable thinning of the lithosphere [Kaila, 1986]. Accordingly, Deccan Traps lavas have the potential to reveal a broad range in extent of crustal or lithospheric assimilation. Complex trends in lithophile isotope systems have led to a variety of models advocating distinct lithospheric and crustal assimilants. For example, common interpretations of the Ambenali Formation include assimilation of low-εNd, low-$^{87}Sr/^{86}Sr$ material, which has been attributed to SCLM [e.g., Lightfoot et al., 1990] or lower crust [Bhattacharya et al., 2013]. In contrast, volcanic rocks from the Ghatkopar-Powai area have lithophile isotope characteristics revealing a limited role for crustal and lithospheric assimilation [Sheth et al., 2014]. The use of Os isotopes, which are sensitive to crustal inputs, combined with improved understanding of lower Indian crust compositions [Peucat et al., 2013], has substantially improved the probability of identifying a parental magma signature to Deccan CFB.

We present new Sr-Nd-Os isotopic and HSE data collected using standard ICP-MS and TIMS methods (*Appendix, Supplementary Information*). While some of our samples have experienced post-emplacement alteration (LOI = 0.6-7.6%), we found no strong

effects of these processes on Sr-Nd-Os isotopes or element ratios and abundances discussed here. The new data spans a wide range of Sr-Nd isotope signatures, as shown previously for Deccan volcanic rocks [Mahoney et al., 1982; Peng et al., 1995; Allègre et al., 1999; Bhattacharya et al., 2013]. Age-corrected $^{87}Sr/^{86}Sr$ extends from 0.703834 to 0.711954 and are negatively correlated with age-corrected εNd, which ranges from -18.3 to 1.9. Enrichment in Sr-Nd isotopic signatures is broadly correlated with highly fractionated HSE signatures, reflecting the combined effects of assimilation and fractional crystallization (*Supplementary Information*). However, samples with the highest primitive mantle (PM)-normalized [McDonough & Sun, 1995] La/Yb, which are more common in the northerly Kutch samples and those from the Pavagadh volcanic complex, have distinctive HSE patterns that are similar to patterns found in Réunion rocks [Peters et al., 2016] (*Supplementary Information*).

Age-corrected $^{187}Os/^{188}Os$ ranges from 0.1128 to 0.6713, which encompasses both the range of subcontinental lithospheric mantle (SCLM) [Aulbach et al., 2016] and continental crust [Asmerom & Walker, 1998]. There is no correlation between Os and Sr isotopes, however there is a distinct negative correlation between Os and Nd isotopes (**Figure 5.2**). While previous studies have claimed isochronous behavior for Deccan lavas from a wide geographic area [Allègre et al., 1999] our samples do not show a statistically significant isochron (MSWD $>10^2$) and do not support a near-chondritic initial $^{187}Os/^{188}Os$ (**Figure 5.3**), as previously reported. Excluding samples with MgO <8 wt.% and $^{187}Re/^{188}Os$ >100, a York-type regression of our data yields an initial $^{187}Os/^{188}Os$ of 0.132 ±0.027 (n = 32). Because Deccan basalts have universally assimilated some amount of

continental crust, all possess elevated $^{187}Re/^{188}Os$, requiring projection of data through low-$^{187}Re/^{188}Os$ space to construct an isochron diagram. Our $^{187}Re/^{188}Os$ range is 1-490 with an average of 64 while published data [Allègre et al., 1999] range from 13 to 1800 with an average of 633 and only two samples possessing $^{187}Re/^{188}Os$ <100. Although both datasets evidence crustal disturbance of the Re-Os system, the extensive disturbance present in the samples of Allègre et al. [1999] may prelude accurate determinations of age and initial $^{187}Os/^{188}Os$.

For the new data, we find that the data can be best explained by sequential assimilation of distinct crustal reservoirs. Mixing between a Réunion-like source, SCLM and/or lower crustal materials can explain Os abundances, however Sr and Nd isotopic signatures are dominated by assimilation of lower and upper crustal materials. Correlations between Nd and Os isotopes support a primary role for assimilation of SCLM with later, subordinate contributions from lower continental crust. Strontium isotopic data arrays require the most contributions from upper continental crust (*Supplementary Information*), which possesses more radiogenic $^{87}Sr/^{86}Sr$ than lower crust, while showing little influence from a deeper assimilant similar to SCLM. In contrast to earlier studies, we find no clear role for a DMM-like assimilant in our dataset. These combined isotope systems reveal the full compositional diversity of likely crustal lithospheric assimilants and require a primary magma composition similar to that expected for Réunion (**Figure 5.2**).

Given the low concentrations of HSE compared to lithophile elements in continental crust [Peucker-Ehrenbrink & Jahn, 2001], they are also candidates to establish

a reasonable elemental composition of a CFB mantle source. We quantify the effects of sulfide saturation and extraction in an evolved melt on a Deccan parental magma and compare the results to measure Deccan HSE (*Supplementary Information*). We find that a Réunion-like parental magma can account for measured HSE concentrations of Maharashtra "main sequence" and Saurashtra low-Ti lavas, which are among the most evolved of our sample suite.

The use of the HSE and Os isotopes offers a more straightforward method to unmask the relationship between differentiated HSE lavas and their mantle sources. Réunion offers both a relatively invariant Sr-Nd-Os isotopic signature and a singular $^{187}Os/^{188}Os$ and HSE composition that provide unique and well-constrained endmembers with which to judge the relationship between Deccan CFB and Réunion OIB. This unique Réunion HSE signature has been recently investigated as a relic of a deep mantle source [Peters et al., 2016], and this quantitative analysis shows that the same source may have supported Deccan magmatism. Thus, despite their disparate geography and distinct volcanic structures, Deccan and Réunion igneous rocks display convincing evidence for a common mantle source that represents a geochemical link between canonical plume head and plume tail volcanism. Such a link is inconsistent with the interpretation that the Réunion hotspot track is derived from continual melting of shallow mantle sources, but rather demonstrates that the mantle source to Réunion hotspot volcanism is more likely a deep mantle plume that has persisted for long periods of geologic time, despite mantle convection and proximity to mid-ocean ridge magmatism. Further, the geochemical homogeneity of the mantle source to the Réunion hotspot is unparalleled among other

global hotspots, and convincingly establishes the durability of mantle heterogeneities despite influence from tens of millions of years of upper mantle dynamics.

Acknowledgements

Chapter 5, in full, is a reformatted version of material to be submitted to Nature: Peters, B.J. and J.M.D. Day (2016) A definitive link between plume head and plume tail volcanism: *in preparation*. I was the primary investigator and author of this paper and of this chapter.

Figures

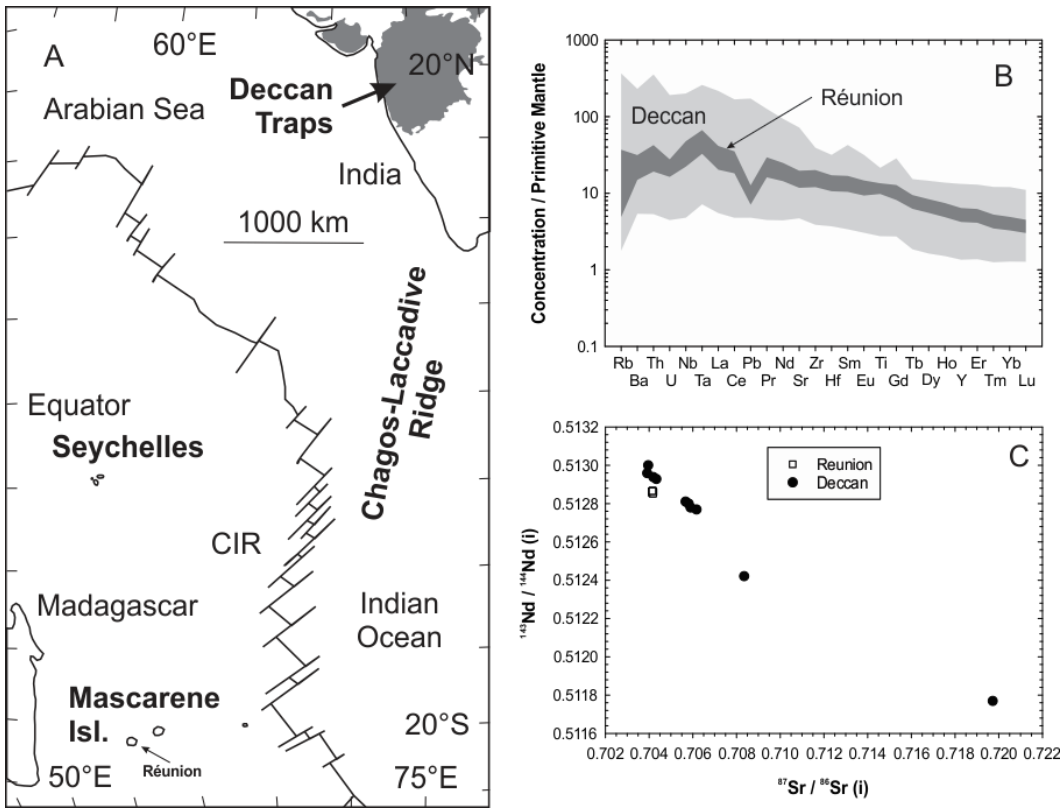

Figure 5.1: (A) Schematic diagram of the Réunion hotspot from the Deccan Traps (gray region within India and including the Seychelles) to the Mascarene Islands. (B) Trace element variations for Réunion [Peters et al., 2016] and Deccan basalts. (C) Sr-Nd isotopic variations for Réunion [DiMuro et al., 2014] and Deccan [Mahoney et al., 1982] basalts.

Figure 5.2: (A) Plot of $^{187}Os/^{188}Os$ versus [Os], with compositions of reservoirs thought to contribute to the isotopic ratios of Deccan parental magmas plotted as mixing lines denoted by 10% mass intervals. In (A), sequential mixing between sub-continental lithospheric mantle (SCLM) and lower continental crust (LCC) is shown with mixing lines between a Réunion-like component and both SCLM and LCC, and an illustrative mixing line drawn between SCLM and LCC. This latter line is not meant to imply that assimilation occurs between these two reservoirs, but rather to define a region in which all possible compositions resulting from sequential SCLM-LCC assimilation are bound. Mixing intervals shown only on the Réunion-LCC line for clarity. (B) Nd-Os and (C) Sr-Os isotopic variations plotted with similar mixing arrays.

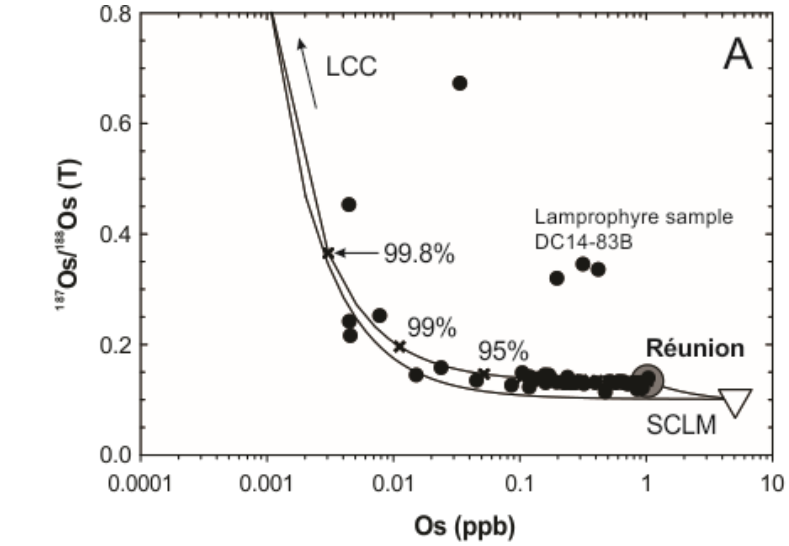
A
LCC
99.8%
99%
95%
Lamprophyre sample
DC14-83B
Réunion
SCLM
$^{187}Os/^{188}Os$ (T)
Os (ppb)
0.0
0.2
0.4
0.6
0.8
0.0001
0.001
0.01
0.1
1
10

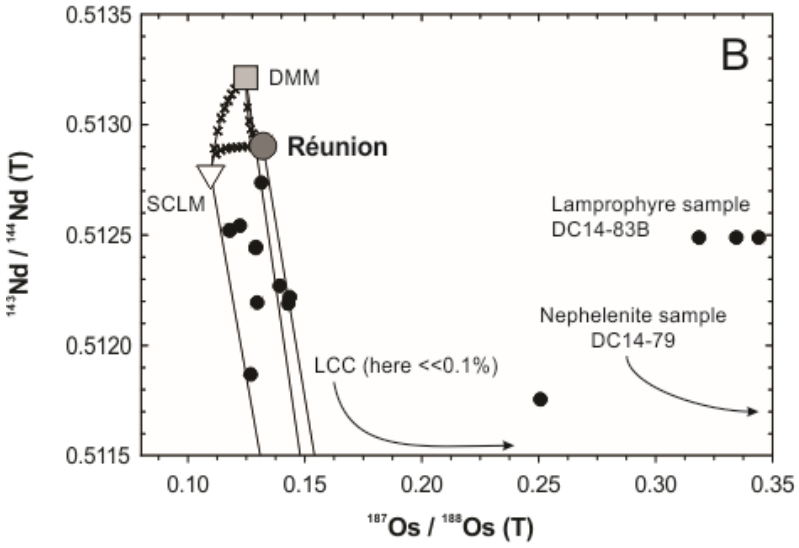
B
DMM
Réunion
SCLM
Lamprophyre sample
DC14-83B
Nephelenite sample
DC14-79
LCC (here <<0.1%)
^{143}Nd / ^{144}Nd (T)
^{187}Os / ^{188}Os (T)
0.5115
0.5120
0.5125
0.5130
0.5135
0.10
0.15
0.20
0.25
0.30
0.35

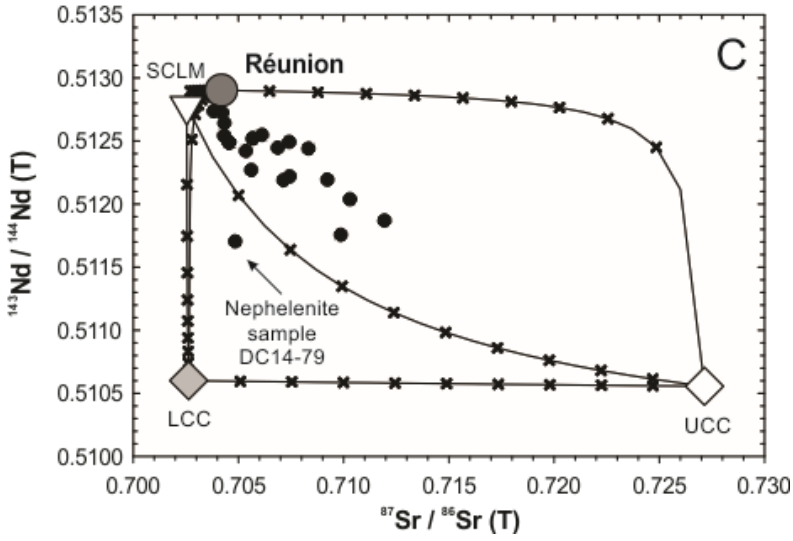
C
SCLM
Réunion
Nephelenite
sample
DC14-79
LCC
UCC
^{143}Nd / ^{144}Nd (T)
^{87}Sr / ^{86}Sr (T)
0.5100
0.5105
0.5110
0.5115
0.5120
0.5125
0.5130
0.5135
0.700
0.705
0.710
0.715
0.720
0.725
0.730

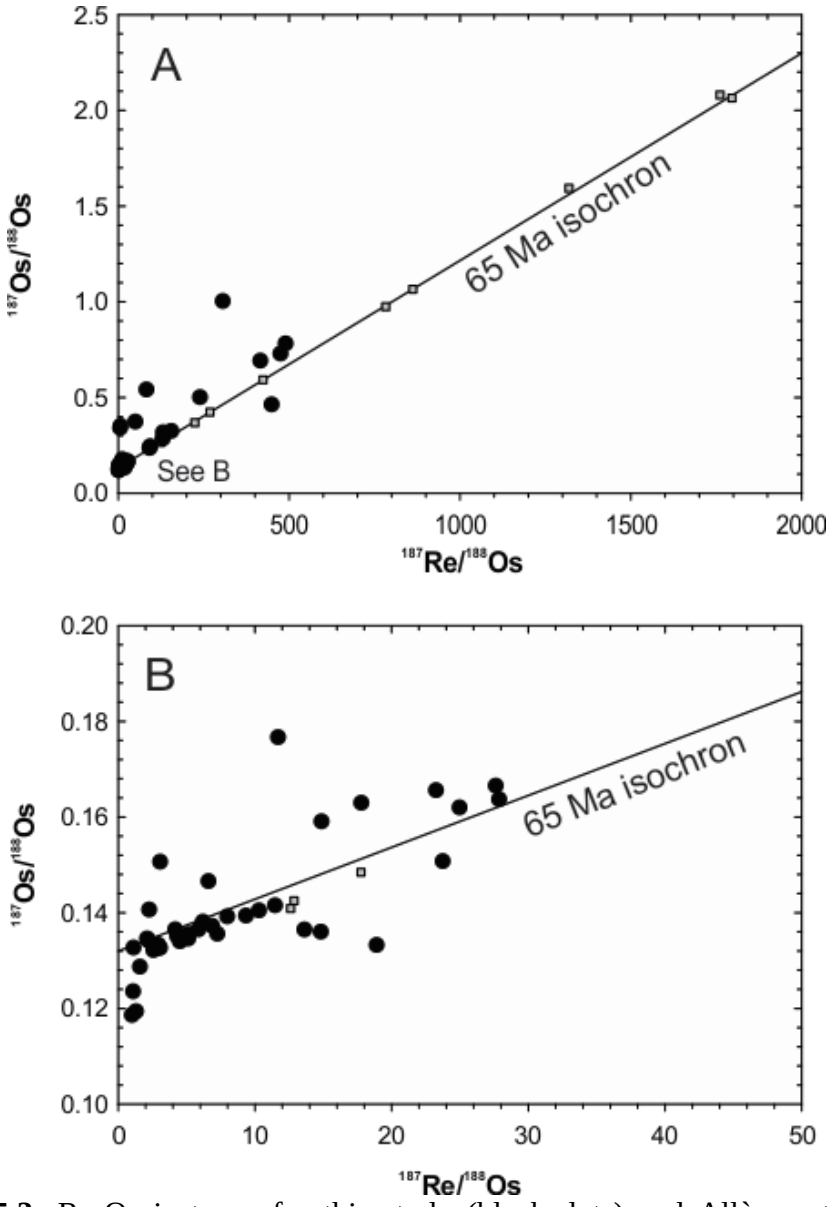

Figure 5.3: Re-Os isotopes for this study (black dots) and Allègre et al. (small gray squares). (B) is a subset of (A). A 65 Ma isochron with an initial $^{187}Os/^{188}Os$ of 0.132 is plotted for reference, but is not a good statistical fit to the data due to extensive crustal assimilation.

References

Allégre, C.J., J.L. Birck, F. Campas and V. Courtillot (1999) Age of the Deccan traps using ^{187}Re-^{187}Os systematics: Earth and Planetary Science Letters, 170, 197-204.

Asmerom, Y. and R.J. Walker (1998) Pb and Os isotopic constraints on the composition and rheology of the lower crust: Geology, 26(4), 359-362.

Aulbach, S., J.E. Mungall and D.G. Pearson (2016) Distribution and processing of highly siderophile elements in cratonic mantle lithosphere, *in* Harvey, J. and J.M.D. Day (*eds.*) Highly siderophile and strongly chalcophile elements in high-temperature geochemistry and cosmochemistry: Reviews in Mineralogy and Geochemistry, 81, 239-304.

Bhattacharya, S.K., G.S.-K. Ma and Y. Matsuhisa (2013) Oxygen isotope evidence for crustal contamination in Deccan basalts: Chemie der Erde, 73(1), 105-112.

Cande, S.C. and D.R. Stegman (2011) Indian and African plate motions driven by the push force of the Réunion plume head: Nature, 475, 47-52.

Day, J.M.D. (2013) Hotspot volcanism and highly siderophile elements: Chemical Geology, 341, 60-74.

Day, J.M.D. (2016) Evidence against an ancient non-chondritic mantle source for North Atlantic Igneous Province lavas: Chemical Geology, *in press*.

DiMuro, A., N. Métrich, D. Vergani, M. Rosi, P. Armienti, T. Fougeroux, E. Deloule, I. Arienzo and L. Civetta (2014) The shallow plumbing system of Piton de la Fournaise Volcano (La Réunion Island, Indian Ocean) revealed by the major 2007 caldera-forming eruption: Journal of Petrology, 55(7), 1287-1315.

Füri, E., D.R. Hilton, B.J. Murton, C. Hémond, J. Dyment and J.M.D. Day (201) Helium isotope vriations between Réunion Island and the Central Indian Ridge (17°-21°S): New evidence for ridge-hot spot interaction: Journal of Geophysical Research, 116, B02207.

Graham, D.W. (2002) Noble gas isotope geochemistry of mid-ocean ridge and ocean island basalts: characterization of mantle source reservoirs, *in*: Porcelli, D., C.J. Ballentine and R. Wieler (eds.) Noble gases in geochemistry and cosmochemistry: Reviews in Mineralogy and Geochemistry, 47, 247-319.

Gupta, S., S.S. Rai, K.S. Prakasam, D. Srinagesh, R.K. Chadha, K. Prisetley and V.K. Gaur (2003) First evidence for anomalous thick crust between the mid-Archean western Dharwar craton: Current Science, 84(9), 1219-1226.

Jay, A. and M. Widdowson (2008) Stratigraphy, structure and volcanology of the SE Deccan continental flood basalt province: implications for eruptive extent and volumes: Journal of the Geological Society, 165, 177-188.

Kaila, K.L. (1986) Tectonic framework of Narmada-Son Lineament – a continental rift system in central India from deep seismic soundings, *in* Barazangi, M. and L. Brown (*eds.*) Reflection seismology: a global perspective: American Geophysical Union, Washington, D.C., 18 pp.

Koppers, A.A.P., H. Staudigel, M.S. Pringle and J.R. Wijbrans (2003) Short-lived and discontinuous intraplate volcanism in the South Pacific: Hot spots or extensional volcanism?: Geochemistry, Geophysics, Geosystems, 4(1), 49 pp.

Lightfoot, P.C., C.J. Hawkesworth, C.W. Devey, N.W. Rogers and P.W.C. Van Calsteren (1990) Source and differentiation of Deccan Trap lavas: Implications of geochemical and mineral chemical variations: Journal of Petrology, 31(5), 1165-1200.

Mahoney, J., J.D. Macougall, G.W. Lugmair, A.V. Murali, M. Sankar Das and K. Gopalan (1982) Origin of the Deccan Trap flows at Mahabaleshwar inferred from Nd and Sr isotopic and chemical evidence: Earth and Planetary Science Letters, 60, 47-60.

McDonough, W.F. and S.-s. Sun (1995) The composition of the Earth: Chemical Geology, 120, 223-253.

Montelli, R., G. Nolet, F.A. Dahlen, G. Masters, E.R. Engdahl and S.-H. Hung (2004) Finite-frequency tomography reveals a variety of plumes in the mantle: Science, 303, 338-343.

Morgan, W.J. (1971) Convection plumes in the lower mantle: Nature, 230, 42-43.

Peng, Z.X., J. Mahoney, P. Hooper, C. Harris and J. Beane (1994) A role for lower continental crust in flood basalt genesis? Isotopic and incompatible element study of the lower six formation of the western Deccan Traps: Geochimica et Cosmochimica Acta, 58, 267-288.

Peng, Z.X. and J.J. Mahoney (1995) Drillhole lavas from the northwestern Deccan Traps, and the evolution of the Réunion hotspot mantle: Earth and Planetary Science Letters, 134, 169-185.

Peters, B.J., J.M.D. Day and L.A. Taylor (2016) Early mantle heterogeneities in the Réunion hotspot source inferred from highly siderophile elements in cumulate xenoliths: Earth and Planetary Science Letters, 448, 150-160.

Peucat, J.-J., M. Jayananda, D. Chardon, R. Capdevila, C.M. Fanning and J.-L. Paquette (2013) The lower crust of the Dharwar Craton, southern India: patchwork of Archean granulitic domains: Precambrian Research, 227, 4-28.

Peucker-Ehrenbrink, B. and B.-M. Jahn, (2001) Rhenium-osmium isotope systematics and the platinum group element concentrations: loess and the upper continental crust: Geochemistry Geophysics Geosystems, 2, 22 pp.

Richards, M.A., R.A. Duncan and V.E. Courtillot (1989) Flood basalts and hot-spot tracks: Plume heads and tails: Science, 246, 103-107.

Schilling, J.-G. (1973) Iceland mantle plume: geochemical study of Reykjanes Ridge: Nature, 242, 565-571.

Schoene, B., K.M. Samperton, M.P. Eddy, G. Keller, T. Adatte, S.A. Bowring, S.F.F. Khadri and B. Gertsch (2015) U-Pb geochronology of the Deccan Traps and relation to the end-Cretaceous mass extinction: Science, 347, 182-184.

Self, S., S. Blake, K. Sharma, M. Widdowson and S. Sephton (2008) Sulfur and chlorine in late Cretaceous Deccan magmas and eruptive gas release: Science, 319, 1654-1657.

Sheth, H.C., G.F. Zellmer, E.I. Demonterova. A.V. Ivanov, R. Kumar and R.K. Patel (2014) The Deccan tholeiite lavas and dykes of Ghatkopar-Powai area, Mumbai, Panvel flexure zone: Geochemistry, stratigraphic status, and tectonic significance: Journal of Asian Earth Sciences, 84, 69-82.

Wellman, P. and M.W. McElhinny (1970) K-Ar age of the Deccan Traps, India: Nature, 227, 595-596.

Wilson, J.T. (1963) A possible origin of the Hawaiian Islands: Canadian Journal of Physics, 41, 863-870.

Supplementary Information

5.2 Geological background and sample details

However, our primary goal was to assess the elemental and isotopic characteristics of Deccan Traps lavas, instead of adopting a detailed approach to flow exposures in specific localities, which has been attempted previously [e.g., Peng et al., 1994]. We sampled broadly throughout the western extent of the Deccan Traps from northerly exposures in the Kutch region of Gujarat to more southerly exposures near Mahabaleshwar in Maharashtra (**Figure 5.4**). Our sampling was most intensive in the Saurashtra region of Gujarat, for which there is relatively little published data despite the availability of lavas with comparatively primitive compositions [e.g., Melluso et al., 2006], and where fresh basaltic material can be found in dyke cores. In order to avoid inadvertently sampling material not related to Deccan Traps volcanism, we avoided sampling in areas where the spatial relationship between Deccan flows and mafic flows of different ages has not been mapped in detail and rather preferentially sampled in areas where all exposed volcanic rocks had bonafide Deccan provenance. We collected samples from singular localities, including the mantle xenolith-bearing volcanic plugs near Bhuj, the Amba Dongar carbonatite and nephelenite and lamprophyre dykes near Murud, Maharashtra. Many samples are aphanitic and display varying degrees of weathering and we removed altered rinds from weathered samples so that our analyses reflect only fresh interiors with the help of Kanchan Pande and staff members at IIT Bombay. For a few phaneritic samples, plagioclase,

clinopyroxene and olivine crystals were separated from bulk rock crush for separate analyses.

5.3 Analytical Methods

Sixty-four samples were selected for major and trace element analyses. From this sample set, 45 were selected for Os isotope and HSE analyses and 20 were selected for Sr and Nd isotope analyses. In addition, olivine, clinopyroxene and plagioclase separates and olivine powders recycled from He-isotopic analyses representing 9 samples were analyzed for their HSE abundances. With the exception of XRF element analyses, all other digestions and analyses were performed at the *Scripps Isotope Geochemistry Laboratory* (*SIGL*).

5.3.1 Major and trace element abundance analyses

Analysis of major and select trace elements, FeO titrations and loss on ignition were performed by X-ray fluorescence (XRF) at Franklin & Marshall University using a PW 2404 PANalytical XRF vacuum spectrometer according to procedures detailed in Boyd and Mertzman [1987] and on the Franklin & Marshall XRF Laboratory website (*http://www.fandm.edu/earth-environment/laboratory-facilities/xrf-and-xrd-lab*).

Precision and accuracy are estimated using repeat analyses of preparations of USGS standard BHVO-2 giving long-term reproducibility (2σ absolute standard deviation, n = 13) at ± 0.13 for SiO_2, ± 0.01 for TiO_2, ± 0.09 for Al_2O_3, ± 0.63 for FeO, ± 0.47 for Fe_2O_3, ± 0.10 for $Fe_2O_3^T$, ± 0.01 for MnO, ± 0.04 for MgO, ± 0.07 for CaO, ± 0.03 for Na_2O, ± 0.01 for K_2O, and ± <0.01 for P_2O_5. Accuracy for the average of 13 runs of BHVO-2

relative to USGS accepted values is estimated at <0.2 % for SiO_2 and TiO_2, <1 % for Al_2O_3, MgO, Fe_2O_3(T), CaO, Na_2O, P_2O_5, and <3 % for K_2O.

Trace element abundances were determined on 0.1g of homogenized rock powder. Powders were precisely weighed and digested at 140°C in a 1:4 solution of Teflon-distilled HNO_3 and Optima-grade HF for >72 hours. Total procedural blanks and rock standards BHVO-2, BCR-2 and BIR-1 were digested in batches with the samples. After drying down, the samples were taken up twice in Teflon-distilled HNO_3 and digested for >1 hour. Digested powders were diluted by a factor of 5000 in a dilute HNO_3 solution and doped with a 1 ppb In solution to monitor instrumental drift. Clear solutions were measured using a *ThermoScientific iCAPq-c* quadrupole inductively coupled plasma mass spectrometer (ICPMS) in standard mode. Reproducibility of the rock standards was generally better than 3 % (RSD) for standards, and element abundances were generally within given errors (1σ standard deviation) on the recommended values. Trace element concentrations determined by ICPMS generally agreed with those determined by XRF.

5.3.2 Sr-Nd isotopic analyses

0.1 to 0.15 g of homogenized rock powder of fresh basalt interior fragments were weighed into Teflon beakers and digested in a 1:4 mixture of Teflon-distilled HNO_3 and Optima-grade HF (72 hours), dried down and subsequently equilibrated in Teflon-distilled HNO_3 (24 hours) and Teflon-distilled HCl (24 hours) until clear solutions were achieved. Digested powders were taken up in 1 mL of 2.5M HCl: 1M HF and passed through a preliminary cation exchange column containing pre-cleaned AG-50W X8 resin. Major

elements, Sr, large ion lithophile elements (LILE) and rare earth elements (REE) were sequentially washed off in 2.5M HCl: 1M HF (major elements and Sr), 2M HNO_3 (LILE) and 6M HCl (REE). Aliquots containing Sr were taken up in 1 mL 4M HNO_3 and passed through a column containing Eichrom Sr-Spec resin. After eluting 3 mL 4M HNO_3 into REE cut, Rb and Sr were sequentially washed off and collected in 6 mL 4M HNO_3 and 2 mL 0.05M HNO_3, respectively. Aliquots containing the REE were taken up in 1 mL 0.25M HCl and passed through a column containing Eichrom LN-Spec resin, where REE were sequentially washed off in 0.25M HCl (light REE, 2 mL discarded and 2 mL collected for Nd) and 0.75M HCl (heavy REE, HREE). Isotopic compositions of Sr and Nd were measured as metals in positive-ion mode on a *ThermoScientific Triton* thermal ionization mass spectrometer (TIMS). Blank contributions were monitored by analysis of Sr and Nd abundances on the iCAP-q ICPMS using stock solutions diluted to 0.01, 0.1, 1, 5 and 10 ppb. Using these data, we constructed a calibration curve using a least-squares regression forced through 0,0 and determined blank abundances using this curve. The r-squared fits for the Sr and Nd calibration curves were >0.99. The Sr blanks averaged 460 pg and had a measured $^{87}Sr/^{86}Sr$ of 0.70782. The Nd blanks averaged 61 pg and could not be precisely analyzed for their $^{143}Nd/^{144}Nd$ due to the very small available quantity; consequently, the natural $^{143}Nd/^{144}Nd$ abundance of 0.5128 was used for blank corrections. Blanks were <<1% of measured Sr and Nd abundances. Long-term precision of isotopic measurements was monitored by repeated measurements of NIST NBS987 (Sr) and La Jolla (Nd) standards, with results of 0.710234 ±0.000019 (n = 6) and 0.511836 ±0.000004 (n = 5).

5.3.3 Os isotopic analyses and highly siderophile element abundances

Osmium isotope and HSE abundance analyses were performed according to methods described in Day et al. [2016]. Homogenized powders were precisely weighed and digested in sealed borosilicate Carius tubes with 'spikes' and 10 mL of a 2:3 mixture of multiply Teflon-distilled HCl and Teflon-distilled HNO_3 that had been purged of Os. Powders were equilibrated with isotopically enriched multi-element HSE spikes (^{99}Ru, ^{106}Pd, ^{185}Re, ^{190}Os, ^{191}Ir, ^{194}Pt); approximately half were enriched with a spike containing a set Re/Os ≈ 0.25 and the remainder were spiked for Re and Os separately. Replicate analyses revealed no significant difference between samples spiked with the combined Re-Os spike and the separate Re and Os spikes. Samples were digested at 240°C in an oven for 72 hours. Osmium was then triply extracted from the acid using CCl4, back-extracted into HBr [Cohen & Waters, 1996] and purified by micro-distillation [Birck et al., 1997]. Rhenium and platinum group elements were recovered and purified from the residual solutions by anion exchange separation [Day et al., 2016], and then analyzed on a *Thermo Scientific iCAPq-c* ICPMS in standard mode. Isotopic compositions of Os were measured in negative-ion by peak-jumping on the Triton TIMS and were oxide and fractionation corrected using ^{192}Os/^{188}Os = 3.08271. Concentrations of Os were determined from the same data using a ^{190}Os spike subtraction, and were appropriately blank-corrected. Repeated measurements of 36 and 72 pg UMCP Johnson-Matthey standards were used to monitor precision of the Os-isotopic measurements, and averaged 0.11397±0.00059 (2σ, *n* = 23). Total procedural blanks for Os analyses (*n* = 8) had an average corrected ^{187}Os/^{188}Os of 0.2748 and [Os] of 2.2 ±2.3 pg. Measured Re, Ir, Pt, Pd and Ru isotopic ratios for sample solutions were corrected for mass fractionation using the deviation of the standard average run on the day over the natural ratio for the element, and all reported values are blank

corrected. HSE abundances of these blanks (n = 14) were (in pg): 75-202 for Ir, 14-525 for Ru, 7-46 for Pt, 13-94 for Pd and 15-100 for Re. Full tabulated blank percentages for each sample are available in the *Appendix*.

5.4 Supplementary Results

5.4.1 Major and trace elements

Analyzed rock samples span a large compositional range, with SiO_2 spanning from 42 to 73 wt.%. Plotted with total alkali contents, these results reveal that the sample suite are geochemically classified as basalts, with alkali basalts occurring primarily in the Kutch region (**Figure 5.5**). This corresponds to our field observations. Two melanocratic, silicic rocks were analyzed: a rhyolite from the Saurashtra region (sample DC14-29) and a trachyandesite from the Girnar volcanic complex of Saurashtra (sample DC14-40A). Several basaltic andesites and one basanite were also collected from the Saurashtra region, making it the most compositionally diverse sampled region of our dataset. The sample suite includes both primitive (up to MgO = 15.7 wt.% and Mg# = 84) and evolved (to MgO = 1.3 wt.%, Mg# = 39, excluding highly silicic samples) rocks. The majority of the high-MgO samples come from Kutch, however a number of samples, including basalts from Saurashtra dykes, flows from the Kalsubai volcanic complex, and both intrusive and extrusive rocks from the Mumbai area have MgO > 10 wt.%. Conversely, high-Ti (TiO_2 > 1.5 wt.%) samples from Saurashtra and samples from the Deccan "main sequence" near Mahabaleshwar tend to have more evolved compositions (MgO commonly < 8 wt.%). Although our strategy was to sample primarily fresh, primitive samples, which tend to have

the highest concentrations of the HSE, only five of our samples have MgO > 12 wt.%, despite documentation of picrites in the areas that we sampled.

The samples comprise both fresh (LOI = 0.7 wt.%) and altered (up to LOI = 7.6 wt.%) rocks. Abundances of Al_2O_3 generally reflect the control of plagioclase accumulation (7.9-19.2 wt.%) with corresponding variability in K_2O (0.11-7.38 wt.%) and CaO (1.8-13.5 wt.%). Ranges of Ni (0.9-486 ppm) and Cr (12-1649 ppm) also indicate significant olivine (± clinopyroxene) accumulation in some samples. Variable Cu contents (12-369 ppm) imply that sulfide saturation has affected some lavas.

Correlations between MgO and TiO_2, Al_2O_3, Fe_2O_3(T) and CaO are evident when considering all sampled localities (**Figure 5.6**), including exotic lithologies such as lamprophyres. Remarkable enrichment in TiO_2 for a given MgO exist amongst the Kutch basanites and Pavagadh lavas, implying that these derived from melt batches with relatively high TiO_2 contents [e.g., Prytulak & Elliott, 2007]. In contrast, highly evolved samples, including the Saurashtra rhyolite and Girnar trachyandesite, show magnetite control on TiO_2 compositions. A complex relationship between MgO and Al_2O_3 indicates a prominent role for olivine, clinopyroxene and plagioclase fractionation, and precludes determination of an accurate MgO content for the Deccan parental magma. Notwithstanding, the inflection point of many other MgO-major/minor element arrays lies around 7 to 8 wt.% MgO.

Correlations between MgO, major and minor elements reveal strong fractional crystallization controls (**Figure 5.6**). An inflection point exists on a plot of Cu versus Mg at MgO ≈ 7 wt.% MgO, implying that this is the threshold below which sulfide saturation began affecting bulk rock compositions. A similar inflection point exists around 8 wt. % MgO for plots of Ni and Cr, consistent with removal of sulfide and spinel (magnetite). It is notable, however, that several of the most primitive samples lie on parallel trend with lower Ni contents for a given MgO, implying they may have derived from a compositionally distinct parental magma with a similar differentiation history. Notwithstanding this evidence for significant mineral fractionation, there is a robust negative correlation between MgO and Y/Ho, suggesting that such "canonical" ratios may remain relatively unaltered through extensive crustal transits. Primitive mantle-normalized [McDonough & Sun, 1995] La/Yb ratios do not show such a correlation to MgO, implying that they have been disturbed during crustal assimilation.

Primitive-mantle normalized trace element contents [McDonough & Sun, 1995] (**Figure 5.7**) reveal variably steep incompatible element patterns. The steepest patterns are observed among basalts and basanites from Kutch and Pavagadh, while the flattest patterns are observed in flows near Kalsubai, basaltic dykes from the Maharashtra coast and low-Ti basalts from Saurashtra. High-Ti basalts from Saurashtra show relatively steep patterns, with high-Ti Girnar basalts showing characteristic relative depletions in Zr and Hf. Kutch, Pavagadh and high-Ti Saurashtra samples all show strong relative depletions in Cs and generally have relative enrichments in Ta without being enriched in Nb. The REE patterns amongst this subset show smooth negative trends with occasional depletions in Y relative

to the middle REE. Basalts comprising the flattest trace element patterns also have flat middle-heavy REE trends with strong relative depletions in Ti. Relatively flat patterns among samples from near Mumbai also show characteristic relative enrichments in Rb and depletions in Sr. All samples from Kalusbai, which are among the flattest trends, possess relative depletions in Nb and Sr, and many also possess a strong relative depletion in K.

Nephelenite and lamprophyre dykes near Murud, Maharashtra show enrichments in incompatible trace elements relative to basalts from the same locality. One lamprophyre sample exhibits relative depletions in Th and U and relative enrichments in K, Pb and Sr, while the other sampled lamprophyre, and the nephelenite have opposing patterns across K, Pb and Sr, and notable relative enrichments in Sm. Two dyke samples from the same locality have strong relative enrichments in Cs, which are not observed in any other samples across the Deccan. These complex patterns may be a result of unusually low degree of partial melting combined with fractional crystallization of unique phases during emplacement through normal faulting along the western Indian seaboard in the waning stages of Deccan volcanism.

5.4.2 Highly siderophile elements

Within the Deccan suite, HSE contents are highly variable, but are generally depleted relative to primitive upper mantle (PUM) [Becker et al., 2006] (**Figure 5.8**). For example, Os concentrations range from 4 ppt to more than 1 ppb, and Pd concentrations from 99 ppt to more than 21 ppb, with the highest concentrations generally found in the low-Ti Saurashtra group. Concentrations of Ir are generally low (0.008-0.839 ppb), with

many samples possessing Ir within the range of our total analytical blanks, meaning that blank approaches 100% of the measured Ir in these samples (**Table 5.7**). These concentrations approach those of Réunion cumulates and basalts [Peters et al., 2016] only at the highest ranges; many samples are markedly depleted relative to Réunion and global OIB.

Olivine and clinopyroxene separates have relatively flat PUM-normalized [Becker et al., 2006] HSE patterns (**Figure 5.9**), whereas plagioclase separates show more fractionated patterns with relative enrichments in Pt, Pd and Re. All but one separate (olivine separate DC14-47B) show relative depletions in Ir, with concentrations ranging from 0.0004-1.478 ppb. HSE concentrations are generally enriched relative to their host rock, whereas in clinopyroxene and plagioclase separates, HSE concentrations are relatively depleted.

5.4.3 Sr-Nd-Os isotopic compositions

Measured $^{87}Sr/^{88}Sr$ ratios ranged from 0.70386 to 0.71197. Coupled with a range in $^{87}Rb/^{86}Sr$ ratios of 0.005 to 0.09, these age-corrected to a similar range from 0.70383 to 0.71195 at 65 Ma. Measured $^{143}Nd/^{144}Nd$ ranged from 0.512839 to 0.511806, age-correcting to 0.511701 to 0.512733 (or -18.3 to 1.9 in ε units) at 65 Ma with $^{147}Sm/^{144}Nd$ ratios of 0.16 to 0.32. These results are well within the range of published Deccan Sr-Nd isotope data [e.g., Mahoney et al., 1982, 1985, 2000; Cox & Hawkesworth, 1985; Lightfoot et al., 1987, 1990; Lightfoot & Hawkesworth, 1988; Peng et al., 1994, 1995, 1998; Simonetti et al., 1998; Melluso et al., 2002, 2006; Sheth et al., 2008; Crocket et al., 2008;

Vanderkluysen et al., 2011], which span to much more enriched (crustal signatures) than our own ($^{87}Sr/^{88}Sr_T$ = 0.703-0.786; $^{143}Nd/^{144}Nd_T$ = 0.5114-0.5129). The most enriched samples are DC14-28 and 59 ($^{87}Sr/^{86}Sr_T$ of 0.711954 and 0.709875, respectively and εNd_T of -15.0 and -17.3, respectively). A strong negative correlation exists between $^{87}Sr/^{86}Sr$ and $^{143}Nd/^{144}Nd$ (r^2 = 0.77, excluding nephelenite sample 79; **Figure 5.2**). Samples with moderately enriched Sr-Nd isotopic signatures are spread throughout all measured localities. The range of Sr-Nd-Pb compositions found in the Deccan has widely been ascribed to variable crustal assimilation, with possible distinct contributions from lower and upper crust, or to assimilation of a heterogeneous group of contaminants [e.g., Peng et al., 1994].

Osmium-isotopic compositions are highly variable, spanning compositions consistent with assimilation of continental lithospheric mantle, to highly radiogenic crust (0.1186 to 1.44). Some samples are clearly disturbed with unsupported Os isotopic compositions, after age-correction (γOs = -134 to 1033). Accounting for these samples, and those with lithospheric contamination the average γOs of samples with high Os (>0.5 ppb) concentrations is +2.5 ±3.7. Correlations between $^{187}Os/^{188}Os$ and $^{87}Sr/^{86}Sr$ data are indistinct, even when excluding lamprophyre sample DC14-83B, but samples do not simultaneously possess relatively radiogenic Sr and relatively radiogenic Os. In contrast, there is a distinct negative correlation between $^{187}Os/^{188}Os$ and $^{143}Nd/^{144}Nd$ (r^2 = 0.41, sample DC14-83B excluded).

5.5 Supplementary Discussion

5.5.1 Post-emplacement alteration

Nearly all Deccan Traps outcrops show evidence for weathering and alteration, which is sometimes extensive. Zeolite-filled vesicles (i.e., amygdules) were present in at least a third of our total sample set. Nonetheless, we were able to confidently remove these secondary minerals from samples analyzed in this study. We find positive trends between LOI and Na_2O, P_2O_5, Sr, Nb, Ta, Ba and the LREE (**Figure 5.10**) in these samples. The trends gradually diminish with increasing atomic mass among the REE, demonstrating a relationship between fluid mobility and enrichment of these elements in rocks with high LOI. Although the maximum extent of the trends are defined by the coastal lamprophyre dykes, which are probably enriched in these elements because of their magmatic histories, it is difficult to deconvolve the relative effects of magmatic and weathering processes acting on the coastal rocks. Given the high LOI of these rocks, the latter certainly plays some role, however lamprophyres in particular can have high magmatic volatile contents that may also strongly alter their bulk chemistry [e.g., Esperança & Holloway, 1987]. The presence of such enrichments at high LOI raises the possibility that alteration exists at moderate LOI, even though it is not clearly visible in **Figure 5.10**. Wood et al. [1976] noted significant mobilization of Sr and LREE during zeolite facies metamorphism of Icelandic lavas, but little mobility of the high field strength elements (HFSE) including P, Zr, Nb and Ta. Analyses of weathered material from metamorphic lower crustal rocks led Mongelli et al. [1998] to conclude that modest, but significant amounts of these elements can be lost during protracted surface weathering.

Although the trends between LOI and elemental abundances do not affect every rock, the observed trend may affect rocks with as low as ~2 wt.% LOI. Additionally, enrichment in the affected elements is greatest in high and moderate LOI rocks from highly eroded volcanic complexes, such as Bhujia Hill (sample DC14-05) and Girnar (samples DC14-40A and 41). If topographic relief can be related to the degree of weathering evidenced by these trends, then the moderate LOI (many >2 wt.%) found in main sequence basalt flows near Mahabaheshwar, where chemostratigraphic divisions rely on accurate knowledge of elemental concentrations, requires that these samples receive extra scrutiny. Notwithstanding, we note many rocks with extremely high LOI that do not show signs of elemental perturbation. At least some of these are samples were collected from roadcuts, indicating that subterranean basalts may have been subjected to infiltration of low-temperature fluid that did not remove mass from the rock.

5.5.2 The role of degassing and a possible role in atmospheric chemistry

Eruptions of CFB represent the most intensive periods of volcanic activity known in Earth history [e.g., Richards et al., 1989; Self et al., 2008]. Although the primary constituents of volcanic gases include H_2O, CO_2 and SO_2 or H_2S which affect only the volatile mass balance of a lava, gaseous halides, sulfides, oxides, hydroxides and flourides can complex with immobile metals to form volatile compounds [Symonds et al., 1987, 1992; Craciun et al., 2010]. These compounds may be lost to the atmosphere, or may sublimate to form mineral condensate deposits, as has been observed at Piton de la Fournaise on Réunion Island [Nativel, 1972; Toutain & Meyer, 1989; Gannoun et al., 2015]. Analogous gas condensates for the Deccan have likely been entirely lost to

weathering (see above), however the geochemical evidence for extensive degassing is preserved in lavas, which are the residuum after evaporation of metals. In recent decades, gas condensates have been recognized for their enrichment in Re and Os [Crocket, 2000; Mather et al., 2012], despite their high condensation temperatures [Lodders, 2003]. Gannoun et al. [2015] noted strong Re enrichments in gas sublimates from Piton de la Fournaise relative to nearby lavas, but no relative enrichment in Os, despite notable concentrations (88-157 ppt in thenardite assemblages and 13-132 ppt in aphthitalite-thenardite assemblages). Similarly, Toutain & Meyer [1989] reported Ir contents of up to 7.5 ppb in gas condensates, which are >1 to 2 orders of magnitude greater than concentrations measured in Piton de la Fournaise lavas (0.02-0.39 ppb) [Peters et al., 2016]. The amount of lava or gas required to generate such condensates, however, is unclear. However, the origin of Ir volatility in volcanic systems is unclear, since although Ir is found in fluoride deposits, the Ir-F compounds are unstable in the presence of water [Wood, 1987]. Volatilization of native sulfide compounds has the capability to strongly deplete the HSE from lavas [e.g., Crocket, 2000; Gannoun et al., 2015], but these are usually small in volume compared to other condensed phases.

The relative effects of degassing on HSE can be determined by comparing HSE concentrations to those of elements that behave similarly during partial melting and fractional crystallization, but do not form volatile compounds during magmatism [Day et al., 2010]. For example, Re, a known volatile phase, can be compared to Yb, an incompatible element and Cu, a chalcophile element (**Figure 5.11**); neither Yb nor Cu are known to form volatile compounds. Similarly to Canary OIB [Day et al., 2010] and

Coppermine CFB [Day, 2013], Re/Yb and Re/Cu decrease exponentially with decreasing [Re], implying that Re is lost at a faster pace than either Yb or Cu during Deccan magmatism. If the same relationship holds for Re/Os, variations in Re/Os due to degassing of Re would lead to lower Re/Os in samples containing residue and higher Re/Os in samples containing condensate. This may explain why $^{187}Os/^{188}Os$ model ages are highly variable for Deccan lavas, and also explains large variations in Re corrections to $^{187}Os/^{188}Os$, even for samples collected in the same locality. Similar patterns exist between [Ir], Ir/Cr (Ir and Cr both behave compatibly during melting) and Ir/Cu (**Figure 5.11**), and for analogous treatment of other HSE, however there is no relationship between [Re] and Ir/Yb and Ir/Cu. This may imply that the trends in **Figure 5.11B** do not trace outgassing, however the use of Ir/Yb ratios may be inappropriate because Yb is incompatible while Ir is moderately compatible; a correlation does exist between [Re] and Ir/Cr. The lack of correlation between [Re] and Ir/Cu may indicate that the role of sulfide volatilization was not as great for Ir as it was for Re, and rather Ir was degassed as a fluoride as it is on Réunion [Toutain & Meyer, 1989]. If the trends for Ir do reflect degassing, they do not affect PUM-normalized depletions of Ir relative to Ru (or similarly enrichments in Pd relative to Pt), since $(Ru/Ir)_{PUM}$ displays a flat pattern relative to [Ir]. Given the lack of significant correlation between MgO and HSE, it is likely that silicate fractionation played less of a role in determining HSE concentrations than other processes, and degassing may help explain some of the variations, particularly variable depletions in Ir and Re. However, it is more likely that thick Indian crust and lithosphere had a commanding role to play in the elemental systematics of Deccan CFB.

5.5.3 Environmental impacts of CFB volcanism

Common volcanic gases such as H_2O and CO_2 that were presumably released in Deccan Traps eruptions may have had a major impact on the Cretaceous environment [e.g., McLean, 1985], especially as the Deccan eruptive lifecycle was longer than previously thought [Widdowson et al., 2000; Cucciniello et al., 2015]. Degassing of CO_2 during CFB volcanism may be insufficient to affect global climates [Wingall, 2001; Self et al., 2006], but emplacement of lavas over carbon-rich sedimentary rocks in the Deccan may have caused contact metamorphism that generated greenhouse gases with more acute effects [Ganino & Arndt, 2009]. Given the estimated total volume of Deccan eruptions, the total release of S- and Cl-bearing gases would be on the order of 10^6 teragrams [Self et al., 2008]. The coincidence of a flood basalt emplacement with many mass extinction events has been noted by many researchers [e.g., Chung et al., 1998; Kamo et al., 2003; Schoene et al., 2010], verifying the potential of these eruptions to affect the global environment. In the case of the Deccan, these arguments are complicated by the contemporaneous Chicxulub impact, which would have equal or greater potential to affect global climates [Pierazzo et al., 1998; Schulte et al., 2010]. Further study of the Deccan and other CFB therefore has the potential to enhance our grasp of the geological and biological histories of the Earth.

5.5.4 Assimilation of lithospheric and crustal materials

The Dharwar craton, which underlies much of the Deccan Traps, represents more than 200 km of continental crust and lithosphere [Gupta et al., 1991], with 33-52 km of this representing crust [Gupta et al., 2003]. In contrast, the crust thins to a minimum thickness

of <20 km south of the Narmada Rift, which correlates to a large positive Bouguer anomaly extending north from Mumbai and protruding both east and west at the Narmada Rift [Kaila, 1986]. Accordingly, there exists the potential for a large range of crustal and lithospheric assimilation for Deccan mantle-derived melts. In addition, complex arrays in Sr-Nd-Pb isotopic space have led many researchers to adopt multi-stage and multi-component mixing to explain the compositions of Deccan lavas, including distinct roles for lithospheric, lower and upper crustal materials. For example, common interpretations of the Ambenali formation, which primarily crops out in the Western Ghats, include contamination by low-ε_{Nd} and low-$^{87}Sr/^{86}Sr$ materials, variably envisioned as subcontinental lithospheric mantle (SCLM) [e.g., Lightfoot & Hawkesworth, 1988; Lightfoot et al., 1990] or lower crust [Mahoney et al., 1982]. Qualitative modeling efforts have also evoked specific crustal contaminants to explain anomalous trends found in commonly-cited chemostratigraphic units [e.g., Peng et al., 1996]. In some areas throughout the Deccan, however, age-corrected Sr-Nd isotopic compositions reveal a relatively minor role for crustal assimilation [e.g., Melluso et al., 2006; Sheth et al., 2014].

Our data range from isotopically enriched ($^{87}Sr/^{86}Sr_T$ = 0.711954, ε_{Nd} = -18.3, $^{187}Os/^{188}Os_T$ = 0.67132) to depleted ($^{87}Sr/^{86}Sr_T$ = 0.703834, ε_{Nd} =1.9, $^{187}Os/^{188}Os_T$ = 0.11797), and show clear assimilation trends when plotted versus elemental abundances (**Figure 5.1**). We consider the effect of SCLM, lower and upper continental crust [Peucat et al., 1989, 2013; Aulbach et al., 2016] on a Réunion-like Sr-Nd-Os isotopic and elemental composition. We use the calculated parental $^{187}Os/^{188}Os$ and [Os] values of Peters et al. [2016] and similarly project [Sr] = 57 ppm and [Nd] = 21 ppm from plots of MgO versus

Sr [Albaréde et al., 1997; DiMuro et al., 2014] and Nd [Albaréde et al., 1997; Bosch et al., 2008; DiMuro et al., 2014]. Isotopic compositions of Sr and Nd were then determined from isotope-element plots using the same datasets, and were set at $^{87}Sr/^{86}Sr = 0.704189$ and $^{143}Nd/^{144}Nd = 0.512902$. Empirical data were used to represent the composition of the assimilated reservoirs, and used measurements on regional upper and lower crustal crust where these were available; all of this information is tabulated in the *Appendix*.

The array of $^{87}Sr/^{86}Sr$ versus [Sr] does not conform to mixing between Réunion, upper and lower continental crust, but rather lies within the mixing lines for all three components (main text **Figure 5.1A**). A mixing line fit to the majority of the data represents preliminary assimilation of lower crustal materials representing ~25% of the magma's Sr mass followed by assimilation of upper crustal materials representing 10-40% of the new magma Sr mass. Few empirical constraints exist on the relative mass involvement of crust during assimilation, but it is easy to envision a Sr-poor mantle melt being affected by crustal materials to this degree. A similar mixing relationship exists between a Réunion source and the lower continental crust for Nd isotopes (**Figure 5.12**), which explains the majority of the Nd data without the need for secondary assimilation of upper continental crust. However, some basaltic samples are enriched in Nd relative to what would be expected from this mixing relationship alone, and may have been subject to enrichment by fractional crystallization, which would not have affected their $^{143}Nd/^{144}Nd$. Alternatively, they may represent a parental magma batch that formed after an unusually low degree of partial melting of a Réunion-like source. This would again enrich REE without affecting initial $^{143}Nd/^{144}Nd$, and would provide a satisfactory explanation for the two lamprophyre

samples, which lie off the main trend in the same direction. A melt of this composition is not easily generated by preliminary mixing of a Réunion-like source with an upper mantle domain, such as DMM or SCLM, both of which have less Nd than the projected Réunion source. An even more simplistic mixing scenario exists for Os isotopes, which show good fit around a binary mixture between a Réunion-like parental magma and lower continental crust (main text **Figure 5.12**). There is almost certainly a role for SCLM in the assimilation history of Os, however we do not plot the mixtures here because they visually crowd the image.

Multi-element plots show evidence for similar mixing histories (**Figure 5.2**). The negative correlation between $^{87}Sr/^{86}Sr_T$ and $^{143}Nd/^{144}Nd_T$ fits well in a two-stage assimilation scenario, in which a Réunion-like parental magma first assimilates a relatively large proportion of lower continental crust (visually estimated as 40-70% of the Sr-Nd mass) and smaller amounts of upper continental crust (0-40% by mass). This solution is not unique, however, and arrays in the same space may be created by a primary mixture between a Réunion-like parental magma and SCLM. However, one would expect the inflection of the secondary mixing curve (between the Réunion-SCLM material and upper continental crust) to be subparallel to the Réunion-upper continental crust mixing curve until unrealistically high amounts of SCLM are assimilated. Further, if the Sr-Nd isotopic systems were open to assimilation of SCLM, they would also likely be open to assimilation of lower continental crust, which would drag the data array below the SCLM-upper continental crust mixing curve even at low degrees of lower continental crust assimilation. In Nd-Os space, a subordinate role for UCC is seen, with primary mixtures occurring

between a Réunion-like parental magma and secondary assimilation of lower continental crust. Some samples, including the one analyzed main sequence lava, may be explained instead by a primary mixture of a Réunion-like parental magma and DMM, followed by assimilation of lower continental crust. However, we prefer a unified explanation for all of our data, some of which cannot be explained by such an assimilation history, and it is more likely that significant SCLM exists in the ascent pathways of liquid Deccan primary magmas than DMM. However, some studies invoke DMM or Central Indian Ridge-like MORB as an assimilation component responsible for the trace element and isotopic compositions of Deccan basalts [e.g., Melluso et al., 2006]. Despite clear Nd-Os and Sr-Nd isotope correlations, decoupling between the Sr and Os isotopic systems strongly implies that the two experienced distinct differentiation histories (**Figure 5.12**). Considering the dominant mineral hosts of Sr, Nd and Os, it is possible that the Os isotope system was closed to assimilation early in magma ascent, whereas Sr, which is bound mostly in late-crystallizing phases such as plagioclase, remained open to lithologies seen late in the ascent process, such as upper continental crust. Accordingly, decoupling of the Sr and Os isotopic systems does not imply a role for multiple mantle sources to Deccan magmas.

In both Nd-Sr and Nd-Os space, nephelenite sample DC14-79 lies far from the main data array, while lamprophyre samples DC14-80 and 83B lie far from the main data array only in Nd-Os space. This implies that both the Sm/Nd and Re/Os systematics are distinct during nephelenite genesis, but that only the Re/Os systematics are distinct during lamprophyre genesis, despite both lithologies being present in the same geographic region.

This may have occurred if the nephelenites were generated by lower degree of partial melting than the lamprophyres, generating lower Sm/Nd, but this degree of partial melting was sufficient for both to have initial Re/Os higher than and $^{187}Os/^{188}Os$ more radiogenic than basalts from other parts of the Deccan. The Re/Os of the nephelenite must have been still greater than that of the lamprophyre, however, because its initial $^{187}Os/^{188}Os$ is 0.67132, the greatest of the whole suite. In general, however, the clear trend toward our assigned Réunion endmember strongly implies that our selected representative composition reflects the composition of the Deccan parental magma.

5.5.5 A protracted ascent for Deccan magmas?

The clear coupling between the Sr-Nd and Nd-Os systems is not unusual amongst hotspot localities; however, a relationship between Sr and Os isotopic systematics may be more difficult to derive [Molzahn et al., 1996]. In the case of a Deccan, despite clear negative correlations between Nd isotopes and both Sr and Os isotopes, no relationship exists between Sr and Os isotopes themselves. The mineral hosts to these systems are distinct: Re and Os are found in sulfides, REE are strongly compatible in phosphates and Rb and Sr are generally found in silicates. Each of these phases have distinct cooling temperatures, with sulfides and phosphates generally crystallizing at high temperatures [e.g., Bhatnagar, 1969; Wendlandt, 1982] and silicates, such as plagioclase, crystallizing at relatively low temperatures. If the ascent of the Deccan parental magma through continental crust and lithosphere were protracted, the potential exists for the Re-Os and Rb-Sr systems to equilibrate at distinct times. Early-formed sulfides containing Re-Os would be shielded from the effects of late-stage assimilation of upper continental crust,

whereas the Rb-Sr system would be least likely to preserve evidence for assimilation of Sr-poor SCLM. If the Sm-Nd system remained open from lithospheric to upper crustal depths, it may preserve evidence for assimilation events experienced by both the Re-Os and Rb-Sr systems, thus creating the observed correlations. In order for this to occur, saturation and equilibration of sulfide and Sr- and Rb-bearing silicate phases must have occurred at distinct times.

Recent Ar-Ar geochronological work on the Deccan Traps have revealed that magmatism may have initiated as early as ~67 Ma in the far northern regions of the Traps [Cucciniello et al., 2015] and terminated as late as ~63 Ma in the far south [Widdowson et al., 2000], with both ages being well-resolved. This range of ages implies that Deccan CFB volcanism was significantly more protracted than previously thought [e.g., Courtillot et al., 1988; Richards et al., 1989; Jaeger et al., 1989], but may have had a duration of less than one million years [Schoene et al., 2015]. Our field observations noted few occurrences of paleosols, which has previously been used as evidence of a short-duration eruptive event [Mahoney et al., 1989], but may also simply indicate that volcanism was relatively continuous. The Sr-Nd-Os isotopic evidence indicate that magma ascents were elongated rather than brief, which supports the idea that Traps volcanism persisted for a long period of time.

5.5.6 HSE composition of the Deccan Traps

Despite the existence of primitive isotopic characteristics, there is compelling evidence that differentiation played a dominant role in the determination of lava HSE

signatures. Outside of Kutch, nearly all measured lavas show the characteristic "stepwise" break between relatively low concentrations of the IPGE and relatively high concentrations of the PPGE (**Figure 5.8**). This feature is common amongst CFB [e.g., Rocha-Júnior et al., 2012; Day et al., 2013] and likely results from sulfide saturation in evolved melts, causing rapid loss of IPGE to sulfide phases and preferential retention of PPGE in residual melts [e.g., Jamais et al., 2008]. This process can be traced on a plot of PPGE versus Cu (**Figure 5.13**), where PPGE contents below a certain level indicated by sulfur accumulation (traced by Cu) indicates previous extraction of sulfides. Many of our samples lie above the qualitative line separating S-saturated and S-undersaturated melts [e.g., Keays & Lightfoot, 2007, 2010; Day et al., 2013] but still overlap with the field of S-saturated West Greenland lavas [Keays & Lightfoot, 2007], which, considering the low MgO contents of many lavas, strongly implies they indeed represent S-saturated melts.

The effects of sulfide saturation and crustal assimilation on HSE concentrations can be effectively avoided by considering the HSE contents of early-formed mineral phases such as olivine. We reconstruct a parental magma composition by regressing Ir versus MgO data for mineral separates and determining concentrations of the remaining HSE using the HSE/Ir ratios of the olivine separates. We can then quantify the effects of sulfide extraction using the partitioning data of Jamais et al. [2008] and empirically-determined partition coefficients of Day [2013] (**Figure 5.13B**) and this assumed parental melt HSE concentration. With an assumed tholeiitic parental magma MgO composition of 16 wt.%, we model extraction of an olivine-clinopyroxene-orthopyroxene-plagioclase assemblage and assimilation of upper continental crust [Peucker-Ehrenbrink & Jahn, 2001; Nishimura,

2012]. Concentrations of MgO are monitored using experimentally-determined partition coefficients [Beattie, 1994; Bindeman & Davis, 2000; Adam & Green, 2006] to approximate sulfur saturation at ~8 wt.% MgO. At that point (~8% mass extraction), HSE partition coefficients are changed to reflect increased compatibility of IPGE relative to PPGE. Model results overlap measured concentrations of Saurashtra low-Ti and Maharashtra main sequence samples, which are some of the most evolved of the sample suite, and generally reproduce the range of PUM-normalized HSE concentrations measured in the lavas.

The model predicts relative depletions in Pd for evolved lavas despite input of a parental magma with modest enrichment in Pd, and this is reflected in the measured data for evolved lavas (**Figure 5.8**). A notable exception is found among main sequence lavas from near Mahabaleshwar (samples DC14-99, 103, 108 and 110), as well as two relatively high-MgO lavas from Saurashtra (samples DC14-20 and 31A), which preserve relative Pd enrichments. Given that main sequence lavas from the formations represented by these samples exhibit Sr-Nd-Pb evidence consistent with them being the least contaminated members of the main sequence [e.g., Peng et al., 1994], and that high-MgO lavas may be resistant to crustal assimilation, this may signify the persistence of a relative Pd enrichment present in the parental magma. Additionally, the model predicts relative enrichments in Ir for high-MgO lavas and relative depletions in Ir for lower-MgO lavas, an effect that would be compounded by degassing. This result closely matches the measured data, which show relative enrichments in Ir amongst primitive lavas from Pavagadh and coastal regions of Maharashtra, but generally flat-to-negative patterns across Ir elsewhere. One sample,

DC14-02, an alkali basalt from Kutch, does not follow these trends and instead has a nearly flat PUM-normalized pattern. Given its relatively unradiogenic $^{187}Os/^{188}Os$ (0.131578) and $^{87}Sr/^{86}Sr$ (0.703834) signatures, it is possible that this sample has experienced significant assimilation of SCLM, a result that is consistent with other samples from Kutch [Peters et al., 2016].

The results of any fractional crystallization model are input-dependent, and in the case of modeling HSE concentrations, the determination of partition coefficients is complicated by a number of factors unique to siderophile elements. For example, there is relatively little data regarding the partitioning of HSE into silicate phases, which may be significant [e.g., Brenan et al., 2003]. Additionally, selection of experimental conditions for determination of HSE K_D values includes additional variables, such as initial S content and FeS activity in melts, which are unnecessary while determining K_D for lithophile elements. However, use of the partition coefficients we select here has been successful in other applications [e.g., Day et al., 2013], so we accordingly support their continued use.

5.5.7 A Deccan-Réunion geochemical connection

The assimilation histories of Sr, Nd and Os isotopes measured on rocks from throughout the Deccan Traps clearly permit a primary role for a parental magma possessing a composition similar to that of Réunion (**Figures 5.2 & 5.12**). In addition, a clear chemo-physiographic link exists between the Deccan Traps and Réunion Island, which includes ancient volcanic centers along the Chagos-Laccadive Ridge, enriched signatures occurring in 34 Ma Central Indian Ridge basalts [Fisk et al., 1989; Duncan et al. 1990], and more

recent volcanism on the island of Mauritius [e.g., Moore et al. 2011]. Hotspot traces like this one exist elsewhere, including for the Kerguelen hotspot [Morgan, 1981] and the Hawaii-Emperor seamount chain [Wilson, 1963]. Displaced hotspots and CFB provinces, which display no clear physiographic link to other volcanic features, include the Ontong-Java Plateau, the Emeishan flood basalt, the North Atlantic Igneous Province, Iceland, the Canary Islands, the Comoros and many others. Some of these features are linked based on plate reconstructions and/or geochemical evidence [e.g., Saunders et al., 1997], however the Réunion hotspot provides the basis for the strongest link between canonical plume head and plume tail volcanism [Richards et al., 1989]. Notwithstanding, strong crustal and lithospheric signatures in the isotopic compositions of flood basalts can preclude positive identification of a geochemical link between Deccan and Réunion volcanism. Here, we have shown that Os isotopes show the least complex assimilation history of the Sr, Nd and Os isotope systems, and that Os would be most likely to preserve a deep source because it is primarily held in early-formed sulfides and because the crust is essentially devoid of Os. Modeled assimilation that presumes a Réunion-like parental magma to the Deccan can accurately predict the isotopic compositions of Deccan basalts, strongly suggesting that the two volcanic episodes are geochemically related. Given the singularity of the Réunion isotopic signature [e.g., Albarède et al., 1997; Vlastélic et al., 2005, 2007; Bosch et al., 2008; Füri et al., 2011; Peters et al., 2016], it seems most likely that a single mantle feature is responsible for both Deccan Traps and Réunion volcanism.

In addition to the Sr-Nd-Os isotopic evidence, there is also a clear link between the HSE compositions of Deccan and Réunion basalts. Using a calculated HSE composition

for a Deccan parental magma, we successfully modeled both the range and detailed features of HSE in Deccan basalts (**Figure 5.13B**). The HSE signature of this parental magma has a very similar pattern to one determined for Réunion [Peters et al., 2016], meaning that the HSE compositions of Deccan lavas could have arisen from a mantle source with a similar composition to the one fueling active volcanism on Réunion today. Taken together, these data provide strong evidence for a geochemical link between the initial flood basalt and waning OIB volcanism of the Réunion hotspot. It is plain that, whatever the exact physical construction of the Réunion hotspot mantle source, its ability to deliver magmas to Earth's surface is an enduring feature that can last for long periods of geologic time, despite mantle convection, interaction with tectonically-induced magmatism and other fundamental facets of mantle dynamics.

Figures

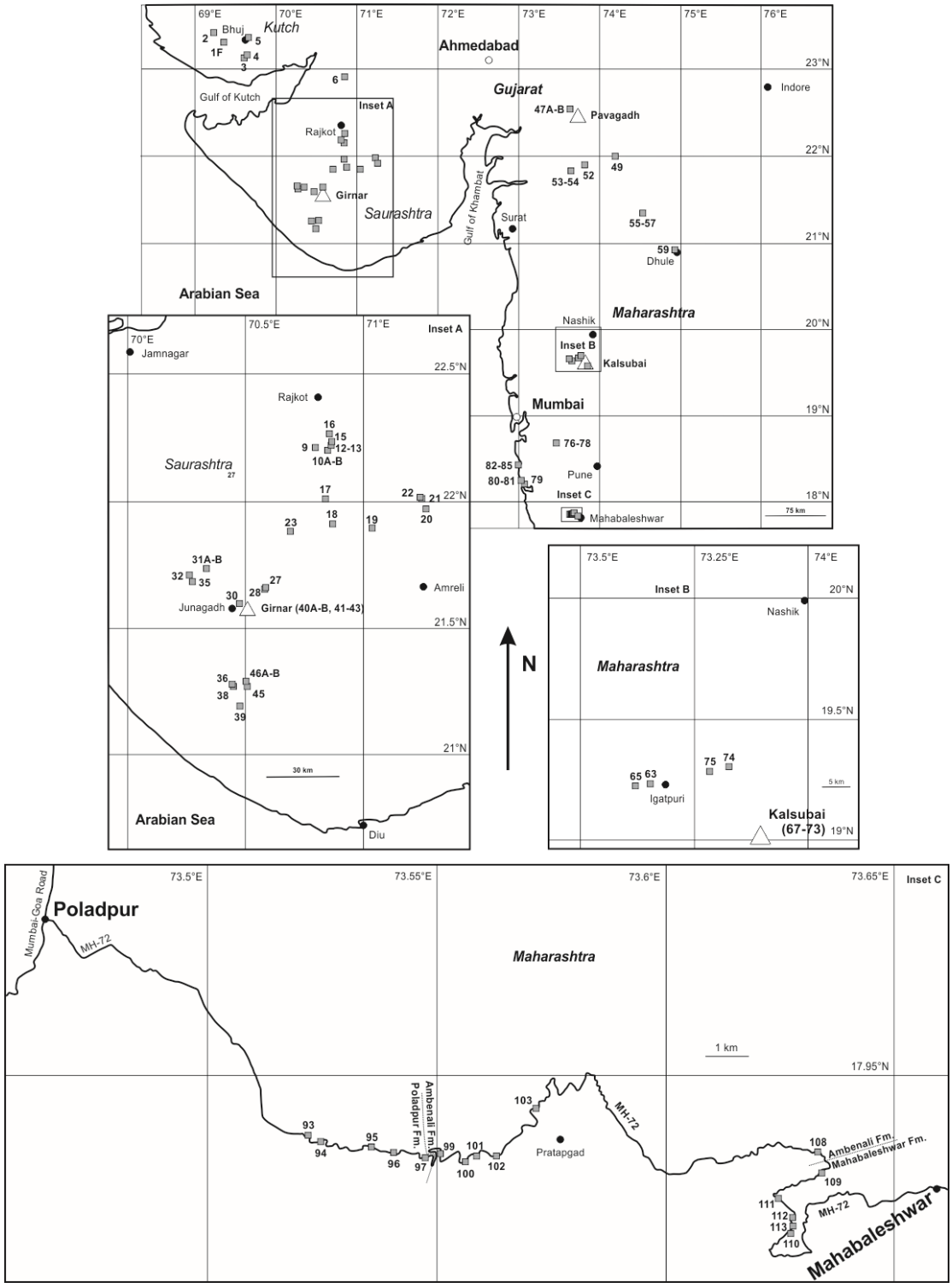

Figure 5.4: Map showing sampling locations of Deccan lavas.

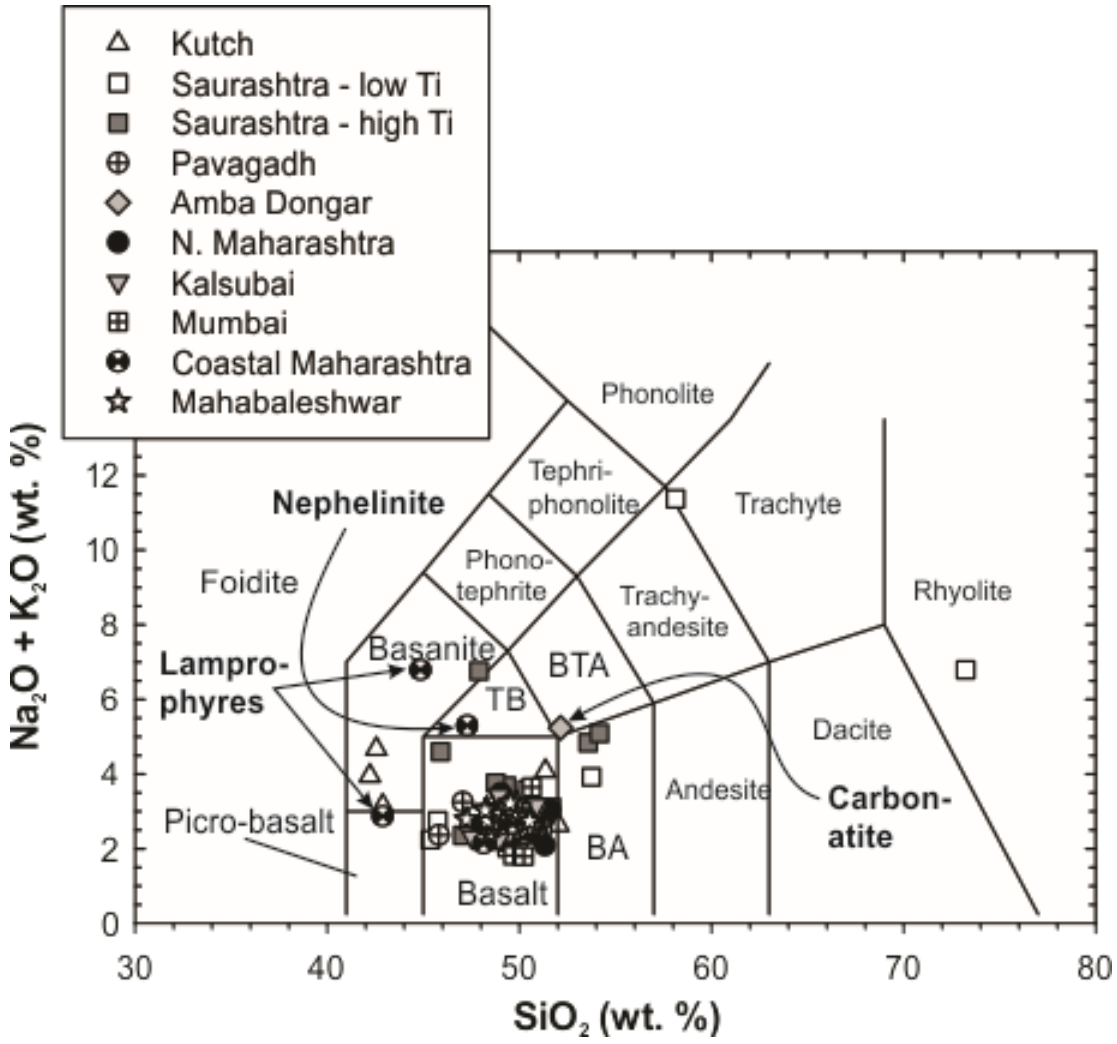

Figure 5.5: Total alkali versus silica plot for Deccan lavas.

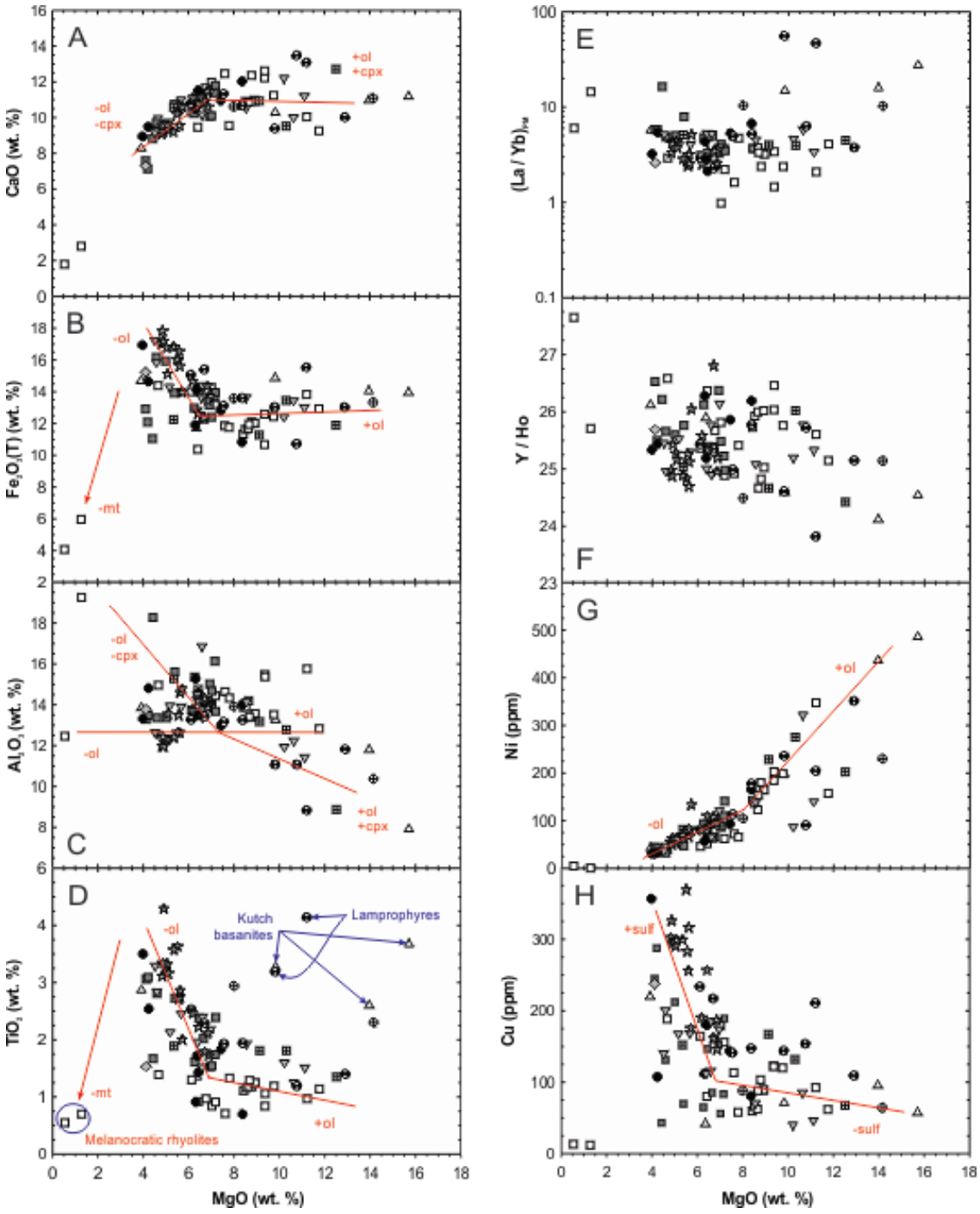

Figure 5.6: MgO versus major and minor elements with approximate fractionation pathways relative to an assumed melt composition. Symbols as in **Figure 5.5**.

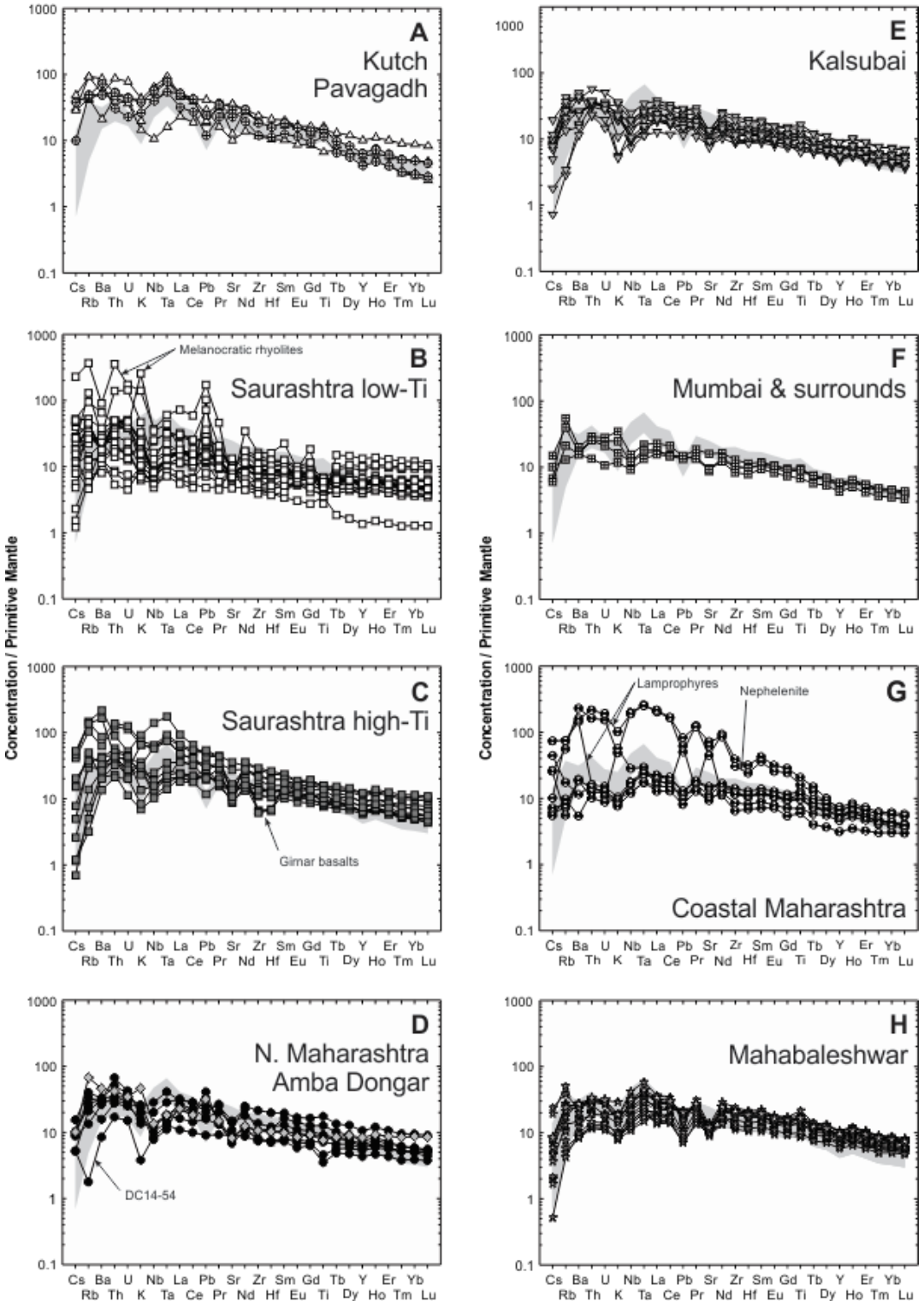

Figure 5.7: Trace element variation diagrams for Deccan lavas, normalized to primitive mantle [McDonough & Sun, 1995]. Gray field represent range of Réunion lava compositions (unpublished data). Symbols as in **Figure 5.5**.

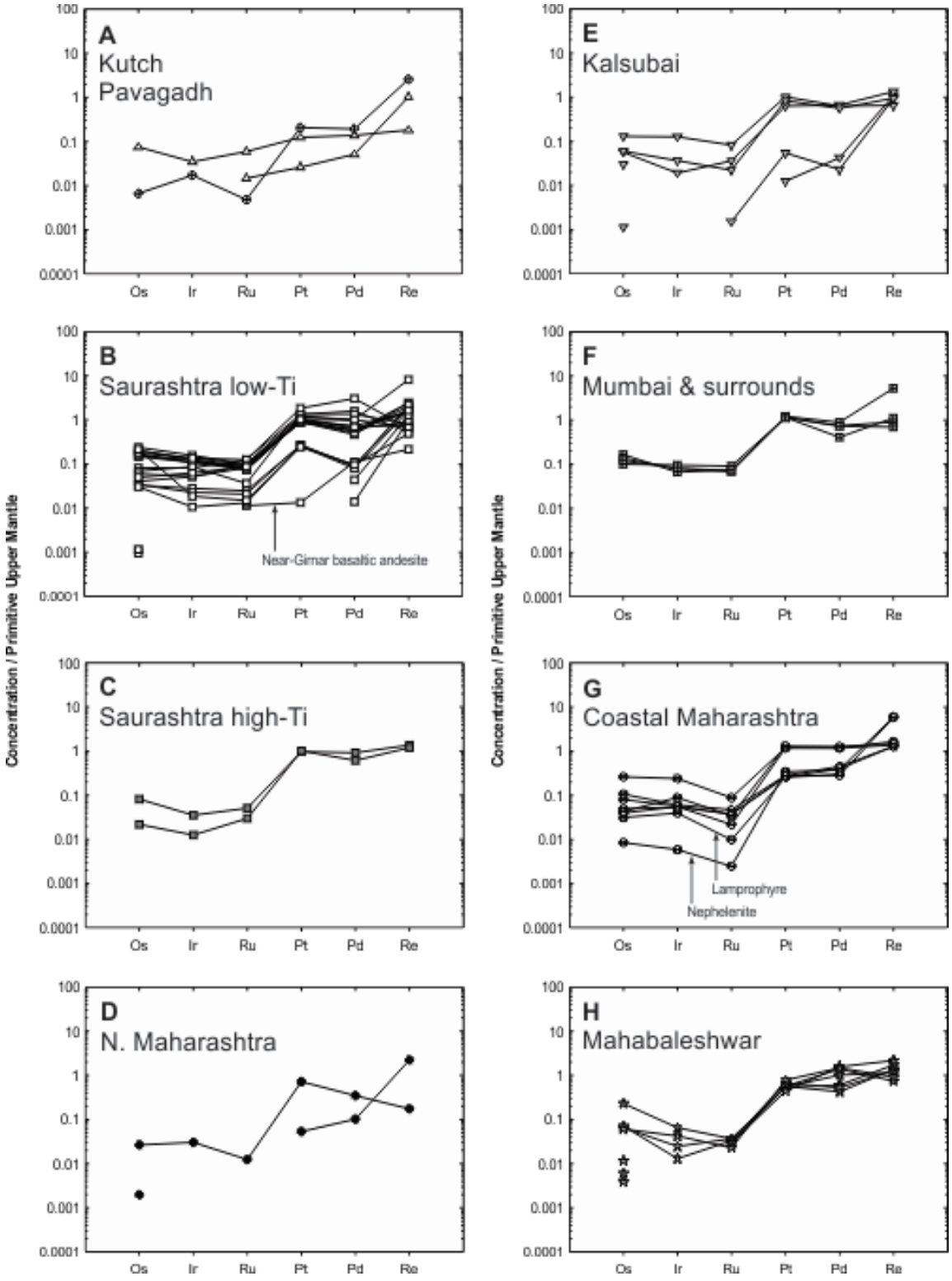

Figure 5.8: Primitive upper mantle [Becker et al., 2006] normalized highly siderophile element plots for Deccan lavas. Symbols as in **Figure 5.5**.

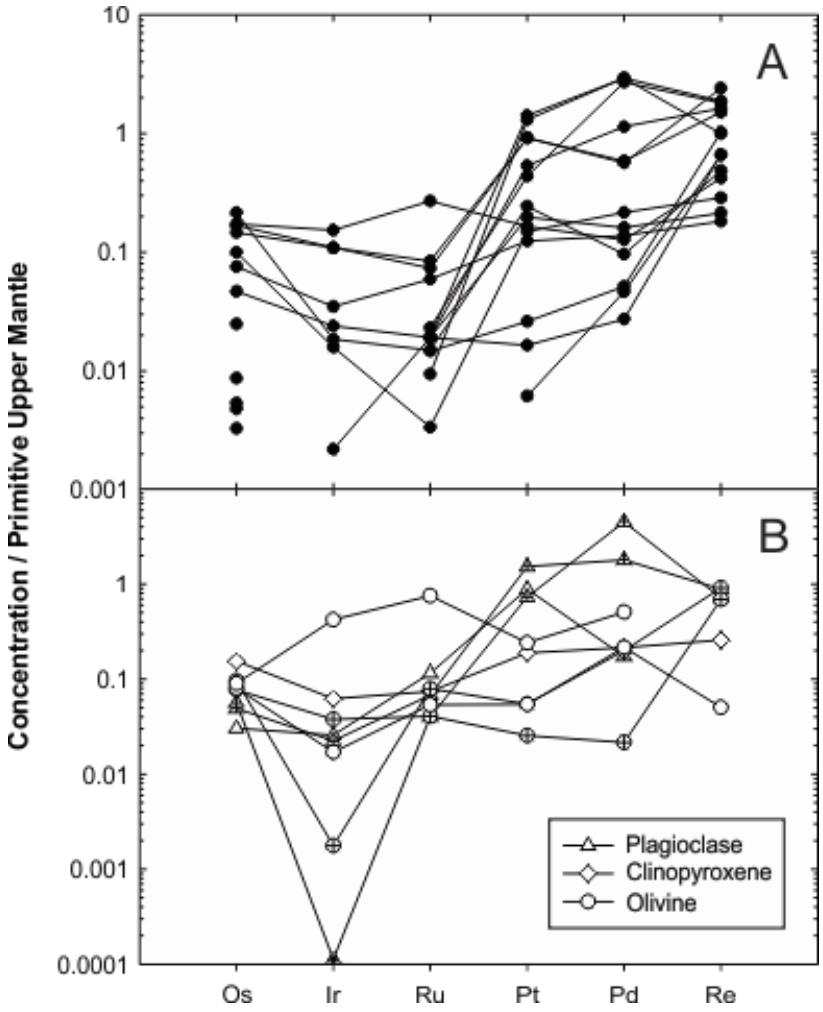

Figure 5.9: PUM-normalized [Becker et al., 2006] HSE concentrations for host lavas (A) and mineral separates (B).

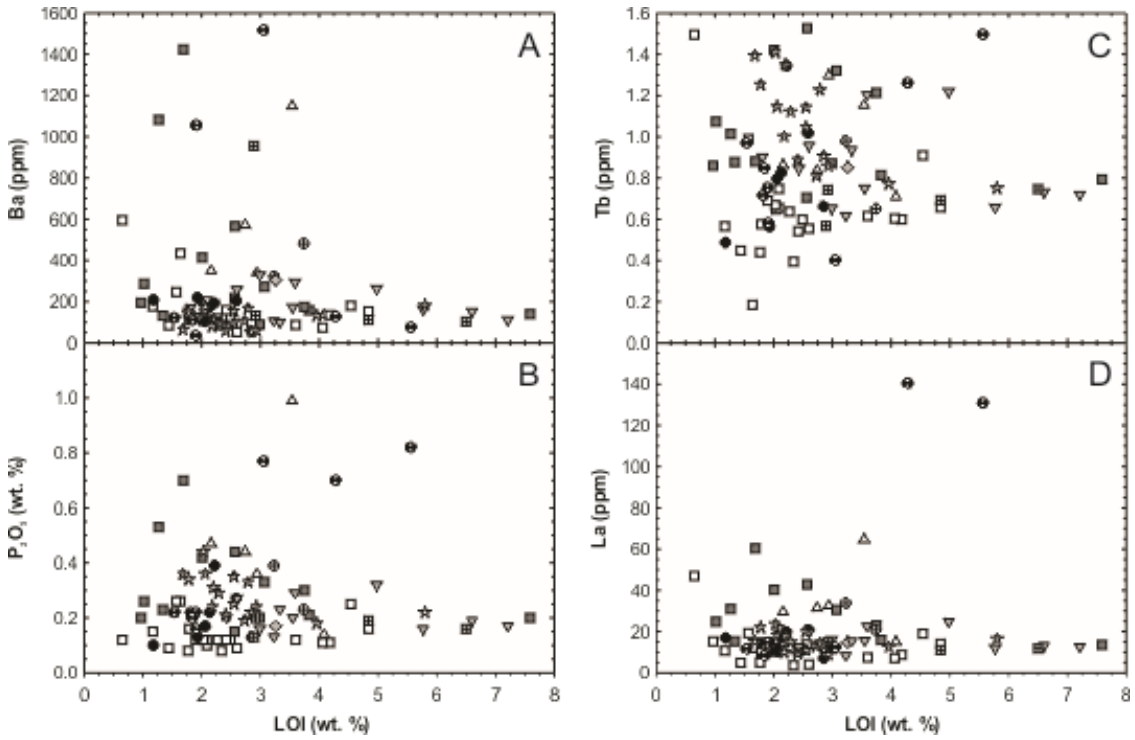

Figure 5.10: Loss on ignition versus elements suspected for post-emplacement alteration. The subordinate positive trend diminishes with increasing atomic number for rare earth elements and is virtually gone for atomic numbers greater than that of Tb. Symbols as in **Figure 5.5**.

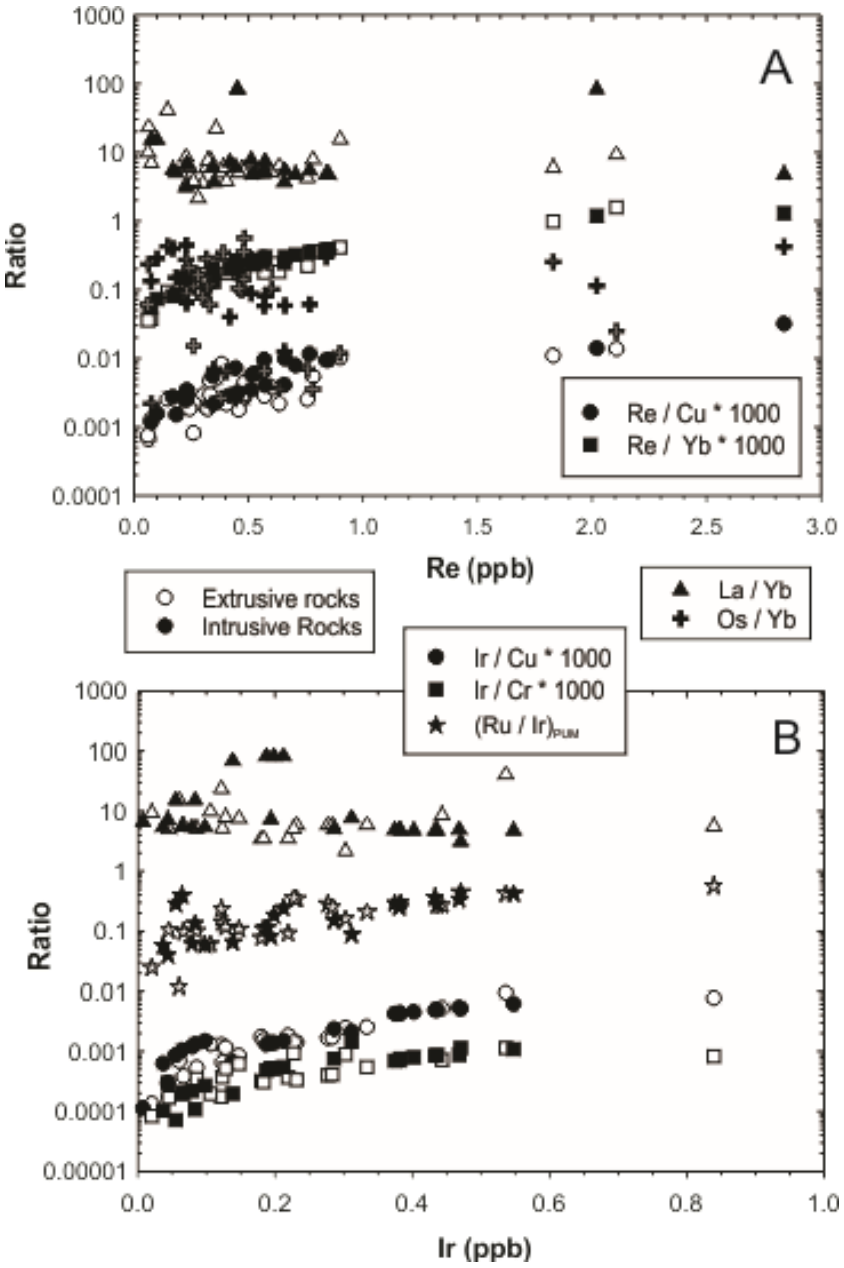

Figure 5.11: Re (A) and Ir (B) versus HSE/Cu and HSE/Yb ratios to trace the effects of degassing on Re and Ir contents. Plots of La/Yb and Os/Yb are shown for comparison, as these ratios should be unaffected by degassing. Filled symbols represent intrusive rocks (most commonly dykes) and open symbols represent extrusive lava flows.

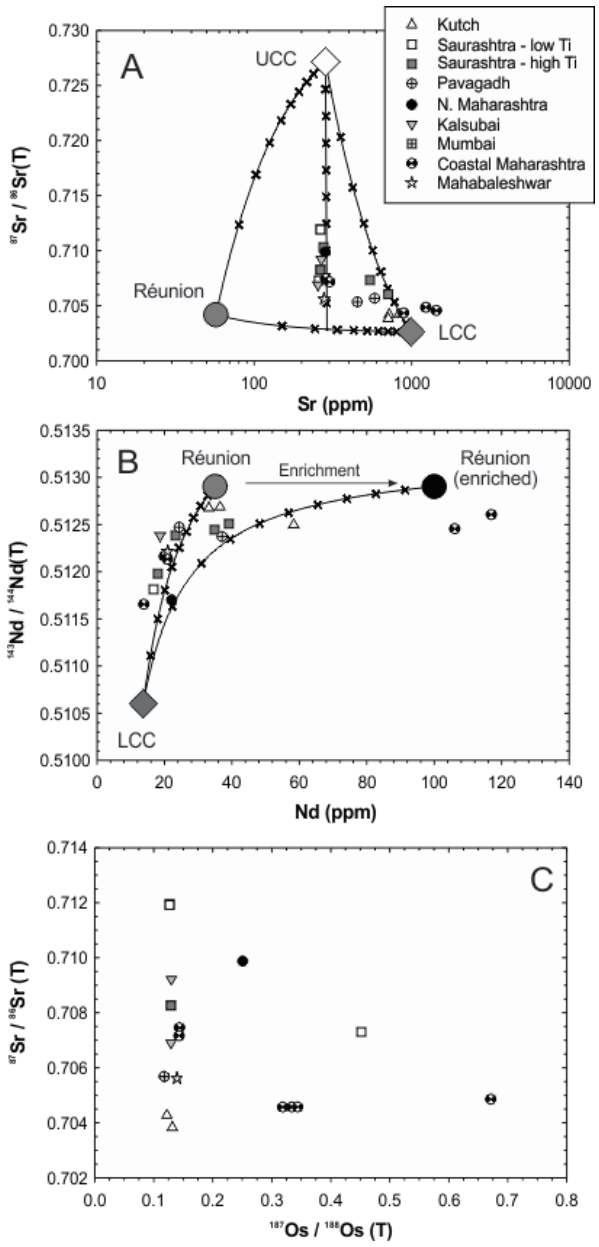

Figure 5.12: Plots of $^{87}Sr/^{86}Sr$ versus [Sr] (A), $^{143}Nd/^{144}Nd$ versus [Nd] (B) and $^{187}Os/^{188}Os$ versus [Os]. Compositions of reservoirs thought to contribute to the isotopic ratios of Deccan parental magmas are plotted with mixing lines denoted by 10% mass intervals. In (a), an intermediate mixing line is drawn illustrating the effect of sequential assimilation of lower continental crust (LCC) and upper continental crust (UCC). In (B), an arrow is drawn representing enrichment in Nd without changing $^{143}Nd/^{144}Nd$, however the placement of this line is arbitrary; Nd enrichment could occur at any point while maintaining this type of relationship (for example, as a result of partial melting or fractional crystallization). (C) Sr-Os isotopic array. No mixing models are shown in panel (C) due to the lack of correlation between Sr and Os (see text).

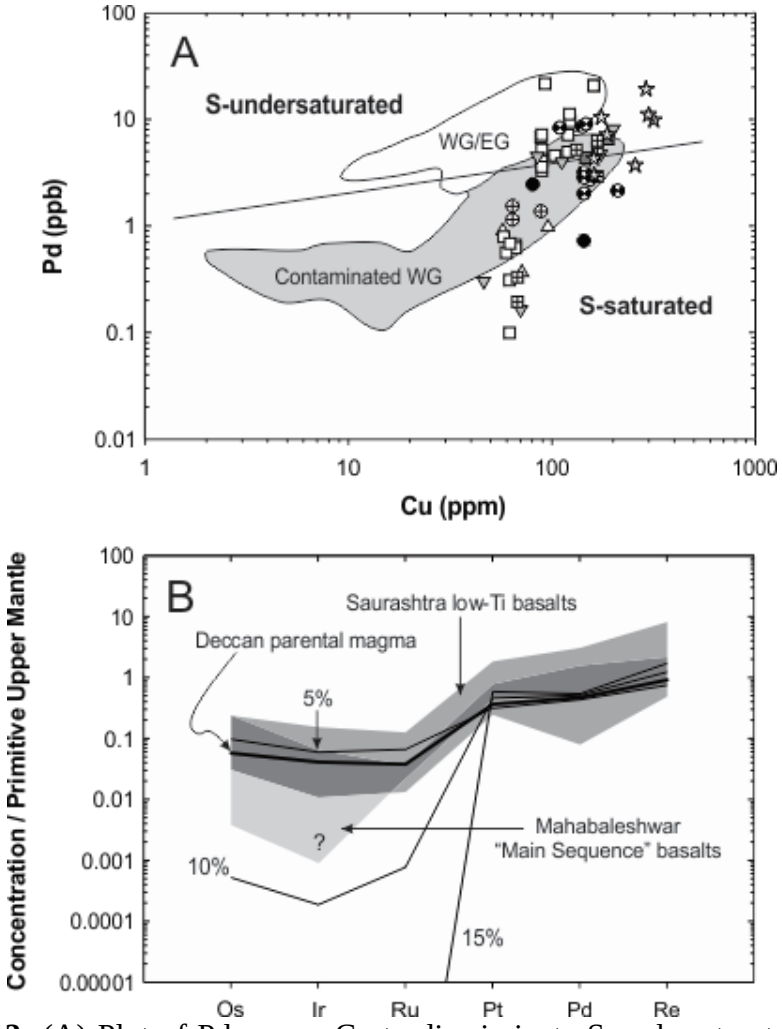

Figure 5.13: (A) Plot of Pd versus Cu to discriminate S-undersaturated and S-saturated lavas [e.g., Keays & Lightfoot, 2007]. Although many Deccan lava samples lie above the qualitative line denoting the boundary between the S-saturated and S-undersaturated fields, most overlap the field of S-saturated ("contaminated") West Greenland (WG) lavas [Keays & Lightfoot, 2007], which we take to imply that these lavas are also S-saturated. WG/EG: S-undersaturated ("uncontaminated") West and East Greenland lavas [Keays & Lightfoot, 2007]. Symbols as in **Figure 5.5**. (B) Assimilation-fractional crystallization model for a calculated Deccan parental magma [Peters et al., 2016a], using partition coefficients of Jamais et al. [2009] and Day [2013] and an upper continental crust HSE composition of Peucker-Ehrenbrink & Jahn [2001]. Shown for comparison are composition ranges of Mahabaleshwar main sequence basalts (light gray), Saurashtra low-Ti basalts (medium gray) and the field in which these ranges overlap (dark gray). Question mark denotes unknown minimum Ir composition after several analyses for which measured Ir contents were less than the Ir contents of associated blanks.

References

Adam, J. and T. Green (2006) Trace element partitioning between mica- and amphibole-bearing garnet lherzolite and hydrous basanitic melt: 1. Experimental results and the investigation of controls on partitioning behavior: Contributions to Mineralogy and Petrology, 152, 1-17.

Albaréde, F., B. Luais, G. Fitton, M. Semet, E. Kaminski, B.G.J. Upton, P. Bachélery an J.-L. Cheminée (1997) The geochemical regimes of Piton de la Fournaise Volcano (Réunion) during the last 530,000 years: Journal of Petrology, 38(2), 171-201.

Aulbach, S., J.E. Mungall and D.G. Pearson (2016) Distribution and processing of highly siderophile elements in cratonic mantle lithosphere, *in* Harvey, J. and J.M.D. Day (*eds.*) Highly siderophile and strongly chalcophile elements in high-temperature geochemistry and cosmochemistry: Reviews in Mineralogy and Geochemistry, 81, 239-304.

Beattie, P. (1994) Systematics and energetics of trace-element partitioning between olivine and silicate melts: Implications for the nature of mineral/melt partitioning: Chemical Geology, 117, 57-71.

Becker, H., M.F. Horan, R.J. Walker, S. Gao, J.-P. Lorand and R.L. Rudnick (2006) Highly siderophile element composition of the Earth's primitive upper mantle: constraints rom new data on peridotite massifs and xenoliths: Geochimica et Cosmochimica Acta, 70, 4528-4550.

Bhatnagar, V.M. (1969) The melting points of synthetic apatites: Mineralogical Magazine, 37(288), 527-528.

Bindeman, I. and A. Davis (2000) Trace element partitioning between plagioclase and melt: Investigation of dopant influence on partition behavior: Geochimica et Cosmochimica Acta, 64(2), 2863-2878.

Birck, J.-L., M. Roy-Barman and F. Capmas (1997) Re-Os isotopic measurements at the femtomole level in natural samples: Geostandards Newsletter, Journal of Geostandards and Geoanalysis, 21, 19-27.

Bosch, D., J. Blichert-Toft, F. Moynier, B.K. Nelson, P. Telouk, P.-Y. Gillot and F. Albarede (2008) Pb, Hf and Nd isotope compostiions of the two Réunion volcanoes (Indian Ocean): A tale of two small-scale mantle "blobs"?: Earth and Planetary Science Letters, 265, 748-765.

Boyd, F.R. and S.A. Mertzman (1987) Composition and structure of the Kaapvaal lithosphere, southern Africa, *in:* Mysen, B.O. (ed.) Magmatic Processes: Physicochemical Principles: Geochemical Society Special Publications, 1, 13-24.

Brenan, J., W.F. McDonough and C. Dalpé (2003) Experimental constraints on the partitioning of rhenium and some platinum-group elements between olivine and silicate melt: Earth and Planetary Science Letters, 212, 135-150.

Chung, S.-L., B.-M. Jahn, W. Ganyao, C.-H. Lo and C Bollin (1998) The Emeishan flood basalt in SW China: A mantle plume initiation model and its connection with continental breakup and mass extinction at the Permian-Triassic boundary, *in* Flower, M.F.J., S.-L. Chung, C.-H. Lo and T.-Y. Lee (*eds.*) Mantle Dynamics and Plate Interactions in East Asia: American Geophysical Union, Washington, DC, 47-58.

Cohen, A.S. and F.G. Waters (1996) Separation of osmium from geological materials by solvent extraction for analysis by thermal ionization mass spectrometry: Analytica Chimica Acta, 332, 269-275.

Courtillot, V., G. Féraud, M. Maluski, D. Vandamme, M.G. Moreau and J. Besse (1988) Deccan flood basalts and the Cretaceous/Tertiary boundary: Nature, 333, 843-846.

Cox, K.G. and C.J. Hawkesworth (1985) Geochemical stratigraphy of the Deccan Traps at Mahabaleshwar, Western Ghats, India, with implication for open system magmatic processes: Journal of Petrology, 26(2), 355-377.

Craciun, R., D. Picone, R.T. Long, S. Li and D.A. Dixon (2010) Third row transition metal hexafluorides, extraordinary oxidizers, and Lewis acids: Electron affinities, fluoride affinities, and heats of formation of WF_6, ReF_6, OsF_6, IrF_6, PtF_6, and AuF_6: Inorganic Chemistry, 49, 1056-1070.

Crocket, J.H. (2000) PGE in fresh basalt, hydrothermal alteration products, and volcanic incrustations of Kilauea volcano, Hawaii: Geochimica et Cosmochimica Acta, 64(10), 1791-1807.

Cucciniello, C., E.I. Demonterova, H. Sheth, K. Pande and A. Vijayan (2015) $^{40}Ar/^{39}Ar$ geochronology and geochemistry of the central Saurashtra mafic dyke swarm: insights into magmatic evolution, magma transport, and dyke-flow relationships in the northwestern Deccan Traps: Bulletin of Volcanology, 77(45), 19 pp.

Day, J.M.D. (2013) Hotspot volcanism and highly siderophile elements: Chemical Geology, 341, 60-74.

Day, J.M.D., D.G. Pearson and L.J. Hulbert (2013) Highly siderophile lement behavior during flood basalt genesis and evidence for melts from intrusive chromitite formation in the Mackenzie large igneous province: Lithos, 182-183, 242-258.

Day, J.M.D., D.G. Pearson, C.G. Macpherson, D. Lowry and J.-C. Carracedo (2010) Evidence for distinct proportions of subducted oceanic crust and lithosphere in HIMU-type mantle beneath El Hierro and La Palma, Canary Islands: Geochimica et Cosmochimica Acta, 74, 6565-6589.

Day, J.M.D., C.L. Waters, B.F. Schaefer, R.J. Walker and S. Turner (2016) Use of hydrofluoric acid desilicification in the determination of highly siderophile element abundances and Re-Pt-Os isotope systematics in mafic-ultramafic rocks: Geostandards and Geoanalytical Research, 40, 49-65.

DiMuro, A., N. Métrich, D. Vergani, M. Rosi, P. Armienti, T. Fougeroux, E. Deloule, I. Arinzo and L. Civetta (2014) The shallow plumbing system of Piton de la Fournaise volcano (La Réunion Island, Indian Ocean) revealed by the major 2007 caldera-forming eruption: Journal of Petrology, 55(7), 1287-1315.

Duncan, R.A., J. Backman and L.C. Peterson (1990) The volcanic record of the Réunion hot spot: Proceedings of the Ocean Drilling Program, Scientific Results, 115, 3-10.

Esperança, S. and J.R. Holloway (1987) On the origin of some mica-lamprophyres: experimental evidence from a mafic minette: Contributions to Mineralogy and Petrology, 95, 207-216.

Fisk, M.R., B.G.J. Upton and C.E. Ford (1988) Geochemical and experimental study of the genesis of magmas of Reunion Island, Indian Ocean: Journal of Geophysical Research, 93(B5), 4933-4950.

Füri, E., D.R. Hilton, B.J. Murton, C. Hémond, J. Dyment and J.M.D. Day (201) Helium isotope vriations between Réunion Island and the Central Indian Ridge (17°-21°S): New evidence for ridge-hot spot interaction: Journal of Geophysical Research, 116, B02207.

Gannoun, A., I. Vlastélic and P. Schiano (2015) Escape of unradiogenic osmium during sub-aerial lava degassing: Evidence from fumarolic deposits, Piton de la Fournaise, Réunion Island: Geochimica et Cosmochimica Acta, 166, 312-326.

Ganino, C. and N.T. Arndt (2009) Climate changes caused by degassing of sediments during the emplacement of large igneous provinces: Geology, 37(4), 323-326.

Gupta, M.L., A. Sundar and S.R. Sharma (1991) Heat flow and heat generation in the Archaean Dharwar cratons and implications for the southern Indian shield geotherm and lithospheric thickness: Tectonophysics, 194, 107-122.

Gupta, S., S.S. Rai, K.S. Prakasam, D. Srinagesh, R.K. Chadha, K. Prisetley and V.K. Gaur (2003) First evidence for anomalous thick crust between the mid-Archean western Dharwar craton: Current Science, 84(9), 1219-1226.

Jaeger, J.-J., V. Courtillot and P. Tapponnier (1989) Paleontological view of the ages of the Deccan Traps, the Cretaceous/Tertiary boundary, and the India-Asia collision: Geology, 17, 316-319.

Jamais, M. J.C. Lassiter and G. Brügmann (2008) PGE and Os-isotopic variations in lavas from Kohala Volcano, Hawaii: constraints on PGE behavior and melt/crust interaction: Chemical Geology, 250, 16-28.

Kaila, K.L. (1986) Tectonic framework of Narmada-Son Lineament – a continental rift system in central India from deep seismic soundings, *in* Barazangi, M. and L. Brown (*eds.*) Reflection seismology: a global perspective: American Geophysical Union, Washington, D.C., 18 pp.

Kamo, S., G.K. Czamanske, Y. Amelin, V.A. Fedorenko, D.W. Davis and V.R. Trofimov (2003) Rapid eruption of Siberian flood-volcanic rocks and evidence for coincidence with the Permian-Triassic boundary and mass extinction at 251 Ma: Earth and Planetary Science Letters, 214, 75-91.

Keays, R.R. and P.C. Lightfoot (2007) Siderophile and chalcophile metal variations in Tertiary picrites and basalts from West Greenland with implications for the sulphide saturation history of continental flood basalt magmas: Mineralium Deposita, 40, 451-472.

Keays, R.R. and P.C. Lightfoot (2010) Crustal sulfur is required to form magmatic Ni-Cu sulfide deposits: evidence from chalcophile element signatures of Siberian and Deccan Trap basalts: Mineralium Deposita, 45, 241-257.

Lightfoot, P. and C. Hawkesworth (1988) Origin of Deccan Trap lavas: evidence from combined trace element and Sr-, Nd- and Pb-isotope studies: Earth and Planetary Science Letters, 91, 89-104.

Lightfoot, P.C., C.J. Hawkesworth and S.F. Sethna (1987) Petrogenesis of rhyolites and trachytes from the Deccan Trap: Sr, Nd and Pb isotope and trace element evidence: Contributions to Mineralogy and Petrology, 95, 44-54.

Lightfoot, P.C., C.J. Hawkesworth, C.W. Devey, N.W. Rogers and P.W.C. Van Calsteren (1990) Source and differentiation of Deccan Trap lavas: Implications of geochemical and mineral chemical variations: Journal of Petrology, 31(5), 1165-1200.

Lodders, K. (2003) Solar system abundances and condensation temperatures of the elements: The Astrophysical Journal, 591(2), 1220-1247.

Mahoney, J.J. (1989) Deccan Traps, *in* Macdougall, J.D. (*ed.*) Continental Flood Basalts: Springer, Dordrecht, 151-194.

Mahoney, J., J.D. Macduogall, G.W. Lugmair, A.V. Murali, M. Sankar Das and K. Gopalan (1982) Origin of the Deccan Trap flows at Mahabaleshwar inferred from Nd and Sr isotopic and chemical evidence: Earth and Planetary Science Leters, 60, 47-60.

Mahoney, J.J., J.D. Macdougall, G.W. Lugmair, K. Gopalan and P. Krishnamurthy (1985) Origin of contemporaneous tholeiitic and K-rich alkalic lavas: a case study from the northern Deccan Plateau, India: Earth and Planetary Science Letters, 72, 39-53.

Mahoney, J.J., H.C. Sheth, D. Chandrasekharam and Z.X. Peng (2000) Geochemistry of flood basalts of the Toranmal Section, northern Deccan Traps, India: Implications for regional Deccan stratigraphy: Journal of Petrology, 41(7), 1099-1120.

Mather, T.A., M.L.I. Witt, D.M. Pyle, B.M. Quayle, A. Aiuppa, E. Bagnato, R.S. Martin, K.W.W. Sims, E. Edmonds, A.J. Sutton and E. Ilyinskaya (2012) Halogens and trace metal emissions from the ongoing 2008 summit eruption of Kilauea volcano, Hawai'i: Geochimica et Cosmochimica Acta, 83, 292-323.

McDonough, W.F. and S.-s. Sun (1995) The composition of the Earth: Chemical Geology, 120, 223-253.

McLean, D.M. (1985) Deccan Traps mantle degassing in the terminal Cretaceous marine extinctions: Cretaceous Research, 6, 235-259.

Melluso, L., S.F. Sethna, M. D'Antonio, P. Javeri and L. Bennio (2002) Geochemistry and petrogenesis of sodic and potassic mafic alkaline rocks in the Deccan Volcanic Province, Mumbai Area (India): Mineralogy and Petrology, 74, 323-342.

Melluso, L., J.J. Mahoney and L. Dallai (2006) Mantle sources and crustal input as recorded in high-Mg Deccan Traps basalts of Gujarat (India): Lithos, 89, 259-274.

Molzahn, M., L. Reisberg and G. Wörner (1996) Os, Sr, Nd, Pb, O isotope and trace element data from the Ferrar flood basalts, Antarctica: evidence for an enriched subcontinental lithospheric source: Earth and Planetary Science Letters, 144, 529-546.

Mongelli, G., R.L. Cullers, E. Dinelli and A. Rottura (1998) Elemental mobility during the weathering of exposed lower crust: the kinzigitic parageneisses from the Serre, Calabria, southern Italy: Terra Nova, 10, 190-195.

Moore, J., W.M. White, D. Paul, R.A. Duncan, W. Abouchami and S.J.G. Galer (2011) Evolution of shiled-building and rejuvenescent volcanism of Mauritius: Journal of Volcanology and Geothermal Research, 207, 47-66.

Morgan, W.J. (1981) Hotspot tracks and the opening of the Atlantic and Indian Oceans, *in* Emiliani, C. (*ed.*) The oceanic lithosphere: Wiley, New York, 443-487.

Nativel, P. (1972) Découverte de thénardite dans les dépôts fumerolliens de la Fournaise (île de la Réunion): Bulletin de la Société Française de Minéralogie et de Crystallographie, 95, 529-531.

Nishimura, K. (2012) A mathematical model of trace element and isotopic behavior during simultaneous assimilation and imperfect fractional crystallization: Contributions to Mineralogy and Petrology, 164, 427-440.

Peng, Z.X. and J.J. Mahoney (1995) Drillhole lavas from the northwestern Deccan Traps, and the evolution of the Réunion hotspot mantle: Earth and Planetary Science Letters, 134, 169-185.

Peng, Z.X., J. Mahoney, P. Hooper, C. Harris and J. Beane (1994) A role for lower continental crust in flood basalt genesis? Isotopic and incompatible element study of the lower six formation of the western Deccan Traps: Geochimica et Cosmochimica Acta, 58, 267-288.

Peng, Z.X., J.J. Mahoney, P.R. Hooper, J.D. Macdougall and P. Krishnamurthy (1998) Basalts of the northeastern Deccan Traps, India: Isotopic and elemental geochemistry and relation to the southwestern Deccan stratigraphy: Journal of Geophysical Research, 103, 29843-29865.

Peters, B.J., J.M.D. Day and L.A. Taylor (2016) Early mantle heterogeneities in the Réunion hotspot source inferred from highly siderophile elements in cumulate xenoliths: Earth and Planetary Science Letters, 448, 150-160.

Peucat, J.-J., P. Vidal, J. Bernard-Griffiths and K.C. Condie (1989) Sr, Nd and Pb isotopic systematics in Archean low- to high-grade transition zone of southern India: Syn-accretion vs. post-accretion granulites: The Journal of Geology, 97(5), 537-549.

Peucat, J.-J., M. Jayananda, D. Chardon, R. Capdevila, C.M. Fanning and J.-L. Paquette (2013) The lower crust of the Dharwar Craton, southern India: patchwork of Archean granulitic domains: Precambrian Research, 227, 4-28.

Peucker-Ehrenbrink, B. and B.-M. Jahn, (2001) Rhenium-osmium isotope systematics and the platinum group element concentrations: loess and the upper continental crust: Geochemistry Geophysics Geosystems, 2, 22 pp.

Pierazzo, E., D.A. Kring and H.J. Melosh (1998) Hydrocode simulation of the Chicxulub impact event and the production of climatically active gases: Journal of Geophysical Research, 103(E12), 28607-28625.

Prytulak, J. and T. Elliott (2007) TiO_2 enrichment in ocean island basalts: Earth and Planetary Science Letters, 263, 388-403.

Richards, M.A., R.A. Duncan and V.E. Courtillot (1989) Flood basalts and hot-spot tracks: Plume heads and tails: Science, 246, 103-107.

Rocha-Júnior, E.R.V., I.S. Puchtel, L.S. Marques, R.J. Walker, F.B. Machado, A.J.R. Nardy, M. Babinski and A.M.G. Figueiredo (2012) Re-Os isotope and highly siderophile element systematics of the Paraná continental flood basalts (Brazil): Earth and Planetary Science Letters, 337-338, 164-173.

Saunders, A.D., J.G. Fitton, A.C. Kerr, M.J. Norry and R.W. Kent (1997) The North Atlantic Igneous Province, *in* Large igneous provinces: Mahoney, J.J. and M.F. Coffin (*eds.*) Continental, oceanic and planetary flood volcanism: American Geophysical Union, Washington, D.C., 45-93.

Schoene, B., J. Guex, A. Bartolini, U. Schaltegger and T.J. Blackburn (2010) Correlating the end-Triassic mass extinction and flood basalt volcanism at the 100 ka level: Geology, 38(5), 387-390.

Schoene, B., K.M. Samperton, M.P. Eddy, G. Keller, T. Adatte, S.A. Bowring, S.F.R. Khadri and B. Gertsch (2015) U-Pb geochronology of the Deccan Traps and relation to the end-Cretaceous mass extinction: Geology, 347, 182-185.

Schulte, P., L. Alegret, I. Arenillas, J.A. Arz, P.J. Barton, P.R. Brown, T.J. Bralower, G.L. Christeson, P. Claeys, C.S. Cockell, G.S. Collins, A. Deutsch, T.J. Goldin, K. Goto, J.M. Grajales-Nishimura, R.A.F. Grieve, S.P.S. Gulick, K.R. Johnson, W. Kiessling, R.A.F. Grieve, S.P.S. Gulick, K.R. Johnson, W. Kiessling, C. Koeberl, D.A. Kring, K.G. MacLeod, T. Matsui, J. Melosh, A. Montanari, J.V. Morgan, C.R. Neal, D.J. Nichols, R.D. Norris, E. Pierazzo, G. Ravizz, M. Rebolledo-Vieyra, W.U. Reimold, E. Robin, T. Salge, R.P. Speijer, A.R. Sweet, J. Urrutia-Fucugauchi, V. Vajda, M.T. Whalen and P.S. Willumsen (2010) The Chicxulub asteroid impact and mass extinction at the Cretaceous-Paleogene boundary: Science, 327, 1214-1218.

Self, S., M. Widdowson, T. Thordarson and A.E. Jay (2006) Volatile fluxes during flood basalt eruptions and potential effects on the global environment: A Deccan perspective: Earth and Planetary Science Letters, 258, 518-532.

Self, S., S. Blake, K. Sharma, M. Widdowson and S. Sephton (2008) Sulfur and chlorine in late Cretaceous Deccan magmas and eruptive gas release: Science, 319, 1654-1657.

Sheth, H.C. (2005) From Deccan to Réunion: No trace of a mantle plume: Geological Society of America Special Papers, 388, 477-501.

Sheth, H.C., G.F. Zellmer, E.I. Demonterova. A.V. Ivanov, R. Kumar and R.K. Patel (2014) The Deccan tholeiite lavas and dykes of Ghatkopar-Powai area, Mumbai, Panvel flexure zone: Geochemistry, stratigraphic status, and tectonic significance: Journal of Asian Earth Sciences, 84, 69-82.

Simonetti, A., S.L. Goldstein, S.S Schmidberger and S.G. Viladkar (1998), Geochemical and Nd, Pb, and Sr isotope data from Deccan alkaline complexes – inferences for mantle sources and plume-lithosphere interaction: Journal of Petrology, 39(11-12), 1847-1864.

Symonds, R.B., W.I. Rose, M.H. Reed, F.E. Lichte and D.L. Finnegan (1987) Volatilization, transport and sublimation of metallic and non-metallic elements in high temperature gases at Merapi Volcano, Indonesia: Geochimica et Cosmochimica Acta, 51, 2083-2101.

Toutain, J.-P. and G. Meyer (1989) Iridium-bearing sublimates at a hot-spot volcano (Piton de la Fournaise, Indian Ocean): Geophysical Research Letters, 16(12), 1391-1394.

Vanderkluysen, L., J.J. Mahoney, P.R. Hooper, H.C. Sheth and R. Ray (2011) The feeder system of the Deccan Traps (India): Insights from dike geochemistry: Journal of Petrology, 52(2), 315-343.

Vlastélic, I., T. Staudacher and M. Semet (2005) Rapid change of lava composition from 1998 to 2002 at Piton de la Fournaise (Réunion) inferred from Pb isotopes and trace elements: Evidence for variable crustal contamination: Journal of Petrology, 46(1), 79-107.

Vlastélic, I., A. Peltier and T. Staudacher (2007) Short-term (1998-2006) fluctuations of Pb isotopes at Piton de la Fournaise volcano (Reunion Island): Origins and constraints on the size and shape of the magma reservoir: Chemical Geology, 244, 202-220.

Wendlandt, R.F. (1982) Suflide saturation of basalt and andesite melts at high pressures and temperatures: American Mineralogist, 67, 877-885.

White, R. and D. McKenzie (1989) Magmatism at rift zones: The generation of volcanic continental margins and flood basalts: Journal of Geophysical Research, 94(B6) 7685-7729.

Widdowson, M., M.S. Pringle and O.A. Fernandez (2000) A post K-T boundary (early Palaeocene) age for Deccan-type feeder dykes, Goa, India: Journal of Petrology, 41(7), 1177-1194.

Wilson, J.T. (1963) A possible origin of the Hawaiian Islands: Canadian Journal of Earth Sciences, 41, 863-870.

Wingall, P.B. (2001) Large igneous provinces and mass extinctions: Earth-Science Reviews, 53, 1-33.

Wood, D.A., I.L. Gibson and R.N. Thompson (1976) Elemental mobility during zeolite facies metamorphism of the Tertiary basalts of eastern Iceland: Contributions to Mineralogy and Petrology, 55, 241-254.

Chapter 6:

Concluding remarks

This dissertation has discussed some emerging research utilizing geochemistry to address questions regarding the origins of hotspot magmas in the mantle and the relationship between continental flood basalt (CFB) and ocean island basalt (OIB) provinces. It examines geochemical data from the Deccan Traps of India, Réunion Island and an array of other global hotspots.

In **Chapter 2**, I discussed the origins of commonly observed enrichments in Ti, Ta and Nb (TITAN) in many global ocean island basalts. I mathematically evaluated the compositions of parental magmas to many global hotspots and found that TITAN enrichments are statistically pervasive features, but are unlikely to reflect similar enrichments in hotspot mantle sources. Rather, this geochemical feature is likely created during partial melting and differentiation processes as a magma rises to the surface. In particular, relative enrichments in Ti can be created by crystallization of olivine and oxide phases, and the high incompatibility of Ta and Nb means that enrichments in these elements

can be generated during partial melting. TITAN enrichments bear no relationship to He isotopic signatures of hotspots or mantle buoyancy flux. Together, modeled partial melting and differentiation processes can recreate the range of TITAN enrichments, Os and He isotopic signatures found in global OIB, meaning that great caution should be exercised when using trace elements to evaluate the composition of mantle domains. Future work might attempt to assess the likelihood that TITAN enrichments may occur during the genesis of mantle domains, but should also focus on the propensity of these enrichments to survive magma transport without being overprinted by domains that lack the enrichments, or processes that serve to diminish or mask them.

Chapter 3 concerned several unusual highly siderophile element (HSE) patterns present in cumulate xenoliths and lavas from Réunion Island. In addition, it explored the implications of an exceptionally consistent Os isotopic signature present in Réunion igneous rocks. The HSE patterns strongly suggest that the Réunion mantle source is non-chondritic with respect to its siderophile element patterns, a feature which may arise due to limited core-mantle interaction shortly after core formation, or due to assimilation of impactor material that may carry a fractionated HSE signature. The highly invariant and relatively unradiogenic $^{187}Os/^{188}Os$ signature reflects a mantle source that is less refractory than those to other global hotspots. The survival of both features suggests that the Réunion mantle source differentiated early in Earth's history and has remained closed since that time. This hypothesis requires further testing using short-lived radioactive (e.g., ^{142}Nd) and

stable isotope systems, but has the potential to reveal new information about the history of the early Earth.

In **Chapter 4**, I detailed the helium, oxygen and osmium isotopic composition of mineral separates from Deccan Traps igneous rocks. In addition, I employed an emerging *in situ* technique utilizing olivine major and minor element compositions to identify the presence of recycled material in the source of global hotspots. Both the isotopic and elemental methods are sensitive to crustal assimilation, which is pervasive in Deccan igneous rocks, however the analysis of early-formed mineral phases such as olivine may capture the compositions of parental magmas before crustal assimilation persisted to an advanced stage. In conjunction with analyses of later-formed phases, I detailed a history of progressive crustal assimilation present in Deccan magmas that is reflected most in plagioclase and least in olivine. Then, using the olivine from the most primitive rocks as the preferred probe of parental magma compositions, I evaluated the maximum proportion of recycled material in the Deccan Traps primary magma to be approximately 20-25%. However, correlations between the *in situ* and isotopic methods were weak, which may reflect how strongly various mantle and differentiation processes affect the two methods. Future work evaluating the relationship between these methods should make use of rocks that contain more olivine with fewer inclusions, as Deccan rocks are generally olivine-poor and contain olivine with a high proportion of inclusions, which may substantially affect measurements. A greater body of measurements attempted on a larger mass of material may clarify the relationship between the *in situ* and isotopic methods.

Finally, in **Chapter 5** I examined the Os, Sr and Nd isotopic and HSE characteristics of a large suite of Deccan lavas from sampling areas comprising most of the Deccan Traps. I found that, while crustal assimilation signatures are pervasive in Deccan lavas, Os isotopes proved to be an especially sensitive measure of crustal assimilation that helped clarify the isotopic composition of the Deccan Traps parental magma. Employing measurements on regional lower and upper crustal rocks, and idealized compositions of continental lithospheric mantle, I found that Os revealed signatures lithospheric and lower crustal assimilation, while Nd and Sr were able to effectively trace lower and upper crustal assimilants. In multi-isotopic space, the assimilation trends clearly trended from a common composition similar to the Sr-Nd-Os isotopic composition of Réunion magmas. In addition, Deccan HSE signatures can be explained by differentiation of a magma with a parental HSE signature similar to the calculated parental magma HSE composition of Réunion. This analysis represents the first clear geochemical link between a CFB and OIB domain and strongly suggests that the mantle sources to hotspots can persist in the mantle over long periods of geologic time, despite the influences of convection and other shallow mantle processes. This conclusion is incompatible with the notion that hotspots are generated by shallow processes such as lithospheric cracking or localized shallow mantle convection. Instead, it supports the long-discussed hypothesis that volcanism along the Réunion hotspot is generated by an actively upwelling, deep mantle plume that has endured for 65 million years of Earth history.

Appendix

This section contains essential data tables for Chapter 3, Chapter 4 and Chapter 5. The first number on each table corresponds to the chapter to which it belongs.

Table A3.1: Full geochemical data for Piton Chisny cumulate xenoliths and Piton de la Fournaise basaltic lavas. Begins next page for clarity.

Major Elements (XRF)	*Unit*	**CH0701**	**CH0701 Dunite**	**CH0702**	**CH0702A**
SiO_2	wt. %	38.42	39.06	38.18	38.08
TiO_2	wt. %	0.14	0.20	0.10	0.11
Al_2O_3	wt. %	0.63	0.90	0.45	0.57
Fe_2O_3T	wt. %	15.39	15.36	15.75	15.76
MnO	wt. %	0.20	0.20	0.21	0.21
MgO	wt. %	43.70	41.67	44.60	44.41
CaO	wt. %	1.08	2.20	0.39	0.45
Na_2O	wt. %	0.10	0.12	0.10	0.10
K_2O	wt. %	0.00	0.00	0.00	0.00
P_2O_5	wt. %	0.02	0.02	0.02	0.02
Total	wt. %	99.68	99.74	99.81	99.71
LOI	wt. %	0.60	0.63	0.67	0.59
FeO	wt. %	12.13	12.32	12.00	12.07
Fe_2O_3	wt. %	1.91	1.67	2.41	2.35
Mg-number		86.53	85.78	86.89	86.77
Fe^{2+}/Fe^*	mole fraction	0.93	0.94	0.92	0.92
Trace Elements (XRF)					
Rb	ppm	0.6	0.8	0.6	1
Sr	ppm	6	8	6	9
Y	ppm	0.6	1.7	0.5	<0.5
Zr	ppm	11	8	8	8
V	ppm	42	59	26	35
Ni	ppm	1733	1614	2003	2000
Cr	ppm	3625	3846	2358	2710
Nb	ppm	<0.5	<0.5	<0.5	<0.5
Ga	ppm	3	3.7	2.6	2.5
Cu	ppm	17	43	29	26
Zn	ppm	103	104	100	101
Co	ppm	171	166	164	167
Ba	ppm	4	7	<3	<3
La	ppm	<1	1	1	<1
Ce	ppm	<1	2	4	<1
U	ppm	<0.5	<0.5	<0.5	<0.5
Th	ppm	<0.5	<0.5	<0.5	<0.5
Sc	ppm	8	12	7	7
Pb	ppm	<1	<1	<1	<1
Trace Elements (ICPMS)					
Li	ppm	1.21	2.24	1.16	1.98
Sc	ppm	6.40	11.90	4.64	4.89
V	ppm	32.5	51.7	21.1	27.4
Cr	ppm	3717	3910	2459	2726
Co	ppm	182	176	188	173
Ni	ppm	2028	1991	2420	2288
Cu	ppm	14.6	36.9	23.6	20.0

Zn	ppm	86.5	100.4	80.9	88.8
Ga	ppm	1.67	2.14	1.18	1.43
Ge	ppm	1.40	1.47	1.53	1.57
Rb	ppm	0.11	0.10	0.26	0.29
Sr	ppm	2.87	4.85	4.39	5.96
Y	ppm	0.88	1.64	0.48	0.61
Zr	ppm	2.53	3.78	2.40	3.48
Nb	ppm	0.16	0.15	0.35	0.41
Cs	ppm	0.00	0.00	0.00	0.01
Ba	ppm	0.79	0.38	1.97	1.95
La	ppm	0.22	0.27	0.30	0.38
Ce	ppm	0.59	0.87	0.63	0.87
Pr	ppm	0.10	0.15	0.09	0.11
Nd	ppm	0.56	0.88	0.40	0.51
Sm	ppm	0.17	0.30	0.09	0.12
Eu	ppm	0.06	0.10	0.03	0.04
Gd	ppm	0.17	0.34	0.10	0.13
Tb	ppm	0.03	0.05	0.01	0.02
Dy	ppm	0.19	0.34	0.09	0.12
Ho	ppm	0.04	0.07	0.02	0.02
Er	ppm	0.10	0.17	0.05	0.07
Tm	ppm	0.01	0.02	0.01	0.01
Yb	ppm	0.09	0.15	0.06	0.07
Lu	ppm	0.02	0.02	0.01	0.01
Hf	ppm	0.10	0.15	0.07	0.08
Ta	ppm	0.02	0.02	0.03	0.04
W	ppm	0.01	0.00	0.01	0.00
Pb	ppm	0.04	0.07	0.04	0.03
Th	ppm	0.02	0.02	0.03	0.04
U	ppm	0.00	0.00	0.01	0.01
Highly Siderophile Elements (ICPMS)					
Ir	ppb	0.297	0.304	1.045	0.255
Ru	ppb	1.736	1.250	5.825	1.456
Pt	ppb	0.926	1.147	0.250	0.745
Pd	ppb	0.403		0.347	1.062
Re	ppb	0.027	0.049	0.012	0.008
Osmium (TIMS)					
Os	ppb	0.982	0.627	2.896	1.477
$^{187}Os/^{188}Os$		0.13225	0.13223	0.13225	0.13206
± 2σ		0.00010	0.00013	0.00010	0.00008

Major Elements (XRF)	*Unit*	**CH0703A**	**CH0703B**	**CH0703C**	**CH0703D**	**CH0703E**
SiO_2	wt. %	37.8	41.1	38.4	38.1	38.7
TiO_2	wt. %	0.09	0.45	0.07	0.09	0.05
Al_2O_3	wt. %	0.39	1.78	0.36	0.41	0.27
Fe_2O_3(T)	wt. %	17.3	14.7	16.1	17.1	13.6
MnO	wt. %	0.24	0.19	0.22	0.22	0.18
MgO	wt. %	43.5	33.1	44.2	43.4	46.4
CaO	wt. %	0.35	7.74	0.40	0.40	0.28
Na_2O	wt. %	0.08	0.43	0.08	0.10	0.08
K_2O	wt. %	0.00	0.02	0.00	0.00	0.01
P_2O_5	wt. %	0.01	0.22	0.01	0.02	0.01
Total	wt. %	99.8	99.7	99.9	99.8	99.6
LOI	wt. %	0.86	0.78	0.66	0.66	0.65
FeO	wt. %	14.1	10.4	11.4	11.4	11.2
Fe_2O_3	wt. %	1.70	3.09	3.43	4.47	1.17
Mg-number		84.6	85.0	87.4	87.2	88.1
Fe^{2+}/Fe^*	mole fraction	0.95	0.88	0.88	0.85	0.96
Trace Elements (XRF)						
Rb	ppm	<0.5	0.6	0.7	0.5	1.2
Sr	ppm	6	19	4	3	3
Y	ppm	<0.5	4.6	<0.5	<0.5	0.5
Zr	ppm	9	15	8	9	10
V	ppm	27	130	30	30	14
Ni	ppm	1657	979	1692	1720	2701
Cr	ppm	2533	2521	3205	3258	1348
Nb	ppm	<0.5	<0.5	<0.5	<0.5	<0.5
Ga	ppm	2.7	4.8	2.6	2.7	2
Cu	ppm	16	64	7	38	9
Zn	ppm	107	92	101	116	78
Co	ppm	181	135	180	182	143
Ba	ppm	6	24	3	7	4
La	ppm	1	3	1	1	<1
Ce	ppm	1	5	2	<1	1
U	ppm	<0.5	<0.5	<0.5	<0.5	<0.5
Th	ppm	<0.5	<0.5	<0.5	<0.5	<0.5
Sc	ppm	8	28	7	8	5
Pb	ppm	<1	<1	<1	<1	<1
Trace Elements (ICPMS)						
Li	ppm	1.12	2.59	1.77	2.65	2.40
Sc	ppm	5.13	32.79	3.31	5.04	4.46
V	ppm	21.1	120.8	21.0	28.3	11.6
Cr	ppm	2619	2507	2899	3414	1346
Co	ppm	194	137	177	176	158

Ni	ppm	2047	1241	1932	1935	2922
Cu	ppm	13.3	67.7	3.4	32.3	6.5
Zn	ppm	95.7	86.3	87.2	99.0	77.9
Ga	ppm	2.25	3.84	1.10	2.53	0.65
Ge	ppm	1.69	1.50	1.63	1.65	1.44
Rb	ppm	0.09	0.20	0.01	0.09	0.52
Sr	ppm	1.37	17.97	0.85	2.61	0.93
Y	ppm	0.29	5.24	0.22	0.30	0.29
Zr	ppm	1.30	14.66	0.66	1.76	0.87
Nb	ppm	0.13	0.35	0.08	0.14	0.37
Cs	ppm	0.01	0.01	0.00	0.01	0.01
Ba	ppm	0.88	14.93	0.22	0.96	
La	ppm	0.12	1.06	0.07	0.13	0.12
Ce	ppm	0.26	3.44	0.16	0.30	0.29
Pr	ppm	0.04	0.60	0.02	0.04	0.04
Nd	ppm	0.18	3.32	0.10	0.18	0.15
Sm	ppm	0.05	1.09	0.03	0.05	0.04
Eu	ppm	0.01	0.37	0.01	0.01	0.01
Gd	ppm	0.05	1.21	0.03	0.05	0.04
Tb	ppm	0.01	0.19	0.00	0.01	0.01
Dy	ppm	0.05	1.17	0.03	0.05	0.05
Ho	ppm	0.01	0.23	0.01	0.01	0.01
Er	ppm	0.03	0.54	0.03	0.04	0.04
Tm	ppm	0.01	0.07	0.00	0.01	0.01
Yb	ppm	0.04	0.41	0.04	0.05	0.05
Lu	ppm	0.01	0.06	0.01	0.01	0.01
Hf	ppm	0.04	0.56	0.02	0.05	0.02
Ta	ppm	0.02	0.04	0.01	0.02	0.03
W	ppm	0.02	0.01	0.00	0.01	0.05
Pb	ppm	0.07	0.22	0.03	0.17	0.16
Th	ppm	0.02	0.08	0.01	0.02	0.03
U	ppm	0.01	0.02	0.00	0.01	0.02
Highly Siderophile Elements (ICPMS)						
Ir	ppb	1.071	0.239	1.047	0.257	0.405
Ru	ppb	3.715	0.814	3.967	1.172	1.173
Pt	ppb	0.720	1.090	0.076	0.595	0.289
Pd	ppb	0.580	1.276	0.517	0.782	0.216
Re	ppb	0.009	0.110	0.131	0.030	
Osmium (TIMS)						
Os	ppb	1.993	1.003	2.896	1.861	0.903
^{187}Os/^{188}Os		0.13312	0.13385	0.13296	0.13161	0.13262
± 2σ		0.00013	0.00010	0.00010	0.00009	0.00013

Major Elements (XRF)	Unit	**CH0703 Dunite**	**CH0703 Pyroxenite**	**CH0704**
SiO_2	wt. %	38.2	38.4	37.8
TiO_2	wt. %	0.19	0.13	0.12
Al_2O_3	wt. %	0.67	0.65	0.50
Fe_2O_3(T)	wt. %	17.8	15.9	16.7
MnO	wt. %	0.23	0.21	0.22
MgO	wt. %	40.7	43.8	43.2
CaO	wt. %	1.81	0.45	0.43
Na_2O	wt. %	0.11	0.11	0.09
K_2O	wt. %	0.00	0.01	0.00
P_2O_5	wt. %	0.02	0.02	0.02
Total	wt. %	99.7	99.7	99.1
LOI	wt. %	0.76	0.61	0.61
FeO	wt. %	15.2	11.2	12.5
Fe_2O_3	wt. %	0.91	3.54	2.78
Mg-number		82.7	87.5	86.0
Fe^{2+}/Fe^*	mole fraction	0.97	0.88	0.91
Trace Elements (XRF)				
Rb	ppm	0.9	1	<0.5
Sr	ppm	9	9	6
Y	ppm	1.2	0.7	<0.5
Zr	ppm	11	9	11
V	ppm	52	39	37
Ni	ppm	1610	1824	1814
Cr	ppm	2220	3827	3660
Nb	ppm	<0.5	<0.5	<0.5
Ga	ppm	3.3	3.1	3.4
Cu	ppm	68	11	18
Zn	ppm	128	105	114
Co	ppm	175	177	173
Ba	ppm	3	<3	<3
La	ppm	<1	<1	1
Ce	ppm	<1	1	<1
U	ppm	<0.5	<0.5	<0.5
Th	ppm	<0.5	<0.5	<0.5
Sc	ppm	10	7	7
Pb	ppm	<1	<1	<1
Trace Elements (ICPMS)				
Li	ppm	1.69	2.35	2.08
Sc	ppm	10.31	3.10	29.59
V	ppm	40.4	31.2	31.4
Cr	ppm	2275	3555	3171

Co	ppm	187	173		170	
Ni	ppm	1997	2038		1999	
Cu	ppm	55.4	5.8		11.0	
Zn	ppm	104.1	94.5		98.6	
Ga	ppm	1.91	1.81		1.66	
Ge	ppm	1.60	1.61		1.68	
Rb	ppm	0.10	0.35		0.03	
Sr	ppm	4.31	6.90		1.38	
Y	ppm	1.82	0.64		0.34	
Zr	ppm	4.98	3.94		1.30	
Nb	ppm	0.13	0.47		0.12	
Cs	ppm	0.01	0.01		0.00	
Ba	ppm	0.67	7.16			
La	ppm	0.40	0.45		0.12	
Ce	ppm	1.21	1.04		0.30	
Pr	ppm	0.22	0.13		0.04	
Nd	ppm	1.14	0.57		0.20	
Sm	ppm	0.35	0.13		0.05	
Eu	ppm	0.11	0.05		0.02	
Gd	ppm	0.39	0.14		0.06	
Tb	ppm	0.06	0.02		0.01	
Dy	ppm	0.39	0.12		0.06	
Ho	ppm	0.08	0.03		0.01	
Er	ppm	0.19	0.07		0.04	
Tm	ppm	0.03	0.01		0.01	
Yb	ppm	0.17	0.08		0.06	
Lu	ppm	0.03	0.01		0.01	
Hf	ppm	0.19	0.10		0.04	
Ta	ppm	0.02	0.04		0.01	
W	ppm	0.01	0.01		0.00	
Pb	ppm	0.21	0.07		0.03	
Th	ppm	0.02	0.07		0.01	
U	ppm	0.00	0.02		0.00	

Highly Siderophile Elements (ICPMS)

Ir	ppb	0.841	0.206	0.435	0.414	0.299
Ru	ppb	1.621	1.268	2.891	2.234	2.152
Pt	ppb	1.969	0.391	0.302	0.238	0.244
Pd	ppb	1.913	0.989	0.174	0.921	1.092
Re	ppb	0.046	0.035	0.007	0.010	0.001

Osmium (TIMS)						
Os	ppb	0.698	0.600	0.435	0.414	0.299
$^{187}Os/^{188}Os$		0.13179	0.13310	0.13050	0.13224	0.13223
± 2σ		0.00008	0.00011	0.00022	0.00009	0.00010

Major Elements (XRF)	*Unit*	**CH0704A**	**CH0705A**	**CH0705B**	**CH0705C**
SiO_2	wt. %	38.1	38.4	38.3	37.5
TiO_2	wt. %	0.08	0.10	0.08	0.19
Al_2O_3	wt. %	0.42	0.50	0.33	0.83
Fe_2O_3(T)	wt. %	16.1	15.0	16.1	16.6
MnO	wt. %	0.21	0.20	0.22	0.21
MgO	wt. %	44.4	45.0	44.3	42.9
CaO	wt. %	0.31	0.40	0.28	0.83
Na_2O	wt. %	0.08	0.09	0.08	0.09
K_2O	wt. %	0.00	0.00	0.00	0.00
P_2O_5	wt. %	0.01	0.02	0.02	0.02
Total	wt. %	99.8	99.7	99.7	99.1
LOI	wt. %	0.56	0.55	0.60	0.64
FeO	wt. %	12.0	10.9	12.7	12.6
Fe_2O_3	wt. %	2.85	2.90	2.01	2.56
Mg-number		86.9	88.0	86.2	85.8
Fe^{2+}/Fe*	mole fraction	0.90	0.89	0.93	0.92
Trace Elements (XRF)					
Rb	ppm	0.8	0.7	0.6	0.6
Sr	ppm	3	2	5	3
Y	ppm	<0.5	<0.5	<0.5	<0.5
Zr	ppm	9	7	7	11
V	ppm	29	34	20	62
Ni	ppm	1770	1831	2068	1882
Cr	ppm	4013	3051	2215	6055
Nb	ppm	<0.5	<0.5	<0.5	<0.5
Ga	ppm	2.7	2.5	2.7	3.6
Cu	ppm	7	12	7	72
Zn	ppm	102	96	108	111
Co	ppm	176	180	164	165
Ba	ppm	<3	11	6	<1
La	ppm	1	<1	<1	1
Ce	ppm	<1	1	1	<1
U	ppm	<0.5	<0.5	<0.5	<0.5
Th	ppm	<0.5	<0.5	<0.5	<0.5
Sc	ppm	7	5	6	8
Pb	ppm	<1	<1	<1	<1
Trace Elements (ICPMS)					
Li	ppm	1.48	3.03	2.63	2.46
Sc	ppm	4.74	9.12	26.45	7.03
V	ppm	23.3	27.3	16.0	59.3
Cr	ppm	4133	3274	2014	6008
Co	ppm	193	201	168	180

Ni	ppm	2110	2200	2314		2289
Cu	ppm	3.6	8.0	2.6		65.9
Zn	ppm	89.8	83.9	97.2		112.8
Ga	ppm	1.22	1.47	1.20		2.84
Ge	ppm	1.53	1.59	1.68		1.50
Rb	ppm	0.07	0.13	0.07		0.17
Sr	ppm	1.01	2.27	1.31		2.89
Y	ppm	0.23	0.45	0.45		0.79
Zr	ppm	0.90	1.51	2.06		2.67
Nb	ppm	0.12	0.19	0.10		0.21
Cs	ppm	0.00	0.00	0.00		0.00
Ba	ppm	0.64	1.04	0.21		3.38
La	ppm	0.10	0.19	0.15		0.23
Ce	ppm	0.20	0.44	0.42		0.64
Pr	ppm	0.03	0.06	0.06		0.10
Nd	ppm	0.12	0.26	0.29		0.49
Sm	ppm	0.03	0.07	0.07		0.14
Eu	ppm	0.01	0.02	0.02		0.05
Gd	ppm	0.04	0.07	0.08		0.16
Tb	ppm	0.01	0.01	0.01		0.03
Dy	ppm	0.04	0.07	0.08		0.16
Ho	ppm	0.01	0.02	0.02		0.03
Er	ppm	0.03	0.05	0.06		0.09
Tm	ppm	0.01	0.01	0.01		0.01
Yb	ppm	0.04	0.06	0.08		0.09
Lu	ppm	0.01	0.01	0.01		0.02
Hf	ppm	0.03	0.04	0.06		0.09
Ta	ppm	0.02	0.02	0.01		0.02
W	ppm	0.00	0.01	0.01		0.01
Pb	ppm	0.01	0.05	0.00		0.19
Th	ppm	0.01	0.03	0.02		0.06
U	ppm	0.00	0.01	0.00		0.01
Highly Siderophile Elements (ICPMS)						
Ir	ppb	0.944	0.448	0.222	0.066	0.546
Ru	ppb	3.011	2.006	1.512	0.790	2.558
Pt	ppb	0.098	0.803	0.240	0.087	0.984
Pd	ppb	0.958	1.916	0.496	0.484	1.248
Re	ppb		0.001	0.004		0.018
Osmium (TIMS)						
Os	ppb	2.410	1.197		0.262	3.096
^{187}Os/^{188}Os		0.13285	0.13197		0.13218	0.13251
± 2σ		0.00008	0.00010		0.00015	0.00015

Major Elements (XRF)	*Unit*	**CH0705X**	**CH0705Y**	**CH0706A**	**CH0706B**
SiO_2	wt. %	38.1	38.0	38.7	37.8
TiO_2	wt. %	0.20	0.07	0.09	0.08
Al_2O_3	wt. %	0.99	0.39	0.57	0.28
Fe_2O_3(T)	wt. %	15.4	16.4	13.0	16.8
MnO	wt. %	0.20	0.22	0.17	0.22
MgO	wt. %	44.1	44.2	46.3	43.8
CaO	wt. %	0.48	0.26	0.29	0.52
Na_2O	wt. %	0.13	0.10	0.08	0.09
K_2O	wt. %	0.01	0.02	0.00	0.00
P_2O_5	wt. %	0.03	0.02	0.02	0.02
Total	wt. %	99.7	99.7	99.3	99.6
LOI	wt. %	0.74	0.76	0.66	0.82
FeO	wt. %	11.8	13.0	8.2	11.7
Fe_2O_3	wt. %	2.33	2.00	3.89	3.75
Mg-number		87.0	85.9	91.0	86.9
Fe^{2+}/Fe*	mole fraction	0.92	0.94	0.82	0.87
Trace Elements (XRF)					
Rb	ppm	0.6	1.1	<0.5	<0.5
Sr	ppm	8	6	4	2
Y	ppm	<0.5	<0.5	<0.5	0.5
Zr	ppm	9	8	8	10
V	ppm	63	26	34	15
Ni	ppm	2159	1943	2503	2335
Cr	ppm	3767	2521	5609	1235
Nb	ppm	<0.5	<0.5	<0.5	<0.5
Ga	ppm	3.6	2.6	2.6	2.3
Cu	ppm	39	5	5	145
Zn	ppm	105	104	73	108
Co	ppm	160	175	148	147
Ba	ppm	4	<3	<3	<3
La	ppm	<1	<1	<1	1
Ce	ppm	<1	2	<1	<1
U	ppm	<0.5	<0.5	<0.5	<0.5
Th	ppm	<0.5	<0.5	<0.5	<0.5
Sc	ppm	7	7	5	8
Pb	ppm	<1	<1	<1	<1
Trace Elements (ICPMS)					
Li	ppm	2.72	2.40	3.07	2.83
Sc	ppm	36.75	4.78	26.34	8.79
V	ppm	49.8	19.6	24.6	17.1
Cr	ppm	3387	2695	4810	1345
Co	ppm	163	198	153	195

Ni	ppm	2334	2384		2469	2887
Cu	ppm	33.2	2.0		3.3	115.6
Zn	ppm	96.9	92.2		73.8	179.8
Ga	ppm	2.92	1.15		4.90	0.87
Ge	ppm	1.56	1.60		1.37	1.64
Rb	ppm	0.05	0.72		0.13	0.06
Sr	ppm	6.47	0.85		1.92	1.11
Y	ppm	0.70	0.31		0.32	0.43
Zr	ppm	2.59	4.28		2.79	1.17
Nb	ppm	0.28	0.37		0.26	0.12
Cs	ppm	0.00	0.02		0.01	0.00
Ba	ppm		1.43		1.02	1.11
La	ppm	0.29	0.33		0.21	0.16
Ce	ppm	0.69	0.63		0.48	0.33
Pr	ppm	0.10	0.08		0.06	0.05
Nd	ppm	0.45	0.28		0.25	0.23
Sm	ppm	0.12	0.05		0.06	0.06
Eu	ppm	0.04	0.01		0.02	0.02
Gd	ppm	0.13	0.06		0.06	0.07
Tb	ppm	0.02	0.01		0.01	0.01
Dy	ppm	0.13	0.05		0.06	0.07
Ho	ppm	0.03	0.01		0.01	0.02
Er	ppm	0.09	0.04		0.04	0.05
Tm	ppm	0.01	0.01		0.01	0.01
Yb	ppm	0.11	0.05		0.06	0.06
Lu	ppm	0.02	0.01		0.01	0.01
Hf	ppm	0.07	0.10		0.09	0.04
Ta	ppm	0.03	0.04		0.03	0.01
W	ppm	0.01	0.04		0.02	0.01
Pb	ppm	0.24	0.07		0.12	0.10
Th	ppm	0.02	0.15		0.06	0.03
U	ppm	0.01	0.04		0.02	0.00

Highly Siderophile Elements (ICPMS)

Ir	ppb	0.210	0.464	0.425	3.020	1.157
Ru	ppb	2.493	1.349	2.531	4.791	4.090
Pt	ppb	2.159	0.350	0.363	13.333	1.795
Pd	ppb	3.070	0.196	0.416	21.244	2.845
Re	ppb	0.046	0.002		0.235	0.066

Major Elements (XRF)	*Unit*	**CH0706B,3**	**CH0706C**	**CH0706E**	**CH0706F**
SiO_2	wt. %	38.1	37.9	38.4	38.8
TiO_2	wt. %	0.10	0.10	0.10	0.10
Al_2O_3	wt. %	0.48	0.42	0.56	0.42
Fe_2O_3(T)	wt. %	16.5	15.8	15.6	13.4
MnO	wt. %	0.21	0.21	0.21	0.18
MgO	wt. %	43.7	43.6	44.5	46.2
CaO	wt. %	0.56	0.68	0.28	0.42
Na_2O	wt. %	0.09	0.09	0.08	0.09
K_2O	wt. %	0.00	0.00	0.02	0.00
P_2O_5	wt. %	0.02	0.02	0.02	0.02
Total	wt. %	99.7	98.8	99.7	99.6
LOI	wt. %	0.62	0.54	0.38	0.59
FeO	wt. %	11.5	9.7	9.2	8.6
Fe_2O_3	wt. %	3.73	5.02	5.43	3.93
Mg-number		87.1	88.9	89.6	90.6
Fe^{2+}/Fe^*	mole fraction	0.87	0.81	0.79	0.83
Trace Elements (XRF)					
Rb	ppm	<0.5	0.8	0.6	1.3
Sr	ppm	3	3	3	3
Y	ppm	<0.5	<0.5	<0.5	<0.5
Zr	ppm	9	9	9	8
V	ppm	37	39	28	22
Ni	ppm	1964	2291	1826	2206
Cr	ppm	3425	2495	3825	3166
Nb	ppm	<0.5	<0.5	<0.5	<0.5
Ga	ppm	2.4	3.2	2.5	2.6
Cu	ppm	100	21	21	8
Zn	ppm	104	99	103	88
Co	ppm	169	149	181	149
Ba	ppm	<3	4	4	<3
La	ppm	1	1	<1	<1
Ce	ppm	<1	<1	<1	<1
U	ppm	<0.5	<0.5	<0.5	<0.5
Th	ppm	<0.5	<0.5	<0.5	<0.5
Sc	ppm	8	8	6	5
Pb	ppm	<1	<1	<1	<1
Trace Elements (ICPMS)					
Li	ppm	1.32	1.51	1.64	2.62
Sc	ppm	5.42	5.50	4.33	5.51
V	ppm	28.7	36.9	27.6	25.3
Cr	ppm	3446	3408	4523	3527
Co	ppm	196	181	196	168

Ni	ppm	2371	2685	2155	2591
Cu	ppm	85.5	17.7	11.9	8.7
Zn	ppm	87.5	94.9	91.8	93.7
Ga	ppm	1.31	1.75	1.64	1.35
Ge	ppm	1.56	1.49	1.56	1.36
Rb	ppm	0.06	0.08	0.05	0.09
Sr	ppm	1.48	1.16	0.84	1.89
Y	ppm	0.34	0.64	0.41	0.80
Zr	ppm	1.02	1.67	1.44	2.21
Nb	ppm	0.11	0.09	0.12	0.15
Cs	ppm	0.00	0.00	0.01	0.00
Ba	ppm	0.58	0.63	0.77	4.00
La	ppm	0.11	0.21	0.21	0.29
Ce	ppm	0.25	0.52	0.46	0.73
Pr	ppm	0.04	0.09	0.07	0.11
Nd	ppm	0.18	0.44	0.31	0.56
Sm	ppm	0.05	0.12	0.08	0.15
Eu	ppm	0.02	0.04	0.03	0.05
Gd	ppm	0.05	0.13	0.08	0.16
Tb	ppm	0.01	0.02	0.01	0.02
Dy	ppm	0.06	0.12	0.08	0.15
Ho	ppm	0.01	0.03	0.02	0.03
Er	ppm	0.04	0.07	0.05	0.09
Tm	ppm	0.01	0.01	0.01	0.01
Yb	ppm	0.04	0.08	0.06	0.09
Lu	ppm	0.01	0.01	0.01	0.02
Hf	ppm	0.03	0.05	0.04	0.06
Ta	ppm	0.02	0.02	0.02	0.02
W	ppm	0.00	0.01	0.03	0.01
Pb	ppm	0.04	0.03	1.25	0.02
Th	ppm	0.01	0.01	0.02	0.02
U	ppm	0.00	0.00	0.00	0.00
Highly Siderophile Elements (ICPMS)					
Ir	ppb	0.614	1.115	0.327	0.129
Ru	ppb	1.587	3.923	1.758	1.626
Pt	ppb	3.574	0.627	0.102	0.755
Pd	ppb	6.680	1.159	3.037	1.725
Re	ppb	0.047	0.238	0.257	0.046
Osmium (TIMS)					
Os	ppb	1.621	0.716	0.175	0.437
$^{187}Os/^{188}Os$		0.13187	0.13231	0.13180	0.13332
± 2σ		0.00016	0.00008	0.00037	0.00008

Major Elements (XRF)	*Unit*	**CH0707B**	**CH0707C**	**CH0708A**	**CH0708B**
SiO_2	wt. %		38.1	37.8	38.2
TiO_2	wt. %		0.14	0.08	0.08
Al_2O_3	wt. %		0.71	0.39	0.57
Fe_2O_3(T)	wt. %		15.6	17.4	15.5
MnO	wt. %		0.20	0.23	0.20
MgO	wt. %		44.2	43.3	44.8
CaO	wt. %		0.56	0.34	0.28
Na_2O	wt. %		0.09	0.08	0.08
K_2O	wt. %		0.00	0.00	0.00
P_2O_5	wt. %		0.02	0.01	0.01
Total	wt. %		99.6	99.7	99.6
LOI	wt. %		0.64	0.76	0.63
FeO	wt. %		11.2	12.8	10.9
Fe_2O_3	wt. %		3.09	3.16	3.30
Mg-number			87.6	85.8	88.0
Fe^{2+}/Fe^*	mole fraction		0.89	0.90	0.88
Trace Elements (XRF)					
Rb	ppm		<0.5	<0.5	<0.5
Sr	ppm		3	2	3
Y	ppm		<0.5	<0.5	<0.5
Zr	ppm		11	9	8
V	ppm		52	34	36
Ni	ppm		1956	1856	2251
Cr	ppm		4684	2702	4314
Nb	ppm		<0.5	<0.5	<0.5
Ga	ppm		3.4	2.8	3
Cu	ppm		16	37	26
Zn	ppm		102	120	99
Co	ppm		168	174	158
Ba	ppm		<3	<3	<3
La	ppm		<1	1	<1
Ce	ppm		<1	1	<1
U	ppm		<0.5	<0.5	<0.5
Th	ppm		<0.5	<0.5	<0.5
Sc	ppm		6	7	5
Pb	ppm		<1	<1	<1
Trace Elements (ICPMS)					
Li	ppm	2.29	1.06	1.27	
Sc	ppm	23.19	4.65	4.76	
V	ppm	26.1	37.2	28.3	
Cr	ppm	3808	4623	3190	
Co	ppm	162	185	204	

Ni	ppm	2370	2303	2359	
Cu	ppm	16.1	8.1	25.9	
Zn	ppm	92.6	87.1	104.9	
Ga	ppm	1.65	2.12	1.35	
Ge	ppm	1.58	1.49	1.74	
Rb	ppm	0.00	0.10	0.07	
Sr	ppm	2.08	1.87	0.89	
Y	ppm	0.27	0.58	0.22	
Zr	ppm	1.27	2.09	0.94	
Nb	ppm	0.11	0.15	0.12	
Cs	ppm	0.00	0.00	0.00	
Ba	ppm	-0.73	0.64	0.48	
La	ppm	0.11	0.22	0.10	
Ce	ppm	0.27	0.54	0.20	
Pr	ppm	0.03	0.08	0.03	
Nd	ppm	0.15	0.39	0.12	
Sm	ppm	0.03	0.11	0.03	
Eu	ppm	0.01	0.03	0.01	
Gd	ppm	0.04	0.11	0.03	
Tb	ppm	0.01	0.02	0.01	
Dy	ppm	0.04	0.11	0.04	
Ho	ppm	0.01	0.02	0.01	
Er	ppm	0.04	0.06	0.03	
Tm	ppm	0.01	0.01	0.00	
Yb	ppm	0.05	0.07	0.04	
Lu	ppm	0.01	0.01	0.01	
Hf	ppm	0.03	0.06	0.02	
Ta	ppm	0.01	0.02	0.01	
W	ppm	0.01	0.03	0.01	
Pb	ppm	0.02	0.26	0.07	
Th	ppm	0.02	0.04	0.01	
U	ppm	0.00	0.01	0.00	
Highly Siderophile Elements (ICPMS)					
Ir	ppb	0.251	0.155	1.085	0.371
Ru	ppb	2.190	1.056	1.996	1.531
Pt	ppb	0.517	0.207	2.708	1.936
Pd	ppb	1.699	0.958	9.196	3.638
Re	ppb	0.004	0.004	0.044	0.013
Osmium (TIMS)					
Os	ppb	1.724	0.521	3.807	1.248
$^{187}Os/^{188}Os$		0.13182	0.13130	0.13259	0.13330
± 2σ		0.00007	0.00012	0.00007	0.00152

Major Elements (XRF)	*Unit*	**CH0708D**	**CH0704CL**	**RU0701**	**RU0702**
SiO_2	wt. %	38.0	45.8	43.3	42.8
TiO_2	wt. %	0.09	2.73	1.56	1.46
Al_2O_3	wt. %	0.39	13.72	8.15	7.73
Fe_2O_3(T)	wt. %	17.0	13.9	14.5	14.6
MnO	wt. %	0.23	0.18	0.19	0.20
MgO	wt. %	43.7	10.7	23.5	24.8
CaO	wt. %	0.36	9.74	6.55	6.36
Na_2O	wt. %	0.08	2.33	1.45	1.26
K_2O	wt. %	0.00	0.70	0.37	0.37
P_2O_5	wt. %	0.01	0.32	0.18	0.17
Total	wt. %	99.8	100.1	99.8	99.7
LOI	wt. %	0.71	1.87	0.82	0.73
FeO	wt. %	11.9	7.3	11.2	8.6
Fe_2O_3	wt. %	3.68	5.84	1.98	4.97
Mg-number		86.7	72.5	78.9	83.7
Fe^{2+}/Fe*	mole fraction	0.88	0.73	0.93	0.79
Trace Elements (XRF)					
Rb	ppm	<0.5	12.6	8	8.9
Sr	ppm	2	327	190	185
Y	ppm	0.5	27.2	25.6	26.1
Zr	ppm	8	184	81	76
V	ppm	37	307	205	204
Ni	ppm	1686	227	753	746
Cr	ppm	3247	618	1651	1634
Nb	ppm	<0.5	24.8	9.1	10.1
Ga	ppm	2.7	16.9	11.6	11.1
Cu	ppm	10	144	76	63
Zn	ppm	103	105	99	96
Co	ppm	178	67	102	105
Ba	ppm	10	126	72	67
La	ppm	1	11	8	6
Ce	ppm	<1	23	25	27
U	ppm	<0.5	0.8	<0.5	<0.5
Th	ppm	<0.5	1.1	0.9	0.5
Sc	ppm	7	34	22	22
Pb	ppm	<1	<1	<1	2
Trace Elements (ICPMS)					
Li	ppm	1.10	5.57		2.67
Sc	ppm	4.39	28.1		3.4
V	ppm	24.0	279		104
Cr	ppm	3351	556		2116
Co	ppm	194	63.5		138.8

Ni	ppm	2034	264		1602
Cu	ppm	4.7	132		41
Zn	ppm	88.1	105		95
Ga	ppm	1.16	19.5		6.7
Ge	ppm	1.61	1.64		1.51
Rb	ppm	0.07	17.0		5.3
Sr	ppm	1.20	311		98
Y	ppm	0.25	24.9		7.5
Zr	ppm	0.76	190		53
Nb	ppm	0.10	23.9		6.2
Cs	ppm	0.01	0.26		0.07
Ba	ppm	1.08	134.5		39.5
La	ppm	0.11	19.7		5.6
Ce	ppm	0.19	45.8		13.0
Pr	ppm	0.03	5.91		1.72
Nd	ppm	0.13	26.0		7.6
Sm	ppm	0.03	5.97		1.84
Eu	ppm	0.01	1.91		0.59
Gd	ppm	0.03	6.20		1.89
Tb	ppm	0.01	0.86		0.27
Dy	ppm	0.04	5.08		1.59
Ho	ppm	0.01	1.00		0.31
Er	ppm	0.03	2.50		0.78
Tm	ppm	0.00	0.32		0.10
Yb	ppm	0.04	2.01		0.66
Lu	ppm	0.01	0.28		0.09
Hf	ppm	0.02	4.07		1.28
Ta	ppm	0.01	1.75		0.52
W	ppm	0.03	0.29		0.08
Pb	ppm	0.01	1.59		0.47
Th	ppm	0.01	2.31		0.60
U	ppm	0.00	0.56		0.17
Highly Siderophile Elements (ICPMS)					
Ir	ppb	1.509	0.049	0.393	0.364
Ru	ppb	4.430	0.126	1.075	0.819
Pt	ppb	0.662	0.821	0.901	1.552
Pd	ppb	2.340	1.945	1.243	1.126
Re	ppb	0.034	2.472	0.037	0.037
Osmium (TIMS)					
Os	ppb	2.694	0.126	0.416	0.830
$^{187}Os/^{188}Os$		0.13344	0.13252	0.13302	0.13205
± 2σ		0.00006	0.00019	0.00013	0.00007

Major Elements (XRF)	*Unit*	**RU0703**	**RU0705**	**RU0706**
SiO_2	wt. %	48.7	42.2	42.3
TiO_2	wt. %	2.69	1.20	1.29
Al_2O_3	wt. %	14.12	6.10	6.59
Fe_2O_3(T)	wt. %	12.7	14.6	14.9
MnO	wt. %	0.17	0.20	0.20
MgO	wt. %	7.5	29.2	27.6
CaO	wt. %	10.94	4.95	5.34
Na_2O	wt. %	2.61	1.04	1.12
K_2O	wt. %	0.72	0.26	0.27
P_2O_5	wt. %	0.32	0.14	0.15
Total	wt. %	100.5	99.8	99.7
LOI	wt. %	0.86	0.95	0.86
FeO	wt. %	10.1	12.4	12.5
Fe_2O_3	wt. %	1.42	0.82	0.97
Mg-number		56.9	80.8	79.7
Fe^{2+}/Fe*	mole fraction	0.94	0.97	0.97
Trace Elements (XRF)				
Rb	ppm	14.2	5.7	6.3
Sr	ppm	345	140	145
Y	ppm	26.9	23.4	25.4
Zr	ppm	183	56	67
V	ppm	310	167	174
Ni	ppm	92	986	959
Cr	ppm	313	2096	1975
Nb	ppm	21.9	6.6	7.8
Ga	ppm	18.3	9.6	9.9
Cu	ppm	110	68	74
Zn	ppm	92	102	104
Co	ppm	48	122	117
Ba	ppm	139	60	45
La	ppm	12	5	5
Ce	ppm	25	20	21
U	ppm	2.2	<0.5	<0.5
Th	ppm	1.5	1.6	5.4
Sc	ppm	32	18	19
Pb	ppm	1	<1	<1
Trace Elements (ICPMS)				
Li	ppm	3.71	3.63	3.85
Sc	ppm	18.0	15.2	17.8
V	ppm	153	149	164
Cr	ppm	1576	2086	1896
Co	ppm	111.5	139.7	126.3

Ni	ppm	1019	1393	1232
Cu	ppm	54	76	81
Zn	ppm	96	109	108
Ga	ppm	11.2	9.9	11.3
Ge	ppm	1.58	1.68	1.61
Rb	ppm	9.4	7.5	8.1
Sr	ppm	169	146	164
Y	ppm	14.2	12.5	14.6
Zr	ppm	94	79	90
Nb	ppm	11.1	8.9	9.6
Cs	ppm	0.13	0.10	0.11
Ba	ppm	70.5	56.0	60.6
La	ppm	10.0	7.8	8.7
Ce	ppm	23.5	18.2	20.3
Pr	ppm	3.06	2.46	2.77
Nd	ppm	13.6	11.0	12.7
Sm	ppm	3.31	2.76	3.21
Eu	ppm	1.08	0.91	1.07
Gd	ppm	3.50	2.88	3.41
Tb	ppm	0.50	0.42	0.50
Dy	ppm	2.99	2.49	2.99
Ho	ppm	0.60	0.49	0.59
Er	ppm	1.47	1.22	1.47
Tm	ppm	0.19	0.16	0.19
Yb	ppm	1.17	0.99	1.18
Lu	ppm	0.17	0.14	0.17
Hf	ppm	2.34	1.91	2.23
Ta	ppm	0.93	0.70	0.77
W	ppm	0.15	0.12	0.13
Pb	ppm	0.81	0.64	0.75
Th	ppm	1.21	0.87	0.99
U	ppm	0.30	0.23	0.25

Highly Siderophile Elements (ICPMS)

Ir	ppb	0.029	0.318	0.296	0.334	0.284
Ru	ppb		0.896	0.750	1.327	1.233
Pt	ppb	1.044	0.823	0.742	0.741	0.835
Pd	ppb	4.008	1.177	0.763	1.048	1.582
Re	ppb	0.209	0.101	0.089	0.112	0.116

Osmium (TIMS)

Os	ppb	0.092	0.481	0.680
$^{187}Os/^{188}Os$		0.13110	0.13194	0.13308
± 2σ		0.00024	0.00006	0.00011

Major Elements (XRF)	*Unit*	**RU0707**	**RU0708**	**RU0709**
SiO_2	wt. %	48.4	45.0	46.1
TiO_2	wt. %	2.61	2.10	2.51
Al_2O_3	wt. %	14.24	10.83	12.72
Fe_2O_3(T)	wt. %	12.5	13.7	13.2
MnO	wt. %	0.17	0.18	0.18
MgO	wt. %	7.2	16.5	11.2
CaO	wt. %	11.20	8.89	10.93
Na_2O	wt. %	2.64	1.87	2.26
K_2O	wt. %	0.67	0.53	0.73
P_2O_5	wt. %	0.31	0.25	0.29
Total	wt. %	99.9	99.9	100.1
LOI	wt. %	0.68	0.69	0.79
FeO	wt. %	10.5	10.9	11.0
Fe_2O_3	wt. %	0.80	1.57	1.00
Mg-number		54.9	73.0	64.4
Fe^{2+}/Fe^*	mole fraction	0.97	0.94	0.96
Trace Elements (XRF)				
Rb	ppm	13.5	11.2	15.3
Sr	ppm	332	272	324
Y	ppm	26.6	28.1	25.7
Zr	ppm	177	128	154
V	ppm	311	266	307
Ni	ppm	80	433	202
Cr	ppm	294	1155	610
Nb	ppm	19.9	15.4	21.4
Ga	ppm	17.9	14.3	15.9
Cu	ppm	169	93	104
Zn	ppm	93	95	91
Co	ppm	52	79	58
Ba	ppm	124	103	144
La	ppm	11	9	11
Ce	ppm	22	26	26
U	ppm	1.2	<0.5	1.2
Th	ppm	<0.5	<0.5	<0.5
Sc	ppm	33	28	34
Pb	ppm	<1	2	<1
Trace Elements (ICPMS)				
Li	ppm	5.58	4.98	5.55
Sc	ppm	31.4	28.6	35.0
V	ppm	292	253	319
Cr	ppm	241	1116	570
Co	ppm	52.6	82.7	65.3
Ni	ppm	91	573	275

Cu	ppm	178	92		111
Zn	ppm	109	108		110
Ga	ppm	21.3	17.5		20.3
Ge	ppm	1.52	1.67		1.73
Rb	ppm	16.5	15.2		22.2
Sr	ppm	332	290		355
Y	ppm	27.5	23.0		25.8
Zr	ppm	185	162		178
Nb	ppm	20.1	17.9		23.5
Cs	ppm	0.23	0.21		0.30
Ba	ppm	126.7	113.5		170.7
La	ppm	18.0	16.2		19.3
Ce	ppm	43.5	38.0		45.0
Pr	ppm	5.62	5.07		5.85
Nd	ppm	25.6	22.6		25.9
Sm	ppm	6.23	5.50		6.07
Eu	ppm	2.06	1.82		2.00
Gd	ppm	6.48	5.69		6.27
Tb	ppm	0.94	0.81		0.88
Dy	ppm	5.60	4.80		5.18
Ho	ppm	1.12	0.95		1.03
Er	ppm	2.74	2.33		2.56
Tm	ppm	0.36	0.30		0.34
Yb	ppm	2.16	1.86		2.05
Lu	ppm	0.31	0.26		0.29
Hf	ppm	4.34	3.85		4.18
Ta	ppm	1.60	1.46		1.87
W	ppm	0.27	0.23		0.30
Pb	ppm	1.56	1.30		1.66
Th	ppm	2.05	1.86		2.25
U	ppm	0.52	0.47		0.55
Highly Siderophile Elements (ICPMS)					
Ir	ppb	0.100	0.180	0.128	0.064
Ru	ppb	0.107	0.398	0.222	0.109
Pt	ppb	1.838	1.217	1.514	1.373
Pd	ppb	1.526	2.381	9.984	1.635
Re	ppb	0.450	0.459	0.107	0.106
Osmium (TIMS)					
Os	ppb	0.528			0.105
^{187}Os/^{188}Os		0.13179			0.13328
± 2σ		0.00028			0.00013

Major Elements (XRF)	*Unit*	**RU0719**	**RU1515**	**RU1516B**
SiO_2	wt. %	43.7	46.9	46.7
TiO_2	wt. %	1.73	2.17	2.53
Al_2O_3	wt. %	8.94	12.63	12.76
Fe_2O_3(T)	wt. %	14.2	13.3	13.5
MnO	wt. %	0.19	0.19	0.19
MgO	wt. %	21.5	11.0	10.5
CaO	wt. %	7.43	10.23	10.20
Na_2O	wt. %	1.55	2.42	2.46
K_2O	wt. %	0.47	0.69	0.68
P_2O_5	wt. %	0.20	0.30	0.30
Total	wt. %	100.0	99.8	99.8
LOI	wt. %	0.83	0.64	0.34
FeO	wt. %	11.7	9.8	0.6
Fe_2O_3	wt. %	1.27	2.39	12.81
Mg-number		76.7	62.1	93.6
Fe^{2+}/Fe^*	mole fraction	0.95	0.90	0.10
Trace Elements (XRF)				
Rb	ppm	10.3	16.1	12.4
Sr	ppm	229	330	315
Y	ppm	26.6	27.2	28.7
Zr	ppm	99	175	171
V	ppm	231	316	302
Ni	ppm	604	265	251
Cr	ppm	1519	566	576
Nb	ppm	13.7	23.9	24.3
Ga	ppm	12.4	17.9	17.9
Cu	ppm	102	94	159
Zn	ppm	99	105	107
Co	ppm	97	62	65
Ba	ppm	92	125	120
La	ppm	8	12	11
Ce	ppm	27	19	20
U	ppm	<0.5	<0.5	0.8
Th	ppm	4.5	4.3	4.1
Sc	ppm	25	2	32
Pb	ppm	<1	<1	4
Trace Elements (ICPMS)				
Li	ppm	4.65	5.77	5.57
Sc	ppm	25.7	30.3	29.9
V	ppm	227	288	272
Cr	ppm	1656	584	532
Co	ppm	108.2	61.2	60.3
Ni	ppm	852	293	270

Cu	ppm	103	88.2	135.6
Zn	ppm	110	106	105
Ga	ppm	14.8	19.8	19.5
Ge	ppm	1.71	1.63	1.61
Rb	ppm	14.5	19.2	16.6
Sr	ppm	246	341	339
Y	ppm	19.0	25.2	24.8
Zr	ppm	133	180	178
Nb	ppm	17.3	22.4	22.3
Cs	ppm	0.19	0.29	0.27
Ba	ppm	105.1	131.8	133.5
La	ppm	15.0	19.4	19.6
Ce	ppm	34.2	45.5	45.7
Pr	ppm	4.40	5.89	5.88
Nd	ppm	19.2	25.4	25.6
Sm	ppm	4.42	5.84	5.91
Eu	ppm	1.45	1.94	1.91
Gd	ppm	4.57	6.07	6.15
Tb	ppm	0.65	0.86	0.86
Dy	ppm	3.82	5.11	5.10
Ho	ppm	0.76	1.00	1.00
Er	ppm	1.90	2.47	2.43
Tm	ppm	0.25	0.32	0.32
Yb	ppm	1.52	1.97	1.93
Lu	ppm	0.22	0.28	0.27
Hf	ppm	3.09	4.19	4.11
Ta	ppm	1.35	1.77	1.76
W	ppm	0.23	0.26	0.28
Pb	ppm	1.09	0.94	1.60
Th	ppm	1.80	2.27	2.28
U	ppm	0.43	0.55	0.57

Highly Siderophile Elements (ICPMS)

Ir	ppb	0.118	0.158	0.042	0.029
Ru	ppb	0.451	0.465	0.088	0.028
Pt	ppb	0.950	0.979	0.265	0.322
Pd	ppb	1.192	0.138	0.594	1.046
Re	ppb	0.173	0.168	0.235	0.236

Osmium (TIMS)

Os	ppb	0.226	0.334
^{187}Os/^{188}Os		0.13387	0.13273
± 2σ		0.00022	0.00013

Major Elements (XRF)	*Unit*	**RU1517**
SiO_2	wt. %	46.7
TiO_2	wt. %	2.51
Al_2O_3	wt. %	12.70
Fe_2O_3(T)	wt. %	13.1
MnO	wt. %	0.19
MgO	wt. %	10.9
CaO	wt. %	10.28
Na_2O	wt. %	2.45
K_2O	wt. %	0.69
P_2O_5	wt. %	0.31
Total	wt. %	99.8
LOI	wt. %	0.59
FeO	wt. %	9.5
Fe_2O_3	wt. %	2.55
Mg-number		62.3
Fe^{2+}/Fe^*	mole fraction	0.89
Trace Elements (XRF)		
Rb	ppm	16.6
Sr	ppm	330
Y	ppm	27
Zr	ppm	174
V	ppm	318
Ni	ppm	250
Cr	ppm	547
Nb	ppm	24
Ga	ppm	17.6
Cu	ppm	93
Zn	ppm	103
Co	ppm	59
Ba	ppm	137
La	ppm	11
Ce	ppm	19
U	ppm	<0.5
Th	ppm	4.2
Sc	ppm	30
Pb	ppm	<1
Trace Elements (ICPMS)		
Li	ppm	5.64
Sc	ppm	29.5
V	ppm	280
Cr	ppm	554
Co	ppm	58.5
Ni	ppm	278

Cu	ppm	85.1
Zn	ppm	104
Ga	ppm	19.2
Ge	ppm	1.61
Rb	ppm	19.2
Sr	ppm	336
Y	ppm	24.7
Zr	ppm	178
Nb	ppm	22.2
Cs	ppm	0.29
Ba	ppm	133.5
La	ppm	19.6
Ce	ppm	45.7
Pr	ppm	5.88
Nd	ppm	25.6
Sm	ppm	5.91
Eu	ppm	1.91
Gd	ppm	6.15
Tb	ppm	0.86
Dy	ppm	5.10
Ho	ppm	1.00
Er	ppm	2.43
Tm	ppm	0.32
Yb	ppm	1.93
Lu	ppm	0.27
Hf	ppm	4.11
Ta	ppm	1.76
W	ppm	0.28
Pb	ppm	1.60
Th	ppm	2.28
U	ppm	0.57

Highly Siderophile Elements (ICPMS)

Ir	ppb	0.022	0.136
Ru	ppb	0.060	
Pt	ppb	0.238	0.223
Pd	ppb	1.321	0.552
Re	ppb	0.220	0.222

Osmium (TIMS)

Os	ppb	0.329
^{187}Os/^{188}Os		0.13221
± 2σ		0.00008

Table A3.2: Modal mineralogy (modal %) for select Piton Chisny cumulate xenoliths and Piton de la Fournaise basaltic lavas

Sample	Type	Discolored?	Ox	Cpx	Ol	Gm
CH0701	Dunite	**N**				
CH0701 Dunite	Dunite	**N**	1.7	2.3	96	
CH0702	Dunite	**N**				
CH0702A	Dunite	**N**	1.3		99	
CH0703	Dunite	**Y**	0.7			
CH0703A	Dunite	**N**	0.9		99	
CH0703B	Wherlite	**Y**		27	23	51
CH0703C	Dunite	**Y**				
CH0703D	Dunite	**Y**				
CH0703E	Dunite	**Y**	0.3		100	
CH0703 Dunite	Dunite	**N**				
CH0703 Pyroxenite	Dunite	**Y**				
CH0704	Dunite	**Y**	1.2		99	
CH0704A	Dunite	**N**				
CH0705A	Dunite	**Y**	1.2	0.6	98	
CH0705B	Dunite	**Y**	0.5		99	
CH0705C	Dunite	**N**				
CH0705X	Dunite	**Y**	1.2		97	
CH0705Y	Dunite	**Y**				
CH0706A	Dunite	**Y**				
CH0706B	Dunite	**Y**				
CH0706B,3	Dunite	**Y**				
CH0706C	Dunite	**Y**			52	48
CH0706D	Dunite	**Y**	0.7			
CH0706E	Dunite	**Y**	1.4		99	
CH0706F	Dunite	**Y**				
CH0707A	Dunite	**N**	2.5		98	
CH0707B	Dunite	**N**	3.7	2.1	94	
CH0707C	Dunite	**N**	4.6	3.1	92	
CH0708A	Dunite	**Y**	3.6			
CH0708B	Dunite	**Y**			59	41
CH0708D	Dunite	**Y**				
RU0701	Oceanite					
RU0702	Oceanite		0.9	1.5	*44*	10
RU0703	Basalt				*3.4*	
RU0705	Oceanite				*49*	
RU0706	Oceanite				*46*	

RU0707	Basalt				*1.7*	
RU0708	Basalt				*27*	
RU0709	Basalt				*8.5*	
RU0719	Oceanite		0.4		*31*	
RU1515	Basalt				*6.2*	
RU1517	Basalt				*4.2*	

Notes:
*Olivine abundances in italics determined by ImageJ color threshold analysis of sample chips; all other abundances determined by ImageJ analysis of thin sections
*Gray boxes indicate that phase abundance could not be accurately determined by ImageJ; gray boxes across all phases of a single sample indicates that no appropriate rock chip or thin section exists for modal analysis
*Blank, white boxes indicate phase is not present in sample

Table A3.3: Replicate analyses of external standards during trace element analyses of Piton Chisny cumulate xenoliths and Piton de la Fournaise basaltic lavas. Table starts on next page for clarity.

	BHVO-2	BCR-2	BCR-2	BCR-2	BCR-2	BCR-2	BIR-1
Ti (wt. %)	1.62	1.33	1.45	1.29	1.30	1.28	0.57
Mn (wt. %)			0.21	0.19	0.19	0.19	
Fe (wt. %)			10.37	9.26	9.30	9.22	
P (wt. %)	0.12	0.16	0.17	0.15	0.15	0.15	0.02
Li	4.87	10.25	10.69	9.55	9.56	9.46	3.33
Sc	31.9	33.2	36.2	32.3	32.5	31.1	44.6
V	312	412	448	399	401	397	322
Cr	275.3	14.4	16.1	13.9	14.2	11.5	374.4
Co	44.5	37.7	40.1	35.7	35.9	36.3	53.0
Ni	118	12.1	13.4	11.8	11.9	11.8	172
Cu	126	18.9	21.7	19.6	19.8	19.6	119
Zn	102	129	139	125	127	125	64.9
Ga	21.5	22.6	24.3	21.7	21.9	21.7	15.6
Ge	1.60	1.71	1.87	1.67	1.67	1.72	1.20
Rb	9.7	50.3	54.3	48.4	48.7	46.4	0.19
Sr	387	335	362	324	325	326	114
Y	25.7	35.8	38.7	34.6	34.8	34.8	15.7
Zr	171	188	203	181	183	184	15
Nb	17.9	12.1	13.2	11.8	11.9	11.9	0.53
Cs	0.10	1.23	1.21	1.09	1.10	1.12	0.01
Ba	129	679	741	666	667	735	5.53
La	15.0	24.7	26.5	23.8	23.8	24.5	0.60
Ce	38.4	54.4	58.0	52.0	52.0	55.0	1.91
Pr	5.38	6.88	7.41	6.63	6.64	6.86	0.37
Nd	24.8	30.2	31.7	28.4	28.4	30.0	2.45

Sm	6.11	6.78	7.26	6.50	6.49	6.76	1.11
Eu	2.07	2.11	2.26	2.02	2.02	2.12	0.51
Gd	6.31	7.04	7.54	6.76	6.77	7.08	1.71
Tb	0.90	1.02	1.10	0.98	0.98	1.04	0.34
Dy	5.25	6.46	6.93	6.21	6.19	6.68	2.56
Ho	1.03	1.37	1.48	1.33	1.33	1.43	0.60
Er	2.50	3.71	3.97	3.55	3.54	3.72	1.70
Tm	0.33	0.53	0.56	0.50	0.50	0.52	0.25
Yb	2.01	3.39	3.64	3.25	3.26	3.43	1.65
Lu	0.28	0.51	0.54	0.49	0.49	0.52	0.25
Hf	4.14	4.62	4.95	4.41	4.44	4.80	0.55
Ta	1.42	0.95	1.01	0.91	0.92	0.97	0.05
W	0.21	0.46	0.50	0.44	0.45	0.45	0.02
Pb	1.60	9.54	10.69	9.43	9.96	9.67	3.15
Th	1.20	5.87	6.29	5.64	5.66	6.13	0.03
U	0.39	1.61	1.73	1.55	1.55	1.69	0.01

	BIR-1	*BCR-2 Avg.*	*BCR-2 RSD (%)*	*BIR-1 Avg.*	*BIR-1 RSD*
Ti (wt. %)	0.58	1.3	5.1	0.6	0.9
Mn (wt. %)	0.17	0.2	5.9	0.2	
Fe (wt. %)	7.87	9.5	5.8	7.9	
P (wt. %)	0.01	0.2	4.8	0.0	36.8
Li	3.28	9.9	5.5	3.3	1.1
Sc	44.0	33.1	5.8	44.3	1.0
V	326	411.4	5.2	324.1	0.7
Cr	384.3	14.0	11.9	379.4	1.9
Co	52.5	37.1	4.9	52.8	0.7
Ni	170	12.2	5.4	171.2	0.9
Cu	118	19.9	5.4	118.5	0.2
Zn	68.2	129.2	4.6	66.6	3.5
Ga	15.6	22.4	4.9	15.6	0.2
Ge	1.22	1.7	4.7	1.2	1.1
Rb	0.20	49.6	5.9	0.2	6.8
Sr	105	334.3	4.9	109.8	5.6
Y	15.5	35.7	4.8	15.6	1.2
Zr	14	187.9	4.6	14.4	4.6
Nb	0.52	12.2	4.6	0.5	1.4
Cs	0.00	1.1	5.9	0.0	8.9
Ba	5.68	697.6	5.4	5.6	1.9
La	0.59	24.6	4.6	0.6	1.7
Ce	1.86	54.3	4.6	1.9	1.8

Pr	0.37	6.9	4.6	0.4	1.0
Nd	2.38	29.7	4.7	2.4	2.0
Sm	1.09	6.8	4.7	1.1	0.9
Eu	0.51	2.1	4.6	0.5	0.8
Gd	1.67	7.0	4.5	1.7	1.9
Tb	0.33	1.0	4.7	0.3	2.6
Dy	2.50	6.5	4.8	2.5	1.5
Ho	0.59	1.4	4.8	0.6	1.4
Er	1.64	3.7	4.7	1.7	2.6
Tm	0.24	0.5	4.7	0.2	2.1
Yb	1.60	3.4	4.7	1.6	2.0
Lu	0.24	0.5	4.7	0.2	2.3
Hf	0.53	4.6	4.9	0.5	2.8
Ta	0.05	1.0	4.5	0.0	3.7
W	0.02	0.5	5.3	0.0	6.6
Pb	2.78	9.9	5.1	3.0	8.9
Th	0.03	5.9	4.9	0.0	3.8
U	0.01	1.6	5.0	0.0	5.5

Table A3.4: Blank abundances and statistics for HSE analyses of Piton Chisny cumulate xenoliths and Piton de la Fournaise basaltic lavas.

Lab code	**Os (ng)**	**Ru (ng)**	**Pd (ng)**	**Re (ng)**	**Ir (ng)**	**Pt (ng)**	**$^{187}Os/^{188}Os$**
B1-8	0.002	0.094	0.051	0.007	0.018	0.051	0.1432
B2-4	0.003	0.106	0.025	0.010	0.118	0.041	0.1105
B2-8	0.003	0.114	0.089	0.007	0.127	0.057	0.1291
B4-4	0.016	0.095	0.032	0.008	0.084	0.064	0.1598
B4-8	0.020	0.106	0.021	0.010	0.057	0.039	0.1308
B5-4	0.007	0.140	0.008	0.012	0.045	0.052	0.1699
B11-4		0.097	0.058	0.008	0.032	0.024	
B13-4	0.001	0.184	0.025	0.013	0.128	0.022	0.1932
Average (B1-B5)	0.009	0.109	0.037	0.009	0.075	0.051	0.1405
Average (B11, B13)	0.001	0.140	0.042	0.011	0.080	0.023	0.193

Sample	**Type**	**Os % blank**	**Ir % blank**	**Ru % blank**	**Pt % blank**	**Pd % blank**	**Re % blank**
CH0704CL	Basalt	6.8	60.4	46.3	5.8	1.9	0.4
RU0702	Oceanite	0.3	7.6	8.2	2.6	4.5	17.2
[Duplicate]		0.1	26.0	18.3	1.4	2.2	26.3
RU0703	Basalt	1.3	81.4	100.0	2.1	0.6	5.9
RU0705	Oceanite		9.2	9.7	2.8	4.7	7.2
[Duplicate]		0.3	30.2	19.7	2.9	3.2	12.9
RU0706	Oceanite		8.8	6.8	3.1	5.3	6.5
[Duplicate]		0.2	31.1	13.0	2.6	1.6	10.2
RU0707	Basalt	0.2	24.4	47.4	1.3	3.7	1.7
RU0708	Basalt		15.2	19.5	1.9	2.4	1.7
RU0709	Basalt		20.1	30.3	1.6	0.6	6.8

[Duplicate]		1.2	66.7	62.7	1.6	1.5	11.1
RU0719	Oceanite	0.5	21.5	17.6	2.4	4.7	4.3
[Duplicate]		0.4	44.8	28.4	2.2	15.5	7.3
RU1515	Basalt		43.7	52.2	8.3	8.9	3.2
[Duplicate]			81.3	86.7	6.5	2.4	5.3
RU1517	Basalt, oxidized	0.4	59.9	61.8	9.1	4.2	3.4
[Duplicate]			48.5	106.1	9.1	4.4	5.6
CH0701	Dunite	0.9	20.0	5.9	5.2	8.5	24.5
CH0701 Dunite	Dunite	1.4	19.7	8.0	4.2		15.3
CH0702	Dunite	0.3	6.7	1.8	16.9	9.8	42.1
CH0702A	Dunite	0.6	22.7	7.0	6.4	3.4	51.7
CH0703 Dunite	Dunite	1.3	8.2	6.3	2.5	1.9	16.2
CH0703 Pyroxenite	Dunite	1.5	26.6	7.9	11.5	3.6	20.1
CH0703A	Dunite	0.5	6.5	2.9	6.6	6.1	49.0
CH0703B	Wherlite	0.9	23.9	11.8	4.4	2.9	7.5
CH0703C	Dunite	0.3	6.7	2.7	40.2	6.8	6.4
CH0703D	Dunite	0.5	22.6	8.5	7.9	4.6	22.7
CH0703E	Dunite	1.0	15.6	8.5	14.9	14.8	148.7
CH0704	Dunite	0.4	14.7	3.6	14.4	17.7	55.7
[Replicate]		0.7	15.3	4.7	17.5	3.9	47.5
[Replicate]		3.0	20.0	4.8	17.2	3.3	93.0
CH0704A	Dunite	0.4	7.3	3.5	34.1	3.8	199.9
CH0705A	Dunite	0.8	14.3	5.2	5.9	1.9	93.3
CH0705B	Dunite		25.0	6.7	17.3	7.0	70.7
[Duplicate]		3.4	53.2	12.1	36.8	7.2	636.6

CH0705C	Dunite	0.3	12.1	4.1	4.9	2.9	33.5
CH0705X	Dunite	2.6	26.3	4.2	2.3	1.2	16.2
CH0705Y	Dunite	0.9	13.9	7.5	12.7	16.0	85.2
[Duplicate]		1.2	15.0	4.1	12.3	8.3	212.2
CH0706A	Dunite	0.2	2.4	2.2	0.4	0.2	3.7
CH706B	Dunite	0.3	6.1	2.6	2.7	1.3	12.0
CH0706B,3	Dunite	0.6	10.9	6.4	1.4	0.6	15.8
CH0706C	Dunite	1.3	6.3	2.7	7.5	3.1	3.6
CH0706E	Dunite	5.0	18.6	5.8	33.3	1.2	3.4
CH0706F	Dunite	2.1	36.7	6.3	6.3	2.1	16.4
CH0707B	Dunite	0.5	23.0	4.7	8.9	2.2	69.0
CH0707C	Dunite	1.7	32.5	9.4	19.7	3.8	70.6
CH0708A	Dunite	0.2	6.5	5.2	1.8	0.4	16.9
CH0708B	Dunite	0.7	16.8	6.6	2.6	1.0	39.9
CH0708D	Dunite	0.3	4.7	2.4	7.1	1.6	20.8
Average		1.1	24.3	18.1	8.9	4.5	46.2

Table A3.5: Example calculation for primary magma composition for use in empirical P-T model of Lee et al. (2009); yellow highlighted cells indicate input required. Table is attached as a supplemental file.

Table A3.6: Electron microprobe (EMP) run statistics

(A) Average standard deviation (wt. %) for EMP analyses of given phase determined from analysis standard materials.

	Si	Na	Fe	Mn	Cr	Al	Ca	K	Ti	Mg	O	Ni	P	V
Olivine	0.24		0.15	0.026	0.019	0.009	0.013		0.014	0.43		0.031	0.010	
Pyroxene	0.26	0.029	0.086	0.021	0.037	0.038	0.14	0.012	0.033	0.17				
Spinel	0.024		0.26	0.029	0.18	0.093	0.016		0.044	0.09				0.025

(B) Average detection limits (ppm) for EMP analyses of given phase determined from analysis of standard materials

	Si	Na	Fe	Mn	Cr	Al	Ca	K	Ti	Mg	O	Ni	P	V
Olivine	192		276	239	222	98	126		160	170		302	118	
Pyroxene	192	171	272	214	236	107	185	138	215	145				
Spinel	180		325	300	270	158	175		219	173				225

Table A3.7: Average compositions for olivine, pyroxene and spinel in dunite and wherlite cumulate xenolith samples (in wt.%). Uncertainty represents 1 standard deviation of sample population on last reported digit of each analyte (i.e., it does not represent run precision, which is tabulated separately).

Lithology	*Dunite*		*Dunite*		*Dunite*		*Wherlite*		*Wherlite*		*Wherlite*	
Phase	*Olivine*		*Pyroxene*		*Spinel*		*Olivine*		*Pyroxene*		*Spinel*	
n	*367*		*177*		*219*		*63*		*115*		*27*	
	Conc.	*S.D.*[1]	*Conc.*	*S.D.*[1]	*Conc.*	*S.D.*[1]	*Conc.*	*S.D.*[1]	*Conc.*	*S.D.*[1]	*Conc.*	*S.D.*[1]
SiO_2	39.8	4	50.6	7	0.060	4	39.5	3	50.4	4	0.120	3
TiO_2	0.012	8	1.10	3	2.70	6	0.020	5	1.00	1	5.00	1
Al_2O_3	0.020	5	3.90	8	16.0	3	0.050	15	4.10	4	15.0	3
MgO	45.7	9	16.0	5	10.0	2	43.3	9	15.9	4	10	2
CaO	0.110	5	21.7	8	0.010	3	0.200	2	21.2	3	0.090	9
MnO	0.200	2	0.100	2	0.240	4	0.230	1	0.130	1	0.200	4
FeO	14.0	1	4.50	5			17.1	7	5.80	2		
Fe_2O_3 (calc)					15.0	3					20.0	9
FeO (calc)					21.0	3					22.0	3
Na_2O			0.500	1					0.490	5		
K_2O			0.004	5					0.003	3		
P_2O_5	0.008	8					0.010	1				
V_2O_3					0.220	4					0.4	8
NiO	0.300	4					0.210	3				
Cr_2O_3	0.01	1	0.900	3	33.0	3	0.030	3	0.700	1	25.0	6
Total	100.4	4			99.8	5	100.6	4			97.0	1
Fo	85	1					82	1				
Fs			7.4	9					9.4	2		
En			47	1					46.2	7		
Wo			46	2					44.4	8		
Cr#					58	5					52	3

Table A3.8: Analyses of olivine in Piton Chisny cumulate xenoliths (wt.%).

Sample	SiO_2	TiO_2	Al_2O_3	MgO	CaO	MnO	FeO	P_2O_5	NiO	Cr_2O_3	Total
CH0701	40.0	0.02	0.029	46.1	0.16	0.20	14.5	0.005	0.27	0.03	101.3
CH0701	39.9	0.00	0.038	46.3	0.14	0.17	14.5	0.039	0.29	0.00	101.3
CH0701	39.7	0.01	0.021	45.8	0.13	0.21	14.5	0.008	0.29	0.01	100.7
CH0701	39.9	0.00	0.019	46.2	0.16	0.18	14.4	0.008	0.29	0.02	101.2
CH0701	40.0	0.01	0.028	46.1	0.20	0.19	14.3	0.009	0.26	0.04	101.1
CH0701	39.8	0.00	0.035	46.0	0.13	0.17	14.6	0.016	0.27	0.00	101.0
CH0701	39.7	0.01	0.029	46.0	0.12	0.20	14.4	0.000	0.26	0.01	100.8
CH0701	40.0	0.02	0.032	46.0	0.15	0.18	14.3	0.000	0.27	0.03	101.0
CH0701	40.0	0.02	0.037	46.1	0.13	0.19	14.6	0.000	0.28	0.01	101.3
CH0701	39.9	0.01	0.028	46.1	0.13	0.19	14.5	0.000	0.27	0.01	101.2
CH0701	39.9	0.02	0.036	46.1	0.13	0.18	14.7	0.004	0.28	0.01	101.3
CH0701	40.0	0.01	0.025	45.9	0.14	0.20	14.5	0.006	0.26	0.03	101.2
CH0701	40.0	0.02	0.027	46.3	0.13	0.18	14.6	0.014	0.26	0.10	101.6
CH0701	39.7	0.02	0.034	45.9	0.13	0.20	14.6	0.000	0.27	0.03	100.9
CH0701	40.0	0.02	0.028	46.0	0.15	0.19	14.3	0.015	0.29	0.05	101.0
CH0701	39.8	0.03	0.028	46.1	0.13	0.19	14.2	0.011	0.30	0.01	100.9
CH0701	40.1	0.02	0.029	46.1	0.13	0.21	14.3	0.017	0.28	0.03	101.2
CH0701	39.9	0.02	0.022	46.1	0.12	0.18	14.3	0.005	0.27	0.01	100.9
CH0701	39.8	0.01	0.027	46.1	0.12	0.19	14.3	0.000	0.26	0.01	100.8
CH0701	39.7	0.01	0.045	46.1	0.13	0.17	14.4	0.016	0.29	0.01	101.0
CH0701	39.9	0.01	0.019	46.1	0.19	0.18	14.1	0.020	0.26	0.02	100.8
CH0701	39.9	0.01	0.032	46.2	0.13	0.20	14.4	0.014	0.28	0.03	101.1
CH0701	39.7	0.03	0.026	45.9	0.11	0.19	14.4	0.040	0.28	0.03	100.7
CH0701	39.9	0.01	0.028	45.7	0.13	0.20	14.7	0.011	0.29	0.01	100.9
CH0701	39.7	0.01	0.030	45.7	0.12	0.22	14.6	0.004	0.28	0.01	100.7
CH0701	39.7	0.01	0.034	45.9	0.13	0.18	14.7	0.000	0.30	0.02	101.0
CH0701	39.8	0.00	0.026	45.8	0.13	0.18	14.8	0.006	0.28	0.01	101.0
CH0701	39.8	0.02	0.020	45.8	0.13	0.20	14.6	0.009	0.29	0.02	100.9
CH0701	39.6	0.02	0.031	45.9	0.14	0.18	14.6	0.000	0.26	0.02	100.8
CH0701	39.8	0.02	0.027	45.9	0.13	0.19	14.7	0.000	0.30	0.02	101.1
CH0701	39.8	0.01	0.028	45.6	0.14	0.21	14.9	0.000	0.26	0.00	100.9
CH0701	39.7	0.02	0.034	45.6	0.16	0.20	14.9	0.007	0.28	0.01	100.8
CH0701	39.7	0.03	0.014	45.5	0.12	0.17	14.2	0.022	0.30	0.00	100.1
CH0701	39.8	0.01	0.028	45.6	0.14	0.21	14.4	0.000	0.28	0.02	100.5
CH0701	39.9	0.02	0.022	45.2	0.11	0.22	14.7	0.000	0.28	0.02	100.6
CH0701	39.8	0.02	0.022	45.4	0.12	0.19	14.6	0.004	0.27	0.00	100.5
CH0701	40.1	0.00	0.024	45.5	0.14	0.18	14.2	0.005	0.27	0.02	100.4
CH0701	39.9	0.01	0.015	45.7	0.13	0.18	14.2	0.022	0.30	0.01	100.5
CH0701	39.6	0.02	0.019	45.9	0.13	0.19	14.2	0.002	0.26	0.02	100.4

Sample	SiO_2	TiO_2	Al_2O_3	MgO	CaO	MnO	FeO	P_2O_5	NiO	Cr_2O_3	Total
CH0701	40.0	0.02	0.029	46.1	0.16	0.20	14.5	0.005	0.27	0.03	101.3
CH0701	39.9	0.00	0.038	46.3	0.14	0.17	14.5	0.039	0.29	0.00	101.3
CH0701	39.7	0.01	0.021	45.8	0.13	0.21	14.5	0.008	0.29	0.01	100.7
CH0701	39.9	0.00	0.019	46.2	0.16	0.18	14.4	0.008	0.29	0.02	101.2
CH0701	40.0	0.01	0.028	46.1	0.20	0.19	14.3	0.009	0.26	0.04	101.1
CH0701	39.8	0.00	0.035	46.0	0.13	0.17	14.6	0.016	0.27	0.00	101.0
CH0701	39.7	0.01	0.029	46.0	0.12	0.20	14.4	0.000	0.26	0.01	100.8
CH0701	40.0	0.02	0.032	46.0	0.15	0.18	14.3	0.000	0.27	0.03	101.0
CH0701	40.0	0.02	0.037	46.1	0.13	0.19	14.6	0.000	0.28	0.01	101.3
CH0701	39.9	0.01	0.028	46.1	0.13	0.19	14.5	0.000	0.27	0.01	101.2
CH0701	39.9	0.02	0.036	46.1	0.13	0.18	14.7	0.004	0.28	0.01	101.3
CH0701	40.0	0.01	0.025	45.9	0.14	0.20	14.5	0.006	0.26	0.03	101.2
CH0701	40.0	0.02	0.027	46.3	0.13	0.18	14.6	0.014	0.26	0.10	101.6
CH0701	39.7	0.02	0.034	45.9	0.13	0.20	14.6	0.000	0.27	0.03	100.9
CH0701	40.0	0.02	0.028	46.0	0.15	0.19	14.3	0.015	0.29	0.05	101.0
CH0701	39.8	0.03	0.028	46.1	0.13	0.19	14.2	0.011	0.30	0.01	100.9
CH0701	40.1	0.02	0.029	46.1	0.13	0.21	14.3	0.017	0.28	0.03	101.2
CH0701	39.9	0.02	0.022	46.1	0.12	0.18	14.3	0.005	0.27	0.01	100.9
CH0701	39.8	0.01	0.027	46.1	0.12	0.19	14.3	0.000	0.26	0.01	100.8
CH0701	39.7	0.01	0.045	46.1	0.13	0.17	14.4	0.016	0.29	0.01	101.0
CH0701	39.9	0.01	0.019	46.1	0.19	0.18	14.1	0.020	0.26	0.02	100.8
CH0701	39.9	0.01	0.032	46.2	0.13	0.20	14.4	0.014	0.28	0.03	101.1
CH0701	39.7	0.03	0.026	45.9	0.11	0.19	14.4	0.040	0.28	0.03	100.7
CH0701	39.9	0.01	0.028	45.7	0.13	0.20	14.7	0.011	0.29	0.01	100.9
CH0701	39.7	0.01	0.030	45.7	0.12	0.22	14.6	0.004	0.28	0.01	100.7
CH0701	39.7	0.01	0.034	45.9	0.13	0.18	14.7	0.000	0.30	0.02	101.0
CH0701	39.8	0.00	0.026	45.8	0.13	0.18	14.8	0.006	0.28	0.01	101.0
CH0701	39.8	0.02	0.020	45.8	0.13	0.20	14.6	0.009	0.29	0.02	100.9
CH0701	39.6	0.02	0.031	45.9	0.14	0.18	14.6	0.000	0.26	0.02	100.8
CH0701	39.8	0.02	0.027	45.9	0.13	0.19	14.7	0.000	0.30	0.02	101.1
CH0701	39.8	0.01	0.028	45.6	0.14	0.21	14.9	0.000	0.26	0.00	100.9
CH0701	39.7	0.02	0.034	45.6	0.16	0.20	14.9	0.007	0.28	0.01	100.8
CH0701	39.7	0.03	0.014	45.5	0.12	0.17	14.2	0.022	0.30	0.00	100.1
CH0701	39.8	0.01	0.028	45.6	0.14	0.21	14.4	0.000	0.28	0.02	100.5
CH0701	39.9	0.02	0.022	45.2	0.11	0.22	14.7	0.000	0.28	0.02	100.6
CH0701	39.8	0.02	0.022	45.4	0.12	0.19	14.6	0.004	0.27	0.00	100.5
CH0701	40.1	0.00	0.024	45.5	0.14	0.18	14.2	0.005	0.27	0.02	100.4
CH0701	39.9	0.01	0.015	45.7	0.13	0.18	14.2	0.022	0.30	0.01	100.5
CH0701	39.6	0.02	0.019	45.9	0.13	0.19	14.2	0.002	0.26	0.02	100.4

Sample	SiO_2	TiO_2	Al_2O_3	MgO	CaO	MnO	FeO	P_2O_5	NiO	Cr_2O_3	Total
CH0701	40.0	0.01	0.019	45.9	0.12	0.19	13.8	0.000	0.30	0.01	100.3
CH0701	40.0	0.01	0.018	45.9	0.14	0.18	13.9	0.012	0.29	0.02	100.4
CH0701	39.7	0.01	0.018	46.0	0.12	0.18	13.8	0.000	0.30	0.03	100.2
CH0701	39.8	0.02	0.021	46.2	0.11	0.19	13.9	0.014	0.29	0.02	100.5
CH0701	39.9	0.01	0.021	46.5	0.12	0.19	13.9	0.008	0.26	0.00	101.0
CH0701	40.1	0.02	0.019	45.9	0.13	0.18	13.8	0.019	0.32	0.02	100.5
CH0701	39.8	0.03	0.030	46.1	0.13	0.17	13.7	0.001	0.29	0.01	100.3
CH0701	39.9	0.01	0.016	45.9	0.12	0.19	13.9	0.002	0.27	0.08	100.4
CH0701	40.0	0.02	0.014	46.2	0.14	0.19	13.8	0.005	0.30	0.03	100.7
CH0701 Dunite	39.7	0.00	0.018	44.8	0.14	0.20	15.0	0.009	0.27	0.00	100.2
CH0701 Dunite	39.4	0.01	0.019	45.0	0.13	0.21	14.9	0.011	0.26	0.00	99.9
CH0701 Dunite	39.6	0.02	0.022	45.1	0.13	0.20	14.8	0.004	0.24	0.03	100.2
CH0701 Dunite	39.8	0.01	0.007	45.3	0.11	0.19	14.4	0.006	0.28	0.02	100.1
CH0701 Dunite	39.7	0.01	0.032	45.3	0.12	0.19	14.2	0.001	0.26	0.02	99.8
CH0701 Dunite	39.7	0.02	0.015	45.5	0.13	0.18	14.4	0.001	0.28	0.02	100.2
CH0701 Dunite	39.7	0.02	0.025	45.2	0.13	0.19	14.5	0.025	0.28	0.03	100.1
CH0701 Dunite	39.6	0.01	0.025	45.3	0.13	0.19	14.5	0.002	0.27	0.02	100.0
CH0701 Dunite	39.6	0.00	0.025	45.4	0.13	0.18	14.6	0.007	0.27	0.01	100.3
CH0701 Dunite	39.7	0.01	0.019	45.7	0.13	0.20	14.2	0.000	0.28	0.01	100.2
CH0701 Dunite	39.7	0.02	0.026	45.8	0.13	0.20	14.3	0.000	0.28	0.00	100.5
CH0701 Dunite	39.6	0.02	0.029	45.8	0.14	0.19	14.4	0.002	0.27	0.01	100.4
CH0701 Dunite	40.0	0.01	0.018	45.6	0.14	0.17	14.2	0.007	0.25	0.02	100.3
CH0701 Dunite	39.7	0.02	0.026	45.6	0.14	0.18	14.3	0.004	0.29	0.01	100.2
CH0701 Dunite	39.9	0.01	0.015	45.8	0.14	0.20	14.2	0.011	0.29	0.02	100.5
CH0701 Dunite	39.6	0.00	0.017	45.4	0.13	0.19	14.5	0.020	0.29	0.02	100.2
CH0701 Dunite	39.6	0.01	0.012	45.3	0.12	0.18	14.2	0.012	0.27	0.02	99.8
CH0701 Dunite	39.5	0.01	0.024	45.5	0.13	0.18	14.4	0.001	0.30	0.02	100.1
CH0701 Dunite	39.4	0.00	0.026	45.5	0.14	0.21	14.3	0.009	0.29	0.01	99.8
CH0701 Dunite	39.7	0.00	0.024	45.7	0.12	0.20	14.0	0.008	0.26	0.02	100.1

Sample	SiO_2	TiO_2	Al_2O_3	MgO	CaO	MnO	FeO	P_2O_5	NiO	Cr_2O_3	Total
CH0701 Dunite	39.6	0.02	0.009	45.6	0.12	0.19	14.3	0.002	0.27	0.02	100.1
CH0701 Dunite	39.4	0.01	0.013	45.7	0.12	0.19	14.1	0.007	0.28	0.02	99.9
CH0701 Dunite	39.7	0.02	0.025	45.6	0.12	0.19	14.2	0.011	0.29	0.02	100.1
CH0701 Dunite	39.7	0.02	0.015	45.8	0.13	0.18	14.2	0.010	0.28	0.03	100.3
CH0701 Dunite	39.7	0.01	0.027	45.7	0.14	0.18	14.2	0.006	0.27	0.00	100.3
CH0701 Dunite	39.5	0.01	0.021	45.6	0.15	0.19	14.2	0.022	0.27	0.02	99.9
CH0701 Dunite	39.6	0.02	0.011	45.9	0.13	0.19	14.1	0.000	0.30	0.01	100.2
CH0702	39.7	0.01	0.002	45.7	0.14	0.19	14.4	0.000	0.33	0.01	100.4
CH0702	39.8	0.02	0.006	45.7	0.13	0.22	14.2	0.001	0.32	0.02	100.4
CH0702	39.8	0.00	0.025	45.6	0.17	0.22	14.2	0.000	0.33	0.01	100.4
CH0702	39.5	0.01	0.013	45.5	0.16	0.20	14.3	0.012	0.31	0.00	100.0
CH0702	39.9	0.00	0.016	45.7	0.16	0.21	14.2	0.012	0.33	0.00	100.4
CH0702	39.6	0.02	0.017	45.8	0.16	0.18	14.2	0.000	0.32	0.01	100.3
CH0702	39.9	0.00	0.018	45.6	0.14	0.21	14.2	0.000	0.32	0.02	100.4
CH0702	40.0	0.01	0.019	45.8	0.18	0.20	14.2	0.010	0.32	0.02	100.7
CH0702	39.9	0.01	0.022	45.8	0.15	0.18	14.3	0.019	0.32	0.01	100.7
CH0702	39.8	0.01	0.024	45.7	0.16	0.19	14.3	0.010	0.32	0.00	100.5
CH0702	39.7	0.03	0.026	45.6	0.12	0.19	14.4	0.000	0.32	0.01	100.3
CH0702	39.7	0.02	0.014	45.6	0.12	0.19	14.3	0.015	0.32	0.00	100.3
CH0702	39.6	0.01	0.013	45.6	0.13	0.19	14.3	0.013	0.31	0.02	100.2
CH0702	39.7	0.00	0.017	45.6	0.16	0.18	14.3	0.000	0.32	0.00	100.4
CH0702	39.5	0.01	0.017	45.5	0.15	0.20	14.2	0.009	0.34	0.01	100.0
CH0702	39.8	0.00	0.020	45.6	0.15	0.19	14.3	0.000	0.34	0.02	100.4
CH0702	40.0	0.01	0.022	45.7	0.14	0.18	14.2	0.000	0.31	0.02	100.6
CH0702	39.6	0.02	0.013	45.6	0.15	0.20	14.4	0.000	0.29	0.00	100.3
CH0702	39.7	0.00	0.015	45.2	0.19	0.20	14.1	0.009	0.32	0.02	99.8
CH0702	39.8	0.00	0.009	45.9	0.15	0.18	14.3	0.003	0.32	0.01	100.6
CH0702	39.7	0.01	0.012	45.7	0.15	0.20	14.3	0.000	0.29	0.02	100.4
CH0702	39.7	0.01	0.012	45.5	0.15	0.19	14.2	0.008	0.27	0.01	100.1
CH0702	39.7	0.03	0.010	45.7	0.13	0.20	14.2	0.000	0.34	0.01	100.3
CH0702	39.6	0.01	0.009	45.6	0.12	0.19	14.3	0.005	0.30	0.00	100.2
CH0702	39.9	0.01	0.014	45.6	0.15	0.18	14.3	0.000	0.32	0.00	100.4
CH0702	39.8	0.00	0.018	45.7	0.12	0.20	14.2	0.003	0.31	0.00	100.4
CH0702	39.5	0.00	0.018	45.7	0.15	0.20	14.3	0.009	0.33	0.01	100.2
CH0702	39.6	0.01	0.018	45.9	0.15	0.18	14.2	0.001	0.33	0.02	100.3
CH0702	39.7	0.01	0.013	45.7	0.16	0.20	14.1	0.002	0.30	0.00	100.2
CH0702	39.8	0.02	0.013	45.7	0.15	0.21	14.3	0.032	0.31	0.01	100.5

Sample	SiO_2	TiO_2	Al_2O_3	MgO	CaO	MnO	FeO	P_2O_5	NiO	Cr_2O_3	Total
CH0702	39.9	0.01	0.014	45.6	0.15	0.18	14.3	0.000	0.32	0.00	100.4
CH0702	39.8	0.00	0.018	45.7	0.12	0.20	14.2	0.003	0.31	0.00	100.4
CH0702	39.5	0.00	0.018	45.7	0.15	0.20	14.3	0.009	0.33	0.01	100.2
CH0702	39.6	0.01	0.018	45.9	0.15	0.18	14.2	0.001	0.33	0.02	100.3
CH0702	39.7	0.01	0.013	45.7	0.16	0.20	14.1	0.002	0.30	0.00	100.2
CH0702	39.8	0.02	0.013	45.7	0.15	0.21	14.3	0.032	0.31	0.01	100.5
CH0702A	39.9	0.00	0.012	45.9	0.23	0.19	14.3	0.018	0.34	0.01	100.9
CH0702A	39.8	0.00	0.028	45.9	0.31	0.19	14.2	0.007	0.31	0.02	100.8
CH0702A	39.8	0.01	0.011	46.1	0.16	0.19	14.3	0.001	0.33	0.01	100.9
CH0702A	40.1	0.01	0.011	46.1	0.18	0.19	14.2	0.007	0.31	0.02	101.1
CH0702A	39.8	0.01	0.013	45.8	0.18	0.19	14.2	0.004	0.33	0.01	100.4
CH0702A	39.6	0.02	0.030	45.8	0.29	0.19	14.4	0.008	0.29	0.04	100.7
CH0702A	39.9	0.02	0.016	46.1	0.13	0.20	14.3	0.007	0.32	0.00	101.1
CH0702A	39.6	0.04	0.221	44.6	0.46	0.20	15.0	0.021	0.29	0.05	100.4
CH0702A	39.9	0.02	0.017	45.9	0.16	0.18	14.3	0.007	0.34	0.00	100.9
CH0702A	39.9	0.00	0.019	46.2	0.14	0.19	14.3	0.001	0.29	0.00	101.0
CH0702A	38.4	0.02	0.050	45.7	0.16	0.20	14.3	0.004	0.33	0.00	99.1
CH0702A	40.2	0.02	0.115	45.6	0.13	0.20	14.2	0.007	0.31	0.02	100.8
CH0702A	39.2	0.02	0.055	44.9	0.14	0.19	14.2	0.003	0.31	0.01	99.0
CH0702A	39.8	0.01	0.041	45.4	0.14	0.18	14.2	0.005	0.32	0.01	100.1
CH0703 Dunite	38.1	0.01	0.061	45.3	0.07	0.24	16.8	0.010	0.36	0.00	101.0
CH0703 Pyroxenite	38.4	0.01	0.069	42.3	0.12	0.22	17.6	0.017	0.28	0.02	99.0
CH0703 Pyroxenite	38.7	0.01	0.023	43.1	0.11	0.23	17.4	0.007	0.27	0.03	99.9
CH0703 Pyroxenite	38.6	0.02	0.099	42.3	0.12	0.23	17.4	0.011	0.29	0.02	99.0
CH0703 Pyroxenite	38.9	0.01	0.018	42.8	0.10	0.24	17.6	0.012	0.28	0.00	100.0
CH0703A	39.4	0.02	0.006	44.8	0.03	0.20	15.4	0.003	0.26	0.00	100.2
CH0703A	39.3	0.01	0.001	44.8	0.03	0.20	15.6	0.005	0.28	0.00	100.3
CH0703A	39.2	0.00	0.002	44.5	0.07	0.21	15.6	0.000	0.26	0.00	99.9
CH0703A	39.5	0.01	0.011	44.7	0.04	0.22	15.4	0.004	0.28	0.01	100.2
CH0703A	39.7	0.01	0.014	44.8	0.05	0.23	15.6	0.000	0.29	0.02	100.7
CH0703A	39.4	0.01	0.012	44.8	0.05	0.22	15.4	0.000	0.26	0.00	100.2
CH0703A	39.8	0.01	0.008	44.9	0.05	0.22	15.6	0.012	0.26	0.01	100.9
CH0703A	39.5	0.00	0.004	44.6	0.07	0.25	15.8	0.003	0.26	0.01	100.5
CH0703A	39.2	0.00	0.010	44.9	0.09	0.19	15.2	0.009	0.26	0.00	99.8
CH0703A	39.4	0.01	0.008	44.9	0.09	0.22	15.5	0.012	0.29	0.00	100.4
CH0703A	39.5	0.01	0.008	44.6	0.09	0.21	15.6	0.000	0.26	0.01	100.3
CH0703A	39.3	0.00	0.009	44.5	0.06	0.23	15.6	0.000	0.25	0.00	100.0

Sample	SiO_2	TiO_2	Al_2O_3	MgO	CaO	MnO	FeO	P_2O_5	NiO	Cr_2O_3	Total
CH0703A	39.4	0.02	0.002	44.8	0.15	0.22	15.5	0.009	0.25	0.00	100.3
CH0703A	39.5	0.01	0.015	44.3	0.28	0.22	15.8	0.009	0.25	0.02	100.4
CH0703A	39.5	0.01	0.015	44.6	0.11	0.22	15.8	0.003	0.28	0.00	100.5
CH0703A	39.3	0.01	0.010	44.5	0.08	0.20	15.9	0.003	0.27	0.00	100.4
CH0703A	39.3	0.01	0.009	44.6	0.08	0.24	15.7	0.000	0.27	0.00	100.3
CH0703A	39.3	0.00	0.008	44.4	0.09	0.22	15.8	0.007	0.30	0.00	100.1
CH0703A	39.5	0.03	0.017	45.0	0.05	0.21	15.6	0.011	0.27	0.00	100.7
CH0703A	39.5	0.01	0.008	44.8	0.05	0.24	15.7	0.002	0.25	0.01	100.6
CH0703A	39.6	0.00	0.016	44.6	0.06	0.23	15.9	0.016	0.25	0.00	100.7
CH0703A	39.6	0.00	0.003	44.5	0.07	0.23	15.7	0.004	0.26	0.00	100.4
CH0703A	39.6	0.01	0.006	45.0	0.03	0.22	15.3	0.011	0.25	0.00	100.4
CH0703A	39.3	0.02	0.009	44.7	0.05	0.24	15.6	0.015	0.26	0.01	100.2
CH0703A	39.2	0.00	0.010	44.3	0.06	0.25	15.8	0.019	0.25	0.01	99.9
CH0703A	39.3	0.00	0.007	44.7	0.07	0.21	15.7	0.009	0.23	0.01	100.3
CH0703A	39.6	0.01	0.007	44.7	0.07	0.23	15.7	0.008	0.25	0.01	100.6
CH0703A	39.4	0.00	0.010	44.9	0.06	0.22	15.2	0.006	0.28	0.01	100.1
CH0703A	39.3	0.00	0.015	45.0	0.04	0.20	15.2	0.009	0.30	0.02	100.2
CH0703B	39.5	0.02	0.053	42.1	0.10	0.22	18.7	0.013	0.21	0.02	100.9
CH0703B	39.3	0.02	0.024	43.4	0.09	0.22	17.3	0.006	0.19	0.01	100.5
CH0703B	39.6	0.02	0.019	43.2	0.11	0.25	17.3	0.008	0.20	0.02	100.7
CH0703B	39.4	0.01	0.019	43.6	0.37	0.23	16.9	0.000	0.19	0.04	100.8
CH0703B	39.4	0.02	0.015	43.6	0.12	0.23	17.2	0.015	0.22	0.00	100.9
CH0703B	39.0	0.01	0.198	43.5	0.09	0.23	17.2	0.021	0.21	0.04	100.5
CH0703B	39.4	0.02	0.016	43.8	0.29	0.21	16.4	0.016	0.23	0.03	100.5
CH0703B	39.4	0.02	0.022	43.7	0.09	0.23	17.2	0.000	0.21	0.01	100.9
CH0703B	39.3	0.00	0.030	43.6	0.09	0.24	17.2	0.018	0.24	0.00	100.8
CH0703B	39.4	0.01	0.020	43.6	0.08	0.23	17.4	0.006	0.23	0.03	101.0
CH0703B	39.1	0.01	0.020	43.8	0.10	0.23	17.3	0.012	0.22	0.00	100.7
CH0703B	39.5	0.00	0.024	43.7	0.11	0.22	17.1	0.014	0.23	0.00	100.9
CH0703B	39.3	0.01	0.022	43.8	0.09	0.25	17.3	0.011	0.23	0.02	101.0
CH0703B	39.2	0.01	0.013	43.6	0.09	0.24	17.2	0.005	0.22	0.00	100.6
CH0703B	39.5	0.01	0.027	43.2	0.14	0.23	17.1	0.024	0.20	0.02	100.5
CH0703B	39.6	0.01	0.019	43.4	0.12	0.22	17.1	0.000	0.21	0.01	100.7
CH0703B	39.4	0.02	0.030	43.0	0.13	0.22	17.7	0.017	0.19	0.01	100.8
CH0703B	39.2	0.03	0.025	43.4	0.09	0.25	17.6	0.005	0.21	0.01	100.8
CH0703B	39.3	0.01	0.024	43.3	0.14	0.23	17.6	0.012	0.20	0.03	100.9
CH0703B	39.7	0.01	0.013	43.3	0.14	0.22	17.3	0.017	0.21	0.03	100.9
CH0703B	39.5	0.01	0.013	43.6	0.21	0.24	17.2	0.020	0.19	0.03	101.1
CH0703B	39.2	0.02	0.025	44.1	0.34	0.22	16.9	0.044	0.23	0.04	101.1

Sample	SiO_2	TiO_2	Al_2O_3	MgO	CaO	MnO	FeO	P_2O_5	NiO	Cr_2O_3	Total
CH0703B	39.5	0.02	0.022	43.1	0.26	0.23	17.3	0.049	0.20	0.03	100.7
CH0703B	39.5	0.01	0.014	43.0	0.21	0.24	17.6	0.006	0.20	0.01	100.8
CH0703B	40.3	0.01	0.017	42.9	0.32	0.23	17.0	0.009	0.19	0.02	101.0
CH0703B	39.3	0.04	0.072	43.8	0.48	0.24	15.7	0.038	0.22	0.05	99.9
CH0703B	40.0	0.04	0.020	42.0	0.33	0.24	16.8	0.053	0.20	0.03	99.7
CH0703B	40.0	0.01	0.023	42.4	0.31	0.20	16.8	0.088	0.22	0.04	100.1
CH0703B	40.7	0.02	0.080	42.2	0.38	0.24	16.7	0.031	0.19	0.03	100.6
CH0703B	39.4	0.02	0.031	43.0	0.19	0.25	17.4	0.022	0.20	0.00	100.5
CH0703B	39.5	0.00	0.044	43.6	0.10	0.22	17.4	0.015	0.19	0.02	101.0
CH0703B	39.1	0.01	0.027	43.4	0.33	0.21	16.9	0.020	0.21	0.04	100.3
CH0703B	39.3	0.01	0.010	43.0	0.11	0.24	17.9	0.007	0.18	0.00	100.7
CH0703B	39.5	0.02	0.056	43.2	0.20	0.21	17.1	0.002	0.21	0.03	100.6
CH0703B	39.4	0.01	0.025	43.3	0.11	0.24	17.4	0.013	0.20	0.00	100.7
CH0703B	39.4	0.02	0.015	42.8	0.09	0.22	17.7	0.001	0.19	0.02	100.4
CH0703B	39.3	0.02	0.032	42.7	0.28	0.23	16.6	0.015	0.18	0.06	99.4
CH0703B	39.8	0.01	0.032	42.8	0.25	0.22	16.5	0.019	0.19	0.03	99.8
CH0703B	39.7	0.01	0.029	43.0	0.15	0.23	17.1	0.006	0.19	0.03	100.4
CH0703B	39.8	0.00	0.019	42.8	0.18	0.24	17.9	0.006	0.21	0.04	101.1
CH0703B	40.6	0.01	0.029	40.8	0.37	0.22	17.0	0.013	0.19	0.05	99.2
CH0703B	39.4	0.01	0.006	43.7	0.16	0.23	17.1	0.014	0.19	0.04	100.9
CH0703B	40.4	0.38	1.184	39.1	1.39	0.20	17.5	0.018	0.19	0.15	100.6
CH0703B	39.9	0.01	0.024	41.4	0.29	0.21	17.0	0.028	0.18	0.10	99.3
CH0703B	39.1	0.00	0.020	43.1	0.27	0.25	17.0	0.019	0.20	0.05	100.0
CH0703B	39.5	0.00	0.017	43.5	0.09	0.23	17.5	0.000	0.22	0.01	101.1
CH0703B	39.3	0.01	0.025	43.0	0.12	0.25	17.8	0.005	0.20	0.06	100.8
CH0703B	39.1	0.00	0.023	43.4	0.10	0.22	17.2	0.017	0.23	0.00	100.3
CH0703B	39.3	0.01	0.017	43.5	0.10	0.23	17.4	0.005	0.21	0.02	100.8
CH0703B	39.2	0.01	0.026	43.6	0.08	0.22	17.4	0.013	0.24	0.01	100.9
CH0703B	39.5	0.02	0.014	43.6	0.09	0.25	17.1	0.005	0.21	0.06	100.8
CH0703B	39.0	0.03	0.010	44.2	0.08	0.25	16.1	0.008	0.21	0.09	100.0
CH0703B	39.4	0.01	0.015	42.7	0.35	0.24	17.6	0.018	0.18	0.05	100.5
CH0703B	39.3	0.01	0.021	43.8	0.12	0.21	16.7	0.007	0.24	0.01	100.5
CH0703B	39.2	0.02	0.019	43.8	0.09	0.23	16.8	0.005	0.26	0.00	100.5
CH0703B	39.3	0.00	0.029	44.1	0.10	0.21	16.8	0.011	0.26	0.01	100.8
CH0703B	39.5	0.02	0.031	44.0	0.17	0.23	16.6	0.005	0.26	0.03	100.8
CH0703B	39.3	0.01	0.026	44.1	0.19	0.25	16.4	0.023	0.25	0.00	100.6
CH0703B	39.4	0.01	0.035	41.6	0.09	0.21	18.8	0.009	0.23	0.02	100.4
CH0703B	39.3	0.02	0.008	44.0	0.10	0.21	17.0	0.007	0.25	0.00	100.8
CH0703B	39.6	0.00	0.009	45.4	0.05	0.21	15.0	0.002	0.31	0.00	100.6

Sample	SiO_2	TiO_2	Al_2O_3	MgO	CaO	MnO	FeO	P_2O_5	NiO	Cr_2O_3	Total
CH0703B	39.8	0.02	0.021	45.5	0.08	0.21	15.1	0.000	0.23	0.02	101.0
CH0703B	39.8	0.00	0.012	45.4	0.05	0.21	15.0	0.000	0.30	0.02	100.7
CH0703C	40.5	0.02	0.053	43.0	0.09	0.23	15.2	0.023	0.29	0.04	99.5
CH0703C	39.5	0.00	0.055	45.6	0.12	0.21	14.5	0.005	0.28	0.01	100.2
CH0703D	39.8	0.02	0.043	44.8	0.15	0.18	15.5	0.012	0.26	0.01	100.8
CH0703D	39.9	0.01	0.009	45.3	0.14	0.22	15.1	0.004	0.29	0.01	101.0
CH0703D	39.7	0.01	0.013	45.5	0.15	0.22	15.2	0.000	0.28	0.00	101.1
CH0703D	39.5	0.01	0.019	45.2	0.16	0.19	15.3	0.020	0.28	0.02	100.7
CH0703D	39.8	0.03	0.016	45.4	0.16	0.21	15.1	0.010	0.29	0.00	101.0
CH0703D	39.7	0.02	0.013	45.5	0.16	0.21	15.0	0.008	0.26	0.01	100.9
CH0703D	39.6	0.00	0.015	45.1	0.15	0.20	15.5	0.028	0.26	0.02	100.9
CH0703D	39.9	0.01	0.007	45.8	0.16	0.23	14.8	0.014	0.25	0.00	101.1
CH0703D	40.1	0.01	0.013	44.9	0.17	0.21	15.3	0.004	0.27	0.00	100.9
CH0703D	39.6	0.01	0.016	45.0	0.14	0.22	15.4	0.009	0.25	0.02	100.7
CH0703D	39.7	0.02	0.013	45.0	0.15	0.21	15.7	0.007	0.27	0.00	101.1
CH0703D	39.7	0.02	0.012	45.6	0.16	0.19	15.0	0.005	0.29	0.01	101.1
CH0704	39.5	0.01	0.005	45.1	0.06	0.19	14.9	0.000	0.28	0.02	100.1
CH0704	39.4	0.01	0.010	44.9	0.08	0.19	15.0	0.015	0.29	0.01	99.9
CH0704	39.5	0.02	0.011	45.0	0.07	0.20	15.1	0.003	0.27	0.01	100.1
CH0704	39.7	0.01	0.005	45.0	0.07	0.18	15.1	0.023	0.30	0.01	100.4
CH0704	39.6	0.02	0.017	44.9	0.07	0.20	15.0	0.011	0.30	0.01	100.1
CH0704	39.5	0.01	0.018	45.0	0.18	0.22	14.8	0.001	0.31	0.02	100.2
CH0704	39.5	0.01	0.006	45.3	0.16	0.20	14.9	0.012	0.32	0.02	100.4
CH0704	39.7	0.01	0.022	45.0	0.15	0.19	14.9	0.006	0.28	0.01	100.3
CH0704	39.3	0.01	0.019	44.6	0.08	0.19	15.6	0.020	0.28	0.00	100.1
CH0704	39.4	0.00	0.007	44.5	0.07	0.23	15.5	0.003	0.26	0.01	99.9
CH0704	39.4	0.02	0.015	44.6	0.07	0.22	15.4	0.018	0.28	0.01	100.1
CH0704	39.6	0.00	0.012	44.9	0.16	0.20	15.1	0.007	0.26	0.00	100.2
CH0704	39.6	0.00	0.005	45.0	0.16	0.22	15.1	0.007	0.28	0.02	100.3
CH0704	39.5	0.00	0.015	44.9	0.16	0.20	15.0	0.015	0.29	0.04	100.1
CH0704	39.7	0.02	0.019	46.1	0.06	0.21	13.2	0.006	0.33	0.00	99.6
CH0704	40.0	0.00	0.009	46.4	0.07	0.19	13.4	0.019	0.33	0.01	100.5
CH0704	39.8	0.02	0.010	46.2	0.08	0.18	13.6	0.014	0.34	0.00	100.3
CH0704A	39.9	0.00	0.016	46.2	0.11	0.19	14.4	0.015	0.28	0.00	101.0
CH0704A	39.9	0.01	0.022	46.2	0.07	0.20	14.4	0.000	0.28	0.00	101.1
CH0704A	40.0	0.01	0.007	46.2	0.10	0.19	14.3	0.012	0.27	0.01	101.1
CH0704A	39.9	0.02	0.006	46.1	0.08	0.20	14.5	0.003	0.27	0.01	101.0
CH0704A	40.0	0.02	0.005	46.0	0.08	0.21	14.5	0.012	0.28	0.00	101.1
CH0704A	40.2	0.00	0.142	45.0	0.09	0.19	14.5	0.000	0.27	0.01	100.4

Sample	SiO_2	TiO_2	Al_2O_3	MgO	CaO	MnO	FeO	P_2O_5	NiO	Cr_2O_3	Total
CH0705A	39.8	0.01	0.012	46.5	0.14	0.19	13.3	0.014	0.31	0.01	100.3
CH0705A	39.8	0.02	0.016	46.3	0.14	0.18	13.5	0.003	0.28	0.01	100.2
CH0705A	39.9	0.02	0.018	46.2	0.14	0.20	13.5	0.007	0.30	0.01	100.4
CH0705A	39.8	0.02	0.014	46.4	0.15	0.20	13.7	0.015	0.28	0.00	100.5
CH0705A	40.0	0.02	0.008	46.3	0.13	0.19	13.6	0.005	0.29	0.00	100.5
CH0705A	39.8	0.02	0.023	46.3	0.12	0.19	13.4	0.013	0.29	0.01	100.2
CH0705A	39.8	0.01	0.018	46.5	0.11	0.19	13.5	0.000	0.27	0.01	100.4
CH0705A	39.9	0.01	0.002	46.3	0.14	0.17	13.5	0.000	0.24	0.02	100.3
CH0705A	40.0	0.02	0.019	46.2	0.14	0.20	13.5	0.014	0.27	0.02	100.3
CH0705A	39.7	0.02	0.012	46.2	0.15	0.18	13.5	0.009	0.27	0.02	100.1
CH0705A	40.0	0.01	0.025	46.2	0.12	0.20	13.6	0.004	0.31	0.00	100.5
CH0705A	39.9	0.01	0.018	46.4	0.14	0.18	13.4	0.006	0.29	0.00	100.4
CH0705A	39.8	0.00	0.016	46.4	0.19	0.20	13.6	0.016	0.28	0.00	100.5
CH0705A	40.1	0.00	0.020	46.3	0.13	0.21	13.6	0.000	0.28	0.02	100.6
CH0705A	39.9	0.01	0.015	46.1	0.11	0.20	13.6	0.005	0.25	0.04	100.3
CH0705A	39.8	0.01	0.011	46.5	0.12	0.19	13.6	0.018	0.28	0.00	100.5
CH0705A	40.0	0.02	0.014	46.3	0.12	0.19	13.6	0.016	0.31	0.02	100.5
CH0705A	39.9	0.01	0.015	46.4	0.14	0.19	13.5	0.004	0.26	0.01	100.5
CH0705A	39.8	0.02	0.019	46.3	0.14	0.18	13.4	0.000	0.26	0.01	100.1
CH0705A	39.8	0.01	0.020	46.2	0.13	0.18	13.5	0.000	0.27	0.01	100.0
CH0705A	39.8	0.02	0.024	46.1	0.20	0.19	13.5	0.008	0.29	0.01	100.2
CH0705A	39.8	0.01	0.015	46.3	0.15	0.17	13.4	0.002	0.30	0.01	100.2
CH0705A	39.8	0.02	0.008	46.3	0.14	0.16	13.5	0.015	0.28	0.01	100.2
CH0705A	39.8	0.00	0.019	46.4	0.15	0.18	13.5	0.005	0.29	0.01	100.4
CH0705A	39.9	0.02	0.019	46.1	0.14	0.19	13.5	0.008	0.31	0.01	100.3
CH0705C	39.8	0.01	0.033	45.8	0.09	0.20	14.8	0.011	0.33	0.02	101.1
CH0705C	39.7	0.00	0.054	45.4	0.11	0.18	15.0	0.003	0.29	0.05	100.8
CH0705C	39.9	0.02	0.045	44.6	0.11	0.18	15.1	0.008	0.30	0.00	100.3
CH0705C	39.5	0.01	0.029	45.8	0.10	0.20	14.8	0.003	0.32	0.02	100.8
CH0705C	39.4	0.00	0.040	45.5	0.10	0.21	14.9	0.000	0.31	0.02	100.5
CH0705C	39.8	0.02	0.075	45.0	0.11	0.19	14.8	0.000	0.29	0.00	100.4
CH0705X	39.6	0.02	0.015	45.9	0.11	0.20	14.2	0.008	0.32	0.01	100.4
CH0705X	39.9	0.02	0.004	46.0	0.10	0.20	14.0	0.021	0.33	0.01	100.6
CH0705X	39.8	0.01	0.012	46.0	0.11	0.21	13.9	0.004	0.34	0.00	100.3
CH0705X	39.7	0.02	0.016	46.0	0.11	0.19	14.0	0.014	0.36	0.02	100.4
CH0705X	39.7	0.01	0.026	45.8	0.11	0.18	14.3	0.012	0.35	0.01	100.6
CH0705X	39.6	0.01	0.005	45.8	0.10	0.18	14.2	0.029	0.33	0.02	100.3
CH0705X	39.8	0.01	0.021	45.8	0.10	0.19	14.1	0.018	0.33	0.02	100.4
CH0705X	39.6	0.01	0.028	46.2	0.11	0.20	13.7	0.008	0.35	0.00	100.2

Sample	SiO_2	TiO_2	Al_2O_3	MgO	CaO	MnO	FeO	P_2O_5	NiO	Cr_2O_3	Total
CH0705X	39.8	0.01	0.025	46.0	0.10	0.17	13.8	0.000	0.34	0.02	100.3
CH0705X	39.9	0.02	0.023	46.1	0.10	0.18	13.7	0.000	0.34	0.02	100.4
CH0705X	39.6	0.02	0.025	45.3	0.10	0.20	14.8	0.000	0.34	0.01	100.4
CH0705X	39.6	0.02	0.027	45.4	0.11	0.18	14.7	0.012	0.31	0.02	100.4
CH0705X	39.9	0.02	0.028	46.2	0.10	0.20	13.9	0.008	0.34	0.00	100.7
CH0705X	40.0	0.02	0.023	46.2	0.11	0.18	13.7	0.017	0.32	0.01	100.6
CH0705X	40.0	0.03	0.017	46.2	0.10	0.19	13.7	0.008	0.34	0.03	100.7
CH0705X	39.8	0.01	0.025	45.7	0.11	0.22	14.2	0.014	0.33	0.02	100.4
CH0705X	39.9	0.02	0.019	45.6	0.10	0.20	14.2	0.006	0.31	0.02	100.3
CH0705X	39.7	0.02	0.019	45.6	0.10	0.21	14.8	0.000	0.30	0.00	100.7
CH0705X	39.8	0.00	0.014	45.4	0.10	0.21	14.5	0.017	0.30	0.00	100.4
CH0705X	39.6	0.03	0.023	45.6	0.12	0.20	14.8	0.004	0.31	0.02	100.6
CH0705X	39.6	0.02	0.032	45.3	0.19	0.20	14.7	0.008	0.31	0.00	100.4
CH0705X	39.6	0.03	0.013	45.4	0.12	0.21	14.7	0.001	0.27	0.01	100.4
CH0705X	39.7	0.01	0.018	45.7	0.10	0.18	14.2	0.018	0.32	0.02	100.3
CH0705X	39.9	0.01	0.027	46.1	0.11	0.18	13.7	0.006	0.33	0.02	100.4
CH0705X	39.9	0.02	0.020	46.2	0.10	0.20	13.8	0.008	0.35	0.00	100.6
CH0705Y	39.6	0.01	0.000	45.5	0.02	0.19	14.6	0.029	0.29	0.01	100.3
CH0705Y	39.6	0.02	0.000	45.4	0.03	0.20	14.7	0.048	0.32	0.01	100.4
CH0705Y	39.6	0.01	0.003	45.1	0.03	0.20	14.8	0.023	0.31	0.00	100.1
CH0705Y	39.8	0.01	0.011	45.6	0.01	0.21	14.3	0.015	0.31	0.01	100.3
CH0705Y	39.7	0.01	0.021	45.4	0.28	0.19	14.4	0.000	0.33	0.01	100.3
CH0705Y	39.9	0.00	0.008	45.2	0.03	0.21	14.7	0.020	0.31	0.02	100.4
CH0705Y	39.6	0.01	0.013	45.3	0.03	0.20	14.6	0.000	0.28	0.00	100.0
CH0705Y	39.6	0.00	0.005	45.3	0.01	0.21	14.8	0.009	0.31	0.01	100.3
CH0705Y	39.6	0.00	0.008	45.2	0.03	0.21	14.7	0.010	0.30	0.02	100.1
CH0705Y	39.8	0.01	0.010	45.4	0.03	0.23	14.7	0.018	0.32	0.00	100.5
CH0705Y	39.6	0.01	0.013	45.3	0.04	0.21	14.6	0.016	0.33	0.02	100.1
CH0705Y	39.5	0.00	0.012	45.4	0.04	0.21	14.7	0.004	0.32	0.02	100.2
CH0705Y	39.9	0.00	0.003	45.6	0.01	0.21	14.7	0.015	0.29	0.00	100.6
CH0705Y	39.7	0.02	0.011	45.3	0.02	0.21	14.7	0.005	0.32	0.02	100.3
CH0705Y	39.6	0.00	0.003	45.4	0.03	0.23	14.5	0.011	0.29	0.00	100.0
CH0705Y	39.5	0.00	0.007	45.4	0.03	0.21	14.7	0.003	0.34	0.01	100.3
CH0705Y	39.5	0.01	0.014	45.3	0.02	0.21	14.5	0.014	0.32	0.01	99.9
CH0705Y	39.3	0.01	0.005	45.2	0.05	0.21	14.7	0.011	0.30	0.00	99.8
CH0705Y	39.5	0.02	0.026	45.3	0.05	0.19	14.7	0.005	0.31	0.00	100.1
CH0705Y	39.6	0.01	0.007	45.3	0.05	0.19	14.6	0.017	0.31	0.01	100.1
CH0705Y	39.4	0.00	0.018	45.3	0.04	0.19	14.4	0.019	0.32	0.00	99.6
CH0705Y	39.2	0.02	0.000	44.5	0.02	0.20	15.2	0.001	0.31	0.01	99.6

Sample	SiO_2	TiO_2	Al_2O_3	MgO	CaO	MnO	FeO	P_2O_5	NiO	Cr_2O_3	Total
CH0705Y	39.5	0.00	0.005	45.0	0.02	0.19	15.2	0.008	0.31	0.01	100.3
CH0705Y	39.3	0.03	0.006	45.4	0.02	0.19	14.8	0.022	0.29	0.01	100.0
CH0705Y	39.5	0.01	0.009	45.3	0.03	0.19	14.7	0.007	0.31	0.00	100.1
CH0706A	40.5	0.01	0.008	48.2	0.05	0.16	11.3	0.013	0.39	0.00	100.7
CH0706A	40.3	0.01	0.013	48.4	0.05	0.17	11.2	0.019	0.39	0.02	100.6
CH0706A	40.4	0.00	0.019	47.5	0.05	0.15	11.1	0.016	0.38	0.01	99.6
CH0706A	40.4	0.02	0.015	48.0	0.07	0.17	11.3	0.013	0.39	0.02	100.3
CH0706A	40.4	0.01	0.009	48.0	0.08	0.16	11.5	0.016	0.38	0.02	100.5
CH0706A	40.4	0.02	0.036	46.7	0.08	0.13	12.5	0.000	0.34	0.01	100.3
CH0706A	40.4	0.00	0.000	48.2	0.08	0.16	11.5	0.000	0.36	0.01	100.8
CH0706A	40.4	0.00	0.010	48.4	0.07	0.16	11.1	0.000	0.37	0.01	100.5
CH0706A	40.3	0.00	0.021	47.9	0.06	0.16	11.5	0.018	0.39	0.00	100.4
CH0706A	40.3	0.00	0.007	47.7	0.07	0.17	11.7	0.000	0.38	0.02	100.4
CH0706A	40.5	0.00	0.003	47.8	0.07	0.17	11.7	0.016	0.35	0.02	100.7
CH0706A	40.4	0.01	0.011	47.7	0.06	0.17	11.7	0.011	0.38	0.00	100.5
CH0706A	40.5	0.00	0.007	47.9	0.05	0.17	11.6	0.023	0.40	0.00	100.6
CH0706A	40.3	0.00	0.007	47.6	0.07	0.16	12.1	0.003	0.36	0.00	100.6
CH0706A	40.4	0.00	0.010	47.8	0.06	0.16	12.0	0.016	0.39	0.01	100.8
CH0706A	40.3	0.02	0.000	47.6	0.08	0.17	11.9	0.000	0.36	0.01	100.4
CH0706A	40.4	0.01	0.016	47.8	0.07	0.16	11.8	0.002	0.37	0.00	100.6
CH0706A	40.6	0.01	0.003	48.7	0.07	0.16	11.0	0.005	0.40	0.00	100.9
CH0706A	40.5	0.02	0.001	48.0	0.07	0.18	11.3	0.003	0.36	0.00	100.5
CH0706A	40.4	0.01	0.006	48.2	0.07	0.14	11.2	0.003	0.38	0.00	100.3
CH0706A	40.6	0.01	0.009	48.1	0.07	0.14	11.7	0.004	0.37	0.01	101.0
CH0706A	40.5	0.02	0.006	47.8	0.06	0.16	11.6	0.012	0.36	0.01	100.5
CH0706A	40.6	0.01	0.018	48.0	0.06	0.16	11.6	0.010	0.37	0.01	100.7
CH0706A	40.6	0.00	0.008	48.2	0.08	0.16	11.6	0.004	0.37	0.00	101.0
CH0706A	40.5	0.00	0.002	48.1	0.07	0.16	11.5	0.008	0.40	0.00	100.9
CH0706A	40.4	0.00	0.000	48.3	0.08	0.16	11.4	0.024	0.39	0.01	100.7
CH0706A	40.4	0.00	0.011	48.3	0.08	0.15	11.5	0.013	0.40	0.02	100.9
CH0706A	40.5	0.01	0.006	48.1	0.08	0.16	11.4	0.016	0.38	0.00	100.6
CH0706A	40.4	0.01	0.015	48.1	0.05	0.16	11.4	0.001	0.39	0.00	100.5
CH0706B	39.1	0.02	0.026	44.4	0.11	0.21	15.3	0.015	0.34	0.00	99.5
CH0706B	39.1	0.02	0.022	44.7	0.11	0.20	15.4	0.023	0.37	0.01	99.9
CH0706B	38.9	0.00	0.016	44.0	0.12	0.22	16.2	0.001	0.32	0.00	99.9
CH0706B	38.8	0.02	0.022	43.8	0.11	0.21	16.2	0.017	0.35	0.00	99.6
CH0706B	40.2	0.03	0.032	43.8	0.14	0.21	14.6	0.020	0.36	0.01	99.5
CH0706B,3	39.8	0.01	0.000	45.5	0.16	0.22	14.2	0.003	0.30	0.00	100.2
CH0706B,3	39.7	0.02	0.008	45.2	0.18	0.20	14.7	0.000	0.30	0.01	100.4

Sample	SiO_2	TiO_2	Al_2O_3	MgO	CaO	MnO	FeO	P_2O_5	NiO	Cr_2O_3	Total
CH0706B,3	39.7	0.00	0.014	45.2	0.10	0.20	14.6	0.009	0.34	0.02	100.2
CH0706B,3	39.6	0.01	0.024	43.5	0.17	0.19	16.5	0.000	0.29	0.01	100.3
CH0706B,3	39.8	0.02	0.023	45.2	0.22	0.20	14.7	0.014	0.28	0.01	100.5
CH0706B,3	39.7	0.01	0.012	45.2	0.20	0.18	14.7	0.011	0.35	0.00	100.5
CH0706B,3	39.9	0.01	0.019	45.1	0.20	0.20	14.6	0.001	0.30	0.00	100.3
CH0706B,3	39.9	0.01	0.015	45.3	0.20	0.22	14.8	0.000	0.33	0.00	100.8
CH0706B,3	40.0	0.01	0.016	43.9	0.22	0.20	15.8	0.004	0.33	0.02	100.6
CH0706B,3	39.6	0.01	0.008	44.9	0.18	0.20	14.6	0.010	0.29	0.00	99.8
CH0706B,3	39.9	0.01	0.017	44.9	0.16	0.21	14.9	0.000	0.27	0.01	100.4
CH0706B,3	39.8	0.01	0.006	45.3	0.20	0.21	14.7	0.009	0.31	0.00	100.6
CH0706B,3	39.7	0.01	0.015	45.1	0.19	0.20	14.7	0.000	0.29	0.01	100.3
CH0706B,3	39.8	0.01	0.017	45.4	0.15	0.21	14.6	0.000	0.31	0.00	100.5
CH0706B,3	39.7	0.02	0.005	45.4	0.15	0.19	14.7	0.000	0.28	0.00	100.4
CH0706B,3	39.8	0.02	0.007	45.2	0.14	0.21	14.9	0.012	0.27	0.01	100.6
CH0706B,3	39.6	0.03	0.010	45.1	0.18	0.20	14.8	0.000	0.30	0.01	100.2
CH0706B,3	39.7	0.00	0.005	45.1	0.17	0.21	14.7	0.013	0.32	0.02	100.2
CH0706B,3	39.7	0.01	0.010	45.2	0.16	0.20	14.8	0.018	0.33	0.01	100.5
CH0706B,3	39.7	0.02	0.003	45.2	0.16	0.21	14.7	0.006	0.30	0.00	100.4
CH0706B,3	39.8	0.01	0.019	45.2	0.15	0.20	14.8	0.015	0.28	0.00	100.5
CH0706B,3	39.6	0.02	0.021	45.2	0.15	0.20	14.9	0.013	0.29	0.03	100.5
CH0706B,3	39.8	0.01	0.018	45.2	0.18	0.20	14.7	0.023	0.32	0.01	100.5
CH0706B,3	39.9	0.02	0.016	45.1	0.17	0.20	15.0	0.000	0.29	0.01	100.6
CH0706B,3	39.7	0.01	0.005	44.9	0.17	0.22	14.9	0.011	0.30	0.00	100.3
CH0706B,3	39.5	0.01	0.014	45.2	0.15	0.24	14.8	0.000	0.29	0.03	100.2
CH0706B,3	39.5	0.01	0.013	44.9	0.21	0.21	15.2	0.004	0.30	0.01	100.4
CH0706B,3	39.5	0.02	0.018	44.9	0.21	0.20	15.1	0.019	0.30	0.01	100.3
CH0706C	40.2	0.02	0.006	47.1	0.07	0.22	13.3	0.003	0.32	0.02	101.3
CH0706C	40.5	0.02	0.022	46.9	0.06	0.20	13.6	0.015	0.39	0.00	101.7
CH0706C	39.2	0.01	0.703	45.5	0.07	0.22	13.8	0.000	0.34	0.00	99.9
CH0706C	39.7	0.01	0.005	46.0	0.08	0.21	14.2	0.010	0.37	0.02	100.6
CH0706C	39.8	0.01	0.007	46.2	0.08	0.20	14.0	0.006	0.37	0.01	100.8
CH0706C	39.8	0.00	0.012	46.3	0.09	0.20	14.3	0.013	0.36	0.04	101.0
CH0706C	39.8	0.00	0.009	46.1	0.10	0.20	14.1	0.005	0.34	0.02	100.7
CH0706C	39.5	0.00	0.024	45.9	0.10	0.21	14.2	0.010	0.35	0.00	100.3
CH0706C	40.3	0.01	0.016	46.1	0.09	0.19	13.9	0.004	0.37	0.01	101.1
CH0706C	40.0	0.01	0.011	46.0	0.09	0.21	14.3	0.006	0.37	0.01	100.9
CH0706C	40.2	0.01	0.024	45.1	0.09	0.20	14.2	0.007	0.36	0.01	100.2
CH0706C	40.4	0.00	0.030	44.9	0.08	0.22	13.9	0.015	0.38	0.00	100.0
CH0706C	39.7	0.00	0.023	46.2	0.09	0.21	14.1	0.005	0.37	0.02	100.7

Sample	SiO_2	TiO_2	Al_2O_3	MgO	CaO	MnO	FeO	P_2O_5	NiO	Cr_2O_3	Total
CH0706C	40.0	0.01	0.057	45.5	0.08	0.19	14.2	0.000	0.38	0.00	100.4
CH0706D	40.6	0.01	0.030	45.3	0.13	0.23	12.9	0.003	0.27	0.02	99.5
CH0706D	40.5	0.01	0.032	45.2	0.14	0.22	14.8	0.000	0.29	0.00	101.1
CH0706E	39.8	0.00	0.021	46.3	0.03	0.19	14.1	0.000	0.28	0.00	100.7
CH0706E	40.2	0.01	0.198	44.0	0.05	0.22	14.1	0.000	0.29	0.00	99.1
CH0706E	39.0	0.01	0.149	46.1	0.07	0.18	14.1	0.000	0.29	0.00	100.0
CH0706E	39.1	0.01	0.065	45.5	0.08	0.19	14.1	0.003	0.30	0.02	99.3
CH0706E	39.4	0.02	0.446	44.4	0.04	0.21	14.4	0.002	0.29	0.03	99.3
CH0706E	39.6	0.05	0.080	46.2	0.04	0.22	14.0	0.018	0.29	0.00	100.5
CH0706E	38.8	0.00	0.064	45.8	0.03	0.19	14.0	0.000	0.28	0.01	99.2
CH0706E	39.7	0.01	0.012	46.3	0.04	0.20	14.2	0.002	0.28	0.01	100.8
CH0706E	40.4	0.00	0.077	45.9	0.04	0.20	14.1	0.000	0.27	0.00	101.1
CH0706E	39.3	0.01	0.064	45.9	0.03	0.20	14.2	0.019	0.30	0.01	100.0
CH0706F	40.2	0.01	0.020	47.8	0.10	0.17	11.8	0.013	0.34	0.03	100.4
CH0706F	39.9	0.00	0.038	47.9	0.09	0.18	11.9	0.000	0.32	0.02	100.3
CH0706F	39.9	0.01	0.053	46.8	0.11	0.17	12.3	0.009	0.35	0.05	99.7
CH0706F	39.9	0.01	0.049	46.2	0.08	0.17	12.5	0.023	0.32	0.02	99.2
CH0706F	39.3	0.01	0.080	46.4	0.12	0.17	12.9	0.008	0.31	0.04	99.4
CH0707C	38.6	0.01	0.033	45.8	0.08	0.19	13.9	0.053	0.30	0.01	99.0
CH0708B	38.5	0.01	0.019	46.2	0.14	0.20	14.9	0.009	0.32	0.00	100.3
CH0708B	39.5	0.03	0.030	45.5	0.16	0.21	15.0	0.014	0.30	0.02	100.8

Table A3.9: Analyses of pyroxene in Piton Chisny cumulate xenoliths (wt.%)

Sample	SiO_2	TiO_2	Al_2O_3	MgO	CaO	MnO	FeO	Na_2O	K_2O	Cr_2O_3	Total
CH0701	49.0	0.96	8.78	15.6	19.82	0.09	4.19	0.50	0.00	0.91	99.9
CH0701	50.5	1.05	4.04	16.5	20.92	0.10	4.67	0.52	0.00	0.91	99.1
CH0701	50.5	1.09	4.66	16.6	20.78	0.12	4.83	0.50	0.00	0.99	100.0
CH0701	50.1	1.07	4.06	16.2	21.38	0.11	4.58	0.53	0.00	1.01	99.1
CH0701	49.6	1.01	5.09	16.0	21.19	0.08	4.56	0.54	0.01	0.99	99.0
CH0701	50.0	1.13	4.53	16.4	20.88	0.12	4.95	0.47	0.01	0.99	99.5
CH0701	49.8	1.06	5.28	16.1	21.02	0.09	4.55	0.48	0.00	0.80	99.2
CH0701	50.3	1.12	4.29	16.0	21.48	0.11	4.67	0.48	0.00	0.98	99.4
CH0701	50.4	1.03	4.16	16.4	21.07	0.12	4.82	0.46	0.00	0.94	99.4
CH0701	49.9	1.11	4.78	16.2	21.16	0.10	4.60	0.55	0.00	1.01	99.4
CH0701	50.2	1.04	4.14	16.7	20.66	0.11	4.94	0.43	0.00	1.07	99.2
CH0701	50.1	1.01	4.89	16.0	21.18	0.10	4.60	0.49	0.00	1.03	99.4
CH0701	49.3	1.01	4.41	17.9	19.90	0.11	5.18	0.47	0.01	0.99	99.3
CH0701	49.2	0.94	5.06	16.4	20.86	0.08	4.92	0.48	0.01	1.05	99.0
CH0701	51.2	0.97	3.24	16.9	21.06	0.13	5.18	0.41	0.00	0.30	99.3
CH0701	51.1	0.95	3.02	17.0	20.76	0.12	5.49	0.39	0.00	0.29	99.1
CH0701	51.1	0.99	3.03	16.9	21.13	0.13	4.98	0.40	0.00	0.30	98.9
CH0701	51.0	1.01	3.31	16.9	21.22	0.12	5.13	0.39	0.00	0.30	99.3
CH0701	50.7	1.00	3.17	16.7	20.47	0.13	6.21	0.38	0.00	0.32	99.1
CH0701	50.3	1.08	4.29	16.4	21.62	0.10	4.43	0.38	0.00	0.41	99.0
CH0701	49.5	1.39	5.01	15.8	20.80	0.13	5.75	0.41	0.01	0.42	99.3
CH0701	50.2	1.17	4.12	16.4	21.54	0.10	4.85	0.38	0.00	0.50	99.3
CH0701	49.9	1.27	4.49	16.1	21.43	0.11	4.99	0.43	0.00	0.45	99.2
CH0701	49.9	1.29	4.48	16.2	21.24	0.10	5.17	0.42	0.00	0.40	99.2
CH0701	49.7	1.31	4.59	16.2	21.32	0.12	5.05	0.43	0.00	0.44	99.1
CH0701	49.1	1.63	5.47	15.6	21.46	0.11	4.96	0.53	0.00	0.54	99.4
CH0701	50.4	1.24	4.41	16.0	21.27	0.12	5.24	0.46	0.00	0.35	99.5
CH0701	50.1	1.26	4.31	15.6	21.28	0.10	5.31	0.47	0.00	0.66	99.2
CH0701	50.3	1.28	4.52	15.8	21.16	0.13	5.11	0.49	0.01	0.58	99.4
CH0701	49.5	1.44	5.26	15.5	20.69	0.12	5.75	0.43	0.01	0.40	99.1
CH0701	51.0	0.97	3.29	16.4	20.81	0.12	5.63	0.39	0.00	0.31	99.0
CH0701	50.6	1.20	4.08	16.2	21.16	0.11	5.02	0.49	0.00	0.42	99.2
CH0701	51.1	0.83	3.67	16.6	20.77	0.11	5.14	0.42	0.01	0.90	99.6
CH0701	51.4	0.91	3.61	16.6	20.96	0.10	5.17	0.37	0.00	0.72	99.8
CH0701	51.0	0.95	3.94	16.5	20.72	0.11	4.89	0.43	0.01	0.74	99.3
CH0701	51.5	0.81	3.15	17.0	20.47	0.13	5.33	0.39	0.00	0.53	99.3
CH0701	50.8	0.83	3.40	16.5	20.82	0.12	5.46	0.37	0.00	0.70	99.1
CH0701	50.7	0.99	3.94	16.5	20.72	0.14	4.91	0.43	0.00	0.92	99.2
CH0701	50.5	0.94	4.13	16.2	20.62	0.14	5.30	0.39	0.01	0.96	99.2

Sample	SiO_2	TiO_2	Al_2O_3	MgO	CaO	MnO	FeO	Na_2O	K_2O	Cr_2O_3	Total
CH0701	50.7	1.03	3.93	16.4	20.96	0.10	4.87	0.43	0.00	0.75	99.2
CH0701	50.8	0.95	3.85	16.3	21.05	0.12	5.30	0.40	0.01	0.81	99.5
CH0701	50.7	1.05	3.96	16.2	21.06	0.11	4.56	0.51	0.01	0.96	99.1
CH0701	50.9	0.96	4.05	16.7	20.52	0.10	4.89	0.48	0.00	0.97	99.6
CH0701	50.7	1.02	4.14	16.2	20.76	0.10	4.65	0.49	0.02	0.99	99.1
CH0701	50.2	1.18	4.37	16.0	20.81	0.11	5.84	0.36	0.00	0.34	99.2
CH0701	50.0	1.26	4.70	15.7	20.76	0.11	5.88	0.38	0.00	0.37	99.2
CH0701	50.6	1.08	3.88	16.4	20.50	0.14	5.90	0.38	0.01	0.25	99.1
CH0701	50.6	1.09	4.21	16.2	20.74	0.12	5.68	0.37	0.01	0.27	99.3
CH0701	50.4	1.28	4.74	16.1	20.96	0.13	4.97	0.54	0.01	0.27	99.4
CH0701 Dunite	50.2	1.12	4.37	16.3	20.66	0.11	4.92	0.42	0.00	0.90	99.0
CH0701 Dunite	50.2	1.09	4.25	16.2	20.45	0.13	5.45	0.39	0.01	0.93	99.1
CH0701 Dunite	50.1	1.22	4.50	16.1	20.58	0.12	4.94	0.44	0.00	0.97	99.0
CH0702	52.4	0.46	1.84	17.4	21.24	0.11	4.39	0.26	0.00	1.05	99.1
CH0702	50.3	1.18	4.27	15.3	22.35	0.08	4.05	0.65	0.01	1.07	99.2
CH0702	50.4	1.07	4.05	15.3	22.28	0.09	4.04	0.75	0.00	1.12	99.1
CH0702	51.5	1.18	2.23	16.0	22.52	0.08	4.69	0.49	0.00	0.74	99.4
CH0702A	49.9	1.02	3.78	16.9	20.33	0.12	4.84	0.58	0.00	1.50	99.0
CH0702A	50.1	1.04	3.97	16.7	20.45	0.12	4.67	0.66	0.00	1.25	99.0
CH0702A	51.2	0.91	3.56	16.3	21.41	0.08	4.34	0.65	0.01	1.15	99.7
CH0702A	51.0	0.86	3.49	16.6	21.04	0.12	4.49	0.55	0.01	1.14	99.2
CH0702A	50.8	1.06	3.89	15.9	22.28	0.08	4.10	0.66	0.00	1.03	99.8
CH0702A	51.0	0.98	3.66	16.3	21.52	0.11	4.31	0.61	0.00	1.13	99.6
CH0702A	51.0	0.87	3.35	16.7	21.13	0.11	4.45	0.56	0.00	1.07	99.3
CH0702A	50.5	1.04	4.05	16.2	21.08	0.11	4.45	0.67	0.01	1.25	99.4
CH0702A	51.0	1.07	3.99	16.4	20.95	0.11	4.62	0.66	0.00	1.29	100.1
CH0702A	51.2	0.87	3.35	15.8	22.18	0.11	3.97	0.67	0.00	0.99	99.2
CH0702A	50.3	1.18	4.28	16.0	22.44	0.08	3.92	0.75	0.03	0.98	99.9
CH0702A	50.4	1.02	3.90	16.1	22.39	0.08	3.91	0.61	0.00	1.02	99.5
CH0702A	51.1	0.92	3.47	16.4	21.12	0.10	4.51	0.53	0.00	1.09	99.2
CH0702A	51.6	0.81	3.22	16.9	21.15	0.10	4.18	0.53	0.02	1.32	99.8
CH0703 Pyroxenite	50.1	1.21	4.32	15.3	21.10	0.14	5.55	0.54	0.00	0.79	99.1
CH0703 Pyroxenite	50.8	1.19	4.28	15.2	21.70	0.12	5.24	0.54	0.00	0.79	99.9
CH0703 Pyroxenite	50.6	0.88	3.40	16.0	21.32	0.13	5.38	0.52	0.00	0.98	99.2

Sample	SiO_2	TiO_2	Al_2O_3	MgO	CaO	MnO	FeO	Na_2O	K_2O	Cr_2O_3	Total
CH0703 Pyroxenite	49.0	1.63	4.90	16.2	21.27	0.11	5.50	0.64	0.01	0.64	99.9
CH0703 Pyroxenite	49.7	1.52	4.84	15.4	21.22	0.12	5.65	0.59	0.00	0.77	99.8
CH0703B	50.0	1.17	4.61	15.4	21.32	0.10	5.83	0.53	0.00	0.79	99.8
CH0703B	51.0	0.98	4.08	16.1	21.27	0.12	5.93	0.51	0.00	0.72	100.7
CH0703B	50.6	0.89	3.87	16.2	21.29	0.12	5.85	0.51	0.00	0.70	100.0
CH0703B	49.9	1.21	4.72	15.4	21.27	0.12	5.75	0.55	0.00	0.69	99.6
CH0703B	50.8	0.90	3.78	16.0	21.31	0.13	5.80	0.50	0.01	0.69	99.9
CH0703B	50.4	0.82	3.90	16.2	20.94	0.15	5.71	0.51	0.00	0.77	99.4
CH0703B	50.4	0.99	5.51	15.4	21.14	0.12	5.57	0.53	0.00	0.83	100.5
CH0703B	50.4	0.94	3.84	16.0	21.23	0.14	5.72	0.52	0.01	0.67	99.5
CH0703B	50.0	1.11	4.41	15.5	21.33	0.14	5.73	0.55	0.00	0.91	99.7
CH0703B	51.0	0.91	3.88	16.1	21.30	0.13	5.88	0.51	0.00	0.72	100.4
CH0703B	50.5	1.06	3.88	16.0	21.23	0.13	5.79	0.48	0.00	0.58	99.6
CH0703B	50.5	0.98	3.69	16.0	21.34	0.12	5.69	0.45	0.00	0.60	99.3
CH0703B	50.6	1.00	3.80	16.1	21.31	0.11	5.66	0.45	0.00	0.67	99.7
CH0703B	50.6	1.09	3.92	15.9	21.48	0.13	5.78	0.44	0.01	0.59	99.9
CH0703B	50.6	1.04	3.87	15.9	21.40	0.12	5.71	0.47	0.01	0.59	99.7
CH0703B	50.7	1.03	3.84	16.0	21.21	0.15	5.69	0.48	0.00	0.55	99.6
CH0703B	50.7	1.09	4.08	15.8	21.33	0.13	5.72	0.49	0.00	0.61	100.0
CH0703B	50.3	1.13	4.33	15.7	21.42	0.10	5.73	0.49	0.00	0.55	99.8
CH0703B	50.5	1.01	3.81	16.0	21.33	0.13	5.63	0.49	0.01	0.59	99.5
CH0703B	50.4	1.06	3.99	16.1	21.05	0.13	5.85	0.45	0.01	0.64	99.6
CH0703B	50.2	1.00	3.97	15.9	21.48	0.13	5.73	0.47	0.00	0.72	99.6
CH0703B	49.9	1.11	4.29	15.6	21.26	0.14	5.68	0.52	0.00	0.72	99.3
CH0703B	50.2	1.01	4.03	15.8	21.35	0.14	5.80	0.51	0.00	0.69	99.5
CH0703B	50.0	1.05	4.17	15.7	21.32	0.13	5.70	0.52	0.00	0.71	99.3
CH0703B	50.5	0.80	2.89	16.7	20.95	0.14	6.14	0.24	0.01	0.75	99.2
CH0703B	50.3	0.99	4.05	15.8	21.28	0.13	5.75	0.52	0.01	0.74	99.6
CH0703B	50.6	0.96	4.11	16.8	21.24	0.14	5.89	0.52	0.00	0.66	100.9
CH0703B	50.5	0.99	4.02	15.9	21.16	0.13	5.95	0.50	0.00	0.69	99.8
CH0703B	50.3	1.05	4.12	15.8	21.14	0.13	5.71	0.50	0.00	0.71	99.5
CH0703B	50.0	1.12	4.53	15.7	21.27	0.14	5.70	0.53	0.00	0.71	99.7
CH0703B	50.3	1.03	4.18	15.7	21.36	0.14	5.70	0.49	0.00	0.70	99.6
CH0703B	50.4	0.95	3.85	16.0	21.30	0.14	5.82	0.50	0.00	0.61	99.6
CH0703B	50.5	0.97	3.89	15.9	21.30	0.12	5.64	0.49	0.00	0.60	99.4
CH0703B	50.7	0.93	3.69	16.1	21.46	0.15	5.85	0.46	0.00	0.59	99.9
CH0703B	50.5	0.97	3.77	16.0	21.31	0.13	5.86	0.48	0.00	0.64	99.7
CH0703B	50.2	1.07	4.11	15.8	21.31	0.14	5.76	0.50	0.00	0.55	99.4
CH0703B	50.5	0.96	3.76	15.9	21.32	0.11	5.85	0.48	0.00	0.61	99.4

Sample	SiO_2	TiO_2	Al_2O_3	MgO	CaO	MnO	FeO	Na_2O	K_2O	Cr_2O_3	Total
CH0703B	50.1	0.98	3.90	15.9	21.28	0.12	5.83	0.49	0.00	0.65	99.2
CH0703B	50.1	1.09	4.08	15.8	21.35	0.12	5.76	0.48	0.00	0.69	99.4
CH0703B	49.1	1.34	4.98	15.2	21.43	0.13	5.75	0.56	0.00	0.77	99.2
CH0703B	49.4	1.24	4.76	15.3	21.47	0.13	5.85	0.52	0.00	0.81	99.5
CH0703B	50.4	0.97	3.92	16.0	21.26	0.13	5.93	0.46	0.00	0.65	99.7
CH0703B	49.2	1.22	4.63	15.5	21.37	0.13	5.96	0.54	0.00	0.73	99.2
CH0703B	52.4	0.69	2.33	17.9	19.28	0.16	6.51	0.30	0.01	0.82	100.4
CH0703B	50.3	1.17	4.30	15.8	21.27	0.15	6.02	0.53	0.00	0.64	100.2
CH0703B	50.2	1.14	4.09	15.9	21.44	0.12	6.01	0.51	0.00	0.62	100.0
CH0703B	50.3	1.12	4.14	15.8	21.26	0.14	6.01	0.52	0.00	0.68	100.1
CH0703B	50.7	0.63	2.25	18.5	19.68	0.13	6.82	0.33	0.00	0.37	99.4
CH0703B	49.9	1.16	4.21	15.6	21.36	0.14	5.89	0.49	0.01	0.68	99.4
CH0703B	50.5	0.97	4.15	15.8	21.24	0.12	5.73	0.51	0.00	0.84	99.9
CH0703B	50.1	0.96	4.13	15.7	21.40	0.14	5.76	0.50	0.00	0.87	99.6
CH0703B	50.9	0.98	4.06	15.8	21.23	0.14	5.75	0.51	0.01	0.73	100.1
CH0703B	50.3	0.95	4.10	15.8	21.24	0.14	5.76	0.51	0.00	0.85	99.7
CH0703B	50.4	0.94	4.01	15.8	21.25	0.14	5.60	0.51	0.00	0.96	99.7
CH0703B	49.9	1.01	4.28	15.7	21.28	0.12	5.85	0.52	0.00	0.87	99.5
CH0703B	50.3	1.01	4.33	15.9	21.16	0.14	5.75	0.55	0.01	0.93	100.0
CH0703B	50.1	1.04	4.26	15.7	21.43	0.12	5.71	0.52	0.00	0.85	99.8
CH0703B	50.4	0.99	4.16	15.6	21.21	0.12	5.63	0.53	0.01	0.91	99.5
CH0703B	50.1	1.02	4.27	15.6	21.36	0.13	5.73	0.54	0.00	0.82	99.7
CH0703B	50.0	1.05	4.31	15.7	21.43	0.13	5.70	0.54	0.00	0.83	99.7
CH0703B	50.4	1.02	4.23	15.4	21.30	0.13	5.80	0.51	0.00	0.86	99.6
CH0703B	50.9	0.95	4.13	15.9	21.27	0.12	5.69	0.51	0.00	0.74	100.2
CH0703B	50.2	0.97	4.07	15.7	21.35	0.13	5.79	0.49	0.00	0.77	99.5
CH0703B	50.2	1.03	4.33	15.5	21.32	0.13	5.67	0.52	0.01	0.90	99.6
CH0703B	49.9	1.02	4.22	15.7	21.23	0.12	5.89	0.53	0.01	0.87	99.5
CH0703B	50.0	1.01	4.26	15.6	21.38	0.13	5.75	0.50	0.00	0.83	99.5
CH0703B	50.5	0.95	4.08	15.8	21.25	0.12	5.71	0.53	0.00	0.74	99.7
CH0703B	50.8	0.93	4.14	15.8	21.29	0.13	5.78	0.52	0.00	0.78	100.1
CH0703B	49.8	1.07	4.42	15.8	21.24	0.14	5.77	0.53	0.00	0.78	99.6
CH0703B	50.2	1.09	4.31	15.6	21.28	0.14	5.72	0.52	0.01	0.88	99.7
CH0703B	49.9	1.07	4.31	15.6	21.27	0.13	5.60	0.55	0.00	0.87	99.3
CH0703B	49.7	0.94	4.47	15.3	21.26	0.14	5.90	0.49	0.00	0.78	99.0
CH0703B	50.7	0.93	4.06	15.9	21.23	0.13	5.72	0.52	0.00	0.87	100.1
CH0703B	50.3	0.96	4.09	15.7	21.25	0.14	5.71	0.52	0.00	0.97	99.6
CH0703B	50.2	1.03	4.19	15.8	21.25	0.14	5.70	0.55	0.01	0.93	99.7
CH0703B	50.2	1.01	4.20	15.6	21.17	0.13	5.62	0.52	0.00	0.92	99.4

Sample	SiO_2	TiO_2	Al_2O_3	MgO	CaO	MnO	FeO	Na_2O	K_2O	Cr_2O_3	Total
CH0703B	50.5	0.95	4.09	15.9	21.22	0.14	5.68	0.51	0.01	0.87	99.9
CH0703B	50.8	0.97	4.22	15.9	21.29	0.13	5.75	0.52	0.00	0.81	100.3
CH0703B	50.5	0.98	4.05	15.8	21.26	0.13	5.56	0.53	0.00	0.94	99.7
CH0703B	50.1	1.04	4.12	15.7	21.34	0.13	5.59	0.54	0.01	0.95	99.5
CH0703B	50.3	0.97	4.01	15.7	21.30	0.13	5.58	0.52	0.00	0.91	99.5
CH0703B	50.2	1.01	4.16	15.6	21.29	0.13	5.59	0.56	0.00	0.91	99.5
CH0703B	50.0	1.13	4.49	15.6	21.40	0.11	5.50	0.52	0.01	0.91	99.6
CH0703B	49.8	1.09	4.41	15.7	21.32	0.11	5.46	0.53	0.00	0.95	99.3
CH0703B	49.7	1.21	4.78	15.6	21.18	0.12	5.56	0.55	0.00	0.91	99.6
CH0703B	50.8	0.93	3.71	16.1	21.31	0.13	5.77	0.38	0.00	0.60	99.7
CH0703B	50.7	0.95	3.61	16.3	21.15	0.12	5.91	0.33	0.00	0.54	99.6
CH0703B	50.2	1.06	4.00	16.0	21.14	0.11	5.77	0.40	0.00	0.59	99.3
CH0703B	50.6	1.03	3.87	16.0	21.17	0.12	5.90	0.48	0.00	0.60	99.8
CH0703B	50.1	1.20	4.15	15.8	21.19	0.12	5.82	0.46	0.00	0.54	99.3
CH0703B	50.8	0.92	3.54	16.0	21.20	0.12	5.65	0.44	0.00	0.59	99.3
CH0703B	50.0	1.18	4.45	15.9	21.07	0.13	5.90	0.43	0.00	0.55	99.5
CH0703B	50.1	1.20	4.38	15.7	20.95	0.13	5.88	0.46	0.00	0.60	99.5
CH0703B	50.5	1.09	4.30	15.9	21.37	0.13	5.36	0.53	0.00	0.87	100.1
CH0703B	50.4	1.02	4.18	15.9	21.41	0.11	5.24	0.55	0.00	0.93	99.7
CH0703B	50.3	1.07	4.21	15.8	21.44	0.12	5.29	0.52	0.00	0.96	99.8
CH0703B	50.2	1.15	4.12	15.9	21.12	0.14	5.88	0.48	0.00	0.58	99.5
CH0703B	50.4	1.01	3.73	15.9	21.15	0.14	5.84	0.45	0.00	0.62	99.2
CH0703B	50.8	0.94	3.61	16.2	21.45	0.12	5.62	0.38	0.02	0.63	99.8
CH0703B	51.1	0.93	3.78	16.3	21.16	0.13	5.73	0.35	0.00	0.67	100.1
CH0703B	50.7	0.99	3.87	16.0	21.19	0.13	5.79	0.47	0.01	0.54	99.7
CH0703B	51.1	0.92	3.55	16.3	21.27	0.14	5.68	0.45	0.00	0.62	100.0
CH0703B	50.4	1.09	4.07	16.1	21.12	0.13	5.90	0.48	0.00	0.59	99.9
CH0703B	50.6	0.98	3.70	16.1	21.13	0.11	5.78	0.48	0.00	0.66	99.5
CH0703B	50.5	1.07	3.76	16.0	21.06	0.13	5.79	0.46	0.00	0.62	99.4
CH0703B	50.2	1.16	4.28	15.9	21.00	0.13	5.96	0.47	0.00	0.61	99.7
CH0703B	50.5	1.20	3.92	16.1	20.89	0.16	6.01	0.46	0.00	0.52	99.8
CH0703B	49.9	1.21	4.27	15.6	21.10	0.12	5.92	0.48	0.01	0.59	99.2
CH0703B	50.2	1.05	3.75	16.0	20.99	0.14	5.84	0.49	0.00	0.66	99.1
CH0703B	50.7	0.94	3.66	16.1	21.11	0.13	5.78	0.46	0.00	0.62	99.5
CH0703B	50.4	1.23	4.34	15.8	21.18	0.13	5.77	0.48	0.00	0.61	99.9
CH0703B	50.1	1.08	3.94	16.0	21.12	0.11	5.76	0.42	0.00	0.66	99.2
CH0703B	51.0	1.05	3.42	16.3	20.94	0.13	5.89	0.46	0.01	0.53	99.8
CH0703B	50.7	0.97	3.72	16.0	21.53	0.11	5.70	0.41	0.00	0.55	99.6
CH0703B	51.2	0.99	3.80	16.3	21.31	0.11	5.64	0.43	0.00	0.54	100.3

Sample	SiO_2	TiO_2	Al_2O_3	MgO	CaO	MnO	FeO	Na_2O	K_2O	Cr_2O_3	Total
CH0703C	50.2	1.71	5.16	16.1	21.19	0.11	4.83	0.57	0.00	0.91	100.9
CH0703D	49.9	1.40	4.47	15.3	22.90	0.08	4.51	0.49	0.01	0.63	99.7
CH0703D	50.8	1.13	3.68	15.7	22.86	0.07	4.35	0.48	0.00	0.59	99.6
CH0703D	50.7	1.18	3.97	15.6	23.00	0.08	4.38	0.47	0.01	0.70	100.1
CH0703D	50.5	1.16	4.04	15.4	23.12	0.06	4.57	0.48	0.00	0.80	100.1
CH0704	50.7	0.86	3.65	15.6	22.07	0.10	4.46	0.54	0.01	1.02	99.0
CH0704	50.7	0.87	3.67	15.7	21.80	0.10	4.61	0.52	0.00	1.02	99.0
CH0704	50.2	1.01	4.06	15.5	21.82	0.08	4.58	0.57	0.00	1.08	98.9
CH0704	50.5	0.92	3.82	15.3	22.80	0.08	4.26	0.51	0.00	0.88	99.1
CH0704	50.3	0.99	4.03	15.2	22.69	0.08	4.31	0.55	0.02	0.94	99.2
CH0704	49.9	1.00	4.36	15.0	22.54	0.09	4.47	0.53	0.01	0.98	98.9
CH0704	49.8	1.10	4.51	15.1	22.20	0.11	4.69	0.54	0.00	1.00	99.1
CH0704	50.3	1.06	4.24	15.1	22.38	0.09	4.37	0.56	0.01	0.98	99.0
CH0704	50.2	1.00	4.23	15.1	22.26	0.10	4.51	0.58	0.00	1.06	99.1
CH0704	50.2	0.98	4.26	15.3	22.20	0.09	4.61	0.52	0.00	0.99	99.2
CH0704	50.2	1.01	4.23	15.5	21.88	0.12	4.75	0.54	0.00	0.98	99.2
CH0704	50.3	0.95	4.02	15.6	21.94	0.10	4.66	0.54	0.00	0.97	99.1
CH0704A	51.9	0.69	2.71	16.4	22.76	0.08	3.98	0.48	0.01	1.01	100.0
CH0704A	51.9	0.62	2.71	16.0	23.39	0.08	3.78	0.50	0.00	0.95	99.9
CH0704A	51.8	0.68	2.74	16.4	22.84	0.08	4.00	0.45	0.01	0.94	100.0
CH0704A	51.8	0.69	2.77	16.4	22.63	0.08	3.96	0.52	0.01	0.99	99.9
CH0704A	51.8	0.74	2.87	16.1	22.95	0.09	3.75	0.58	0.00	1.00	100.0
CH0704A	51.6	0.68	2.84	16.2	22.72	0.08	3.95	0.47	0.00	1.03	99.6
CH0704A	51.6	0.73	2.87	16.3	22.78	0.09	3.98	0.51	0.00	1.04	99.9
CH0704A	52.1	0.70	2.81	16.5	22.44	0.09	4.12	0.39	0.00	0.95	100.1
CH0704A	51.9	0.66	2.68	16.6	22.16	0.09	4.22	0.43	0.00	1.00	99.7
CH0704A	51.9	0.69	2.69	16.6	22.23	0.10	4.23	0.43	0.02	0.98	99.8
CH0704A	51.9	0.78	2.83	16.4	23.09	0.09	3.64	0.49	0.00	0.81	100.1
CH0704A	50.9	0.74	2.93	16.0	22.54	0.09	4.36	0.58	0.02	1.34	99.6
CH0704A	50.8	1.22	3.86	15.9	22.44	0.07	4.28	0.52	0.00	0.95	100.1
CH0705A	49.8	1.41	4.50	15.9	21.84	0.08	4.30	0.43	0.00	1.17	99.4
CH0705A	49.9	1.30	4.25	16.0	21.81	0.09	4.29	0.41	0.00	1.12	99.2
CH0705A	49.1	1.54	4.80	15.6	21.83	0.08	4.31	0.51	0.01	1.23	99.0
CH0705A	49.7	1.32	4.28	16.0	21.87	0.09	4.33	0.38	0.00	1.05	99.0
CH0705A	49.8	1.31	4.27	16.0	21.74	0.10	4.30	0.36	0.00	1.08	99.0
CH0705A	49.6	1.29	4.39	15.9	21.91	0.11	4.29	0.35	0.00	1.18	99.0
CH0705A	50.6	1.10	3.42	16.2	22.16	0.08	3.92	0.53	0.00	0.86	99.0
CH0705A	49.9	1.26	4.12	15.9	21.98	0.09	4.26	0.50	0.00	1.08	99.0
CH0705A	50.5	1.25	3.97	15.9	22.04	0.09	3.94	0.61	0.00	0.99	99.2

Sample	SiO_2	TiO_2	Al_2O_3	MgO	CaO	MnO	FeO	Na_2O	K_2O	Cr_2O_3	Total
CH0705A	49.8	1.32	4.26	15.9	21.78	0.10	4.21	0.39	0.00	1.11	98.9
CH0705A	49.8	1.38	4.35	15.7	22.04	0.08	4.11	0.54	0.00	1.15	99.1
CH0705C	50.9	1.06	3.78	15.9	22.21	0.10	4.34	0.55	0.00	0.82	99.6
CH0705C	50.3	1.06	3.84	15.8	22.38	0.10	4.33	0.53	0.01	0.90	99.3
CH0705C	50.1	1.15	4.13	15.7	22.26	0.10	4.38	0.56	0.01	1.02	99.4
CH0705C	50.4	1.01	4.00	16.1	22.12	0.10	4.35	0.57	0.01	1.11	99.8
CH0705C	50.8	0.85	3.80	16.1	21.73	0.11	4.52	0.50	0.00	1.13	99.6
CH0705C	49.8	1.30	4.63	15.4	21.71	0.10	4.72	0.51	0.00	1.02	99.2
CH0705C	49.9	1.18	4.59	16.0	21.46	0.10	4.85	0.51	0.00	0.99	99.6
CH0705X	48.5	2.15	5.64	15.2	21.25	0.12	4.68	0.66	0.01	1.03	99.2
CH0705X	48.7	2.07	5.59	15.4	21.02	0.09	4.55	0.60	0.01	1.03	99.0
CH0705X	48.7	2.05	5.51	15.3	21.16	0.11	4.71	0.62	0.00	1.04	99.2
CH0705X	50.0	1.03	4.42	16.0	21.28	0.10	4.39	0.49	0.01	1.22	98.9
CH0705X	50.6	0.96	4.03	16.3	21.29	0.09	4.36	0.52	0.01	1.15	99.3
CH0705X	50.5	1.18	4.09	16.2	21.34	0.10	4.33	0.57	0.00	1.12	99.5
CH0705X	50.3	1.14	4.54	16.2	21.21	0.10	4.47	0.51	0.00	0.93	99.4
CH0705X	50.2	1.33	4.24	16.0	21.32	0.14	4.46	0.60	0.00	1.20	99.4
CH0705X	50.3	1.29	4.14	15.9	21.31	0.11	4.47	0.60	0.00	1.15	99.3
CH0705X	50.6	1.00	3.76	16.3	21.22	0.11	4.38	0.57	0.00	1.11	99.0
CH0705X	49.2	1.60	5.11	15.4	21.30	0.11	4.46	0.65	0.01	1.06	99.0
CH0705X	50.0	1.54	4.36	15.8	21.56	0.11	4.26	0.59	0.00	0.88	99.1
CH0705X	49.8	1.60	4.60	15.7	21.56	0.11	4.39	0.61	0.00	0.91	99.2
CH0706A	51.9	0.77	2.70	16.4	23.47	0.05	3.00	0.53	0.00	0.88	99.7
CH0706A	51.5	0.89	3.03	16.3	23.11	0.05	3.25	0.57	0.00	1.05	99.7
CH0706A	51.9	0.74	2.59	16.5	23.64	0.05	2.93	0.46	0.00	0.73	99.6
CH0706A	52.1	0.67	2.35	16.7	23.37	0.09	2.95	0.49	0.01	0.65	99.4
CH0706B	50.2	1.16	3.87	15.8	23.23	0.09	4.07	0.39	0.00	0.64	99.4
CH0706B	50.1	1.26	4.64	15.5	22.31	0.10	4.55	0.42	0.00	0.88	99.7
CH0706B,3	50.8	0.98	3.61	15.3	22.65	0.10	3.83	0.70	0.01	1.11	99.1
CH0706B,3	50.8	0.97	3.62	15.3	22.56	0.08	3.97	0.75	0.00	1.15	99.2
CH0706B,3	51.1	0.95	3.60	15.6	22.20	0.08	4.09	0.77	0.00	1.10	99.4
CH0706B,3	51.3	0.89	3.14	15.8	22.17	0.08	4.04	0.77	0.01	1.00	99.3
CH0706B,3	51.3	0.88	3.28	15.7	22.44	0.06	3.96	0.67	0.00	0.95	99.3
CH0706B,3	50.9	0.86	3.35	16.3	21.55	0.10	4.57	0.49	0.00	1.07	99.2
CH0706B,3	51.4	0.83	3.18	15.9	22.35	0.09	4.03	0.68	0.00	0.99	99.5
CH0706B,3	51.7	0.83	3.17	15.9	22.11	0.10	4.02	0.77	0.01	1.05	99.6
CH0706B,3	51.5	0.86	3.29	15.8	22.05	0.09	4.05	0.74	0.00	1.00	99.4
CH0706B,3	51.2	0.85	3.38	15.7	22.06	0.07	4.09	0.78	0.01	1.06	99.2
CH0706B,3	51.6	0.82	3.03	16.2	21.80	0.07	4.08	0.72	0.00	0.95	99.3

Sample	SiO_2	TiO_2	Al_2O_3	MgO	CaO	MnO	FeO	Na_2O	K_2O	Cr_2O_3	Total
CH0706B,3	51.2	0.92	3.60	15.4	22.38	0.09	4.05	0.77	0.01	1.19	99.6
CH0706B,3	50.9	0.95	3.66	15.2	22.24	0.09	3.90	0.78	0.02	1.22	99.0
CH0706B,3	51.2	0.97	3.60	15.2	22.69	0.06	3.85	0.75	0.01	1.18	99.5
CH0706C	51.1	0.74	3.51	15.7	22.68	0.08	4.41	0.49	0.02	0.68	99.4
CH0706C	50.7	0.57	3.53	16.0	23.39	0.08	3.93	0.36	0.01	0.59	99.1
CH0706C	51.2	0.58	3.06	16.1	23.53	0.06	4.02	0.35	0.01	0.53	99.4
CH0706C	50.9	0.58	3.40	15.8	23.70	0.07	4.05	0.37	0.00	0.56	99.4
CH0706C	50.6	0.94	3.64	15.8	22.76	0.07	4.26	0.50	0.00	0.98	99.6
CH0706C	50.3	1.13	4.15	15.3	22.54	0.09	4.38	0.52	0.00	0.91	99.4
CH0706C	50.6	1.03	3.72	15.8	22.77	0.10	4.19	0.54	0.00	0.80	99.6
CH0706C	51.3	0.94	3.44	16.3	22.53	0.11	4.28	0.47	0.01	0.57	100.0
CH0706C	51.0	1.01	3.65	16.1	22.39	0.10	4.36	0.54	0.01	0.73	99.8
CH0706C	50.2	1.20	4.00	15.6	22.12	0.09	4.30	0.53	0.01	0.88	98.9
CH0706C	50.6	1.25	3.99	15.7	22.37	0.10	4.24	0.53	0.00	0.88	99.7
CH0706C	50.6	1.15	3.84	16.0	22.43	0.10	4.36	0.50	0.00	0.60	99.5
CH0706C	50.8	0.99	3.85	15.7	22.25	0.08	4.41	0.55	0.00	1.06	99.7
CH0706C	50.2	1.00	3.90	15.7	22.28	0.10	4.36	0.59	0.00	1.07	99.3
CH0706C	51.4	1.08	4.34	15.7	22.12	0.11	4.49	0.59	0.01	1.03	100.9
CH0706C	51.2	0.95	3.40	16.3	22.29	0.11	4.24	0.56	0.00	0.78	99.8
CH0706C	51.4	0.81	3.36	16.2	22.29	0.09	4.28	0.48	0.01	0.89	99.8
CH0708B	50.1	0.95	3.70	16.6	21.47	0.10	4.47	0.54	0.00	1.18	99.2
CH0708B	51.4	1.04	4.14	16.0	21.83	0.09	4.15	0.77	0.00	1.13	100.6
CH0708B	50.0	1.04	3.90	16.4	21.58	0.10	4.75	0.43	0.00	1.14	99.3
CH0708B	51.6	0.90	3.44	16.8	21.59	0.10	4.50	0.50	0.01	1.09	100.5

Table A3.10: Analyses of spinel in Piton Chisny cumulate xenoliths (wt.%).

Sample	SiO_2	TiO_2	Al_2O_3	MgO	CaO	MnO	Fe_2O_3 (calc)	FeO (calc)	Cr_2O_3	V_2O_3	Total (calc)
CH0701	0.09	2.97	22.00	13.1	0.01	0.19	13.3	17.7	29.9	0.24	99.5
CH0701	0.16	3.00	25.78	11.9	0.02	0.17	9.9	20.3	27.7	0.23	99.1
CH0701	0.07	3.79	20.72	12.8	0.00	0.21	12.7	19.0	30.9	0.22	100.3
CH0701	0.07	3.77	20.21	12.3	0.00	0.18	12.2	19.7	31.8	0.22	100.4
CH0701	0.10	3.54	21.55	13.7	0.04	0.19	13.3	17.5	30.1	0.22	100.2
CH0701	0.07	2.80	20.30	11.9	0.02	0.19	12.8	19.5	32.8	0.27	100.6
CH0701	0.07	2.79	20.40	11.7	0.00	0.21	12.5	19.8	32.9	0.24	100.7
CH0701	0.07	2.78	20.83	12.0	0.00	0.19	12.7	19.3	32.3	0.23	100.5
CH0701	0.06	2.86	20.82	12.0	0.00	0.21	12.7	19.5	32.4	0.24	100.7
CH0701	0.13	2.74	21.22	13.0	0.00	0.21	14.2	17.4	30.0	0.25	99.2
CH0701	0.11	2.78	22.48	13.9	0.00	0.22	14.6	16.9	29.9	0.24	101.1
CH0701	0.09	2.80	21.42	13.0	0.00	0.19	13.5	17.8	31.0	0.25	100.1
CH0701	0.08	2.78	21.60	13.4	0.01	0.20	14.0	17.1	30.6	0.23	100.0
CH0701	0.12	2.80	23.46	12.5	0.09	0.18	11.9	18.9	29.7	0.23	99.8
CH0701	0.15	2.83	23.55	13.2	0.02	0.20	12.8	17.8	28.6	0.23	99.4
CH0701	0.06	2.83	18.53	11.6	0.01	0.21	10.8	19.4	36.2	0.20	99.9
CH0701	0.07	2.81	18.72	11.7	0.00	0.20	10.9	19.4	36.1	0.19	100.1
CH0701	0.05	2.54	18.05	11.5	0.01	0.21	10.5	19.4	37.9	0.19	100.3
CH0701	0.07	2.51	17.86	11.6	0.01	0.20	10.4	19.1	37.9	0.19	99.9
CH0701	0.05	2.55	17.96	11.5	0.00	0.20	10.6	19.3	37.7	0.21	100.2
CH0701	0.05	2.52	18.17	11.5	0.00	0.22	10.4	19.5	37.8	0.19	100.3
CH0701	0.05	2.55	18.25	11.5	0.00	0.23	10.8	19.5	37.5	0.20	100.5
CH0701	0.05	2.60	18.29	11.6	0.00	0.22	10.8	19.3	37.0	0.19	100.1
CH0701	0.05	2.55	18.23	11.5	0.00	0.21	10.7	19.4	37.3	0.20	100.1
CH0701	0.05	2.90	19.53	12.1	0.00	0.23	10.5	19.0	35.6	0.20	100.1
CH0701	0.07	2.78	19.07	11.9	0.01	0.22	11.0	19.1	35.9	0.21	100.3
CH0701	0.06	2.73	19.10	11.7	0.00	0.21	10.7	19.3	35.9	0.19	99.9
CH0701 Dunite	0.06	2.60	18.31	11.2	0.00	0.22	11.3	19.6	35.9	0.18	99.4
CH0701 Dunite	0.08	2.59	18.33	11.3	0.00	0.21	11.3	19.6	36.1	0.22	99.9
CH0701 Dunite	0.06	2.64	18.39	11.2	0.00	0.20	11.3	19.7	35.7	0.19	99.4
CH0701 Dunite	0.08	2.76	18.34	11.2	0.00	0.25	11.9	19.9	35.1	0.22	99.7
CH0701 Dunite	0.06	2.71	17.99	11.2	0.00	0.23	12.1	19.8	35.5	0.22	99.8
CH0701 Dunite	0.06	2.74	18.08	11.2	0.00	0.22	11.9	19.9	35.6	0.22	99.8
CH0701 Dunite	0.05	2.80	19.58	11.6	0.00	0.22	12.6	19.5	33.2	0.22	99.9

Sample	SiO_2	TiO_2	Al_2O_3	MgO	CaO	MnO	Fe_2O_3 (calc)	FeO (calc)	Cr_2O_3	V_2O_3	Total (calc)
CH0701 Dunite	0.06	2.74	19.40	11.6	0.00	0.24	12.5	19.3	33.3	0.22	99.4
CH0701 Dunite	0.06	2.60	17.99	11.5	0.01	0.22	10.3	19.4	37.7	0.18	99.9
CH0701 Dunite	0.06	2.62	18.01	11.7	0.00	0.20	10.5	19.1	37.6	0.18	100.0
CH0701 Dunite	0.07	2.84	18.88	11.5	0.01	0.21	11.1	19.6	35.2	0.21	99.5
CH0701 Dunite	0.06	2.81	18.84	11.4	0.01	0.23	11.0	19.5	35.2	0.21	99.3
CH0701 Dunite	0.06	2.81	19.00	11.2	0.00	0.23	13.3	20.0	32.9	0.24	99.7
CH0701 Dunite	0.07	2.80	18.93	11.3	0.01	0.21	13.3	19.8	32.6	0.22	99.1
CH0701 Dunite	0.07	2.69	18.56	11.9	0.00	0.22	11.7	18.9	35.7	0.17	99.9
CH0701 Dunite	0.08	2.73	18.27	11.7	0.00	0.20	11.4	19.2	36.1	0.17	99.8
CH0701 Dunite	0.04	2.45	18.64	11.4	0.01	0.22	11.4	19.3	36.1	0.20	99.8
CH0701 Dunite	0.05	2.46	18.76	11.6	0.00	0.22	11.6	19.1	35.8	0.17	99.7
CH0702	0.07	2.57	16.83	11.0	0.00	0.22	16.6	19.6	32.2	0.21	99.3
CH0702	0.05	2.58	16.70	10.9	0.00	0.21	16.9	19.9	32.4	0.28	99.9
CH0702	0.06	2.59	16.58	10.8	0.00	0.22	16.6	20.0	32.4	0.25	99.5
CH0702	0.04	2.73	16.91	11.5	0.01	0.21	14.3	19.0	34.2	0.24	99.1
CH0702	0.07	2.65	16.94	11.0	0.01	0.21	15.1	19.9	33.9	0.22	100.0
CH0702	0.07	2.63	16.68	11.3	0.02	0.19	14.9	19.4	34.5	0.24	99.9
CH0702	0.04	2.59	16.50	11.0	0.00	0.21	14.8	19.6	34.5	0.23	99.5
CH0702A	0.05	2.80	17.25	10.8	0.02	0.24	13.5	20.4	34.9	0.23	100.3
CH0702A	0.05	2.73	17.29	10.8	0.00	0.23	13.5	20.5	35.0	0.24	100.3
CH0702A	0.04	2.96	17.63	11.2	0.00	0.22	15.2	20.0	32.7	0.21	100.2
CH0702A	0.06	2.96	17.80	11.2	0.01	0.23	14.8	20.3	33.1	0.20	100.5
CH0702A	0.05	2.95	17.58	11.1	0.00	0.22	14.7	20.2	33.2	0.24	100.3
CH0702A	0.04	3.00	18.61	12.7	0.05	0.19	12.9	18.0	34.6	0.23	100.4
CH0702A	0.05	2.99	18.49	12.6	0.04	0.18	12.8	17.9	34.3	0.26	99.7
CH0702A	0.04	2.80	16.98	11.1	0.00	0.22	13.6	20.0	35.2	0.24	100.2
CH0702A	0.06	2.75	16.96	10.9	0.01	0.27	13.6	20.1	35.1	0.24	100.0
CH0702A	0.19	2.77	18.09	14.9	0.05	0.19	16.2	14.7	33.6	0.25	101.0
CH0702A	0.06	2.93	17.80	12.6	0.00	0.23	15.6	18.1	33.3	0.23	100.9

Sample	SiO_2	TiO_2	Al_2O_3	MgO	CaO	MnO	Fe_2O_3 (calc)	FeO (calc)	Cr_2O_3	V_2O_3	Total (calc)
CH0703 Dunite	0.04	2.27	16.33	10.2	0.00	0.23	17.5	21.0	33.3	0.21	101.1
CH0703 Dunite	0.06	2.39	15.31	10.4	0.00	0.22	16.9	20.6	34.5	0.19	100.5
CH0703 Dunite	0.06	2.34	15.26	9.3	0.01	0.23	15.5	21.9	34.8	0.18	99.5
CH0703 Dunite	0.02	2.32	15.02	10.8	0.00	0.22	17.5	19.4	33.8	0.18	99.2
CH0703 Dunite	0.06	2.29	15.54	10.0	0.01	0.21	16.5	20.8	34.3	0.19	99.9
CH0703 Dunite	0.06	2.20	15.29	9.9	0.01	0.21	15.7	20.7	35.0	0.21	99.2
CH0703 Pyroxenite	0.08	4.31	17.63	9.5	0.00	0.19	18.7	23.7	25.0	0.39	99.6
CH0703A	0.04	2.83	16.76	8.2	0.00	0.28	17.8	24.0	29.2	0.22	99.4
CH0703A	0.03	3.15	16.06	8.1	0.01	0.26	18.6	24.3	28.5	0.25	99.2
CH0703A	0.06	2.79	14.81	7.9	0.00	0.26	19.6	24.1	29.7	0.22	99.5
CH0703A	0.04	2.74	15.09	6.8	0.00	0.31	18.6	25.7	29.5	0.20	98.9
CH0703A	0.02	2.71	14.98	7.3	0.00	0.27	19.3	25.1	29.8	0.22	99.7
CH0703A	0.04	2.84	14.96	6.6	0.00	0.32	18.5	26.2	29.9	0.19	99.5
CH0703A	0.04	2.71	15.01	6.4	0.00	0.32	17.8	26.2	30.4	0.20	99.0
CH0703A	0.04	2.70	15.00	7.0	0.00	0.32	18.8	25.5	30.2	0.19	99.8
CH0703A	0.05	2.49	15.89	6.9	0.00	0.31	17.7	25.7	30.6	0.21	99.9
CH0703A	0.03	2.63	15.85	7.6	0.01	0.31	17.7	24.6	30.8	0.18	99.8
CH0703A	0.05	2.72	14.84	8.1	0.02	0.31	19.8	23.8	29.7	0.19	99.5
CH0703A	0.04	2.77	14.91	6.9	0.00	0.34	19.1	25.7	29.7	0.18	99.6
CH0703A	0.03	2.71	15.95	6.7	0.00	0.32	18.2	26.0	29.3	0.16	99.3
CH0703A	0.04	3.08	15.28	7.3	0.00	0.29	17.9	25.4	30.1	0.21	99.7
CH0703A	0.02	3.47	15.95	7.4	0.01	0.31	19.1	25.7	27.4	0.26	99.6
CH0703B	0.12	5.37	16.50	11.9	0.08	0.22	16.5	20.3	26.7	0.37	98.0
CH0703B	0.06	4.76	17.29	9.1	0.00	0.21	15.8	24.1	26.2	0.34	97.8
CH0703B	0.07	4.93	17.03	9.8	0.01	0.18	16.2	23.1	26.2	0.31	97.9
CH0703B	0.10	4.47	16.12	8.8	0.00	0.22	20.2	24.1	23.5	0.31	97.9
CH0703B	0.10	4.34	16.20	8.8	0.01	0.22	19.7	24.3	25.0	0.30	99.0
CH0703B	0.07	4.53	16.22	9.6	0.00	0.23	20.0	23.4	25.1	0.29	99.4
CH0703B	0.09	4.06	17.10	9.4	0.01	0.22	19.0	23.1	25.2	0.30	98.6
CH0703B	0.15	4.13	19.46	10.0	0.01	0.19	17.6	23.2	24.9	0.30	100.0
CH0703B	0.09	4.30	15.94	9.7	0.00	0.24	21.0	22.8	24.4	0.29	98.8
CH0703B	0.15	5.47	14.75	8.6	0.01	0.19	19.0	24.5	22.5	0.42	95.6
CH0703B	0.13	5.62	15.67	9.4	0.07	0.16	16.9	24.0	24.6	0.40	96.9
CH0703B	0.13	5.55	14.78	11.1	0.12	0.17	19.4	21.1	24.6	0.43	97.3

Sample	SiO_2	TiO_2	Al_2O_3	MgO	CaO	MnO	Fe_2O_3 (calc)	FeO (calc)	Cr_2O_3	V_2O_3	Total (calc)
CH0703B	0.19	0.22	1.00	1.7	0.22	0.10	64.4	28.0	1.8	0.03	97.6
CH0703B	0.14	4.61	16.63	9.9	0.24	0.19	18.9	22.5	24.7	0.37	98.3
CH0703B	0.10	4.71	16.74	10.2	0.19	0.21	18.5	22.1	24.9	0.36	98.0
CH0703B	0.12	5.62	14.90	8.6	0.00	0.20	19.3	25.3	23.2	0.38	97.5
CH0703B	0.16	5.06	13.91	10.8	0.38	0.15	17.1	20.3	27.6	0.38	95.9
CH0703B	0.11	5.69	15.13	9.9	0.14	0.20	17.5	22.9	24.6	0.43	96.6
CH0703B	0.13	5.80	14.69	10.8	0.10	0.20	18.3	21.8	24.9	0.40	97.1
CH0703B	0.10	5.88	14.55	10.7	0.07	0.27	19.0	21.7	24.1	0.42	96.8
CH0703B	0.11	5.99	14.83	10.4	0.09	0.21	18.9	22.5	23.6	0.42	97.0
CH0703B	0.14	4.12	15.06	15.0	0.16	0.29	12.5	13.6	35.3	0.33	96.4
CH0703B	0.13	4.33	16.57	15.9	0.09	0.25	10.7	13.4	36.6	0.38	98.2
CH0703B	0.11	5.26	15.21	10.3	0.15	0.20	17.6	22.1	26.0	0.37	97.2
CH0703B	0.09	5.46	14.88	9.1	0.05	0.18	18.8	24.3	24.3	0.38	97.5
CH0703B	0.11	5.38	14.65	10.9	0.08	0.14	18.2	21.1	25.8	0.41	96.8
CH0703B	0.13	5.01	14.25	11.9	0.11	0.17	17.4	19.3	28.4	0.37	97.0
CH0703C	0.09	2.98	16.73	10.8	0.01	0.24	15.6	20.3	32.6	0.19	99.6
CH0703C	0.06	2.97	17.31	10.5	0.00	0.23	15.7	21.0	31.9	0.22	99.9
CH0703D	0.04	2.73	16.45	9.1	0.00	0.23	15.5	22.6	32.3	0.20	99.2
CH0703D	0.04	2.84	15.54	9.5	0.00	0.21	16.0	22.0	33.0	0.22	99.3
CH0703D	0.04	2.59	16.07	9.6	0.00	0.23	16.3	21.8	33.0	0.19	99.8
CH0704	0.03	3.64	17.18	9.8	0.00	0.25	14.3	22.6	31.9	0.20	99.9
CH0704	0.07	3.60	16.93	9.8	0.01	0.26	14.5	22.4	31.7	0.22	99.6
CH0704	0.06	3.67	17.27	10.0	0.00	0.23	14.2	22.4	31.8	0.20	99.9
CH0704	0.07	3.68	17.07	9.6	0.00	0.26	15.3	22.8	30.5	0.24	99.6
CH0704	0.07	3.77	17.18	9.7	0.00	0.22	15.3	23.0	30.5	0.22	99.9
CH0704	0.03	6.05	13.95	9.3	0.00	0.27	17.8	24.8	26.7	0.30	99.2
CH0704	0.07	3.02	15.45	10.1	0.01	0.23	16.0	21.3	33.5	0.21	100.0
CH0704	0.06	3.02	15.41	10.0	0.00	0.22	15.7	21.4	33.6	0.22	99.5
CH0704	0.03	4.30	17.03	9.5	0.00	0.25	16.6	23.5	28.1	0.26	99.5
CH0704	0.02	4.32	16.95	9.8	0.01	0.26	16.5	23.0	28.2	0.25	99.3
CH0704	0.05	2.78	15.29	9.9	0.01	0.23	16.3	21.2	33.4	0.23	99.4
CH0704	0.07	2.91	15.64	10.5	0.01	0.24	16.2	20.5	33.0	0.24	99.3
CH0704A	0.02	2.27	13.77	7.8	0.00	0.29	13.3	24.0	38.5	0.20	100.2
CH0704A	0.05	2.28	13.53	7.2	0.00	0.32	12.8	24.8	38.8	0.17	100.0
CH0704A	0.04	2.23	13.84	8.0	0.00	0.31	13.0	23.7	38.8	0.20	100.1
CH0704A	0.03	2.18	13.74	7.3	0.00	0.32	12.6	24.6	39.1	0.19	100.1
CH0704A	0.03	2.24	13.28	9.2	0.00	0.25	15.4	21.8	37.9	0.16	100.2
CH0704A	0.02	2.14	13.32	9.0	0.00	0.29	15.2	22.0	38.1	0.17	100.2
CH0704A	0.03	2.15	13.30	9.4	0.00	0.25	15.0	21.3	38.5	0.18	100.1

Sample	SiO_2	TiO_2	Al_2O_3	MgO	CaO	MnO	Fe_2O_3 (calc)	FeO (calc)	Cr_2O_3	V_2O_3	Total (calc)
CH0704A	0.03	2.16	13.54	8.9	0.00	0.25	13.5	22.1	39.3	0.20	100.0
CH0704A	0.04	2.43	13.42	7.9	0.01	0.29	13.2	23.9	38.7	0.18	100.1
CH0704A	0.04	2.23	13.56	8.2	0.00	0.29	13.7	23.3	38.8	0.17	100.3
CH0704A	0.04	2.70	13.17	9.7	0.00	0.24	17.4	21.5	35.5	0.20	100.4
CH0704A	0.05	2.47	13.26	9.9	0.01	0.24	16.9	21.1	36.7	0.21	100.8
CH0704A	0.05	2.26	12.84	9.2	0.01	0.26	14.8	21.7	38.9	0.16	100.2
CH0704A	0.02	2.21	13.20	9.6	0.00	0.26	15.1	21.1	38.6	0.18	100.4
CH0704A	0.05	2.05	12.75	7.3	0.01	0.30	15.0	24.4	38.2	0.16	100.2
CH0704A	0.06	2.17	12.79	7.5	0.01	0.30	15.4	24.2	37.6	0.18	100.1
CH0704A	0.05	2.28	14.75	7.4	0.00	0.31	11.8	24.9	39.0	0.18	100.7
CH0704A	0.04	1.89	12.08	9.2	0.00	0.35	19.9	21.0	35.4	0.13	100.1
CH0704A	0.26	2.72	10.28	10.6	0.01	0.26	17.5	19.5	38.0	0.18	99.4
CH0704A	0.15	2.63	10.05	11.2	0.01	0.24	19.3	18.5	37.6	0.22	99.8
CH0704A	0.04	2.11	13.65	8.6	0.01	0.29	16.3	22.5	36.3	0.15	100.0
CH0704A	0.06	2.14	13.13	6.9	0.02	0.27	15.3	24.7	36.3	0.18	98.9
CH0704A	0.10	2.43	11.42	10.4	0.01	0.23	17.0	20.0	39.1	0.17	101.0
CH0705A	0.04	2.85	17.72	11.0	0.00	0.24	15.2	20.1	32.3	0.24	99.6
CH0705A	0.05	2.82	17.59	10.6	0.00	0.26	15.3	20.7	32.2	0.26	99.8
CH0705A	0.06	2.95	17.76	10.5	0.01	0.25	15.3	20.9	31.7	0.24	99.7
CH0705A	0.04	2.93	17.70	10.7	0.00	0.26	14.2	20.8	33.4	0.22	100.3
CH0705A	0.05	2.91	17.65	10.7	0.00	0.24	14.1	20.8	33.4	0.23	100.1
CH0705A	0.05	2.91	17.64	11.0	0.00	0.24	14.1	20.3	33.5	0.26	99.9
CH0705A	0.06	3.07	19.07	11.2	0.00	0.22	13.9	20.1	31.5	0.25	99.4
CH0705A	0.03	2.81	17.84	10.7	0.00	0.24	15.1	20.5	32.2	0.27	99.7
CH0705A	0.04	2.91	18.17	11.0	0.00	0.23	15.0	20.4	32.1	0.21	100.0
CH0705A	0.05	3.04	18.34	10.9	0.01	0.24	12.8	20.7	33.8	0.24	100.1
CH0705A	0.05	2.92	18.23	11.0	0.00	0.23	12.7	20.4	34.2	0.23	99.9
CH0705A	0.05	2.97	18.25	11.4	0.00	0.21	12.4	20.0	34.8	0.27	100.3
CH0705A	0.06	3.27	19.52	11.3	0.00	0.23	14.4	20.4	30.4	0.25	99.8
CH0705A	0.06	2.95	18.43	11.1	0.00	0.23	13.2	20.4	33.7	0.25	100.3
CH0705A	0.05	3.19	18.92	11.1	0.01	0.22	14.1	20.5	31.5	0.23	99.9
CH0705A	0.04	2.93	18.49	11.0	0.00	0.24	13.6	20.5	33.0	0.26	100.1
CH0705B	0.06	3.33	13.64	9.0	0.00	0.28	17.0	23.1	33.5	0.20	100.1
CH0705B	0.04	5.11	11.72	9.4	0.00	0.26	19.3	23.6	30.0	0.25	99.6
CH0705B	0.04	3.60	11.61	9.4	0.01	0.26	18.7	22.0	33.4	0.23	99.3
CH0705B	0.05	2.68	14.41	8.7	0.00	0.27	18.4	23.1	32.3	0.25	100.1
CH0705B	0.02	2.72	14.09	8.7	0.01	0.29	18.3	22.7	32.3	0.23	99.4
CH0705B	0.03	3.79	12.56	9.1	0.00	0.25	17.5	23.0	33.2	0.21	99.7
CH0705Y	0.04	2.29	13.08	6.4	0.01	0.31	18.3	25.6	32.8	0.21	99.0

Sample	SiO_2	TiO_2	Al_2O_3	MgO	CaO	MnO	Fe_2O_3 (calc)	FeO (calc)	Cr_2O_3	V_2O_3	Total (calc)
CH0705Y	0.03	2.35	13.17	6.4	0.00	0.33	18.5	25.8	32.8	0.20	99.5
CH0705Y	0.03	2.39	12.95	6.3	0.00	0.30	18.3	25.8	32.7	0.21	98.9
CH0705Y	0.05	2.21	12.83	6.2	0.00	0.31	20.0	25.8	31.4	0.22	99.0
CH0705Y	0.04	2.17	12.85	6.3	0.00	0.32	20.0	25.7	31.8	0.23	99.4
CH0705Y	0.05	2.24	12.92	5.9	0.00	0.34	19.7	26.3	31.4	0.20	99.1
CH0705Y	0.02	2.16	12.93	5.9	0.00	0.31	19.9	26.2	31.5	0.23	99.0
CH0705Y	0.04	2.46	13.27	6.5	0.01	0.32	19.3	25.6	31.5	0.21	99.3
CH0705Y	0.05	2.49	13.44	6.6	0.00	0.28	18.9	25.6	31.6	0.20	99.2
CH0705Y	0.05	2.45	13.45	7.6	0.02	0.29	19.9	24.1	31.3	0.25	99.4
CH0705Y	0.04	2.54	14.15	8.0	0.00	0.27	17.2	23.7	33.2	0.17	99.3
CH0705Y	0.03	2.61	14.10	6.8	0.00	0.32	16.9	25.5	33.0	0.21	99.5
CH0705Y	0.06	2.50	13.73	6.4	0.00	0.33	18.0	26.0	32.1	0.20	99.2
CH0705Y	0.04	2.36	14.73	7.6	0.00	0.28	17.3	24.2	32.4	0.22	99.0
CH0705Y	0.04	2.36	14.80	7.1	0.00	0.32	17.5	25.0	32.1	0.22	99.4
CH0705Y	0.04	5.81	13.21	8.8	0.01	0.29	18.3	25.1	27.4	0.22	99.3
CH0705Y	0.05	3.05	12.82	7.4	0.00	0.30	18.9	24.7	31.7	0.25	99.3
CH0705Y	0.04	2.15	12.14	6.0	0.01	0.31	20.5	25.8	31.6	0.25	98.9
CH0705Y	0.04	2.15	12.18	5.9	0.01	0.32	20.7	26.1	31.6	0.22	99.2
CH0705Y	0.05	2.20	13.35	6.4	0.00	0.31	18.5	25.5	32.4	0.23	98.9
CH0705Y	0.04	2.13	13.39	6.5	0.01	0.30	18.4	25.4	32.8	0.22	99.2
CH0705Y	0.04	2.16	13.56	8.3	0.01	0.27	18.4	22.6	33.5	0.20	99.1
CH0705Y	0.03	2.58	12.75	6.3	0.00	0.32	18.7	26.0	32.3	0.23	99.2
CH0705Y	0.05	2.57	13.09	8.0	0.01	0.28	18.9	23.6	33.0	0.23	99.7
CH0706A	0.04	1.67	18.74	10.4	0.01	0.22	13.5	20.2	34.9	0.17	99.8
CH0706A	0.03	1.88	15.83	11.5	0.01	0.23	11.5	18.3	40.5	0.16	100.0
CH0706A	0.04	2.20	15.88	10.9	0.01	0.22	10.8	19.5	40.3	0.14	100.1
CH0706A	0.05	1.50	16.04	10.9	0.00	0.26	12.0	18.9	40.4	0.15	100.2
CH0706A	0.04	2.08	16.56	11.2	0.00	0.22	12.4	19.1	38.4	0.18	100.2
CH0706A	0.03	1.64	16.61	11.0	0.01	0.25	12.7	19.0	38.6	0.21	100.1
CH0706A	0.06	2.00	16.39	11.3	0.01	0.24	12.5	18.8	38.4	0.19	99.8
CH0706A	0.05	2.21	15.72	11.0	0.01	0.16	10.9	19.2	40.0	0.18	99.5
CH0706A	0.04	1.92	15.90	11.1	0.00	0.22	13.3	18.8	38.2	0.18	99.7
CH0706A	0.04	2.19	15.99	11.0	0.00	0.20	10.3	19.1	40.1	0.16	99.1
CH0706A	0.06	2.41	15.42	10.8	0.01	0.18	10.7	19.7	39.9	0.18	99.4
CH0706A	0.03	3.09	17.73	14.1	0.02	0.27	8.0	15.5	40.2	0.14	99.1
CH0706A	0.03	1.69	17.24	10.9	0.00	0.18	15.2	19.0	34.8	0.18	99.2
CH0706A	0.03	1.73	17.23	11.3	0.01	0.19	15.2	18.6	35.3	0.19	99.8
CH0706A	0.02	1.81	17.52	11.4	0.01	0.19	15.5	18.8	35.1	0.16	100.5
CH0706A	0.05	2.03	15.33	10.7	0.00	0.18	9.3	19.4	42.0	0.17	99.2

Sample	SiO_2	TiO_2	Al_2O_3	MgO	CaO	MnO	Fe_2O_3 (calc)	FeO (calc)	Cr_2O_3	V_2O_3	Total (calc)
CH0706A	0.06	2.03	16.39	11.2	0.00	0.23	8.3	18.7	41.9	0.15	99.1
CH0706B,3	0.06	4.13	16.44	10.8	0.00	0.24	14.9	21.2	31.2	0.27	99.4
CH0706C	0.06	2.95	16.18	10.5	0.00	0.20	17.5	20.7	31.0	0.29	99.3
CH0706C	0.08	2.87	17.45	11.8	0.01	0.21	17.0	18.6	30.3	0.30	98.5
CH0706C	0.05	2.57	13.58	7.8	0.02	0.15	24.1	23.4	25.8	0.32	97.8
CH0706C	0.05	2.59	14.03	7.7	0.01	0.21	23.8	23.8	25.8	0.31	98.3
CH0706C	0.06	2.63	13.78	8.4	0.01	0.19	24.5	22.7	25.6	0.34	98.1
CH0706C	0.06	2.48	17.00	12.1	0.00	0.23	16.5	18.2	33.5	0.33	100.4
CH0706C	0.04	2.54	16.79	10.9	0.02	0.24	15.6	19.7	33.2	0.36	99.4
CH0706C	0.06	2.92	15.87	9.2	0.01	0.25	19.7	22.7	28.8	0.29	99.8
CH0706D	0.05	2.90	14.21	8.1	0.00	0.28	15.2	24.0	34.8	0.23	99.8
CH0706D	0.05	2.27	14.67	7.3	0.00	0.29	16.8	24.8	33.8	0.23	100.3
CH0706D	0.07	2.47	15.18	9.3	0.01	0.33	17.4	22.2	33.5	0.21	100.7
CH0706D	0.06	2.55	13.81	8.0	0.01	0.30	15.3	23.6	35.2	0.20	99.1
CH0706E	0.06	3.06	16.81	9.1	0.00	0.25	15.5	23.1	31.8	0.23	100.0
CH0706E	0.06	2.62	15.95	8.6	0.00	0.28	17.1	23.6	32.5	0.19	100.9
CH0706E	0.03	2.62	15.30	8.5	0.02	0.31	17.0	23.4	32.9	0.22	100.3
CH0706E	0.10	2.53	14.99	10.3	0.00	0.24	19.1	20.4	31.8	0.16	99.6
CH0706E	0.04	2.48	14.52	8.3	0.00	0.28	18.7	23.3	32.0	0.17	99.8
CH0706E	0.07	3.34	14.78	9.9	0.00	0.21	16.6	21.7	32.4	0.19	99.2
CH0706E	0.05	3.35	16.07	9.7	0.01	0.22	16.2	22.3	31.9	0.20	100.0
CH0706E	0.06	2.35	14.07	8.7	0.01	0.26	17.4	22.4	34.1	0.19	99.6
CH0706F	0.08	1.60	18.69	11.6	0.00	0.22	9.6	18.2	39.2	0.19	99.4
CH0706F	0.08	2.49	20.18	11.9	0.01	0.22	9.4	19.0	36.2	0.26	99.7
CH0706F	0.06	1.96	19.88	13.2	0.01	0.22	10.7	16.4	36.9	0.25	99.6
CH0706F	0.12	3.17	19.02	12.8	0.00	0.21	10.3	18.3	36.3	0.21	100.5
CH0706F	0.06	2.56	19.35	12.2	0.01	0.20	8.9	18.6	38.4	0.15	100.4
CH0707C	0.05	3.13	19.40	13.0	0.01	0.20	15.8	17.9	30.8	0.20	100.5
CH0707C	0.04	3.74	17.36	12.8	0.00	0.22	15.6	18.3	31.7	0.24	100.0
CH0707C	0.05	3.08	19.41	11.9	0.00	0.23	15.0	19.4	30.8	0.24	100.1
CH0707C	0.05	3.15	18.60	12.1	0.00	0.21	14.6	18.8	31.7	0.23	99.5
CH0708B	0.53	3.07	18.91	8.8	0.42	0.26	10.2	23.9	33.0	0.26	99.4

Table A3.11: Laser ablation ICP-MS data for Piton Chisny cumulate xenoliths.

	Sample	**CH0701 Dunite**			**CH0706B**				
	Phase	Olivine	Clinopyroxene	Oxide	Olivine	Clinopyroxene	Pentlandite	Chalcopyrite	Oxide
	Spots analyzed	3	3	9	1	2	2	3	1
Ni	ppm	2991	384	1880	1268	347	60161	48636	1521
Cu	ppm	1	1	6	140	588	21795	136128	177
Mo	ppm	0.045	0.039	0.082	0.042	0.039	0.738	0.171	0.042
W	ppm	0.002	0.006	0.040	b.d.	0.020	0.044	0.590	0.002
Os	ppm	0.000	0.000	0.001	0.001	0.001	0.408	0.269	0.000
Ir	ppm	b.d.	0.001	0.001	b.d.	0.001	0.233	0.111	b.d.
Ru	ppm	b.d.	0.001	0.092	0.006	0.003	0.491	0.247	0.020
Rh	ppm	b.d.	0.001	0.001	0.004	0.016	0.616	3.373	0.003
Pd	ppm	0.000	0.001	b.d.	0.001	0.006	1.484	0.693	b.d.
Pd	ppm	0.002	0.029	0.001	0.007	0.049	3.186	8.679	0.003
Re	ppm	0.001	0.001	0.001	b.d.	0.007	0.072	0.043	0.001
Au	ppm	0.002	b.d.	b.d.	0.001	0.006	0.285	0.453	b.d.

Table A4.1: Sample locations and field descriptions. Coordinates given as degrees/minutes/decimal minutes in WGS84 projection.

Sample Number (DC14-)	Location	Coordinates	Elevation (m)	Field Description
1F	Dhrubiya Hill	**N**23 12.299 **E**069 23.589	47	Fresh basalt
2	Surabapa Hill, Nakhatranya	**N**23 20.808 **E**069 16.383	217	Ol-, cpx-phyric basalt
5	Bhujia Hill	**N**23 14.684 **E**069 41.210	114	Phaneritic basalt
9	Ribda	**N**22 07.747 **E**070 47.081	133	Ol-, plag-pyric basalt with rind
10B	Ribda	**N**22 07.190 **E**070 50.022	132	Ol-, cpx-, plag-phyric basalt
15	Ganghar Farm	**N**22 09.157 **E**070 51.218	140	Ol- & cpx-phyric basalt with rind, sparse sulfide
46C	Malanka	**N**21 15.418 **E**070 30.514	102	Fresh ol- & cpx-phyric basalt
47B	Pavagadh	**N**22 29.869 **E**073 31.211	108	Highly altered ankaramite, up to 50 vol. % phenocrysts
68	Kalsubai	**N**19 35.844 **E**073 42.899	1482	Fresh basalt with sparse ol & cpx macrophenocrysts
111	Mahabaleshwar Fm.	**N**17 55.470 **E**073 37.496	962	Plag- & ol-phyric, vesiculated (but unzeolitized) flow
MMF7	IIT Bombay (courtesy H. Sheth)			Fresh, cpx-phyric basalt

Table A4.2: Bulk rock major (wt.%) and trace (ppm) element abundance data.

Sample:	**DC14-1F**	**DC14-2**	**DC14-5**	**DC14-9**	**DC14-10B**	**DC14-15**
SiO_2	42.6	42.9	42.2	51.0	50.1	48.9
TiO_2	3.27	2.6	3.67	1.29	1.25	0.97
Al_2O_3	13.3	11.8	7.92	13.4	13.6	14.2
Fe_2O_3T	14.9	14.0	14.0	12.0	12.0	14.1
MnO	0.19	0.19	0.18	0.18	0.19	0.23
MgO	9.83	14.0	15.7	8.68	8.93	6.76
CaO	10.3	11.0	11.2	10.9	10.9	11.7
Na_2O	3.45	2.58	2.87	1.98	1.93	2.14
K_2O	1.22	0.57	1.08	0.45	0.57	0.63
P_2O_5	0.44	0.47	0.99	0.12	0.12	0.16
Total	**99.4**	**100.1**	**99.8**	**99.9**	**99.6**	**99.8**
LOI	2.74	2.16	3.54	1.9	2.03	1.79
FeO	8.51	9.46	8.25	8.89	8.88	9.54
Fe_2O_3	5.40	3.53	4.78	2.07	2.16	3.53
Mg no.	67.3	72.5	77.2	63.5	64.2	55.8
Fe2+/Fe* (mol. fract.)	0.78	0.86	0.79	0.91	0.90	0.86
XRF Trace Elements:						
Rb	43.7	17.5	57	17.2	18.3	14.1
Sr	721	709	859	148	147	155
Y	19.5	22	24.5	30	29.2	29.2
Zr	221	201	281	105	104	73
V	323	305	259	278	262	335
Ni	168	373	431	150	148	68
Cr	374	710	605	337	320	62
Nb	45.9	36.2	108.7	4.2	3.7	7.1
Ga	19	17.8	15.7	17.4	17.9	16
Cu	89	116	73	103	103	190
Zn	98	106	106	81	77	90
Co	65	75	71	55	52	57
Ba	526	346	1095	123	121	113
La	13	13	12	12	14	14
Ce	23	31	30	26	18	21
U	3.1	2.7	3.2	<0.5	<0.5	<0.5
Th	5.8	<0.5	8.4	3	3.4	<0.5
Sc	24	27	22	31	28	40
Pb	3	<1	6	<1	<1	2

ICPMS Trace Elements:						
Li	7.7	6.5	8.6	9.7	8.6	4.9
Sc	23	27	20	37	37	49
V	311	301	235	281	281	344
Cr	362	696	473	539	506	74
Co	63	78	72	50	53	52
Ni	198	437	486	154	164	65
Cu	71	96	57	88	89	161
Zn	118	116	122	80	82	92
Ga	22	21	18	18	18	17
Ge	1.7	1.7	1.8	1.4	1.4	1.6
Rb	55.7	24.6	84.0	18.2	20.3	15.7
Sr	719	711	834	147	143	156
Y	20.6	19.0	25.5	24.2	23.8	24.5
Zr	204	197	277	94	91	57
Nb	43	35	98	5	5	9
Mo	1.4	1.3	0.4	0.6	0.5	0.5
Cs	0.6	0.9	1.0	0.3	0.2	0.1
Ba	572	351	1149	121	108	110
La	32	30	65	11	10	10
Ce	65	66	128	25	24	20
Pr	7.92	8.56	14.82	3.22	3.01	2.41
Nd	33.2	36.5	58.3	13.9	13.4	10.1
Sm	6.91	7.67	11.04	3.72	3.58	2.62
Eu	2.39	2.50	3.55	1.20	1.19	0.99
Gd	6.74	7.18	10.09	4.37	4.12	3.32
Tb	0.84	0.86	1.15	0.69	0.67	0.58
Dy	4.45	4.35	5.75	4.64	4.47	4.13
Ho	0.84	0.79	1.04	0.98	0.95	0.96
Er	1.96	1.85	2.37	2.56	2.52	2.74
Tm	0.24	0.22	0.28	0.36	0.36	0.41
Yb	1.43	1.27	1.58	2.29	2.20	2.69
Lu	0.19	0.17	0.21	0.34	0.32	0.41
Hf	4.51	4.52	6.07	2.50	2.42	1.44
Ta	3.45	2.82	6.78	0.51	0.46	0.63
W	0.36	0.35	0.17	0.21	0.18	0.17
Pb	2.77	2.95	4.97	2.42	2.10	1.19
Th	4.03	3.15	9.04	3.45	3.00	1.33
U	0.85	0.73	2.00	0.84	0.76	0.34

Sample:	**DC14-46C**	**DC14-47B**	**DC14-68**	**DC14-111**	**MMF7**
SiO_2	50.5	45.8	50.9	49.3	50.2
TiO_2	1.18	2.3	2.84	3.32	1.35
Al_2O_3	14.2	10.4	12.6	12.3	8.87
Fe_2O_3T	11.7	13.3	15.8	16.8	11.9
MnO	0.17	0.2	0.21	0.23	0.19
MgO	8.65	14.2	4.6	5.05	12.5
CaO	10.9	11.1	9.3	9.35	12.7
Na_2O	1.91	1.61	2.51	2.54	1.46
K_2O	0.68	0.76	0.66	0.55	0.34
P_2O_5	0.12	0.23	0.29	0.34	0.13
Total	**100.0**	**99.9**	**99.7**	**99.8**	**99.7**
LOI	2.27	3.74	3.59	1.78	2.89
FeO	8.22	9.13	8.67	11.74	8.03
Fe_2O_3	2.54	3.18	6.19	3.71	2.97
Mg no.	65.2	73.4	48.6	43.4	73.5
Fe2+/Fe* (mol. fract.)	0.88	0.86	0.76	0.88	0.86
XRF Trace Elements:					
Rb	24.3	23	9.4	11.3	5.2
Sr	142	575	268	227	163
Y	30.1	23.1	37.8	36.2	26
Zr	104	129	250	233	94
V	270	306	366	415	349
Ni	134	220	44	49	217
Cr	332	778	88	94	942
Nb	3.9	24.7	13.7	22.8	4.8
Ga	17	13.7	21.9	21.3	13.7
Cu	72	78	286	377	81
Zn	76	113	123	146	77
Co	52	77	53	54	65
Ba	120	545	289	174	104
La	11	13	17	16	13
Ce	25	30	29	14	22
U	0.9	2.7	1.4	1.8	<0.5
Th	0.6	<0.5	3.1	5.8	<0.5
Sc	30	31	29	35	38
Pb	<1	<1	<1	<1	<1

ICPMS Trace Elements:					
Li	8.2	5.1	5.9	6.7	8.7
Sc	35	40	32	34	42
V	262	297	377	393	333
Cr	328	773	68	72	1649
Co	47	72	45	47	56
Ni	123	230	47	54	202
Cu	62	64	200	290	68
Zn	74	90	123	136	73
Ga	18	15	24	25	14
Ge	1.3	1.6	1.7	1.8	1.4
Rb	27.2	29.6	12.7	14.6	7.8
Sr	139	582	275	243	183
Y	23.5	18.0	38.8	41.1	18.2
Zr	94	126	203	221	86
Nb	5	26	13	21	6
Mo	0.5	0.7	0.7	0.9	0.4
Cs	0.6	0.8	0.2	0.2	0.2
Ba	118	482	293	181	102
La	12	21	23	22	10
Ce	26	46	50	50	24
Pr	3.26	5.72	6.61	6.79	3.31
Nd	14.2	24.4	30.0	31.0	15.2
Sm	3.61	5.16	7.48	7.99	3.82
Eu	1.13	1.74	2.34	2.46	1.23
Gd	4.08	5.08	7.89	8.39	3.94
Tb	0.64	0.65	1.20	1.25	0.57
Dy	4.14	3.76	7.47	7.79	3.54
Ho	0.90	0.72	1.56	1.63	0.74
Er	2.38	1.81	4.00	4.16	1.82
Tm	0.33	0.23	0.53	0.57	0.25
Yb	2.12	1.37	3.20	3.49	1.53
Lu	0.31	0.20	0.47	0.51	0.22
Hf	2.43	3.18	4.97	5.26	2.18
Ta	0.48	2.02	0.97	1.65	0.49
W	0.22	0.16	0.23	0.28	0.14
Pb	2.23	1.80	4.35	3.06	2.23
Th	3.98	2.44	3.03	2.66	1.07
U	0.96	0.46	0.58	0.63	0.21

Table A4.3: Bulk rock HSE abundances and Os isotope compositions

Sample:	**Os (ppb)**	**Ir (ppb)**	**Ru (ppb)**	**Pt (ppb)**	**Pd (ppb)**	**Re (ppb)**	**$^{187}Os/^{188}Os$**	**2σ**	**$^{187}Re/^{188}Os$**	**$^{187}Os/^{188}Os$ (i)**
DC14-01F			0.103	0.198	0.365	0.358				
DC14-02	0.294	0.122	0.415	0.945	0.979	0.064	0.13271	0.00014	1.12	0.13149
DC14-05	0.673	0.536	1.886	1.254	0.900	0.147	0.12356	0.00007	1.09	0.12238
DC14-09	0.571	0.381	0.589	6.958	4.154	0.529	0.13402	0.00009	4.52	0.12913
DC14-10B	0.654	0.383	0.514	6.952	4.002	0.839	0.13811	0.00010	6.20	0.13140
DC14-15	0.019		0.066	9.907	20.740	0.349	0.23546	0.00085	91.7	0.13615
DC14-15	0.034		0.136	10.746	20.702	0.656	0.24480	0.00043	93.6	0.14335
DC14-46C	0.837	0.065	0.105	1.847	0.683	0.170	0.11861	0.00024	1.01	0.11751
DC14-47B	0.388	0.056	0.024	1.134	1.533	0.100	0.11939	0.00013	1.31	0.11797
DC14-47B	0.182	0.084	0.134	1.498	1.142	0.075	0.13459	0.00118	2.11	0.13231
DC14-68	0.021		0.133	4.072	8.096	0.569	0.31762	0.00450	132	0.17506
DC14-111	0.013		0.162	3.322	19.114	0.634	0.50100	0.00090	239	0.24162
MMF7	0.097			0.047	0.329	0.229	0.17666	0.00127	11.69	0.16400
MMF7		0.008	0.133	0.125	0.194	0.232				

Table A4.4: Full mineral separate geochemistry.

	DC14-05 ol	DC14-05 ol MAP	DC14-15 pl	DC14-15 pl MAP
Major element abundances by ICP-MS (wt. %)				
SiO_2*	40.4	26.8		
TiO_2	0.27	0.43		
Al_2O_3	0.80	1.13		
Fe_2O_3T	12.3	15.7		
MnO	0.17	0.21		
MgO	44.6	53.1		
CaO	0.99	1.59		
Na_2O	0.18	0.33		
K_2O	0.18	0.44		
P_2O_5	0.16	0.38		
*SiO_2 is determined by difference to 100 wt. %				
Trace element abundances by ICP-MS (ppm)				
Li	4.2	4.3		4.1
Sc	4.4	5.2		11.1
V	23	26		50
Cr	172	280		90
Co	151	146		13
Ni	2649	2510		54
Cu	7	19		137
Zn	81	104		30
Ga	2.1	2.8		18.7
Ge	1.25	1.20		0.55
Rb	7.0	9.6		14.9
Sr	72	95		248
Y	2.2	2.6		7.5
Zr	23	32		21
Nb	7.3	9.6		2.3
Mo	1.31	3.58		1.50
Cs	0.064	0.090		0.088
Ba	113	180		97
La	4.4	5.9		3.5
Ce	8.3	11.5		7.0
Pr	0.94	1.31		0.81
Nd	3.73	5.14		3.38
Sm	0.72	0.98		0.83

Eu	0.24	0.34	0.46
Gd	0.70	0.94	1.01
Tb	0.08	0.10	0.17
Dy	0.43	0.56	1.21
Ho	0.08	0.10	0.28
Er	0.18	0.22	0.77
Tm	0.02	0.03	0.11
Yb	0.13	0.17	0.75
Lu	0.02	0.02	0.11
Hf	0.45	0.65	0.50
Ta	0.44	0.60	0.18
W	0.03	19.62	0.90
Pb	0.45	0.68	0.71
Th	0.53	0.79	0.45
U	0.13	0.18	0.12

ICPMS Os concentrations (ppb)

Os	0.313	0.376	0.191

TIMS Os isotopic compositions

^{187}Os/^{188}Os	0.12675	0.12805	0.14104
2σ	0.00014	0.00030	0.00034
^{187}Re/^{188}Os	0.00003	0.00041	0.00078
Δ^{187}Os/^{188}Os MAP (%)		1	
ΔOs MAP (%)		20	
^{187}Os/^{188}Os (i)	0.12675	0.12805	0.14104

MAP He isotopic compositions

^{3}He/^{4}He (R_A)	4.2		2.4	
2σ	0.2		0.4	
[^{4}He], µcc/g STP	0.0040		0.0003	
J[^{4}He] µcc/g STP yr-1	2.0E-06	2.8E-06		1.8E-06
^{3}He/^{4}He (i) (R_A)	0.00			

	DC14-10B cpx	DC14-47B ol	DC14-47B ol MAP	DC14-68 pl	DC14-111 pl
Major element abundances by ICP-MS (wt. %)					
SiO_2*	45.9	40.9		53.3	49.7
TiO_2	0.22	0.32		0.34	0.28
Al_2O_3	28.8	1.60		26.1	29.7
Fe_2O_3T	3.80	19.0		3.42	1.85
MnO	0.06	0.24		0.03	0.02
MgO	1.99	34.4		0.72	0.58
CaO	16.2	3.24		12.1	13.5
Na_2O	2.32	0.14		3.47	4.01
K_2O	0.59	0.11		0.36	0.23
P_2O_5	0.12	0.08		0.18	0.07
*SiO_2 is determined by difference to 100 wt. %					
Trace element abundances by ICP-MS (ppm)					
Li	7.1	2.8		13.5	12.6
Sc	61.7	18.5		4.3	3.0
V	354	62		33	26
Cr	2282	947		18	16
Co	51	185		9	5
Ni	258	863		15	15
Cu	16	16		44	20
Zn	43	111		18	14
Ga	11.6	2.8		27.5	28.2
Ge	1.15	1.68		0.55	0.39
Rb	3.8	3.0		2.0	1.0
Sr	101	48		459	455
Y	11.3	2.6		5.7	2.3
Zr	20	14		25	12
Nb	0.8	2.5		1.6	1.4
Mo	0.75	0.54		0.81	0.31
Cs	0.048	0.084		0.024	0.007
Ba	23	47		101	57
La	2.1	1.9		4.0	1.8
Ce	5.2	4.4		8.6	3.7
Pr	0.76	0.56		1.08	0.45
Nd	3.91	2.56		4.61	1.98
Sm	1.30	0.60		1.06	0.46
Eu	0.51	0.21		0.92	0.73
Gd	1.65	0.62		1.13	0.47
Tb	0.29	0.09		0.16	0.07
Dy	2.00	0.52		1.02	0.41
Ho	0.43	0.10		0.21	0.08
Er	1.12	0.26		0.54	0.22
Tm	0.16	0.03		0.08	0.03

Yb	1.01	0.22		0.50	0.19
Lu	0.14	0.03		0.08	0.03
Hf	0.64	0.38		0.58	0.26
Ta	0.08	0.19		0.11	0.08
W	0.05	0.07		0.07	0.02
Pb	0.52	0.26		1.07	0.51
Th	0.46	0.21		0.36	0.13
U	0.11	0.04		0.08	0.03

ICPMS Os concentrations (ppb)

Os	0.603	0.352	0.300	0.118	

TIMS Os isotopic compositions

^{187}Os/^{188}Os	0.13910	0.13082	0.14426568	0.14412	
2σ	0.00010	0.00009	0.00013444	0.00036	
^{187}Re/^{188}Os	0.00007		0.00038711		
Δ^{187}Os/^{188}Os MAP (%)			4		
ΔOs MAP (%)			-15		
^{187}Os/^{188}Os (i)	0.13910	0.13082	0.14427	0.14412	

MAP He isotopic compositions

^{3}He/^{4}He (R_A)		10.7			
2σ		0.5			
[^{4}He], µcc/g STP		0.0003			
J[^{4}He] µcc/g STP yr-1	1.7E-06	7.0E-07		1.3E-06	4.8E-07
^{3}He/^{4}He (i) (R_A)		0.00			

	DC14-111 pl MAP	MMF7 cpx
Major element abundances by ICP-MS (wt. %)		
SiO_2*		56.1
TiO_2		0.75
Al_2O_3		4.44
Fe_2O_3T		8.53
MnO		0.16
MgO		13.8
CaO		15.4
Na_2O		0.59
K_2O		0.16
P_2O_5		0.10
*SiO_2 is determined by difference to 100 wt. %		
Trace element abundances by ICP-MS (ppm)		
Li	13.0	7.1
Sc	2.5	70.5
V	20	471
Cr	82	3680
Co	8	57
Ni	58	278
Cu	252	23
Zn	23	58
Ga	27.9	8.8
Ge	0.40	1.31
Rb	0.9	2.3
Sr	447	86
Y	1.7	13.0
Zr	11	35
Nb	0.9	1.8
Mo	1.55	0.38
Cs	0.006	0.073
Ba	51	30
La	1.5	3.4
Ce	3.2	9.3
Pr	0.39	1.44
Nd	1.67	7.52
Sm	0.37	2.26
Eu	0.68	0.72
Gd	0.38	2.48
Tb	0.05	0.39
Dy	0.32	2.51
Ho	0.06	0.51
Er	0.17	1.30
Tm	0.02	0.17

Yb	0.15	1.07
Lu	0.02	0.15
Hf	0.23	1.06
Ta	0.06	0.15
W	1.27	0.20
Pb	0.65	0.94
Th	0.10	0.32
U	0.02	0.06

ICPMS Os concentrations (ppb)		
Os	0.219	0.335

TIMS Os isotopic compositions		
^{187}Os/^{188}Os	0.14612	0.16317
2σ	0.00021	0.00280
^{187}Re/^{188}Os	0.00055	0.00006
Δ^{187}Os/^{188}Os MAP (%)		
ΔOs MAP (%)		
^{187}Os/^{188}Os (i)	0.14612	0.16317

MAP He isotopic compositions		
^{3}He/^{4}He (R_A)		0.63
2σ		0.03
[^{4}He], µcc/g STP		0.0035
J[^{4}He] µcc/g STP yr-1	3.7E-07	1.1E-06
^{3}He/^{4}He (i) (R_A)		-3.2E-05

Table A4.5: Oxygen isotope data for olivine separates.

Sample		$\delta^{18}O$ (olivine)
DC14-05	*Replicate 1*	4.819
DC14-05	*Replicate 2*	5.035
DC14-05	*Average*	**4.927**
DC14-10B		**6.042**
DC14-15	*Replicate 1*	5.827
DC14-15	*Replicate 2*	5.815
DC14-15	*Average*	**5.821**
DC14-23	*Replicate 1*	5.402
DC14-23	*Replicate 2*	5.534
DC14-23	*Average*	**5.468**
DC14-31A	*Replicate 1*	6.108
DC14-31A	*Replicate 2*	6.269
DC14-31A	*Average*	**6.1885**
DC14-39		**6.389**
DC14-46C		**6.509**
DC14-47B	*Replicate 1*	5.212
DC14-47B	*Replicate 2*	5.09
DC14-47B	*Average*	**5.151**
DC14-53		**12.804**
DC14-54	*Replicate 1*	8.799
DC14-54	*Replicate 2*	5.999
DC14-54	*Average*	**7.399**
DC14-68	*Replicate 1*	6.241
DC14-68	*Replicate 2*	6.213
DC14-68	*Average*	**6.227**
DC14-69	*Replicate 1*	5.904
DC14-69	*Replicate 2*	5.731
DC14-69	*Average*	**5.8175**
DC14-111	*Replicate 1*	5.894
DC14-111	*Replicate 2*	5.791
DC14-111	*Average*	**5.8425**
MMF7	*Replicate 1*	5.106
MMF7	*Replicate 2*	5.098
MMF7	*Average*	**5.102**

Table A4.6: Xpx data compilation statistics. "% in" refers to proportion of values included after filtering for 0 < Xpx < 1; *n* includes only filtered data.

	Canaries	Hawaii	Iceland	Mascarene	Samoa	Deccan	Emeishan	Etendeka	Ethiopia	NAIP	Siberia
Max	1.00	1.00	0.99	1.00	0.92	0.85	1.00	1.00	1.00	0.99	1.00
Min	0.003	0.006	0.001	0.003	0.032	0.002	0.002	0.006	0.081	0.006	0.001
% in	94%	57%	88%	60%	66%	70%	94%	65%	83%	87%	89%
n	2821	1808	5550	170	116	140	1313	427	208	773	1250
Median	0.38	0.59	0.28	0.38	0.50	0.36	0.60	0.44	0.53	0.45	0.24
Average	0.43	0.59	0.29	0.41	0.47	0.38	0.57	0.48	0.55	0.44	0.28
SD (1σ)	0.19	0.20	0.13	0.23	0.19	0.21	0.22	0.25	0.21	0.18	0.17

Table A4.7: Model parameters for Figures 4.2 and 4.7. Concentrations of gases are illustrative of R values and are not meant to reflect natural concentrations with specific dimensions. $^{187}Os/^{188}Os$ of recycled oceanic crust is calculated assuming recycling of a young MORB with $^{187}Os/^{188}Os = 0.15$, $^{187}Re/^{188}Os = 48$ and a 1 Ga recycling time.

Figure 4.2

	$\delta^{18}O$	[O]	$^{187}Os/^{188}Os$	[Os]	Pb/Ce	[Ce]	Nb/U	[U]	References
UCC	10	1	1.900	0.05	0.270	63.0	4.4	2.70	Rudnick & Gao (2003 ToG); Hart et al. (1999 GCA)
LCC	8	1	0.833	0.004	0.200	20.0	25.0	0.20	Rudnick & Fountain (1995 Rev. Geophys.); Kempton & Harmon (1992 GCA); Asmerom & Walker (1998 Geology)
DMM	5.71	1	0.125	10	0.033	0.4	48.0	0.00	Workman & Hart (2005 EPSL); Hart et al. (1999 GCA); Standish et al., 2002 G-Cubed)
Reunion	4.72	1	0.132	1.01	0.034	29.0	45.8	0.31	Boivin & Bachelery (2009 JVGR); Peters et al. (2016 EPSL)

Figure 4.7

	$\delta^{18}O$	[O]	$^{3}He/^{4}He$	[He]	$^{187}Os/^{188}Os$	[Os]	References
ROL	4	1	6	4	0.12	5	Standish et al. (2002 G-Cubed); Day et al. (2009 Geology; 2010 GCA); Graham (2002); Moreira & Kurz (EPSL 2001)
ROC	5.1	1	1	1	0.96	0.1	Day et al. (2009 Geology; 2010 GCA); Day et al. (2015 GCA)
Hi-^{18}O ROC	8	1	1	1	0.96	0.1	Day et al. (2009 Geology; 2010 GCA); Day et al. (2015 GCA); may vary to higher $\delta^{18}O$
Reunion	4.72	1	40	10	0.1324	2	Eiler (2001); Peters et al. (2016 EPSL)

Table A4.8: HSE blank information and statistics.

	Os (ng)	**Ir (ng)**	**Ru (ng)**	**Pt (ng)**	**Pd (ng)**	**Re (ng)**	**$^{187}Os/^{188}Os$**
Average Blank		0.127	0.092	0.020	0.050	0.034	
Os blanks - lavas	0.002						0.27482
Os blanks - olivine	0.002						0.08496
Sample:	**Os (%)**	**Ir (%)**	**Ru (%)**	**Pt (%)**	**Pd (%)**	**Re (%)**	
DC14-01F			55.3	14.7	20.0	5.2	
DC14-02	0.8	28.9	23.5	3.5	8.5	23.6	
DC14-05	0.3	8.5	6.3	2.7	9.2	11.8	
DC14-09	0.4	11.5	17.8	0.5	2.2	3.6	
DC14-10B	0.3	11.5	19.8	0.5	2.2	2.3	
DC14-15	10.7		65.9	0.3	0.4	5.3	
DC14-15	6.2		48.3	0.3	0.4	2.9	
DC14-46C	0.3	43.4	54.8	1.8	11.8	10.4	
DC14-47B	1.2	37.2	48.6	2.2	7.4	20.8	
DC14-47B	0.6	47.2	84.4	2.9	5.6	16.4	
DC14-68	9.6		48.8	0.8	1.1	3.3	
DC14-111	14.8		44.0	1.0	0.5	3.0	
MMF7		86.6	48.8	21.5	32.1	7.8	
MMF7	2.3			42.3	21.7	7.9	
DC14-05 ol	2.8	79.6	61.4	28.1	21.9	83.9	
DC14-05 ol MAP	2.6	97.7	54.9	30.4	25.5	24.7	
DC14-15 ol MAP	3.0	65.7	45.0	0.9	2.1	16.2	
DC14-10B ol	1.2	47.4	49.3	8.7	19.3	46.3	
DC14-47B ol	1.5	8.6	6.4	5.0	6.7		
DC14-47B ol MAP	2.1	55.4	59.6	37.0	66.4	21.2	
DC14-68 ol	14.5	85.2	62.2	5.1	43.7		
DC14-111 ol MAP	2.3	99.7	55.0	1.6	0.8	17.5	

Table A5.1: Major (wt.%) and trace element (ppm) data for Deccan Traps lavas. Figure starts on next page for clarity.

Sample:	**DC14-1F**	**DC14-2**	**DC14-3**	**DC14-4**	**DC14-5**
Locality:	Dhrubiya Hill	Nakhatranya	Bhabar	Bhabar	Bhujia Hill
SiO_2	42.6	42.9	52.1	51.4	42.2
TiO_2	3.27	2.6	1.35	2.87	3.67
Al_2O_3	13.3	11.8	14.5	13.9	7.9
Fe_2O_3T	14.9	14.0	11.7	14.7	14.0
MnO	0.19	0.19	0.16	0.21	0.18
MgO	9.83	13.96	6.36	3.92	15.71
CaO	10.29	10.97	10.77	8.28	11.19
Na_2O	3.45	2.58	2.21	2.83	2.87
K_2O	1.22	0.57	0.42	1.25	1.08
P_2O_5	0.44	0.47	0.14	0.36	0.99
Total	**99.37**	**100.07**	**99.65**	**99.62**	**99.78**
LOI	2.74	2.16	4.08	2.94	3.54
FeO	8.51	9.46	6.39	9.47	8.25
Fe_2O_3	5.40	3.53	4.61	4.17	4.78
Mg no.	67.31	72.46	63.96	42.46	77.25
Fe2+/Fe* (mol. Fraction)	0.78	0.86	0.76	0.83	0.79
XRF Trace Elements:					
Rb	43.7	17.5	23.7	39.6	57
Sr	721	709	192	239	859
Y	19.5	22	28.2	37.9	24.5
Zr	221	201	124	261	281
V	323	305	291	408	259
Ni	168	373	60	44	431
Cr	374	710	172	56	605
Nb	45.9	36.2	5.6	30.1	108.7
Ga	19	17.8	18.1	21.5	15.7
Cu	89	116	45	235	73
Zn	98	106	84	124	106
Co	65	75	44	42	71
Ba	526	346	123	303	1095
La	13	13	14	20	12
Ce	23	31	27	27	30
U	3.1	2.7	<0.5	<0.5	3.2
Th	5.8	<0.5	<0.5	11.3	8.4
Sc	24	27	30	29	22
Pb	3	<1	<1	1	6
ICPMS Trace Elements:					
Li	7.7	6.5	4.7	11.9	8.6
Sc	23	27	34	31	20
V	311	301	290	429	235
Cr	362	696	172	34	473
Co	63	78	41	38	72

Ni	198	437	55	42	486
Cu	71	96	42	220	57
Zn	118	116	87	135	122
Ga	22	21	20	25	18
Ge	1.7	1.7	1.5	1.7	1.8
Rb	55.7	24.6	26.0	55.0	84.0
Sr	719	711	201	251	834
Y	20.6	19.0	24.9	43.4	25.5
Zr	204	197	122	249	277
Nb	43	35	7	27	98
Mo	1.4	1.3	0.6	1.3	0.4
Cs	0.6	0.9	0.6	1.0	1.0
Ba	572	351	139	341	1149
La	32	30	15	33	65
Ce	65	66	32	70	128
Pr	7.92	8.56	4.03	8.77	14.82
Nd	33.2	36.5	17.3	36.7	58.3
Sm	6.91	7.67	4.19	8.35	11.04
Eu	2.39	2.50	1.30	2.46	3.55
Gd	6.74	7.18	4.61	8.95	10.09
Tb	0.84	0.86	0.71	1.30	1.15
Dy	4.45	4.35	4.51	8.07	5.75
Ho	0.84	0.79	0.96	1.66	1.04
Er	1.96	1.85	2.50	4.43	2.37
Tm	0.24	0.22	0.34	0.61	0.28
Yb	1.43	1.27	2.19	3.86	1.58
Lu	0.19	0.17	0.32	0.56	0.21
Hf	4.51	4.52	2.91	5.88	6.07
Ta	3.45	2.82	0.59	2.06	6.78
W	0.36	0.35	0.24	0.65	0.17
Pb	2.77	2.95	4.36	6.18	4.97
Th	4.03	3.15	3.60	6.96	9.04
U	0.85	0.73	0.73	1.55	2.00

Sample:	**DC14-6**	**DC14-8**	**DC14-9**	**DC14-10A**	**DC14-10B**
Locality:	Morbi	Ribda	Ribda	Ribda	Ribda
SiO_2	48.8	54.2	51.0	50.5	50.1
TiO_2	2.81	3.09	1.29	1.24	1.25
Al_2O_3	13.4	13.5	13.4	13.5	13.6
Fe_2O_3T	16.2	12.1	12.0	12.0	12.0
MnO	0.27	0.18	0.18	0.18	0.19
MgO	4.6	4.21	8.68	8.91	8.93
CaO	9.7	7.13	10.86	10.98	10.91
Na_2O	2.85	2.95	1.98	2.04	1.93
K_2O	0.91	2.14	0.45	0.34	0.57
P_2O_5	0.33	0.44	0.12	0.12	0.12
Total	**99.77**	**99.88**	**99.9**	**99.85**	**99.58**
LOI	3.07	2.57	1.9	2.09	2.03
FeO	8.51	5.63	8.89	8.76	8.88
Fe_2O_3	6.71	5.83	2.07	2.28	2.16
Mg no.	49.08	57.14	63.51	64.46	64.20
Fe2+/Fe* (mol. Fraction)	0.74	0.68	0.91	0.89	0.90
XRF Trace Elements:					
Rb	16.4	58.1	17.2	21	18.3
Sr	326	196	148	138	147
Y	44.7	42.9	30	30.7	29.2
Zr	239	314	105	97	104
V	461	464	278	294	262
Ni	30	42	150	160	148
Cr	27	74	337	360	320
Nb	41.9	51.1	4.2	4.7	3.7
Ga	19.5	20.6	17.4	16.8	17.9
Cu	148	337	103	93	103
Zn	138	116	81	80	77
Co	64	34	55	56	52
Ba	230	469	123	121	121
La	19	20	12	11	14
Ce	29	23	26	27	18
U	0.9	0.8	<0.5	<0.5	<0.5
Th	5	22.2	3	1.1	3.4
Sc	32	28	31	33	28
Pb	<1	1	<1	<1	<1
ICPMS Trace Elements:					
Li	6.7	9.5	9.7	8.9	8.6
Sc	39	35	37	37	37
V	471	507	281	281	281
Cr	13	18	539	538	506
Co	58	34	50	51	53
Ni	33	42	154	165	164

Cu	131	288	88	89	89
Zn	150	127	80	81	82
Ga	23	24	18	18	18
Ge	1.9	1.8	1.4	1.5	1.4
Rb	22.2	83.7	18.2	23.1	20.3
Sr	327	214	147	153	143
Y	46.8	52.5	24.2	24.2	23.8
Zr	236	305	94	97	91
Nb	39	42	5	5	5
Mo	1.5	1.5	0.6	0.6	0.5
Cs	0.4	1.0	0.3	0.4	0.2
Ba	272	566	121	109	108
La	31	43	11	11	10
Ce	67	91	25	24	24
Pr	8.21	10.87	3.22	3.09	3.01
Nd	35.3	44.7	13.9	13.7	13.4
Sm	7.88	9.61	3.72	3.62	3.58
Eu	2.42	2.79	1.20	1.17	1.19
Gd	8.66	10.42	4.37	4.12	4.12
Tb	1.32	1.53	0.69	0.65	0.67
Dy	8.57	9.65	4.64	4.35	4.47
Ho	1.82	2.06	0.98	0.93	0.95
Er	4.82	5.50	2.56	2.42	2.52
Tm	0.66	0.78	0.36	0.34	0.36
Yb	4.27	5.01	2.29	2.20	2.20
Lu	0.63	0.74	0.34	0.32	0.32
Hf	5.50	7.29	2.50	2.38	2.42
Ta	2.96	3.39	0.51	0.47	0.46
W	0.51	0.91	0.21	0.19	0.18
Pb	4.11	8.08	2.42	2.32	2.10
Th	4.58	10.92	3.45	3.20	3.00
U	0.91	2.50	0.84	0.78	0.76

Sample:	**DC14-12**	***Rep.***	**DC14-13**	**DC14-15**	**DC14-16**
Locality:	Lothada		Lothada	Ganghar	Vippasana
SiO_2	50.4		53.6	48.9	50.9
TiO_2	1.39		3.06	0.97	2.02
Al_2O_3	15.0		13.3	14.2	13.8
Fe_2O_3T	14.4		12.9	14.1	12.3
MnO	0.21		0.25	0.23	0.17
MgO	4.67		4.12	6.76	6.65
CaO	9.89		7.58	11.65	11.16
Na_2O	2.63		2.95	2.14	2.18
K_2O	0.95		1.89	0.63	0.39
P_2O_5	0.26		0.42	0.16	0.21
Total	**99.78**		**100.06**	**99.75**	**99.77**
LOI	1.57		2.01	1.79	3.83
FeO	6.44		6.44	9.54	6.98
Fe_2O_3	7.23		5.75	3.53	4.53
Mg no.	56.39		53.28	55.82	62.94
Fe2+/Fe* (mol. Fraction)	0.66		0.71	0.86	0.77
XRF Trace Elements:					
Rb	25.4		45.8	14.1	3.9
Sr	176		202	155	259
Y	46.1		42.6	29.2	30.1
Zr	152		301	73	155
V	331		448	335	334
Ni	42		43	68	68
Cr	53		38	62	209
Nb	14.6		47.3	7.1	8.4
Ga	16.6		21.6	16	20.5
Cu	192		299	190	98
Zn	108		94	90	96
Co	45		41	57	47
Ba	224		387	113	147
La	18		21	14	17
Ce	33		22	21	28
U	0.7		2.8	<0.5	0.8
Th	4.2		14.3	<0.5	<0.5
Sc	35		28	40	29
Pb	<1		<1	2	1
ICPMS Trace Elements:					
Li	10.7	11.5	10.6	4.9	7.3
Sc	43	45	34	49	30
V	331	348	504	344	336
Cr	48	49	25	74	217
Co	42	43	33	52	43
Ni	40	40	45	65	64

Cu	188	194	245	161	85
Zn	116	120	122	92	98
Ga	19	19	24	17	22
Ge	1.7	1.7	1.8	1.6	1.5
Rb	31.0	31.5	62.2	15.7	4.4
Sr	189	189	216	156	261
Y	42.2	43.2	50.6	24.5	26.1
Zr	154	152	289	57	151
Nb	16	17	40	9	10
Mo	1.1	1.1	1.4	0.5	0.5
Cs	1.0	1.0	0.9	0.1	0.0
Ba	247	249	414	110	158
La	19	20	40	10	16
Ce	41	42	85	20	37
Pr	5.01	5.16	10.40	2.41	4.91
Nd	21.2	21.5	42.4	10.1	22.5
Sm	5.08	5.14	9.23	2.62	5.37
Eu	1.49	1.50	2.62	0.99	1.69
Gd	6.10	6.20	9.78	3.32	5.78
Tb	0.99	0.99	1.42	0.58	0.81
Dy	7.02	7.11	9.17	4.13	5.11
Ho	1.59	1.58	1.91	0.96	1.03
Er	4.43	4.55	5.13	2.74	2.58
Tm	0.66	0.67	0.71	0.41	0.35
Yb	4.45	4.48	4.69	2.69	2.17
Lu	0.65	0.68	0.69	0.41	0.31
Hf	3.50	3.55	6.62	1.44	3.61
Ta	1.16	1.17	3.05	0.63	0.84
W	0.50	0.52	0.94	0.17	0.11
Pb	3.56	3.70	7.56	1.19	3.13
Th	3.77	3.82	9.85	1.33	3.25
U	0.84	0.82	2.23	0.34	0.83

Sample:	**DC14-17**	**DC14-18**	**DC14-19**	**DC14-20**	**DC14-21**
Locality:	Gondal	Mandan Kundla	Vasavad	Amildha	Kotowar
SiO_2	47.1	50.0	48.1	45.8	49.0
TiO_2	1.74	0.71	2.39	1.06	2.38
Al_2O_3	16.1	14.6	13.7	15.4	13.5
Fe_2O_3T	13.7	11.9	14.0	12.6	14.0
MnO	0.14	0.19	0.19	0.18	0.19
MgO	7.16	7.61	7.19	9.37	6.45
CaO	11.4	12.46	11.79	12.61	11.13
Na_2O	2.16	1.93	2.12	2.15	2.18
K_2O	0.2	0.29	0.24	0.6	0.81
P_2O_5	0.2	0.08	0.2	0.15	0.23
Total	**99.9**	**99.72**	**99.83**	**99.83**	**99.81**
LOI	7.59	1.77	2.99	1.17	1.34
FeO	2.63	8.05	8.27	8.76	7.89
Fe_2O_3	10.79	2.91	4.76	2.85	5.24
Mg no.	82.92	62.76	60.79	65.60	59.31
Fe2+/Fe* (mol. Fraction)	0.35	0.86	0.79	0.87	0.77
XRF Trace Elements:					
Rb	2.8	8.5	2.7	17.1	24.5
Sr	265	141	226	243	257
Y	34.3	25.5	30.6	27.2	26.3
Zr	117	65	140	78	161
V	300	270	367	278	394
Ni	108	82	136	181	83
Cr	79	95	285	289	133
Nb	6	1.5	8.9	9.2	12.3
Ga	18.7	15.3	20.7	15.6	19.8
Cu	98	136	190	138	138
Zn	103	72	87	68	106
Co	63	52	51	55	52
Ba	109	70	87	181	125
La	13	10	12	15	12
Ce	30	18	19	18	18
U	<0.5	<0.5	<0.5	<0.5	<0.5
Th	7.9	<0.5	<0.5	<0.5	1.9
Sc	30	37	31	35	33
Pb	<1	<1	1	<1	4
ICPMS Trace Elements:					
Li	5.3	4.6	4.6	4.7	5.2
Sc	35	41	34	41	31
V	292	256	378	291	388
Cr	79	111	333	381	147
Co	55	46	49	55	49

Ni	110	72	141	203	86
Cu	83	113	189	122	146
Zn	96	74	103	72	117
Ga	21	15	23	16	22
Ge	1.5	1.3	1.6	1.4	1.7
Rb	3.0	8.6	1.9	17.0	29.6
Sr	276	139	244	258	264
Y	27.6	19.1	27.3	22.4	26.6
Zr	118	49	141	72	155
Nb	7	3	10	11	12
Mo	0.4	0.3	0.5	0.4	0.6
Cs	0.0	0.2	0.0	0.2	0.3
Ba	140	147	89	177	132
La	14	5	12	11	15
Ce	31	11	30	23	37
Pr	4.00	1.46	4.24	2.83	5.00
Nd	18.1	7.0	20.0	12.0	23.3
Sm	4.58	2.05	5.45	2.91	5.71
Eu	1.59	0.78	1.78	1.06	1.88
Gd	5.09	2.52	5.66	3.46	5.94
Tb	0.79	0.44	0.87	0.57	0.88
Dy	5.11	3.25	5.39	3.86	5.36
Ho	1.09	0.77	1.09	0.85	1.05
Er	2.86	2.13	2.76	2.31	2.58
Tm	0.40	0.32	0.37	0.34	0.35
Yb	2.50	2.09	2.27	2.13	2.13
Lu	0.37	0.32	0.32	0.32	0.29
Hf	2.95	1.31	3.45	1.80	3.68
Ta	0.51	0.27	0.81	0.83	1.01
W	0.11	0.12	0.14	0.14	0.25
Pb	3.50	1.72	1.76	1.75	2.89
Th	1.84	1.12	1.68	1.72	2.55
U	0.22	0.25	0.40	0.28	0.61

Sample:	**DC14-22**	**DC14-23**	**DC14-27**	**DC14-28**	**DC14-29**
Locality:	Kotowar	Virar	Armatia	Armatia	Damodar Kund
SiO_2	53.8	49.4	49.2	51.7	73.2
TiO_2	0.92	0.84	3.18	1.33	0.55
Al_2O_3	14.8	14.0	13.4	14.3	12.5
Fe_2O_3T	10.4	14.3	15.9	11.8	4.1
MnO	0.16	0.23	0.22	0.17	0.07
MgO	6.42	7.02	5.01	7.8	0.54
CaO	9.46	11.98	9.46	9.55	1.79
Na_2O	2.57	1.94	2.31	2.81	2.74
K_2O	1.35	0.18	0.66	0.3	4.05
P_2O_5	0.1	0.09	0.3	0.16	0.12
Total	**99.86**	**99.92**	**99.62**	**99.88**	**99.62**
LOI	2.09	2.6	3.75	4.84	0.65
FeO	6.08	9.74	7.81	6.59	1.61
Fe_2O_3	3.61	3.45	7.25	4.44	2.28
Mg no.	65.31	56.24	53.35	67.85	37.42
Fe2+/Fe* (mol. Fraction)	0.79	0.86	0.71	0.77	0.61
XRF Trace Elements:					
Rb	63.2	3.5	7	5.8	215.9
Sr	144	88	266	259	92
Y	33.2	30	36.8	32.7	57.3
Zr	104	61	225	113	344
V	248	365	390	309	55
Ni	58	84	65	75	10
Cr	116	99	128	264	12
Nb	7.8	2	15.9	6.2	25
Ga	16.9	16.1	22.1	16.4	23.2
Cu	91	215	246	68	10
Zn	74	98	120	86	54
Co	41	58	55	55	5
Ba	180	49	158	130	611
La	20	13	15	15	48
Ce	41	16	24	31	93
U	<0.5	<0.5	2.3	<0.5	1.5
Th	11.7	<0.5	3.7	6.8	42.2
Sc	31	40	29	30	5
Pb	11	<1	<1	9	12
ICPMS Trace Elements:					
Li	6.6	4.5	5.4	6.7	22.7
Sc	35	47	32	33	9
V	250	352	396	264	46
Cr	106	101	82	292	12
Co	41	54	47	47	7

Ni	52	87	63	66	5
Cu	80	179	212	58	13
Zn	71	94	136	83	58
Ga	19	16	25	17	21
Ge	1.4	1.5	1.8	1.4	1.2
Rb	77.6	4.5	8.2	6.0	219.2
Sr	165	94	275	264	107
Y	28.3	25.1	37.5	22.8	56.8
Zr	103	45	225	115	170
Nb	8	4	16	8	25
Mo	0.7	0.3	1.1	0.3	1.5
Cs	0.5	0.0	0.1	0.0	4.8
Ba	201	53	175	154	595
La	21	4	23	14	47
Ce	43	9	54	31	99
Pr	4.93	1.23	7.30	3.90	11.48
Nd	19.0	6.1	32.6	16.8	42.9
Sm	4.38	2.12	8.16	4.05	9.17
Eu	1.09	0.82	2.36	1.32	1.38
Gd	4.89	2.96	8.42	4.42	9.87
Tb	0.75	0.55	1.21	0.66	1.50
Dy	4.93	4.14	7.44	4.25	9.72
Ho	1.07	0.97	1.47	0.90	2.05
Er	2.90	2.76	3.76	2.31	5.68
Tm	0.42	0.43	0.51	0.32	0.82
Yb	2.78	2.83	3.11	2.02	5.29
Lu	0.41	0.43	0.44	0.30	0.75
Hf	2.89	1.26	5.38	2.88	4.47
Ta	0.99	0.31	1.29	0.58	2.23
W	0.45	0.11	0.25	0.08	1.01
Pb	10.76	0.72	3.03	3.64	25.76
Th	11.12	0.69	4.08	2.43	28.35
U	2.87	0.15	0.87	0.33	3.46

Sample:	**DC14-30**	**DC14-31A**	**DC14-32**	**DC14-35**	**DC14-36**
Locality:	Dolatpara Part	Moti Marad	Osam Hill	Osam Hill	Ambola
SiO_2	48.9	45.4	49.9	51.1	49.9
TiO_2	0.84	0.97	0.91	1.3	1.18
Al_2O_3	15.5	15.8	14.4	13.8	13.4
Fe_2O_3T	10.7	13.8	13.2	14.0	12.1
MnO	0.2	0.19	0.2	0.21	0.18
MgO	9.36	11.22	7.18	6.13	8.79
CaO	12.22	10.04	11.43	10.31	12.36
Na_2O	1.98	1.95	2.14	2.43	1.71
K_2O	0.26	0.29	0.28	0.37	0.2
P_2O_5	0.08	0.09	0.11	0.25	0.11
Total	**100**	**99.71**	**99.78**	**99.82**	**99.94**
LOI	2.34	1.44	4.18	4.54	4.06
FeO	6.64	9.2	5.88	6.94	7.64
Fe_2O_3	3.30	3.61	6.67	6.29	3.61
Mg no.	71.54	68.50	68.52	61.16	67.23
Fe2+/Fe* (mol. Fraction)	0.82	0.85	0.66	0.71	0.82
XRF Trace Elements:					
Rb	7.3	8.7	3.3	10.6	2
Sr	173	160	126	181	149
Y	23.4	24	34.5	47.3	30
Zr	51	64	96	145	86
V	261	228	306	316	283
Ni	181	291	65	48	195
Cr	298	414	67	48	482
Nb	2.9	2.5	3.4	15.6	3.2
Ga	14.9	16.4	16.3	16.4	15.8
Cu	123	103	165	206	125
Zn	88	82	89	115	76
Co	52	78	54	52	61
Ba	79	79	109	165	65
La	10	11	14	18	15
Ce	10	15	35	46	15
U	<0.5	<0.5	0.8	2.3	<0.5
Th	<0.5	<0.5	<0.5	4.5	0.9
Sc	38	26	44	35	35
Pb	5	<1	<1	3	<1
ICPMS Trace Elements:					
Li	6.5	5.3	9.2	6.8	4.8
Sc	42	29	44	44	36
V	258	227	301	309	270
Cr	341	414	52	43	563
Co	51	75	46	43	53

Ni	184	347	62	46	180
Cu	123	93	156	164	103
Zn	80	85	85	100	76
Ga	15	18	17	17	17
Ge	1.4	1.5	1.4	1.5	1.4
Rb	7.7	7.4	3.5	13.4	2.9
Sr	189	179	124	188	146
Y	16.8	17.2	24.7	37.9	21.7
Zr	41	64	83	134	75
Nb	4	5	5	16	4
Mo	0.3	0.4	0.2	1.3	0.3
Cs	0.8	0.1	0.0	0.6	0.3
Ba	87	85	135	180	74
La	4	5	9	19	7
Ce	8	11	19	40	17
Pr	1.12	1.48	2.45	4.81	2.31
Nd	5.5	7.1	10.7	19.9	10.8
Sm	1.70	2.11	2.86	4.81	3.08
Eu	0.85	0.88	0.93	1.38	1.10
Gd	2.22	2.56	3.43	5.53	3.64
Tb	0.39	0.45	0.60	0.91	0.60
Dy	2.89	3.07	4.21	6.38	4.00
Ho	0.64	0.67	0.99	1.49	0.87
Er	1.78	1.76	2.77	4.21	2.34
Tm	0.26	0.25	0.40	0.63	0.32
Yb	1.67	1.59	2.66	4.12	2.04
Lu	0.25	0.24	0.40	0.61	0.29
Hf	1.04	1.51	2.12	3.28	2.01
Ta	0.27	0.39	0.41	1.23	0.41
W	0.07	0.07	0.09	0.45	0.10
Pb	15.34	1.07	2.99	4.26	1.80
Th	0.43	0.65	2.35	3.90	1.41
U	0.09	0.11	0.47	1.02	0.34

Sample:	**DC14-38**	**DC14-39**	**DC14-40A**	**DC14-40B**	**DC14-41**
Locality:	Hedekiya	Jalondar	Girnar	Girnar	Girnar
SiO_2	49.4	49.4	47.9	58.1	45.9
TiO_2	1.19	1.14	1.67	0.7	2.73
Al_2O_3	13.5	12.8	18.3	19.3	15.6
Fe_2O_3T	12.4	12.9	11.1	6.0	13.9
MnO	0.19	0.19	0.2	0.12	0.2
MgO	9.76	11.76	4.43	1.28	5.39
CaO	11.24	9.26	8.81	2.8	10.74
Na_2O	1.83	1.79	4.13	3.99	2.71
K_2O	0.2	0.55	2.63	7.38	1.89
P_2O_5	0.12	0.12	0.7	0.26	0.53
Total	**99.85**	**99.92**	**99.8**	**99.89**	**99.63**
LOI	3.6	2.42	1.69	1.64	1.27
FeO	8.36	9.73	6.95	2.69	8.59
Fe_2O_3	3.14	2.12	3.33	2.98	4.37
Mg no.	67.55	68.30	53.19	45.90	52.80
Fe2+/Fe* (mol. Fraction)	0.86	0.91	0.82	0.67	0.81
XRF Trace Elements:					
Rb	3.1	13.8	74.6	225.3	56.9
Sr	120	181	767	545	541
Y	31.3	27.3	26.7	14.1	27
Zr	77	92	215	226	77
V	287	232	211	55	372
Ni	203	157	42	8	54
Cr	494	365	31	11	48
Nb	3.3	5	98.2	98.9	36.7
Ga	15.2	15.6	16.2	17	17.3
Cu	126	71	50	51	79
Zn	79	87	80	43	95
Co	60	76	29	4	45
Ba	79	158	1117	1386	1028
La	10	12	40	39	16
Ce	19	24	96	87	31
U	<0.5	<0.5	<0.5	0.5	1.3
Th	0.7	1	5.9	16.5	<0.5
Sc	33	26	16	3	23
Pb	<1	<1	25	30	2
ICPMS Trace Elements:					
Li	4.4	7.2	15.3	2.9	6.7
Sc	38	30	15	1	27
V	280	230	192	12	391
Cr	596	385	23		20
Co	57	68	27	2	43
Ni	199	158	37	1	47

Cu	120	62	43	12	70
Zn	81	85	120	13	102
Ga	17	16	18	5	19
Ge	1.4	1.4	1.3	0.3	1.6
Rb	2.8	16.8	88.1	56.8	81.4
Sr	143	172	711	144	544
Y	22.8	18.9	27.6	5.8	31.7
Zr	79	90	198	46	64
Nb	5	6	92	23	38
Mo	0.5	0.4	1.4	0.8	1.1
Cs	0.2	1.0	0.9	1.1	1.1
Ba	87	159	1423	434	1082
La	7	11	60	12	31
Ce	17	23	109	23	68
Pr	2.42	2.88	11.09	2.38	8.45
Nd	11.4	12.8	39.1	8.3	34.9
Sm	3.17	3.16	6.53	1.39	7.08
Eu	1.12	1.11	2.24	0.46	2.34
Gd	3.76	3.55	7.01	1.47	7.36
Tb	0.62	0.54	0.88	0.19	1.01
Dy	4.15	3.47	5.12	1.10	6.16
Ho	0.89	0.75	1.05	0.23	1.23
Er	2.34	2.00	2.78	0.61	3.20
Tm	0.34	0.27	0.38	0.09	0.41
Yb	2.12	1.74	2.49	0.56	2.65
Lu	0.31	0.25	0.37	0.09	0.38
Hf	2.07	2.30	4.38	1.10	1.91
Ta	0.39	0.49	6.44	1.62	2.74
W	0.11	0.08	0.78	0.50	0.27
Pb	1.89	3.42	6.37	5.39	4.57
Th	1.49	1.82	7.15	3.53	3.46
U	0.36	0.26	1.03	0.75	0.55

Sample:	**DC14-42**	**DC14-43**	**DC14-45**	**DC14-46A**	**DC14-46B**
Locality:	Girnar	Girnar	Malanka	Malanka	Malanka
SiO_2	49.3	49.3	50.7	50.7	51.2
TiO_2	1.53	1.61	1.54	1.16	1.11
Al_2O_3	15.0	15.4	14.7	13.9	13.9
Fe_2O_3T	13.2	13.0	12.4	11.6	11.3
MnO	0.19	0.16	0.18	0.17	0.18
MgO	6.93	6.27	7.02	8.52	8.42
CaO	10.08	10.23	10.09	10.9	10.73
Na_2O	2.46	2.65	2.31	1.93	1.98
K_2O	0.82	1.03	0.82	0.75	0.66
P_2O_5	0.2	0.26	0.15	0.12	0.12
Total	**99.68**	**99.87**	**99.93**	**99.79**	**99.63**
LOI	0.97	1.02	2.56	2.04	2.49
FeO	8.43	8.31	7.3	8.12	7.16
Fe_2O_3	3.80	3.74	4.29	2.61	3.37
Mg no.	59.44	57.36	63.16	65.17	67.71
Fe2+/Fe* (mol. Fraction)	0.83	0.83	0.79	0.87	0.83
XRF Trace Elements:					
Rb	15.4	20.1	27.4	22.5	24.5
Sr	163	165	179	126	121
Y	38.4	40.4	29.7	28.2	29.1
Zr	155	221	116	99	91
V	338	256	271	271	264
Ni	100	85	93	135	151
Cr	82	99	154	313	328
Nb	5.1	8.2	7.6	3.7	5.3
Ga	17.8	18.7	18.4	17.3	16.2
Cu	189	72	56	67	64
Zn	92	84	85	72	76
Co	56	49	55	51	52
Ba	186	279	209	95	96
La	16	19	16	11	12
Ce	28	38	27	27	27
U	<0.5	<0.5	0.7	<0.5	<0.5
Th	<0.5	<0.5	4.3	,0.5	4.1
Sc	34	32	27	29	28
Pb	<1	4	3	1	2
ICPMS Trace Elements:					
Li	9.4	8.9	5.8	6.8	7.5
Sc	39	40	34	38	36
V	278	255	279	280	258
Cr	91	95	150	365	361
Co	51	50	49	49	49
Ni	105	93	88	137	143

Cu	153	65	56	66	60
Zn	92	110	90	76	79
Ga	19	21	19	19	17
Ge	1.5	1.7	1.4	1.5	1.3
Rb	17.5	20.4	27.3	25.3	25.1
Sr	173	187	186	151	134
Y	33.4	38.9	25.0	23.8	22.0
Zr	70	68	115	99	88
Nb	7	10	9	6	5
Mo	0.4	0.4	0.6	0.7	0.5
Cs	0.2	0.1	0.3	0.4	0.4
Ba	195	287	218	124	123
La	15	25	14	12	11
Ce	34	53	30	26	24
Pr	4.40	6.79	3.82	3.35	3.07
Nd	19.5	28.9	16.5	14.2	13.4
Sm	4.95	6.61	4.13	3.62	3.37
Eu	1.57	1.96	1.32	1.15	1.06
Gd	5.59	7.24	4.62	4.17	3.82
Tb	0.86	1.07	0.71	0.65	0.60
Dy	5.88	6.92	4.57	4.28	4.01
Ho	1.27	1.49	0.98	0.92	0.86
Er	3.48	3.96	2.57	2.43	2.25
Tm	0.49	0.54	0.36	0.35	0.32
Yb	3.15	3.52	2.28	2.20	2.04
Lu	0.45	0.52	0.33	0.31	0.30
Hf	1.94	1.82	2.94	2.40	2.29
Ta	0.59	0.75	0.75	0.49	0.46
W	0.18	0.16	0.13	0.24	0.33
Pb	4.30	5.46	3.92	2.36	2.53
Th	2.95	3.60	3.54	3.99	3.74
U	0.42	0.42	0.74	0.98	0.91

Sample:	**DC14-46C**	**DC14-47A**	***Rep.***	***DC14-47B***	**DC14-49**
Locality:	Malanka	Pavagadh	Pavagadh	Pavagadh	Amba Dongar
SiO_2	50.5	47.1		45.8	52.2
TiO_2	1.18	2.94		2.3	1.53
Al_2O_3	14.2	13.9		10.4	13.8
Fe_2O_3T	11.7	13.6		13.3	15.2
MnO	0.17	0.2		0.2	0.21
MgO	8.65	8		14.15	4.12
CaO	10.86	10.61		11.09	7.3
Na_2O	1.91	2.18		1.61	3.9
K_2O	0.68	1.07		0.76	1.34
P_2O_5	0.12	0.39		0.23	0.17
Total	**99.99**	**99.93**		**99.86**	**99.74**
LOI	2.27	3.23		3.74	3.26
FeO	8.22	8.16		9.13	8.1
Fe_2O_3	2.54	4.51		3.18	6.23
Mg no.	65.23	63.61		73.43	47.56
Fe2+/Fe* (mol. Fraction)	0.88	0.80		0.86	0.74
XRF Trace Elements:					
Rb	24.3	23		23	37.1
Sr	142	432		575	166
Y	30.1	28.8		23.1	45.3
Zr	104	199		129	123
V	270	330		306	361
Ni	134	105		220	38
Cr	332	287		778	32
Nb	3.9	40.3		24.7	7.7
Ga	17	18.7		13.7	18.9
Cu	72	101		78	298
Zn	76	193		113	123
Co	52	58		77	59
Ba	120	306		545	229
La	11	17		13	17
Ce	25	28		30	30
U	0.9	1.1		2.7	<0.5
Th	0.6	0.5		<0.5	13.6
Sc	30	29		31	29
Pb	<1	<1		<1	1
ICPMS Trace Elements:					
Li	8.2	9.5	8.6	5.1	13.8
Sc	35	33	31	40	37
V	262	333	313	297	360
Cr	328	288	268	773	17
Co	47	53	50	72	43

Ni	123	105	98	230	32
Cu	62	88	83	64	238
Zn	74	107	98	90	119
Ga	18	22	21	15	19
Ge	1.3	1.7	1.6	1.6	1.7
Rb	27.2	29.4	28.8	29.6	40.5
Sr	139	453	448	582	164
Y	23.5	27.6	27.1	18.0	35.8
Zr	94	195	190	126	112
Nb	5	39	37	26	9
Mo	0.5	1.2	1.1	0.7	1.2
Cs	0.6	0.2	0.2	0.8	0.2
Ba	118	322	318	482	305
La	12	34	33	21	15
Ce	26	73	70	46	31
Pr	3.26	9.17	8.71	5.72	3.72
Nd	14.2	37.1	36.7	24.4	15.6
Sm	3.61	7.60	7.46	5.16	4.02
Eu	1.13	2.37	2.32	1.74	1.28
Gd	4.08	7.49	7.40	5.08	4.99
Tb	0.64	0.98	0.97	0.65	0.85
Dy	4.14	5.52	5.57	3.76	6.03
Ho	0.90	1.13	1.08	0.72	1.39
Er	2.38	2.76	2.70	1.81	3.84
Tm	0.33	0.36	0.35	0.23	0.57
Yb	2.12	2.19	2.14	1.37	3.83
Lu	0.31	0.31	0.30	0.20	0.58
Hf	2.43	4.55	4.39	3.18	2.88
Ta	0.48	2.92	2.85	2.02	0.68
W	0.22	0.35	0.35	0.16	2.16
Pb	2.23	3.64	3.61	1.80	4.76
Th	3.98	4.29	4.22	2.44	3.37
U	0.96	0.90	0.87	0.46	0.69

Sample:	**DC14-52**	**DC14-53**	**DC14-54**	**DC14-55**	**DC14-56**
Locality:	Sadar Sarovar Dam	Karjan Dam	Karjan Dam	Ranala	Ranala
SiO_2	50.5	51.3	49.3	51.6	49.0
TiO_2	1.72	0.7	1.43	0.91	3.5
Al_2O_3	13.5	14.0	14.6	15.3	13.3
Fe_2O_3T	14.1	10.8	14.3	11.9	16.9
MnO	0.2	0.12	0.2	0.19	0.24
MgO	6.37	8.37	6.43	6.31	3.98
CaO	10.68	12.02	11.52	10.47	8.94
Na_2O	2.02	1.51	2.09	2.29	2.82
K_2O	0.46	0.58	0.11	0.75	0.67
P_2O_5	0.17	0.1	0.13	0.13	0.39
Total	**99.75**	**99.58**	**100.01**	**99.86**	**99.83**
LOI	2.06	1.18	2.85	1.93	2.22
FeO	9.88	3	8.22	8.34	11.15
Fe_2O_3	3.14	7.50	5.12	2.64	4.54
Mg no.	53.48	83.26	58.24	57.43	38.89
Fe2+/Fe* (mol. Fraction)	0.87	0.47	0.78	0.88	0.85
XRF Trace Elements:					
Rb	11.7	10.9	1.8	22.5	17.1
Sr	150	129	176	157	211
Y	31.8	25.9	30	26.9	38.2
Zr	127	94	92	102	242
V	367	259	366	272	434
Ni	81	174	72	59	23
Cr	128	452	90	86	38
Nb	7.1	4.5	5	5.8	21.8
Ga	19.2	16.2	17.7	16.7	22.6
Cu	223	90	194	136	428
Zn	116	79	75	84	144
Co	56	52	61	46	47
Ba	104	197	54	222	183
La	12	19	11	22	9
Ce	21	34	15	31	11
U	1.2	1.1	<0.5	1.9	<0.5
Th	2.5	2.1	<0.5	0.6	10.6
Sc	34	37	42	34	29
Pb	<1	1	<1	<1	<1
ICPMS Trace Elements:					
Li	4.3	7.8	7.5	8.0	9.8
Sc	37	36	40	38	37
V	343	246	351	254	443
Cr	148	541	69	75	12
Co	48	46	50	42	43

Ni	80	166	69	57	31
Cu	181	80	180	112	357
Zn	96	68	92	75	165
Ga	20	16	19	17	25
Ge	1.5	1.4	1.5	1.3	1.8
Rb	14.5	12.6	1.1	23.9	20.0
Sr	156	136	180	168	216
Y	28.4	18.4	24.8	23.1	45.4
Zr	110	83	77	85	226
Nb	8	5	6	7	19
Mo	0.4	0.3	0.2	0.4	1.1
Cs	0.2	0.1	0.1	0.3	0.2
Ba	103	208	56	219	194
La	10	17	7	15	20
Ce	24	32	17	31	48
Pr	3.27	3.55	2.31	3.61	6.68
Nd	15.1	13.5	10.9	14.7	31.0
Sm	4.30	2.99	3.19	3.31	7.99
Eu	1.43	0.88	1.17	1.06	2.52
Gd	4.89	3.39	3.89	3.67	8.81
Tb	0.80	0.49	0.66	0.56	1.34
Dy	5.25	3.18	4.45	3.86	8.55
Ho	1.13	0.70	0.98	0.88	1.79
Er	2.96	1.90	2.58	2.45	4.67
Tm	0.41	0.26	0.36	0.35	0.65
Yb	2.54	1.70	2.26	2.30	4.16
Lu	0.38	0.25	0.33	0.35	0.61
Hf	2.87	1.97	2.08	2.06	5.55
Ta	0.67	0.41	0.48	0.54	1.52
W	0.21	0.33	0.11	0.21	0.27
Pb	2.37	6.12	1.35	4.89	3.02
Th	2.21	5.36	1.36	2.76	2.38
U	0.50	0.85	0.30	0.68	0.56

Sample:	**DC14-57**	**DC14-59**	**DC14-63**	**DC14-65**	**DC14-66**
Locality:	Ranala	Dhule	Thal Ghat	Thal Ghat	Thal Ghat
SiO_2	50.4	50.8	48.9	47.6	48.7
TiO_2	2.54	1.83	1.51	1.52	1.6
Al_2O_3	14.8	13.0	11.4	16.9	11.9
Fe_2O_3T	14.7	12.8	13.0	13.6	12.4
MnO	0.16	0.18	0.19	0.21	0.18
MgO	4.24	7.43	11.12	6.59	10.22
CaO	9.48	10.94	11.2	11.06	12.21
Na_2O	2.53	2.28	1.76	2.15	1.59
K_2O	0.58	0.39	0.54	0.16	0.7
P_2O_5	0.27	0.22	0.13	0.17	0.16
Total	**99.68**	**99.88**	**99.77**	**99.88**	**99.69**
LOI	2.59	2.13	3.23	7.21	5.77
FeO	6.7	7.81	7.78	4.5	5.22
Fe_2O_3	7.20	4.13	4.36	8.62	6.59
Mg no.	53.01	62.91	71.82	72.31	77.73
Fe2+/Fe* (mol. Fraction)	0.67	0.81	0.80	0.54	0.64
XRF Trace Elements:					
Rb	12.5	6.8	17.4	1.7	14.8
Sr	296	265	145	182	144
Y	30.7	30.1	27.9	38.1	28.7
Zr	198	142	89	104	103
V	351	310	325	307	318
Ni	30	90	141	103	94
Cr	63	295	600	151	478
Nb	13.9	7	4	5.5	5.1
Ga	22.9	19.5	15.7	19.9	19.1
Cu	147	152	48	141	45
Zn	197	94	77	98	93
Co	51	54	66	62	57
Ba	188	165	99	119	133
La	16	11	9	15	14
Ce	20	24	19	23	22
U	<0.5	<0.5	<0.5	<0.5	<0.5
Th	4	2.8	<0.5	6.8	7
Sc	26	29	31	30	26
Pb	3	5	9	2	<1
ICPMS Trace Elements:					
Li	12.2	10.0	7.3	6.9	15.4
Sc	26	33	35	36	35
V	338	319	312	278	318
Cr	50	354	708	157	597
Co	39	51	60	49	49
Ni	33	93	140	90	87

Cu	107	144	46	116	40
Zn	113	100	87	99	85
Ga	26	22	17	21	20
Ge	1.7	1.6	1.5	1.4	1.4
Rb	16.5	8.1	19.2	1.7	17.0
Sr	298	283	161	183	150
Y	31.8	26.4	20.1	27.3	20.9
Zr	112	143	90	98	101
Nb	13	8	5	6	6
Mo	0.8	0.9	0.4	0.4	0.4
Cs	0.2	0.2	0.2	0.0	0.1
Ba	205	173	106	111	162
La	21	17	8	13	12
Ce	47	38	20	28	27
Pr	6.29	5.06	2.71	3.47	3.55
Nd	27.8	22.2	12.7	15.3	16.0
Sm	6.65	5.31	3.61	3.87	4.07
Eu	2.13	1.65	1.20	1.32	1.33
Gd	6.80	5.67	3.93	4.52	4.45
Tb	1.02	0.83	0.62	0.72	0.66
Dy	6.08	4.98	3.88	4.85	4.05
Ho	1.25	1.02	0.79	1.06	0.83
Er	3.17	2.63	2.01	2.79	2.07
Tm	0.42	0.35	0.27	0.40	0.28
Yb	2.59	2.17	1.68	2.57	1.76
Lu	0.36	0.30	0.25	0.38	0.25
Hf	3.15	3.38	2.44	2.59	2.70
Ta	1.05	0.66	0.42	0.50	0.52
W	0.24	0.16	0.11	0.18	0.15
Pb	3.65	2.53	1.91	2.84	2.22
Th	4.12	2.76	2.51	2.78	2.63
U	0.77	0.58	0.58	0.58	0.65

Sample:	**DC14-67**	**DC14-68**	**DC14-69**	**DC14-70**	**DC14-71**
Locality:	Kalsubai	Kalsubai	Kalsubai	Kalsubai	Kalsubai
SiO_2	51.0	50.9	49.5	49.7	49.0
TiO_2	2.13	2.84	1.25	2.45	2.18
Al_2O_3	14.0	12.6	12.2	13.9	14.0
Fe_2O_3T	14.3	15.8	13.4	14.0	13.7
MnO	0.2	0.21	0.18	0.2	0.18
MgO	5.17	4.6	10.64	5.67	6.96
CaO	9.75	9.3	10	10.99	11.45
Na_2O	2.53	2.51	1.81	2.35	2.11
K_2O	0.55	0.66	0.61	0.31	0.15
P_2O_5	0.21	0.29	0.16	0.23	0.2
Total	**99.78**	**99.73**	**99.79**	**99.81**	**99.83**
LOI	1.81	3.59	2.99	3.33	2.43
FeO	9.95	8.67	7.66	8.06	8.14
Fe_2O_3	3.25	6.19	4.92	5.06	4.63
Mg no.	48.09	48.61	71.24	55.64	60.39
Fe2+/Fe* (mol. Fraction)	0.87	0.76	0.78	0.78	0.80
XRF Trace Elements:					
Rb	8.4	9.4	15.2	7.7	2.2
Sr	233	268	211	256	239
Y	32.9	37.8	31	33.6	32.1
Zr	173	250	104	165	136
V	373	366	301	370	354
Ni	53	44	298	82	112
Cr	45	88	517	152	281
Nb	9.3	13.7	5.1	11.5	7.5
Ga	20.2	21.9	16	21.3	20.8
Cu	218	286	95	193	181
Zn	163	123	92	100	95
Co	53	53	71	50	52
Ba	156	289	325	103	76
La	14	17	16	12	11
Ce	25	29	32	24	20
U	<0.5	1.4	<0.5	0.5	0.5
Th	5.5	3.1	1.1	2.5	0.8
Sc	34	29	30	32	35
Pb	<1	<1	<1	<1	<1
ICPMS Trace Elements:					
Li	6.4	5.9	6.3	7.5	7.0
Sc	32	32	35	35	37
V	339	377	291	357	361
Cr	51	68	618	156	338
Co	45	45	66	44	49
Ni	53	47	322	78	121

Cu	167	200	85	168	174
Zn	104	123	90	108	103
Ga	22	24	17	23	23
Ge	1.6	1.7	1.5	1.6	1.7
Rb	10.9	12.7	17.1	8.0	2.1
Sr	247	275	223	263	254
Y	31.0	38.8	22.0	30.2	28.5
Zr	149	203	104	156	133
Nb	9	13	7	11	9
Mo	0.7	0.7	0.5	0.6	0.4
Cs	0.2	0.2	0.2	0.2	0.0
Ba	170	293	328	100	75
La	15	23	16	15	12
Ce	36	50	33	37	28
Pr	4.78	6.61	4.17	4.91	4.06
Nd	21.3	30.0	17.6	22.8	18.7
Sm	5.56	7.48	4.12	5.72	5.15
Eu	1.83	2.34	1.38	1.89	1.73
Gd	6.06	7.89	4.39	6.21	5.56
Tb	0.90	1.20	0.65	0.94	0.85
Dy	5.86	7.47	4.11	5.89	5.30
Ho	1.21	1.56	0.85	1.19	1.09
Er	3.06	4.00	2.22	2.96	2.75
Tm	0.41	0.53	0.30	0.40	0.37
Yb	2.61	3.20	1.87	2.57	2.24
Lu	0.37	0.47	0.27	0.36	0.33
Hf	3.69	4.97	2.38	3.69	3.22
Ta	0.76	0.97	0.41	0.92	0.70
W	0.16	0.23	0.21	0.17	0.09
Pb	3.09	4.35	2.95	2.48	1.70
Th	2.47	3.03	1.82	2.64	1.86
U	0.54	0.58	0.29	0.71	0.39

Sample:	**DC14-72**	**DC14-73**	**DC14-74**	**DC14-75**	**DC14-76**
Locality:	Kalsubai	Kalsubai	Ghoti	Ghoti	Khopoli
SiO_2	50.1	49.1	49.0	48.1	50.7
TiO_2	1.96	2.4	3.29	1.93	1.89
Al_2O_3	14.5	13.4	12.6	14.1	15.3
Fe_2O_3T	12.8	14.4	17.2	13.6	12.3
MnO	0.21	0.21	0.22	0.19	0.13
MgO	6.39	6.61	4.52	8.55	5.35
CaO	10.67	10.16	9.15	10.54	10.58
Na_2O	2.35	2.42	2.39	1.95	2.65
K_2O	0.7	0.96	1.04	0.71	1
P_2O_5	0.2	0.27	0.32	0.19	0.2
Total	**99.87**	**99.92**	**99.75**	**99.9**	**99.98**
LOI	3.55	2.6	4.98	6.6	2.92
FeO	7.16	8.72	7.21	5.52	4.79
Fe_2O_3	4.86	4.70	9.22	7.51	6.93
Mg no.	61.41	57.47	52.78	73.42	66.57
Fe2+/Fe* (mol. Fraction)	0.77	0.80	0.63	0.62	0.61
XRF Trace Elements:					
Rb	15.5	22.6	15.5	12.7	23.4
Sr	275	231	238	183	309
Y	28.1	31.7	37.2	30.8	26.8
Zr	134	171	236	121	137
V	303	371	409	301	281
Ni	87	69	32	157	92
Cr	231	142	50	370	180
Nb	10.8	12.1	16.3	5.1	9.5
Ga	20.5	21.7	21.9	19.7	21
Cu	109	159	170	72	133
Zn	78	111	110	99	92
Co	52	55	56	68	47
Ba	169	210	247	122	114
La	20	15	16	11	16
Ce	30	24	25	25	24
U	<0.5	<0.5	<0.5	<0.5	<0.5
Th	5.7	3.7	10.3	11.6	<0.5
Sc	28	33	28	21	30
Pb	<1	7	2	3	10
ICPMS Trace Elements:					
Li	9.5	9.2	8.8	13.2	8.4
Sc	31	36	35	30	29
V	306	348	418	311	269
Cr	247	145	42	409	180
Co	45	50	48	53	41
Ni	80	66	37	139	82

Cu	112	185	140	70	152
Zn	97	120	147	93	87
Ga	22	25	26	21	23
Ge	1.5	1.8	1.9	1.4	1.5
Rb	16.5	25.6	22.0	16.0	32.8
Sr	267	231	249	187	317
Y	23.2	29.5	38.1	23.3	23.3
Zr	130	164	229	119	135
Nb	11	13	16	7	10
Mo	0.6	0.7	1.1	0.7	0.4
Cs	0.1	0.2	0.4	0.2	0.1
Ba	172	258	263	152	132
La	16	20	25	13	15
Ce	36	44	55	30	35
Pr	4.61	5.82	7.32	4.00	4.64
Nd	20.2	25.6	31.8	18.2	20.4
Sm	4.87	6.23	7.81	4.65	4.86
Eu	1.61	2.00	2.33	1.48	1.59
Gd	5.10	6.55	8.20	4.95	5.12
Tb	0.75	0.96	1.22	0.73	0.74
Dy	4.57	5.87	7.34	4.53	4.49
Ho	0.93	1.18	1.50	0.93	0.93
Er	2.35	3.01	3.83	2.30	2.33
Tm	0.32	0.41	0.51	0.32	0.32
Yb	2.00	2.52	3.24	1.98	1.96
Lu	0.29	0.36	0.47	0.28	0.27
Hf	3.30	4.06	5.44	3.15	3.17
Ta	0.88	1.02	1.26	0.58	0.81
W	0.20	0.21	0.28	0.19	0.28
Pb	3.29	3.60	4.08	2.26	2.18
Th	2.71	3.00	4.54	2.90	2.31
U	0.65	0.62	1.01	0.65	0.56

Sample:	**DC14-77**	**DC14-78**	**DC14-79**	**DC14-80**	**DC14-81**
Locality:	Khopoli	Khopoli	Rajpuri	Beacon Hill, Murud	Beacon Hill, Murud
SiO_2	50.4	49.7	44.9	42.9	48.8
TiO_2	1.81	1.81	1.19	4.14	2.53
Al_2O_3	13.2	12.8	11.1	8.8	13.3
Fe_2O_3T	11.3	13.5	10.7	15.5	15.1
MnO	0.24	0.17	0.21	0.35	0.22
MgO	9.13	10.31	10.77	11.2	6.11
CaO	10.93	9.52	13.48	13.07	10.81
Na_2O	1.91	1.35	5.15	1.47	2.43
K_2O	0.71	0.47	1.64	1.4	0.3
P_2O_5	0.19	0.16	0.77	0.82	0.22
Total	**99.79**	**99.7**	**99.86**	**99.71**	**99.77**
LOI	4.84	6.5	3.05	5.56	1.54
FeO	5.34	6.09	3.58	6.74	10.49
Fe_2O_3	5.35	6.68	6.74	8.04	3.41
Mg no.	75.30	75.11	84.29	74.76	50.94
Fe2+/Fe* (mol. Fraction)	0.69	0.67	0.54	0.65	0.87
XRF Trace Elements:					
Rb	20.9	11	32.6	22.1	8.5
Sr	191	176	1339	1016	209
Y	29	34.1	15.7	27.4	31.5
Zr	108	110	85	414	154
V	311	297	249	295	416
Ni	252	309	99	200	77
Cr	562	689	213	935	92
Nb	6.9	6.3	16	164.7	11.6
Ga	19.6	24.6	13	13.1	20.5
Cu	194	180	172	250	245
Zn	83	95	73	134	120
Co	52	63	40	65	57
Ba	107	116	817	1469	56
La	11	14	12	28	11
Ce	18	22	20	55	16
U	<0.5	<0.5	<0.5	2.2	<0.5
Th	4.5	<0.5	<0.5	18.7	0.7
Sc	27	28	27	29	36
Pb	<1	<1	9	3	<1
ICPMS Trace Elements:					
Li	8.9	5.5	20.5	43.9	5.6
Sc	35	32	29	36	39
V	314	283	228	283	417
Cr	691	612	247	703	124
Co	47	56	40	58	54

Ni	228	275	91	205	81
Cu	167	132	154	211	234
Zn	90	88	82	143	127
Ga	20	24	13	15	23
Ge	1.5	1.4	1.1	2.3	1.8
Rb	23.6	12.6	44.7	33.4	10.4
Sr	191	173	1233	889	220
Y	21.9	25.0	13.5	27.8	31.9
Zr	105	107	68	411	148
Nb	8	8	19	132	12
Mo	0.5	0.4	1.2	2.9	0.6
Cs	0.3	0.1	1.6	0.6	0.9
Ba	111	104	956	1518	76
La	11	12	12	131	12
Ce	26	25	26	278	30
Pr	3.46	3.67	3.33	31.46	4.13
Nd	16.0	17.4	13.9	116.9	20.2
Sm	4.24	4.48	2.92	17.44	5.66
Eu	1.44	1.57	1.07	4.74	1.91
Gd	4.57	4.88	2.93	15.37	6.17
Tb	0.69	0.75	0.40	1.50	0.97
Dy	4.31	4.62	2.46	6.73	6.18
Ho	0.89	0.96	0.52	1.17	1.25
Er	2.21	2.42	1.42	2.88	3.19
Tm	0.30	0.32	0.21	0.32	0.42
Yb	1.87	2.01	1.34	1.89	2.69
Lu	0.27	0.29	0.20	0.26	0.39
Hf	2.74	2.71	1.92	8.85	3.56
Ta	0.61	0.66	1.09	9.55	0.93
W	0.21	0.18	0.56	0.26	0.15
Pb	2.09	1.98	9.29	7.53	1.44
Th	2.06	2.02	1.30	12.99	1.26
U	0.49	0.42	0.21	3.07	0.30

Sample:	**DC14-82**	**DC14-83B**	**DC14-84A**	**DC14-85**	**DC14-86**
Locality:	More	More	More	More	Korlai
SiO_2	48.1	47.3	49.6	49.0	48.2
TiO_2	1.4	3.19	1.93	1.94	2.29
Al_2O_3	11.8	11.1	13.2	13.3	13.4
Fe_2O_3T	13.0	13.0	13.1	13.6	15.4
MnO	0.2	0.2	0.2	0.2	0.22
MgO	12.9	9.81	7.55	8.38	6.7
CaO	10.01	9.39	11.33	10.67	10.73
Na_2O	1.86	2.37	2.4	2.39	2.44
K_2O	0.28	2.93	0.27	0.24	0.22
P_2O_5	0.16	0.7	0.22	0.22	0.2
Total	**99.8**	**99.98**	**99.81**	**99.86**	**99.8**
LOI	1.91	4.28	1.82	1.9	1.84
FeO	9.93	6.24	9.79	10.45	10.32
Fe_2O_3	1.99	6.10	2.24	1.99	3.94
Mg no.	69.84	73.70	57.89	58.84	53.65
Fe2+/Fe* (mol. Fraction)	0.92	0.69	0.91	0.92	0.85
XRF Trace Elements:					
Rb	4.6	30.9	4.4	4.7	5.4
Sr	206	1598	296	290	185
Y	30.3	25.2	27.7	27.8	32.3
Zr	94	350	132	131	127
V	283	230	332	304	423
Ni	368	251	121	172	98
Cr	658	395	371	207	156
Nb	7.5	143.8	12.2	10.8	7.9
Ga	15.8	15.9	18.1	18.3	19.5
Cu	124	162	158	154	251
Zn	99	130	106	111	118
Co	74	66	56	66	62
Ba	105	997	125	114	50
La	11	56	15	11	9
Ce	22	97	22	25	15
U	<0.5	4.1	0.5	<0.5	0.6
Th	1.1	22.9	<0.5	0.5	2.4
Sc	30	14	31	31	36
Pb	<1	2	<1	<1	<1
ICPMS Trace Elements:					
Li	8.0	29.9	8.3	8.8	6.3
Sc	34	23	35	33	38
V	262	212	315	309	405
Cr	1016	388	369	218	153
Co	63	60	51	61	55

Ni	351	236	113	178	97
Cu	109	144	141	147	217
Zn	92	142	105	113	121
Ga	15	17	19	20	22
Ge	1.4	2.0	1.5	1.6	1.6
Rb	4.3	44.6	3.3	4.9	5.8
Sr	200	1436	285	301	185
Y	19.8	24.2	22.4	23.8	28.6
Zr	90	321	120	129	121
Nb	8	125	11	11	8
Mo	0.4	1.8	0.6	0.8	0.5
Cs	0.1	0.2	0.5	0.2	0.1
Ba	122	1056	128	123	36
La	10	140	14	15	8
Ce	25	282	33	35	22
Pr	3.35	29.98	4.42	4.60	3.20
Nd	15.2	106.1	20.0	20.9	16.1
Sm	3.65	14.67	4.87	4.98	4.66
Eu	1.18	3.84	1.58	1.65	1.63
Gd	3.86	13.15	4.97	5.24	5.25
Tb	0.58	1.26	0.72	0.75	0.85
Dy	3.69	5.51	4.36	4.51	5.44
Ho	0.79	0.98	0.90	0.92	1.13
Er	2.05	2.49	2.27	2.33	2.89
Tm	0.29	0.28	0.31	0.32	0.40
Yb	1.82	1.71	1.91	1.91	2.48
Lu	0.27	0.25	0.28	0.27	0.36
Hf	2.27	6.76	2.96	3.00	3.09
Ta	0.63	9.29	0.84	0.87	0.65
W	0.13	0.80	0.14	0.13	0.12
Pb	1.70	12.38	1.91	1.94	1.21
Th	0.81	17.22	1.13	1.16	0.99
U	0.18	3.81	0.26	0.26	0.25

Sample:	**DC14-93**	**DC14-94**	**DC14-95**	**DC14-96**
Locality:	Mahabaleshwar	Mahabaleshwar	Mahabaleshwar	Mahabaleshwar
SiO_2	49.9	49.2	50.3	50.7
TiO_2	3.11	2.75	1.72	1.79
Al_2O_3	12.0	12.6	14.0	14.3
Fe_2O_3T	17.0	16.5	13.4	12.3
MnO	0.24	0.23	0.18	0.19
MgO	4.83	5.61	6.87	6.71
CaO	9.06	9.55	10.59	10.91
Na_2O	2.4	2.48	2.28	2.3
K_2O	0.84	0.57	0.23	0.28
P_2O_5	0.31	0.29	0.18	0.19
Total	**99.63**	**99.79**	**99.82**	**99.72**
LOI	2.2	2.29	3.96	2.73
FeO	9.45	9.84	6.89	7.87
Fe_2O_3	6.50	5.59	5.78	3.59
Mg no.	47.68	50.41	64.00	60.32
Fe2+/Fe* (mol. Fraction)	0.76	0.80	0.73	0.83
XRF Trace Elements:				
Rb	22.6	14.4	6.2	9.1
Sr	196	189	177	182
Y	41.3	38.7	34.9	32.8
Zr	255	177	126	137
V	402	434	307	337
Ni	50	66	104	117
Cr	70	97	216	239
Nb	14.4	12.3	6.4	7.4
Ga	21.4	20.8	20.9	19.9
Cu	324	299	175	162
Zn	129	129	82	95
Co	55	55	52	53
Ba	117	127	92	144
La	10	11	16	13
Ce	20	19	33	21
U	<0.5	<0.5	0.7	<0.5
Th	4.8	6.9	4.1	<0.5
Sc	35	33	28	32
Pb	<1	<1	<1	<1
ICPMS Trace Elements:				
Li	6.6	9.8	8.9	5.3
Sc	34	38	36	32
V	394	421	319	308
Cr	58	76	238	247
Co	46	48	47	44
Ni	56	66	97	108

Cu	302	256	146	161
Zn	133	134	98	89
Ga	25	23	19	21
Ge	1.8	1.7	1.4	1.3
Rb	30.4	16.5	6.7	10.4
Sr	215	188	179	202
Y	43.7	36.4	26.3	29.4
Zr	222	185	117	127
Nb	15	12	7	8
Mo	0.7	0.7	0.5	0.4
Cs	0.4	0.2	0.1	0.2
Ba	112	115	96	132
La	18	15	12	13
Ce	44	37	29	30
Pr	6.38	5.24	3.75	3.95
Nd	30.2	24.8	16.8	17.8
Sm	8.10	6.62	4.30	4.72
Eu	2.51	2.08	1.42	1.57
Gd	8.80	7.22	4.92	5.25
Tb	1.35	1.12	0.77	0.81
Dy	8.52	7.14	4.92	5.15
Ho	1.75	1.47	1.04	1.10
Er	4.48	3.73	2.70	2.89
Tm	0.60	0.51	0.38	0.40
Yb	3.68	3.17	2.36	2.52
Lu	0.53	0.46	0.35	0.37
Hf	5.36	4.61	2.95	3.11
Ta	1.21	1.01	0.55	0.63
W	0.22	0.18	0.12	0.13
Pb	2.54	2.38	3.24	3.05
Th	2.43	2.29	2.21	1.93
U	0.60	0.57	0.36	0.38

Sample:	**DC14-97**	**DC14-99**	**DC14-100**	**DC14-101**
Locality:	Mahabaleshwar	Mahabeleshwar	Mahabaleshwar	Mahabaleshwar
SiO_2	50.5	48.4	48.6	48.6
TiO_2	2.22	2.11	2.46	2.71
Al_2O_3	14.2	13.9	13.7	13.5
Fe_2O_3T	12.6	14.4	14.6	16.0
MnO	0.18	0.21	0.24	0.21
MgO	6.43	6.85	6.19	5.56
CaO	10.8	11.49	11.12	10.41
Na_2O	2.48	2.19	2.34	2.41
K_2O	0.26	0.23	0.24	0.3
P_2O_5	0.22	0.24	0.21	0.24
Total	**99.91**	**99.96**	**99.72**	**99.91**
LOI	2.85	2.93	2.41	2.18
FeO	7.18	8.19	7.96	5.99
Fe_2O_3	4.63	5.26	5.79	9.31
Mg no.	61.49	59.86	58.10	62.33
Fe2+/Fe* (mol. Fraction)	0.78	0.78	0.75	0.59
XRF Trace Elements:				
Rb	11	2.8	2.7	4.6
Sr	197	185	197	193
Y	36.5	32.2	32	35.3
Zr	149	132	145	159
V	363	395	450	408
Ni	115	91	80	78
Cr	255	95	62	59
Nb	10	6.9	7.3	8.5
Ga	20.3	19.8	20.4	20.4
Cu	24	205	195	241
Zn	102	103	116	120
Co	43	54	60	55
Ba	105	43	57	54
La	15	9	9	8
Ce	21	18	15	14
U	0.8	<0.5	<0.5	<0.5
Th	2.4	0.5	1	1.7
Sc	33	34	38	36
Pb	<1	<1	<1	<1
ICPMS Trace Elements:				
Li	6.6	5.3	4.3	6.7
Sc	35	37	34	37
V	367	374	400	426
Cr	268	109	59	73
Co	39	50	50	51
Ni	110	95	80	79

Cu	257	187	190	283
Zn	98	106	109	129
Ga	21	22	23	24
Ge	1.4	1.6	1.5	1.8
Rb	10.5	3.0	3.5	6.2
Sr	199	198	213	214
Y	30.7	28.1	30.5	33.1
Zr	137	127	128	155
Nb	10	9	9	10
Mo	0.5	0.4	0.4	0.5
Cs	0.1	0.0	0.0	0.1
Ba	106	54	60	57
La	13	9	9	10
Ce	30	23	24	26
Pr	4.35	3.37	3.48	3.94
Nd	20.2	17.0	17.1	19.9
Sm	5.29	4.84	5.08	5.68
Eu	1.76	1.63	1.74	1.96
Gd	5.87	5.31	5.64	6.25
Tb	0.91	0.86	0.89	1.00
Dy	5.82	5.40	5.79	6.47
Ho	1.21	1.13	1.19	1.31
Er	3.09	2.84	3.01	3.30
Tm	0.43	0.38	0.40	0.45
Yb	2.65	2.36	2.50	2.79
Lu	0.39	0.34	0.37	0.39
Hf	3.44	3.06	3.24	3.67
Ta	0.79	0.72	0.73	0.81
W	0.14	0.11	0.11	0.14
Pb	2.15	1.06	1.07	1.20
Th	1.72	0.93	0.98	1.03
U	0.33	0.22	0.24	0.26

Sample:	**DC14-102**	**DC14-103**	**DC14-108**	**DC14-109**
Locality:	Mahabaleshwar	Mahabaleshwar	Mahabaleshwar	Mahabaleshwar
SiO_2	48.3	47.3	49.0	48.3
TiO_2	3.63	2.86	3.57	4.29
Al_2O_3	12.6	14.6	12.4	12.0
Fe_2O_3T	16.0	15.6	16.8	17.2
MnO	0.22	0.2	0.27	0.26
MgO	5.51	5.62	5.35	4.9
CaO	10.2	10.69	9.18	9.19
Na_2O	2.5	2.51	2.54	2.57
K_2O	0.25	0.28	0.4	0.51
P_2O_5	0.36	0.25	0.33	0.44
Total	**99.68**	**99.85**	**99.9**	**99.61**
LOI	1.68	2.55	2.79	2.03
FeO	9.26	6.34	10.35	10.37
Fe_2O_3	5.75	8.55	5.33	5.66
Mg no.	51.48	61.25	47.96	45.72
Fe2+/Fe* (mol. Fraction)	0.78	0.62	0.81	0.80
XRF Trace Elements:				
Rb	2.8	2.1	6.8	8.5
Sr	198	218	200	233
Y	43.8	37.6	40.7	35.1
Zr	251	173	221	274
V	509	431	465	451
Ni	77	84	69	60
Cr	93	105	105	73
Nb	16.9	11.3	17.2	32.7
Ga	22.2	22.1	21.4	23.3
Cu	463	259	260	318
Zn	142	120	140	172
Co	52	52	56	62
Ba	79	68	95	145
La	7	10	9	2
Ce	9	17	12	3
U	1.6	<0.5	<0.5	1.4
Th	2.2	<0.5	5.8	3.7
Sc	35	34	36	35
Pb	<1	<1	<1	<1
ICPMS Trace Elements:				
Li	6.2	6.3	7.3	6.8
Sc	33	34	40	33
V	484	421	456	419
Cr	112	113	77	38
Co	43	46	49	51
Ni	78	83	70	63

Cu	369	316	299	294
Zn	126	123	150	163
Ga	26	25	24	27
Ge	1.7	1.6	1.7	1.8
Rb	4.5	2.6	7.9	12.7
Sr	209	226	195	258
Y	45.8	34.8	39.5	44.2
Zr	233	164	198	253
Nb	15	11	16	28
Mo	0.8	0.6	0.8	1.0
Cs	0.0	0.0	0.1	0.1
Ba	80	64	98	166
La	15	11	14	24
Ce	40	29	37	57
Pr	5.86	4.26	5.32	7.78
Nd	29.2	21.0	25.9	35.8
Sm	8.36	6.04	7.15	9.05
Eu	2.66	2.03	2.27	2.69
Gd	9.00	6.62	7.81	9.26
Tb	1.39	1.05	1.23	1.41
Dy	8.88	6.79	7.76	8.64
Ho	1.85	1.38	1.59	1.74
Er	4.63	3.57	4.05	4.46
Tm	0.61	0.48	0.56	0.59
Yb	3.86	2.98	3.43	3.66
Lu	0.55	0.41	0.49	0.53
Hf	5.61	3.91	4.89	5.96
Ta	1.24	0.90	1.27	2.15
W	0.19	0.19	0.20	0.33
Pb	1.69	1.33	1.51	2.34
Th	1.61	1.16	1.53	2.56
U	0.39	0.28	0.37	0.58

Sample:	**DC14-110**	**DC14-111**	**DC14-112**
Locality:	Mahabaleshwar	Mahabaleshwar	Mahabaleshwar
SiO_2	49.7	49.3	48.2
TiO_2	2.00	3.32	3.34
Al_2O_3	14.8	12.3	12.4
Fe_2O_3T	14.0	16.8	17.8
MnO	0.19	0.23	0.22
MgO	5.72	5.05	4.87
CaO	10.6	9.35	9.58
Na_2O	2.41	2.54	2.59
K_2O	0.56	0.55	0.44
P_2O_5	0.22	0.34	0.35
Total	**100.13**	**99.76**	**99.86**
LOI	5.8	1.78	2.55
FeO	4.77	11.74	9.56
Fe_2O_3	8.67	3.71	7.20
Mg no.	68.13	43.40	47.60
Fe2+/Fe* (mol. Fraction)	0.55	0.88	0.75
XRF Trace Elements:			
Rb	7.6	11.3	19.1
Sr	285	227	220
Y	27.5	36.2	38
Zr	149	233	223
V	306	415	427
Ni	147	49	54
Cr	245	94	104
Nb	14.1	22.8	21.9
Ga	19.7	21.3	20.3
Cu	186	377	370
Zn	106	146	140
Co	52	54	54
Ba	186	174	130
La	15	16	15
Ce	24	14	20
U	<0.5	1.8	<0.5
Th	1.7	5.8	8.2
Sc	24	35	34
Pb	<1	<1	2
ICPMS Trace Elements:			
Li	6.0	6.7	6.1
Sc	29	34	37
V	298	393	406
Cr	239	72	73
Co	45	47	45
Ni	133	54	50

Cu	175	290	326
Zn	98	136	148
Ga	20	25	23
Ge	1.5	1.8	1.9
Rb	10.4	14.6	23.1
Sr	278	243	212
Y	24.9	41.1	36.8
Zr	140	221	200
Nb	14	21	19
Mo	0.7	0.9	1.0
Cs	0.1	0.2	0.5
Ba	184	181	147
La	17	22	20
Ce	37	50	47
Pr	4.82	6.79	6.23
Nd	21.0	31.0	28.4
Sm	4.95	7.99	7.13
Eu	1.63	2.46	2.21
Gd	5.17	8.39	7.60
Tb	0.75	1.25	1.14
Dy	4.70	7.79	7.21
Ho	0.96	1.63	1.48
Er	2.52	4.16	3.76
Tm	0.34	0.57	0.52
Yb	2.19	3.49	3.24
Lu	0.32	0.51	0.46
Hf	3.23	5.26	4.81
Ta	1.11	1.65	1.51
W	0.22	0.28	0.31
Pb	3.23	3.06	3.06
Th	2.09	2.66	2.47
U	0.37	0.63	0.56

Sample:	**DC14-113**	***Rep.***	**MMF7**
Locality:	Mahabaleshwar		IIT Bombay
SiO_2	49.5		50.2
TiO_2	3.16		1.35
Al_2O_3	13.5		8.9
Fe_2O_3T	15.1		11.9
MnO	0.22		0.19
MgO	5.09		12.51
CaO	9.59		12.72
Na_2O	2.78		1.46
K_2O	0.44		0.34
P_2O_5	0.36		0.13
Total	**99.81**		**99.7**
LOI	2.06		2.89
FeO	10.02		8.03
Fe_2O_3	3.97		2.97
Mg no.	47.53		73.53
Fe2+/Fe* (mol. Fraction)	0.85		0.86
XRF Trace Elements:			
Rb	13.4		5.2
Sr	221		163
Y	38.8		26
Zr	225		94
V	354		349
Ni	67		217
Cr	133		942
Nb	21.2		4.8
Ga	21.3		13.7
Cu	369		81
Zn	139		77
Co	49		65
Ba	152		104
La	10		13
Ce	15		22
U	<0.5		<0.5
Th	7.4		<0.5
Sc	32		38
Pb	5		<1
ICPMS Trace Elements:			
Li	9.3	9.6	8.7
Sc	35	36	42
V	399	411	333
Cr	115	119	1649
Co	42	43	56

Ni	62	64	202
Cu	299	310	68
Zn	138	144	73
Ga	23	24	14
Ge	1.7	1.7	1.4
Rb	14.5	15.2	7.8
Sr	213	224	183
Y	37.5	39.2	18.2
Zr	202	213	86
Nb	18	19	6
Mo	1.0	1.0	0.4
Cs	0.2	0.2	0.2
Ba	154	174	102
La	18	19	10
Ce	44	45	24
Pr	5.90	6.23	3.31
Nd	27.1	28.3	15.2
Sm	6.96	7.26	3.82
Eu	2.19	2.28	1.23
Gd	7.47	7.82	3.94
Tb	1.15	1.20	0.57
Dy	7.25	7.46	3.54
Ho	1.49	1.56	0.74
Er	3.83	4.00	1.82
Tm	0.53	0.55	0.25
Yb	3.32	3.49	1.53
Lu	0.48	0.49	0.22
Hf	4.88	5.12	2.18
Ta	1.47	1.53	0.49
W	0.28	0.30	0.14
Pb	2.79	2.84	2.23
Th	2.34	2.45	1.07
U	0.53	0.56	0.21

Table A5.2: Sr-Nd isotopic data for Deccan Traps lavas.

	$^{87}Sr/^{86}Sr$	2σ	$^{87}Sr/^{86}Sr(T)$	$^{143}Nd/^{144}Nd$	2σ	$^{143}Nd/^{144}Nd(T)$	εNd(T)
DC14-01F	0.704269	0.000003	0.704205	0.512825	0.000021	0.512721	1.6
DC14-02	0.703863	0.000002	0.703834	0.512839	0.000005	0.512733	1.9
DC14-05	0.704360	0.000002	0.704278	0.512633	0.000002	0.512538	-1.9
DC14-17	0.710338	0.000009	0.710329	0.512162	0.000013	0.512035	-11.8
DC14-20	0.707357	0.000003	0.707304				
DC14-21	0.708363	0.000003	0.708271	0.512561	0.000002	0.512438	-3.9
Rep.	0.708351	0.000003	0.708260				
DC14-28	0.711973	0.000002	0.711954	0.511987	0.000009	0.511866	-15.1
Rep.	0.711936	0.000002	0.711918				
DC14-40A	0.706151	0.000009	0.706050	0.512628	0.000004	0.512544	-1.8
DC14-41	0.707453	0.000012	0.707332	0.512591	0.000003	0.512490	-2.9
DC14-47A	0.705393	0.000003	0.705340	0.512520	0.000005	0.512417	-4.3
DC14-47B	0.705721	0.000003	0.705680	0.512624	0.000039	0.512518	-2.3
DC14-59	0.709898	0.000023	0.709875	0.511873	0.000010	0.511753	-17.3
DC14-71	0.706906	0.000039	0.706899	0.512580	0.000003	0.512442	-3.8
DC14-72	0.709262	0.000024	0.709212	0.512311	0.000009	0.512191	-8.7
DC14-79	0.704883	0.000010	0.704854	0.511806	0.000007	0.511701	-18.3
DC14-80	0.704376	0.000004	0.704345	0.512713	0.000003	0.512638	0.0
DC14-83B	0.704599	0.000004	0.704574	0.512554	0.000003	0.512485	-3.0
DC14-84A	0.707464	0.000067	0.707455	0.512337	0.000009	0.512215	-8.2
DC14-85	0.707176	0.000075	0.707163	0.512305	0.000010	0.512186	-8.8
DC14-110	0.705644	0.000003	0.705614	0.512385	0.000005	0.512267	-7.2

Table A5.3: Highly siderophile element and Os-isotopic data for Deccan Traps lavas.

Sample:	**Os (ppb)**	**Ir (ppb)**	**Ru (ppb)**	**Pt (ppb)**	**Pd (ppb)**	**Re (ppb)**	**$^{187}Re/^{188}Os$**		**$^{187}Os/^{188}Os$**	**2σ**	**γOs**
DC14-01F			0.103	0.198	0.365	0.358					
DC14-02	0.294	0.122	0.415	0.945	0.979	0.064	1.04	0.05	0.13271	0.00014	3.5
DC14-05	0.673	0.536	1.886	1.254	0.900	0.147	1.05	0.05	0.12356	0.00007	-3.7
DC14-05 ol	0.31	0.06	0.38	0.41	1.53	0.02	0.3	0.01	0.12675	0.00014	-0.5
DC14-05 ol MAP	0.38	0.01	0.55	0.42	1.42	0.32	4.1	0.20	0.12805	0.00030	-2.8
DC14-09	0.571	0.381	0.589	6.958	4.154	0.529	4.47	0.22	0.13402	0.00009	1.6
DC14-09	0.777	0.469	0.709	9.211	6.766				0.13488	0.00015	6.1
DC14-10A	0.639	0.375	0.674	6.558	4.180	0.566	4.27	0.21	0.13511	0.00013	2.6
DC14-10B	0.602	0.437	0.535	7.050	5.209	0.515	4.1	0.21	0.13650	0.00007	3.8
DC14-10B	0.799	0.434	0.624	6.820	3.294	0.850	5.13	0.26	0.13553	0.00007	2.2
DC14-10B	0.654	0.383	0.514	6.952	4.002	0.839	6.19	0.31	0.13811	0.00010	3.4
DC14-10B	0.927	0.548	0.697	9.050	7.163	2.838	14.78	0.74	0.13601	0.00008	-5.6
DC14-10B		0.402	0.518	7.007	3.581	0.705					
DC14-10B cpx	0.60	0.22	0.52	1.43	1.52	0.09	0.7	0.04	0.13910	0.00010	8.8
DC14-15	0.019		0.066	9.907	20.740	0.349	91.43	4.57	0.23546	0.00085	7.3
DC14-15	0.034		0.136	10.746	20.702	0.656	94.85	4.74	0.24480	0.00043	11.7
DC14-15 pl											
DC14-15 pl MAP	0.19	0.08	0.47	11.62	12.74	0.31	7.8	0.39	0.14104	0.00034	4.3
DC14-19	0.318	0.124	0.357	7.381	6.526	0.478	7.24	0.36	0.13559	0.00015	0.5
DC14-20	0.317	0.286	0.873	10.047	11.169	0.184	2.80	0.14	0.13260	0.00010	1.9
DC14-21	0.085	0.044	0.210	7.689	4.361	0.418	23.8	1.19	0.15075	0.00033	-1.7
DC14-28	0.004		0.080	0.101	0.790	0.075	86.7	4.34	0.54107	0.00099	252

Sample:	**Os (ppb)**	**Ir (ppb)**	**Ru (ppb)**	**Pt (ppb)**	**Pd (ppb)**	**Re (ppb)**	**$^{187}Re/^{188}Os$**		**$^{187}Os/^{188}Os$**	**2σ**	**γOs**
DC14-30	0.269	0.303	0.253	10.318	9.517	0.280	5.02	0.25	0.13459	0.00046	1.6
DC14-31A	0.705	0.471	0.875	13.891	21.563	0.228	1.56	0.08	0.12870	0.00008	-0.1
DC14-36	0.158	0.180	0.576	7.691	4.571	0.301	9.20	0.46	0.13938	0.00015	1.8
DC14-38	0.231	0.183	0.662	8.002	4.949	0.263	5.49	0.27	0.13643	0.00014	2.6
DC14-38	0.194	0.219	0.608	7.726	7.122	0.231	5.75	0.29	0.13649	0.00012	2.5
DC14-39	0.004				0.099	0.343	468	23.38	0.46312	0.00535	-134
DC14-39	0.005		0.090		0.309	0.443	511	25.55	0.72922	0.00888	38.2
DC14-46A	0.128	0.098	0.173	1.999	0.662	0.659	24.8	1.24	0.16199	0.00019	6.2
DC14-46A	0.134	0.080	0.145	2.061	0.619	0.767	27.7	1.39	0.16652	0.00018	7.4
DC14-46B	0.118	0.037	0.092	1.919	0.561	0.568	23.3	1.17	0.16558	0.00035	10.4
DC14-46C	0.837	0.065	0.105	1.847	0.683	0.170	1.0	0.05	0.11861	0.00024	-7.5
DC14-47B	0.388	0.056	0.024	1.134	1.533	0.100	1.2	0.06	0.11939	0.00013	-7.2
DC14-47B	0.182	0.084	0.134	1.498	1.142	0.075	2.0	0.10	0.13459	0.00118	4.2
DC14-47B ol	0.35	1.48	5.26	1.83	3.60				0.13082	0.00009	2.9
DC14-47B ol MAP	0.30	0.13	0.28	0.19	0.15	0.24	3.9	0.19	0.14427	0.00013	10.2
DC14-53	0.103	0.106	0.087	5.451	2.453	0.061	2.85	0.14	0.15066	0.00079	16.1
DC14-59	0.008			0.404	0.723	0.782	530	26.52	0.78144	0.00091	62.7
DC14-63	0.004			0.095	0.301	0.382	446	22.29	0.69163	0.00179	64.0
DC14-68	0.021		0.133	4.072	8.096	0.569	135	6.73	0.31762	0.00450	35.2
DC14-68 pl	0.12	0.09	0.81	6.72	1.23				0.14412	0.00036	13.4
DC14-69	0.507	0.444	0.578	7.721	4.492	0.227	2.16	0.11	0.13416	0.00009	3.7
DC14-71	0.220	0.067	0.253	4.796	4.707	0.470	10.3	0.52	0.14046	0.00014	1.7

Sample:	**Os (ppb)**	**Ir (ppb)**	**Ru (ppb)**	**Pt (ppb)**	**Pd (ppb)**	**Re (ppb)**	**$^{187}Re/^{188}Os$**		**$^{187}Os/^{188}Os$**	**2σ**	**γOs**
DC14-72	0.234	0.128	0.157	6.346	3.979	0.333	6.86	0.34	0.13723	0.00008	2.1
DC14-75	0.118		0.011	0.417	0.164	0.331	13.6	0.68	0.13647	0.00120	-4.3
DC14-77	0.530	0.277	0.477	8.717	5.314	0.315	2.9	0.14	0.13324	0.00006	2.4
DC14-77	0.642	0.232	0.521	8.736	2.903	0.389	2.92	0.15	0.13327	0.00007	2.3
DC14-77	0.469	0.284	0.500	9.227	6.318	1.831	18.82	0.94	0.13324	0.00009	-11.2
DC14-78	0.391	0.334	0.635	8.580	5.174	0.243	2.99	0.15	0.13266	0.00006	1.8
DC14-79	0.033	0.021	0.017	2.597	2.711	2.106	341	17.03	1.00326	0.00069	399
DC14-80	0.123	0.138	0.068	1.946	2.136				1.44061	0.00103	1033
DC14-82	1.026	0.839	0.619	9.126	8.331	0.482	2.27	0.11	0.14064	0.00006	8.7
DC14-83B	0.413	0.213	0.330	2.142	3.182	0.451	5.4	0.27	0.34018	0.00095	163
DC14-83B	0.312	0.199	0.260	1.947	2.840	0.451	7.16	0.36	0.35165	0.00173	170
DC14-83B	0.194	0.188	0.266	2.083	2.010	2.020	51.67	2.58	0.37294	0.00066	149
DC14-84A	0.156	0.194	0.152	8.993	8.541	0.573	17.8	0.89	0.16297	0.00014	13.0
DC14-85	0.168	0.312	0.242	9.862	9.022	0.511	14.8	0.74	0.15907	0.00015	12.5
DC14-96	0.896	0.227	0.258	4.283	3.020	0.478	2.57	0.13	0.13217	0.00015	1.8
DC14-96	0.253	0.086	0.257	4.076	4.274	0.602	11.5	0.57	0.14153	0.00018	1.5
DC14-97	0.276	0.045	0.232	5.109	3.714	0.457	7.98	0.40	0.13921	0.00014	2.7
DC14-99	0.015		0.192	4.172	7.171	0.404	133	6.63	0.28458	0.00093	10.8
DC14-103	0.045		0.218	4.289	9.818	0.259	27.9	1.40	0.16370	0.00021	4.9
DC14-108	0.024		0.209	3.352	11.099	0.757	159	7.95	0.32497	0.00042	20.2
DC14-110	0.236	0.148	0.160	5.931	10.415	0.322	7	0.33	0.14659	0.00013	9.7
DC14-111	0.013		0.162	3.322	19.114	0.634	250	12.52	0.50100	0.00090	80.6

Sample:	**Os (ppb)**	**Ir (ppb)**	**Ru (ppb)**	**Pt (ppb)**	**Pd (ppb)**	**Re (ppb)**	**$^{187}Re/^{188}Os$**		**$^{187}Os/^{188}Os$**	**2σ**	**γOs**
DC14-111 pl											
DC14-111 ol								0.28			
MAP	0.22	0.00	0.28	5.56	32.01	0.25	5.5		0.14612	0.00021	10.2
MMF7	0.097			0.047	0.329	0.229	11	0.57	0.17666	0.00127	29.2
MMF7		0.008	0.133	0.125	0.194	0.232					
MMF7 cpx	0.06	1.78		0.06		0.22			0.16317	0.00280	

Table A5.4: Tabulated HSE blank concentrations and percent blank contribution to samples.

Blank ID	**Os (ng)**	**Ir (ng)**	**Ru (ng)**	**Pt (ng)**	**Pd (ng)**	**Re (ng)**	**$^{187}Os/^{188}Os$**
B6-4		0.131	0.081	0.029	0.049	0.054	
B6-8		0.125	0.072	0.024	0.055	0.100	
B8-4		0.090	0.028	0.010	0.065		
B9-4		0.077	0.026	0.012	0.058	0.033	
B9-8		0.088	0.029	0.007	0.038		
B10-4		0.075	0.086	0.011	0.083	0.046	
B12-1		0.097	0.039	0.014	0.094	0.049	
B12-2	0.003	0.092	0.015	0.012	0.063	0.021	
B12-3		0.099	0.018	0.016	0.057	0.020	
B12-4	0.004	0.137	0.014	0.011	0.073	0.021	
B12-5	0.004	0.150	0.020	0.015	0.063	0.022	0.683
B14-4	0.001	0.168	0.040	0.031	0.022	0.025	0.231
B15-4	0.001	0.164	0.382	0.046	0.014	0.035	0.310
B16-4	0.001	0.202	0.037	0.019	0.013	0.015	0.255
B17-4	0.001	0.177	0.052	0.034	0.022	0.022	0.033
B18-4	0.003	0.164	0.525	0.024	0.023	0.018	0.137

*Many Os blanks reflected inefficient spike equilibration and were consequently discarded

Average blank	0.002	0.127	0.092	0.020	0.050	0.034	0.27482
Sample:	**Os (%)**	**Ir (%)**	**Ru (%)**	**Pt (%)**	**Pd (%)**	**Re (%)**	
DC14-01F			55.3	14.7	20.0	5.2	
DC14-02	0.8	28.9	23.5	3.5	8.5	23.6	
DC14-05	0.3	8.5	6.3	2.7	9.2	11.8	
DC14-09	0.3	9.6	15.2	0.4	1.3		
DC14-10A	0.3	11.7	15.9	0.5	2.1	3.4	
DC14-10B	0.4	10.2	19.2	0.5	1.7	3.7	
DC14-10B	0.3	10.3	17.0	0.5	2.7	2.3	
DC14-10B	0.3	11.5	19.8	0.5	2.2	2.3	
DC14-10B	0.2	8.3	15.4	0.4	1.3	0.7	
DC14-10B		11.0	19.7	0.5	2.5	2.7	
DC14-15	10.7		65.9	0.3	0.4	5.3	
DC14-15	6.2		48.3	0.3	0.4	2.9	
DC14-19	0.7	28.6	26.3	0.5	1.4	4.0	
DC14-20	0.7	14.8	12.7	0.3	0.8	9.6	
DC14-21	2.6	52.9	37.8	0.4	2.1	4.5	

DC14-28	33.7		41.6	25.1	9.9	19.9
DC14-30	0.8	14.1	33.4	0.3	1.0	6.6
DC14-31A	0.3	9.5	12.7	0.2	0.4	7.9
DC14-36	1.4	21.6	18.1	0.4	2.0	6.1
DC14-38	1.1	18.4	17.3	0.4	1.3	7.8
DC14-38	1.0	21.3	16.1	0.4	1.8	7.0
DC14-39	33.1		53.7	84.2	18.9	4.3
DC14-39	37.7				48.0	5.4
DC14-46A	1.7	33.6	42.4	1.7	12.1	2.9
DC14-46A	1.6	38.4	46.7	1.6	12.9	2.5
DC14-46B	1.9	57.1	58.0	1.8	14.0	3.3
DC14-46C	0.3	43.4	54.8	1.8	11.8	10.4
DC14-47B	1.2	37.2	48.6	2.2	7.4	20.8
DC14-47B	0.6	47.2	84.4	2.9	5.6	16.4
DC14-47A	7.9	45.1	79.0	2.1	6.3	2.1
DC14-53	2.1	31.9	59.5	0.6	3.6	24.4
DC14-59	22.4			7.8	11.2	2.5
DC14-63	33.5			26.4	23.3	4.9
DC14-68	9.6		48.8	0.8	1.1	3.3
DC14-69	0.4	10.0	18.0	0.4	2.0	8.0
DC14-71	1.0	42.5	33.4	0.7	1.9	4.0
DC14-72	0.9	27.9	44.8	0.5	2.2	5.6
DC14-75	1.9		92.3	7.6	35.9	5.6
DC14-77	0.3	17.6	19.6	0.4	3.1	4.8
DC14-77	0.5	14.9	20.3	0.4	1.4	1.1
DC14-77	0.4	15.1	21.1	0.4	1.7	5.9
DC14-78	0.6	12.9	16.7	0.4	1.7	7.5
DC14-79	6.3	70.6	88.0	1.3	3.3	0.9
DC14-80	1.8	26.4	65.0	1.7	4.1	0.0
DC14-82	0.2	5.6	17.1	0.4	1.1	3.9
DC14-83B	0.5	18.9	27.8	1.6	2.8	4.2
DC14-83B	1.1	20.9	32.4	1.6	4.4	1.0
DC14-83B	0.7	20.0	32.8	1.7	3.1	4.2
DC14-84A	1.4	20.4	45.5	0.4	1.1	3.3
DC14-85	1.3	13.7	34.5	0.3	1.0	3.7
DC14-96	0.2	17.9	33.0	0.8	2.9	3.9
DC14-96	0.9	36.6	33.1	0.8	2.1	3.2
DC14-97	0.8	52.2	35.5	0.7	2.4	4.1
DC14-99	12.9		39.9	0.8	1.3	4.6
DC14-103	4.7		36.8	0.8	0.9	7.0
DC14-108	8.6		37.9	1.0	0.8	2.5
DC14-110	0.9	25.1	44.3	0.6	0.9	5.7

DC14-111	14.8		44.0	1.0	0.5	3.0
MMF7		86.6	48.8	21.5	32.1	7.8
MMF7	2.3			42.3	21.7	7.9

Table A5.5: Unspiked Sr-Nd digestion and column separation procedure.

√	***Digestion***
	Precisely weigh 0.100 grams homogenized rock powders into labeled 15 mL or 20 mL PFTE beakers. Adjust powder mass to achieve a target load of ca. 1 µL Sr and 500 ng Nd, but do not load more than 0.200 grams into a 15 mL beaker or 0.300 mL into a 20 mL beaker.
	Add 1 mL teflon distilled HNO_3 per 0.100 grams rock powder to each beaker.
	Add 4 mL Optima HF per 0.100 grams rock powder to each beaker.
	Place tightly capped beakers on vented hotplate at 150°C. Monitor for reaction between powder and acid; this should produce a yellow-ish, gaseous substance above the liquid in the beaker. Allow to flux for at least 72 hours.
	Carefully uncap beakers and evaporate to incipient dryness on a vented hotplate at a maximum temperature of 100°C. Expect this drydown to take 10-12 hours for 5 mL acid at 100°C.
	Add 2 mL teflon distilled HNO_3 per 0.100 grams rock powder to each beaker.
	Place tightly capped beakers on vented hotplate at 120°C. Allow to flux for at least 24 hours.
	Carefully uncap beakers and evaporate to incipient dryness on a vented hotplate at a maximum temperature of 100°C. Expect this drydown to take 4-6 hours for 2 mL acid at 100°C.
	Add 5 mL teflon distilled HCl per 0.100 grams rock powder to each beaker.
	Place tightly capped beakers on vented hotplate at 120°C. Allow to flux for at least 24 hours.
	Carefully uncap beakers and evaporate to incipient dryness on a vented hotplate at a maximum temperature of 100°C. Expect this drydown to take 10-12 hours for 5 mL acid at 100°C.
	Add 2 mL 4M HCl to each beaker.
	Place tightly capped beakers on vented hotplate at a maximum temperature of 100°C for at least three hours to equilibrate sample with dilute acid.
	If desired, extract a ca. 20 uL aliquot for trace element analysis on the iCAP.

	Preliminary cation exchange column
	Prepare new columns with 1.5 mL AG50W-X8 resin, or take used columns from storage. With proper cleaning procedures, each column can be used about 10 times with no loss in functionality.
	Elute 1 column volume mQ H_2O and discard.
	Elute 1 column volume 4M HF and discard into HF-bearing waste container.

	Elute 1 column volume mQ H_2O and discard.
	Elute 1 column volume 6M HCl and discard into acid waste container.
	Elute 1 column volume mQ H_2O and discard.
	Elute 5 mL 4N HCl and discard into acid waste container.
	Load sample in 2 mL 4M HCl and collect in 7 mL beaker (Hf-Pb cut)
	Elute 2 mL 2.5N HCl-1N HF and collect in same 7 mL beaker (Hf-Pb cut)
	Elute 20 mL 2.5N HCl-1N HF and collect in 20 mL beaker (Sr cut)
	Elute 1 column volume 2N HNO_3 and discard into acid waste container (LILE, including Ba).
	Elute 15 mL 6N HCl and collect in 15 mL beaker (REE cut)
	Elute 1 column volume mQ H_2O and discard.
	Elute 5 mL 4N HCl and discard into acid waste container.
	Fill column with 4N HCl so that liquid level in the column is higher than liquid level in the storage container, and return used column to storage. If the column has been used >10 times, discard the column.
	Place uncapped Hf-Pb, Sr and REE beakers on a vented hotplate and evaporate to incipient dryness at a maximum temperature of 100°C.
	Take up Sr cut in 1 mL 4N HNO_3 and allow to equilibrate for at least three hours at a maximum temperature of 70°C.
	Leave REE cut at incipient dryness for now; do not take up in any liquid.

	Sr column
	Prepare new columns with ca. 200 mg Sr-spec resin in a 1 mL pipette tip (ask for direction), or take used columns from storage. With proper cleaning procedures, each column can be reused with no loss in functionality.
	Elute 1 column volume mQ H_2O and discard.
	Elute 1 column volume 4N HNO_3 and discard.
	Elute 1 column volume mQ H_2O and discard.
	Elute 1 column volume 4N HNO_3 and discard.
	Elute 1 column volume mQ H_2O and discard.
	Elute 1 column volume 4N HNO_3 and discard.

	Load sample in 1 mL 4N HNO_3 and collect onto dry REE cut.
	Elute a further 1 mL 4N HNO_3 and collect into REE cut. Evaporate replenished REE cut to incipient dryness at a maximum temperature of 100°C. Expect this drydown to take 2-4 hours. Then, take up REE cut in 1 mL 0.25N HCl and allow to equilibrate for at least three hours at a maximum temperature of 70°C.
	Elute 1 mL 4N HNO_3 and collect into Sr beaker. Repeat 5 further times for a cumulative collection of 6 mL 4N HNO_3 into the Sr beaker.
	Elute 1 mL 0.05N HNO_3 and collect into Sr beaker. Repeat 2 further times for a cumulative collection of 3 mL 0.05N HNO_3 into the Sr beaker. Place uncapped Sr beaker on vented hotplate at a maximum of 100°C and evaporate to incipient dryness. It is now ready for analysis on the Triton.
	Elute 1 mL 0.05N HNO_3 and discard. Repeat 2 further times for a cumulative 3 mL of discarded 0.05N HNO_3.
	Elute 1 column volume mQ H_2O and discard.
	Elute 1 column volume 4N HNO_3 and discard.
	Fill column with 4N HNO_3 so that liquid level in the column is higher than liquid level in the storage container, and return used column to storage in 4N HNO_3.

Nd column

	Prepare new columns with ca. 200 mg LN-spec resin in a 1 mL pipette tip (ask for direction), or take used columns from storage. With proper cleaning procedures, each column can be reused with no loss in functionality.
	Elute 1 column volume mQ H_2O and discard.
	Elute 1 column volume 4N HNO_3 and discard.
	Elute 1 column volume mQ H_2O and discard.
	Elute 1 column volume 6N HCl and discard.
	Elute 1 column volume mQ H_2O and discard.
	Elute 1 column volume 0.25N HCl and discard.
	Load sample in 1 mL 0.25N HCl and discard.
	Elute 1 mL 0.25N HCl and collect into Nd beaker. Repeat 2 further times for a cumulative collection of 3 mL 0.25N HCl into the Nd beaker. Place uncapped Nd beaker on vented hotplate at a maximum of 100°C and evaporate to incipient dryness.
	Elute 1 mL 0.25N HCl and discard. Repeat 2 further times for a cumulative 3 mL of discarded 0.25N HCl (Sm).

	Elute 1 mL 0.75N HCl and discard. Repeat 3 further times for a cumulative 4 mL of discarded 0.75N HCl (HREE).
	Elute 1 column volume mQ H_2O and discard.
	Elute 1 column volume 0.25N HCl and discard.
	Fill column with 0.25N HCl so that liquid level in the column is higher than liquid level in the storage container, and return used column to storage in 0.25N HCl.

Table A5.6: Modeling parameters for **Figure 5.2** and **Figure 5.12**.

	$^{87}Sr/^{86}Sr$	[Sr]	$^{143}Nd/^{144}Nd$	[Nd]	$^{187}Os/^{188}Os$	[Os]	References
Réunion	0.704189[1]	57.24	0.512902[1]	35-100[2]	0.1324	1.01	Albarede et al. (1997 J. Pet.); Bosch (2008 EPSL); DiMuro et al. (2014 J. Pet)
Upper Continental Crust	0.72715	284	0.510556	4.6			Ray et al. (2008 Gondwana); Peucat et al. (1989 J. Geology)
Lower Continental Crust	0.70264	989	0.5106	13.7	0.83335	0.001-0.004	Asmerom & Walker (1998 Geology); Peucat et al. (1989 J. Geology; 2013 Precam. Res.)
Sub-continental Lithospheric Mantle	0.70255	325[3]	0.512777	1.25[3]	0.11[4]	5	Aulbach et al. (2016 RIMG); McBride et al. (1996 Geology)
Depleted MORB Mantle			0.51321	8	0.125	10	Roy-Barman et al. (1998 EPSL); Standish et al. (2002 G-Cubed)

Notes:

1. Elemental concentrations projected from MgO versus element plots assembled from listed references; isotopic ratios projected from element versus isotope ratio plots assembled from listed references
2. Nd noted in the text and represented here is not meant to imply that the Reunion source itself contains variable [Nd]; rather, the upper end of Nd concentration is used in modeling to illustrate the effect of enrichment that precedes or is syncronous with assimilation processes
3. Estimated concentrations to match appropriate R values as discussed in the literature
4. Representing Archean-aged SCLM